

Physico-Chemical Development of Oxide-Based Ceramics for Thermoelectric Energy Harvesting

VON DER NATURWISSENSCHAFTLICHEN FAKULTÄT
DER GOTTFRIED WILHELM LEIBNIZ UNIVERSITÄT HANNOVER

ZUR ERLANGUNG DES GRADES

**Doktor der Naturwissenschaften
(Dr. rer. nat.)**

genehmigte Dissertation

von

Richard Hinterding, M. Sc.

[2021]

Referent: apl. Prof. Dr. rer. nat. habil. Armin Feldhoff

1. Korreferent: Prof. Dr. rer. nat. Oliver Oeckler

2. Korreferent: Prof. Dr. rer. nat. Georg Garnweitner

Tag der Promotion: 10.12.2021

Preface

The last four years have been an unique journey I am glad to have experienced. This thesis represents the distillate of this challenging but fruitful time within the working group of Prof. Dr. Armin Feldhoff. As a research associate, the majority of my work was conducted at the Institute of Physical Chemistry and Electrochemistry of the Gottfried Wilhelm Leibniz University Hannover. In total, I have been involved in eleven peer-reviewed publications and fourteen conference talks or posters of prestigious chemical associations. Seven of these publications are presented within this thesis and I am the first and corresponding author of five of them. In the following, my contributions to the included publications are clarified.

Chapter 1 presents two reviews on the theoretical aspects of this thesis. The first review "*High power factor vs high zT - A review of thermoelectric materials for high-temperature application*" is about comparing various thermoelectric material classes and their applicability at high temperature. Work on this manuscript included literature research, neat visualization of data and concise writing. These three major tasks were carried out by me and M. Sc. Mario Wolf in close collaboration. The initial concept was pitched by Prof. Dr. Armin Feldhoff and elaborated by all three authors. The second review "*Two dimensional oxides: Recent progress in nanosheets*" deals with the synthesis of nanodimensional sheets and their advantages in applications. Similar to the first review, literature research, visualization of data and comprehensive writing was required for the manuscript. In this case, I was responsible for most of the chapters, while Prof. Dr. Armin Feldhoff wrote some parts as well and helped with the scope and revision of the manuscript.

Chapter 2 contains a total of five original research articles. The first article "*Anisotropic growth of $\text{La}_2\text{NiO}_{4+\delta}$: Influential pre-treatment in molten-flux synthesis*" deals with the crystal growth of La_2NiO_4 in the form of microdimensional sheets, which were later used for thermoelectric composites. The manuscript was mainly based on the master thesis of M. Sc. Zhijun Zhao, which I supervised. I was responsible for the concept of the manuscript while M. Sc. Zhijun Zhao executed the syntheses and some of the analyses. Transmission electron microscopy investigation was accomplished by me and the electron probe micro-analysis by Dr. Chao Zhang. In close collaboration with M. Sc. Zhijun Zhao, I developed the original draft of the manuscript, which was revised by Prof. Dr. Armin Feldhoff.

The second article "*Ceramic composites based on $\text{Ca}_3\text{Co}_{4-x}\text{O}_{9+\delta}$ and $\text{La}_2\text{NiO}_{4+\delta}$ with enhanced properties*" is a follow-up to the aforementioned article, focusing on thermoelectric composites. Idea and original draft were composed by myself. M. Sc. Zhijun Zhao was responsible for synthesizing the base material La_2NiO_4 via molten flux. Thermoelectric measurements were conducted by myself and M. Sc. Mario Wolf with the exception of thermal conductivity. The latter was measured in cooperation with Prof. Dr. Oliver Oeckler and M. Sc. Matthias Jakob of the Leipzig University. All authors revised the manuscript carefully.

The third research article "*Improved thermoelectric properties in ceramic composites based on $\text{Ca}_3\text{Co}_4\text{O}_9$ and $\text{Na}_2\text{Ca}_2\text{Nb}_4\text{O}_{13}$* " is conceptually similar to the second one, but $\text{Na}_2\text{Ca}_2\text{Nb}_4\text{O}_{13}$ is used as an additive. Again, the idea and original draft were composed by myself. In addition, all syntheses were performed by myself. The analyses were conducted by myself with support of M. Sc. Mario Wolf, except for the measurements of the thermal conductivity. The latter was again measured in collaboration with Prof. Dr. Oliver Oeckler and M. Sc. Matthias Jakob of the Leipzig University. The concept of the manuscript was designed by myself in consultation with M. Sc. Mario Wolf and Prof. Dr. Armin Feldhoff. All authors revised the manuscript thoroughly.

The fourth research article "*Triple-phase ceramic 2D nanocomposite with enhanced thermoelectric properties*" succeeded in cooperation with Dr. Michael Bittner, who was mainly responsible for the achieved results. I contributed experimentally by testing several dopants in the sol-gel synthesis of $\text{Ca}_3\text{Co}_4\text{O}_9$ to find the proper elemental choices and appropriate amounts for the enhanced thermoelectric properties of the heavily doped $\text{Ca}_3\text{Co}_4\text{O}_9\text{-Na}_x\text{CoO}_2\text{-Bi}_2\text{Ca}_2\text{Co}_2\text{O}_9$ triple-phase composite. Additionally, I helped at revising the manuscript.

The fifth research article "*Reaction sintering of $\text{Ca}_3\text{Co}_4\text{O}_9$ with BiCuSeO nanosheets for high-temperature thermoelectric composites*" deals with the reactions of BiCuSeO at high temperature and their effects on thermoelectricity. I was responsible for the idea and original draft as well as the thermoelectric measurements and electron microscopy. Syntheses were performed and developed by B. Sc. Desiree Rieks and myself. M. Sc. Patrick A. Kießling measured the thermogravimetric analyses under the management of Prof. Dr. Nadja C. Bigall and B. Sc. Lukas Steinbach contributed by developing the used sintering process under my supervision. All authors helped at revising the manuscript.

Finally, this thesis was only possible due to the support of several people. First and foremost my deep gratitude goes to Prof. Dr. Armin Feldhoff for the opportunity to perform my research within his working group. His expeditious and proficient feedback, especially in topics related to electron microscopy and thermoelectrics, was essential for the achieved results. Furthermore, I am thankful for the fruitful cooperation with Prof. Dr. Oliver Oeckler and M. Sc. Matthias Jakob of the Leipzig University, which enabled the completion of two manuscripts. In addition, I thank M. Sc. Mario Wolf for various topic-related collaborations, which resulted in several research articles. A special thanks goes to Frank Steinbach for the vital support regarding transmission electron microscopy and particularly the preparation of proper samples. Thanks are due to my co-workers M. Sc. Felix Rieck genannt Best and Dr. Alexander Mundstock for a pleasant working atmosphere. Various students completed a master thesis or research internship under my supervision. Hence, I thank Zhijun Zhao, Vincent Viebranz, Lukas Steinbach and Desiree Rieks for their effort in research, which always yielded new insights and sometimes resulted in new publications. Additionally, I thank Dr. Michael Bittner for his early advice on the measurement of thermoelectric properties and his competent cooperation. Further thanks goes to Kerstin Janze and Yvonne Gabbey for lab organization and office related topics. Finally, I would like to express my whole-hearted gratitude to my wife Saskia Zailskas and my family members for their constant support and encouragement, whether work-related or else.

Abstract

The thermoelectric effect describes the conversion of heat into electrical energy and it is the pivotal element for the utilization of waste heat via Energy Harvesting. Especially high-temperature applications in industrially relevant areas such as basic materials production or transportation hold enormous potential for unused energy. Proper thermoelectric materials for these high-temperature applications are mandatory to ensure high conversion efficiency and high electrical power output. Oxides are auspicious candidates for this task as they exhibit high thermal stability under air and are less toxic than most alternatives. Therefore, it is expedient to investigate the electrical performance and the energy conversion efficiency of these promising high-temperature materials more intensively. The currently best performing oxide material is $\text{Ca}_3\text{Co}_4\text{O}_9$ (CCO), so improving its thermoelectric properties was the main research focus of this thesis.

Novel composite materials based on CCO in combination with other oxides such as La_2NiO_4 (LNO), $\text{Na}_2\text{Ca}_2\text{Nb}_4\text{O}_{13}$ (NCNO), Na_xCoO_2 (NCO) and $\text{Bi}_2\text{Ca}_2\text{Co}_2\text{O}_9$ (BCCO) as well as the oxyselenide BiCuSeO (BCSO) were synthesized and thoroughly investigated regarding synergistic effects. Close attention was given to the microstructure and elemental composition, which were investigated by various methods such as electron microscopy as well as electron or X-ray diffraction. Further analyses regarding the thermoelectric performance were made by measuring the SEEBECK coefficient, the electrical conductivity and the thermal conductivity. All investigated materials exhibit layered crystal structures and hence anisotropic transport properties. Preferred crystal orientations within the composite ceramics were observed due to uniaxial pressing during processing. In case of LNO or NCNO, the orientation was influenced by using large plate-like particles synthesized by molten-flux synthesis. Sintering resulted in advantageous reactions between the mixing partners. Regarding LNO or NCNO, heavily doped perovskite phases $\text{La}(\text{Co},\text{Ni})\text{O}_3$ and $\text{Ca}(\text{Nb},\text{Co})\text{O}_3$ were ascertained with beneficial impact on the thermoelectric properties. Especially the power factor was positively influenced, either by an enhanced electrical conductivity or by a higher SEEBECK coefficient. Approaches in the nanodimension were realized by a triple-phase ceramic including NCO and BCCO as two-dimensional nanostructures within a CCO matrix or by using BCSO nanosheets as a mixing partner. In both cases, the electrical conductivity and the SEEBECK coefficient were increased simultaneously as a result of doping and emerged phases. While the large particles could increase either the average or even the maximum figure-of-merit compared to CCO, the nanodimensional strategy led to a significantly enhanced power factor.

Keywords: Thermoelectricity; Energy Harvesting; Oxides; Composites.

Zusammenfassung

Der thermoelektrische Effekt beschreibt die Umwandlung von Wärme in elektrische Energie und ist das zentrale Element für die Ausnutzung von Verlustwärme durch "Energy Harvesting". Besonders Hochtemperatur-Anwendungen in industriell relevanten Sektoren, wie der Herstellung von Basismaterialien oder des Transportwesens, umfassen große Potentiale von ungenutzter Energie. Um eine hohe Effizienz beim Umwandeln der Energieformen und eine hohe elektrische Leistungsabgabe zu erreichen, sind für diese Hochtemperatur-Anwendungen geeignete thermoelektrische Materialien erforderlich. Oxide sind vielversprechende Kandidaten, da sie eine hohe Temperaturstabilität und eine geringere Toxizität als die meisten Alternativen aufweisen. Es ist daher zielführend, die elektrische Leistungsfähigkeit und die Effizienz der Energieumwandlung dieser vielversprechenden Hochtemperatur-Materialien intensiver zu untersuchen. Momentan stellt $\text{Ca}_3\text{Co}_4\text{O}_9$ (CCO) das leistungsstärkste oxidische Material dar, weshalb die Verbesserung seiner thermoelektrischen Eigenschaften den Hauptaspekt der vorliegenden Dissertation darstellt. Hierzu wurden neuartige Kompositmaterialien basierend auf CCO in Kombination mit anderen Oxiden wie La_2NiO_4 (LNO), $\text{Na}_2\text{Ca}_2\text{Nb}_4\text{O}_{13}$ (NCNO), Na_xCoO_2 (NCO) und $\text{Bi}_2\text{Ca}_2\text{Co}_2\text{O}_9$ (BCCO) oder dem Oxyselenid BiCuSeO (BCSO) hergestellt und ausgiebig hinsichtlich synergistischer Effekte untersucht. Ein besonderes Augenmerk lag auf der Mikrostruktur und der elementaren Zusammensetzung, welche mittels zahlreicher Analysemethoden wie etwa der Elektronenmikroskopie oder der Elektronen- und RÖNTGEN-Beugung untersucht wurden. Weitere Analysen bezüglich des thermoelektrischen Verhaltens erfolgten durch Messung des SEEBECK-Koeffizienten, der elektrischen sowie der thermischen Leitfähigkeit. Alle untersuchten Materialien weisen geschichtete Kristallstrukturen und damit anisotrope Transporteigenschaften auf. Durch das uniaxiale Pressen während der Prozessierung konnten innerhalb der Komposit-Keramiken bevorzugte Kristall-Orientierungen erzeugt werden. Im Falle von LNO und NCNO wurde die Orientierung durch den Einsatz großer plättchenförmiger Partikel, welche durch Schmelzfluss-Synthese gewonnen wurden, beeinflusst. Das Sintern resultierte in vorteilhaften Reaktionen zwischen den jeweilig gemischten Komponenten. Unter Einsatz von LNO oder NCNO konnten die hochdotierten Perowskit-Phasen $\text{La}(\text{Co},\text{Ni})\text{O}_3$ und $\text{Ca}(\text{Nb},\text{Co})\text{O}_3$ mit vorteilhaften Auswirkungen für die thermoelektrischen Eigenschaften identifiziert werden. Insbesondere der Leistungsfaktor wurde positiv beeinflusst, entweder durch eine erhöhte elektrische Leitfähigkeit oder durch einen größeren SEEBECK-Koeffizienten. Eine auf Nanodimensionalität beruhende Strategie wurde durch eine dreiphasige Keramik mit NCO und BCCO als zweidimensionale Nanostrukturen innerhalb einer CCO Matrix oder durch den Einsatz von BCSO als Mischungspartner realisiert. In beiden Fällen konnten mittels Dotierung und neu entstandener Phasen die elektrische Leitfähigkeit und der SEEBECK Koeffizient simultan erhöht werden. Während die großen Partikel den Durchschnittswert oder sogar den Maximalwert der Gütezahl gegenüber CCO erhöhen konnten, führte der nanodimensionale Ansatz zu einer signifikanten Erhöhung des Leistungsfaktors.

Schlüsselwörter: Thermoelektrizität; Energy Harvesting; Oxide; Komposite.

Abbreviations

2D	Two-dimensional
3D	Three-dimensional
BCCO	$\text{Bi}_2\text{Ca}_2\text{Co}_2\text{O}_9$
BCSO	BiCuSeO
CCO	$\text{Ca}_3\text{Co}_4\text{O}_9$
CMO	CaMnO_3
CS	Conventional sintering
CSP	Cold sintering process
DOS	Density of states
DSC	Differential scanning calorimetry
EDXS	Energy dispersive X-ray spectroscopy
HP	Hot pressing
HRTEM	High-resolution transmission electron microscopy
ITO	$\text{In}_2\text{O}_3:\text{Sn}$ - Indium tin oxide
ktoe	Kilo tons of oil equivalent
LFA	Light-flash analysis
LNO	La_2NiO_4
NCNO	$\text{Na}_2\text{Ca}_2\text{Nb}_4\text{O}_{13}$
NCO	Na_xCoO_2
OC	Open circuit
PF	Power factor
SEM	Scanning electron microscopy
SPS	Spark plasma sintering
STEM	Scanning transmission electron microscopy
STO	SrTiO_3

TEG	Thermoelectric generator
TEM	Transmission electron microscopy
XRD	X-ray diffraction

Contents

Preface	i
Abstract	iii
Zusammenfassung	v
Abbreviations	vii
1 Introduction	1
1.1 Principals of Energy Harvesting by thermoelectricity	3
1.1.1 Basic transport equation	3
1.1.2 Fundamental thermoelectric parameters	4
1.1.3 Influencing thermoelectric properties	7
1.1.4 Composites in thermoelectrics	11
1.2 Thermoelectric materials	13
1.2.1 Overview of state-of-the-art materials	13
1.2.2 Oxide-based materials	16
1.2.3 High power factor vs high zT - A review of thermoelectric materials for high-temperature application	20
1.3 Anisotropy in thermoelectric materials	53
1.3.1 Control of morphology by molten-flux synthesis	54
1.3.2 Anisotropic oxides: La_2NiO_4 and $\text{Na}_2\text{Ca}_2\text{Nb}_4\text{O}_{13}$	55
1.3.3 Two-dimensional oxides: Recent progress in nanosheets	56
List of Figures	107
Bibliography	118
2 Thermoelectric oxide composites based on $\text{Ca}_3\text{Co}_4\text{O}_9$	119
2.1 Concept I: Microdimensional approach	121
2.1.1 Summary	121
2.1.2 Anisotropic growth of $\text{La}_2\text{NiO}_{4+\delta}$: Influential pre-treatment in molten-flux synthesis	122
2.1.3 Ceramic composites based on $\text{Ca}_3\text{Co}_{4-x}\text{O}_{9+\delta}$ and $\text{La}_2\text{NiO}_{4+\delta}$ with enhanced properties	138
2.1.4 Improved thermoelectric properties in ceramic composites based on $\text{Ca}_3\text{Co}_4\text{O}_9$ and $\text{Na}_2\text{Ca}_2\text{Nb}_4\text{O}_{13}$	156
2.2 Concept II: Nanodimensional approach	169
2.2.1 Summary	169
2.2.2 Triple-phase ceramic 2D nanocomposite with enhanced thermoelectric properties	170

2.2.3	Reaction sintering of $\text{Ca}_3\text{Co}_4\text{O}_9$ with BiCuSeO nanosheets for high-temperature thermoelectric composites	190
3	Conclusions and Outlook	213
	Curriculum Vitae	I
	Publications and Conferences	III

1. Introduction

Energy supply and demand is a crucial issue given limited resources and the impact of fossil energy supplies on the global climate. The trend of global energy consumption in Fig. 1.1 further exacerbates the situation, showing that demand has increased steadily over the last 50 years [1] with no decline in sight. In addition, electricity as an energy form gained growing importance, since its share has increased from roughly 10% to 20% [1].

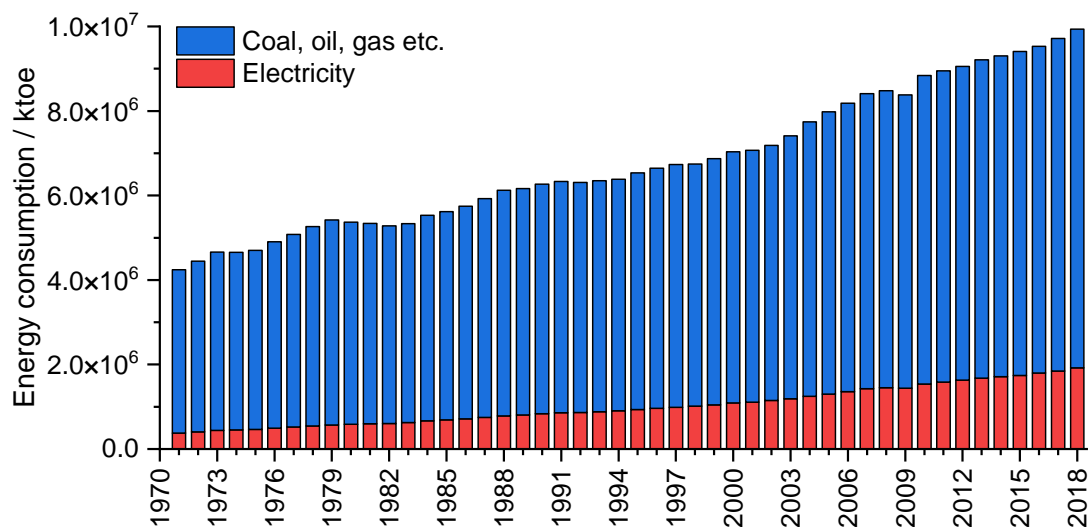


Figure 1.1: Total worldwide energy consumption from 1971 to 2018 in kilo tons of oil equivalent (ktoe). Demand of electricity is displayed separately from other energy sources. Data are extracted from a report of the IEA from 2020 [1].

The usage of energy is always accompanied by some type of energy loss during conversion, based on the second law of thermodynamics. Often this energy is released as heat to the environment. For the conversion of thermal energy into mechanical energy from a heat engine, the maximum efficiency is determined by the CARNOT efficiency and therefore the temperature difference between the hot and cold reservoir. This CARNOT efficiency in combination with unoptimized conversion processes result in an energy loss of approximately 72% for primary resources after conversion [2]. A promising route to utilize wasted energy is *Energy Harvesting*. The term comprises multiple ways of increasing the total efficiency of a process by taking advantage of mechanical energy (vibrations), electromagnetic energy (solar energy, magnetic fields) or thermal energy (heat) [3]. These unused forms of energy can be partially transformed into usable electricity. A requirement and advantage of *Energy Harvesting* systems is long-term stability and their lack of moving parts, which makes them nearly maintenance-free. This is especially useful when power supplies such as batteries can not be replaced easily [4].

The major share of wasted energy is heat, but the possibilities to use it are coupled with factors like continuity, temperature and accessibility. The main part of worldwide waste heat is released by exhausts and effluents as depicted in Fig. 1.2a, followed by energy services such as lighting, heating or cooling [2]. The waste heat of exhausts and effluents holds the greatest potential and accounts for the largest share of the transportation sector. The CARNOT efficiency limit further highlights the aspect of temperature, because higher temperature yields higher potentials regarding efficiency. The different temperature values with regards to the social sectors are given in Fig. 1.2b, where most of the global waste heat is at temperatures below 373 K, but the second largest portion is already above 573 K. This mid-to high temperature region is especially pronounced for the transportation and industrial sector. Therefore, the biggest potential of harvesting waste heat occurs in these sectors and thermoelectricity gets especially relevant.

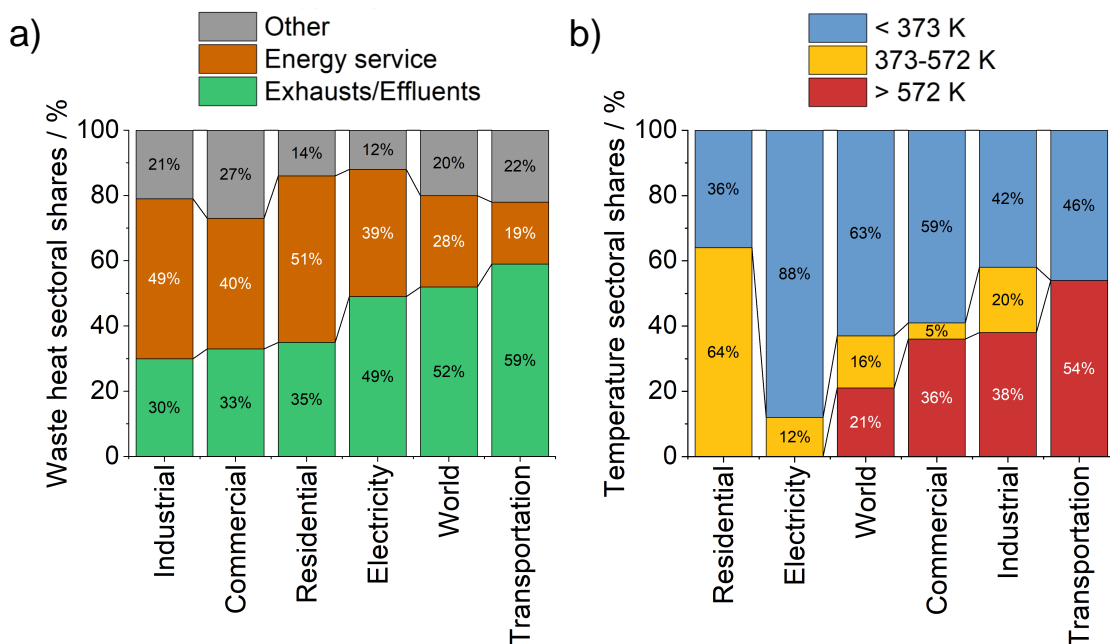


Figure 1.2: Waste heat in the year 2012 assigned to the relevant sectors. a) Shares of exhausts, effluents, energy service and other sources on the worldwide waste heat and specific sectors. Sectors are ordered by their share of exhausts and effluents. b) Waste heat assigned to the sectors and temperature regions. Sectors are ordered by their share in the high-temperature region. Data are extracted from [2].

Thermoelectric energy conversion utilizes the **SEEBECK** effect, which describes the thermal induction of an electrical current [5]. The inversed process is called **PELTIER** effect, where an electrical current is used to transport heat [6]. Despite the attractiveness of thermoelectricity with regards to using waste heat, practical applications in thermoelectric generators (TEGs) are rather scarce until now. Mainly niches like space travel already regularly use thermoelectrics in radioisotope generators to generate electricity for inaccessible devices [7]. One reason for the limited applicability is the cost-benefit ratio, which has so far not been in favor of thermoelectrics because of low electrical power output, availability and efficiency of TEGs. Hence, further research is mandatory to improve the performance of the thermoelectric materials. Within this thesis, oxide-based composite systems are investigated with respect to the improvement of thermoelectric properties.

1.1 Principals of Energy Harvesting by thermoelectricity

1.1.1 Basic transport equation

To understand the concept of energy conversion driven by thermoelectricity, the basic transport equation is indispensable (see Equation 1.1) [8–10]. As only its implications for thermoelectricity in general are discussed within this work, the reader is referred to more in-depth portrayals in publications from Feldhoff [10], Fuchs [11, 12] and Goupil [13]. The transport equation describes the local coupling of the electrical flux density \vec{j}_q and the entropy flux density \vec{j}_S , which results in the thermoelectric effect. On the one hand, the electrical flux density is based on the transport of electrical charge q and corresponds to the electrical potential φ . On the other hand, the entropy flux density is based on the transport of entropy S and corresponds to the thermodynamic potential expressed by the absolute temperature T . The coupling of both entities is represented in Equation 1.1 [10].

$$\begin{pmatrix} \vec{j}_q \\ \vec{j}_S \end{pmatrix} = \begin{pmatrix} \sigma & \sigma \cdot \alpha \\ \sigma \cdot \alpha & \sigma \cdot \alpha^2 + \Lambda_{\text{OC}} \end{pmatrix} \cdot \begin{pmatrix} -\vec{\nabla}\varphi \\ -\vec{\nabla}T \end{pmatrix} \quad (1.1)$$

For a practical approach, the potential gradients within the thermoelectric material can be approximated as potential differences along the length L , which changes the algebraic sign from minus to plus. Furthermore, adding a cross-sectional area A of the material allows the integration of the local flux densities to currents of electrical charge I_q and entropy I_S . As a result, the integrated form of the transport equation follows (see Equation 1.2) [14].

$$\begin{pmatrix} I_q \\ I_S \end{pmatrix} = \frac{A}{L} \begin{pmatrix} \sigma & \sigma \cdot \alpha \\ \sigma \cdot \alpha & \sigma \cdot \alpha^2 + \Lambda_{\text{OC}} \end{pmatrix} \cdot \begin{pmatrix} \Delta\varphi \\ \Delta T \end{pmatrix} \quad (1.2)$$

Special attention should be paid to the thermoelectric material tensor, which includes σ as the isothermal electrical conductivity, α as the SEEBECK coefficient and Λ_{OC} as the open-circuited entropy conductivity. All three parameters are fundamental for thermoelectrics and implicitly temperature-dependent. Historically, the term heat conductivity λ is established, although entropy conductivity can be viewed as a more fundamental term [14]. Within this thesis, the generic term thermal conductivity is used to comprise both, the heat conductivity and the entropy conductivity. A dimensionless figure-of-merit can be derived from the material tensor, which gives information about the energy conversion efficiency of a thermoelectric material. This figure-of-merit in Equation 1.3 is commonly called zT [14, 15] or f [14, 16] and was firstly introduced 1957 by Ioffe [15].

$$f = \frac{\sigma \cdot \alpha^2}{\Lambda_{\text{OC}}} = \frac{\sigma \cdot \alpha^2}{\lambda_{\text{OC}}} \cdot T := zT \quad (1.3)$$

As high energy conversion efficiencies are desired, the numerator of Equation 1.3 needs to be as high and the denominator as low as possible. Considering the importance of this equation, the numerator can be further condensed as the so-called power factor $PF = \sigma \cdot \alpha^2$. All three basic parameters σ , α and Λ_{OC} are decisive for the power factor and the figure-of-merit, wherefore they are explained in more detail in the following.

1.1.2 Fundamental thermoelectric parameters

The basic thermoelectric parameters are the isothermal electrical conductivity σ , the SEEBECK coefficient α and the open-circuited entropy conductivity Λ_{OC} as introduced in Chapter 1.1.1. In the following, their mathematical and experimental origins are discussed in more detail.

Isothermal electrical conductivity

The electrical conductivity within solid state is based on the transport of electrical charges, which can either be electrons or electron holes. First theories of the classical free electron gas model appeared around 1900 and were developed by P. DRUDE [17–19]. Although the assumption that electrons in solid state follow the MAXWELL-BOLTZMANN distribution with respect to their velocity turned out to be inaccurate, the model still provides valid relations for OHM’s-law and describes electrical conductivity vividly [20]. A. SOMMERFELD later expanded the model in terms of quantum mechanics, which led to the DRUDE-SOMMERFELD model [20]. In the classical kinetic approach, the isothermal electrical conductivity follows OHM’s-law and is directly proportional to the electrical flux density \vec{j}_q in a constant electrical field \vec{E} [20, 21]. P. DRUDE assumed the charge carriers with the elemental charge e to be accelerated by the electrical field and slowed down by collisions with the atom cores. Nowadays it is evident, that in a perfect crystal at 0 K theoretically no collisions occur [20]. In a real crystal collisions are possible with phonons, defects, impurities or at the crystal surface [20]. The DRUDE-SOMMERFELD-model corrects this assumption by complying with PAULI’s exclusion principle and the SCHRÖDINGER equation, wherefore only charge carriers within the energy range $k_{\text{B}}T$ around the FERMI energy participate at scattering processes. In the ground state at 0 K, the FERMI energy is the highest energy a particle can possess. The influence of the electrical field on the velocity of the charge carriers is given by the drift velocity \vec{v} . Further assuming a defined charge carrier concentration n , leads to the Equation 1.4 in a steady state [20, 21]. Note that for both, positively charged electron holes and negatively charged electrons, the absolute elemental charge is used [22]. In addition, the transport equation (Equation 1.1) gives the same relation for the special case of isothermal conditions [10].

$$\vec{j}_q = \sigma \vec{E} = |e|n\vec{v} = -\sigma \vec{\nabla}\varphi \quad (1.4)$$

The charge carrier mobility μ is introduced in Equation 1.5 and gives the drift velocity \vec{v} per electrical field strength. It includes the mean time between two scattering processes of the charge carriers τ and the charge carrier mass m [20].

$$\mu = \frac{|e|\tau}{m} \quad (1.5)$$

Therefore, the electrical conductivity is dependent on the charge carrier concentration and the charge carrier mobility [20].

$$\sigma = \frac{ne^2\tau}{m} = |e|n\mu \quad (1.6)$$

The temperature dependency of the electrical conductivity is given by the charge carrier mobility or more precisely by the time dependence of scattering processes. With increasing temperature, the mobility is usually less influenced by scattering

processes of the charge carriers with defects or impurities as scattering with phonons becomes more relevant [20]. Practically, the electrical conductivity can be determined by measuring the voltage $\Delta\varphi$ and the electrical current I_q across the sample [23]. Additionally, the geometry of the sample has to be considered as in Equation 1.7. To neglect internal resistances of the measurement device and contact resistances with the sample, a four-probe method can be used. The resulting unit with relevant dimensions for thermoelectrics is S cm^{-1} .

$$\sigma = \frac{I_q}{\Delta\varphi} \cdot \frac{L}{A} \quad (1.7)$$

Seebeck coefficient

The **SEEBECK** coefficient α , sometimes referred to as thermopower, is defined as the entropy flow of a particle S^* per unit charge q as in Equation 1.8 [10]. Since it can be positive or negative, it describes both the magnitude and direction of the entropy flow [10].

$$\alpha = \frac{S^*}{q} \quad (1.8)$$

Under isothermal conditions, the **SEEBECK** coefficient correlates with the entropy flux density j_S transported in presence of an electrical current [10]. Practically relevant are situations where a temperature gradient within the material occurs, resulting in a hot and cold side. Under electrical open-circuited conditions, the charge carriers at the cold side can accumulate and lead to a gradient of the electrical potential. Important physical values influencing the **SEEBECK** coefficient are the charge carrier concentration, the electronic density of states (DOS) and the effective mass m^* . According to Equation 1.9, which is valid for degenerate semiconductors with parabolic band dispersion, the **SEEBECK** coefficient is proportional to the effective mass and antiproportional to the carrier concentration [24].

$$\alpha_{\text{deg}} = \frac{8\pi^2 k_B^2}{3eh^2} m^* T \left(\frac{\pi}{3n} \right)^{2/3} \quad (1.9)$$

Further constants appearing in the equation are the **BOLTZMANN** constant k_B and the **PLANCK** constant h . For non-degenerate semiconductors, the **SEEBECK** coefficient can be calculated based on **BOLTZMANN** statistics [25]. Under the simplifying assumption of same DOS, charge carrier mobility and transport coefficient A for both types of charge carriers, the Equation 1.10 follows for n -type ("−") and p -type ("+") materials [25, 26].

$$\alpha_{\text{non-deg}} = \pm \frac{k_B}{e} \left(\ln \left(\frac{N}{n} \right) + A \right) \quad (1.10)$$

The variable N represents either the DOS at the conduction band (n -type) or at the valence band (p -type) and includes the effective mass. Hence, a similar trend regarding the effective mass and the carrier concentration follows with $\alpha_{\text{non-deg}} \propto \pm \ln(m^{*3/2} n^{-1})$ [25]. If a semiconductor is classified as degenerate or non-degenerate depends on the electronic band structure and the carrier concentration. High carrier concentrations and an overlap of valence band and conduction band, as in heavily doped semiconductors, lead to a degenerate system, although the boundaries are fluent. A degenerate

semiconductor is characterized by exhibiting characteristics of metals, such as the decrease of electrical conductivity with temperature.

Experimentally, the SEEBECK coefficient can be measured as the fraction of voltage $\Delta\varphi$ and temperature drop ΔT along the thermoelectric material, as long as the electrical flux is suppressed [10, 21]. Hence, the unit of the coefficient is V K^{-1} and the measured dimensions usually $\mu\text{V K}^{-1}$. Despite the sample length not appearing directly in Equation 1.11, it is relevant for the measured temperature difference and voltage.

$$\alpha = -\frac{\Delta\varphi}{\Delta T} \quad (1.11)$$

The SEEBECK coefficient can either be positive for p -type or negative for n -type materials. This is based on the majority of the charge carriers, which can be dominated by electrons (n -type) or electron holes (p -type). Furthermore, the charge carrier concentration is antiproportional to the SEEBECK coefficient in contrast to the electrical conductivity [22]. This exemplifies the major problem in tuning thermoelectric parameters, as they usually interact with each other. Approaches to addressing this problem are discussed in Chapters 1.1.3 and 1.1.4.

Entropy conductivity

Entropy conductivity in terms of thermal conductivity was introduced with the material tensor in Equation 1.1. For the special case of open-circuited conditions, the electrical flux density becomes zero and FOURIER'S law is obeyed, wherefore the entropy flux density j_S is defined by the entropy conductivity and the thermal gradient as in Equation 1.12 [10, 27]. Hence, the entropy conductivity functions as a proportionality constant under these circumstances.

$$\vec{j}_S = -\Lambda_{\text{OC}} \vec{\nabla} T \quad (1.12)$$

The concept of entropy conductivity as a fundamental parameter is relatively new in modern thermoelectrics and traditionally the heat conductivity λ is still often used. Both quantities are linked by the absolute temperature via Equation 1.13 [10, 11, 27]. Naturally, this means an antiproportional temperature dependency of the entropy conductivity as long as the heat conductivity does not increase in equal terms. One advantage of using entropy instead of heat becomes evident in the figure-of-merit from Equation 1.3, because the temperature dependency is incorporated in all three parameters. Furthermore, the power factor and the entropy conductivity share the same unit of $\text{W m}^{-1} \text{K}^{-2}$.

$$\lambda = T \cdot \Lambda \quad (1.13)$$

Another consideration of the entropy conductivity is the approach of separating it in an electronic Λ_{el} and a phonon part Λ_{ph} [15].

$$\Lambda = \Lambda_{\text{el}} + \Lambda_{\text{ph}} \quad (1.14)$$

The electronic part is determined by the WIEDEMANN-FRANZ relation in Equation 1.15, which shows a direct dependence on the electrical conductivity and a constant L [15, 28].

$$\Lambda_{\text{el}} = L\sigma \quad (1.15)$$

The theoretical constant L is denoted as the LORENZ number with a value of $2.45 \cdot 10^{-8} \Omega \text{ W K}^{-2}$ for degenerate electrons as in metallic materials [15,28]. However, according to Ioffe [15] this value is only valid for an electrical conductivity higher than 4000 S cm^{-1} . For values of 2500 S cm^{-1} and less, as it is typically the case for semiconductors, there is again a linear relation between the entropy conductivity and the electrical conductivity, but it shows a lower value of the LORENZ number with $1.48 \cdot 10^{-8} \Omega \text{ W K}^{-2}$ [15]. In addition, the WIEDEMANN-FRANZ relation is only valid for charge carriers with the same sign [15]. If charge carriers with both signs are present within the material, recombinations can set energy free and increase the thermal conductivity [15]. To estimate the LORENZ number fitting to the investigated material, the correlation with the SEEBECK coefficient can be used, as a high coefficient results in a low number [29].

The phonon part includes the thermal vibrations and the transport of entropy via phonons through the crystalline lattice [15,20].

$$\Lambda_{\text{ph}} = \frac{1}{3}Kvl \quad (1.16)$$

Equation 1.16 comprises the sound velocity v , the mean phonon free path length l and entropy capacity K . The latter states the change of entropy with the temperature and fundamentally fulfills the role of a capacity. However, the traditionally used heat capacity at constant volume or pressure can be obtained by multiplying the entropy capacity with the absolute temperature [12]. The mean free path length is influenced by scattering processes of phonons with other phonons, electrons, defects or surfaces [20]. Both, the entropy capacity and the mean free path are temperature-dependent. In the range above the DEBYE temperature of the material, the phonon-phonon scattering is predominant and the heat capacity tends to be constant, which results in a decreasing entropy conductivity [20].

Practically, Equation 1.17 is used to experimentally determine the entropy conductivity of a material [23,30]. The thermal diffusivity coefficient D_{th} with the unit $\text{m}^2 \text{ s}^{-1}$ can be measured by light-flash analysis (LFA), the entropy capacity at constant pressure K_p e.g. by differential scanning calorimetry (DSC) and the density ρ by an ARCHIMEDES setup.

$$\Lambda = D_{\text{th}}K_p\rho \quad (1.17)$$

1.1.3 Influencing thermoelectric properties

The main challenge in researching thermoelectric materials is the optimization of the generated power output and the energy conversion efficiency. Equation 1.3 introduced the figure-of-merit as a function of the power factor and the thermal conductivity. According to Narducci [31], the power factor itself can be at least equally important as the figure-of-merit for a theoretically unlimited heat source, which is realistically closest to find at high temperature [32]. Therefore, future research should focus not only on high values for the figure-of-merit, but also on the power factor. However, the interplay between the three basic parameters makes this task more complicated. In the following, some approaches facing this challenge are presented.

Carrier concentration engineering

All three basic parameters as introduced by the transport equation (Equation 1.1) are influenced by the charge carrier concentration [15, 24, 33]. While the SEEBECK coefficient (see Equations 1.9 and 1.10) decreases with an increasing carrier concentration, the electrical (see Equation 1.6) and the entropy conductivity (see Equation 1.15) rise as depicted in Fig. 1.3.

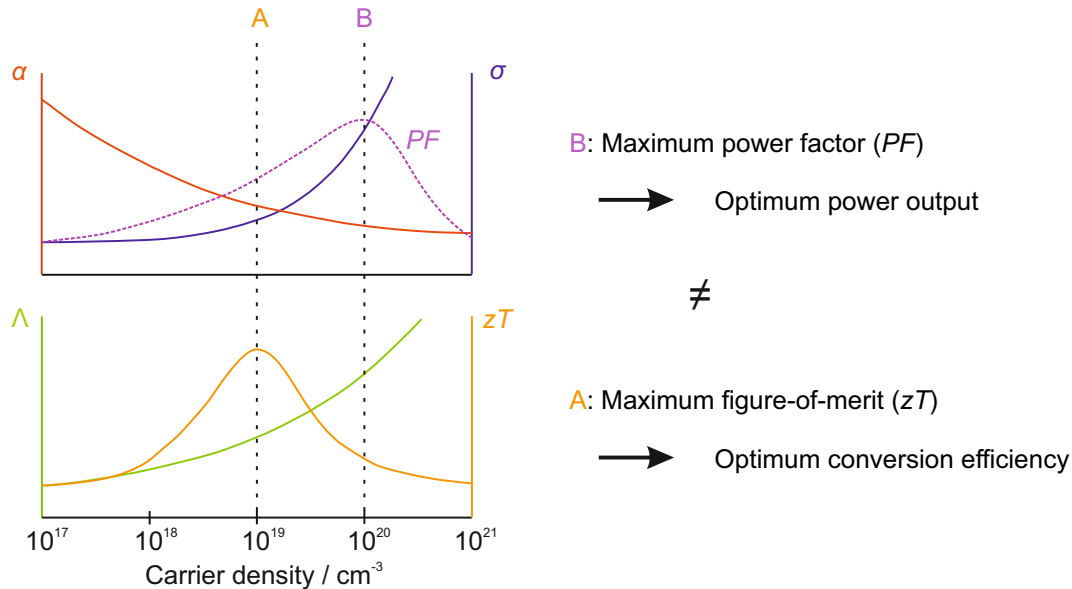


Figure 1.3: Carrier concentration dependency of SEEBECK coefficient α , electrical conductivity σ , power factor PF , entropy conductivity Λ and figure-of-merit zT . Adapted from [15, 34].

Most relevant thermoelectric materials show a carrier concentration between 10^{19} cm^{-3} and 10^{21} cm^{-3} [33]. Typically, the maximum figure-of-merit and the maximum power factor of a material are located at different carrier concentrations, wherefore it is important to know which of both should be optimized. An optimization of the carrier concentration is generally achieved by extrinsic doping [33]. Single element doping requires the substitution of lattice atoms or occupancy of vacancies with aliovalent elements, meaning elements with a different valence or oxidation state than in the surrounding lattice. However, solubility limits emerge by charge imbalances, which further complicates the choice of a suitable dopant [24]. Furthermore, the optimum carrier concentration is temperature-dependent and follows roughly a $T^{3/2}$ curve, wherefore the intended application temperature is highly relevant as well [33]. To expand the temperature range of optimum thermoelectric properties, graded doping or dopants with temperature-dependent solubilities are possible options. By stacking powders with different carrier concentrations before sintering, graded doping can be achieved, but the long term stability is an issue due to diffusion mechanisms [24, 35]. Dopants with temperature-dependent solubilities utilize the thermal gradient within the material to adjust the proper amount of dopants within the system, however they are difficult to figure out for a specific system [24, 36]. Another way to influence the carrier concentration by doping is the regulation of intrinsic point defects such as vacancies or interstitials [33]. Whether these point defects occur often depends on the composition of the thermoelectric material [33].

Band structure engineering

The electronic band structure and DOS are important features when thermoelectric properties are discussed. While the band structure comprises the energy levels of the charge carriers, the DOS shows the proportions of occupied energy levels. Hence, both carrier concentration as well as charge carrier mobility are directly influenced. Just as the carrier concentration, the band structure can also be influenced by doping [24, 33]. Effective band structure engineering either maximizes the band degeneracy, increases the DOS effective mass or enhances the carrier mobility. The first one can be increased by band convergence where multiple bands are degenerate, which means they possess the same energy level or similar ones within a few $k_B T$ [33]. The impact of band convergence on the DOS can be seen in Fig. 1.4b. Possible parameters to control the band structure are temperature, chemical composition and crystal structure [33]. The DOS effective mass is also related to the band structure, but refers to the curvature of the bands. Distortion of these bands is able to increase the DOS in the vicinity of the FERMI level [24].

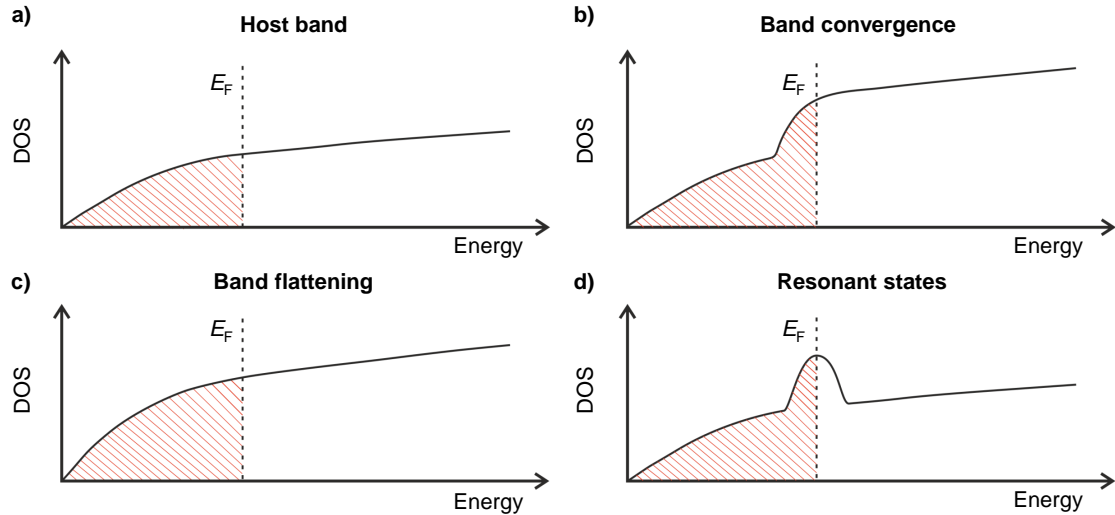


Figure 1.4: Impact of band structure engineering on the DOS near the FERMI energy. a) Host band of the pristine material. b) Band convergence with increased band degeneracy. c) Band flattening caused by doping. d) Resonant state at the FERMI level caused by impurities. Adapted from [37].

One strategy to increase the effective mass is band flattening, where the orbital overlap is diminished by introducing dopants with highly localized orbitals [24, 37]. An increase of the effective mass at a constant carrier concentration favors the SEEBECK coefficient (see Equation 1.9), but disfavors the charge carrier mobility (see Equation 1.5). To benefit from increased effective mass through a higher power factor, it can be necessary to adjust the carrier concentration, since the optimum carrier concentration correlates with the effective mass [24]. As a result of band flattening, the overall DOS increases in comparison to the host band as depicted in Fig. 1.4c.

Another way to influence the effective mass is the introduction of resonant states. These states emerge from impurities, when the electrons of the impurity couple with the electrons of the conduction band or the valence band of the host [24]. As a result, there is an excess DOS at the resonant energy level as shown in Fig. 1.4d, which can increase the effective mass as long as the FERMI level is nearby. However, the effect of

resonant levels diminishes with increasing temperature, because the acoustic phonon scattering becomes more important with shorter relaxation times [24].

The remaining parameter controlled by band structure engineering is the charge carrier mobility. As stated before, an increase of the effective mass negatively effects the carrier mobility. However, the negative effect can be diminished by modulation doping [24] as illustrated in Fig. 1.5. In contrast to the classical uniform doping, where the dopant is homogeneously distributed within the material, modulation doping uses a two-phase composite system. One phase consists of the undoped pristine sample with a higher carrier mobility than the second doped phase. The FERMI levels of both phases are imbalanced, which results in a transition of the charge carriers from the doped to the undoped region [24]. Using this mechanism reduces the ionized impurity scattering of the uniform doping and is beneficial to the charge carrier mobility [24]. However, analogous to graded doping, the long term stability at high temperature is a problem of this technique, because diffusion mechanisms and thermodynamic equilibration can overrule the phase separation.

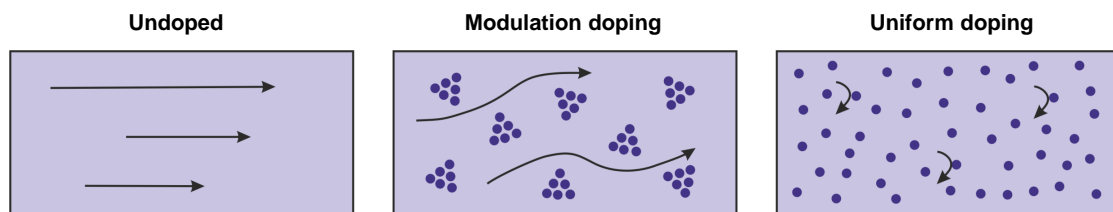


Figure 1.5: Schematic illustration of the electronic transport in an undoped material, a material with modulated doping and for uniform doping. Adapted from [24].

All-scale hierarchical structuring

The last fundamental aspect of tuning thermoelectric materials is the reduction of thermal conductivity by affecting the crystal lattice. The main objective is to hinder the propagation of phonons without too much interference of the SEEBECK coefficient or the electrical conductivity. Phonon propagation can be influenced on the atomic, nano- and mesoscale as shown in Fig. 1.6. When all three structuring methods are combined in a single material, the term all-scale hierarchical architecture is used [38, 39].

The atomic scale has a dimension of a few Å and is dominated by lattice imperfections such as point defects. Analogous to the carrier concentration and band structure engineering, the point defects can be achieved by doping. For single element doping, the reduction of the thermal conductivity correlates with the dopant amount, the mass difference between host element and dopant as well as the lattice mismatch between host and disordered phase [24, 40]. However, these factors are limited by the dopant solubility, which is diminished for an increased mismatch of host element and dopant [24]. A way to partly overcome the solubility limit caused by charge imbalances is cross substituting the host elements with element pairs resulting in a constant valence electron count [24, 41]. The mass difference of host and dopant can be maximized when disordered vacancies are introduced into the lattice [24].

Influencing the nanoscale of thermoelectric materials is usually referred to as nanostructuring [42, 43]. Here, defects with a dimension of several nanometers are interfering with phonon propagation. These defects are commonly produced by a second

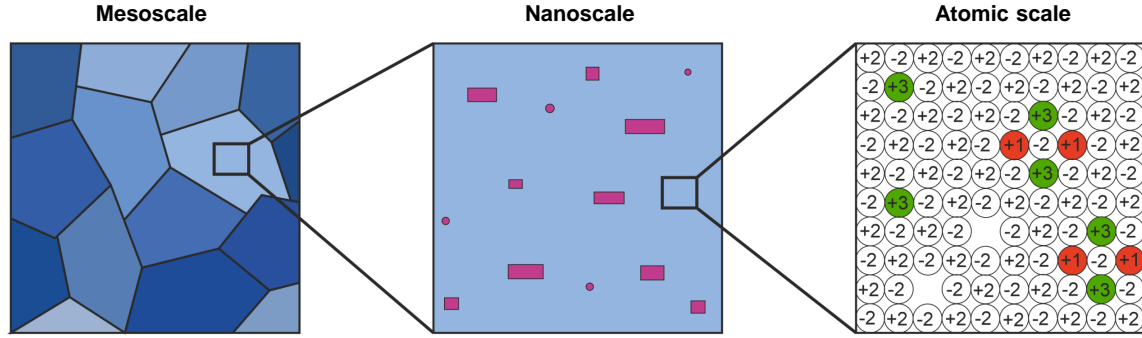


Figure 1.6: Schematic illustration of a material with an all-scale hierarchical structure. Grain boundaries are decisive on the mesoscale, precipitations or inclusions on the nanoscale and point defects on the atomic scale. Based on [24].

phase material, which can be precipitated in-situ by utilizing a solubility-matrix or ex-situ by mixing materials before sintering. The effect of phonon scattering does not increase indefinitely with the amount of second phase, because at some point aggregation and the formation of larger structures occurs [24, 44]. The same problem can appear when temperature-induced diffusion takes place. Furthermore, nanostructures not necessarily decrease the thermal conductivity, as the phonon propagation within them is rather unpredictable [24, 44].

The last scale being relevant for phonon propagation is the mesoscale, where long-wavelength phonons come into play. While point defects and nanostructures are not able to scatter them effectively, structures in the length of micrometers or slightly below can do so. Grain sizes typically in the range of 0.1 to 3 micrometers serve as exemplary structures [24, 38] and can be achieved by densifying mesoscopic particles. As a result, polycrystalline samples are obtained.

1.1.4 Composites in thermoelectrics

Composite thermoelectric systems are related to the aforementioned methods and are discussed in more detail as follows. Multiphase systems aim at synergistic effects between two or more separated phases to gain a superior heteromaterial. However, theoretical limits of two-phase systems with coexisting materials were stated by BERGMAN et al. in the 1990's [45, 46]. The conclusions derived from the mathematical models show that the power factor can be increased compared to the single-phase materials, but not the figure-of-merit. Isotropic components were assumed for the calculations, which means effects of texturing or preferred orientations were excluded. Extensions of the calculations to multiphase composites also were not comprehensive. In addition, research in thermoelectrics intensified dramatically in the last 20 to 30 years, developing methods such as nanostructuring, which has experimentally proven not only to reduce thermal conductivity, but also to increase the figure-of-merit simultaneously [43, 47]. This means that the overall thermoelectric properties can exceed those of the individual components as long as the intrinsic bulk properties of at least one component are altered [48].

Introducing other phases into a host matrix can have several effects on the whole system. First of all, heterointerfaces are introduced with possible benefits to the thermal conductivity [49, 50]. However, depending on the thermal conductivity of the

added phases and the grain sizes, the overall thermal conductivity is not necessarily reduced [51]. Three big material classes are relevant in terms of thermoelectric composites: inorganic, metallic and organic materials. Introducing phases with high electrical conductivity such as silver [49] or graphite [52] has proven to increase the overall thermoelectric properties within the proper system significantly. Organic compounds, on the other hand, convince with their extraordinarily low thermal conductivity, which can increase the figure-of-merit despite a lower power factor [53]. Carbon nanotubes in an organic composite system also proved to increase the power factor beyond the ones of the individual components [54].

Another important factor in composites is the temperature stability of the components. If components with low thermal stability, such as organic compounds, are used with components of high thermal stability, such as oxides, the overall range in the composite can be unfavorably limited [50]. Therefore, components with similar thermal stability are more reasonable when the optimum properties shall be reached. Exceptions are possible if, for example, the minor component is intentionally embedded within a host matrix to benefit from stabilization effects [55]. Different phases can also possibly react at higher temperature, leading to new interesting compounds or indirectly result in doping by temperature-induced atom exchanges. If reactions or atom exchanges occur, the thermoelectric properties are also influenced. However, promising components for composites are not easy to predict, especially when temperature-induced transformations take place.

1.2 Thermoelectric materials

The variety of thermoelectric materials is immense and every few years a new material with promising properties emerges or new mechanisms enable the improvement of established materials. Hence, an overview with the current state-of-the-art materials is given within this chapter. As stated in the previous Chapter 1.1, the optimum thermoelectric properties of a material depend on the application temperature. Therefore, there is no perfect material covering low, mid and high temperature. While materials in one temperature range may compete with each other, materials focusing in other ranges can be viewed as complementary. As the research within this thesis focuses on oxide-based materials, they are discussed more in-depth and a review on thermoelectric materials for high-temperature applications is enclosed.

1.2.1 Overview of state-of-the-art materials

The thermoelectric material classes can be assigned to different temperature ranges, because their properties are optimal at a specific temperature or their thermal stability is limited. Therefore, the overview of the material classes within this thesis is divided with respect to the temperature. The low- to mid-temperature materials cover a temperature range from 300 K to 973 K and the high-temperature range goes beyond. Note that these boundaries are fluent and not consistent throughout the literature. To provide a comprehensive insight into the material properties, the following Fig. 1.7 and Fig. 1.8 are used. They display type-I IOFFE plots, where the power factor is plotted against the electrical conductivity, and plots of power factor against figure-of-merit. As the transport directions differ in n - and p -type materials, they are viewed separately in these plots. Type-I IOFFE plots have the advantage of showing whether the power factor of a material benefits from a high SEEBECK coefficient or rather from a high electrical conductivity [32]. Only polycrystalline materials are included in the IOFFE plots, because they are easier to synthesize in appreciable quantities compared to single-crystal materials.

In the low- to mid-temperature range, bismuth tellurides, lead tellurides, ZNTL phases, skutterudites and oxyselenides were chosen as the most outstanding materials based on their thermoelectric properties. The displayed values are all based on heavily tuned materials, as no raw material can usually exhibit these properties intrinsically. A comparison of the n - and p -type materials with the type-I IOFFE plots in Fig. 1.7a,b shows a typical electrical conductivity in the range of 100 S cm^{-1} to 1000 S cm^{-1} . All these materials show a metallic behavior with a decreasing electrical conductivity at rising temperature. The power factor, on the other hand, varies between $10 \mu\text{W cm}^{-1} \text{ K}^{-2}$ and $100 \mu\text{W cm}^{-1} \text{ K}^{-2}$ and is typically in the lower end of the range. The BiCuSeO (BCSO) is displayed only for the p -type materials as n -type doping has not yet led to comparable results [56]. A complete picture including the energy conversion efficiency is given in Fig. 1.7c,d. An excellent figure-of-merit of 1.8 (n -type) and 2.5 (p -type) could be reached by lead tellurides at a high power factor of $20 \mu\text{W cm}^{-1} \text{ K}^{-2}$ and $30 \mu\text{W cm}^{-1} \text{ K}^{-2}$. The power factor of lead telluride mainly benefits from a high SEEBECK coefficient, especially for the p -type material. Skutterudites, on the other hand, have a high electrical conductivity slightly below 1000 S cm^{-1} , which especially gives the n -type material an outstanding power factor around $50 \mu\text{W cm}^{-1} \text{ K}^{-2}$. In the low-temperature range around 400 K, the bismuth

tellurides are unrivaled with a consistent figure-of-merit around 1.5. The power factor of BCSO is comparatively low with values below $10 \mu\text{W cm}^{-1} \text{K}^{-2}$, although a high figure-of-merit of 1.5 is reached. This is accomplished by the extraordinary low entropy conductivity of up to $5 \mu\text{W cm}^{-1} \text{K}^{-2}$. In general, a high figure-of-merit is achieved by decreasing thermal conductivity rather than increasing power factor, mainly due to the success of hierarchical structures and nanostructuring in particular.

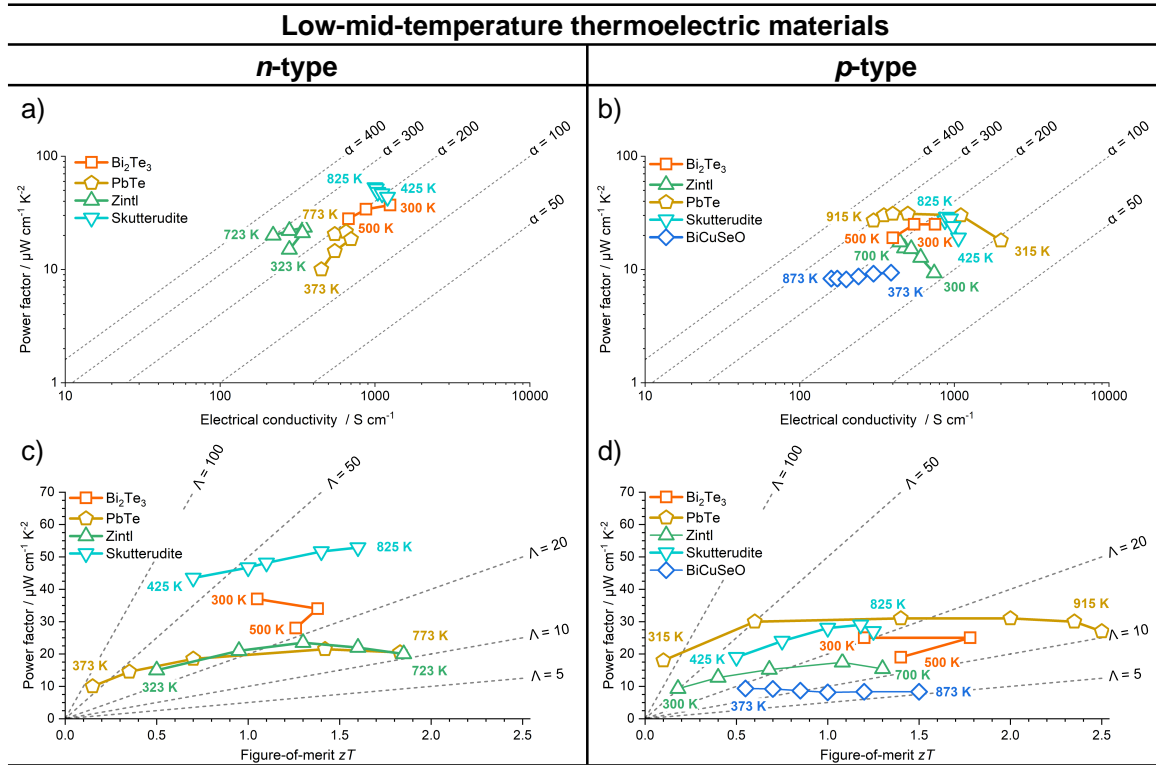


Figure 1.7: Comparison of low- to mid-temperature thermoelectric materials with IOFFE plots (a,b) and power factor vs. figure-of-merit plots (c,d). Dashed lines indicate the SEEBECK coefficient in $\mu\text{V K}^{-1}$ (a,b) and the entropy conductivity in $\mu\text{W cm}^{-1} \text{K}^{-2}$ (c,d). Represented material classes are bismuth tellurides (n -type: $\text{Bi}_{1.8}\text{Sb}_{0.2}\text{Te}_{2.7}\text{Se}_{0.3}/\text{Te}$ [57]; p -type: $\text{Bi}_{0.5}\text{Sb}_{1.5}\text{Te}_3$ [58]), lead tellurides (n -type: PbTe/InSb [59]; p -type: PbTe/SrTe [60]), ZINTL phases (n -type: $\text{Mg}_{3.15}\text{Mn}_{0.05}\text{Sb}_{1.5}\text{Bi}_{0.49}\text{Te}_{0.01}$ [61]; p -type: $\text{Yb}_{0.96}\text{Ba}_{0.04}\text{Cd}_{1.5}\text{Zn}_{0.5}\text{Sb}_2$ [62]), skutterudites (n -type: $(\text{Mn},\text{Sm})_y\text{Co}_4\text{Sb}_{12}$ [63]; p -type: $\text{DD}_y(\text{Fe}_{1-x}\text{Co}_x)_4\text{Sb}_{12}$ [63]) and oxyselenides (p -type: $\text{Bi}_{0.88}\text{Ca}_{0.06}\text{Pb}_{0.06}\text{CuSeO}$ [64]).

Similar relationships can be established for the high-temperature thermoelectric materials with Fig. 1.8. Selected material classes are oxides, half-HEUSLER compounds and SiGe-based materials. The half-HEUSLER compounds show exceptional values for the power factor of around $40 \mu\text{W cm}^{-1} \text{K}^{-2}$ (p -type) or even $60 \mu\text{W cm}^{-1} \text{K}^{-2}$ (n -type), based on a high SEEBECK coefficient between $300 \mu\text{V K}^{-1}$ and $200 \mu\text{V K}^{-1}$ as well as a high electrical conductivity of 500 S cm^{-1} to 1000 S cm^{-1} . Depending on the chosen half-HEUSLER compound, either a metallic or a semiconductor-like behavior at elevated temperature is prevalent and a high figure-of-merit around 1.5 can be achieved. SiGe-based materials reach an even higher figure-of-merit of up to 1.8 at a relatively low power factor of $10 \mu\text{W cm}^{-1} \text{K}^{-2}$ and a much lower entropy conductivity around $7.5 \mu\text{W cm}^{-1} \text{K}^{-2}$. Finally, oxide materials are covered in the high-temperature range. Oxide-based materials suffer from a relatively low thermoelectric performance, as exemplified by the p -type $\text{Ca}_3\text{Co}_4\text{O}_9$ (CCO). A high SEEBECK coefficient of $300 \mu\text{V K}^{-1}$

is reached, but the electrical conductivity does not exceed 100 S cm^{-1} . A moderate thermal conductivity enables a figure-of-merit of 0.74 at 800 K. Note that CCO is usually stable up to approximately 1200 K [65, 66], wherefore it is included in the high-temperature range. For a long time, p -type oxides were superior to the n -type oxides, but recently Acharya et al. [52] managed to achieve a high figure-of-merit of 1.42 at a high power factor of $40 \mu\text{W cm}^{-1} \text{ K}^{-2}$ with SrTiO_3 by doping and the inclusion of graphite. The latter led to a drastic increase in electrical conductivity to more than 1000 S cm^{-1} , but also compromised one of the greatest advantages of oxides: oxidation stability.

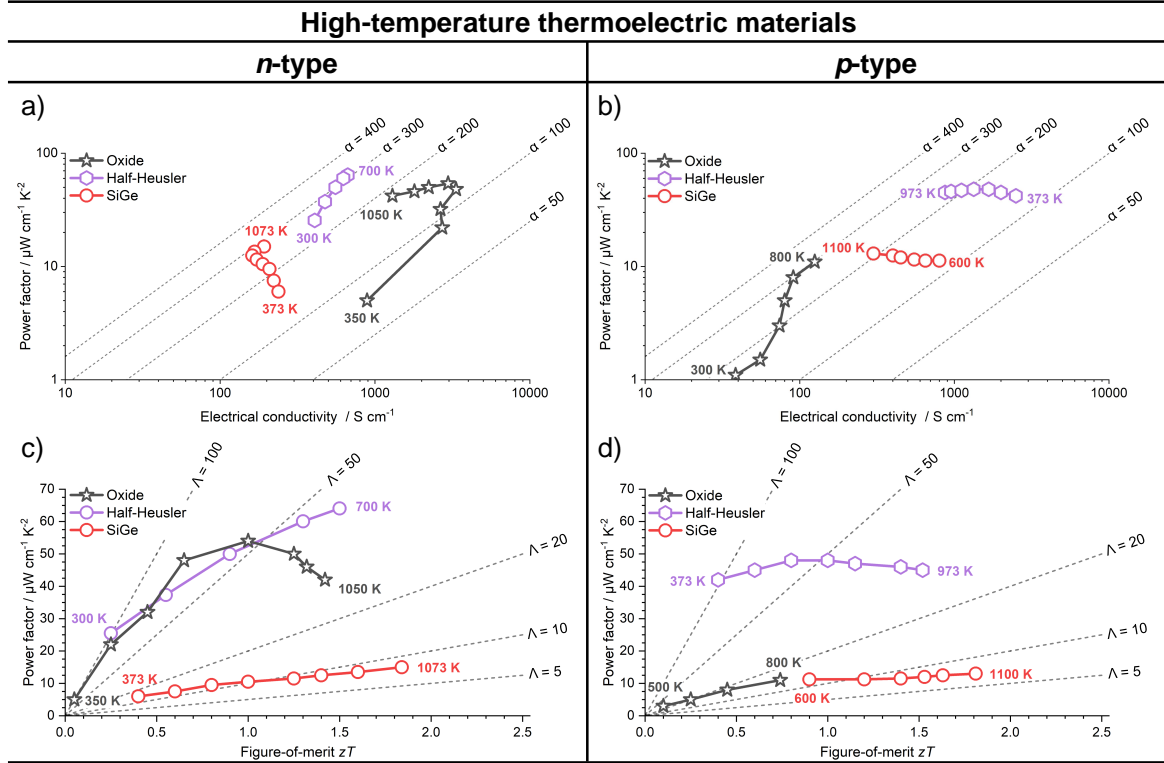


Figure 1.8: Comparison of high-temperature thermoelectric materials with IOFFE plots (a,b) and power factor vs. figure-of-merit plots (c,d). Dashed lines indicate the SEEBECK coefficient in $\mu\text{V K}^{-1}$ (a,b) and the entropy conductivity in $\mu\text{W cm}^{-1} \text{ K}^{-2}$ (c,d). Represented material classes are oxides (n -type: $\text{SrTi}_{0.85}\text{Nb}_{0.15}\text{O}_3$ /graphite [52]; p -type: $\text{Ca}_3\text{Co}_4\text{O}_9$:Tb [67]), half-HEUSLER compounds (n -type: $\text{Ta}_{0.74}\text{V}_{0.1}\text{Ti}_{0.16}\text{FeSb}$ [68]; p -type: $\text{Ti}_{0.5}\text{Zr}_{0.25}\text{Hf}_{0.25}\text{NiSn}_{0.998}\text{Sb}_{0.002}$ [69]) and SiGe (n -type: SiGe:P [70]; p -type: SiGe:Y₂O₃ [71]).

The air stability in dependence of the temperature can be roughly assigned to the presented material classes as shown in Fig. 1.9. Note that composite systems with temperature-sensitive compounds are not considered, as these would reduce applicability. Furthermore, diffusion-controlled mechanisms are promoted at higher temperature and can lower the thermoelectric performance, if graded materials or nanocomposites are used. The biggest competitors of oxides in terms of high-temperature applications are half-HEUSLER compounds and SiGe-based materials. The half-HEUSLER compounds can be stable in air up to 873 K, but their stability strongly depends on the composition [72]. On the other hand, SiGe is more stable up to 973 K and is only surpassed by the oxides, where a much higher temperature is possible depending on the compound. The air-stability of CCO, for example, is limited by decomposition at a temperature of approximately 1200 K [73, 74]. The low temperature stability of

BCSO in air is linked to the crystal structure, where copper selenide layers alternate with bismuth oxide layers [75]. As a consequence, BCSO is not labeled as an oxide material but as an oxyselenide. If we consider combustion engines with a temperature between 773 K and 1273 K as a possible application [76], oxides are the preferred candidate as long as air contact can not be prevented easily.

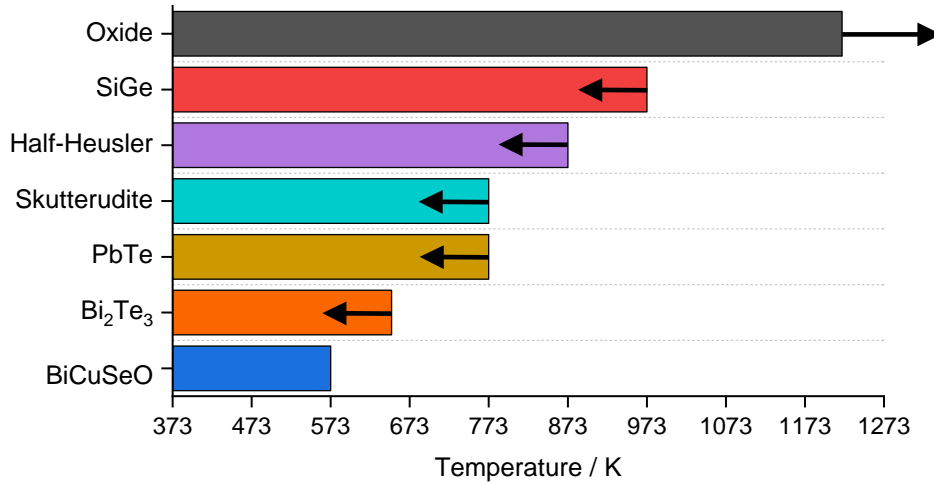


Figure 1.9: Comparison of air and oxidation stability in dependence of the temperature. Selected material classes are oxides [73, 74], SiGe [77], half-HEUSLER compounds [72], skutterudites [78], PbTe [79], Bi₂Te₃ [80] and BiCuSeO [81]. The arrows show the decreasing or increasing trend of other materials within the thermoelectric classes.

1.2.2 Oxide-based materials

In the former section 1.2.1, the state-of-the-art *n*- and *p*-type oxide materials have already been introduced. In the following, a closer look into the oxide material class for thermoelectrics is given with particular attention to CCO, since it is used prominently in this thesis. A general overview of some oxides with reasonable thermoelectric properties is displayed in Fig. 1.10. Similar to the comparison of different material classes before, the IOFFE plots and power factor vs. figure-of-merit plots come in handy. Only the most promising oxide materials are discussed and single-crystals or composites with non-air-stable components were not considered.

Four different materials are displayed for the *n*-type oxides: CaMnO₃ (CMO), In₂O₃ (ITO), SrTiO₃ (STO) and ZnO. Of course, not the pristine materials but the doped or modified ones are shown, as the base materials have significantly reduced thermoelectric properties. Beginning with CMO and ITO, they both have a similar trend within Fig. 1.10c as the maximum power factor is similar. Of all the oxides, ITO has the highest electrical conductivity of around 800 S cm⁻¹, but suffers from a low SEEBECK coefficient, as it is obvious in the IOFFE plot of Fig. 1.10a. STO is in between the two aforementioned materials in terms of electrical conductivity, but can maintain the high SEEBECK coefficient around 200 μV K⁻¹, resulting in a better power factor. However, the high thermal conductivity prevents STO from achieving a figure-of-merit higher than 0.4. The highest figure-of-merit and at the same time highest power factor of the shown *n*-type oxides is obtained by doped ZnO at a high temperature of 1250 K. The thermal conductivity of the doped ZnO is relatively high,

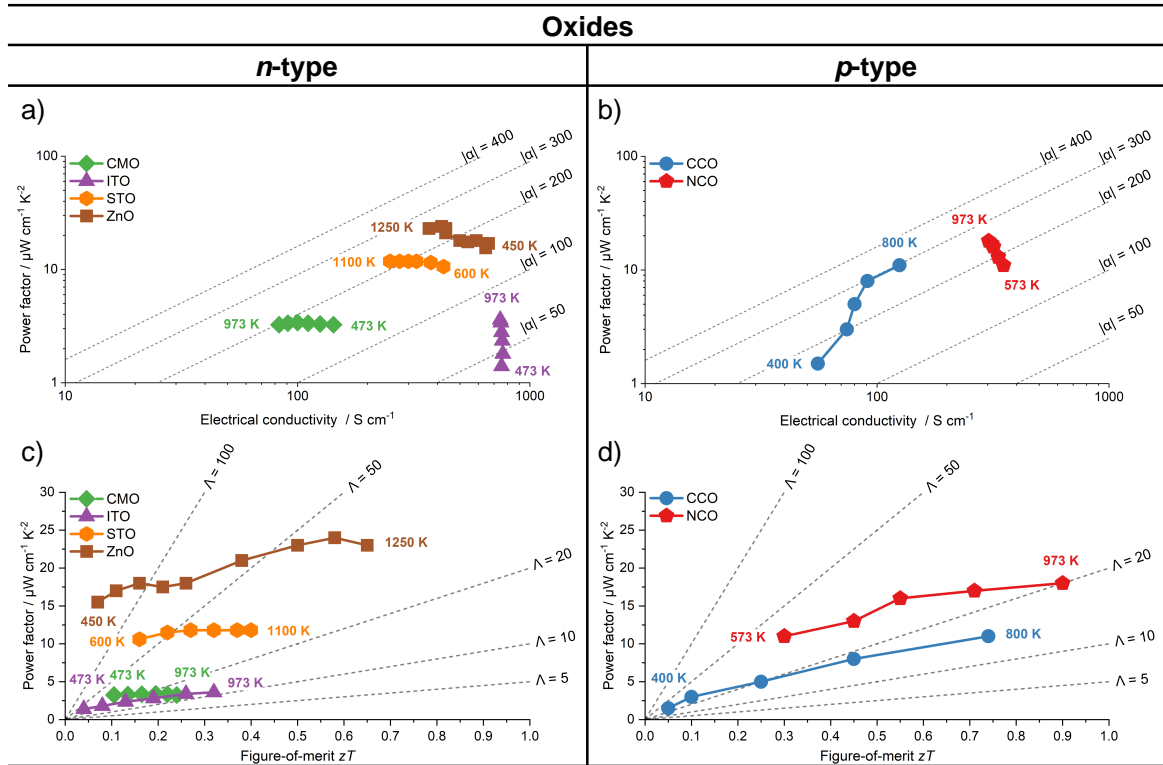


Figure 1.10: Comparison of oxide thermoelectric materials with IOFFE plots (a,b) and power factor vs. figure-of-merit plots (c,d). Dashed lines indicate the SEEBECK coefficient in $\mu\text{V K}^{-1}$ (a,b) and the entropy conductivity in $\mu\text{W cm}^{-1} \text{K}^{-2}$ (c,d). Represented materials are CaMnO_3 (CMO; *n*-type: $\text{Ca}_{0.92}\text{Pr}_{0.04}\text{Yb}_{0.04}\text{O}_3$ [82]), In_2O_3 (ITO; *n*-type: $\text{In}_{1.76}\text{Zn}_{0.12}\text{Sn}_{0.12}\text{O}_3$ [83]), SrTiO_3 (STO; *n*-type: $\text{SrTiO}_3:\text{Nb}$ [84]) ZnO (*n*-type: $\text{ZnAl}_{0.02}\text{Ga}_{0.02}\text{O}$ [85]), $\text{Ca}_3\text{Co}_4\text{O}_9$ (CCO; *p*-type: $\text{Ca}_3\text{Co}_4\text{O}_9:\text{Tb}$ [67]) Na_xCoO_2 (NCO; *p*-type: $\text{Na}_x\text{CoO}_2/10\text{wt}\% \text{Ag}$ [86]).

but the improved power factor compared to STO enables an increase of the figure-of-merit.

On the other hand, there the *p*-type oxides are dominated by layered calcium cobalt oxides. CCO and Na_xCoO_2 (NCO) in particular show excellent thermoelectric properties. While NCO achieves a higher figure-of-merit than CCO due to a higher electrical conductivity, it suffers from a lower thermal stability in air of approximately 960 K associated with volatile sodium [55]. The biggest downside of CCO is its relatively low electrical conductivity, which can be adjusted by doping or composite systems. A closer look into the material is given in the following.

Structure and thermoelectric properties of $\text{Ca}_3\text{Co}_4\text{O}_9$

Several layered cobaltates exist, but one of the most promising in terms of thermoelectrics is CCO. Its thermoelectric properties are directly linked to the layered crystal structure, which is built up from two incommensurate subsystems. As depicted in Fig. 1.11, one subsystem contains CoO_2 in a misfit-layered CdI_2 structure and the other subsystem contains Ca_2CoO_3 units as a layered cutout of the rock-salt type [87]. Both subsystems alternate along the shared *c*-axis with the same *a* and distinct *b* lattice parameters [88]. Hence, the structure-revealing formula $[\text{Ca}_2\text{CoO}_3]_{0.62}\text{CoO}_2$ is also often used instead of $\text{Ca}_3\text{Co}_4\text{O}_9$, especially in the early stage of research on CCO [88]. The incommensurate structure of CCO has also consequences on the LAUE indexing,

because the classical three-dimensional (3D) approach does not apply. Instead, the approach of a four-dimensional superspace group can be used, where the 3D symmetry is complemented by rationally independent modulation vectors based on the divergent crystallographic axes [89, 90].

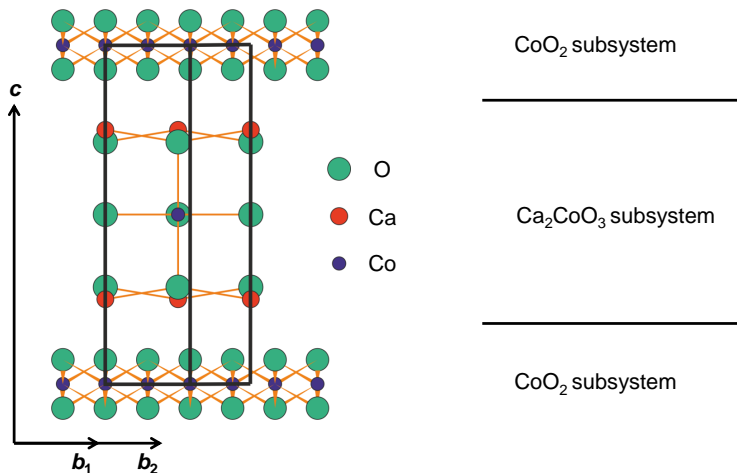


Figure 1.11: Misfit-layered structure of $[\text{Ca}_2\text{CoO}_3]_{0.62}\text{CoO}_2$ ($\text{Ca}_3\text{Co}_4\text{O}_9$) containing CoO_2 (b_1) and Ca_2CoO_3 (b_2) subsystems with an irregular axis ratio of $b_1/b_2 \approx 0.62$. Based on [55].

According to the anisotropic crystal structure, the thermoelectric properties of CCO are also highly anisotropic. In a polycrystal, the bulk properties can only be assumed as isotropic when the grains are randomly orientated. However, usually there is some kind of anisotropy or texture caused by pressing and sintering methods. As CCO typically has plate-like crystals, they orientate when pressure is uniaxially applied for densification. Pressure is involved in several densification methods such as conventional sintering (CS) [91], spark plasma sintering (SPS) [92], hot pressing (HP) [93], cold sintering process (CSP) [94] and pressure-assisted sintering [95]. Depending on the sintering method used, the degree of texturing and the density vary. In general, electrical conductivity of CCO is higher along the a, b -direction because of the CoO_2 subsystem [87]. In contrast, the thermal conductivity is lower along the c -axis because of the enhanced phonon scattering at the different subsystems [87]. This logically leads to a higher power factor for the a, b -direction, which is also proven by experimental results where up to a 13.6 times higher power factor was found for hot pressed and highly textured CCO [96]. Furthermore, the figure-of-merit is also increased in the a, b -direction [97]. Therefore, the a, b -direction is preferred for thermoelectric applications. The vast difference of the transport properties between the crystallographic directions makes it important to measure the power factor and the thermal conductivity in the same direction to avoid overestimations of the figure-of-merit. More details about the relevance of anisotropy in thermoelectrics is given in Chapter 1.3.

Besides texturing, porosity is another important factor controlled by the sintering method. To reach high electrical conductivity, a high density and a good grain connectivity are mandatory. However, porosity lowers the thermal conductivity and can increase the figure-of-merit compared to a dense ceramic [91]. Hence, a trade-off between the electrical conductivity and the figure-of-merit can be made as the SEEBECK coefficient remains mainly unaffected by the porosity [91]. As the material is only stable up to 1198 K in air [73, 74], conventional sintering at 1173 K is not enough to

create a fully dense ceramic and naturally leads to a porosity of approximately 30% to 40% [91].

For a *p*-type material, the electron hole concentration is directly related to the electrical conductivity. As the Ca_2CoO_3 subsystem is prone to exhibit oxygen vacancies while maintaining the overall structure [98], the oxygen content within CCO plays an important role. In fact, the hole concentration increases for the fully oxidized CCO and a high charge carrier concentration of $5.7 \cdot 10^{21} \text{ cm}^{-3}$ can be reached, which favors the electrical conductivity [98]. Due to the sensitivity to oxygen content in the CCO, it is important to operate and measure the material in an oxygen-containing atmosphere, otherwise the thermoelectric properties will change or even premature decomposition will occur at elevated temperature [66].

1.2.3 High power factor vs high zT - A review of thermoelectric materials for high-temperature application

Mario Wolf, Richard Hinterding and Armin Feldhoff

Entropy, 21 **2019**, 1058
DOI: 10.3390/e21111058



Review

High Power Factor vs. High zT —A Review of Thermoelectric Materials for High-Temperature Application

Mario Wolf ^{*}, Richard Hinterding ^{*} and Armin Feldhoff ^{*}

Institute of Physical Chemistry and Electrochemistry, Leibniz University Hannover, Callinstr. 3A, D-30167 Hannover, Germany

^{*} Correspondence: mario.wolf@pci.uni-hannover.de (M.W.); richard.hinterding@pci.uni-hannover.de (R.H.); armin.feldhoff@pci.uni-hannover.de (A.F.)

Received: 27 September 2019; Accepted: 25 October 2019; Published: 29 October 2019



Abstract: Energy harvesting with thermoelectric materials has been investigated with increasing attention over recent decades. However, the vast number of various material classes makes it difficult to maintain an overview of the best candidates. Thus, we revitalize Ioffe plots as a useful tool for making the thermoelectric properties of a material obvious and easily comparable. These plots enable us to consider not only the efficiency of the material by the figure of merit zT but also the power factor and entropy conductivity as separate parameters. This is especially important for high-temperature applications, where a critical look at the impact of the power factor and thermal conductivity is mandatory. Thus, this review focuses on material classes for high-temperature applications and emphasizes the best candidates within the material classes of oxides, oxyselenides, Zintl phases, half-Heusler compounds, and SiGe alloys. An overall comparison between these material classes with respect to either a high efficiency or a high power output is discussed.

Keywords: thermoelectric materials; energy harvesting; energy materials

1. Introduction

At a time when raw fossil materials are becoming scarcer and the demand for regenerative energies is relentlessly rising, the use of energy harvesting systems has gained an ever-increasing interest [1]. Regardless of whether it is from industrial processes, mechanical processes, or the transportation sector, the amount of wasted energy currently remains enormous. In 2017, the estimated energy consumption in the U.S. was shown to be approximately 67% wasted energy [2]. At this point, energy harvesting comes into play, converting even small amounts of wasted energy in the form of heat, light, vibration, or movement into usable energy [3]. Since most of this wasted energy is in the form of heat, the conversion of thermal energy to electrical energy via thermoelectric generators is an attractive solution. The associated energy conversion is based on the thermoelectric effect, which is the simplest way for direct energy conversion from dissipated heat into electrical energy.

Discovered by T.J. Seebeck in 1821, the first thermoelectric effect (Seebeck effect) describes the direct conversion of thermal energy into electrical energy, which Seebeck demonstrated by thermally inducing an electrical current by heating two different electrical conductors. Together with the Peltier effect (1834), which describes the heating or cooling effect of an electrical current in a thermocouple, and the work of W. Thomson on the thermoelectric effect in homogeneous conductors (Thomson effect), the basis of thermoelectricity was laid [4]. In the first half of the 20th century, the term ‘figure of merit’ was introduced, and the first theoretical approaches were made in designing a material with a high energy conversion efficiency. In 1957, A.F. Ioffe defined the figure of merit zT as a

function of the electrical conductivity, the Seebeck coefficient, and the thermal conductivity of the material [5]. However, thermoelectric energy conversion has been too inefficient for most applications for a long time. Theoretical descriptions of nanostructural engineering and superlattice structures paved the way to significantly improved zT values, which strongly increased research on thermoelectric materials in the mid 1990s [6]. Today, the improvement and development of thermoelectric materials still have the goals of gaining higher efficiencies and power outputs. Within this research field, various materials from wide-ranging material classes, such as metallics and intermetallics [7,8], oxide-based ceramics [9–11], chalcogenide compounds [12], and polymers [13] have been investigated. It is important to compare the efficiencies and resulting power outputs of these materials to draw the correct conclusions when actual generators for applications are manufactured. The purpose of this review is to convey descriptive comparisons, which is realized by two different types of Ioffe plots. These plots allow a direct comparison of the thermoelectric properties of different materials, which is vital for prospective research [14].

1.1. Thermoelectric Parameters

Discussing thermoelectricity requires an understanding of some fundamental parameters, which are briefly described in the following. Thermoelectric energy conversion is based on local coupling of fluxes of charge carriers and entropy. When a thermoelectric material is simultaneously exposed to local gradients of temperature (i.e., ∇T) and an electrochemical potential of charge carriers (i.e., $\nabla \frac{\tilde{\mu}}{q}$) the local flux densities of charge j_q and entropy j_s are given by the following transport equation [15]:

$$\begin{pmatrix} j_q \\ j_s \end{pmatrix} = \begin{pmatrix} \sigma & \sigma \cdot \alpha \\ \sigma \cdot \alpha & \sigma \cdot \alpha^2 + \Lambda \end{pmatrix} \cdot \begin{pmatrix} -\nabla \frac{\tilde{\mu}}{q} \\ -\nabla T \end{pmatrix}. \quad (1)$$

The thermoelectric material tensor, which appears here, is characterized by three material parameters: the isothermal electrical conductivity σ , the Seebeck coefficient α , and the electrically open-circuited entropy conductivity Λ . The latter is linearly related to the traditionally used heat conductivity λ via the absolute temperature T as described in Equation (2) [15–17]. In the context of this review, thermal conductivity is a generic term, that covers both entropy conductivity and heat conductivity. Here, it is advantageous to address the thermal conductivity by the more fundamental entropy conductivity, as we will see when comparing materials.

Considering entropy as a central primitive quantity of equal rank to electric charge comes with the benefit of an easy understanding of the physics of thermoelectricity. A local coupling of the fluxes of these substance-like quantities is described by Equation (1) [15]; this is in contrast to the cumbersome traditional approach, which introduces generalized forces and a kinetic matrix [18] instead of thermodynamic potential gradients and a material tensor. Naturally, for each substance-like quantity, a conductivity is assigned to the material. The material tensor is symmetric by principle, and an elaborate discussion of the reciprocity of Onsager coefficients is superfluous [15]. A further advantage is that the currents of thermal energy (heat) and electrical energy (or electrochemical energy), which accompany the fluxes of entropy and charge, can be treated separately. The entropy and charge fluxes allow us to consider energy conversion and its efficiency in a thermoelectric material apart from the device. When expressed with the entropy conductivity, the figure of merit zT in Equation (2) is purely a material parameter that depends only implicitly on temperature. Moreover, the appearance of two substance-like quantities in Equation (1) to be transported through a thermoelectric material allows for an integration of thermoelectricity into a broad picture of coupled transport processes (e.g., diffusion, viscous flow, entropy conduction and electric conduction) and benefits from analogies. A reader who is interested in more details is referred to the discussion about the properties of heat by Fuchs [19] and the comparative overview by Job and R uffler [17].

The tensor element M_{22} in Equation (1) directly leads to parameters that describe the performance of a thermoelectric material. The most commonly used parameter is the dimensionless figure of merit zT , which describes the relation of the power factor $\sigma\alpha^2$ and the entropy conductivity Λ in Equation (2).

$$zT = \frac{\sigma \cdot \alpha^2}{\Lambda} = \frac{\sigma \cdot \alpha^2}{\lambda} \cdot T. \quad (2)$$

The figure of merit zT indicates the maximum achievable power conversion efficiency of a thermoelectric material [16]:

$$\eta_{\max} = \frac{\sqrt{1+zT}-1}{\sqrt{1+zT}+1} \cdot \eta_{\text{Carnot}}. \quad (3)$$

In contrast, the power factor $\sigma\alpha^2$ is proportional to the maximum achievable power output of a material and the temperature difference ΔT [20]:

$$P_{\text{el,max}} \propto \sigma\alpha^2 \cdot (\Delta T)^2. \quad (4)$$

For some applications, the power factor may have the same relevance as the efficiency described by the zT value. As shown in Figure 1a, for a thermoelectric material, the optimum efficiency and optimum power output as a function of the carrier density differ, leading to a possible optimization of one parameter for the desired properties or a special application.

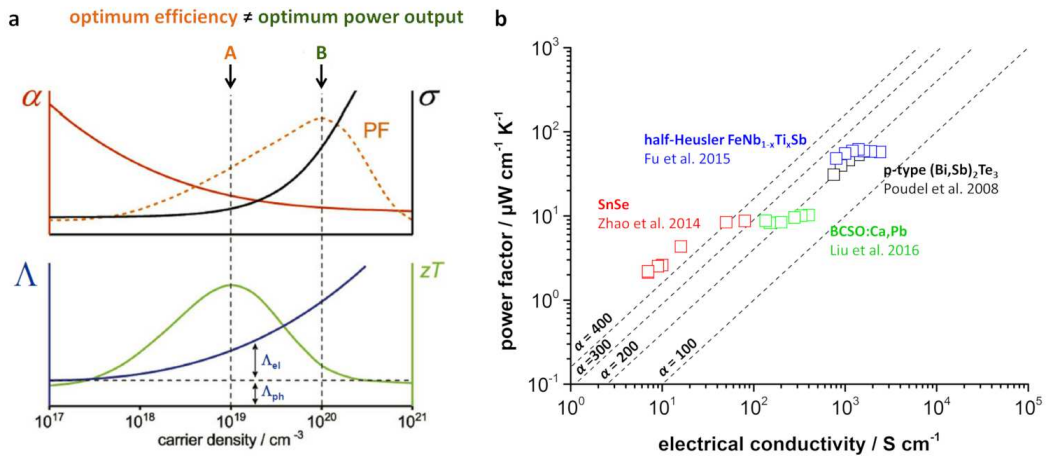


Figure 1. (a) Seebeck coefficient α , electrical conductivity σ , entropy conductivity Λ , and the resulting power factor $\sigma\alpha^2$ and zT value as a function of the charge carrier density; adapted from [20] with permission from Elsevier; (b) Type-I Ioffe plot of various reported high- zT materials [11,12,21,22]. Seebeck coefficient α is given in $\mu\text{V K}^{-1}$. Different data points for the same material refer to different temperatures.

Narducci [23] also emphasized that the figure of merit zT may be an inappropriate parameter to rate and compare different materials for some applications. Especially for applications at high temperature, the power factor $\sigma\alpha^2$ could be a better quality criterion. In this review, rather than just comparing the figure of merit zT , we will also look at the power output and the entropy conductivity of different materials by comparing them via Ioffe plots. We distinguish between a type-I Ioffe plot, which considers the power factor $\sigma\alpha^2$ as a function of the electrical conductivity σ , and a type-II Ioffe plot, which considers the entropy conductivity Λ as a function of the electrical conductivity σ . Figure 1b displays a type-I Ioffe plot of various reported materials from different classes with high figure of merit zT values. Although all of the shown materials exhibit exceptionally high zT values in their specific material class, the electrical conductivity σ as well as the power factor vary over several orders

of magnitude. Furthermore, type-II Ioffe plots will be vital for an in-depth comparison of different thermoelectric materials later on. Since the entropy conductivity can be displayed in the same unit and scale as the power factor, the type-II Ioffe plot enables an easy comparison of electrical and thermal properties and observable zT values.

1.2. Doping and Band Structure Engineering

A prevailing challenge when facing the improvement of a thermoelectric material is coupling all three relevant material parameters with each other, which can be managed to a certain degree. The most common approach to enhancing the performance of thermoelectric materials is doping, which can have a huge impact on the electrical conductivity, Seebeck coefficient, and thermal conductivity. Several parameters, such as carrier density, mobility, effective mass, and the band structure, are effectively influenced by proper doping.

Figure 1a shows an optimum carrier density for a balanced electrical conductivity and Seebeck coefficient at a given temperature, which varies between an optimum power factor and zT value. This means that adjusting the carrier density via doping is highly advised for either high power or high efficiency applications [23]. The dopant may influence the carrier density of a material by introducing defect-enabled mechanisms including point defects [1]. However, the optimum carrier density is temperature-dependent and increases approximately with $T^{3/2}$ [5]. Thus, either further material engineering is required or the carrier density needs to be optimized for a specific temperature range according to the application field.

Generally, the Seebeck coefficient decreases with increasing carrier concentration, as shown in Figure 1, and the electrical conductivity is oppositely coupled. However, the doping-induced convergence of valence or conduction bands to increased valley degeneracy has proven to increase the electrical conductivity while maintaining the Seebeck coefficient [24]. This is explained by the Seebeck coefficient being dominated by the smaller value of several bands. If degeneracy of several bands is achieved, the Seebeck coefficient is stable, but the electrical conductivity substantially rises [24,25]. Therefore, band convergence is an effective way to improve the power factor of a material.

Additionally, doping strongly influences the thermal properties of the material. The thermal conductivity expressed as entropy conductivity Λ was introduced in the tensor element M_{22} in Equation (1). Conventionally, the thermal conductivity is divided into a phonon contribution and an electronic contribution [5]. Influencing the phonon contribution to the thermal conductivity via scattering mechanisms is well investigated and can be divided into size-relevant dimensions. The atomic scale is influenced by single doping or cross substitution, which results in point defects within the crystal lattice. These defects effectively delay the phonon propagation by scattering when the lattice mismatch between the host and the dopant is sufficient and the mass difference as well as the dopant amount are high [26]. The next relevant dimension for scattering phonons is the nanoscale, which leads to so-called nanostructuring [27]. Nanoscaled defects can be introduced in-situ by forcing the precipitation of a second phase [28] or ex-situ by mixing the nanoscaled second phase with a host phase [29]. However, the phonon propagation within the second phase is rather unpredictable, making it difficult to design a proper system. Temperature stability is another issue since elevated temperatures may change the scale of the precipitates and diminish the achieved effect [27]. The main part of the thermal energy is propagated by short- and medium-wavelength phonons, which are effectively hindered by point defects and nanostructuring. The residual long-wavelength phonons can be influenced by defects in the range of a few micrometers or submicrometers, namely, the mesoscale. This effect is typically active for polycrystalline materials with mesoscale grains [30]. Additional phonon scattering may appear at heteromaterial interfaces of composite systems [31]. However, the electronic transport may be reduced by these grains, making a consideration of maximum power output vs. efficiency necessary. If the scattering of the phonons is achieved at all three length scales, the term all-scale hierarchical architecture is used [32]. Only a few studies achieve all-scale phonon scattering,

but when regarding the overall reduction of the phonon contribution to the thermal conductivity, decreases of more than 50% are possible [33].

While the phonon contribution to the thermal conductivity has been widely studied, the electronic contribution is not straightforward. For degenerate semiconductors with charge carriers of the same sign, the commonly used separation into both contributions fits well, and the Wiedemann–Franz relation $\Lambda = L_0 \cdot \sigma$ with the Sommerfeld value of the Lorenz number $L_0 = 2.4453 \cdot 10^{-8} \text{ W } \Omega / \text{ K}^2$ [34] can be applied to describe the electronic contribution. However, for nondegenerate semiconductors and especially for materials with charge carriers of both signs, the electronic contribution significantly increases, resulting in a deviation of the Sommerfeld value, as stated by Ioffe [5]. Thus, the relationship may lead to questionable results when applied to all kinds of thermoelectric materials and must be considered carefully. As a result, doping may have a nonnegligible influence on the electronic contribution to the thermal conductivity.

1.3. Thermoelectric Materials for High-Temperature Applications

As state-of-the-art materials for thermoelectric power conversion, bismuth telluride (Bi_2Te_3) and lead chalcogenide PbX ($X = \text{S}, \text{Se}$ or Te) compounds long exhibited the highest zT near room temperature and approximately 600 to 700 K, respectively [35]. However, due to the toxicity of telluride and lead, investigations into less toxic alternatives have attracted strong attention in recent years. Several promising materials or material classes have been reported since and have been discussed in detailed reviews, e.g., copper and tin chalcogenides [35], oxide-based materials [9,36], intermetallic compounds [8,37], and organic polymers [13,38]. Since each material typically has an optimum temperature range for its most efficient thermoelectric power conversion, the materials do not necessarily compete but complement each other with respect to a specific application. Figure 2 shows the zT values of several different thermoelectric material classes as a function of temperature. There are multiple promising alternatives for commercially used bismuth telluride at high operating temperatures.

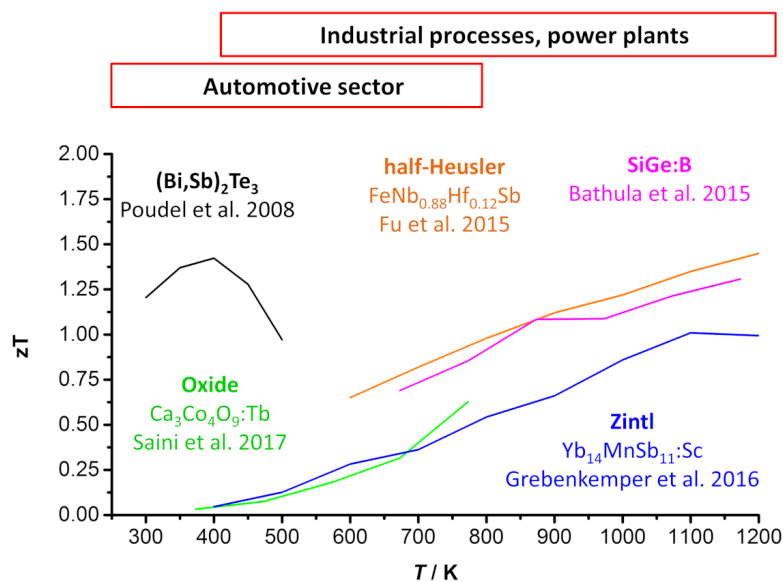


Figure 2. zT values as a function of temperature for several thermoelectric material classes [21,22,39–41]. While bismuth telluride shows the highest zT value at low temperatures, different kinds of materials are interesting for high-temperature applications.

In this review, we take a closer look at these promising materials for high-temperature applications (>700 K), e.g., power plants, industrial processes, and the automobile industry [20,42]. Therefore, oxide-based materials and several intermetallic compounds such as Zintl phases and half-Heusler compounds will be discussed and compared in terms of the power factor and the figure of merit zT . In this context, the focus is on the thermoelectric properties at the material level. Please note that the utilization of thermoelectric materials in a device comes alongside additional important tasks such as contact resistivity and the variation in thermoelectric properties in an applied temperature gradient. It has been emphasized that for a thermoelectric device, the average properties, such as the average zT , within the respective temperature range are the key parameters instead of the peak properties [43–45]. As mentioned, within this review, the discussed thermoelectric compounds will only be evaluated at their respective material level.

2. Oxides and Oxyselenides

2.1. Thermoelectric Oxides

Oxide-based thermoelectric materials generally exhibit an inferior zT compared to that of telluride and selenide compounds, but show a much higher chemical and thermal stability, thus allowing high operating temperatures and large temperature gradients [46]. Consequently, such materials are very promising for high-temperature applications in areas such as the automobile sector or industrial furnaces. Additionally, raw materials of such oxide-based ceramics are less toxic than other materials and therefore easier to process. The first works that predicted good thermoelectric properties in layered crystal structures [47] and the first report of Na_xCoO_2 [48] were published in the mid 1990s. Later, manganites and cobaltites, which show strong spin and orbital fluctuations in the d -electron system and a strong Jahn–Teller effect, became the focus of research [9]. Today, oxide-based thermoelectric materials represent a group of materials with good chemical and temperature stability. In general, oxide-based thermoelectric materials exhibit high Seebeck coefficients, but only a medium electrical conductivity and moderate thermal conductivity. By adjusting these parameters via nanostructuring, doping, and defect engineering, these materials can be tuned to reach high zT values up to 1. In this context, we will have a close look at p -type layered cobaltites (Na_xCoO_2 , $\text{Ca}_3\text{Co}_4\text{O}_9$, $\text{Bi}_2\text{Ca}_2\text{Co}_2\text{O}_9$) and the most common n -type oxide-based materials (ZnO , CaMnO_3 , SrTiO_3). As already mentioned, the focus of this work is on a comparison and evaluation of the power factor and the figure of merit zT . For a more detailed discussion of the physical properties of thermoelectric oxides, e.g., for oxide-based materials [9,36,49] or BiCuSeO [49–51], the reader is referred to other review articles.

2.1.1. p -Type Layered Cobaltites

Since the discovery of Na_xCoO_2 , several layered cobaltite compounds with analogous structures have been found. In addition to Na_xCoO_2 , two other promising compounds, namely, $\text{Ca}_3\text{Co}_4\text{O}_9$ and $\text{Bi}_2\text{A}_2\text{Co}_2\text{O}_9$ ($A =$ alkaline-earth metal), will be discussed. Figure 3 shows the crystal structures of these compounds. Na_xCoO_2 consists of a hexagonal-layered structure with CoO_2 sheets separated by disordered Na layers. In $\text{Ca}_3\text{Co}_4\text{O}_9$ and $\text{Bi}_2\text{A}_2\text{Co}_2\text{O}_9$ ($A =$ alkaline-earth metal), the Na layer is replaced by Ca_2CoO_3 or $\text{Bi}_2\text{A}_2\text{O}_4$ substructures, respectively. In these structures, the CoO_2 sheets represent an electron-conducting layer, which is described as an ‘electron crystal’, while the salt-like separating layers work as a ‘phonon glass’ and reduce the thermal conductivity of the material, resulting in a high zT [1,46].

The thermoelectric parameters of these layered cobaltites are strongly influenced by the exact stoichiometry of the compound. In Na_xCoO_2 , the amount of Na in the disordered phonon glass layer influences the phonon scattering and the electronic properties [52,53]. In $\text{Bi}_2\text{A}_2\text{Co}_2\text{O}_9$ ($A =$ alkaline-earth metal), the thermoelectric properties can be influenced by the amount of Co [54]. The most investigated compounds of $\text{Bi}_2\text{A}_2\text{Co}_2\text{O}_9$ have $A =$ Ca or Sr [55]. The practical use of

Na_xCoO_2 and $\text{Bi}_2\text{A}_2\text{Co}_2\text{O}_9$ is limited by the volatility of Na and Bi at high temperatures and the hygroscopicity of the compounds. Therefore, $\text{Ca}_3\text{Co}_4\text{O}_9$ represents the most interesting layered cobaltite for thermoelectric applications, especially at high operating temperatures. Due to its structure, which consists of electron conducting layers separated by nonconducting layers that cause phonon scattering, the thermoelectric properties of $\text{Ca}_3\text{Co}_4\text{O}_9$ are highly anisotropic. The in-plane direction is characterized by a high electrical conductivity within the CoO_2 layers, resulting in a high power factor $\sigma\alpha^2$. However, in the out-of-plane direction, the phonon scattering is very high, resulting in an even lower thermal conductivity.

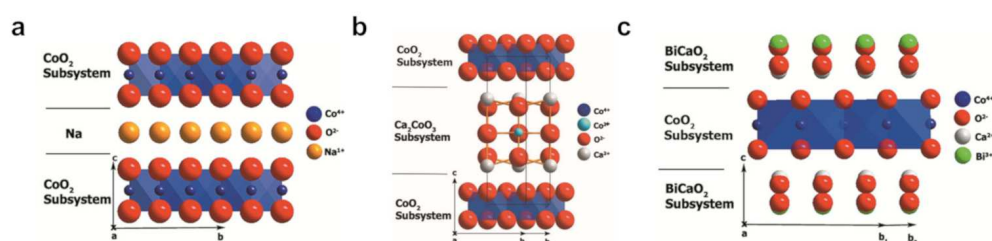


Figure 3. Crystal structures of (a) Na_xCoO_2 , (b) $\text{Ca}_3\text{Co}_4\text{O}_9$ (CCO) and (c) $\text{Bi}_2\text{Ca}_2\text{Co}_2\text{O}_9$. Adapted from [10] with permission from Elsevier.

In general, the thermoelectric properties of bulk $\text{Ca}_3\text{Co}_4\text{O}_9$ can be strongly influenced by the parameters of the synthesis and the sintering method, which have a strong influence on the resulting density, grain size, and orientation of the material [56]. $\text{Ca}_3\text{Co}_4\text{O}_9$ can be synthesized via a solid-state mechanism or a sol-gel procedure. Krolicka et al. investigated the effect of these techniques on the structural and thermoelectric properties, and showed increased zT values in the sample prepared by the sol-gel route due to improved grain alignment [57]. The corresponding ceramics can be prepared by different sintering methods, such as spark plasma sintering (SPS) or pressureless sintering methods, all again leading to different grades of grain orientation and densification [56,58–60]. Bittner et al. showed that the porosity of a bulk $\text{Ca}_3\text{Co}_4\text{O}_9$ ceramic strongly influences the resulting thermoelectric parameters [61]. A high porosity leads to a reduced electrical conductivity and simultaneously decreased thermal conductivity, thus improving the figure of merit zT . Therefore, the porosity as well as the synthesis method is one way to tune such oxide-based materials for an increased power factor (dense ceramic) or zT (high porosity).

As mentioned before, doping and nanostructuring are common ways to tune the thermoelectric parameters of thermoelectric materials. Table 1 shows the figure of merit zT and the power factor $\sigma\alpha^2$ of several doped $\text{Ca}_3\text{Co}_4\text{O}_9$, Na_xCoO_2 and $\text{Bi}_2\text{Ca}_2\text{Co}_2\text{O}_9$ compounds. Here, Na_xCoO_2 exhibits the highest power factor, while $\text{Ca}_3\text{Co}_4\text{O}_9$ is the most promising layered cobaltite when high efficiency and therefore high zT is desired. A nanocomposite containing all three layered cobaltites discussed here is also included, showing promising synergistic effects in its thermoelectric properties as well as its thermal stability [10].

Overall, the thermoelectric properties of layered cobaltites, and all oxide-based materials in general, strongly depend on many parameters, such as the synthesis route, morphology of the crystals, doping, nanostructuring, texturing, and densification into a bulk material, thus leading to a possible control of tuning oxide-based thermoelectric materials to a high power factor $\sigma\alpha^2$ or a high zT value for different application fields. However, more research on the enhancement of the power factor is required to increase the potential of these materials for high-temperature applications.

Table 1. Dimensionless figure of merit zT and power factor $\sigma\alpha^2$ of p -type $\text{Ca}_3\text{Co}_4\text{O}_9$, Na_xCoO_2 and $\text{Bi}_2\text{Ca}_2\text{Co}_2\text{O}_9$ with different dopants.

Material	Dopant	T/K	zT	$\sigma\alpha^2/\mu\text{W cm}^{-1}\text{K}^{-2}$
$\text{Ca}_3\text{Co}_4\text{O}_9$	Cr [62]	1000 K	0.16	3.5
	Sm [63]	1000 K	0.15	2.4
	Tb [39]	1000 K	0.73	11.5
	K [64]	1000 K	0.22	2.85
	Cd [65]	1000 K	0.35	5.25
	Sr [66]	1000 K	0.22	3.95
	Na,W codopants [67]	1000 K	0.21	2.7
	La,Fe codopants [68]	1000 K	0.32	4.15
	NCO,BCCO nanocomposite [10]	1100 K	0.34	6.08
Na_xCoO_2	Ag,Au [69]	1000 K	0.4–0.5	13–15
	Ni [70]	1073 K	-	10.8
	Cu [71]	1000 K	-	15.5
	K, Sr, Y, Nd, Sm, Yb [72]	1000 K	0.36–0.5	6.8–7.3
$\text{Bi}_2\text{Ca}_2\text{Co}_2\text{O}_9$	Na [73]	900 K	-	2.1
	K [74]	1000 K	0.305	1.92
	Pb,La [75]	1000 K	-	1.6–2.2

2.1.2. n -Type Oxides

Around the same time as the first layered cobaltite compounds, other transition metal oxides were reported to have promising thermoelectric properties. Since then, the most studied oxide-based n -type materials have been the aforementioned ZnO, as well as SrTiO₃ and CaMnO₃. ZnO exhibits a hexagonal wurtzite structure with a large direct band gap of 3.44 eV [76], SrTiO₃ has a cubic perovskite structure and is also characterized by a large band gap of 3.25 eV [77] and CaMnO₃ crystallizes in an orthorhombic perovskite structure with an indirect band gap of 0.7 eV [78]. All these materials are characterized by a high Seebeck coefficient and a very low electrical conductivity due to a low carrier concentration without doping [9].

Based on the large band gap of undoped ZnO, increasing the carrier density by doping and defect engineering is used to ensure good thermoelectric properties. For ZnO, doping with Al has been widely studied and shows the highest zT values from 0.3 to 0.45 with moderate power factor values of approximately 5–8 $\mu\text{W cm}^{-1}\text{K}^{-2}$ thus far [79–81]. Again, the synthesis parameters as well as the morphology of the crystals strongly influence the resulting thermoelectric parameters. Han et al. reported, that the zT value of ZnO with nanoparticle morphology is 1.5 times higher than that of a platelet-shaped morphology [82]. In addition to doping, defect engineering is another promising way to enhance the thermoelectric properties, as shown by Tian et al.; by increasing the Al solubility and therefore the carrier concentration and electrical conductivity, the thermal conductivity decreases due to introduced defects [83]. Undoped SrTiO₃ also has a very large band gap, making it electrically insulating. However, by electron doping with group III elements (mostly lanthanides) on the Sr sites or group V elements (Nb, Ta) on the Ti sites, a strong increase in carrier density (up to approximately 10^{20} cm^{-3}) and electrical conductivity (up to 50–1000 S cm^{-1}) in single crystals can be observed [84]. In addition to doping and codoping with several lanthanides, the influences of Sr vacancies have been investigated and were reported to have a positive effect on thermoelectric properties [85,86]. Similarly to SrTiO₃, CaMnO₃ exhibits a high Seebeck coefficient but an electrically insulating character before doping. Here, rare-earth metals as dopants for the Ca sites as well as transition metals for the Ti sites have been investigated. CaMnO₃ and SrTiO₃ have perovskite structures with octahedral coordination of Mn and Ti, respectively. The symmetry of the MnO₆ and TiO₆ octahedrons also influences the resulting parameters. A distortion of the octahedron, e.g., that due to a Jahn–Teller distortion as a result of a partial reduction of Mn⁴⁺ to Mn³⁺ or due to doping with smaller or larger elements, influences the electrical and thermal conductivity of the material [9].

Additionally, *n*-type In₂O₃ was investigated as a promising oxide-based thermoelectric material [20,87]. Undoped In₂O₃ is a semiconductor with a band gap of 1.2 eV that can be strongly influenced via doping. The crystal structure can be described as a cubic bixbyite structure with two nonequivalent cation sites that can be substituted with different dopants [88]. The electron effective mass as well as the carrier concentration of this material strongly depend on the amount of doping within the structure. As a result, a very high carrier mobility can be achieved, making tuning the thermoelectric properties very promising [89]. Bittner et al. [20] presented Sn,Al-doped *n*-type In₂O₃, which reached a comparatively high power factor of 7.1 μW cm⁻¹ K⁻² at 1200 K. However, doped In₂O₃ suffers from its high thermal conductivity and thus shows a noteworthy *zT* only above 1000 K at this time. Nevertheless, doped In₂O₃ represents an interesting *n*-type thermoelectric material for high-temperature applications due to the high power factor resulting from high electrical conductivity.

Table 2 shows the figure of merit *zT* and the power factor $\sigma\alpha^2$ of several doped ZnO, SrTiO₃, CaMnO₃, and In₂O₃ bulk compounds. As described before, the thermoelectric properties also strongly depend on the synthesis method and the sintering parameters. Here, SrTiO₃ compounds exhibit the highest power factor, while the other materials reach *zT* values of approximately 0.3–0.4, except for doped In₂O₃, which only reaches a *zT* value of 0.15.

Table 2. Figure of merit *zT* and power factor $\sigma\alpha^2$ of *n*-type ZnO, SrTiO₃, CaMnO₃, and In₂O₃ with different dopants.

Material	Dopant	T/K	<i>zT</i>	$\sigma\alpha^2/\mu\text{W cm}^{-1}\text{ K}^{-2}$
ZnO	Al [79–81]	1073	0.3–0.45	5–8
	Ni [90]	1073	0.09	5.8
	Al,Ni codopants [91]	773	0.06	5.6
	Ga [92]	973	0.25	12
SrTiO ₃	La,Nb,Sm,Gd,Dy [93]	1073	0.2–0.28	5.5–9
	La [94]	973	0.365	11.6
	Gd [95]	1023	0.37	10.9
	Nb [96]	1023	0.39	11.3
	Nb,Nd codopants [97]	1073	0.315	8.8
CaMnO ₃	Nb [98]	1073	0.325	1.9
	Dy,Ho,Er,Yb [99]	1000	0.15–0.2	2–3.5
	W [100]	1073	0.16	3.2
	Y,Dy codopants [101]	800	0.18	3.1
	Pr,Yb codopants [102]	973	0.24	3.3
In ₂ O ₃	Sn,Al [20]	1200	0.08	7.1
	Ge,Mn,Zn [20]	1200	0.15	3.6

2.2. BiCuSeO

Doped BiCuSeO is one of the newest and most promising thermoelectric materials. The first works presenting the thermoelectric properties of this compound were published from 2010 to 2012 [103–105]. BiCuSeO is one of several isostructural RMChO (R = Bi, Ce to Dy; M = Cu or Ag; Ch = S, Se or Te) compounds and exhibits a two-dimensional layered structure with Bi₂O₂ and Cu₂Se₂ layers, as shown in Figure 4a–d [50]. Due to this layered structure, BiCuSeO also shows anisotropic thermoelectric properties, which strongly depend on the synthesis method and the sintering parameters, analogous to the layered cobaltite compounds [50,106,107]. Due to the similar behavior between BiCuSeO and the oxide-based cobaltites, the former material is discussed here, although it is an oxyarsenide and not an oxide material. BiCuSeO can be synthesized via hydrothermal methods, solid state reactions, sol-gel methods, or mechanical alloying. The bulk materials are again prepared via cold-pressing, hot-pressing, or SPS [50,51,108–110]. The electrical conductivity of undoped BiCuSeO is relatively low because of a low carrier concentration and carrier mobility, while the material exhibits an exceptionally high Seebeck coefficient of approximately 450 μV K⁻¹ and a very low thermal conductivity of approximately

$0.4 \text{ W m}^{-1} \text{ K}^{-1}$ [50,111]. Based on this, BiCuSeO can be described as a high- zT material but offers a relatively low power factor $\sigma\alpha^2$ comparable to those of the layered cobaltites. Although a very high $zT > 1$ can be reached. Additionally, BiCuSeO struggles with thermal stability in an air atmosphere showing surface oxidation at 573 K and complete decomposition at 773 K [112].

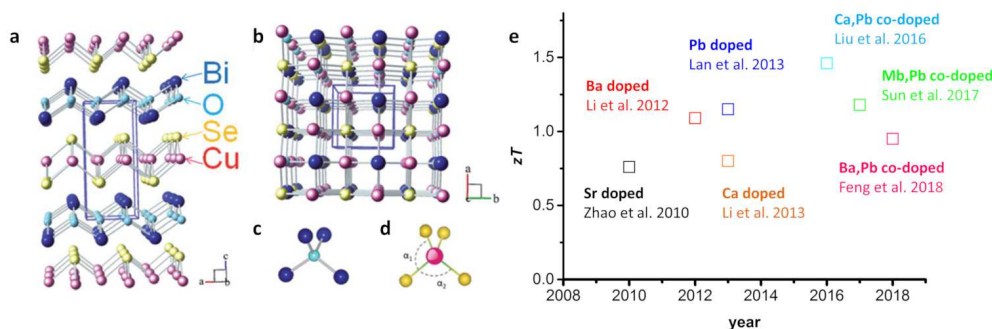


Figure 4. Crystal structure of BiCuSeO (a) along the b-axis and (b) along the c-axis; (c) Bi_4O coordination tetrahedra, and (d) CuSe_4 coordination tetrahedra. Reproduced from [50] with permission from The Royal Society of Chemistry; (e) zT values of various doped bulk BiCuSeO materials under an inert gas atmosphere [11,103,105,113–116].

To improve the thermoelectric properties of BiCuSeO, adjusting the electrical conductivity by enhancing the carrier concentration via doping has been extensively studied. For this purpose, element doping with divalent cations at Bi sites to enhance the p -type electron conduction is very promising. Here, doping and codoping with various elements have been investigated. Figure 4e shows the reported peak zT of various doped BiCuSeO materials in recent years.

BiCuSeO is an intrinsic p -type semiconductor due to Bi and Cu vacancies. Recently, Pan et al. realized n -type BiCuSeO by iron incorporation [117] and Zhang et al. [118] presented the realization of n -type BiCuSeO by filling these vacancies with additional Bi and Cu and simultaneously introducing Br and I at the Se site for electron doping; the above resulted with Seebeck coefficients of up to $-550 \mu\text{V K}^{-1}$.

2.3. Comparison of Oxides and Oxyselenides

Overall, the discussed oxide-based thermoelectric materials exhibit good zT values of approximately 0.2–0.8 with the oxyselenide compound BiCuSeO reaching zT values >1 , while generally showing a medium power factor of $1\text{--}11 \mu\text{W cm}^{-1} \text{ K}^{-2}$. Preparation parameters, doping, defect engineering, and nanostructuring can be utilized to tune the material behavior, thus enhancing the power factor or decreasing the thermal conductivity to reach higher zT values. Figure 5 shows the type-I and type-II Ioffe plots and zT plots for several of the doped p - and n -type oxide-based bulk materials and oxyselenides. Here, it can be easily seen that doped BiCuSeO and doped SrTiO_3 exhibit the highest power factor in relation to electrical conductivity and are therefore the closest to the desired area. In comparison, Figure 5b displays the related zT values of the materials, where the BiCuSeO and $\text{Ca}_3\text{Co}_4\text{O}_9$ reach the highest zT values. However, the BiCuSeO is not stable in an air atmosphere, as mentioned before. As oxide-based materials are of special interest for high-temperature applications, enhancement of the power factor and thus increasing the resulting power output must be further investigated.

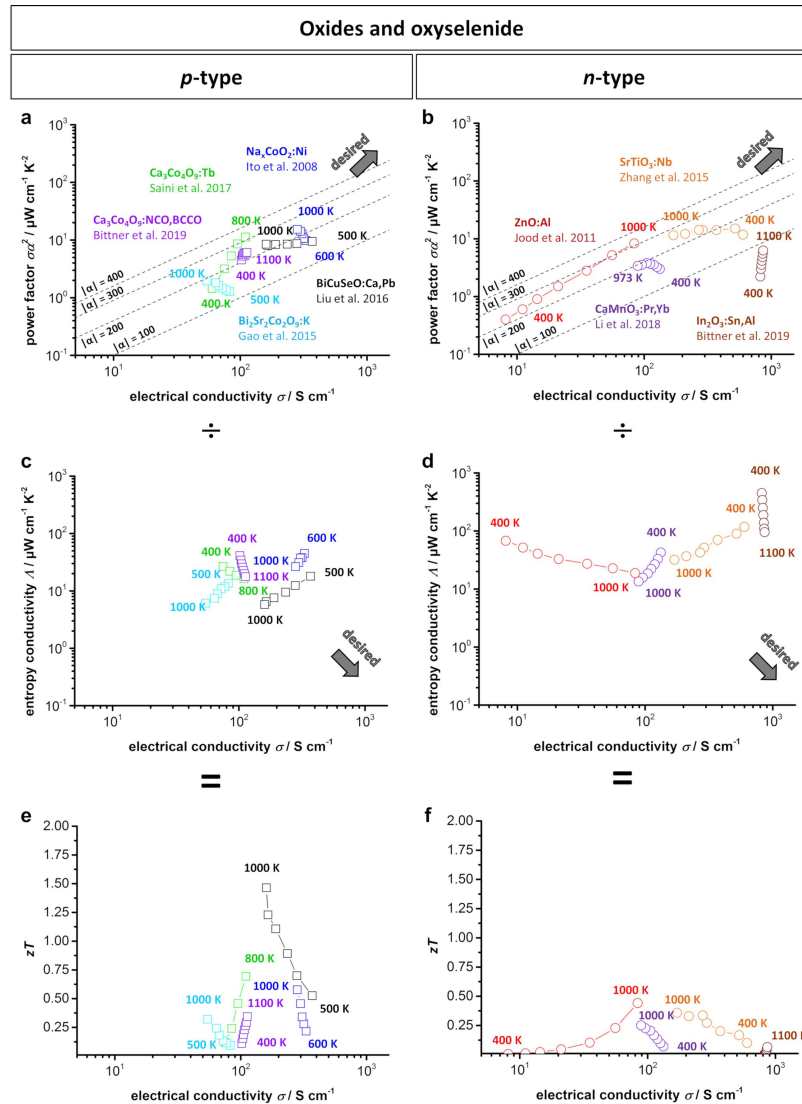


Figure 5. (a) *p*-type; (b) *n*-type type-I Ioffe plots; (c) *p*-type; (d) *n*-type type-II Ioffe plots and (e) *p*-type and (f) *n*-type zT -electrical conductivity plots for several doped oxitic thermoelectric materials and BiCuSeO [10,11,39,69,74,80,96,102]. Dashed lines show the corresponding absolute values of the Seebeck coefficient α given in $\mu\text{V K}^{-1}$. In the type-I Ioffe plot, a desired material would be located at a high power factor and simultaneously high electrical conductivity in the top right. In the type-II Ioffe plot, a desired material would be located at a low entropy conductivity and simultaneously high electrical conductivity in the bottom right. Note that the data in Ioffe plots of type-I and type-II can be divided by each other according to Equation (2) to give the dimensionless figure of merit zT as a function of the electrical conductivity.

3. Metals and Intermetallics

3.1. Zintl Phases

Zintl phases are high-melting intermetallic compounds that are characterized by an ionic structure containing covalently bonded polyanions that build an ‘electron crystal’, while the cation layers act as a ‘phonon glass’. Although this form of intermetallics was discovered in the 1930s and has been highly

investigated since, the first reports about their good thermoelectric properties were not published until 2005 [119]. The thermoelectric properties of many different Zintl families and structures have been investigated. The general composition of a Zintl phase can be described as A_aBX_x with A = active, electropositive metal (mostly alkaline and earth alkaline metals); X = noble, electronegative metal from group 13, 14 and 15, and B = ternary transition metal (Zn, Cd, Mn). Based on this, different groups of Zintl phases can be named after their stoichiometry, e.g., 14-1-11 compounds such as $Yb_{14}MnSb_{11}$. In Figure 6 the T -dependent zT values of several p - and n -type Zintl groups can be seen. The investigated Zintl compounds exhibit varying zT values between 0.5 and 1.5. Due to their complex structure, Zintl phases are usually characterized by a very low glass-like thermal conductivity. The electronic structure strongly depends on the respective material, varying between extremely low carrier mobility and high carrier concentration in 0D 14-1-11 compounds, and very high carrier mobility and low carrier concentration in 2D 1-2-2 compounds [8]. In this section, several p -type (14-1-11, 5-2-6, 9-4.5-9, and 1-2-2) and the most recently investigated n -type 1-2-2 Zintl compounds will be discussed. Again, the reader is referred to other review articles for more details on the respective physical properties of Zintl phases [8,49,120].

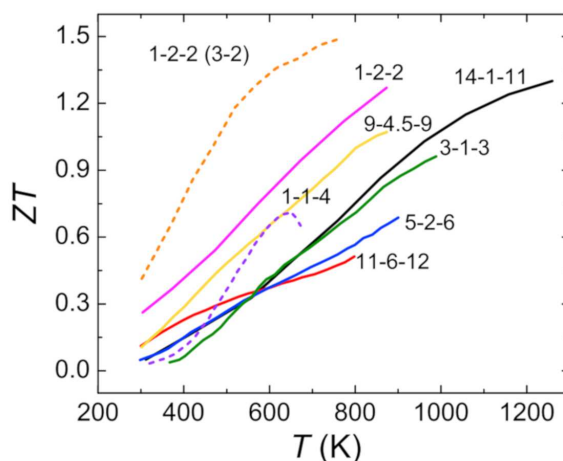


Figure 6. Temperature-dependent zT -values of Zintl phases with different stoichiometries. Solid lines represent p -type Zintl phases and dashed lines represent n -type Zintl phases. Different Zintl families are named after their respective stoichiometry (see also Table 3). Reused from [8] with permission from Elsevier.

3.1.1. p -Type Zintl Phases

Currently, the best p -type Zintl family are the 14-1-11 compounds, reaching a $zT > 1$ at an operating temperature of up to 1200 K. These 14-1-11 compounds with the general formula $A_{14}MPn_{11}$ (A = alkaline-earth or rare earth element, M = Al, Mn, Zn, Ga, Nb, In or Cd and Pn = group 15 element) exhibit covalently bonded $[MPn_4]^{9-}$ tetrahedra and $[Pn_3]^{7-}$ linear components with Pn^{3-} and A^{2+} ions [121]. Due to their large unit cell and semiconductor nature with low electrical resistivity and low thermal conductivity, these compounds are very promising candidates for achieving good thermoelectric properties via doping. Within this family, $Yb_{14}MnSb_{11}$ showed the highest zT values of up to 1.3 [122]. Compared to its isostructural analog $Yb_{14}AlSb_{11}$, which was the first reported 14-1-11 Zintl compound, $Yb_{14}MnSb_{11}$ has the Al^{3+} replaced by Mn^{2+} resulting in p -type conduction. To optimize the extremely high carrier concentration of approximately 10^{21} cm^{-3} , several different dopants at various sites have been investigated, e.g., La, Ca, Sc and Y at the Yb site [41,123,124] or Al and Mg at the Mn site [122]. Several doped 14-1-11 Zintl compounds are shown in Table 3. The resulting power factor is approximately $5\text{--}10 \mu\text{W cm}^{-1} \text{ K}^{-2}$ and therefore, slightly higher than

that of oxide-based materials. $\text{Yb}_{14}\text{MnSb}_{11}$ is usually prepared by a Sn-flux method or ball milling and densification via hot pressing or SPS sintering.

The 11-6-12 compounds are somewhat newly investigated thermoelectric materials. In 2014, the first work on the thermoelectric properties of *p*-type $\text{Eu}_{11}\text{Cd}_6\text{Sb}_{12}$ was published [125]. The 11-6-12 compounds exhibiting a $\text{Sr}_{11}\text{Cd}_6\text{Sb}_{12}$ structure type consist of $[\text{Cd}_6\text{Sb}_{12}]^{22-}$ ribbons forming a 1D structure filled with Sr^{2+} cations [126] and are mostly prepared by the Sn-flux method. Due to the infinite 1D structure of polyanions, these compounds feature comparatively high thermal conductivity. For Zn-doped $\text{Sr}_{11}\text{Cd}_6\text{Sb}_{12}$ a *zT* of 0.5 with a power factor of $5.6 \mu\text{W cm}^{-1} \text{K}^{-2}$ could be achieved [127]. The rather low power factor in 11-6-12 compounds is mainly due to the low carrier mobility of approximately $20\text{--}30 \text{ cm}^2 \text{V}^{-1} \text{s}^{-1}$ [127]. However, investigations of thermoelectric 11-6-12 have only started, and further optimization and tuning are still the focus of research. Similarly, the thermoelectric properties of 5-2-6 Zintl compounds were also recently reported. It can be described by the general formula $\text{A}_5\text{M}_2\text{Pn}_6$ with A = alkaline earth or rare earth metal, M = trivalent metal and Pn = As, Sb or Bi. The 5-2-6 compounds are mainly produced via ball milling and hot pressing. Within this family, the two basic structure types are $\text{Ca}_5\text{Ga}_2\text{As}_6$ and $\text{Ca}_5\text{Al}_2\text{Bi}_6$, which both consist of infinite $[\text{M}_2\text{Pn}_6]^{10-}$ chains and A^{2+} cations [128]. A peak *zT* of 0.7 with a power factor of $6.5 \mu\text{W cm}^{-1} \text{K}^{-2}$ can be reached in Zn-doped $\text{Ga}_5\text{In}_2\text{Sb}_6$ [129]. Several other doped materials of the 11-6-12 and 5-2-6 families are shown in Table 3.

The 9-4+x-9 Zintl compounds with a general formula of $\text{A}_9\text{M}_{4+x}\text{Pn}_9$ where A = Ca, Sr, Eu, or Yb, M = transition metal and Pn = Bi or Sb also consist of infinite ribbons of $[\text{M}_4\text{Pn}_9]^{19-}$ components and exhibit partially filled interstitial sites filled with transition metal [130]. Therefore, the thermoelectric properties can be influenced by occupancy of the interstitial sites and by the exact stoichiometry [131]. To date, several doped and undoped compounds in this family have been investigated, including $\text{Yb}_9\text{Mn}_{4+x}\text{Sb}_9$ [132], $\text{Eu}_9\text{Cd}_{4+x}\text{Sb}_9$ [133], and $\text{Ca}_9\text{Zn}_{4+x}\text{Sb}_9$ [131], reaching *zT* values of approximately 0.7 and a power factor of $5\text{--}7 \mu\text{W cm}^{-1} \text{K}^{-2}$ (compare Table 3). Here, again the Sn-flux technique as well as a combination of ball milling and hot pressing or SPS were utilized for preparation.

Table 3. Dimensionless figure of merit *zT* and power factor $\sigma\alpha^2$ of several *p*-type Zintl phases with different dopants.

Composition	Materials	Dopant	T/K	<i>zT</i>	$\sigma\alpha^2/\mu\text{W cm}^{-1} \text{K}^{-2}$	
14-1-11	$\text{Yb}_{14}\text{MnSb}_{11}$ [121]	-	1200 K	1.02	6.1	
		Al [122]	1200 K	1.28	8.82	
		Sc [41]	1200 K	1.02	8.38	
	$\text{Yb}_{14}\text{MgSb}_{11}$ [134]	Y [41]	1200 K	1.01	6.85	
		-	1200 K	1.03	6.5	
		$\text{Sr}_{14}\text{MgBi}_{11}$ [135]	-	1200 K	0.71	9.5
11-6-12	$\text{Eu}_{11}\text{Cd}_6\text{Sb}_{12}$	Zn [127]	800 K	0.51	5.55	
		As [125]	800 K	0.185	1.69	
5-2-6	$\text{Ca}_5\text{Al}_2\text{Sb}_6$	Na [136]	1050 K	0.605	4.44	
		Zn [137]	800 K	0.4	3.75	
		Mn [138]	850 K	0.42	4.12	
	$\text{Ga}_5\text{In}_2\text{Sb}_6$	Zn [129]	950 K	0.72	6.56	
		$\text{Eu}_5\text{In}_2\text{Sb}_6$	Zn [139]	800 K	0.28	4.08
		Cd [140]	850 K	0.46	5.2	
$\text{Sr}_5\text{In}_2\text{Sb}_6$	Zn [141]	800 K	0.36	4.13		
9-4+x-9	$\text{Yb}_9\text{Mn}_{4.2}\text{Sb}_9$ [132]	-	1000 K	0.74	4.53	
		$\text{Ca}_9\text{Zn}_{4+x}\text{Sb}_9$	Cu [131]	850 K	0.71	6.72
1-2-2	CaZn_2Sb_2	Na, Mg [142]	800 K	0.85	9.24	
		Cd [143]	650 K	1.05	22.5	
		Mn [144]	650 K	1.13	10	
	YbCd_2Sb_2	Zn [145]	700 K	1.22	19.2	
		Mg [146]	650 K	1.06	16.8	
		Na [147]	850 K	0.88	12.3	
	CaMg_2Bi_2	Yb [148]	850 K	0.96	12.2	
		Ca [149]	850 K	1.26	13.5	
		Na [150]	750 K	0.58	4.2	
$\text{Eu}_{0.5-x}\text{Yb}_{0.5-x}\text{Mg}_2\text{Bi}_2$	Mg_3Sb_2					

Next, to the 14-1-11 compounds, the family of 1-2-2 Zintl phases show very good thermoelectric properties, reaching a $zT > 1$. This group can be described as AB_2X_2 with $A = Ca, Ba, Sr, Yb$ or Eu , $B = Mn, Zn, Cd$ or Mg and $X = As, Sb$ or Bi . The $CaAl_2Si_2$ -type structure contains two-dimensional $[B_2X_2]^{2-}$ sheets separated by A^{2+} cations [151]. Most p -type 1-2-2 Zintl phases are characterized by an extremely high p -type carrier concentration due to the vacancies on the A cation sites. Thus, substitution and doping at this site proves to be promising for tuning the thermoelectric properties. Subsequently, doped $EuZn_2Sb_2$ [143] and doped $YbCd_2Sb_2$ [144–146] reached zT values above $zT = 1$. Shuai et al. reported a zT value of 1.3 and a power factor of $13.5 \mu W cm^{-1} K^{-2}$ for $Eu_{0.5-x}Yb_{0.5-x}Mg_2Bi_2$ [149]. Additionally, binary p -type 1-2-2 compounds with $A=B$, e.g., Mg_3Sb_2 , have been widely investigated [150,152]. However, due to their high resistivity, only a moderate zT at high temperatures can be reached. The thermoelectric properties of several ternary and binary 1-2-2 Zintl compounds are shown in Table 3. Similar to that of the other families, the 1-2-2 Zintl compounds are mostly prepared by melting or ball milling and densification via hot pressing or SPS.

3.1.2. n -Type Zintl Phases

As described above, several p -type 1-2-2 compounds have been investigated resulting in zT values of up to 1.3. In this group, the stoichiometric Mg_3Sb_2 has taken a special role in research, due to its characteristically low carrier concentration, which opens a pathway to thermoelectric n -type Zintl phases [8]. Since the first report, in 2014, of n -type conduction in Mn-doped Mg_3Sb_2 [153], many different dopants have been investigated. Doping with Te as an electron donor and Bi to reduce the lattice thermal conductivity proved to be an effective way to realize high zT values in n -type Zintl phases. Most recently, Chen et al. [154] reached a zT value of 1.7 at a power factor of $20 \mu W cm^{-1} K^{-2}$ by combining Mn doping at the Mg site and Te and Bi doping at the Sb site. Table 4 gives an overview of several doped n -type Zintl phases based on Mg_3Sb_2 . To date, zT values of approximately 1.5–1.7 and a power factor of up to $20 \mu W cm^{-1} K^{-2}$ have been reached.

Table 4. Dimensionless figure of merit zT and power factor $\sigma\alpha^2$ of several n -type Zintl phases with different dopants.

Basis	Material	T/K	zT	$\sigma\alpha^2/\mu W cm^{-1} K^{-2}$
Mg_3Sb_2	$Mg_{3+\delta}Sb_{1.99}Te_{0.01}$ [155]	700 K	0.61	9.16
	$Mg_{3+\delta}Sb_{1.48}Bi_{0.48}Te_{0.04}$ [156]	700 K	1.59	12.56
	$Mg_{3+\delta}Sb_{1.48}Bi_{0.49}Te_{0.01}$ [157]	700 K	1.45	15.14
	$Mg_{3+\delta}Nb_{0.15}Sb_{1.5}Bi_{0.49}Te_{0.01}$ [158]	700 K	1.52	18.5
	$Mg_{3+\delta}Mn_{0.025}Sb_{1.5}Bi_{0.49}Te_{0.01}$ [154]	700 K	1.71	20.02

3.1.3. Comparison of Zintl phases

Figure 7 shows the type-I and type-II Ioffe plots and zT plots from several of the doped p -type and n -type bulk Zintl materials. As described above, within the p -type Zintl phases, the 14-1-11 compounds show the best temperature stability up to 1200 K and reach the highest zT values. However, the Ioffe plots show that ternary 1-2-2 compounds and the 9-4+x-9 compounds feature a comparable or even higher power factor than 14-1-11 compounds at lower temperatures. Improvement of temperature stability could therefore lead to even higher power outputs at high operating temperatures. Within the n -type 1-2-2 Zintl phases, heavily doped $Mg_{3+\delta}Sb_2$ exhibits the highest zT reported for Zintl phases thus far and a high power factor of approximately $20 \mu W cm^{-1} K^{-2}$. However, the operating temperature is limited to approximately 700 K for the heavily doped $Mg_{3+\delta}Sb_2$ and up to 1000 K for previously reported compounds. Additionally, the Ioffe plots show a maximum power factor and electrical conductivity at approximately 700 K with decreasing values afterward. Enhancing the temperature stability and improving the thermoelectric properties at temperatures above 700 K may lead to a very promising n -type Zintl phase for application at high temperatures.

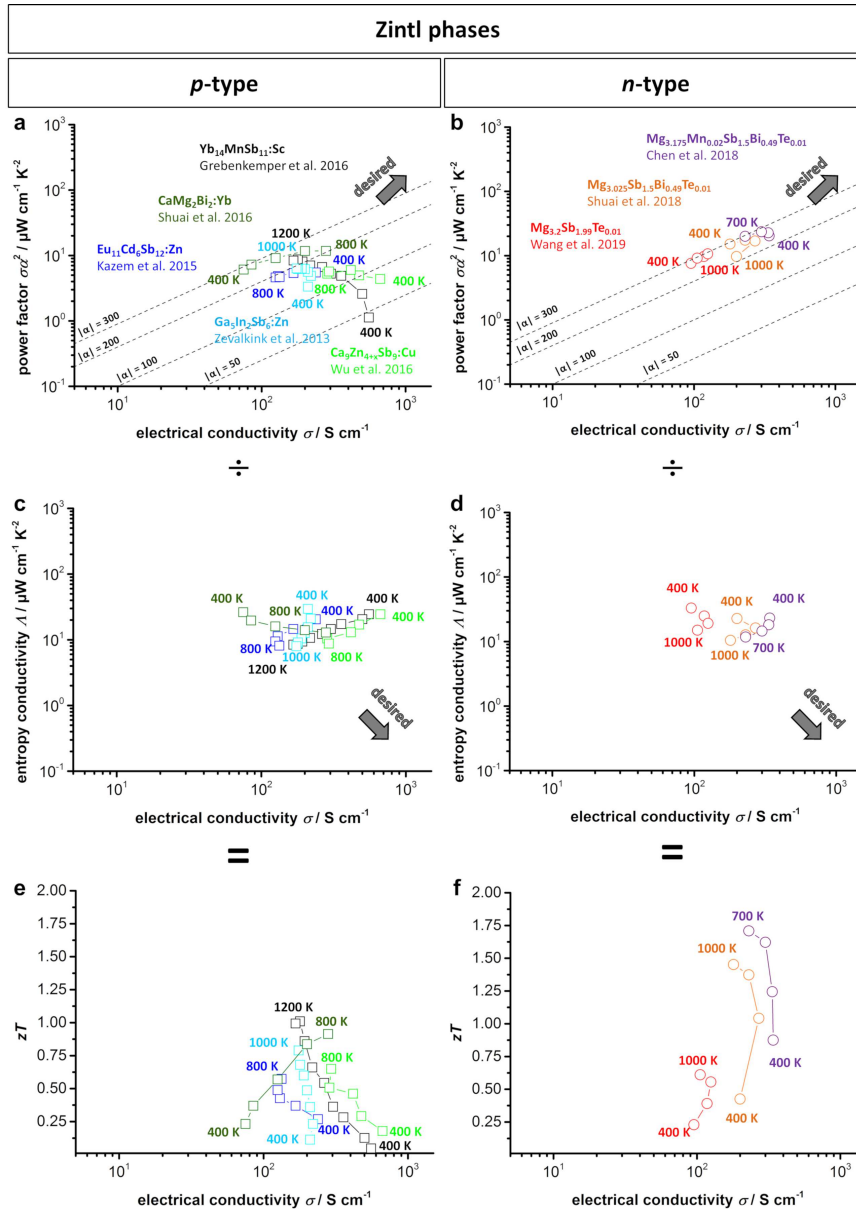


Figure 7. (a) *p*-Type; (b) *n*-type type-I Ioffe plots; (c) *p*-type; (d) *n*-type type-II Ioffe plots as well as (e) *p*-type and (f) *n*-type *zT*-electrical conductivity plots of several doped Zintl materials [41,127,129,131,148,154,155,157]. Dashed lines show the corresponding absolute values of the Seebeck coefficient α given in $\mu\text{V K}^{-1}$.

3.2. Heusler and Half-Heusler Compounds

Heusler compounds are intermetallics with the formula X_2YZ and are characterized by their cubic structure with the space group $Fm\bar{3}m$ [159]. The X and Y within this formula represent transition metals, while Z is a main group element. The half-Heusler compounds are derived from this and have the formula XYZ with the $F\bar{4}3m$ space group [7,159]. The structures for both compounds are displayed in Figure 8. The full-Heusler structure (Figure 8a) can be described by four interpenetrating face-centered-cubic sublattices, where two of them are equally occupied by the X. In contrast, one

of the equally occupied sublattices is vacant for the half-Heusler compounds (Figure 8b) [7]. The difference in the structures greatly affects the valence electrons and thereby the band structures of both compounds, typically leading to increased effective mass carrier concentrations and a high power factor for half-Heusler compounds, which is the reason for our focus on them within this review [159]. Half-Heusler materials are generally stable if 18 valence electrons are present, because only bonding states are occupied in this case [159]. Notably, this restricts the choice of elements for stable phases. The resulting phases usually show semiconducting behavior, e.g., with band gaps of 0.5 eV for $XNiSn$ compounds or semimetallic behavior for $(Zr,Hf)CoSb$ compounds [159–161]. This narrow electronic band structure results in a characteristically high power factor for half-Heusler compounds in comparison to other thermoelectric material classes [159]. Since the states near the Fermi level are mainly based on $d-d$ orbital bonding, the density of states results in large Seebeck coefficients and high electrical conductivities [162]. A more detailed discussion of the physical properties of different half-Heusler compounds can be found in the respective review articles [35,37,49,159,163].

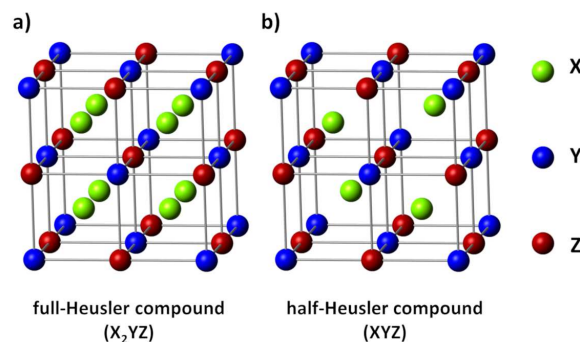


Figure 8. (a) Crystal structure of (a) full-Heusler- (X_2YZ) and (b) half-Heusler-compounds (XYZ). The half-Heusler compounds exhibit an unoccupied sublattice of X resulting in promising thermoelectric characteristics.

The first studies on half-Heusler compounds started in the early 1990s, but intensified with respect to thermoelectrics in the 2000s [164]. Recently, Poon presented an approach for dividing the advances of half-Heusler development for thermoelectrics into three different generations [163]. The first generation in the 2000s was characterized by alloying and doping as main modification factors providing zT values below 1, while in the second generation around 2010, more advanced synthesis techniques were introduced, namely, SPS for densification and nanostructuring, which led to zT values of approximately 1. In the current third generation, band engineering and structure ordering are becoming increasingly famous in addition to the previous techniques, which results in zT values of approximately 1.5 [163]. Advantages of half-Heusler compounds are their nontoxicity and stability to mechanical stress as well as high temperatures [7]. The optimum working temperature with regard to the thermoelectric performance is typically within 700–1000 K when in a vacuum or inert gas. The materials exhibit remarkable oxygen stability, but recent research has shown a sensitivity to oxygen at working temperatures for $TiNiSn$ and $ZrNiSn$, resulting in the formation of oxides at the surface. Thus, the oxygen influence on the thermoelectric properties still needs to be investigated [165,166].

The elements of the half-Heusler compounds usually maintain very high melting points above 1773 K, which means high-temperature alloying, such as arc melting in a chamber with inert gas, is necessary for synthesis [162]. The usage of rather costly elements such as Hf further increases the production costs, which are major disadvantages of half-Heusler compounds despite their excellent thermoelectric properties.

3.2.1. *p*-Type Half-Heusler Compounds

State-of-the-art *p*-type half-Heusler compounds are mainly based on FeNbSb, where Nb is substituted by Ti or Hf as shown in Table 5. By comparing the power factors of the compounds in Table 5, the high zT values were mainly reached by reducing the thermal conductivity with heavy dopants at relatively high doping amounts. The best properties were achieved for FeNb_{0.88}Hf_{0.12}Sb by Fu et al. [22] and reached a power factor of 51 $\mu\text{W cm}^{-1} \text{K}^{-2}$ and a zT value of 1.45. However, a ZrCoBi-based compound recently reached zT values of up to 1.42, opening the way for research at a competing level. A similar half-Heusler system is based on XCoSb (X=Zr or Hf), which shows a decreased power factor at approximately 28 $\mu\text{W cm}^{-1} \text{K}^{-2}$ but simultaneously a lower thermal conductivity compared to that of the FeNbSb-based compounds. The XCoSb compounds play a special role in thermoelectric research due to their possible *p*- and *n*-type doping, both leading to zT values of up to 1. [167,168] Therefore, these compounds can be found in both Tables 5 and 6 depending on their respective dopants.

Table 5. Dimensionless figure of merit zT and power factor $\sigma\alpha^2$ of several *p*-type half-Heusler phases.

Material	<i>T</i> /K	zT	$\sigma\alpha^2/\mu\text{W cm}^{-1} \text{K}^{-2}$
FeNb _{0.88} Hf _{0.12} Sb [22]	1200 K	1.45	51
FeNb _{0.86} Zr _{0.14} Sb [22]	1050 K	0.80	46
FeNb _{0.95} Ti _{0.05} Sb [169]	973 K	0.70	50
FeNb _{0.8} Ti _{0.2} Sb [169]	973 K	1.10	53
ZrCoBi _{0.65} Sb _{0.15} Sn _{0.20} [170]	973 K	1.42	38
Hf _{0.44} Zr _{0.44} Ti _{0.12} CoSb _{0.8} Sn _{0.2} [167]	973 K	1	28

3.2.2. *n*-Type Half-Heusler Compounds

Research on *n*-type half-Heusler compounds mainly focuses on MNiSn (M=Ti, Zr or Hf) compounds as parent materials. These compounds inherit quite remarkable zT values in the range of 0.4–0.55 as pure bulk materials, as shown in Table 6, but these values begin to rise to 1–1.5 when the materials are engineered properly toward improved thermoelectric performances. Reduction of grain size, alloying, and carrier doping are suitable tools to significantly improve the zT value [162]. Another parent material is XCoSb (X=Ti or Nb), which shows rather poor thermoelectric performance as a pure material due to high thermal conductivity, but drastically improves when doped [171,172]. The record zT value of 1.5 was reached with Ti_{0.5}Zr_{0.25}Hf_{0.25}NiSn_{0.998}Sb_{0.002} by Shutoh et al. [173]. Unfortunately, this value cannot be reproduced independently at this time; however, slightly lower values were achieved by similar chemical compositions [37]. As described for *p*-type half-Heusler materials, the XCoSb (X=Zr or Hf) compounds can also show *n*-type behavior when doped accordingly. Here, (Zr_{0.4}Hf_{0.6})_{0.88}Nb_{0.12}CoSb shows a power factor of 27 $\mu\text{W cm}^{-1} \text{K}^{-2}$ and a zT value of 0.99, as demonstrated by Liu et al. [168] in 2018.

Table 6. Dimensionless figure of merit zT and power factor $\sigma\alpha^2$ of several *n*-type half-Heusler phases.

Material	<i>T</i> /K	zT	$\sigma\alpha^2/\mu\text{W cm}^{-1} \text{K}^{-2}$
TiNiSn [174]	775 K	0.4	24
ZrNiSn [175]	1000 K	0.55	33
HfNiSn [175]	1000 K	0.48	35
Ti _{0.5} Zr _{0.25} Hf _{0.25} NiSn _{0.998} Sb _{0.002} [173]	700 K	1.50	62
Hf _{0.6} Zr _{0.4} Hf _{0.25} NiSn _{0.995} Sb _{0.005} [176]	900 K	1.20	47
NbCoSb _{0.8} Sn _{0.2} [172]	973 K	0.56	21
TiFe _{0.15} Co _{0.85} Sb [177]	850 K	0.45	22
(Zr _{0.4} Hf _{0.6}) _{0.88} Nb _{0.12} CoSb [168]	1173 K	0.99	27

3.2.3. Comparison of Half-Heusler Compounds

Figure 9 shows type-I and type-II Ioffe plots as well as zT plots from several of the doped p -type and n -type bulk half-Heusler materials. The comparatively high power factor that can be easily seen in the type-I Ioffe plots is attributed to the narrow electronic band structure and d - d orbital bonding, as already discussed. The half-Heusler compounds are therefore especially interesting for thermoelectric generators when a high power output is desired. A comparison of p - and n -type compounds shows similar results for the maximum values of the power factor of approximately $50 \mu\text{W cm}^{-1} \text{K}^{-2}$ and the zT up to 1.5, which results in no clear advantage of one specific type. However, the p -type compounds exhibit slightly higher thermal stability up to 1200 K for FeNbSb-based materials. The high power factor also means a rather high impact of thermal conductivity on the efficiency of a half-Heusler compound. Thus, further engineering is mainly targeted at reducing thermal conductivity.

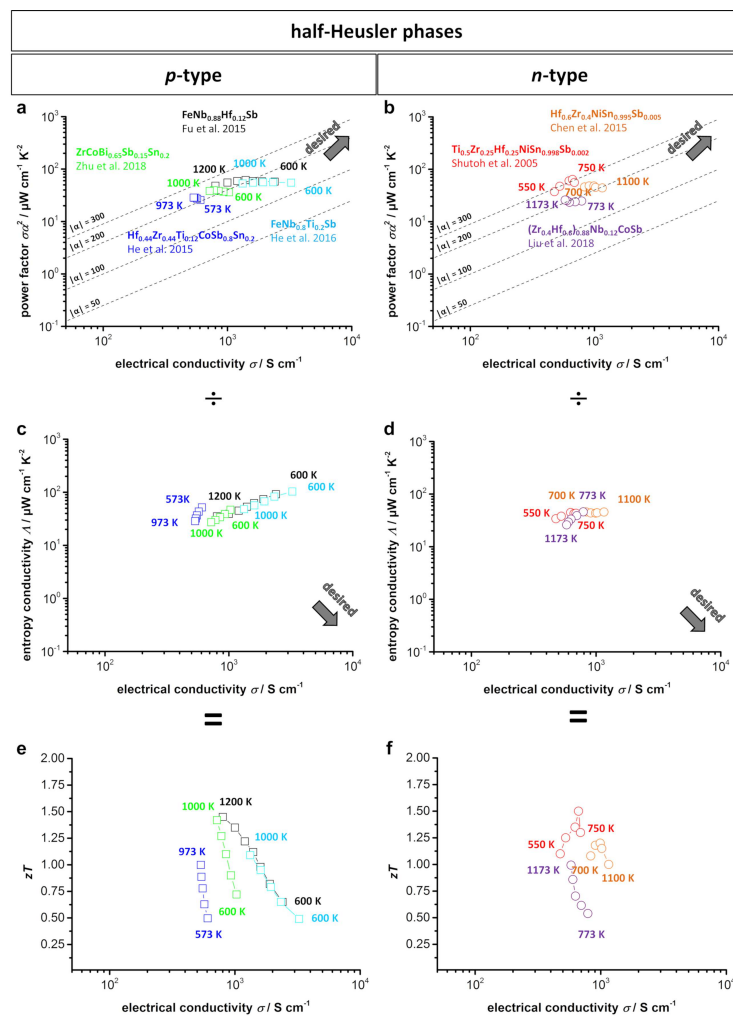


Figure 9. (a) p -Type; (b) n -type type-I Ioffe plots; (c) p -type; (d) n -type type-II Ioffe plots; (e) p -type; (f) n -type zT -electrical conductivity plots of several doped half-Heusler compounds [22,167–170,173,176]. Dashed lines show the corresponding absolute values of the Seebeck coefficient α given in $\mu\text{V K}^{-1}$.

3.3. SiGe Alloys

Electrical supply of deep-space missions was one of the first application fields of thermoelectric power conversion. Here, mostly *n*- and *p*-type silicon–germanium alloys have been used [178]. This intermetallic material with a diamond crystal structure is characterized by a high thermal stability of up to 1200–1300 K when tested in vacuum. While Si exhibits a very high thermal conductivity of $148 \text{ W m}^{-1} \text{ K}^{-1}$, the introduction of Ge atoms in the Si matrix strongly enhances the phonon scattering, resulting in a thermal conductivity of approximately $2\text{--}5 \text{ W m}^{-1} \text{ K}^{-1}$ and a $zT > 1$ in nanostructured SiGe alloys [120]. Achieving *p*- and *n*-type conduction is realized via doping with B [40] or Ga [179] (*p*-type) and P [180] or Sb [181] (*n*-type). The thermoelectric properties can be strongly influenced by the exact stoichiometry of the SiGe alloy. Materials with an ideal ratio of $\text{Si}_{80}\text{Ge}_{20}$ have been found and widely studied. In SiGe alloys, the large difference in the mean free path between electron (approximately 5 nm) and phonon (approximately 200–300 nm) contributions leads to a strong influence of nanostructuring in a range of 10–100 nm, which reduces the thermal conductivity without significantly reducing the electrical conductivity [182]. Therefore, nanostructuring [183–185] and the use of nanoinclusions [184,186–189] are common strategies to further improve the thermoelectric properties of SiGe alloys. For preparation of SiGe alloys, solid-state ball milling [180,183,186,187,190–194] or melt spinning (MS) [182,189] in combination with subsequent SPS are commonly used. Bathula et al. [192] reported a peak zT of 1.72 with a power factor of $28.7 \mu\text{W cm}^{-1} \text{ K}^{-2}$ for *n*-doped $\text{Si}_{80}\text{Ge}_{20}$ with SiC nanoinclusions. In 2016, Ahmad et al. [191] presented a strong increase in *p*-type $\text{Si}_{80}\text{Ge}_{20}$ performance up to a zT of 1.81 and a power factor of $39.05 \mu\text{W cm}^{-1} \text{ K}^{-2}$ via Y_2O_3 nanoinclusions. Table 7 shows the zT value and power factor of several *n*- and *p*-type doped $\text{Si}_{80}\text{Ge}_{20}$ materials.

Table 7. Dimensionless figure of merit zT and power factor $\sigma\alpha^2$ of several doped *p*- and *n*-type SiGe alloys.

Composition	Dopant	Inclusion	T/K	zT	$\sigma\alpha^2/\mu\text{W cm}^{-1} \text{ K}^{-2}$
<i>n</i> -type $\text{Si}_{80}\text{Ge}_{20}$	P [190]	-	1073	1.78	30.3
	P [185]	-	1173	1.3	30.61
	Sb [181]	-	1073	0.61	18.5
	P	SiC [192]	1173	1.72	28.74
	P	Mg_2Si [193]	1173	1.27	29.84
	P	FeSi_2 [194]	1173	1.18	27.8
	P	WSi_2 [187]	1173	1.16	35.27
	<i>p</i> -type $\text{Si}_{80}\text{Ge}_{20}$	B [40]	-	1173	1.22
B [180]		-	1073	0.96	22
Ga [179]		-	1073	0.52	15.5
B		Y_2O_3 [191]	1073	1.81	39.05
B		CrSi_2 [186]	1073	0.65	21.25
B		YSi_2 [189]	1073	0.53	16.57
B		WSi_2 [187]	1173	0.66	17.63

Figure 10 shows the type-I and type-II Ioffe plots and zT plots from several doped $\text{Si}_{80}\text{Ge}_{20}$ alloys. In general, Si-Ge alloys are characterized by a relatively high power factor of approximately $15\text{--}40 \mu\text{W cm}^{-1} \text{ K}^{-2}$ due to their high electrical conductivity, which is why they are located at the top right of the type-I Ioffe plot. The drawback of a simultaneously high thermal conductivity can be mitigated via nanostructuring and nanoinclusions without significantly reducing the electrical conductivity, resulting in zT values of up to 1.7 for *n*-type and 1.8 for *p*-type materials. Combined with a high thermal stability of up to 1200–1300 K in vacuum, Si-Ge alloys are perfect candidates as thermoelectric materials for deep-space missions. Further adjustment of the thermal conductivity of such alloys is especially interesting if a high conversion efficiency is desired.

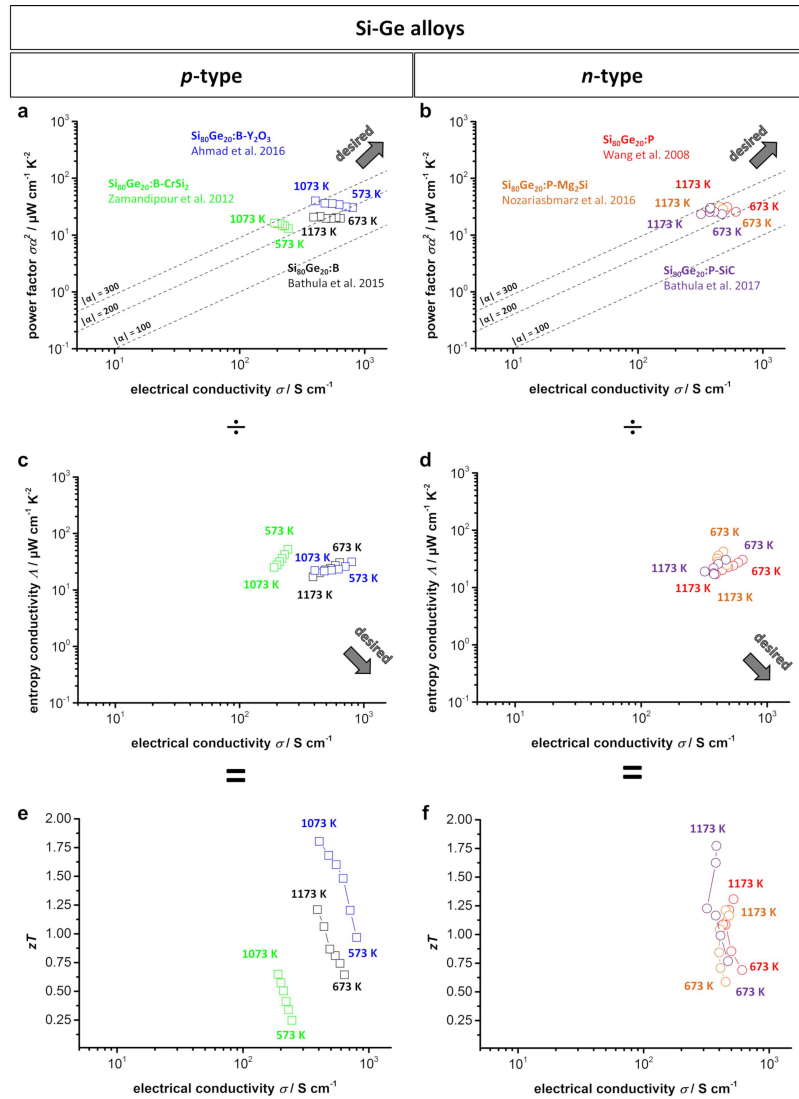


Figure 10. (a) *p*-Type; (b) *n*-type type-I Ioffe plots; (c) *p*-type; (d) *n*-type type-II Ioffe plots; (e) *p*-type; (f) *n*-type zT -electrical conductivity plots of several doped Si-Ge alloys [40,185,186,191–193]. Dashed lines show the corresponding absolute values of the Seebeck coefficient α given in $\mu\text{V K}^{-1}$.

4. Comparison of High-Temperature Thermoelectric Materials

Figure 11 shows the type-I and type-II Ioffe plots and zT plots from several of the doped *p*- and *n*-type materials for possible high temperature applications and their comparison to those of the commercially used Bi_2Te_3 . Here, the half-Heusler compounds exhibit the highest power factor values with a simultaneously high electrical conductivity as a result of their electronic band structure, described above. Therefore, the half-Heusler compounds are the closest to the desired area for both *p*- and *n*-type materials. The conventional Bi_2Te_3 and the SiGe alloys also show a comparably high power factor at a slightly lower electrical conductivity. Of the compared thermoelectric materials, the oxide-based materials have the lowest power factor and electrical conductivity. This trend corresponds to the type-II Ioffe plots, where the half-Heusler compounds and Bi_2Te_3 exhibit the highest entropy conductivity, while the oxide materials show a significantly lower entropy conductivity, especially at high temperatures. Furthermore, the Zintl phases are also characterized by a low thermal

conductivity, which culminates in the n -type Zintl phase of $\text{Mg}_{3.175}\text{Mn}_{0.025}\text{Sb}_{1.5}\text{Bi}_{0.49}\text{Te}_{0.01}$ having the lowest entropy conductivity of all compared n -type materials. As a result, the half-Heusler compounds as well as BiCuSeO show the highest zT values within the p -type materials, and the Zintl compounds have the highest zT value within the n -type materials. As described before, the power factor corresponds to the maximum power output of the material, making the half-Heusler compounds the most interesting bulk materials for high-temperature application from this point of view. Yet, the Zintl compounds and oxyselenides provide a high efficiency in power conversion due to their significantly lower entropy conductivity. The oxide-based thermoelectric materials show comparatively low thermoelectric properties, but are characterized by high chemical and thermal stability, especially in air. As mentioned within the introduction, extension to a functional device always comes alongside additional tasks. In particular, contact resistivity is crucial to reach full potential, when applying highly electrical conducting materials such as half-Heusler compounds in a device.

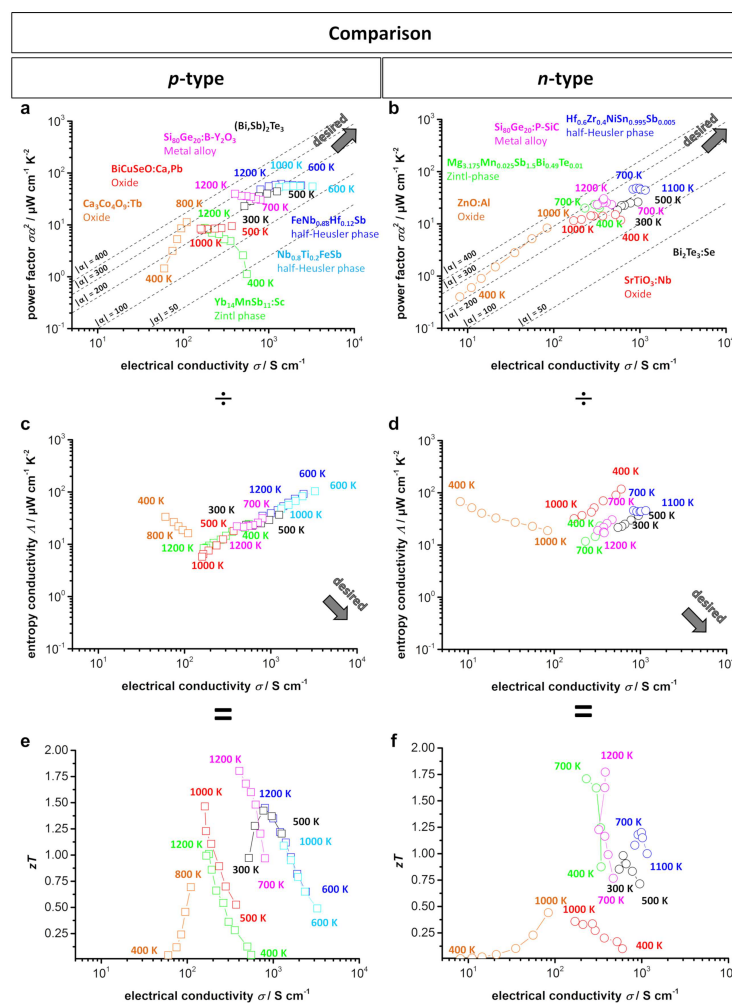


Figure 11. (a) p -type; (b) n -type type-I Ioffe plots; (c) p -type; (d) n -type type-II Ioffe plots; (e) p -type; (f) n -type zT -electrical conductivity plots of several doped oxide materials [11,39,80,96], Zintl phases [41,154], half-Heusler compounds [169,173,176], and Si-Ge alloys [191,192] as compared to doped Bi_2Te_3 [21,195]. Dashed lines show the corresponding absolute values of the Seebeck coefficient α given in $\mu\text{V K}^{-1}$.

A similar comparison of the material properties can be performed by displaying the power factor as a function of the entropy conductivity, shown in Figure 12. Note that the dashed lines within the plot represent the dimensionless zT value. It can be easily observed that within the p -type thermoelectric materials, several compounds from different classes, such as BiCuSeO, SiGe alloys, and half-Heusler alloys, all reach a zT value of up to 1.5, whereas the power factor shows a strong deviation between 10 and 65 $\mu\text{W cm}^{-1} \text{K}^{-2}$. Within the compared n -type materials, the same behavior can be observed, although the materials show overall slightly lower zT values. Therefore, this power factor vs. entropy conductivity plot presents the respective advantages of each kind of thermoelectric material discussed in terms of a high power factor or high zT value.

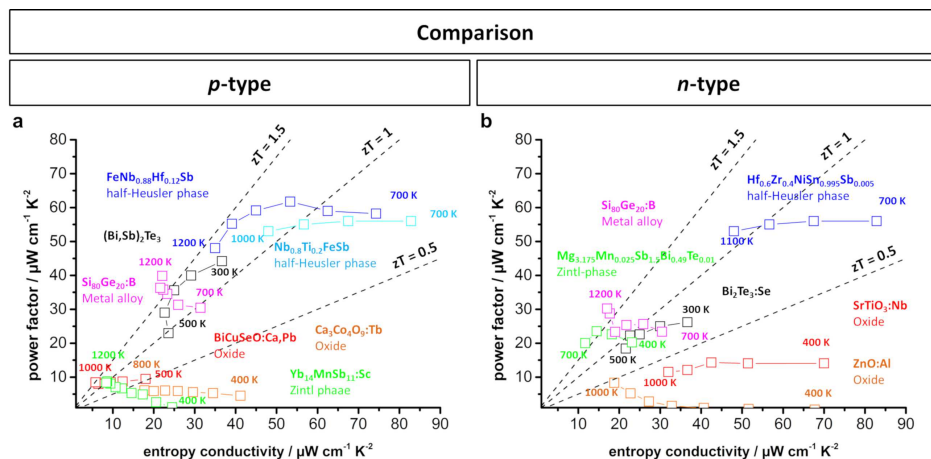


Figure 12. (a) p -Type; (b) n -type power factor vs. entropy conductivity plots of several doped oxide materials [11,39,80,96], Zintl phases [41,154], half-Heusler compounds [169,176,196] and Si-Ge alloys [191,192] as compared to doped Bi_2Te_3 [21,195]. Dashed lines show the corresponding zT values.

In addition to the thermoelectric materials discussed above, there are a few material classes with noteworthy thermal stability of up to 800–900 K, which should also be mentioned here. Cage compounds such as clathrates [197] and skutterudites [198] are both characterized by good electronic transport properties while reducing thermal conductivity by filling the cages with guest atoms [49]. In this way, high zT values of up to 1.3 and 1.7 at 800 K can be reached in multiple filled clathrates [199] and skutterudites [200,201], respectively. However, despite the similarity of these cage compounds, the respective power factor shows a strong variation with approximately 10 $\mu\text{W cm}^{-1} \text{K}^{-2}$ for clathrates [199] and approximately 50 $\mu\text{W cm}^{-1} \text{K}^{-2}$ for skutterudites [201] at 800 K. This also results in a possible tuning for either a high power output or a high conversion efficiency. Last, solid solutions of Mg_2Si intermetallic silicides are also a focus of interest as mid-temperature thermoelectric materials of up to 800 K [49]. Solid solutions of $\text{Mg}_2\text{Si}_{1-x}\text{Ge}_x$ and $\text{Mg}_2\text{Si}_{1-x}\text{Sn}_x$, with an optimized carrier concentration via doping, reached a power factor of approximately 30 $\mu\text{W cm}^{-1} \text{K}^{-2}$ and a zT value > 1 at 800 K [202,203]. For respective applications at mid-temperatures, a similar comparison to this work could be performed for evaluation and comparison of these materials and their respective parameters.

5. Conclusions

Different kinds of bulk thermoelectric materials have been compared with respect to their high-temperature performance and stability. Within the respective thermoelectric material classes, much research has been conducted within recent decades, however, very few works have compared these classes. Here, the concept of using Ioffe plots to compare and evaluate the power factor and the zT value as two different parameters that can be useful for optimization was successfully presented. Hereby, the strengths and weaknesses of each material class were revealed, which could be useful

for prospective research and associated applications. Out of all of the compared materials, the class of half-Heusler compounds exhibited the highest power factor and electrical conductivity, which is applicable for reaching a high power output at high operating temperatures. Si-Ge alloys reached the highest zT values but had a significantly lower power factor than the half-Heusler compounds. Other materials, such as oxide-based materials, oxyselenides, and Zintl compounds, also reached reasonable zT values, which made these promising materials for reaching high conversion efficiencies.

Author Contributions: M.W., R.H. and A.F. worked on the conceptualization. M.W. and R.H. wrote the original draft. M.W., R.H. and A.F. critically revised and edited the manuscript draft. A.F. is responsible for the acquisition of funding.

Funding: This work was funded by the Deutsche Forschungsgemeinschaft (DFG, German Research Foundation)—project number 325156807. The publication of this article was funded by the Open Access fund of Leibniz University Hannover.

Conflicts of Interest: The authors declare no conflict of interest.

References

1. He, J.; Tritt, T.M. Advances in Thermoelectric Materials Research: Looking Back and Moving Forward. *Science* **2017**, *357*, eaak9997. [[CrossRef](#)] [[PubMed](#)]
2. *Energy Flow Chart U.S. 2017*; Technical Report; Lawrence Livermore National Laboratory (LLNL) and the Department of Energy: Livermore, CA, USA, 2018.
3. Kishore, R.A.; Marin, A.; Wu, C.; Kumar, A.; Priya, S. *Energy Harvesting—Materials, Physics, and System Design with Practical Examples*; DEStech Publications: Lancaster, PA, USA, 2019.
4. Goldsmid, H.J. *Introduction to Thermoelectricity*; Springer: Berlin/Heidelberg, Germany, 2010.
5. Ioffe, A.F. *Semiconductor Thermoelements, and Thermoelectric Cooling*, 1st ed.; Info-search Ltd.: London, UK, 1957.
6. Snyder, G.J.; Toberer, E. Complex Thermoelectric Materials. *Nat. Mater.* **2008**, *7*, 105–114. [[CrossRef](#)] [[PubMed](#)]
7. Chen, S.; Ren, Z. Recent Progress of half-Heusler for Moderate Temperature Thermoelectric Applications. *Mater. Today* **2013**, *16*, 387–395. [[CrossRef](#)]
8. Shuai, J.; Mao, J.; Song, S.; Zhang, Q.; Chen, G.; Ren, Z. Recent Progress and Future Challenges on Thermoelectric Zintl Materials. *Mater. Today Phys.* **2017**, *1*, 74–95. [[CrossRef](#)]
9. Yin, Y.; Tudu, B.; Tiwari, A. Recent Advances in Oxide Thermoelectric Materials and Modules. *Vacuum* **2017**, *146*, 356–374. [[CrossRef](#)]
10. Bittner, M.; Kanas, N.; Hinterting, R.; Steinbach, F.; Groeneveld, D.; Wemhoff, P.; Wiik, K.; Einarsrud, M.A.; Feldhoff, A. Triple-phase Ceramic 2D Nanocomposite with Enhanced Thermoelectric Properties. *J. Eur. Ceram. Soc.* **2019**, *39*, 1237–1244. [[CrossRef](#)]
11. Liu, Y.; Zhao, L.D.; Zhu, Y.; Liu, Y.; Li, F.; Yu, M.; Liu, D.B.; Xu, W.; Lin, Y.H.; Nan, C.-W. Synergistically Optimizing Electrical and Thermal Transport Properties of BiCuSeO via a Dual-Doping Approach. *Adv. Energy Mater.* **2016**, *6*, 1–9. [[CrossRef](#)]
12. Zhao, L.D.; Lo, S.H.; Zhang, Y.; Sun, H.; Tan, G.; Uher, C.; Wolverton, C.; Dravid, V.P.; Kanatzidis, M.G. Ultralow Thermal Conductivity and High Thermoelectric Figure of Merit in SnSe Crystals. *Nature* **2014**, *508*, 373–377. [[CrossRef](#)]
13. Tushima, N. Recent Progress of Organic and Hybrid Thermoelectric Materials. *Synth. Met.* **2017**, *225*, 3–21. [[CrossRef](#)]
14. Wolf, M.; Menekse, K.; Mundstock, A.; Hinterting, R.; Nietschke, F.; Oeckler, O.; Feldhoff, A. Low Thermal Conductivity in Thermoelectric Oxide-Based Multiphase Composites. *J. Electron. Mater.* **2019**, *48*, 7551–7561. [[CrossRef](#)]
15. Feldhoff, A. Thermoelectric Material Tensor Derived from the Onsager–de Groot–Callen Model. *Energy Harvest. Syst.* **2015**, *2*, 5–13. [[CrossRef](#)]
16. Fuchs, H.U. A Direct Entropic Approach to Uniform and Spatially Continuous Dynamical Models of Thermoelectric Devices. *Energy Harvest. Syst.* **2014**, *1*, 1–18. [[CrossRef](#)]
17. Job, G.; Ruffler, R. *Physical Chemistry from a Different Angle*, 1st ed.; Springer: Berlin/Heidelberg, Germany, 2014. [[CrossRef](#)]

18. Goupil, C.; Seifert, W.; Zbrocki, K.; Müller, E.; Snyder, G.J. Thermodynamics of Thermoelectric Phenomena and Applications. *Entropy* **2011**, *13*, 1481–1517. [[CrossRef](#)]
19. Fuchs, H. *The Dynamics of Heat—A Unified Approach to Thermodynamics and Heat Transfer*, 2nd ed.; Springer: New York, NY, USA, 2010. [[CrossRef](#)]
20. Bittner, M.; Kanas, N.; Hinterding, R.; Steinbach, F.; Räthel, J.; Schrade, M.; Wiik, K.; Einarsrud, M.A.; Feldhoff, A. A Comprehensive Study on Improved Power Materials for High-Temperature Thermoelectric Generators. *J. Power Sources* **2019**, *410–411*, 143–151. [[CrossRef](#)]
21. Poudel, B.; Hao, Q.; Ma, Y.; Lan, Y.; Minnich, A.; Yu, B.; Yan, X.; Wang, D.; Muto, A.; Vashaee, D.; et al. High-Thermoelectric Performance of Nanostructured Bismuth Antimony Telluride Bulk Alloys. *Science* **2008**, *320*, 634–638. [[CrossRef](#)] [[PubMed](#)]
22. Fu, C.; Bai, S.; Liu, Y.; Tang, Y.; Chen, L.; Zhao, X.; Zhu, T. Realizing High Figure of Merit in Heavy-Band p-Type half-Heusler Thermoelectric Materials. *Nat. Commun.* **2015**, *6*, 1–7. [[CrossRef](#)] [[PubMed](#)]
23. Narducci, D. Do we Really need High Thermoelectric Figures of Merit? A Critical Appraisal to the Power Conversion Efficiency of Thermoelectric Materials. *Appl. Phys. Lett.* **2011**, *99*, 102104. [[CrossRef](#)]
24. Pei, Y.; Shi, X.; Lalonde, A.; Wang, H.; Chen, L.; Snyder, G.J. Convergence of Electronic Bands for High Performance Bulk Thermoelectrics. *Nature* **2011**, *473*, 66–69. [[CrossRef](#)]
25. Pei, Y.; Wang, H.; Snyder, G.J. Band Engineering of Thermoelectric Materials. *Adv. Mater.* **2012**, *24*, 6125–6135. [[CrossRef](#)]
26. Hu, L.; Zhu, T.; Liu, X.; Zhao, X. Point Defect Engineering of High-Performance Bismuth-Telluride-Based Thermoelectric Materials. *Adv. Funct. Mater.* **2014**, *24*, 5211–5218. [[CrossRef](#)]
27. Kanatzidis, M.G. Nanostructured Thermoelectrics: The New Paradigm? *Chem. Mater.* **2010**, *22*, 648–659. [[CrossRef](#)]
28. Cook, B.A.; Kramer, M.J.; Haringa, J.L.; Han, M.K.; Chung, D.Y.; Kanatzidis, M.G. Analysis of Nanostructuring in High Figure-of-Merit $\text{Ag}_{1-x}\text{Pb}_m\text{SbTe}_{2+m}$ Thermoelectric Materials. *Adv. Funct. Mater.* **2009**, *19*, 1254–1259. [[CrossRef](#)]
29. Li, J.; Tan, Q.; Li, J.F.; Liu, D.W.; Li, F.; Li, Z.Y.; Zou, M.; Wang, K. BiSbTe-based Nanocomposites with High zT: The Effect of SiC Nanodispersion on Thermoelectric Properties. *Adv. Funct. Mater.* **2013**, *23*, 4317–4323. [[CrossRef](#)]
30. Lan, Y.; M., A.J.; Chen, G.; Ren, Z. Enhancement of Thermoelectric Figure-of-Merit by a Bulk Nanostructuring Approach. *Adv. Funct. Mater.* **2010**, *20*, 357–376. [[CrossRef](#)]
31. Miyazaki, K.; Kuriyama, K.; Yabuki, T. Printable Thermoelectric Device. In Proceedings of the PowerMEMS 2018 Conference, Daytona Beach, FL, USA, 4–7 December 2018.
32. Biswas, K.; He, J.; Blum, I.D.; Wu, C.I.; Hogan, T.P.; Seidman, D.N.; Dravid, V.P.; Kanatzidis, M.G. High-Performance Bulk Thermoelectrics with All-Scale Hierarchical Architectures. *Nature* **2012**, *489*, 414–418. [[CrossRef](#)] [[PubMed](#)]
33. Zheng, Y.; Zhang, Q.; Su, X.; Xie, H.; Shu, S.; Chen, T.; Tan, G.; Yan, Y.; Tang, X.; Uher, C.; et al. Mechanically Robust BiSbTe Alloys with Superior Thermoelectric Performance: A Case Study of Stable Hierarchical Nanostructured Thermoelectric Materials. *Adv. Energy Mater.* **2015**, *5*, 1401391. [[CrossRef](#)]
34. Tritt, T.M. *Thermal Conductivity—Theory, Properties and Applications*; Kluwer Academic/Plenum Publishers: New York, NY, USA, 2004.
35. Tan, G.; Zhao, L.D.; Kanatzidis, M.G. Rationally Designing High-Performance Bulk Thermoelectric Materials. *Chem. Rev.* **2016**, *116*, 12123–12149. [[CrossRef](#)]
36. Fergus, J.W. Oxide Materials for High Temperature Thermoelectric Energy Conversion. *J. Eur. Ceram. Soc.* **2012**, *32*, 525–540. [[CrossRef](#)]
37. Poon, S. Recent Advances in Thermoelectric Performance of half-Heusler Compounds. *Metals* **2018**, *8*, 989. [[CrossRef](#)]
38. Cowen, L.M.; Atoyo, J.; Carnie, M.J.; Baran, D.; Schroeder, B.C. Review—Organic Materials for Thermoelectric Energy Generation. *ECS J. Solid State Sci. Technol.* **2017**, *6*, N3080–N3088. [[CrossRef](#)]
39. Saini, S.; Yaddanapudi, H.S.; Tian, K.; Yin, Y.; Maggini, D.; Tiwari, A. Terbium Ion Doping in $\text{Ca}_3\text{Co}_4\text{O}_9$: A Step Towards High-Performance Thermoelectric Materials. *Sci. Rep.* **2017**, *7*, 1–9. [[CrossRef](#)] [[PubMed](#)]
40. Bathula, S.; Jayasimhadri, M.; Gahtori, B.; Singh, N.K.; Tyagi, K.; Srivastava, A.K.; Dhar, A. The Role of Nanoscale Defect Features in Enhancing the Thermoelectric Performance of p-Type Nanostructured SiGe Alloys. *Nanoscale* **2015**, *7*, 12474–12483. [[CrossRef](#)] [[PubMed](#)]

41. Grebenkemper, J.H.; Klemenz, S.; Albert, B.; Bux, S.K.; Kauzlarich, S.M. Effects of Sc and Y Substitution on the Structure and Thermoelectric Properties of $\text{Yb}_{14}\text{MnSb}_{11}$. *J. Solid State Chem.* **2016**, *242*, 55–61. [[CrossRef](#)]
42. Bell, L.E. Cooling, Heating, Generating Power, and Recovering Waste Heat with Thermoelectric Systems. *Science* **2008**, *321*, 1457–1461. [[CrossRef](#)]
43. Kim, H.S.; Liu, W.; Ren, Z. The Bridge Between the Materials and Devices of Thermoelectric Power Generators. *Energy Environ. Sci.* **2017**, *10*, 69–85. [[CrossRef](#)]
44. Snyder, G.J.; Snyder, A.H. Figure of Merit zT of a Thermoelectric Device Defined from Materials Properties. *Energy Environ. Sci.* **2017**, *10*, 2280–2283. [[CrossRef](#)]
45. Tan, G.; Ohta, M.; Kanatzidis, M.G. Thermoelectric Power Generation: From New Materials to Devices. *Philos. Trans. R. Soc. A Math. Phys. Eng. Sci.* **2019**, *377*. [[CrossRef](#)]
46. He, J.; Liu, Y.; Funahashi, R. Oxide Thermoelectrics: The Challenges, Progress, and Outlook. *J. Mater. Res.* **2011**, *26*, 1762–1772. [[CrossRef](#)]
47. Hicks, L.D.; Dresselhaus, M.S. Effect of Quantum-Well Structures on the Thermoelectric Figure of Merit. *Phys. Rev. B* **1993**, *47*. [[CrossRef](#)]
48. Terasaki, I.; Sasago, Y.; Uchinokura, K. Large Thermoelectric Power in NaCo_2O_4 Single Crystals. *Phys. Rev.* **1997**, *56*, 12685–12687. [[CrossRef](#)]
49. Shi, X.; Chen, L.; Uher, C. Recent Advances in High-Performance Bulk Thermoelectric Materials. *Int. Mater. Rev.* **2016**, *61*, 379–415. [[CrossRef](#)]
50. Zhao, L.D.; He, J.; Berardan, D.; Lin, Y.; Li, J.F.; Nan, C.W.; Drago, N. BiCuSeO Oxyselenides: New Promising Thermoelectric Materials. *Energy Environ. Sci.* **2014**, *7*, 2900–2924. [[CrossRef](#)]
51. Zhang, X.; Chang, C.; Zhou, Y.; Zhao, L.D. BiCuSeO Thermoelectrics: An Update on Recent Progress and Perspective. *Materials* **2017**, *10*, 198. [[CrossRef](#)] [[PubMed](#)]
52. Liu, P.; Chen, G.; Cui, Y.; Zhang, H.; Xiao, F.; Wang, L.; Nakano, H. High Temperature Electrical Conductivity and Thermoelectric Power of Na_xCoO_2 . *Solid State Ionics* **2008**, *179*, 2308–2312. [[CrossRef](#)]
53. Krasutskaya, N.S.; Klyndyuk, A.I.; Evseeva, L.E.; Tanaeva, S.A. Synthesis and Properties of Na_xCoO_2 ($x = 0.55, 0.89$) Oxide Thermoelectrics. *Inorg. Mater.* **2016**, *52*, 393–399. [[CrossRef](#)]
54. Klyndyuk, A.I.; Krasutskaya, N.S.; Chizhova, E.A. Synthesis and Thermoelectric Properties of Ceramics based on $\text{Bi}_2\text{Ca}_2\text{Co}_{1.7}\text{O}_y$ Oxide. *Glass Phys. Chem.* **2018**, *44*, 100–107. [[CrossRef](#)]
55. Sun, N.; Dong, S.T.; Zhang, B.B.; Chen, Y.B.; Zhou, J.; Zhang, S.T.; Gu, Z.B.; Yao, S.H.; Chen, Y.F. Intrinsically Modified Thermoelectric Performance of Alkaline-Earth Isovalently Substituted $[\text{Bi}_2\text{AE}_2\text{O}_4][\text{CoO}_2]_y$ Single Crystals. *J. Appl. Phys.* **2013**, *114*, 1–7. [[CrossRef](#)]
56. Chen, Y.; Chen, C.; Li, X. Effect on the Properties of Different Preparation Processes in $\text{Ca}_3\text{Co}_4\text{O}_9$ Thermoelectric Material. *Int. Conf. Electr. Control. Eng.* **2010**, 4672–4676. [[CrossRef](#)]
57. Królicka, A.K.; Piersa, M.; Mirowska, A.; Michalska, M. Effect of Sol-Gel and Solid-State Synthesis Techniques on Structural, Morphological and Thermoelectric Performance of $\text{Ca}_3\text{Co}_4\text{O}_9$. *Ceram. Int.* **2018**. [[CrossRef](#)]
58. Noudem, J.G.; Kenfaui, D.; Chateigner, D.; Gomina, M. Toward the Enhancement of Thermoelectric Properties of Lamellar $\text{Ca}_3\text{Co}_4\text{O}_9$ by Edge-Free Spark Plasma Texturing. *Scr. Mater.* **2012**, *66*, 258–260. [[CrossRef](#)]
59. Schulz, T.; Töpfer, J. Thermoelectric Properties of $\text{Ca}_3\text{Co}_4\text{O}_9$ Ceramics Prepared by an Alternative Pressure-Less Sintering/Annealing Method. *J. Alloy. Compd.* **2016**, *659*, 122–126. [[CrossRef](#)]
60. Huang, Y.; Zhao, B.; Fang, J.; Ang, R.; Sun, Y. Tuning of Microstructure and Thermoelectric Properties of $\text{Ca}_3\text{Co}_4\text{O}_9$ Ceramics by High-Magnetic-Field Sintering. *J. Appl. Phys.* **2011**, *110*. [[CrossRef](#)]
61. Bittner, M.; Helmich, L.; Nietschke, F.; Geppert, B.; Oeckler, O.; Feldhoff, A. Porous $\text{Ca}_3\text{Co}_4\text{O}_9$ with Enhanced Thermoelectric Properties Derived from Sol-Gel Synthesis. *J. Eur. Ceram. Soc.* **2017**, *37*, 3909–3915. [[CrossRef](#)]
62. Prasoesopha, N.; Pinitsoontorn, S.; Kamwanna, T.; Amornkitbamrung, V.; Kurosaki, K.; Ohishi, Y.; Muta, H.; Yamanaka, S. The Effect of Cr Substitution on the Structure and Properties of Misfit-Layered $\text{Ca}_3\text{Co}_{4-x}\text{Cr}_x\text{O}_{9+\delta}$ Thermoelectric Oxides. *J. Alloy. Compd.* **2014**, *588*, 199–205. [[CrossRef](#)]
63. Cha, J.S.; Choi, S.; Kim, G.H.; Kim, S.; Park, K. High-Temperature Thermoelectric Properties of Sm^{3+} -Doped $\text{Ca}_3\text{Co}_4\text{O}_{9+\delta}$ Fabricated by Spark Plasma Sintering. *Ceram. Int.* **2018**, *44*, 6376–6383. [[CrossRef](#)]
64. Wang, K.X.; Wang, J.; Wu, H.; Shaheen, N.; Zha, X.Y.; Gao, L.J.; Bai, H.C. Thermoelectric Properties of Lower Concentration K-Doped $\text{Ca}_3\text{Co}_4\text{O}_9$ Ceramics. *Chin. Phys. B* **2018**, *27*. [[CrossRef](#)]

65. Butt, S.; Xu, W.; He, W.Q.; Tan, Q.; Ren, G.K.; Lin, Y.; Nan, C.W. Enhancement of Thermoelectric Performance in Cd-Doped $\text{Ca}_3\text{Co}_4\text{O}_9$ via Spin Entropy, Defect Chemistry and Phonon Scattering. *J. Mater. Chem. A* **2014**, *2*, 19479–19487. [[CrossRef](#)]
66. Delorme, F.; Martin, C.F.; Marudhachalam, P.; Ovono Ovono, D.; Guzman, G. Effect of Ca Substitution by Sr on the Thermoelectric Properties of $\text{Ca}_3\text{Co}_4\text{O}_9$ Ceramics. *J. Alloy. Compd.* **2011**, *509*, 2311–2315. [[CrossRef](#)]
67. Hira, U.; Han, L.; Norrman, K.; Christensen, D.V.; Pryds, N.; Sher, F. High-Temperature Thermoelectric Properties of Na- and W-Doped $\text{Ca}_3\text{Co}_4\text{O}_9$ System. *RSC Adv.* **2018**, *8*, 12211–12221. [[CrossRef](#)]
68. Butt, S.; Liu, Y.C.; Lan, J.L.; Shehzad, K.; Zhan, B.; Lin, Y.; Nan, C.W. High-Temperature Thermoelectric Properties of La and Fe co-Doped Ca-Co-O Misfit-Layered Cobaltites Consolidated by Spark Plasma Sintering. *J. Alloy. Compd.* **2014**, *588*, 277–283. [[CrossRef](#)]
69. Ito, M.; Furumoto, D. Effects of Noble Metal Addition on Microstructure and Thermoelectric Properties of $\text{Na}_x\text{Co}_2\text{O}_4$. *J. Alloy. Compd.* **2008**, *450*, 494–498. [[CrossRef](#)]
70. Park, K.; Choi, J.W. High-Temperature Thermoelectric Properties of $\text{Na}(\text{Co}_{0.91}\text{Ni}_{0.09})_2\text{O}_4$ Fabricated by Solution Combustion Method for Power Generation. *J. Nanosci. Nanotechnol.* **2012**, *12*, 3624–3628. [[CrossRef](#)] [[PubMed](#)]
71. Park, K.; Jang, K.U.; Kwon, H.C.; Kim, J.G.; Cho, W.S. Influence of Partial Substitution of Cu for Co on the Thermoelectric Properties of NaCo_2O_4 . *J. Alloy. Compd.* **2006**, *419*, 213–219. [[CrossRef](#)]
72. Nagira, T.; Ito, M.; Katsuyama, S.; Majima, K.; Nagai, H. Thermoelectric Properties of $(\text{Na}_{1-y}\text{M}_y)_x\text{Co}_2\text{O}_4$ ($M = \text{K}, \text{Sr}, \text{Y}, \text{Nd}, \text{Sm}$ and $\text{Yb}; Y = 0.01 - 0.35$). *J. Alloy. Compd.* **2003**, *348*, 263–269. [[CrossRef](#)]
73. Karakaya, G.C.; Özçelik, B.; Nane, O.; Sotelo, A. Improvement of $\text{Bi}_2\text{Sr}_2\text{Co}_2\text{O}_y$ Thermoelectric Performances by Na Doping. *J. Electroceramics* **2018**, *2*, 11–15. [[CrossRef](#)]
74. Gao, F.; He, Q.; Cao, R.; Wu, F.; Hu, X.; Song, H. Enhanced Thermoelectric Properties of the Hole-Doped $\text{Bi}_{2-x}\text{K}_x\text{Sr}_2\text{Co}_2\text{O}_y$ Ceramics. *Int. J. Mod. Phys. B* **2015**, *29*, 1–7. [[CrossRef](#)]
75. Hao, H.S.; Ye, J.Q.; Liu, Y.T.; Hu, X. High-Temperature Thermoelectric Properties of Pb- and La-Substituted $\text{Bi}_2\text{Sr}_2\text{Co}_2\text{O}_y$ Misfit Compounds. *Adv. Mater. Res.* **2010**, *105-106*, 336–338. [[CrossRef](#)]
76. Janotti, A.; Van De Walle, C.G. Fundamentals of Zinc Oxide as a Semiconductor. *Rep. Prog. Phys.* **2009**, *72*. [[CrossRef](#)]
77. Van Benthem, K.; Elsässer, C.; French, R.H. Bulk Electronic Structure of SrTiO_3 : Experiment and Theory. *J. Appl. Phys.* **2001**, *90*, 6156–6164. [[CrossRef](#)]
78. Zhang, F.P.; Lu, Q.M.; Zhang, X.; Zhang, J.X. First Principle Investigation of Electronic Structure of CaMnO_3 Thermoelectric Compound Oxide. *J. Alloy. Compd.* **2011**, *509*, 542–545. [[CrossRef](#)]
79. Tsubota, T.; Ohtaki, M.; Eguchi, K.; Arai, H. Thermoelectric Properties of Al-Doped ZnO as a Promising Oxide Material for High-Temperature Thermoelectric Conversion. *J. Mater. Chem.* **1997**, *7*, 85–90. [[CrossRef](#)]
80. Jood, P.; Mehta, R.J.; Zhang, Y.; Peleckis, G.; Wang, X.; Siegel, R.W.; Borca-Tasciuc, T.; Dou, S.X.; Ramanath, G. Al-Doped Zinc Oxide Nanocomposites with Enhanced Thermoelectric Properties. *Nano Lett.* **2011**, *11*, 4337–4342. [[CrossRef](#)] [[PubMed](#)]
81. Nam, W.H.; Lim, Y.S.; Choi, S.M.; Seo, W.S.; Lee, J.Y. High-Temperature Charge Transport and Thermoelectric Properties of a Degenerately Al-Doped ZnO Nanocomposite. *J. Mater. Chem.* **2012**, *22*, 14633–14638. [[CrossRef](#)]
82. Han, L.; Van Nong, N.; Zhang, W.; Hung, L.T.; Holgate, T.; Tashiro, K.; Ohtaki, M.; Pryds, N.; Linderroth, S. Effects of Morphology on the Thermoelectric Properties of Al-Doped ZnO. *RSC Adv.* **2014**, *4*, 12353–12361. [[CrossRef](#)]
83. Tian, T.; Cheng, L.; Zheng, L.; Xing, J.; Gu, H.; Bernik, S.; Zeng, H.; Ruan, W.; Zhao, K.; Li, G. Defect Engineering for a Markedly Increased Electrical Conductivity and Power Factor in Doped ZnO Ceramic. *Acta Mater.* **2016**, *119*, 136–144. [[CrossRef](#)]
84. Ohta, S.; Nomura, T.; Ohta, H.; Koumoto, K. High-Temperature Carrier Transport and Thermoelectric Properties of Heavily La- Or Nb-Doped SrTiO_3 Single Crystals. *J. Appl. Phys.* **2005**, *97*. [[CrossRef](#)]
85. Han, J.; Sun, Q.; Song, Y. Enhanced Thermoelectric Properties of La and Dy co-Doped, Sr-deficient SrTiO_3 Ceramics. *J. Alloy. Compd.* **2017**, *705*, 22–27. [[CrossRef](#)]
86. Chen, Y.; Liu, J.; Li, Y.; Zhang, X.; Wang, X.; Su, W.; Li, J.; Wang, C. Enhancement of Thermoelectric Performance of $\text{Sr}_{1-x}\text{Ti}_{0.8}\text{Nb}_{0.2}\text{O}_3$ Ceramics by Introducing Sr Vacancies. *J. Electron. Mater.* **2019**, *48*, 1147–1152. [[CrossRef](#)]

87. Bittner, M.; Geppert, B.; Kanas, N.; Singh, S.P.; Wiik, K.; Feldhoff, A. Oxide-Based Thermoelectric Generator for High-Temperature Application using p-Type $\text{Ca}_3\text{Co}_4\text{O}_9$ and n-Type $\text{In}_{1.95}\text{Sn}_{0.05}\text{O}_3$ Legs. *Energy Harvest. Syst.* **2016**, *3*, 213–222. [[CrossRef](#)]
88. Yan, Y.L.; Wang, Y.X. Electronic Structure and Low Temperature Thermoelectric Properties of $\text{In}_{24}\text{M}_8\text{O}_{48}$ ($\text{M} = \text{Ge}^{4+}, \text{Sn}^{4+}, \text{Ti}^{4+}, \text{and Zr}^{4+}$). *J. Comput. Chem.* **2012**, *33*, 88–92. [[CrossRef](#)]
89. Guilmeau, E.; Brardan, D.; Simon, C.; Maignan, A.; Raveau, B.; Ovono Ovono, D.; Delorme, F. Tuning the Transport and Thermoelectric Properties of In_2O_3 Bulk Ceramics through Doping at In-Site. *J. Appl. Phys.* **2009**, *106*. [[CrossRef](#)]
90. Colder, H.; Guilmeau, E.; Harnois, C.; Marinel, S.; Retoux, R.; Savary, E. Preparation of Ni-Doped ZnO Ceramics for Thermoelectric Applications. *J. Eur. Ceram. Soc.* **2011**, *31*, 2957–2963. [[CrossRef](#)]
91. Zhang, D.B.; Zhang, B.P.; Ye, D.S.; Liu, Y.C.; Li, S. Enhanced Al/Ni Co-Doping and Power Factor in Textured ZnO Thermoelectric Ceramics Prepared by Hydrothermal Synthesis and Spark Plasma Sintering. *J. Alloy. Compd.* **2016**, *656*, 784–792. [[CrossRef](#)]
92. Jung, K.H.; Hyoung Lee, K.; Seo, W.S.; Choi, S.M. An Enhancement of a Thermoelectric Power Factor in a Ga-Doped ZnO System: A Chemical Compression by Enlarged Ga Solubility. *Appl. Phys. Lett.* **2012**, *100*, 3–7. [[CrossRef](#)]
93. Liu, J.; Wang, C.L.; Li, Y.; Su, W.B.; Zhu, Y.H.; Li, J.C.; Mei, L.M. Influence of Rare Earth Doping on Thermoelectric Properties of SrTiO_3 Ceramics. *J. Appl. Phys.* **2013**, *114*. [[CrossRef](#)]
94. Park, K.; Son, J.S.; Woo, S.I.; Shin, K.; Oh, M.W.; Park, S.D.; Hyeon, T. Colloidal Synthesis and Thermoelectric Properties of La-Doped SrTiO_3 Nanoparticles. *J. Mater. Chem. A* **2014**, *2*, 4217. [[CrossRef](#)]
95. Li, L.; Liu, Y.; Qin, X.; Li, D.; Zhang, J.; Song, C.; Wang, L. Enhanced Thermoelectric Performance of Highly Dense and Fine-Grained $(\text{Sr}_{1-x}\text{Gd}_x)\text{TiO}_{3-\delta}$ Ceramics Synthesized by Sol-Gel Process and Spark Plasma Sintering. *J. Alloy. Compd.* **2014**, *588*, 562–567. [[CrossRef](#)]
96. Zhang, B.; Wang, J.; Zou, T.; Zhang, S.; Yaer, X.; Ding, N.; Liu, C.; Miao, L.; Li, Y.; Wu, Y. High Thermoelectric Performance of Nb-Doped SrTiO_3 Bulk Materials with Different Doping Levels. *J. Mater. Chem. C* **2015**, *3*, 11406–11411. [[CrossRef](#)]
97. Chen, Y.; Liu, J.; Li, X.; Li, Y.; Su, W.; Li, J.; Zhao, L.; Wang, C.; Lu, M. Enhancement of Thermoelectric Performance of $\text{Sr}_{0.9-x}\text{Nd}_{0.1}\text{Ti}_{0.9}\text{Nb}_{0.1}\text{O}_3$ Ceramics by Introducing Sr Vacancies. *Phys. Status Solidi A* **2018**, *215*. [[CrossRef](#)]
98. Bocher, L.; Aguirre, M.H.; Logvinovich, D.; Shkabko, A.; Robert, R.; Trottmann, M.; Weidenkaff, A. $\text{CaMn}_{1-x}\text{Nb}_x\text{O}_3$ ($x < 0.08$) Perovskite-Type Phases As Promising New High-Temperature n-Type Thermoelectric Materials. *Inorg. Chem.* **2008**, *47*, 8077–8085.
99. Wang, Y.; Sui, Y.; Su, W. High Temperature Thermoelectric Characteristics of $\text{Ca}_{0.9}\text{R}_{0.1}\text{MnO}_3$ ($\text{R}=\text{La, Pr, Yb}$). *J. Appl. Phys.* **2008**, *104*. [[CrossRef](#)]
100. Thiel, P.; Eilertsen, J.; Populoh, S.; Saucke, G.; Döbeli, M.; Shkabko, A.; Sagarna, L.; Karvonen, L.; Weidenkaff, A. Influence of Tungsten Substitution and Oxygen Deficiency on the Thermoelectric Properties of $\text{CaMnO}_{3-\delta}$. *J. Appl. Phys.* **2013**, *114*. [[CrossRef](#)]
101. Seo, J.W.; Cha, J.; Won, S.O.; Park, K. Electrical Transport and Thermoelectric Properties of $\text{Ca}_{0.8}\text{Y}_{0.2-x}\text{Dy}_x\text{MnO}_{3-\delta}$ ($0 < x < 0.2$). *J. Am. Ceram. Soc.* **2017**, *100*, 3608–3617. [[CrossRef](#)]
102. Li, C.; Chen, Q.; Yan, Y. Effects of Pr and Yb Dual Doping on the Thermoelectric Properties of CaMnO_3 . *Materials* **2018**, *11*, 1–13. [[CrossRef](#)] [[PubMed](#)]
103. Zhao, L.D.; Berardan, D.; Pei, Y.L.; Byl, C.; Pinsard-Gaudart, L.; Dragoë, N. $\text{Bi}_{1-x}\text{Sr}_x\text{CuSeO}$ Oxyselenides as Promising Thermoelectric Materials. *Appl. Phys. Lett.* **2010**, *97*, 10–13. [[CrossRef](#)]
104. Li, F.; Li, J. F.; Zhao, L.D.; Xiang, K.; Liu, Y.; Zhang, B.P.; Lin, Y.H.; Nan, C.W.; Zhu, H.M. Polycrystalline BiCuSeO Oxide as a Potential Thermoelectric Material. *Energy Environ. Sci.* **2012**, *5*, 7188–7195. [[CrossRef](#)]
105. Li, J.; Sui, J.; Pei, Y.; Barreateau, C.; Berardan, D.; Dragoë, N.; Cai, W.; He, J.; Zhao, L.D. A High Thermoelectric Figure of Merit $zT > 1$ in Ba Heavily Doped BiCuSeO Oxyselenides. *Energy Environ. Sci.* **2012**, *5*, 8543–8547. [[CrossRef](#)]
106. Feng, B.; Li, G.; Pan, Z.; Xiaoming, H.; Peihai, L.; Zhu, H.; Yawei, L.; Fan, X. Effect of Synthesis Processes on the Thermoelectric Properties of BiCuSeO Oxyselenides. *J. Alloy. Compd.* **2018**, *754*, 131–138. [[CrossRef](#)]
107. Sui, J.; Li, J.; He, J.; Pei, Y.L.; Berardan, D.; Wu, H.; Dragoë, N.; Cai, W.; Zhao, L.D. Texturation Boosts the Thermoelectric Performance of BiCuSeO Oxyselenides. *Energy Environ. Sci.* **2013**, *6*, 2916–2920. [[CrossRef](#)]

108. Bhaskar, A.; Lai, R.T.; Chang, K.C.; Liu, C.J. High Thermoelectric Performance of BiCuSeO Prepared by Solid State Reaction and Sol-Gel Process. *Scr. Mater.* **2017**, *134*, 100–104. [[CrossRef](#)]
109. Pele, V.; Barreateau, C.; Berardan, D.; Zhao, L.; Dragoe, N. Direct Synthesis of BiCuChO-Type Oxychalcogenides by Mechanical Alloying. *J. Solid State Chem.* **2013**, *203*, 187–191. [[CrossRef](#)]
110. Stampler, E.S.; Sheets, W.C.; Bertoni, M.I.; Prellier, W.; Mason, T.O.; Poeppelmeier, K.R. Temperature Driven Reactant Solubilization Synthesis of BiCuOSe. *Inorg. Chem.* **2008**, *47*, 10009–10016. [[CrossRef](#)] [[PubMed](#)]
111. Pei, Y.L.; He, J.; Li, J.F.; Li, F.; Liu, Q.; Pan, W.; Barreateau, C.; Berardan, D.; Dragoe, N.; Zhao, L.D. High Thermoelectric Performance of Oxyselenides: Intrinsically Low Thermal Conductivity of Ca-Doped BiCuSeO. *NPG Asia Mater.* **2013**, *5*. [[CrossRef](#)]
112. Li, F.; Wei, T.R.; Kang, F.; Li, J.F. Thermal Stability and Oxidation Resistance of BiCuSeO Based Thermoelectric Ceramics. *J. Alloy. Compd.* **2014**, *614*, 394–400. [[CrossRef](#)]
113. Lan, J.L.; Liu, Y.C.; Zhan, B.; Lin, Y.H.; Zhang, B.; Yuan, X.; Zhang, W.; Xu, W.; Nan, C.W. Enhanced Thermoelectric Properties of Pb-Doped BiCuSeO Ceramics. *Adv. Mater.* **2013**, *25*, 5086–5090. [[CrossRef](#)]
114. Li, F.; Wei, T.R.; Kang, F.; Li, J.F. Enhanced Thermoelectric Performance of Ca-Doped BiCuSeO in a Wide Temperature Range. *J. Mater. Chem. A* **2013**, *1*, 11942–11949. [[CrossRef](#)]
115. Sun, Y.; Zhang, C.; Cao, C.; Fu, J.; Peng, L. Co-Doping for Significantly Improved Thermoelectric Figure of Merit in p-Type Bi_{1-2x}Mg_xPb_xCuSeO Oxyselenides. *Ceram. Int.* **2017**, *43*, 17186–17193. [[CrossRef](#)]
116. Feng, B.; Li, G.; Pan, Z.; Hou, Y.; Zhang, C.; Jiang, C.; Hu, J.; Xiang, Q.; Li, Y.; He, Z.; Fan, X. Effect of Ba and Pb Dual Doping on the Thermoelectric Properties of BiCuSeO Ceramics. *Mater. Lett.* **2018**, *217*, 189–193. [[CrossRef](#)]
117. Pan, L.; Lang, Y.; Zhao, L.; Berardan, D.; Amzallag, E.; Xu, C.; Gu, Y.; Chen, C.; Zhao, L.D.; Shen, X.; et al. Realization of n-Type and Enhanced Thermoelectric Performance of p-Type BiCuSeO by Controlled Iron Incorporation. *J. Mater. Chem. A* **2018**, *6*, 13340–13349. [[CrossRef](#)]
118. Zhang, X.; Feng, D.; He, J.; Zhao, L.D. Attempting to Realize n-Type BiCuSeO. *J. Solid State Chem.* **2018**, *258*, 510–516. [[CrossRef](#)]
119. Gascoin, F.; Ottensmahn, S.; Stark, D.; Haïle, S.M.; Snyder, G.J. Zintl phases as thermoelectric materials: Tuned transport properties of the compounds CaYb_{1-x}Zn₂Sb₂. *Adv. Funct. Mater.* **2005**, *15*, 1860–1864. [[CrossRef](#)]
120. Gayner, C.; Kar, K.K. Recent Advances in Thermoelectric Materials. *Prog. Mater. Sci.* **2016**, *83*, 330–382. [[CrossRef](#)]
121. Brown, S.R.; Kauzlarich, S.M.; Gascoin, F.; Snyder, G.J. Yb₁₄MnSb₁₁: New High Efficiency Thermoelectric Material for Power Generation. *Chem. Mater.* **2006**, *18*, 1873–1877. [[CrossRef](#)]
122. Toberer, E.S.; Cox, C.A.; Brown, S.R.; Ikeda, T.; May, A.F.; Kauzlarich, S.M.; Snyder, G.J. Traversing the Metal-Insulator Transition in a Zintl phase: Rational Enhancement of Thermoelectric Efficiency in Yb₁₄Mn_{1-x}Al_xSb₁₁. *Adv. Funct. Mater.* **2008**, *18*, 2795–2800. [[CrossRef](#)]
123. Toberer, E.S.; Brown, S.R.; Ikeda, T.; Kauzlarich, S.M.; Snyder, G.J. High Thermoelectric Efficiency in Lanthanum Doped Yb₁₄MnSb₁₁. *Appl. Phys. Lett.* **2008**, *93*, 11–14. [[CrossRef](#)]
124. Cox, C.A.; Brown, S.R.; Snyder, G.J.; Kauzlarich, S.M. Effect of Ca Doping on the Thermoelectric Performance of Yb₁₄MnSb₁₁. *J. Electron. Mater.* **2010**, *39*, 1373–1375. [[CrossRef](#)]
125. Kazem, N.; Xie, W.; Ohno, S.; Zevalkink, A.; Miller, G.J.; Snyder, G.J.; Kauzlarich, S.M. High-Temperature Thermoelectric Properties of the Solid-Solution Zintl Phase Eu₁₁Cd₆Sb_{12-x}As_x (x < 3). *Chem. Mater.* **2014**, *26*, 1393–1403. [[CrossRef](#)]
126. Park, S.M.; Kim, S.J. Sr₁₁Cd₆Sb₁₂: A New Zintl Compound with Infinite Chains of Pentagonal Tubes. *J. Solid State Chem.* **2004**, *177*, 3418–3422. [[CrossRef](#)]
127. Kazem, N.; Hurtado, A.; Sui, F.; Ohno, S.; Zevalkink, A.; Snyder, J.G.; Kauzlarich, S.M. High Temperature Thermoelectric Properties of the Solid-Solution Zintl Phase Eu₁₁Cd_{6-x}Zn_xSb₁₂. *Chem. Mater.* **2015**, *27*, 4413–4421. [[CrossRef](#)]
128. Aydemir, U.; Zevalkink, A.; Ormeci, A.; Wang, H.; Ohno, S.; Bux, S.; Snyder, G.J. Thermoelectric Properties of the Zintl Phases Yb₅M₂Sb₆ (M = Al, Ga, In). *Dalton Trans.* **2015**, *44*, 6767–6774. [[CrossRef](#)]
129. Zevalkink, A.; Swallow, J.; Snyder, G.J. Thermoelectric Properties of Zn-Doped Ca₅In₂Sb₆. *Dalton Trans.* **2013**, *42*, 9713. [[CrossRef](#)] [[PubMed](#)]

130. Bobev, S.; Thompson, J.D.; Sarrao, J.L.; Olmstead, M.M.; Hope, H.; Kauzlarich, S.M. Probing the Limits of the Zintl Concept: Structure and Bonding in Rare-Earth and Alkaline-Earth Zinc-Antimonides $\text{Yb}_9\text{Zn}_{4+x}\text{Sb}_9$ and $\text{Ca}_9\text{Zn}_{4.5}\text{Sb}_9$. *Inorg. Chem.* **2004**, *43*, 5044–5052. [[CrossRef](#)] [[PubMed](#)]
131. Wu, Z.; Li, J.; Li, X.; Zhu, M.; Wu, K.C.; Tao, X.T.; Huang, B.B.; Xia, S.Q. Tuning the Thermoelectric Properties of $\text{Ca}_9\text{Zn}_{4+x}\text{Sb}_9$ by Controlled Doping on the Interstitial Structure. *Chem. Mater.* **2016**, *28*, 6917–6924. [[CrossRef](#)]
132. Bux, S.K.; Zevalkink, A.; Janka, O.; Uhl, D.; Kauzlarich, S.; Snyder, J.G.; Fleurial, J.P. Glass-Like Lattice Thermal Conductivity and High Thermoelectric Efficiency in $\text{Yb}_9\text{Mn}_{4.2}\text{Sb}_9$. *J. Mater. Chem. A* **2014**, *2*, 215–220. [[CrossRef](#)]
133. Kazem, N.; Zaikina, J.V.; Ohno, S.; Snyder, G.J.; Kauzlarich, S.M. Coinage-Metal-Stuffed $\text{Eu}_9\text{Cd}_4\text{Sb}_9$: Metallic Compounds with Anomalous Low Thermal Conductivities. *Chem. Mater.* **2015**, *27*, 7508–7519. [[CrossRef](#)]
134. Hu, Y.; Wang, J.; Kawamura, A.; Kovnir, K.; Kauzlarich, S.M. $\text{Yb}_{14}\text{MgSb}_{11}$ and $\text{Ca}_{14}\text{MgSb}_{11}$ —New Mg-Containing Zintl Compounds and their Structures, Bonding, and Thermoelectric Properties. *Chem. Mater.* **2015**, *27*, 343–351. [[CrossRef](#)]
135. Tan, W.; Wu, Z.; Zhu, M.; Shen, J.; Zhu, T.; Zhao, X.; Huang, B.; Tao, X.T.; Xia, S.Q. $\text{A}_{14}\text{MgBi}_{11}$ (A = Ca, Sr, Eu): Magnesium Bismuth Based Zintl Phases as Potential Thermoelectric Materials. *Inorg. Chem.* **2017**, *56*, 10576–10583. [[CrossRef](#)]
136. Toberer, E.S.; Zevalkink, A.; Crisosto, N.; Snyder, G.J. The Zintl Compound $\text{Ca}_5\text{Al}_2\text{Sb}_6$ for Low-Cost Thermoelectric Power Generation. *Adv. Funct. Mater.* **2010**, *20*, 4375–4380. [[CrossRef](#)]
137. Zevalkink, A.; Toberer, E.S.; Bleith, T.; Flage-Larsen, E.; Snyder, G.J. Improved Carrier Concentration Control in Zn-Doped $\text{Ca}_5\text{Al}_2\text{Sb}_6$. *J. Appl. Phys.* **2011**, *110*. [[CrossRef](#)]
138. Zevalkink, A.; Swallow, J.; Snyder, G.J. Thermoelectric Properties of Mn-Doped $\text{Ca}_5\text{Al}_2\text{Sb}_6$. *J. Electron. Mater.* **2012**, *41*, 813–818. [[CrossRef](#)]
139. Chanakian, S.; Aydemir, U.; Zevalkink, A.; Gibbs, Z.M.; Fleurial, J.P.; Bux, S.; Snyder, G.J. High Temperature Thermoelectric Properties of Zn-Doped $\text{Eu}_5\text{In}_2\text{Sb}_6$. *J. Mater. Chem. C* **2015**, *3*, 10518–10524. [[CrossRef](#)]
140. Lv, W.; Yang, C.; Lin, J.; Hu, X.; Guo, K.; Yang, X.; Luo, J.; Zhao, J.T. Cd Substitution in Zintl Phase $\text{Eu}_5\text{In}_2\text{Sb}_6$ Enhancing the Thermoelectric Performance. *J. Alloy. Compd.* **2017**, *726*, 618–622. [[CrossRef](#)]
141. Chanakian, S.; Zevalkink, A.; Aydemir, U.; Gibbs, Z.M.; Pomrehn, G.; Fleurial, J.P.; Bux, S.; Snyder, G.J. Enhanced Thermoelectric Properties of $\text{Sr}_5\text{In}_2\text{Sb}_6$ via Zn-Doping. *J. Mater. Chem. A* **2015**, *3*, 10289–10295. [[CrossRef](#)]
142. Wood, M.; Aydemir, U.; Ohno, S.; Snyder, G.J. Observation of Valence Band Crossing: The Thermoelectric Properties of CaZn_2Sb_2 - CaMg_2Sb_2 Solid Solution. *J. Mater. Chem. A* **2018**, *6*, 9437–9444. [[CrossRef](#)]
143. Zhang, H.; Baitinger, M.; Tang, M.B.; Man, Z.Y.; Chen, H.H.; Yang, X.X.; Liu, Y.; Chen, L.; Grin, Y.; Zhao, J.T. Thermoelectric Properties of $\text{Eu}(\text{Zn}_{1-x}\text{Cd}_x)_2\text{Sb}_2$. *Dalton Trans.* **2010**, *39*, 1101–1104. [[CrossRef](#)] [[PubMed](#)]
144. Guo, K.; Cao, Q.G.; Feng, X.J.; Tang, M.B.; Chen, H.H.; Guo, X.; Chen, L.; Grin, Y.; Zhao, J.T. Enhanced Thermoelectric Figure of Merit of Zintl Phase $\text{YbCd}_{2-x}\text{Mn}_x\text{Sb}_2$ by Chemical Substitution. *Eur. J. Inorg. Chem.* **2011**, *2011*, 4043–4048. [[CrossRef](#)]
145. Wang, X.J.; Tang, M.B.; Chen, H.H.; Yang, X.X.; Zhao, J.T.; Burkhardt, U.; Grin, Y. Synthesis and High Thermoelectric Efficiency of Zintl Phase $\text{YbCd}_{2-x}\text{Zn}_x\text{Sb}_2$. *Appl. Phys. Lett.* **2009**, *94*, 2007–2010. [[CrossRef](#)]
146. Cao, Q.; Zheng, J.; Zhang, K.; Ma, G. Thermoelectric Properties of YbCd_2Sb_2 Doped by Mg. *J. Alloy. Compd.* **2016**, *680*, 278–282. [[CrossRef](#)]
147. Shuai, J.; Kim, H.S.; Liu, Z.; He, R.; Sui, J.; Ren, Z. Thermoelectric Properties of Zintl Compound $\text{Ca}_{1-x}\text{Na}_x\text{Mg}_2\text{Bi}_{1.98}$. *Appl. Phys. Lett.* **2016**, *108*. [[CrossRef](#)]
148. Shuai, J.; Liu, Z.; Kim, H.S.; Wang, Y.; Mao, J.; He, R.; Sui, J.; Ren, Z. Thermoelectric Properties of Bi-Based Zintl Compounds $\text{Ca}_{1-x}\text{Yb}_x\text{Mg}_2\text{Bi}_2$. *J. Mater. Chem. A* **2016**, *4*, 4312–4320. [[CrossRef](#)]
149. Shuai, J.; Geng, H.; Lan, Y.; Zhu, Z.; Wang, C.; Liu, Z.; Bao, J.; Chu, C.W.; Sui, J.; Ren, Z. Higher Thermoelectric Performance of Zintl Phases $(\text{Eu}_{0.5}\text{Yb}_{0.5})_{1-x}\text{Ca}_x\text{Mg}_2\text{Bi}_2$ by Band Engineering and Strain Fluctuation. *Proc. Natl. Acad. Sci. USA* **2016**, *113*, E4125–E4132. [[CrossRef](#)] [[PubMed](#)]
150. Bhardwaj, A.; Rajput, A.; Shukla, A.K.; Pulikkotil, J.J.; Srivastava, A.K.; Dhar, A.; Gupta, G.; Auluck, S.; Misra, D.K.; Budhani, R.C. Mg_3Sb_2 -Based Zintl Compound: A Non-Toxic, Inexpensive and Abundant Thermoelectric Material for Power Generation. *RSC Adv.* **2013**, *3*, 8504–8516. [[CrossRef](#)]
151. Zheng, C.; Hoffmann, R.; Nesper, R.; von Schnering, H.G. Site Preferences and Bond Length Differences in CaAl_2Si_2 -Type Zintl Compounds. *J. Am. Chem. Soc.* **1986**, *108*, 1876–1884. [[CrossRef](#)]

152. Shuai, J.; Wang, Y.; Kim, H.S.; Liu, Z.; Sun, J.; Chen, S.; Sui, J.; Ren, Z. Thermoelectric Properties of Na-Doped Zintl Compound: $Mg_{3-x}Na_xSb_2$. *Acta Mater.* **2015**, *93*, 187–193. [[CrossRef](#)]
153. Kim, S.; Kim, C.; Hong, Y.K.; Onimaru, T.; Suekuni, K.; Takabatake, T.; Jung, M.H. Thermoelectric Properties of Mn-Doped Mg-Sb Single Crystals. *J. Mater. Chem. A* **2014**, *2*, 12311–12316. [[CrossRef](#)]
154. Chen, X.; Wu, H.; Cui, J.; Xiao, Y.; Zhang, Y.; He, J.; Chen, Y.; Cao, J.; Cai, W.; Pennycook, S.J.; et al. Extraordinary Thermoelectric Performance in n-Type Manganese Doped Mg_3Sb_2 Zintl: High Band Degeneracy, Tuned Carrier Scattering Mechanism and Hierarchical Microstructure. *Nano Energy* **2018**, *52*, 246–255. [[CrossRef](#)]
155. Wang, Y.; Zhang, X.; Wang, Y.; Liu, H.; Zhang, J. Enhanced Thermoelectric Properties of n-Type Mg_3Sb_2 by Excess Magnesium and Tellurium Doping. *Appl. Mater. Sci.* **2019**, *1800811*, 1–6.
156. Zhang, J.; Song, L.; Pedersen, S.H.; Yin, H.; Hung, L.T.; Brummerstedt Iversen, B. Discovery of High-Performance Low-Cost n-Type Mg_3Sb_2 -Based Thermoelectric Materials with Multi-Valley Conduction Bands. *Nat. Commun.* **2017**, *8*, 1–8. [[CrossRef](#)]
157. Shuai, J.; Ge, B.; Mao, J.; Song, S.; Wang, Y.; Ren, Z. Significant Role of Mg Stoichiometry in Designing High Thermoelectric Performance for $Mg_3(Sb,Bi)_2$ -based n-Type Zintls. *J. Am. Chem. Soc.* **2018**, *140*, 1910–1915. [[CrossRef](#)]
158. Shuai, J.; Mao, J.; Song, S.; Zhu, Q.; Sun, J.; Wang, Y.; He, R.; Zhou, J.; Chen, G.; Singh, D.J.; Ren, Z. Tuning the Carrier Scattering Mechanism to Effectively Improve the Thermoelectric Properties. *Energy Environ. Sci.* **2017**, *10*, 799–807. [[CrossRef](#)]
159. Graf, T.; Felser, C.; Parkin, S. Simple Rules for The Understanding of Heusler Compounds. *Prog. Solid State Chem.* **2011**, *39*, 1–50. [[CrossRef](#)]
160. Larson, P.; Mahanti, S.D.; Sportouch, S.; Kanatzidis, M.G. Electronic Structure of Rare-Earth Nickel Prictides: Narrow-Gap Thermoelectric Materials. *Phys. Rev. B Condens. Matter Mater. Phys.* **1999**, *59*, 15660–15668. [[CrossRef](#)]
161. Xia, Y.; Bhattacharya, S.; Ponnambalam, V.; Pope, A.L.; Poon, S.J.; Tritt, T.M. Thermoelectric Properties of Semimetallic (Zr, Hf)CoSb half-Heusler Phases. *J. Appl. Phys.* **2000**, *88*, 1952–1955. [[CrossRef](#)]
162. Bos, J.W.G.; Downie, R.A. Half-Heusler Thermoelectrics: A Complex Class of Materials. *J. Phys. Condens. Matter* **2014**, *26*. [[CrossRef](#)]
163. Poon, S.J. Half-Heusler Compounds: Promising Materials For Mid-To-High Temperature Thermoelectric Conversion. *J. Phys. D Appl. Phys.* **2019**, *52*, 493001. [[CrossRef](#)]
164. Aliev, F.G.; Kozyrkov, V.V.; Moshchalkov, V.V.; Scolozdra, R.V.; Durczewski, K. Narrow Band in the Intermetallic Compounds $MNiSn$ ($M=Ti, Zr, Hf$). *Z. Für Phys. B Condens. Matter* **1990**, *80*, 353–357. [[CrossRef](#)]
165. Appel, O.; Cohen, S.; Beeri, O.; Shamir, N.; Gelbstein, Y.; Zalkind, S. Surface Oxidation of $TiNiSn$ (half-Heusler) Alloy by Oxygen and Water Vapor. *Materials* **2018**, *11*, 1–16. [[CrossRef](#)]
166. Appel, O.; Breuer, G.; Cohen, S.; Beeri, O.; Kyratsi, T.; Gelbstein, Y.; Zalkind, S. The Initial Stage in Oxidation of $ZrNiSn$ (half Heusler) Alloy by Oxygen. *Materials* **2019**, *12*, 1–14. [[CrossRef](#)]
167. He, R.; Kim, H.S.; Lan, Y.; Wang, D.; Chen, S.; Ren, Z. Investigating the Thermoelectric Properties of p-Type half-Heusler $Hf_x(ZrTi)_{1-x}CoSb_{0.8}Sn_{0.2}$ by reducing Hf concentration for power generation. *RSC Adv.* **2015**, *4*, 64711–64716. [[CrossRef](#)]
168. Liu, Y.; Fu, C.; Xia, K.; Yu, J.; Zhao, X.; Pan, H.; Felser, C.; Zhu, T. Lanthanide Contraction as a Design Factor for High-Performance Half-Heusler Thermoelectric Materials. *Adv. Mater.* **2018**, *30*, 1–7. [[CrossRef](#)]
169. He, R.; Kraemer, D.; Mao, J.; Zeng, L.; Jie, Q.; Lan, Y.; Li, C.; Shuai, J.; Kim, H.S.; Liu, Y.; et al. Achieving High Power Factor and Output Power Density in p-Type half-Heuslers $Nb_{1-x}Ti_xFeSb$. *Proc. Natl. Acad. Sci. USA* **2016**, *113*, 13576–13581. [[CrossRef](#)] [[PubMed](#)]
170. Zhu, H.; He, R.; Mao, J.; Zhu, Q.; Li, C.; Sun, J.; Ren, W.; Wang, Y.; Liu, Z.; Tang, Z.; et al. Discovery of $ZrCoBi$ Based half-Heuslers with High Thermoelectric Conversion Efficiency. *Nat. Commun.* **2018**, *9*, 1–9. [[CrossRef](#)] [[PubMed](#)]
171. Barth, J.; Balke, B.; Fecher, G.H.; Stryhanyuk, H.; Gloskovskii, A.; Naghavi, S.; Felser, C. Thermoelectric Properties of $CoTiSb$ Based Compounds. *J. Phys. D Appl. Phys.* **2009**, *42*. [[CrossRef](#)]
172. Huang, L.; Zhang, Q.; Wang, Y.; He, R.; Shuai, J.; Zhang, J.; Wang, C.; Ren, Z. The Effect of Sn Doping on Thermoelectric Performance of n-Type half-Heusler $NbCoSb$. *Phys. Chem. Chem. Phys.* **2017**, *19*, 25683–25690. [[CrossRef](#)]

173. Shutoh, N.; Sakurada, S. Thermoelectric Properties of the $Ti_x(Zr_{0.5}Hf_{0.5})_{1-x}NiSn$ half-Heusler Compounds. *J. Alloy. Compd.* **2005**, *389*, 204–208. [[CrossRef](#)]
174. Muta, H.; Kanemitsu, T.; Kurosaki, K.; Yamanaka, S. High-Temperature Thermoelectric Properties of Nb-Doped $MNiSn$ ($M = Ti, Zr$) half-Heusler Compound. *J. Alloy. Compd.* **2009**, *469*, 50–55. [[CrossRef](#)]
175. Kimura, Y.; Ueno, H.; Mishima, Y. Thermoelectric Properties of Directionally Solidified half-Heusler ($M_{0.5}^a, M_{0.5}^b$) $NiSn$ ($M^a, M^b = Hf, Zr, Ti$) Alloys. *J. Electron. Mater.* **2009**, *38*, 934–939. [[CrossRef](#)]
176. Chen, L.; Gao, S.; Zeng, X.; Mehdizadeh Dehkordi, A.; Tritt, T.M.; Poon, S.J. Uncovering High Thermoelectric Figure of Merit in (Hf,Zr) $NiSn$ half-Heusler Alloys. *Appl. Phys. Lett.* **2015**, *107*. [[CrossRef](#)]
177. Wu, T.; Jiang, W.; Li, X.; Zhou, Y.; Chen, L. Thermoelectric Properties of p-Type Fe-Doped $TiCoSb$ half-Heusler Compounds. *J. Appl. Phys.* **2007**, *102*, 1–6. [[CrossRef](#)]
178. Rowe, D. *CRC Handbook of Thermoelectrics*; CRC Press: Boca Raton, FL, USA, 1995.
179. Lin, S.; Wang, C.; Chen, H.; Huo, D.; Savvides, N.; Chen, X. Microstructure and Thermoelectric Properties of Ga-Doped $SiGe$ Alloys Prepared by Mechanical Alloying and Induction Hot Pressing. *Funct. Mater. Lett.* **2013**, *07*, 1450008. [[CrossRef](#)]
180. Joshi, G.; Lee, H.; Lan, Y.; Wang, X.; Zhu, G.; Wang, D.; Gould, R.; Cuff, D.; Tang, M.; Dresselhaus, M.; et al. Enhanced Thermoelectric Figure-of-Merit in Nanostructured p-type Silicon Germanium Bulk Alloys. *Nano Lett.* **2008**, *8*, 4670–4674. [[CrossRef](#)] [[PubMed](#)]
181. Wang, C.; Lin, S.; Chen, H.; Zhao, Y.; Zhao, L.; Wang, H.; Huo, D.; Chen, X. Thermoelectric Performance of $Si_{80}Ge_{20-x}Sb_x$ Based Multiphase Alloys with Inhomogeneous Dopant Distribution. *Energy Convers. Manag.* **2015**, *94*, 331–336. [[CrossRef](#)]
182. Wongprakarn, S.; Pinitsoontorn, S.; at Tanusilp, S.; Kurosaki, K. Enhancing Thermoelectric Properties of p-Type $SiGe$ Alloy through Optimization of Carrier Concentration and Processing Parameters. *Mater. Sci. Semicond. Process.* **2018**, *88*, 239–249. [[CrossRef](#)]
183. Bathula, S.; Jayasimhadri, M.; Singh, N.; Srivastava, A.K.; Pulikkotil, J.; Dhar, A.; Budhani, R.C. Enhanced Thermoelectric Figure-of-Merit in Spark Plasma Sintered Nanostructured n-Type $SiGe$ Alloys. *Appl. Phys. Lett.* **2012**, *101*. [[CrossRef](#)]
184. Nozariasbmarz, A.; Agarwal, A.; Coutant, Z.A.; Hall, M.J.; Liu, J.; Liu, R.; Malhotra, A.; Norouzzadeh, P.; Öztürk, M.C.; Ramesh, V.P.; et al. Thermoelectric Silicides: A Review. *Jpn. J. Appl. Phys.* **2017**, *56*, 27. [[CrossRef](#)]
185. Wang, X.; Lee, H.; Lan, Y.; Zhu, G.; Joshi, G.; Wang, D.; Yang, J.; Muto, A.; Tang, M.; Klatsky, J.; et al. Enhanced Thermoelectric Figure-of-Merit in Nanostructured n-Type Silicon Germanium Bulk Alloys. *Appl. Phys. Lett.* **2008**, *93*, 193121. [[CrossRef](#)]
186. Zamanipour, Z.; Vashaeae, D. Comparison of Thermoelectric Properties of p-Type Nanostructured Bulk $Si_{0.8}Ge_{0.2}$ Alloy with $Si_{0.8}Ge_{0.2}$ Composites Embedded with $CrSi_2$ Nano-Inclusions. *J. Appl. Phys.* **2012**, *112*, 0–9. [[CrossRef](#)]
187. Mackey, J.; Dynys, F.; Sehirlioglu, A. Si/Ge - WSi_2 Composites: Processing and Thermoelectric Properties. *Acta Mater.* **2015**, *98*, 263–274. [[CrossRef](#)]
188. Usenko, A.; Moskovskikh, D.; Korotitskiy, A.; Gorshenkov, M.; Voronin, A.; Arkhipov, D.; Lyange, M.; Isachenko, G.; Khovaylo, V. Thermoelectric Properties of n-Type $Si_{0.8}Ge_{0.2}$ - $FeSi_2$ Multiphase Nanostructures. *J. Electron. Mater.* **2016**, *45*, 3427–3432. [[CrossRef](#)]
189. Wongprakarn, S.; Pinitsoontorn, S.; Tanusilp, S.A.; Kurosaki, K. The Effect of YSi_2 Nanoinclusion on the Thermoelectric Properties of p-Type $SiGe$ Alloy. *Phys. Status Solidi (A) Appl. Mater. Sci.* **2017**, *214*, 1–5. [[CrossRef](#)]
190. Basu, R.; Bhattacharya, S.; Bhatt, R.; Roy, M.; Ahmad, S.; Singh, A.; Navaneethan, M.; Hayakawa, Y.; Aswal, D.K.; Gupta, S.K. Improved Thermoelectric Performance of Hot Pressed Nanostructured n-Type $SiGe$ Bulk Alloys. *J. Mater. Chem. A* **2014**, *2*, 6922–6930. [[CrossRef](#)]
191. Ahmad, S.; Singh, A.; Bohra, A.; Basu, R.; Bhattacharya, S.; Bhatt, R.; Meshram, K.N.; Roy, M.; Sarkar, S.K.; Hayakawa, Y.; et al. Boosting Thermoelectric Performance of p-Type $SiGe$ Alloys through in-situ Metallic YSi_2 Nanoinclusions. *Nano Energy* **2016**, *27*, 282–297. [[CrossRef](#)]
192. Bathula, S.; Jayasimhadri, M.; Gahtori, B.; Kumar, A.; Srivastava, A.K.; Dhar, A. Enhancement in Thermoelectric Performance of $SiGe$ Nanoalloys Dispersed with SiC Nanoparticles. *Phys. Chem. Chem. Phys.* **2017**, *19*, 25180–25185. [[CrossRef](#)] [[PubMed](#)]

193. Nozariasbmarz, A.; Roy, P.; Zamanipour, Z.; Dycus, J.H.; Cabral, M.J.; LeBeau, J.M.; Krasinski, J.S.; Vashaee, D. Comparison of Thermoelectric Properties of Nanostructured Mg_2Si , $FeSi_2$, $SiGe$, and Nanocomposites of $SiGe-Mg_2Si$, $SiGe-FeSi_2$. *APL Mater.* **2016**, *4*. [[CrossRef](#)]
194. Nozariasbmarz, A.; Zamanipour, Z.; Norouzzadeh, P.; Krasinski, J.S.; Vashaee, D. Enhanced Thermoelectric Performance in a Metal/Semiconductor Nanocomposite of Iron Silicide/Silicon Germanium. *RSC Adv.* **2016**, *6*, 49643–49650. [[CrossRef](#)]
195. Zheng, G.; Su, X.; Liang, T.; Lu, Q.; Yan, Y.; Uher, C.; Tang, X. High Thermoelectric Performance of Mechanically Robust n-Type $Bi_2Te_{3-x}Se_x$ Prepared by Combustion Synthesis. *J. Mater. Chem. A* **2015**, *3*, 6603–6613. [[CrossRef](#)]
196. Fu, C.; Zhu, T.; Liu, Y.; Xie, H.; Zhao, X. Band Engineering of High Performance p-Type FeNbSb Based half-Heusler Thermoelectric Materials for Figure of Merit $zT > 1$. *Energy Environ. Sci.* **2015**, *8*, 216–220. [[CrossRef](#)]
197. Kleinke, H. New Bulk Materials for Thermoelectric Power Generation: Clathrates and Complex Antimonides. *Chem. Mater.* **2010**, *22*, 604–611. [[CrossRef](#)]
198. Nolas, G.S.; Morelli, D.T.; Tritt, T.M. Skutterudites: A Phonon-Glass-Electron Crystal Approach to Advanced Thermoelectric Energy Conversion Applications. *Annu. Rev. Mater. Sci.* **1999**, *29*, 89–116. [[CrossRef](#)]
199. Shi, X.; Yang, J.; Bai, S.; Yang, J.; Wang, H.; Chi, M.; Salvador, J.R.; Zhang, W.; Chen, L.; Wong-Ng, W. On the Design of High-Efficiency Thermoelectric Clathrates Through a Systematic Cross-Substitution of Framework Elements. *Adv. Funct. Mater.* **2010**, *20*, 755–763. [[CrossRef](#)]
200. Zhang, L.; Grytsiv, A.; Rogl, P.; Bauer, E.; Zehetbauer, M. High Thermoelectric Performance of Riple-Filled n-Type Skutterudites $(Sr,Ba,Yb)_yCo_4Sb_{12}$. *J. Phys. D Appl. Phys.* **2009**, *42*. [[CrossRef](#)]
201. Shi, X.; Yang, J.; Salvador, J.R.; Chi, M.; Cho, J.; Wang, H.; Bai, S.; Yang, J.; Zhang, W.; Chen, L. Multiple-Filled Skutterudites: High Thermoelectric Figure of Merit Through Separately Optimizing Electrical and Thermal Transports. *J. Am. Chem. Soc.* **2011**, *133*, 7837–7846. [[CrossRef](#)] [[PubMed](#)]
202. Zaitsev, V.K.; Fedorov, M.I.; Gurieva, E.A.; Eremin, I.S.; Konstantinov, P.P.; Samunin, A.Y.; Vedernikov, M.V. Highly Effective $Mg_2Si_{1-x}Sn_x$ Thermoelectrics. *Phys. Rev. B Condens. Matter Mater. Phys.* **2006**, *74*, 2–6. [[CrossRef](#)]
203. Khan, A.U.; Vlachos, N.V.; Hatzikraniotis, E.; Polymeris, G.S.; Lioutas, C.B.; Stefanaki, E.C.; Paraskevopoulos, K.M.; Giapintzakis, I.; Kyratsi, T. Thermoelectric Properties of Highly Efficient Bi-Doped $Mg_2Si_{1-x-y}Sn_xGe_y$ Materials. *Acta Mater.* **2014**, *77*, 43–53. [[CrossRef](#)]



© 2019 by the authors. Licensee MDPI, Basel, Switzerland. This article is an open access article distributed under the terms and conditions of the Creative Commons Attribution (CC BY) license (<http://creativecommons.org/licenses/by/4.0/>).

1.3 Anisotropy in thermoelectric materials

In the previous section 1.2, the state-of-the-art thermoelectric materials and especially CCO were introduced. While the role of anisotropy was shortly discussed for CCO, a more general view will be given in this section. Furthermore, ways to exploit anisotropy by controlling crystal shape, in particular by selectively reducing dimensions as in nanosheets, are analyzed.

The electronic and thermal transport properties of a single material are directly linked to its crystal and band structure. While isotropic transport properties are easier to handle during processing, many relevant materials show some form of anisotropy. Naturally, layered crystal structures exhibit anisotropic transport properties, and there are several other state-of-the-art materials besides CCO showing them. First of all, the flagship thermoelectric material for applications near room temperature Bi_2Te_3 also shows anisotropic behavior. The structure consists of quintuple layers of Te-Bi-Te-Bi-Te along the c -axis linked by VAN DER WAALS forces, which results in a higher electrical and thermal conductivity along the a, b -plane [99]. Another oxide besides CCO having a layered structure is Na_xCoO_2 . Similar to CCO, the structure consists of CoO_2 layers along the a, b -plane, but they are separated by sodium ion layers with variable occupations [100]. The x in the formula indicates the occupation of sodium and has a significant impact on the thermoelectric properties [101, 102]. Analogous to CCO, the in-plane orientation is preferred for thermoelectrics due to the high electrical conductivity. Another example for a layered thermoelectric compound is the oxyselenide BCSO, which benefits from an exceptionally low thermal conductivity based on the layered structure. Bi_2O_3 layers with Bi_4O tetrahedra and Cu_2Se_2 layers with CuSe_4 tetrahedra alternate along the c -axis [75]. Again, this leads to a lower thermal conductivity along the c -axis and a higher charge carrier mobility along the a, b -plane [75, 103].

An extreme form of anisotropic transport is given in two-dimensional quantum-well structures, where the ratio between lateral and axial dimensions varies by 2 to 5 orders of magnitude [104, 105]. These so-called nanosheets could drastically enhance the power factor and the figure-of-merit for some thermoelectric materials [42, 106]. Extremely thin sheets lead to the quantum confinement effect, where the movement of charge carrier is possible only in-plane due to the quantization of energy out-of-plane [107]. As a result, a two-dimensional electron gas emerges, increasing the electrical conductivity. Furthermore, the DOS at the FERMI level is increased, which benefits the SEEBECK coefficient [108]. The thermoelectric properties of unit-cell thin STO were investigated and confirmed the huge possibilities regarding nanosheets or artificial superlattices [109]. Nevertheless, fully exploiting the properties of nanosheets within bulk materials remains problematic, as simply stacking them almost nullifies the benefits [110]. Possible approaches are the design of ceramics with nanostructured grain-boundaries [111] or the embedding of nanosheets within a matrix. Further explanation regarding the synthesis and possible applications of oxide nanosheets is given by the review in section 1.3.2.

To utilize the anisotropic transport behavior in polycrystals, a preferred orientation or a texture has to be induced. For thin films, chemical deposition techniques [112] or pulsed laser deposition [113] are appropriate techniques to get grain-oriented polycrystals. Pressure-assisted orientation is preferred, when the crystal morphology is plate-like or sheet-like. To achieve even better texture, elaborated techniques such

as templated grain growth can be utilized, where the same material is used with two different crystal sizes. While the matrix material is a powder with small crystal sizes, the template particles have an anisotropic habitus with several microns in size. Tape-casting the template particles aligns them and the matrix powder supports the crystal growth by OSTWALD ripening during sintering [114]. To control the morphology of a material, the crystal growth is crucial. Depending on the used method, either the thermodynamically stable crystal shape with the lowest surface energy or kinetically metastable forms are possible. One way to reliably obtain large crystals is the molten-flux synthesis, which is discussed in the following.

1.3.1 Control of morphology by molten-flux synthesis

Anisotropically structured materials tend to exhibit anisotropic morphologies [115], which can be utilized to get a preferred orientation or texture in a polycrystal during pressing and sintering. The molten-flux synthesis is an excellent method for synthesizing metal-oxide particles with high purity and a well-defined morphology. Crystal sizes are typically on the microscale, but the nanoscale is possible as well if the reaction parameters are adjusted accordingly.

A major advantage compared to the classical solid-state route is the improved homogeneity of the reactant mixture due to solvent-induced diffusion, which enables larger and better defined crystals [115]. In addition, depending on the melting temperature of the flux used, a lower reaction temperature is possible. The procedure can be divided into four steps as displayed in Fig. 1.12 [116]. In the first step, the reactants dissolve in the molten flux and in the second step, diffusion leads to a homogeneous mixture. Nucleation of the reaction product occurs in the third step, followed by crystal growth based on OSTWALD ripening in the fourth step [115].

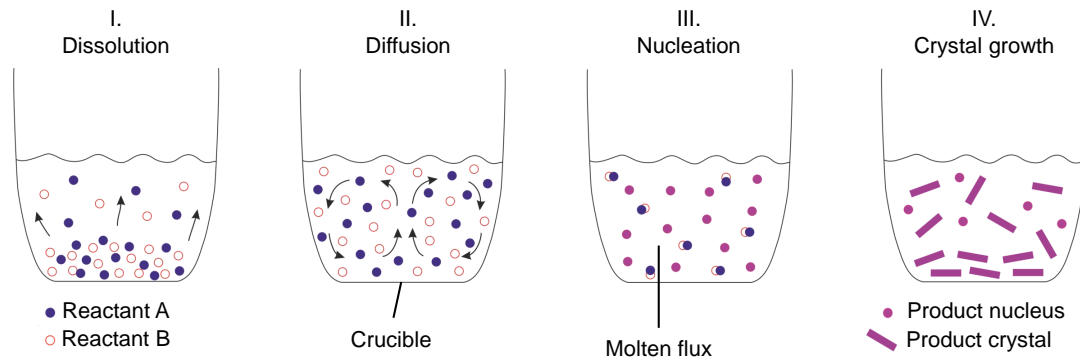


Figure 1.12: Step-wise procedure of the molten-flux synthesis. First, the reactants dissolve in the molten flux and diffusion mixes the reactants. Next, the nucleation of the product starts and crystal growth by OSTWALD ripening leads to large crystals.

The outcome of the procedure mainly depends on the chosen flux, the reactants, the flux-to-reactant molar ratio, the temperature, the heating duration and the cooling time [115, 117, 118]. To avoid impurities in the product, ideally the cations of the flux used match the cations of the product. However, impurities in terms of doping can also be desired to change the electronic properties [119]. Typical inorganic fluxes consist of salt-like hydroxides (NaOH, KOH, LiOH), carbonates (Na_2CO_3), sulfates (Na_2SO_4) or halides (NaCl, KCl, NaF) [115]. The flux should have a low melting point compared

to the reactants and should be removable without residue after the reaction. Another important aspect is the flux-to-reactant molar ratio, which is typically between 1:1 and 50:1 and is important for the solubility of the reactants and their reaction rate [115]. To obtain smaller particles or even nanoparticles by molten-flux synthesis, the reaction temperature should be low and the precursors have to be nanosized to allow fast dissolution and short reaction times [120].

Relatively little is known about the kinetic mechanisms during the reaction in the molten-flux that are responsible for the morphology, but two approaches are of particular importance. When thermodynamic equilibrium is reached by rapid kinetic processes, the minimum total surface energy is crucial for the habitus and leads to the WULFF-CURIE shape [121, 122]. However, for large crystals, the small surface-to-volume ratio hinders equilibrium, and the crystal facets with low growth velocities are decisive according to the WULFF-CHEKHOV theorem [123, 124].

Overall, the method allows the synthesis of metal oxides with a controlled morphology, which can be utilized in thermoelectrics to benefit from a preferred orientation or even a texture within a polycrystal. Of particular interest are plate-like crystals with favorable thermoelectric properties in the desired direction, since they can be arranged perpendicular to the pressing direction.

1.3.2 Anisotropic oxides: La_2NiO_4 and $\text{Na}_2\text{Ca}_2\text{Nb}_4\text{O}_{13}$

The two oxide materials La_2NiO_4 (LNO) and $\text{Na}_2\text{Ca}_2\text{Nb}_4\text{O}_{13}$ (NCNO) with layered structures and hence anisotropic transport properties are investigated within Chapter 2 for thermoelectric composites. Therefore, a short introduction of these materials is given in this section. As for the molten-flux synthesis, both materials can be successfully synthesized with a plate-like crystal shape [118, 125], although in the case of LNO, further modifications were required to obtain a suitable composite material. Furthermore, both are rather unusual in terms of thermoelectric materials, because as a single material they do not stand out for their thermoelectric properties. As a result, information about their thermoelectric properties is rather scarce. The LNO is built up from LaO rock-salt layers and LaNiO_3 perovskite layers alternating along the c -axis [126, 127]. It is a p -type material with a moderate SEEBECK coefficient around $50 \mu\text{V K}^{-1}$ at 1237 K [128], but a relatively high electrical conductivity of up to 200 S cm^{-1} [129]. As a mixed ionic-electronic conductor, it is used in gas separation membranes for oxygen, microelectronics and catalysis [130, 131]. The NCNO, on the other hand, consists of $[(\text{Ca}_2\text{Na})\text{Nb}_4\text{O}_{13}]^-$ perovskite-type layers linked by Na^+ cations [132, 133]. Due to its large band gap of 3.3 eV [118] it shows electrically insulating characteristics, wherefore the material is not used in thermoelectrics but rather photocatalysis [134]. The SEEBECK coefficient for NCNO is not recorded in literature, but the inversed coupling of the electrical conductivity should result in noteworthy values. As single materials, both are clearly inferior to CCO concerning their thermoelectric performance, but the high electrical conductivity of LNO and the high SEEBECK coefficient of NCNO could possibly result in interesting composites.

1.3.3 Two-dimensional oxides: Recent progress in nanosheets

Richard Hinterding and Armin Feldhoff

Zeitschrift für Physikalische Chemie, 233 **2019**, 117-165

DOI: 10.1515/zpch-2018-1125

Review

Richard Hinterding* and Armin Feldhoff

Two-Dimensional Oxides: Recent Progress in Nanosheets

A Retrospection on Synthesis, Microstructure and Applications

<https://doi.org/10.1515/zpch-2018-1125>

Received January 26, 2018; accepted February 27, 2018

Abstract: Two-dimensional (2D) materials have been widely investigated for the last few years, introducing nanosheets and ultrathin films. The often superior electrical, optical and mechanical properties in contrast to their three-dimensional (3D) bulk counterparts offer a promising field of opportunities. Especially new research fields for already existing and novel applications are opened by downsizing and improving the materials at the same time. Some of the most promising application fields are namely supercapacitors, electrochromic devices, (bio-) chemical sensors, photovoltaic devices, thermoelectrics, (photo-) catalysts and membranes. The role of oxides in this field of materials deserves a closer look due to their availability, durability and further advantages. Here, recent progress in oxidic nanosheets is highlighted and the benefit of 2D oxides for applications discussed in-depth. Therefore, different synthesis techniques and microstructures are compared more closely.

Keywords: nanosheet; oxide; thermoelectric; two-dimensional; ultrathin film.

1 Introduction

With the enablement of measuring functional properties of two-dimensional (2D) graphene sheets and the discovery of electrons being able to behave like Dirac-type fermions without restmass [1], new interest in 2D materials was awoken. Actual research considers all elements of the periodic table and their

*Corresponding author: Richard Hinterding, Leibniz University Hannover, Institute of Physical Chemistry and Electrochemistry, Callinstraße 3A, D-30176 Hannover, Germany, e-mail: richard.hinterding@pci.uni-hannover.de

Armin Feldhoff: Leibniz University Hannover, Institute of Physical Chemistry and Electrochemistry, Callinstraße 3A, D-30176 Hannover, Germany

combinations with the aim to synthesize materials with improved functionality. This research includes 2D oxides and got triggered by sophisticated analytical methods and new models, which led to a significant boost in attention and acceleration of investigations regarding this topic. The determining features of 2D materials are their molecular thickness with structural resemblance to graphene. Since graphene is a monolayer sheet of carbon atoms with lateral sizes up to millimeters, the ratio between lateral and axial dimensions in 2D materials is usually between 2 and 5 orders of magnitude [2]. Despite the monolayer in graphene, molecular thickness in so-called nanosheets also provides a significant change in functional properties in comparison to their corresponding 3D bulk materials [3]. These shifts in properties show huge potential for a wide range of applications and have been investigated intensively in the recent years.

Accompanying the novel interest in 2D materials, several reviews have been published in the last few years covering various aspects of 2D materials. While some of them discuss 2D materials in general [2, 4–6], others focus on specific functional properties like electrical capacity [7], charge transport [8] or dielectrics [9]. Furthermore, synthesis methods like the liquid exfoliation process [10] or special application fields as biosensing [11] are covered in-depth. Reviews on 2D oxides and hydroxides in particular are either a subcategory in the generalized reviews, do not cover the most recent research because new methods have been established since the publication [12] or focus on exfoliated materials exclusively [13]. The work from ten Elshof et al. [13] is also recommended for further insights into hydroxides, since they are only peripherally mentioned here.

This review focuses on novel 2D oxide nanosheets and provides an overview of the currently researched compounds, the state-of-the-art synthesis routes, the microstructures within the 2D compounds leading to their extraordinary properties and the resulting application fields.

2 Elemental compositions

Two-dimensional oxide materials have been researched comprehensively in the past few years, which includes research of practical work in synthesis and theoretical calculations of properties with *ab initio* methods. The Tables 1–5 offer an overview of the by now most investigated oxidic compounds. Therefore, the tables are oriented to the order of appearance from specific atoms in the periodic table. While this order is easily maintained with binary oxides, ternary and quaternary compounds are listed separately. The tables do not claim to be complete, but they surely give an insight on the versatility of research in 2D oxide materials. Moreover, specific application fields as supercapacitors, (photo-) catalysis,

Tab. 1: Selected oxidic compounds containing alkali metals with approved synthesis methods and possible application fields.

Elemental composition	Synthesis method	Application field	Reference
$\text{NaCo}_2\text{O}_4, \text{Na}_{0.7}\text{CoO}_2$	Template, pyrolysis	Thermoelectrics	[14, 15]
$\text{CsW}_{11}\text{O}_{36}^{2-}$	Ion intercalation	Electrochromic devices	[16]
$\text{Rb}_{4-x}\text{W}_{11}\text{O}_{35}^{x-}$	Ion intercalation	Electrochromic devices	[17]
$\text{K}_2\text{W}_6\text{O}_{19}, \text{K}_{0.3}\text{WO}_3$	CVD	Electrochromic devices	[18]

Tab. 2: Selected oxidic compounds containing earth-alkali metals with approved synthesis methods and possible application fields.

Elemental composition	Synthesis method	Application field	Reference
BeO	Oxidation	Gas sensors, catalysis	[19, 20]
MgO	Laser deposition, pyrolysis	Adsorbent, catalysis	[21–23]
$\text{Mg}(\text{OH})_2$	Template	Adsorbent	[24]
CaO	Template	Adsorbent	[15]
$\text{Ca}_2\text{Na}_{m-3}\text{Nb}_m\text{O}_{3m+1}^-$	Ion intercalation	Catalysis, supercapacitors	[25–28]
$\text{CaNb}_3\text{O}_{10}^-$	Ion intercalation	Photocatalysis	[29]
$\text{CaNaTa}_3\text{O}_{10}^{2-}$	Ion intercalation	Catalysis	[30]
$\text{CaNb}_2\text{TiO}_{10}^{2-}$	Ion intercalation	Catalysis	[30]
$\text{A}_2\text{Ta}_2\text{TiO}_{10}^{2-}$ (A = Ca, Sr)	Ion intercalation	Catalysis	[30]
$\text{SrA}_2\text{TiO}_{10}^{2-}$ (A = Ta, Nb)	Ion intercalation	Catalysis	[30]
$\text{SrNb}_2\text{O}_{10}^-$	Ion intercalation	Catalysis	[31]

thermoelectrics, electrochromic devices or (bio-) chemical sensors play a decisive role as motivation for further investigations. They will be discussed later on in the Section Applications. It should be stated, that several charged compounds appear in the tables, which result from ion intercalation. Their characteristics will be discussed in the Sections Synthesis and Microstructures.

Alkali and earth-alkali metals (see Tables 1 and 2) play a minor but not unimportant role in two-dimensional materials in comparison to transition metals, which has various explanations. First of all, there is a numerical reason with simply less existing elements of alkali and earth-alkali metals than transition metals, but this is not the main reason. Binary bulk oxides of alkali and earth-alkali metals find unfrequent usage in nowadays applications and are either a side component of larger production chains or of little use for industrial processes. Since the bulk materials already find limited merit, the properties of their nanosheets need to be extraordinary and not only improved to increase the production value. While this is not the case for the binary oxides of these groups, especially the smaller elements as lithium, sodium and potassium have a special role in the synthesis of

Tab. 3: Selected ternary and quaternary oxidic compounds containing transition metals with approved synthesis methods and possible application fields.

Elemental composition	Synthesis method	Application field	Reference
ANb_2O_7^- (A = La, Pr)	Ion intercalation	Catalysis	[32]
AWO_6^- (A = Ta, Nb)	Ion intercalation	Catalysis	[33]
NbMoO_6^-	Ion intercalation	Catalysis	[34]
TiAO_5^- (A = Ta, Nb)	Ion intercalation	Catalysis	[35]
$\text{Ti}_2\text{NbO}_7^-$	Ion intercalation	Catalysis	[35]
$\text{Ba}_5\text{Ta}_4\text{O}_{15}$	Solvothermal	Photocatalysis	[36]
NiFe_2O_4	Template	Supercapacitors	[37]
NiCo_2O_4	Solvothermal	Batteries, catalysis	[38, 39]
ZnCo_2O_4	Solvothermal	Supercapacitors	[40]
$\text{CoCr}_2\text{O}_4/\text{C}$	Calcination	Electrocatalysis	[41]
LaNiO_3	Sol-gel	Supercapacitors	[42]
FeVO_4	CVD	Batteries	[43]
$\text{Bi}_{0.2}\text{Sr}_{0.8}\text{Ta}_2\text{O}_7^{-1.8}$	Ion intercalation	Luminescence	[44]
Bi_2MoO_6	Solvothermal	Photocatalysis	[45, 46]

Tab. 4: Selected oxidic compounds containing metals and non-metals of a higher main group with approved synthesis methods and possible application fields.

Elemental composition	Synthesis method	Application field	Reference
Al_2O_3	Rapid heating	Undefined	[47]
Bi_2O_3	Solvothermal	Photocatalysis	[48, 49]
SnO_2	Template	Supercapacitors	[50–52]
SnO_2/ZnO	Template	Gas sensors	[53]
$\text{In}_2\text{O}_3/\text{SnO}_2$ (ITO)	Laser deposition	Electronics	[54]
Graphene oxide	Various	Template	[55]
CeO_2/PdO doped	Self assembly	Catalysis	[56]

nanosheets. As further explained in the Section Synthesis, layered materials are required for top-down synthesis techniques and their delamination is crucial for gaining nanosheets. Their small ionic radii and the singular charge provides the possibility of ion exchange with H^+ ions in acidic solutions. This method gets commonly used in the liquid exfoliation method, wherefore alkali metals are welcomed within the layered materials as in KNb_3O_8 , $\text{RbLaNb}_2\text{O}_7$, $\text{Rb}_4\text{W}_{11}\text{O}_{35}$ or $\text{K}_{0.45}\text{Mn}_{1-x}\text{Ru}_x\text{O}_2$ to exercise this technique [17, 32, 72, 90]. Despite of this, earth-alkali metals in particular are used in combination with Ruddlesden-Popper phases with a composition of $\text{A}_2[\text{A}^*_{n-1}\text{B}_n\text{O}_{3n+1}]$ (A = alkali, A^* = earth-alkali, B = transition metal) [30] due to high research interest caused by superior catalytic properties of the exfoliated nanosheets in comparison to their 3D bulk counterparts.

Tab. 5: Selected binary-oxidic compounds containing transition metals with approved synthesis methods and possible application fields.

Composition	Synthesis method	Application field	Reference
TiO ₂	Sol-gel, template, ion intercalation	Catalysis	[52, 57–60]
Ti ₂ O ₃	Electron irradiation	Catalysis	[61]
Ti _{1-x} O _{2-x} ^{2x-}	Ion intercalation	Catalysis	[62, 63]
Ti _{1-x} Fe _x O ₂	Ion intercalation	Catalysis	[15, 64]
Ti _{1-x} Nb _x O ₂	Ion intercalation	Catalysis	[65]
V ₂ O ₅	Ion intercalation	Batteries	[66]
V ₆ O ₁₂	Self-assembly	Catalysis	[67]
Cr ₂ O ₃	Rapid heating	Batteries	[47]
MnO, MnO ₂ , Mn ₂ O ₃	Template, ion intercalation	Supercapacitors, catalysis, biosensors	[37, 68–71]
Mn _{1-x} Ru _x O ₂	Ion intercalation	Supercapacitors	[72]
Fe ₂ O ₃ , Fe ₃ O ₄	Template, pyrolysis	Batteries, catalysis	[37, 73, 74]
[CoO ₂] ⁻	Ion intercalation	Catalysis, batteries	[63, 75, 76]
Co ₃ O ₄	Pyrolysis, solvo-thermal, template	Catalysis, supercapacitors	[23, 37, 38]
NiO	Template, pyrolysis, solvothermal	Supercapacitors, catalysis	[23, 37, 38, 77, 78]
CuO/Cu ₂ O	Oxidation	Photocatalysis	[79]
CuO, Cu _{1-x} Ag _x O	Growth method	Supercapacitors	[80, 81]
ZnO	Solvothermal, electrochemical deposition	Gas sensors, photo-electrochemical device	[82–84]
ZnO/SnO ₂	Template	Gas sensors	[53]
Y ₂ O ₃	Rapid heating, solvothermal	Photoluminescence	[47, 85]
ZrO ₂	Sol-gel, template, rapid heating	Biosensors	[47, 52, 58, 86]
NbO	Solvothermal	Catalysis, membranes	[87, 88]
Nb ₂ O ₅	Template	Photocatalysis	[52]
K _{4-x} Nb ₆ O ₁₇ ^{x-}	Ion intercalation	Photocatalysis	[89]
Nb ₃ O ₈ ⁻	Ion intercalation	Photocatalysis	[90]
MoO ₂ , MoO ₃	Ion intercalation, template	Supercapacitors	[71, 91]
[Ru ⁴⁺ O _{2.1}] ^{0.2-}	Ion intercalation	Supercapacitors	[63, 92, 93]
Rh ₂ O ₃	Oxidation	Electrocatalysis	[94]
CdO	Self-assembly	Gas sensors, solar cell	[95]
Yb ₂ O ₃	Solvothermal	Biosensor	[96]
HfO ₂	Interface mediated	Electronics	[97]
Ta ₂ O ₅ , TaO ₃ ⁻	Template, ion intercalation	Batteries, electrochromic devices	[52, 98]
W ₂ O ₇ , WO ₃	Template, ion intercalation	Supercapacitors, electrochromic devices	[33, 71]
IrO ₂	Ion intercalation	Supercapacitors	[99]

Transition metal oxides (TMOs) on the other hand cause wide interest in research due to multiple promising application fields in catalysis, supercapacitors, sensing and more (see Tables 3 and 5). With the increasing atomic number, the atomic radii and the electronic d- or f-orbitals grow, wherefore the electron configurations allow more interactions with upcoming d- and f-electrons. This widens the field of possible interesting interactions, which can be used in several applications. The research regarding binary TMOs is numerous, which becomes partly evident by the length of Table 5. Binary compounds allow an easier understanding of effects and are already investigated as 3D bulk materials in-depth, which explains this imbalance towards more complex compounds. Prominent layered compounds as family members of perovskite-related structures aside with Ruddlesden-Popper phases are the Aurivillius $\text{Bi}_2\text{A}_{n-1}\text{B}_n\text{O}_{3n+1}$ (A = alkali or earth-alkali metals, B = Ti, Nb, Ta) and Dion-Jacobson phases $\text{A}[\text{A}^*_{n-1}\text{B}_n\text{O}_{3n+1}]$ (A = alkali metal, A* = earth-alkali, B = Ti, Nb, Ta). Another useful structure-type is the spinel-type AB_2O_4 , whose nanosheets showed promising catalytic characteristics as for NiFe_2O_4 , NiCo_2O_4 , ZnCo_2O_4 or CoCr_2O_4 .

Other oxides containing metals and non-metals of a higher main group are shown in Table 4. The benefit of graphene oxide as a non-metal compound lies within its removability during calcination, which allows the usage as a template for other oxides. Additionally, it has shown good separation properties of gases for membrane applications.

Overall, the results of downsizing the crystal dimensions and exploiting the morphology show promising results regarding improved properties. The TMOs are currently the main focus of research in utilizing the benefits of nanosheets, which does not imply worse applicability for the other oxides by all means. In-depth discussions regarding differences of application fields and the most promising candidates are held in the Section Applications.

3 Synthesis

Generally, there are two different approaches for the construction of 2D oxide nanosheets, namely the top-down and bottom-up synthesis route. The top-down route comprises layered 3D bulk materials, which can be chemically, physically or mechanically split into 2D materials. This process is called delamination, exfoliation or cleavage. On the other hand, the bottom-up route uses the formation of 2D materials on a molecular level in a specific medium or on a substrate. A selection of commonly used synthesis variants for synthesizing oxide nanosheets or ultrathin oxide films is displayed in Figure 1. The shown methods are all applicable for 2D oxides and most of them will be presented within this

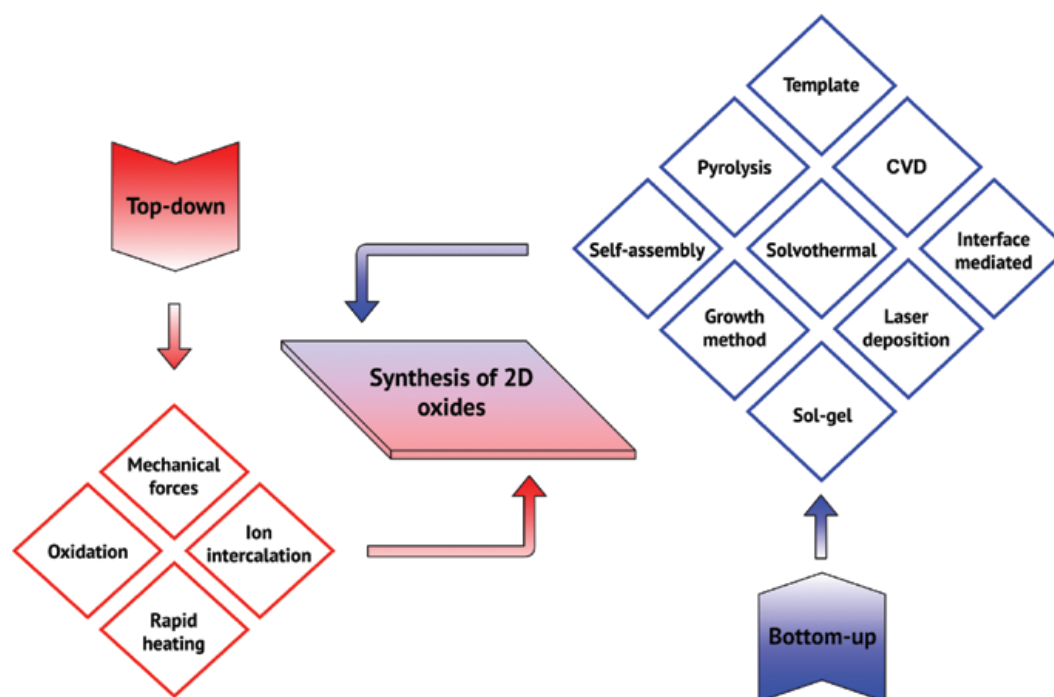


Fig. 1: Overview of different suitable synthesis methods for 2D oxides divided into top-down and bottom-up routes.

section. It is worth noting, that ultrathin oxide films may also appear naturally as a passivation of specific elemental materials as for Al, Ni or Cr. Since these appear rarely and do not provide the versatility of nanosheets, they will not be considered in the following sections. Further methods for synthesizing nanosheets as ion intercalation with Li ions, selective etching or the hot-injection method are also established but not suitable for oxidic materials and discussed by Tan et al. in-depth [6].

3.1 Top-down synthesis: ion exchange and intercalation

In the 1990s first syntheses of oxide nanosheets were published, which used top-down techniques of ion intercalation for layered materials [25, 57, 58]. This method is still one of the most used synthesis routes for layered materials, although some modifications and improvements were established. Today, the common synthesis route for 2D oxidic nanosheets is a multistep top-down technique. The internal layers of the 3D material initially proceeds an ion exchange due to acid treatment followed by an ion intercalation caused by large organic molecules like the tetrabutylammonium cation (TBA^+) [76, 100, 101]. Optionally, the exfoliation of the intercalated layers is subsequently assisted by sonication

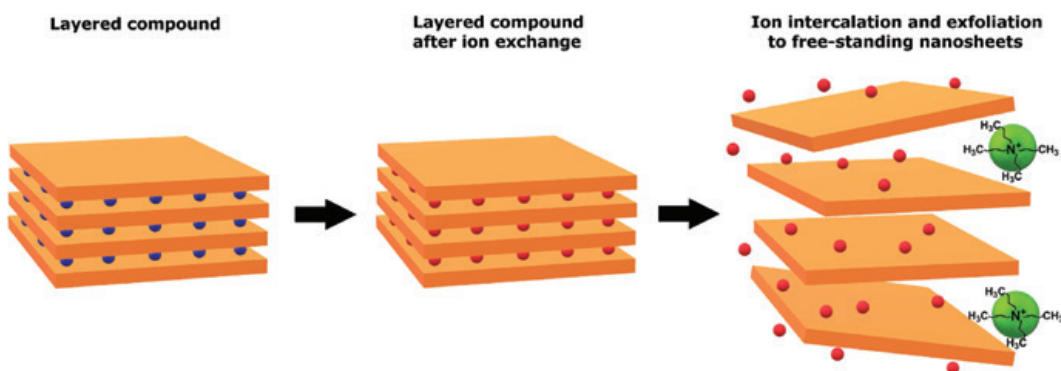


Fig. 2: Schematic synthesis route for liquid exfoliation of layered oxides. In the first step, the alkali or earth-alkali cations (blue orbs) in the interlayers are partially or entirely exchanged caused by acid treatment (red orbs). Afterwards, the layers are separated by large organic cations like the TBA⁺ (green orbs), which function as an exfoliation agent, assisted by osmotic swelling or sonication. As a result, the free-standing nanosheets remain dispersed in the liquid medium. Inspired by Nicolosi et al. [10].

or shear forces. Adequate precursors for this method are layered materials with alkali or earth-alkali metals located inbetween the layers. The position of these metals can easily be exchanged by H⁺ cations trough immersing the layered materials in acid aqueous solution. A second cation exchange process occurs in basic aqueous solution with TBA⁺. Due to the large radius of the organic cation compared to H⁺, the distance of the interlayer increases (see Figure 2).

By applying further energy with sonication or shear forces, the exfoliation is completed with a positively charged surface on the oxidic nanosheets. Alternatively, further driving forces as the formation of insoluble solids during the exfoliation process can be used to improve the outcome [102]. Besides, the exchange of anions is applicable for layered double hydroxides (LDHs) in particular. Overall, the exchange of ions and subsequently intercalation provides high yields and upscaling possibilities [6]. Nevertheless, the chemical formula of the nanosheets deviates compared to the 3D bulk material due to occurred chemical reactions during the exfoliation.

3.2 Top-down synthesis: mechanical forces

The synthesis of graphene was initially performed by the use of Scotch tape, which provided a mechanical cleavage of the 3D graphite into 2D graphene [103, 104]. The method exploits the cleavage of relatively weak van der Waals bonds in layered bulk materials, but in-plane the stronger covalent bonds remain [105]. It provides a product with high crystallinity while the technique itself is easily and

extensively applicable. Furthermore, the 2D material can be attached to many different surfaces after the cleavage. Although, several disadvantages make other techniques more viable. Since the Scotch tape has to be used several times until the nanosheets are obtained, the yield of the process is rather low. Furthermore, the process itself is quite slow and not applicable for upscaling. As the process is managed by hand, the controllability of thickness, size and shape of the nanosheets is lacking and repeatability is an issue. Another problem concerning layered oxides are the mainly covalent and ionic bonds, which require more appropriate techniques. Therefore, the Scotch tape lacks in applicability and is replaced by a wide range of various techniques.

Other possibilities of applying mechanical forces are sonication and shear forces. These methods require a liquid medium, which only disperses the layered material and does not dissolve it. The advantages of these techniques are high yields and the possibility of upscaling at rather low costs by utilizing a cheap solvent [106]. The idea of sonication is using bubbles and their implosions induced by acoustic cavitations to create tension between the layers [107]. Therefore, the surface energy of the layered material and the liquid medium have to match [106]. Furthermore, the medium should prevent the aggregation of nanosheets and their restacking. Thus, the selection and adjusting of the solvent is critical for a successful exfoliation. For using easily applicable and available solvents as water, the modulation of the surface tension is necessary by using ionic or nonionic polymers. As a downside, the attachment of residual polymer on the surface of the nanosheets is often an exclusion criterion for electrical applications. A further issue of sonication concerns the size of the nanosheets, because the mechanical force shatters sheets of large dimensions into smaller ones. The amount of defects in comparison to the Scotch tape is increasing as well due to the possible interaction with the liquid medium [6]. Hence, the controllability of the technique is limited to selecting the sonication time, solvent, additives, temperature and parameters of the sonication device. The utilization of shear forces contributes similar characteristics but with even bigger upscaling possibilities for industry standards. For example, $\text{Ti}_5\text{NbO}_{14}$ nanosheets were synthesized by Zhang et al. [108] with the help of a specialized milling machine. Hereby, additional parameters as rotor diameter and shear rate are determining factors [109].

3.3 Top-down synthesis: rapid heating

In recent years, a novel method with a potentially high production rate for oxidic nanosheets arised by Zhao et al. [47]. Simply by rapid heating of hydrous chloride compounds containing the desired metal species, freestanding nanosheets could

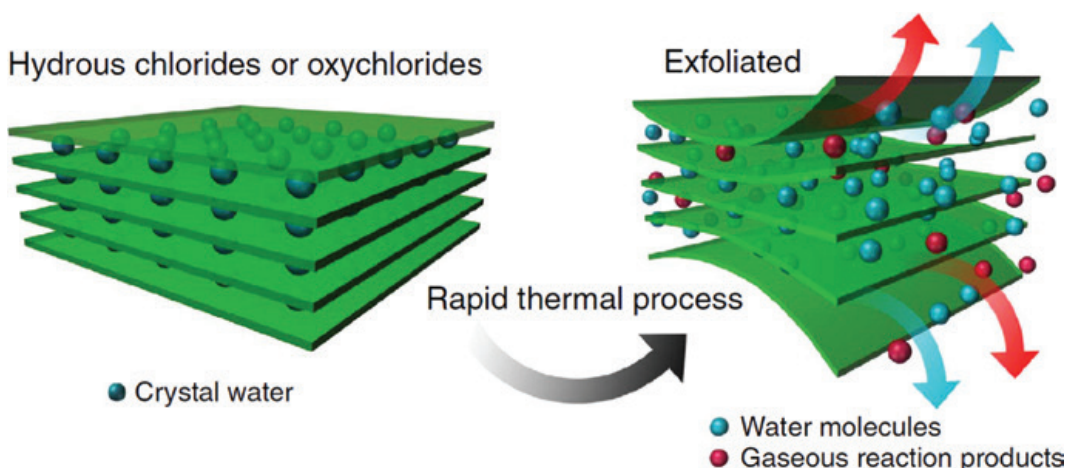


Fig. 3: Schematic principle of the exfoliation process realized by rapid heating of hydrous chlorides. The gaseous products are released in between the layers due to the rapid heating, leading to exfoliation and nanosheets consecutively. Reproduced with permission from [47]. Copyright 2016 Springer Nature. Creative Commons License CC BY 4.0.

be produced. The succeeded nanosheets consisted of Cr_2O_3 , ZrO_2 , Al_2O_3 or Y_2O_3 , while the Cr_2O_3 nanosheets showed the most consistent results. The principle of this method is using the releasing gaseous molecules as water and hydrochloric acid at the heating process to exfoliate the sheets (see Figure 3).

A critical parameter is the heating rate, because rapid heating is necessary to effectively separate the layers and gain monolayers or few multilayer sheets. For example, direct heating in an alcohol lamp flame led to inhomogenous results, but placement in a preheated muffle furnace showed significant improvement. Since the non-layered or anhydrous materials did not lead to nanosheets, the technique seems limited to hydrous chlorides. Though, the simplicity and swiftness of the synthesis route is promising for producing nanosheets in industry orders of magnitude.

3.4 Top-down synthesis: oxidation

The aforementioned methods all require layered oxide materials, but gaining oxide products out of non-oxidic materials is another route. Therefore, the synthesis of non-oxide nanosheets and the oxidation afterwards is possible as shown by Bai et al. [94]. In this example, Rh nanosheets were oxidized chemically by HClO to Rh_2O_3 nanosheets. Other works showed the oxidation of large surfaces to exploit the properties of 2D sheets as shown for $\text{CuO}/\text{Cu}_2\text{O}$ on a Cu surface [79]. Here, the nanosheet array was formed electrochemically via anodization. When using non-oxide nanosheets this method is only superior to other methods, if it is

used for oxide compounds, which else can not be obtained. Otherwise it simply includes another oxidation step, which is already included or not necessary in the other methods. The modification of non-oxide surfaces on the other hand is well controllable if realized electrochemically by adjusting the anodization time, current density, temperature and viscosity of the electrolyte. Simple oxidation as in passivation does not enlarge the surface area and is not easily adjustable.

3.5 Bottom-up synthesis: chemical vapor deposition

A highly valuable synthesis for the bottom-up route is the chemical vapor deposition (CVD). Typically, one precursor is heated in a furnace and led to a reaction chamber via a gaseous flux. The gaseous flux may consist of transport gases and/or further gaseous precursors. Within the chamber, the gaseous precursors react on the surface of a specific substrate and form nanosheets or ultrathin films at proper experimental parameters [110]. In some cases, catalysts are necessary for enabling the desired reaction. The process itself provides a high level of control due to parameters as the choice of precursor, substrates and catalysts, temperature, atmosphere and the gaseous flow rate. Under appropriate experimental conditions, the amount of impurities and defects within the sheets or ultrathin films are negligible [6]. As a downside of this powerful technique, usually high temperatures and cost-intensive inert atmospheres are required. Furthermore, the nanosheets are developed on a specific substrate, which requires further transferring steps for applications or substrates with direct applicability.

3.6 Bottom-up synthesis: solvothermal method

The solvothermal synthesis is a typical bottom-up synthesis in a liquid medium. If water is used as a medium, the synthesis is called hydrothermal. Characteristic for these solvent-driven syntheses is the usage of closed autoclaves for reaching a higher reaction temperature than the boiling point of the selected solvent. The high temperature leads to an increasing pressure inside the vessel and promotes the formation of nanocrystals within the reaction chamber. For the formation of nanosheets commonly additives as Pluronic P123 or ethylene glycol are used [111], which function as a surfactant due to hydrophobic forces. The method enables a high yield at usually low costs, but the optimum experimental parameters for the desired size and thickness are difficult to determine and have to be adjusted to the used materials [6]. Critical parameters are the concentration of the precursors, the used solvent, surfactants, temperature and the oxygen partial pressure.

Even the used oven and autoclave may have an impact on the gained product and may influence the experimental results. These circumstances are inconvenient for a production on industrial scale.

3.7 Bottom-up synthesis: templated method

A relatively new technique for synthesizing anisotropic nanosheets is the use of 2D templates. For example, graphene oxide (GO) can be used for nanosheets consisting of TiO_2 , ZrO_2 , Nb_2O_5 , SnO_2 or Ta_2O_5 [52]. Therefore, dried GO was dispersed in cyclohexane together with the respective metal alkoxide, which resulted in adsorbed metal alkoxides on the surface of GO. In an autoclave, the GO was subsequently reduced and metal oxide nanofilms were formed. GO is especially suitable in this case, since the functional groups of GO hydrolyze the organic ligands of the adsorbed metal alkoxides. Free-standing nanosheets were finally obtained by calcining at 723 K in air [52]. Besides, multiple approaches using templates for the formation of nanosheets exist. Another route presented by Gao et al. [15] utilized a successive ion-layer adsorption and reaction (SILAR) technique, which was interrupted half-way to gain the nanosheets. The route also uses GO as a 2D template, where metal ions are adsorbed on the surface. The difference consists in the further treatment, which starts with a stacking of the sheets via centrifugation. Afterwards, the sheets are dispersed again, quickly frozen and freeze-dried to maintain the structure under mild conditions and not risk fissures or stacking of the sheets caused by drying. At last, the calcination removes the template and nanosheets of the metal oxide remain. Since the removal of 2D templates often requires high temperatures, the technique is especially viable for oxidic materials, because no inert gases are required. As a downside of this technique, 2D templates are required beforehand, which increases the expenses significantly. Therefore, another template-oriented technique is worth mentioning, where 3D structured salt is used (see Figure 4).

Xiao et al. [71] used this technique to synthesize nanosheets consisting of MnO , MoO_3 or WO_3 . An excess of cheap and easily obtainable salt as KCl or NaCl was used and mixed with a precursor solution containing the inorganic metal-salt. After annealing by heating, the oxidic nanosheets were formed with an intermediatic hydroxide phase and dissolving the salt in water led to the free-standing sheets. While in 2D templates the morphology is predefined, the mechanisms in the 3D salt are different. It is assumed, that the crystal geometry of the salt and the oxide have to be similar to allow Frank-van der Merwe film growth on the surface of the salt crystals and favor the lateral growth [71]. Though more investigations are necessary to fully understand the mechanism, not matching

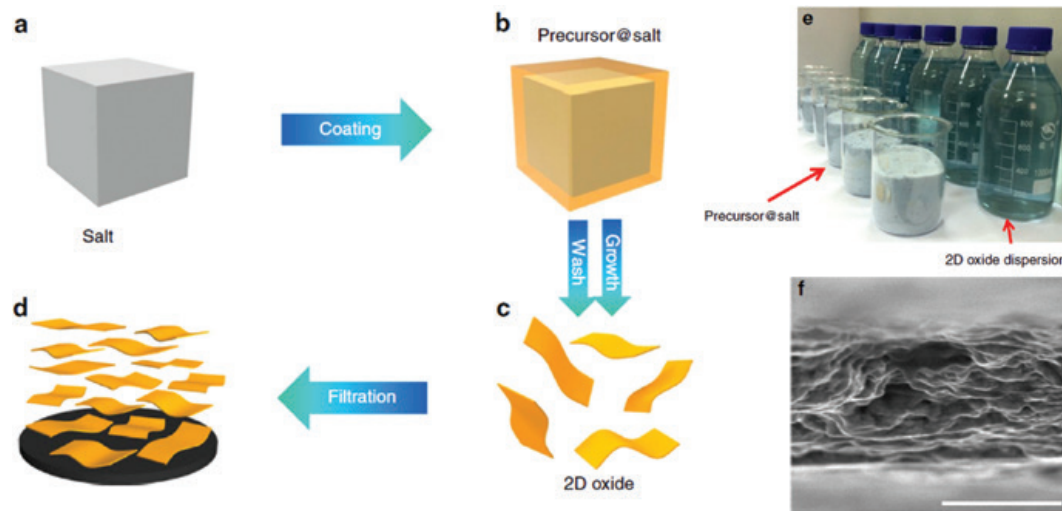


Fig. 4: Salt-templated synthesis of 2D oxide nanosheets: (a–c) Schematic principle of salt-templated synthesis of nanosheets. (a, b) The first step includes the coating of the salt with the precursor solution, (c) followed by the growth and washing to gain the 2D oxide nanosheets. (d) In this case, the dispersion containing the nanosheets were filtrated to utilize the nanosheets on electrodes for their pseudocapacitory characteristics. (e) Photography of the salt mixed with the precursor solution in the front row and the dispersion with the gained MoO_3 nanosheets in the back row. (f) Cross-sectional SEM image of stacked 2D oxide nanosheets with a scalebar of $1\ \mu\text{m}$. Adapted with permission from [71]. Copyright 2016 Springer Nature. Creative Commons License CC BY 4.0.

crystal geometries showed no formation of nanosheets. To control the thickness of the sheets, the ratio of salt to precursor volume can be adjusted and increases with larger volume. The advantage of this technique lies within the utilization of a cheap and reusable template with few reaction steps, which is favorable for large-scale productions.

3.8 Bottom-up synthesis: self-assembly of nanosheets

By utilizing non-covalent interactions like van der Waals or electrostatic forces as in hydrogen bonds, the self-assembling of nanocrystals is a neat way to create nanosheets [111]. It is obvious, that for so-called self-assembling an accomodated driving force is still required, because the attractive forces have to operate in two dimensions or the repulsive forces in only one dimension. For this, the general synthesis contains structure-directing agents (SDAs) as surfactant molecules with amphiphilic structure properties (e.g. block copolymers) and a co-surfactant (e.g. alcohol). The metal species for the formation of nanosheets can be added as alkoxides or salts. The amphiphilic properties of the SDA provides attractive forces between one end of the molecule and the metal species as well as van der

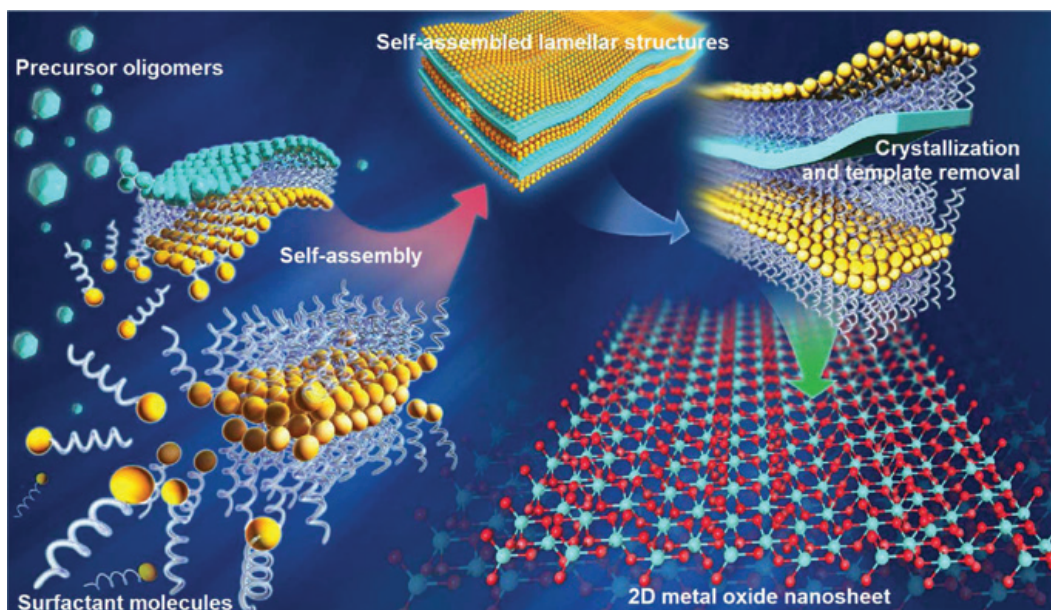


Fig. 5: Schematic principle of self-assembly for 2D oxide nanosheets. In the first step, the metal precursor gets orientated in two dimensions due to surfactant molecules to form a stacked lamellar structure. In the second step, the precursor oligomers get crystallized and the template is removed to gain the nanosheets. Adapted with permission from [111]. Copyright 2014 Springer Nature.

Waals forces between the long chains, thus leading to a stacking and formation of inverse lamellar micelles (see Figure 5). Hereby, the role of the co-surfactant is to ensure a stable lamellar phase. When the amount of lamellar phase is sufficient, a solvothermal treatment is added for crystallization and free-standing nanosheets are obtained after oxidative removal of the SDAs [111]. The advantages of this synthesis are a formation of a structured host material on a molecular basis and a scalable process. Although, the amounts of SDAs have to be carefully adjusted to the sensitive equilibrium of the lamellar phase.

3.9 Bottom-up synthesis: interface-mediated methods

Another technique, similar to self-assembling, is the interface-mediated synthesis. In a typical approach, a metal salt is dissolved and supersaturated in an aqueous solution and an anionic organic molecule with a long hydrophobic tail is added, whose localization at the interface is essential for the nanosheet formation. To ensure a monolayer of the surfactant at the water/air interface, the polymer can first be dissolved in a hydrophobic medium and afterwards added to the water. Once the surfactants form a monolayer at the interface, the attraction of the negatively charged molecules with the positively charged metal cations is essential. In

a supersaturated solution, the precipitation of the oxide is controlled at the interface, despite the formation of nanocrystallites elsewhere in the solution. Since the oxide is already crystallized, a calcination step can be avoided. For the formation of ZnO it was shown, that the reaction time and the cation concentration are crucial to the crystallinity of the sheets [112]. While this method enables especially the formation of large nanosheets due to missing calcination steps, it still contains a monolayer of the surfactant after extraction. Although, its removal may influence the stability of the sheets. Hence, at this state this method is limited to nanosheets where the monolayer of surfactant does not hinder the application fields.

A recently emerged synthesis route utilizes self-limiting thin interfacial oxides for the formation of atomically thin metal oxides [97]. It is especially useful for the synthesis of 2D nanosheets from compounds with non stratified crystal structures. In contrast to most other synthesis methods, a metal-based alloy is used as a solvent (e.g. eutectic gallium melts). In this case, the formation of an oxide skin at the liquid/air interface is mandatory (see Figure 6b).

Zavabeti et al. [97] managed to gain nanosheets of HfO_2 , Al_2O_3 and Gd_2O_3 to show the large compound variety of the technique by co-alloying the gallium

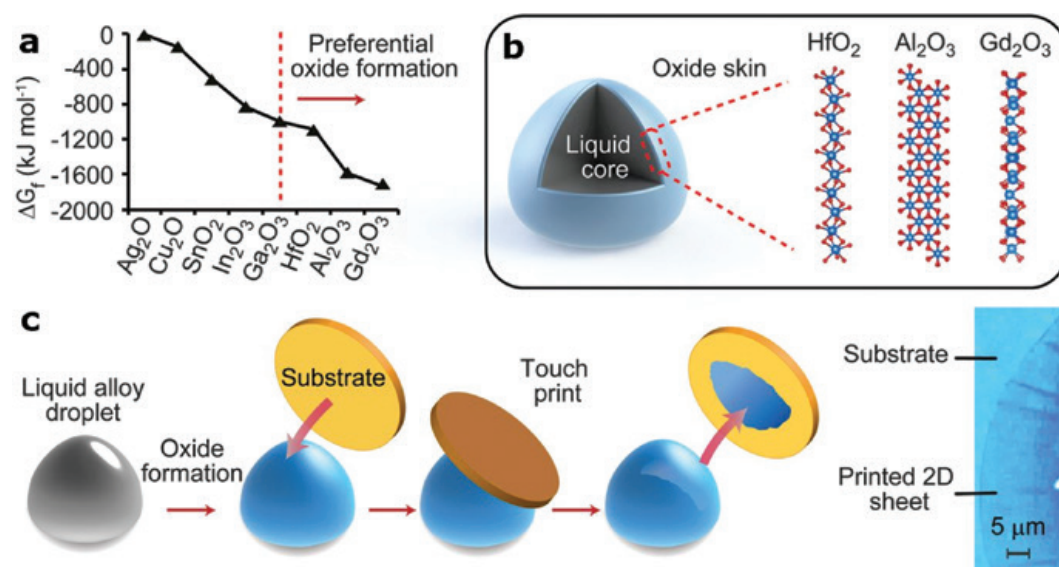


Fig. 6: Principles for the interface-mediated synthesis of 2D oxide nanosheets using metal alloys: (a) Gibbs free energy of several oxides in relation to Ga_2O_3 , which is formed without co-alloying. (b) Schematic composition of a liquid-alloy droplet with a liquid core and an oxide skin at the liquid/air interface with possible crystal structures of displayed oxides. (c) Schematic principle for the attachment of the oxide skin to a solid substrate. Based on van der Waals forces, the oxide skin adheres to the solid surface. An optical image of the 2D nanosheets is presented at the right. Adapted with permission from [97]. Copyright 2017 The American Association for the Advancement of Science.

melt with suitable metals. The suitability is proposed to be dependent on thermodynamic aspects, because the surface oxide with the highest absolute value of Gibbs free energy is preferentially formed at the interface (see Figure 6a). With no co-alloying, Ga_2O_3 is formed at the interface, therefore only oxides with enhanced Gibbs free energy can be synthesized by this method. To separate the oxide skin from the melt, two different approaches are presented. For the attachment on a specific surface, a substrate can be contacted to the liquid-alloy droplet as shown in Figure 6c. To gain the 2D nanosheets in suspension, water can be placed above the melt while gaseous air is injected into the melt below. By this, the amount of required interface is manually controlled and scalability is possible [97]. Although, due to the polycrystalline structure of the gained nanosheets, the method is limited to applications where single-crystals play a subordinated role.

3.10 Bottom-up synthesis: sol-gel method

The sol-gel method has its origins in the 1990s [58] and partly resembles the interface-mediated synthesis. Analogous to the interface-mediated synthesis, the metal species is dissolved in water and hydrolyzed. An amphiphilic chelating agent is placed in a monolayer at the water/air interface as well. The first reaction step includes the condensation of the metal species at the interface due to the complexation of the amphiphilic molecules with the metal centers. This process can be used to gain large nanosheets by using the Langmuir-Blodgett technique, where the singular oxide-based gel islands are merged by reducing the interface area. After sufficient condensation, an ultrathin gel is formed at the interface, which further can be extracted onto a substrate. Therefore, the Langmuir-Blodgett technique is convenient and the dipping of the substrate into the solution leads to a gel-film on both sides of the substrate surface. In the last reaction step of calcination, the complexing agent is removed and the gel is substituted by the oxide species. While this synthesis is in fact interface mediated, it is well established and the gel-formation as a characteristic step distinguishes it sufficiently. Moriguchi et al. [58] accomplished to gain heterolayers of TiO_2 and ZrO_2 with a thickness of 20 nm by this technique on a Si-substrate. The homogeneity of the films are superior to some other synthesis methods, but upscaling this process is unresolved.

3.11 Bottom-up synthesis: growth method

A simple method for growing an array of CuO nanosheets on a nickel foam substrate was shown by Wang et al. [80]. Therefore, a basic growth solution includ-

ing the metal salt was prepared and the nickel substrate hung into it for 6 h at 90 °C. It is similar to solvothermal methods, but does not require an autoclave or high temperatures. The gained nanosheets showed sufficient homogeneity on the substrate, but did not lead to dense sheets. Instead, they were formed by interconnecting nanoparticles, which allowed irregularities and pores. Nevertheless, the synthesis is easily manageable and delivered beneficial properties regarding pseudo-supercapacitors. Determining parameters are temperature, concentration and growth time. The transferability for other metal species has yet to be shown though.

4 Microstructures

Different synthetic processes are able to produce 2D nanosheets free-standing, stacked, arranged into arrays or into ultrathin films with process-dependent microstructures. The nature of the nanosheets can be single-crystalline or polycrystalline. The latter can be considered as planar assemblies of nanoparticles. To reveal the microstructure of 2D oxides, their arrays or assemblies, microscopic and microspectroscopic as well as diffraction methods are indispensable. For some of the most prominent methods, examples are given to show their particular advantage in this context: Atomic force microscopy (AFM), scanning tunneling microscopy (STM), scanning electron microscopy (SEM), transmission electron microscopy (TEM), high-resolution transmission electron microscopy (HRTEM), scanning transmission electron microscopy (STEM), high-angle annular dark-field (HAADF), selected area electron diffraction (SAED), electron energy-loss spectroscopy (EELS), energy-dispersive X-ray spectroscopy (EDXS) and X-ray diffraction (XRD).

4.1 Free-standing nanosheets

Free-standing nanosheets can be synthesized via top-down and bottom-up routes as described in the Section Synthesis. The commonly used top-down route by exfoliation of layered 3D bulk compounds due to intercalation of an exfoliation agent (see Figure 2) is able to produce single-crystalline 2D oxide nanosheets. Often, the freestanding 2D nanosheets have similar structures as the parent material with slight in-plane expansion and eventually change in symmetry. In the following, structurally examined examples of exfoliated free-standing 2D nanosheets will be described and subsequently examples for bottom-up results.

The AFM-measured thickness of exfoliated 2D nanosheets is systematically higher than expected from crystallographic data, which is mainly caused by the absorption of water and other species from solution. Anyway, these measurements allow to elucidate if unilamellar or multiple-layered (e.g. bi- or tri-layer) nanosheets were obtained and moreover resolve differences in ionic radii of the center ion in structure-defining octahedra [113]. The example in Figure 7 exhibits clearly different thicknesses for perovskite-related $\text{Ca}_2\text{Na}_{m-3}\text{Nb}_m\text{O}_{3m+1}^-$ nanosheets, which confirms the high precision of AFM measurements and the possibility to distinguish between unilamellar or multiple layer nanosheets [28].

Due to surface charges, unilamellar nanosheets of oxides like graphene oxide (GO), $\text{Ti}_{0.87}\text{O}_2^{0.52-}$ and $\text{Ca}_2\text{Nb}_3\text{O}_{10}^-$ can be well dispersed in solvents in the form of 2D unilamellar anionic, i.e. negatively charged nanosheets [114]. By the aid of AFM, Cai et al. [114] have shown, that 2D nanosheets of $\text{Ti}_{0.87}\text{O}_2^{0.52-}$ have a uniform thickness of ca. 1.1 nm and that the surfactant polyethylenimine (PEI) which interacts with its oxidative functional groups to the 2D nanosheet, can increase its thickness uniformly to 2.9 nm (see Figure 8). This study also shows, that by using PEI it is possible to preserve the monodispersibility and avoid restacking-induced flocculation of nanosheets, which could be expected in the case of simple addition of cationic species.

To observe expansions of certain crystallographic planes attributed to the exfoliation, SAED in a TEM can be used. Body-centered orthorhombic $\text{RbLaNb}_2\text{O}_7$ ($a = 5.4941 \text{ \AA}$, $b = 21.9901 \text{ \AA}$, $c = 5.4925 \text{ \AA}$) and $\text{RbPrNb}_2\text{O}_7$ ($a = 5.4534 \text{ \AA}$, $b = 22.012 \text{ \AA}$, $c = 5.4549 \text{ \AA}$) of double-layer Dion-Jacobson type were exfoliated into nanosheets using microwave heating in the presence of TBA^+ [32]. It resulted in TBA^+ -attached 2D nanosheets of the type $\text{TBA}^+\text{-LaNb}_2\text{O}_7$ and $\text{TBA}^+\text{-PrNb}_2\text{O}_7$. The delamination of

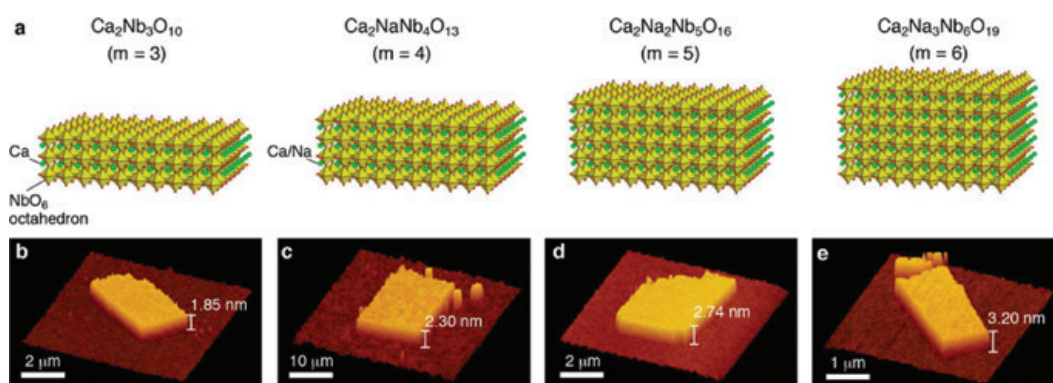


Fig. 7: AFM-analysis of Dion-Jacobson phases: (a) Theoretical structures of $\text{Ca}_2\text{Na}_{m-3}\text{Nb}_m\text{O}_{3m+1}$ 2D nanosheets. (b–e) Morphology of 2D nanosheets, as received from the exfoliation of bulk Dion-Jacobson phases, measured with AFM in tapping mode under vacuum. Reproduced with permission from [28]. Copyright 2017 American Chemical Society.

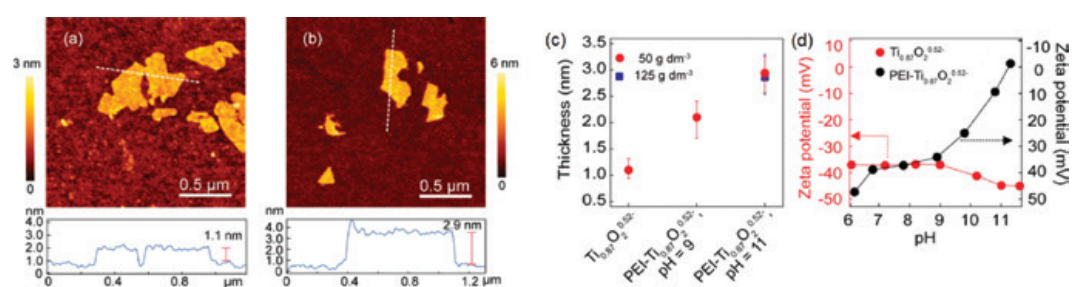


Fig. 8: Tapping mode AFM analysis of exfoliated $\text{Ti}_{0.87}\text{O}_2^{0.52-}$ nanosheets: (a) Original 2D nanosheets and (b) nanosheets modified with polyethylenimine (PEI). (c) Thickness of original and modified 2D nanosheets at different PEI concentrations (50 and 125 g dm^{-3}) and pH values (9 and 11) of the solution. (d) ζ potential of the original and the PEI-modified 2D nanosheets as function of pH value. Adapted with permission from [114]. Copyright 2015 American Chemical Society.

the crystalline structure occurred in the (a,c)-plane, so that SAED patterns along the former b-axis (i.e. [010] zone axis in the bulk material) could be observed as shown in Figure 9. These SAED patterns could still be indexed on a body-centered cell and gave values for the 2D lattice parameters a and c being close to

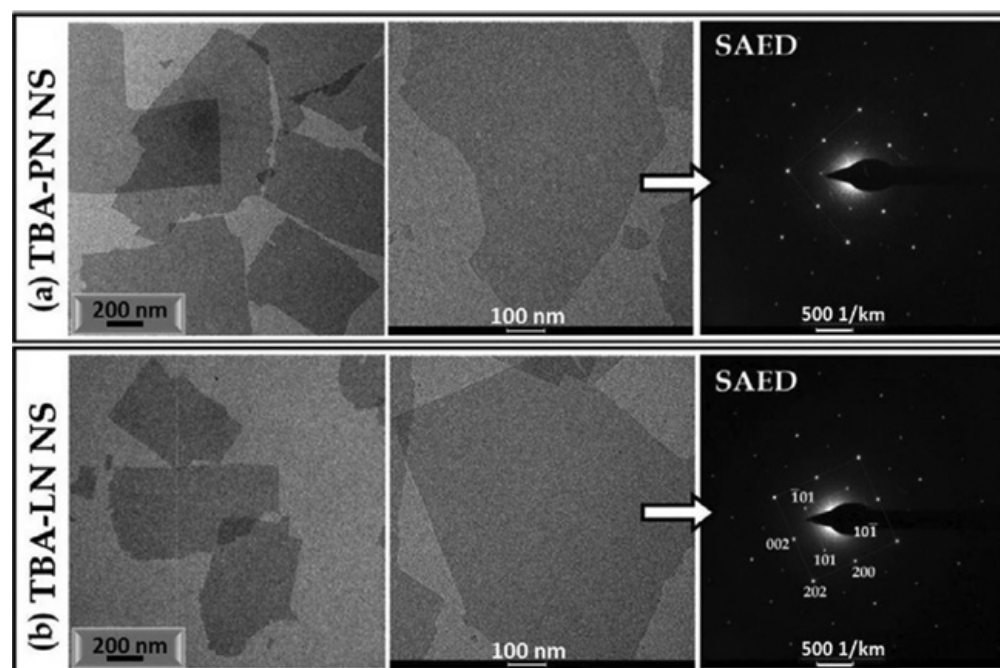


Fig. 9: TEM micrographs and SAED patterns of TBA-functionalized 2D nanosheets: (a) $\text{TBA}^+\text{-PrNb}_2\text{O}_7$, (b) $\text{TBA}^+\text{-LaNb}_2\text{O}_7$. Nanosheets are viewed along the corresponding b-axis in the orthorhombic bulk two-layer Dion-Jacobson phases. Reproduced with permission from [32]. Copyright 2017 Wiley-VCH.

those in the starting material: $\text{TBA}^+\text{-LaNb}_2\text{O}_7$ ($a=5.71 \text{ \AA}$, $c=5.71 \text{ \AA}$), $\text{TBA}^+\text{-PrNb}_2\text{O}_7$ ($a=5.68 \text{ \AA}$, $c=5.74 \text{ \AA}$). However, in both cases the nanosheets have expanded about 4%–5% in the (a,c)-plane [32].

Moreover, orthorhombic $\text{Rb}_4\text{W}_{11}\text{O}_{14}$ ($a=14.64 \text{ \AA}$, $b=25.78 \text{ \AA}$, $c=7.64 \text{ \AA}$) was exfoliated in the (a,c)-plane and SAED revealed a rectangular unit cell for the resulting 2D nanosheets ($a=14.0 \text{ \AA}$, $c=7.8 \text{ \AA}$), which dimensions are close to those of the corresponding bulk material [17]. The perovskite-type monoclinic RbTaO_3 ($a=9.60 \text{ \AA}$, $b=8.426 \text{ \AA}$, $c=7.33 \text{ \AA}$, $\beta=94.2$) was exfoliated in the (a,b)-plane and the 2D nanosheets ($a=9.8 \text{ \AA}$, $b=8.7 \text{ \AA}$) showed an in-plane expansion of 2%–3% compared to the corresponding bulk material. However, a particular feature of the nanosheets were open channels of the 1×1 width of a TaO_6 octahedron [98]. It is worth to note, that for the investigation of 2D nanosheets SAED and AFM are complementary to each other, as the former gives in-plane information and the latter gives out-of plane information.

Upon a tetramethylammonium hydroxide (TMA^+OH^-)-mediated delamination of $\text{Bi}_2\text{W}_2\text{O}_9$ to single-crystalline WO_3 2D nanosheets, the nanosheets undergo a structural change from tetragonal symmetry in the parent material to monoclinic in their free-standing form, which resembles bulk WO_3 ($a=7.297 \text{ \AA}$, $b=7.539 \text{ \AA}$, $c=7.688 \text{ \AA}$, and $\beta=90.85$) and was elucidated by powder XRD, HRTEM and high-resolution STEM-HAADF [101]. In the WO_3 2D nanosheets with the formal composition $\text{H}_2\text{W}_2\text{O}_7$, the WO_6 octahedral units were stacked in two levels, giving the sheets a thickness of only 0.75 nm while the average edge length was $90 \pm 38 \text{ nm}$ [101].

For a rapid and reliable identification of unilamellar and up to five-layer oxide nanosheets, Kim et al. [100] have proposed an universal optical method by analyzing $\text{Ti}_{0.87}\text{O}_2$, $\text{Ca}_3\text{Nb}_3\text{O}_{10}$, and $\text{Ca}_2\text{NaNb}_4\text{O}_{13}$ nanosheets. The method is based on changes in the interference-based optical reflectivity of 2D nanosheets on SiO_2/Si substrates, which is dependent on the nanosheet thickness, SiO_2 film thickness and the optical wavelength. In an optical microscope, the contrast, which can be inverted in some cases, was carefully evaluated for varied parameters.

Considering the exfoliation behavior of protonated Ruddlesden-Popper phases $\text{H}_2[\text{A}_{n-1}\text{B}_n\text{O}_{3n+1}]$, Schaak and Mallouk [30] mention their unpredictable tendency to curl and form scrolls rather than sheets and they give several possible explanations for why they do so. One explanation for the formation of scrolls is that, upon exfoliation, the individual sheets have asymmetric distributions of A- or B-site cations, creating a polarization that is relieved by curling. A second possibility is that the sheets curl as a result of cooperative distortions of the BO_6 octahedra, which is frequently observed in displacive ferroic phase transitions in perovskites. Curling may also occur due to the intrinsic bonding character of water or the intercalated base, which is used in the exfoliation process, with the interlayer atoms of the perovskite block. Anyway, there is still not a

clear understanding of how intercalation affects the interlayer bonding and why certain Ruddlesden-Popper phases as well as some Dion-Jacobson and Aurivillius phases curl rather than remain as sheets [30].

For analyzing the impact of the chosen intercalating agent on the 2D nanosheets, a work from Takagaki et al. [35] should be mentioned. Several 2D nanosheets (TiNbO_5^- , $\text{Ti}_2\text{NbO}_7^-$, and TiTaO_5^-) were prepared by TBA-mediated exfoliation of the corresponding H^+ -exchanged layered oxides (HTiNbO_5 , HTi_2NbO_7 , and HTiTaO_5) [35]. However, the addition of TBA^+OH^- solution did not result in the exfoliation of layered HTiTaO_5 , which was only achieved by adding ethylamine in an aqueous environment. SAED patterns of the titanium niobate nanosheets (TiNbO_5^- and $\text{Ti}_2\text{NbO}_7^-$) exhibited single-crystalline nature (discrete spots pattern), while those of the TiTaO_5^- nanosheets showed polycrystalline nature (diffuse Debye-Scherrer rings). TEM revealed, that the TiTaO_5^- 2D nanosheets were decorated by equiaxial nanoparticles of 2–10 nm in diameter. This obviously shows, there is a definitive distinction between the exfoliation behavior of TBA^+OH^- and ethylamine [35].

After describing multiple examples with their characteristics in top-down exfoliated 2D nanosheets, in the following nanosheets obtained from bottom-up routes will be discussed. Generally, bottom-up routes produce rather polycrystalline free-standing nanosheets as is described in the following examples. Although, single-crystalline nanosheets can also be obtained if the synthesis is appropriately adjusted.

The bottom-up hydrothermal method from $\text{Lu}(\text{OH})_3$ -based colloidal precursor produced Eu- or Tb-doped Lu_2O_3 square 2D nanosheets with thicknesses of ca. 40 nm and side lengths of 200–400 nm [115]. As revealed by HRTEM, the single 2D nanosheet has a polycrystalline structure and is composed of planar arrangement of equiaxial nanocrystals with 10–15 nm in diameter each. As a result, each individual Lu_2O_3 square free-standing 2D nanosheet is a nanoparticle 2D assembly. Similar results were observed for NiCo_2O_4 2D nanosheets, prepared by a hydrothermal method and subsequent annealing. Planar 2D nanosheets with lateral dimensions of more than 300 nm were gained, which consisted of randomly arranged NiCo_2O_4 nanoparticles with diameters of less than 10 nm and of mesopores [39]. Thus, these free-standing nanosheets can be considered as nanoparticle assemblies. Subsequently, irregular arrays of stacked NiCo_2O_4 nanosheets were obtained by immersing stainless steel gauzes in the solution for hydrothermal method in polytetrafluoroethylene (PTFE)-lined autoclaves.

On the other hand, single-crystalline ZnO nanosheets were gained by an interface-mediated synthesis. Surfactant monolayers were used as soft templates to produce 1–2 nm thick single-crystalline ZnO 2D nanosheets at the water-air interface with lateral sizes of up to tens of nanometers [112]. By collecting nanosheets

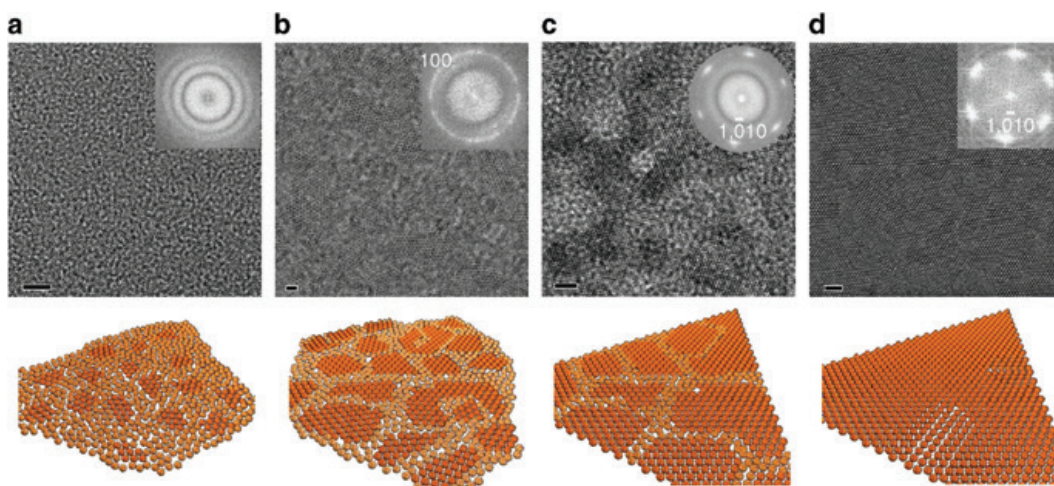


Fig. 10: Plan-view HRTEM analysis of time-dependent evolution of ZnO 2D nanosheets obtained by an interface-mediated synthesis: (a) Mostly amorphous film with tiny crystallites, (b) more crystallized nanosheet with randomly in-plane oriented 2–3 nm crystallites, (c) in-plane crystallites had grown larger and aligned orientation, (d) large-area single-crystalline nanosheet. Insets show fast Fourier transforms (FFTs) of the respective HRTEM micrographs. In the structural models, regions with gold-colored spheres are amorphous and regions with deeper gold-colored spheres are crystalline. Scale bars are 2 nm each. Reproduced with permission from [112]. Copyright 2016 Springer Nature. Creative Commons License CC BY 4.0.

at different reactions times (see Figure 10), HRTEM revealed that at first there was a continuous amorphous film at the interface with tiny crystallites embedded in it. Then, these crystallites grew in lateral size and were all oriented with the same hexagonal crystal plane exposed. However, their in-plane rotation appeared to be stochastic. As the crystallites grew larger, they merged at an aligned orientation into a contiguous, single-crystalline network coexisting with a decreasing amorphous region confined between the nanosheets. Eventually, the amorphous area was fully crystallized and the nanosheet became single crystalline with few dislocations that were probably formed by the misorientation of merged crystalline areas during the formation process [112]. This synthetic process, which has similar attributes as those found in biomineralization, has the potential to produce single-crystalline 2D nanosheets from a wide range of inorganic materials.

4.2 Stacked nanosheets

SEM has the capability to image material microstructures over six orders of magnitude from the mm- down to the nm-scale. So, it is of particular use in investigating assemblies of individual nanosheets. An example is given in Figure 11, which shows 2D $\text{Na}_{0.7}\text{CoO}_2$ nanosheets turbostratically stacked into macro-scale

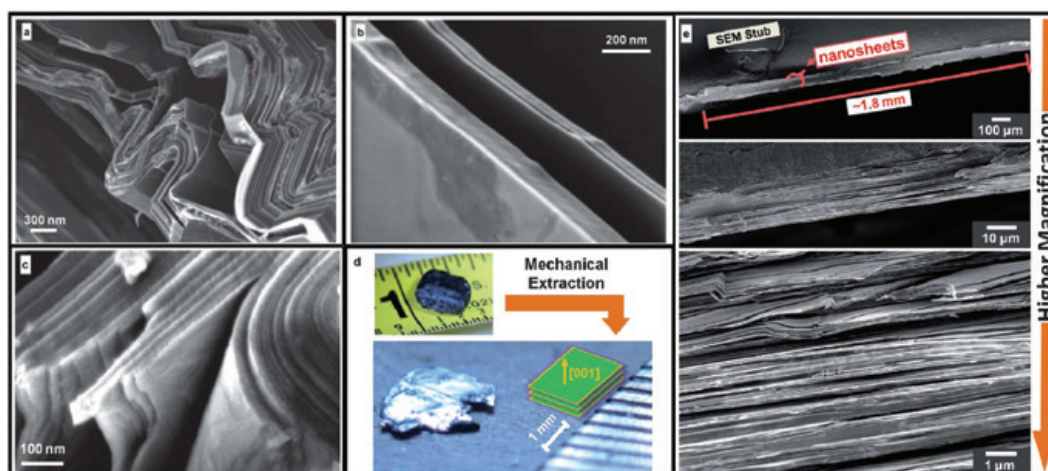


Fig. 11: Millimeter-length 2D $\text{Na}_{0.7}\text{CoO}_2$ nanosheets fabricated from a bottom-up sol-gel process followed by autocombustion, alignment, calcination and electric field-induced kinetic demixing: (a–c) High-magnification SEM shows the thickness of individual sheets to vary from ca. 20 to 100 nm. (d) The bulk pellet consists of thousands of stacked nanosheets from which a single nanosheet stack was mechanically extracted with the individual nanosheets being aligned as drawn. (e) Low-magnification SEM shows the total length of nanosheets to be 1.8 mm and the stack thickness to be around 100 μm . Adapted with permission from [14]. Copyright 2012 Royal Society of Chemistry.

pellets [14]. The length of the nanosheets is exceeding 1.5 mm as can be seen from Figure 11e at low magnification. At the higher magnification in Figure 11a–c, it is revealed that lamellae made of the stacked nanosheets are partly wrinkled. In Figure 11c, individual nanosheets of less than 20 nm in thickness are resolved within a wrinkled lamella. SEM investigation covering macro-scale and nano-scale was made on water-stabilized, millimeter-length, stacked $\text{K}_x\text{CoO}_2 \cdot y\text{H}_2\text{O}$ nanosheets, which were obtained by an analogous synthesis method [116].

Apart from this, another type of stacked nanosheet assemblies is conceivable with focus on the transition of nanoscopic characteristics to macroscopic materials. For this, separately gained 2D oxide nanosheets can be aligned to each other by organic fibers to macroscopic fiber assemblies [117, 118]. As shown in Figure 12a, a dispersion of exfoliated $\text{Ti}_{0.87}\text{O}_2^{0.52-}$ nanosheets in a liquid crystal were successfully assembled with the biopolymer chitosan via a wet-spinning method using a coagulation bath to gain the fibers. The nanosheets within the fiber assemblies (see Figure 12b,c) were highly ordered and led to extraordinary mechanical enhancements competing with those of graphene. This is particularly important, because generally metal oxides only provide few hundredths of the intrinsic tensile strength in a single nanosheet compared to graphene [117]. The mechanical stability together with mechanical flexibility is e.g. useful for energy storage in flexible lithium-ion fiber batteries [119].

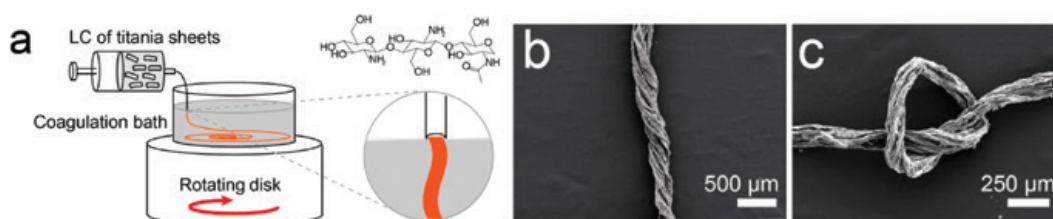


Fig. 12: Stacked nanosheets in macroscopic fiber assemblies: (a) Schematic principle of a wet-spinning method for the assembly of titania nanosheets in a liquid crystal (LC) with a coagulation agent chitosan in a rotating bath. (b, c) SEM micrographs showing the macroscopic fibers with stacked nanosheets as building blocks and flexible characteristics. Adapted with permission from [117]. Copyright 2015 American Chemical Society.

4.3 Nanosheet arrays

SEM micrographs of mesoporous ZnCo_2O_4 nanosheet arrays, which were uniformly grown on the ridges of a Ni foam substrate by hydrothermal method followed by calcination [40] are shown in Figure 13. At low magnification, pores within the Ni foam having diameters of up to $100\ \mu\text{m}$ can be seen. At higher magnification, individual upright standing 2D nanosheets with a thickness of less than $100\ \text{nm}$ are resolved. Due to their deposition on the surface, they can obviously be distinguished from free-standing nanosheets. The high electrical conductivity of the Ni foam combined with the large accessible surface of the mesoporous ZnCo_2O_4 nanosheets give prospect to integrated electrodes for electrochemical supercapacitors for energy storage at high cycling rate.

Arrays of vertically standing CuO 2D nanosheets on Ni foam as a substrate were prepared via the bottom-up template-free growth method from aqueous copper nitrate NH_4NO_3 /ammonia solution [80]. The thickness of the obtained 2D nanosheet film was about several μm , while the individual nanosheets were about $150\ \text{nm}$ in thickness and parallelly clustered into stacks.

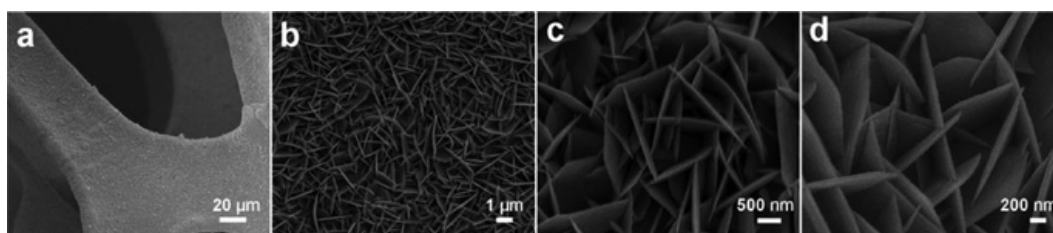


Fig. 13: Mesoporous ZnCo_2O_4 2D nanosheet arrays, which were uniformly grown on Ni foam substrate by a bottom-up hydrothermal method followed by calcination: (a) Low magnification SEM micrograph showing the macroporous Ni-foam and the deposited nanosheets on the surface. (b–c) SEM micrographs at higher magnifications showing the nanosheet arrays. Adapted with permission from [40]. Copyright 2013 Royal Society of Chemistry.

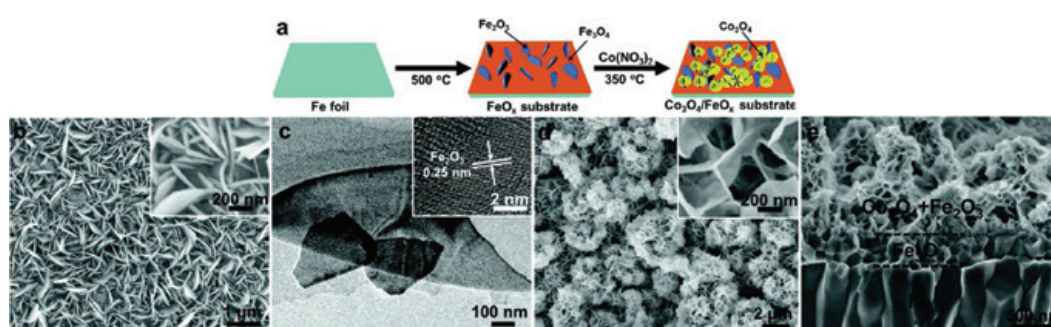


Fig. 14: Hierarchical Co_3O_4 2D nanosheet array on FeO_x substrate: (a) Schematic illustration of the preparation by oxidation of Fe foil in air to exhibit a Fe_3O_4 surface film with Fe_2O_3 nanosheet array to which cobalt nitrate was deposited and thermally decomposed to a crossed Co_3O_4 2D nanosheet array, (b) plan-view SEM micrograph of FeO_x substrate, (c) TEM micrograph of FeO_x substrate, (d) plan-view SEM micrograph of Co_3O_4 nanosheet array on FeO_x substrate, (e) side-view SEM micrograph of Co_3O_4 nanosheet array on FeO_x substrate. Adapted with permission from [23]. Copyright 2016 Royal Society of Chemistry.

Hierarchically crossed metal oxide 2D nanosheet arrays (Co_3O_4 , NiO, MgO) were produced by bottom-up pyrolysis of a thin nitrate film on a FeO_x substrate, which was obtained by annealing an iron foil in air [23]. In the case of Co_3O_4 (see Figure 14), 2D nanosheets with an average thickness of about 40 nm were uniformly and vertically distributed on the iron foil after annealing. The hierarchical 2D nanosheet arrays showed promising catalytic activity for the elimination of soot from Diesel exhaust.

By an anodic process in a double-electrode cell, vertical standing nanosheet arrays composed of coexisting Cu_2O and CuO with a nanosheet thickness of ca. 30 nm were produced on a copper foil substrate [79]. High intensity diffraction peaks of CuO and low intensity diffraction peaks of Cu_2O were detected in XRD patterns of the anodization products obtained at temperatures of 60 and 70 °C.

Moreover, arrays of vertical standing ZnO 2D nanosheets were deposited onto an indium tin oxide (ITO) coated transparent conducting glass substrate, using a galvanic deposition process in a $\text{Al}/\text{ZnSO}_4//\text{NaOH}/\text{ITO}/\text{glass}$ cell with aqueous electrolytes. The ZnO 2D nanosheets were of hexagonal wurtzite structure and had lateral dimensions of up to 1 μm at thicknesses of less than 50 nm [84].

4.4 Ultrathin films

Technically, every film with a thickness lower than 10 nm can be considered ultrathin, which can be accomplished by several bottom-up routes as laser-deposition or molecular beam epitaxy. Another approach to obtain ultrathin films lies within utilizing nanosheets. As an example, bulk triple-layer Dion-Jacobson phase $\text{KCa}_2\text{Nb}_3\text{O}_{10}$

was exfoliated to a colloidal suspension of $\text{Ca}_2\text{Nb}_3\text{O}_{10}$ 2D nanosheets with lateral dimensions of about 3–10 μm from which, as shown in Figure 15, a multilayered ultrathin film was prepared by a layer-by-layer assembly using the Langmuir-Blodgett technique [120]. In the first step, the atomically-flat SrRuO_3 perovskite substrate is effective in obtaining an atomically uniform monolayer film with high dense characteristics. Repeated Langmuir-Blodgett deposition yielded $(\text{Ca}_2\text{Nb}_3\text{O}_{10})_n$ with $n=3$ (4.5 nm, shown in Figure 15c, d), $n=5$ (7.5 nm), $n=10$ (15 nm), $n=15$ (22.5 nm). Besides SrRuO_3 , also quartz glass, Pt or $\text{SrTiO}_3:\text{Nb}$ were used as substrates [120].

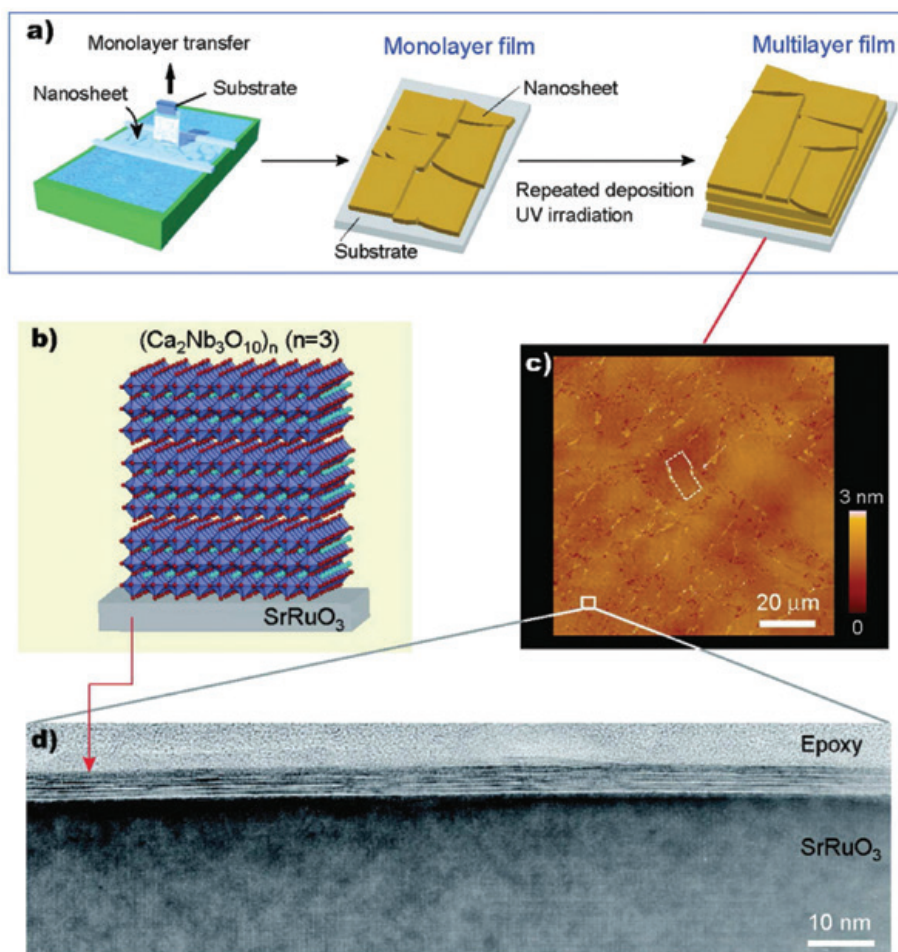


Fig. 15: Ultrathin films gained by using the Langmuir-Blodgett method: (a) Layer-by-layer assembly of delaminated 2D metal oxide nanosheets into multilayer films using the Langmuir-Blodgett method. (b) Schematic crystallographic orientation of a $(\text{Ca}_2\text{Nb}_3\text{O}_{10})_3$ Dion-Jacobson phase relative to a SrRuO_3 perovskite substrate. (c) AFM plan-view with color scale referring to altitude. (d) HRTEM cross-sectional view of a $(\text{Ca}_2\text{Nb}_3\text{O}_{10})_3$ 2D film on a perovskite substrate. These 2D films are prospective high- κ dielectrics/ferroelectrics for use in ultrascaled electronics and post-graphene technology [28]. Reproduced with permission from [120]. Copyright 2010 American Chemical Society.

The Langmuir-Blodgett technique was also used to produce about 10 nm thin superlattices of double-layer LaNb_2O_7 ($d=1.2$ nm) and triple-layer $\text{Ca}_2\text{Nb}_3\text{O}_{10}$ ($d=1.4$ nm) Dion-Jacobson phases from their 2D nanosheets by a layer-by-layer assembly [121]. Interface coupling in these $(\text{LaNb}_2\text{O}_7)_{n_L}(\text{Ca}_2\text{Nb}_3\text{O}_{10})_{n_C}$ superlattices gave rise to ferroelectricity regardless of the stacking sequence (n_L/n_C) of the two different 2D nanosheets. Cross-sectional HRTEM confirmed that wide-ranging uniform artificial superlattices could be produced on an atomically-flat SrRuO_3 substrate. Compositional modulation in alternating lamellae was elucidated by EELS of the La- $M_{2,3}$ (192 eV) and Ca- $L_{2,3}$ (347 eV) ionization edges in the STEM. From the viewpoint of crystal chemistry, unique intergrowth structures were obtained for the $(\text{LaNb}_2\text{O}_7)_{n_L}(\text{Ca}_2\text{Nb}_3\text{O}_{10})_{n_C}$ superlattices, which do not naturally exist in the bulk form.

A 2D bottom-up sol-gel process has been described, in which the hydrolysis and polycondensation reactions occur at the air/water interface and the Langmuir-Blodgett technique is used to deposit a gel film on a substrate [122]. The 2D sol-gel process was further developed by involving repeated layer-by-layer Langmuir-Blodgett technique to produce $(\text{ZrO}_2/\text{TiO}_2)_n$ hetero-multilayered nanofilms [58]. The multilayered nanostructure made up of TiO_2 and ZrO_2 ultrathin laminae with thicknesses of about 10–15 nm was observed throughout the Si substrate surface. A $(\text{ZrO}_2/\text{TiO}_2)_5$ film had a total thickness of about 130 nm. It exhibited alternate stacking of ZrO_2 -lamina and TiO_2 -lamina in the direction from the outer-most surface to the substrate with the diameter of the nanoparticles being 3 nm or less in the ZrO_2 layers and 5–10 nm in the TiO_2 layers as shown by HRTEM.

A more exotic example for ultrathin films is the using of a chemically driven self-assembly process in the gaseous phase, where 2D planar vanadium oxide $[\text{V}_6\text{O}_{12}]$ clusters were produced on a Rh(111) surface and subsequently monitored in the ultra-high vacuum using the STM [67]. In a reducing environment ($p_{\text{H}_2} \approx 10^{-8}$ mbar) at a substrate temperature of 250 °C, the $[\text{V}_6\text{O}_{12}]$ clusters assembled into nano-islands with a well-ordered 2D vanadium oxide monolayer structure. STM revealed a rectangular ($5 \times 3\sqrt{3}$)-rect structure and incorporated star-shaped $[\text{V}_6\text{O}_{12}]$ clusters at the boundary to the free Rh(111) surface [67]. The star-shaped $[\text{V}_6\text{O}_{12}]$ clusters became mobile on the surface above 100 °C.

4.5 Nanoparticle assemblies

As already mentioned for hydrothermally gained free-standing nanosheets, 2D nanosheets can also be obtained as nanoparticle assemblies. In contrast to the single-crystalline nanosheets, the functional properties may vary substantially, because the nanoparticle assemblies are polycrystalline and have a lower density

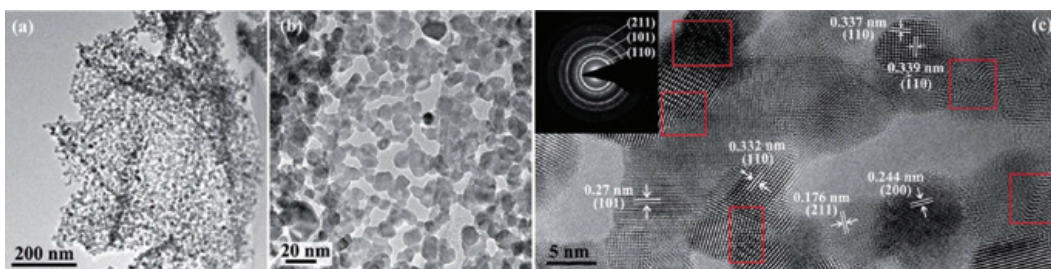


Fig. 16: TEM analysis of net-like SnO_2 2D homo-nanostructure as obtained from a wet-chemical process with graphene as a 2D template: (a, b) TEM bright-field micrographs, (c) HRTEM micrograph. Inset shows SAED pattern with indexed Debye-Scherrer rings. Adapted with permission from [53]. Copyright 2015 Royal Society of Chemistry.

with irregular pores between the particles. Nevertheless, they can be of significant interest as shown for a net-like SnO_2 2D nanostructure in Figure 16. TEM is unrivaled in elucidating the arrangement of individual nanoparticles when assembled to 2D nanostructures. Here, particles are less than 10 nm in diameter with narrow size distribution. The HRTEM in Figure 16c reveals lattice plane distances, which enable the identification of the relative orientations of individual nanoparticles. However, both HRTEM and the SAED in the inset, which shows narrow Debye-Scherrer rings, suggest the individual particles to be oriented randomly. As an approach for complementary investigations, when TEM is operated in STEM mode, it provides with HAADF contrast, EDXS and EELS [123] powerful techniques to unequivocally distinguish different phases in hetero-nanostructures like SnO_2/ZnO as they were fabricated also by Fu et al. [53].

5 Applications

The functional properties of 2D oxides are defining their value for possible applications. The unique 2D morphology and the low thickness in dimensions of few nanometers influence the electrical, optical, mechanical and chemical properties of the materials. Typical functional properties of 2D oxides are a high specific surface area, one-directional quantum confinement, increased charge carrier mobility, high in-plane mechanical strength with out-of-plane flexibility and optical transparency. In a world where technical applications are favorably getting smaller and mobile while maintaining or even increasing their performance, the 2D materials represent a versatile option to face these challenges. For this, ultrathin films, nanosheet arrays or free-standing nanosheets can be used. To use free-standing nanosheets in particular, they often have to be transferred into an applicable form as in ultrathin films. For this, multiple techniques are

suitable, e.g. the commonly used Langmuir-Blodgett technique. A more versatile technique is the layer-by-layer method, where different materials can be applied alternately to gain hybrid films of stacked compounds, which extends the possibilities in applications. Typically, other nanostructures as nanoparticles, nanodots, nanowires, nanorods, nanotubes or nanocables are the competitors to 2D materials when it comes to applicable forms, as long as they are not combined [124]. While each appearance may have its advantages and disadvantages, the specific advantages of 2D oxides in terms of actual applications are focused here. In the following, functional properties of some 2D oxides are presented together with already established or promising but not yet market-ripe applications. This overview of the presented research fields is not meant to be exhaustively in-depth but rather give introductions into each topic. The comprised topics are namely electrochemical energy storage, electrochromic devices, (bio-) chemical sensors, photoelectrochemistry, thermoelectrics, (photo-) catalysis and separation technologies.

5.1 Electrochemical energy storage

A highly promising application field especially for 2D oxides is the utilization in rechargeable batteries and supercapacitors. The setups for both applications are roughly the same containing negative and positive electrodes, electrolytes and the separators [125]. However, they distinguish in functionality, properties and different requirements in materials. In rechargeable batteries, an electrochemical cell with an anode and cathode is formed to ensure the electrical current caused by redox reactions. The large usage in nowadays applications, as all sorts of mobile technical devices, shows the indispensable importance of this technology. On the other side, capacitors are designed to store potential energy by the alignment of opposing charges at two electric conductors in an electric field. In the case of supercapacitors, they nowadays are used as a replacement of batteries or complementarily to them to gain additional power as in electrical vehicles or hybrid electric vehicles by converting acceleration energy during regenerative braking [126]. The main advantage of supercapacitors versus batteries lies within their ability to store substantially more energy and have way more stable and faster cycling characteristics, although they are yet limited to low voltage applications due to lower energy densities. Usually, the life span of a battery is limited by non-reversible reaction products, which slowly decrease the energy density after each recharging. The replacement or combining of commonly used rechargeable batteries with supercapacitors may solve this issue satisfactorily. Supercapacitors can be separated in electrochemical double-layer capacitors

(EDLCs) and pseudocapacitors [126]. The EDLCs contain electrolyte ions, whose adsorption on preferably large specific surface areas of porous electrodes is essential to the charging of the capacitor. For the energy storage of pseudocapacitors, reversible surface-faradaic redox reactions at the interface of electrode and electrolyte occur [126]. Therefore, pseudocapacitors are closer to the functionality of batteries than EDLCs, but their efficiency is diffusion limited. Crucial to the performance of a supercapacitor is the choice of materials and their design at the electrodes.

At this point, the 2D oxides come into play. Due to their faradaic behavior, metal oxides are prominent for their pseudocapacitive behavior rather than the utilization in EDLCs. In EDLCs various appearances of carbon are the currently state-of-the-art [126]. Prominent representative 2D oxides with very high capacities are RuO_2 and IrO_2 , which suffer from their scarce availability though. Cheaper alternatives with likewise or slightly lower capacities are NiO , CuO , SnO_2 , Co_3O_4 , FeO_x , MoO_2 , Cr_2O_3 , MnO_2 , V_2O_5 , NiCo_2O_4 , ZnCo_2O_4 and their doped deviates [38, 40, 81, 93, 99, 125, 126]. As proof of principle, the results of Rui et al. [66] gained with V_2O_5 nanosheets are qualified for the general utilization of nanosheets in hybrid Li-ion batteries. As shown in Figure 17, the usage of 2D nanosheets shows significant improvement in specific capacitance, coulombic efficiency and power density compared to the 3D bulk V_2O_5 . Possible explanations for this outcome are, that in contrast to the 3D bulk counterpart, the electrolyte can penetrate assembled nanosheets due to the large specific surface area, which leads to an increasing number of surface reactions. Furthermore, the small thickness of only 2.1–3.8 nm shortens the diffusion paths for the charge carriers, which results in much higher charge and discharge kinetics [66]. By this, hybrid Li-ion batteries with faster charging processes and longer cycle-lifetimes are possible.

Another promising example of utilized nanosheets, is the formation and characterization of a hybrid graphene/ Cr_2O_3 hetero-nanostructured anode by a layer-by-layer approach [47]. Compared to graphene/ Cr_2O_3 nanoparticles or other Cr_2O_3 based electrodes as a whole, the performance of the electrode could be significantly improved in terms of cycling stability and capacity. This approach exploits the very high theoretical capacity of 1.058 mAhg^{-1} from Cr_2O_3 and solves problems with cycling performance and electron transport within the material. Again, this could be achieved by the 2D arrangement, which causes a better electronic contact of the active materials and led to a way more stable connection between graphene and Cr_2O_3 compared to the nanoparticles. Another attempt to utilize 2D oxides for batteries, is the intercalation of useful Li ions within the layered 3D bulk material by exfoliation and subsequent reassembly of the nanosheets to form an electrode with improved characteristics [76]. Overall, metal oxides appear indispensable for future electrochemical storage applications and the usage of 2D

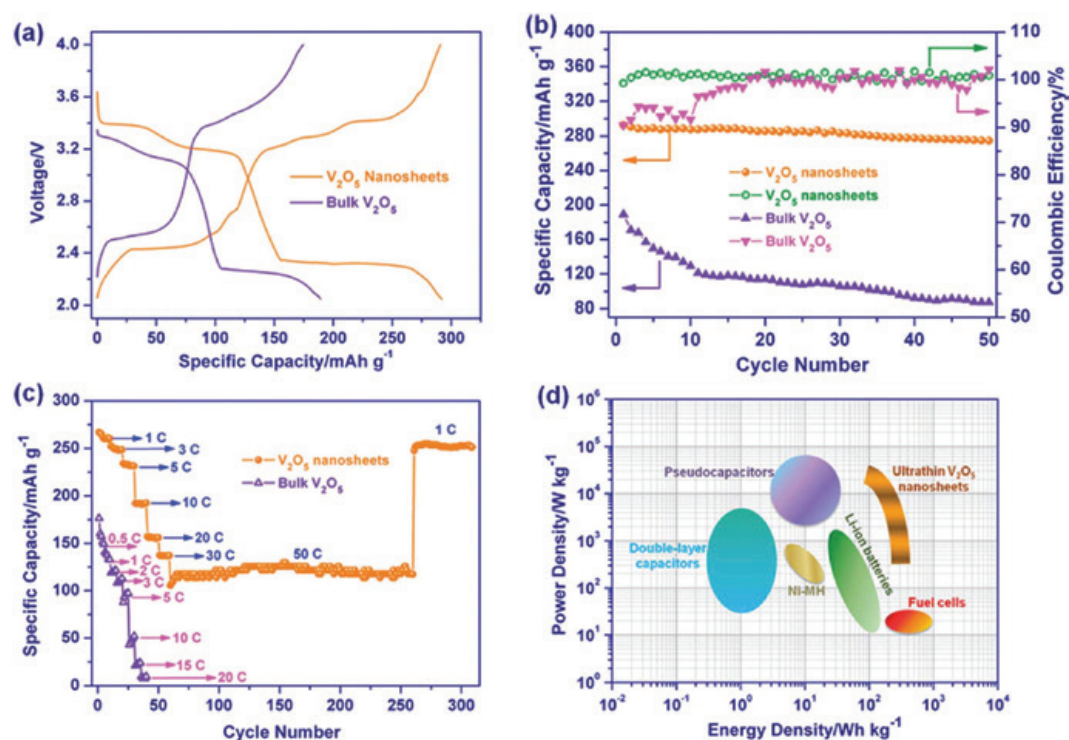


Fig. 17: Vanadium pentoxide V_2O_5 2D nanosheets, as observed from direct exfoliation of bulk crystals in formamide solvent, were tested on coin cells for their lithium storage capacity as prospective cathode material in the lithium-ion battery (LIB). A metallic lithium counter electrode was used and the 2D nanosheet material was compared to bulk V_2O_5 . (a) Charge-discharge curves show voltage over specific charge capacity. For 2D nanosheet material, the latter is distinctly enhanced over the bulk material. (b) At a rate capability of 0.2 C, whether the specific capacity nor the Coulomb efficiency fade away for the 2D nanosheet material. The C-rate describes the rate of charge or discharge in a cell or battery with respect to the nominal rated capacity [127]. (c) The 2D nanosheet material shows a stable rate capability at different charge and discharge rates (up to 50 C). (d) The Ragone plot suggests that a LIB with V_2O_5 2D nanosheet electrode might outperform over various energy storage and conversion devices with respect to both power density and energy density. Reproduced with permission from [66]. Copyright 2012 Royal Society of Chemistry.

nanosheets show highly promising improvements in capacity, cycle-lifetime and energy density.

5.2 Electrochromic devices

Optical properties of a material are defined by their electronic band structures, which are on the other hand influenced by size effects. Moreover, when the thickness of a film is lower than the penetration depth of the wavelengths of the

observed light, the absorption gets drastically reduced. For usual applications at visible and UV light, this occurs at a thickness of less than 10 nm [128]. Practically, this means materials may get more transparent with reducing thickness. This effect becomes even more interesting, if the transparency and absorbance are reversibly controllable, e.g. by applying an electrical current. Materials possessing this property are called electrochromic.

An attractive application for these materials are the so-called smart or switchable windows [129], which could help to reduce the energy consumption within buildings. The idea behind this is, to ensure normally transparent windows when people are within the room and add the possibility to cool and dim the brightness by applying a voltage to the electrochromic window. This leads to a doping of the electrochromic material and a change in color, light absorbance and reflection. Especially, the absorbance of light within the infrared spectrum may lead to an increased cooling effect. Therefore, the choice of the electrochromic material is one key factor within the whole electrochromic device alongside to the glass, transparent conductors and the electrolyte. Metal oxides as WO_3 , MoO_3 , Ta_2O_5 , TiO_2 , V_2O_5 and a few more are by far the most relevant electrochromic materials for this kind of application besides some polymers [129, 130]. Hereby, the tungsten oxides play an outstanding role compared to other metal oxides. In the application itself a film is structurally required, which can be attached to one side of the transparent conductor, respectively electrode (see Figure 18). The transparent conductor can likewise be composed of an ultrathin 2D oxide as indium-tin-oxide (ITO), which appears transparent due to its small thickness but does not show electrochromic characteristics.

Regarding the influence of 2D materials, few attempts have been made to investigate WO_3 nanosheets as a component for building the film [17, 18, 132]. The nanosheets consisting of WO_3 showed intense UV absorption and switchable IR absorption, which is favorable application-wise. An actual film consisting of nanosheets was obtained with the layer-by-layer technique by Wang et al. [132],

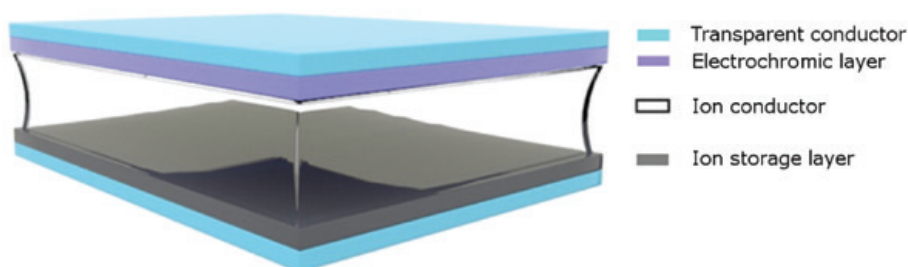


Fig. 18: Schematic setup with different thin layers for an electrochromic window application. Adapted with permission from [131]. Copyright 2016 Royal Society of Chemistry.

which showed good coloration efficiency together with nearly no reduced efficiency after over 800 cycles. The unique property of the film is a slow coloration process compared with a quick bleaching process, which can be attributed to the nanosheets implemented in the film. The suggested reason for this is the repulsion of charged intercalates at the top nanosheet layers during the coloring process, while at the opposing bleaching process the intercalates can easily be extracted from the top side without facing repulsion forces. Nevertheless, the calculated coloration time of 660 s is in reasonable limits and the bleaching time with 11 s [132] especially reliable. Therefore, further investigations of 2D materials within this research field could lead to even better results and pave the way for a market-ripe production of electrochromic devices.

5.3 (Bio-) chemical sensors

One important feature of 2D materials is their high surface-area-to-volume ratio in a chemical reaction. Due to this, the reactivity and accessibility of the material is drastically increased compared to their 3D bulk counterparts. Other competitive nanostructured appearances as nanoparticles or nanorods admittedly have an even greater specific surface area, but the nanosheets often allow better or further manageability regarding stability and applying on surfaces. One research field with 2D oxides as candidates is the detection and immobilization of specific molecules. Due to their large specific surface area, nanosheets are especially suitable for detecting small amounts of molecules, which allows detectors with high sensitivity. Two important detectors utilizing 2D oxides are gas sensors and biosensors.

Regarding gas sensors, several 2D metal oxides show highly promising results for electrochemic detectors. As the materials have to be selective towards the analyzed gas, different materials are required for different gases. Typically, the sensing of toxic or harmful compounds as H_2S , NO_x , ethanol or formaldehyde is asked for. For example, SnO_2/ZnO hetero-nanostructures built by nanosheets reach a detection limit of 10 ppb for H_2S at a relatively low working temperature of 100 °C [53]. Since this is lower than the acceptable concentrations of at least 20–100 ppb for humans, it is within applicable ranges [133]. Other highly toxic gases are nitric oxide NO and nitrogen dioxide NO_2 , which can be summed as NO_x . NiO as a p-type semiconductor with a high chemical stability shows reasonable sensing properties regarding NO_2 . Hereby, the N-doping within nanostructures of NiO nanosheets leads to a two-fold higher gas responsivity and sensitivity [134]. A single-crystal nanosheet of In_2O_3 was also used for detecting NO_2 and NO at room temperature recently [135]. Concerning NiO , the difference

of nanosheet-assembled hierarchical nanoflowers and nanoneedle-assembled structures was observed. The nanosheets showed a substantially higher gas response, but faster gas responses and recovery were gained with the needles [136]. These results show the importance of the used nanostructures and their significant influence on the sensing properties. For ethanol, ZnO nanosheets show high sensitivities and can be directly grown upon the electrode via a hydrothermal method [82]. Detection ranges of 25–1000 ppm at a working temperature of 400 °C and a high gas response could be reached coupled with fast response recovery. It has been shown, that even the type of surface-exposed crystal facets may influence the gas sensing properties substantially [137]. In the proposed study of Xu et al. the sensitivity of ZnO nanosheets towards low ethanol concentrations of 50 ppm was doubled with exposed (0001) planes in comparison to (10 $\bar{1}$ 0) planes and an even greater performance gap at 1 ppm. Even lower detection limits of 0.127 nM for ethanol were achieved by a CdO/ZnO/Yb₂O₃ ternary oxide nanosheet system [138]. Another compound worth mention is the WO₃, which also plays a significant role in electrochromic devices. It was shown, that Cr-doped WO₃ nanosheets can be used for formaldehyde sensing [139].

In terms of biosensing, 2D metal oxides just earned growing attention over the last few years with enormous potential discovering further appropriate materials [11]. First successful attempts have been made with MnO₂ nanosheets for sensing ochratoxin A (OTA) within single-strand desoxyribonucleic acid or cathepsin D (Cat D) using peptide chains [69]. For OTA, low quantification limits of 0.02 ng mL⁻¹ were found, which are competitive towards other detection methods in aqueous solutions. Further attempts with MnO₂ nanosheets regarding a fluorescence polarization-based detection of Ag⁺ ions were accomplished with low detection limits of 9.1 nM [140]. For a non-enzymatic glucose sensor, Co₃O₄ nanosheets with incorporated NiO or Ni(OH)₂ [141] and Ni(OH)₂/NiO nanosheets [142] showed low detection limits of 1.08 μM and 5 μM, respectively. Further 2D metal oxides with proven value regarding biosensors are MoO₃ nanosheets for field-effect-transistor based biosensing [143], ZrO₂ nanolayers for improving the reliability of impedimetric biosensors [86] and Yb₂O₃ nanosheets for the detection of the biomolecule urea [96].

5.4 Photoelectrochemistry

An increasingly important research field concerns regenerative energy usage as in photovoltaic devices. For the last decades, solar cells based on silicon were the most prominent ones, but remaining high manufacturing costs make the search for alternatives attractive.

One greatly promising alternative using metal oxides are perovskite solar cells (PSCs), which offer low costs at possibly high efficiencies. While the active perovskite is not built of oxides but rather organic metal halides as $\text{CH}_3\text{NH}_3\text{PbI}_3$, an electron transporting layer (ETL) is additionally required for loading the perovskite, blocking holes, transmitting light and transporting electrons [144]. Therefore, the ETL actively effects the performance and the stability of the device. Nanosheets with small thicknesses of less than 10 nm usually provide high transmissions of light, which also is used in electrochromic devices. Furthermore, metal oxides are currently state-of-the-art forming these ETLs [145, 146].

Utilizing TiO_2 nanosheets instead of other nanostructures led to power conversion efficiencies of 6.99% [147] and 10.7% [148]. By looking at the rapid evolution of the power conversion efficiencies from 3.8% to roughly 20% since their introduction in 2009 [146, 149], the date of research seems to be essential when comparing different results. The best efficiencies are currently gained by using thin films of mesoporous TiO_2 as the ETL, but the long-term stability lacks due to fast degradation of the devices under UV illumination. As an alternative, SnO_2 shows high chemical and UV illumination stability [150], but slightly lower efficiencies. By using SnO_2 nanosheet arrays, power conversion efficiencies of 17.36% were reached and even further increased to stable 18.00% when coupled with a C_{60} interlayer [144]. While the stability is not yet sufficient for application purposes with maintaining 90% of the original efficiency after storing at ambient conditions for 500 h, it could be further improved in the following years.

5.5 Thermoelectrics

In several kinds of chemical processes temperatures higher than room temperature are required. Although, there is a significant amount of heat loss in most of these processes. To gain a better energy efficiency, the heat energy can be transferred into a more usable form of energy, e.g. electrical energy. A promising way of converting heat loss into an electrical current is accomplished by thermoelectric materials. The efficiencies of such materials are determined by the dimensionless figure-of-merit zT , as given in Equation 1.

$$zT = \frac{\alpha^2 \cdot \sigma}{\Lambda} \quad (1)$$

The figure-of-merit increases with a high Seebeck coefficient α , high electrical conductivity σ and low entropy conductivity Λ [151]. The numerator in the fraction is also described as the power factor and should be observed separately for specific applications where high electrical current densities are required.

The problem in adjusting these parameters is typically their intercorrelation. Various different oxides as $\text{Ca}_3\text{Co}_4\text{O}_9$, CaMnO_3 , SrTiO_3 or In_2O_3 are interesting due to their thermoelectric properties [152]. Although, they mainly show rather poor zT values, mostly in the range of 0.1–0.5 if being unmodified [153]. An usual attempt at increasing the zT value is made by doping, which may effect all three parameters incorporated in zT . Although, doping itself did not increase the thermoelectric properties of the aforementioned oxide materials enough to gain a significant improvement. As a novel material resembling classical oxides, the oxyselenide BiCuSeO is worth mentioning [154]. It is a layered compound with insulating Bi_2O_2 layers and conducting Cu_2Se_2 layers with zT values of up to 1.4 if doped properly. Nevertheless, it is properly observed not a classical oxide and only resistant to surface oxidation up to 573 K and to decomposition reactions up to 773 K under air [155]. In comparison to this, non-oxide based thermoelectrics, if adjusted properly, gain higher zT values between 1 and 2 near room temperature. Though, oxides maintain significant benefits as stability at higher temperatures or the working mode at ambient conditions.

It has been suggested to increase the thermoelectric figure-of-merit of certain materials by more than one order of magnitude by preparing them in 2D quantum-well structures [156–158]. In fact, the extremely high zT of 2.4 [159] at room temperature for a one unit-cell thin $\text{SrTi}_{0.8}\text{Nb}_{0.2}\text{O}_3$ layer with a 2D electron gas shows huge possibilities in utilizing the quantum confinement effect for thermoelectrics. The quantum confinement is described by the restriction of the movement for charge carriers in-plane and the quantization of energy out-of plane [160]. This leads to an enhanced electronic density of states at the Fermi level, which subsequently increases the Seebeck coefficient drastically [161]. The confinement of the electrons additionally increases the in-plane electrical conductivity. Nevertheless, superlattice thin films are not easily applicable and the effective $zT=0.24$ of nine unit-cell layers including barrier layers between the unit cells mentioned by Ohta et al. [159] is still quite low. Therefore, Koumoto et al. [153] proposed to utilize the quantum confinement effect in 3D bulk nanoceramics. For example, nanometer-sized grains would affect the phonon confinement and boundary-scattering to decrease the lattice thermal conductivity significantly. In a “brick-and-mortar”-type SrTiO_3 with nanostructured grain-boundaries and grain interiors these effects could theoretically be utilized. For non-oxide Bi_2Se_3 nanosheets it was exemplary shown by actual measurements, that about 10 times higher zT values compared to the 3D bulk material can be reached [162, 163], wherefore the nanosheets were spark-plasma-sintered to 3D bulk pellets.

Only a few attempts have been made to investigate the thermoelectric properties of stacked 2D oxide nanosheets. In the case of the oxyselenide BiCuSeO , 3–4 nm thin nanosheets were synthesized by a solvothermal reaction and

afterwards restacked to dense pellets via hot pressing [164]. The entropy conductivity could be lowered due to enhanced phonon scattering at the nanoscaled grains and the power factor was increased due to a better electrical conductivity. This led to overall improved zT value of 0.2 for undoped BiCuSeO at 722 K compared to undoped 3D bulk material. Since values of up to 1.4 can be reached with modified BiCuSeO [154], the nanosheet restacking could easily be further optimized by using doped nanosheets. Ultrathin films of Na_xCoO_2 were also investigated by calculations within the Green-Kubo theory with rather poor outcomes regarding beneficial properties. Due to weak coupling of CoO_2 sheets within the layered structure, the in-plane lattice thermal conductivity seems to be insensitive to the thickness of nanosheets and stacks thereof [165]. Actual ultrathin films of Na_xCoO_2 were investigated and showed a decrease of the electrical conductivity for films below 10 nm and a constant Seebeck coefficient, but not measured thermal conductivities, which also does not recommend the utilization of Na_xCoO_2 in terms of nanosheets [166]. But, restacking of nanosheets is only one possible way to exploit the quantum confinement effect in 3D bulk oxides. Another possibility are self-assembled nanostructures within a matrix. A promising example is a nanocomposite of heavily doped $\text{Ca}_3\text{Co}_4\text{O}_9$, which contains stacked 2D hetero-oxide building blocks and exhibits a relatively high 3D bulk zT value for oxides at 1073 K, which is state-of-the-art concerning high-temperature ranges [167]. Thus, the assembly of 2D nanosheets for creating similar nanocomposites with other oxides is quite promising. Overall it can be stated, that the future of oxide-based thermoelectrics lies within utilizing the quantum confinement effect of nanostructures.

5.6 (Photo-) catalysis

Generally, catalysts lower the activation energy of chemical processes without being consumed. Due to this, they do not intervene in the chemical equilibrium but influence the reaction kinetics. Hence, they are indispensable for some of the most important industrially-sized productions of chemicals. Interesting catalyst types for 2D oxides are primarily electrocatalysts and photocatalysts.

Electrocatalysts are e.g. used for electrochemical water splitting for H_2 fuel production. The efficiency of the process is essential to ensure it is economically reasonable. Since the storage of electricity is a far from satisfactorily resolved problem, overproduced capacities of wind turbines are especially interesting for the electrochemical production of H_2 . However, the slow kinetics of the essential oxygen evolution reaction (OER) within this process is a big issue, which usually requires the use of electrocatalysts as RuO_2 or IrO_2 . The price of these compounds

diminishes the manufacturing process in applicability though. The utilization of different nanosheets as an electrocatalyst for the OER has shown substantial improvements in the most recent years. First of all, nanosheets of IrO_2 with a thickness of 0.7 nm exhibit a 6 times higher mass activity for the OER than nanoparticles [99]. Serious competitors are CoOOH nanosheets with a thickness of 1.4 nm, which show 2.4 times higher electrocatalytic activity than currently used IrO_2 and 20 times higher activity in comparison to 3D bulk CoOOH [168]. Further examples are Rh_2O_3 nanosheet assemblies or spinel-structured NiCo_2O_4 nanosheets, which all overcome currently used electrocatalysts for OER due to their 2D structure [94, 169]. Furthermore, the oxygen reduction reaction (ORR) can also be improved by using 2D metal oxide nanosheets like CoO_2 , $\text{Ti}_{1-x}\text{O}_2$ or RuO_2 as additives to graphene [63]. Especially by using CoO_2 , the electrocatalytic activity could be greatly increased while the long-term stability and selectivity were improved as well. The superior benefits of nanosheets compared to nanoparticles are assumed to be linked to the surface expansion in nanosheets. Despite this, the transport and storage of produced H_2 is also an issue. Recently, urea has been shown to be a promising candidate as a solid hydrogen carrier, which simplifies transport and storage of gaseous hydrogen. For gaining the hydrogen out of urea, electrocatalysts are necessary. For improving the current systems, mesoporous NiCo_2O_4 2D nanosheets were directly synthesized on collectors, which led to a decrease of the onset potential in comparison to 3D bulk $\text{Ni}(\text{OH})_2$ electrodes and enhancement of the urea oxidation current simultaneously [39].

An even more promising way to supply the necessary energy for the production of H_2 is the usage of solar energy. Although, low quantum efficiencies in the spectral region of visible light of most suitable materials are an issue. Generally, quantum efficiency is strongly dependent on the recombination rate of electrons and electron holes, namely excitons. A high recombination rate prevents the reactions of the excitons with the water and conclusively the quantum efficiency. Short lifetimes of less than 1 μs [170] for the excitons lead to a transporting problem, because the reactions occur at the surfaces. An approach to shorten the transporting ways to the surface is by using nanocrystals. Since defects within the crystals may trap the excitons, the crystallinity also effects the efficiency. Simply enhancing the reactive surface area would recommend nanoparticles as the most effective way to modify the materials. Nevertheless, nanoparticles have to deal with increasing durations for absorbing photons, which for a diameter of 1 nm already means 4 ms [170]. A solution to this problem could be the utilization of 2D photocatalysts as displayed in Figure 19.

The large areas of 2D nanosheets provide reasonable photon absorbing times, while the transport distance of the excitons to the surface remains short as in nanoparticles due to the small sheet thickness. Suitable semiconducting

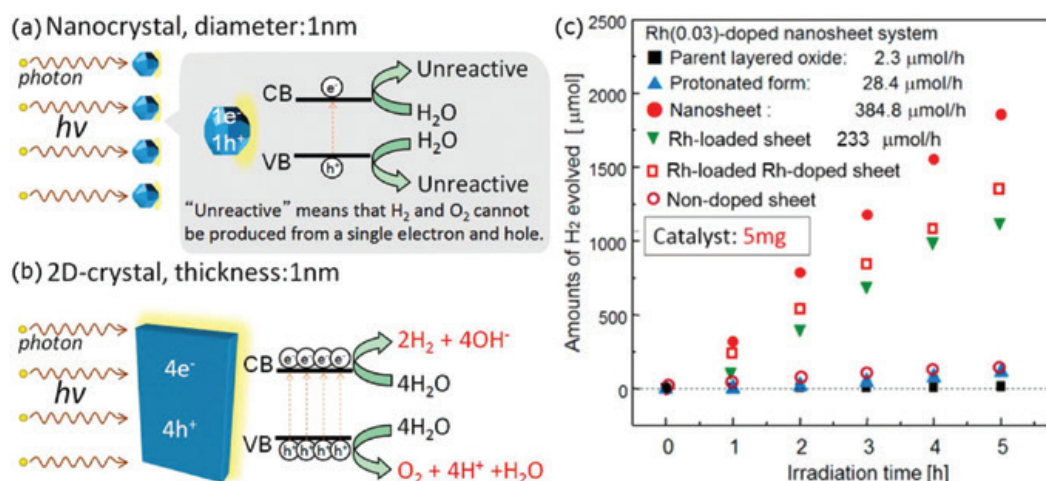


Fig. 19: Schematic comparison of (a) nanocrystals and (b) 2D crystals as photocatalysts. Due to the large sheet area of the 2D crystals, the photons can be absorbed in a reasonable time and catalyze the water splitting more effectively as nanoparticles. (c) H_2 production rates for differently treated $KCa_2Nb_3O_{10}$ compounds with methanol as a sacrificial agent. The non-exfoliated compounds and the unmodified nanosheets do only have small photocatalytic activities, but the Rh-doped or loaded nanosheets have a significantly better performance. The Rh(0.03)-doped nanosheets have the highest production rate while subsequently doping and loading diminish the performance slightly. Adapted with permission from [170]. Copyright 2014 American Chemical Society.

nanosheet oxides with a wide band gap are e.g. exfoliated Ruddlesden-Popper phases as $KCa_2Nb_3O_{10}$ or the Aurivillius phase Bi_2MoO_6 [46, 171]. Generally, there are two different options with co-catalysts and doping to enhance the photocatalytic activity of catalysts. While loading the surface with co-catalysts reliably improves the performance, doping usually does not have a huge impact in comparison [170]. The reason for this is the localization of the dopants within the catalyst and the resulting distance to the surface. In ultrathin 2D nanosheets the dopants are close to the surface, which means a direct involvement in catalytic activities of the dopants and a comparable improvement as caused by co-catalysts. The impact of doped but non-exfoliated compounds result in low photocatalytic activities confirming the influence of the 2D structure [171]. The adjustment of the doping amount is also important to gain high quantum efficiencies for $KCa_2Nb_3O_{10}$ nanosheets as it is shown in Figure 20.

By this, maximum H_2 production rates of $400 \mu\text{mol h}^{-1}$ with 5 mg catalyst were reached. An additional possibility for further improvements of the photocatalytic performance may be the addition of non-expensive co-catalysts. It was shown, that loading niobate nanosheets with small amounts of MoS_2 and graphene with a molar ratio of 99.0:0.5:0.5 leads to significantly increased H_2 production rates [87]. As catalyst for the O_2 production, hetero-structured Bi_2MoO_6 nanosheets

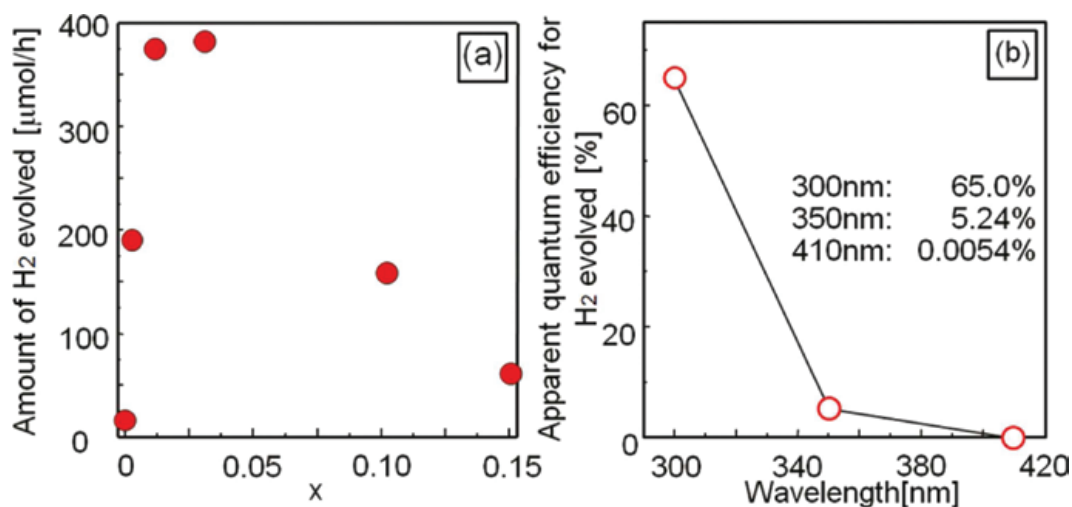


Fig. 20: Nanosheets as a photocatalyst for hydrogen production: (a) Amount of photocatalytically produced H₂ dependent on the Rh doping amount x in $\text{Ca}_2\text{Nb}_3\text{O}_{10} - 2\text{D}$ nanosheets. (b) Quantum efficiency for Rh($x=0.03$)-doped nanosheets regarding the H₂ production and the absorbed wavelengths. Reproduced with permission from [171]. Copyright 2011 American Chemical Society.

coupled with TiO₂ nanobelts were promoted [87]. Oxygen production rates of 0.668 mmol h⁻¹g⁻¹ were gained hereby. The remaining problem of these photocatalysts is their low activity under visible light irradiation. N-doped TiO₂ [172] and NbO_{*x*} [173] nanosheets improve the absorption under visible irradiation, but the absorption maximum continues to be in the ultraviolet (UV) spectrum and the doping amount is limited. Another problem for nanosheets in particular is attributed to their synthesis with ion intercalation. Organic intercalates may remain on the nanosheet surface even after washing and hinder the photocatalytic activity, which requires additional removing steps as UV light irradiation for several hours [170]. Therefore, alternative exfoliation techniques without the need of organic intercalates may be more appropriate.

Another application field for photocatalysts is the photodegradation of hazardous organics for water purification. Unmodified nanosheets as SnNb₂O₆ show higher selectivity and photocatalytic activity for positively charged pollutants in particular in comparison to the 3D bulk SnNb₂O₆, TiO₂ or N-doped TiO₂ [174]. Most recently, even better results were gained by creating 2D/2D heterojunctions between different nanosheets [175]. For niobate nanosheets $\text{Ca}_2\text{Nb}_3\text{O}_{10}$ - other oxide nanosheets as WO₃ or non-oxides as g-C₃N₄ are proven candidates. For both combinations, the photodegradation of tetracycline hydrochloride under simulated sunlight was investigated and both times led to a significantly enhanced performance due to improved charge carrier separations and transfers in strongly interacting hetero-interfaces. In terms of adding 20% WO₃, the optimum efficiency was gained with 5.1-fold and two-fold higher photocatalytic activity compared to

WO_3 and $\text{Ca}_2\text{Nb}_3\text{O}_{10}^-$ single nanosheets [176]. Similar results were accomplished with the combination of 20% g- C_3N_4 , which led to 6.6 and 1.8 times higher degradation rates compared to bare g- C_3N_4 or $\text{Ca}_2\text{Nb}_3\text{O}_{10}^-$ single nanosheets [175].

5.7 Separation technologies

A more exotic application field for 2D oxides comprises separation technologies as membranes or filters. While ceramic-based membranes maintain several disadvantages as brittleness or high costs, graphene oxide (GO) as a carbon-based material showed promising separation characteristics in the recent years [177–179]. Zeolites as a group of microporous aluminosilicates oxides are well-known for their applicability in separation technologies like membranes. The formation of 2D nanosheets with zeolites is also possible and shows auspicious results [180]. Because they are only oxide-related, further consideration is not envisaged within this review.

Several techniques for the arrangement of nanosheets to usable membranes have been tested as drop-casting, spray- and spin-coating, Langmuir-Blodgett method and vacuum filtration [178]. Vacuum filtration has also been shown to be suitable for 2D compounds as MXenes, which are mainly characterized as ultrathin layers composed of transition metal carbides and nitrides. Separating

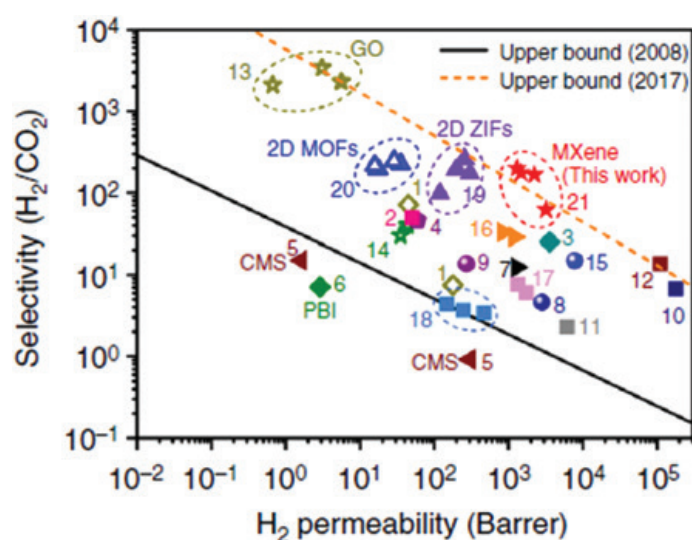


Fig. 21: Separation performance of graphene oxide (GO) membranes compared to other state-of-the-art membranes with highlighting MXene membranes. Abbreviations represent metal-organic-frameworks (MOFs), zeolitic-imidazolate-frameworks (ZIFs), compact-membrane-systems (CMS) and polybenzimidazole (PBI). Reproduced with permission from [181]. Copyright 2018 Nature Springer. Creative Commons License CC BY 4.0.

membranes built of MXenes recently showed substantially enhanced performances regarding permeability and selectivity as shown in Figure 21 [181, 182]. The nanosheet-composed membranes allow the separation of molecules with respect to their size, because larger gases as CO_2 have a longer transporting way moving along the nanosheet grains compared to smaller H_2 .

In comparison of GO-based to MXene-based membranes, the latter reaches higher permeabilities, but with lower selectivities. The disordered assembling of the nanosheets hindered better selectivities, which could be further improved by another assembling route.

2D metal oxides as membranes play only a minor role yet, because other materials show usually better performance. Nevertheless, exemplarily NbO nanosheets were assembled to a membrane by vacuum filtration and showed a high stability. The creation of nanochannels within the membranes allows the usage for high-flux nanofiltration as salts are retained [88].

6 Prospects

Several state-of-the-art compounds, synthesis techniques and related application fields have been presented in this review. The field of 2D oxide nanosheets is still in its infancy, but it is dynamically developing and has overrun the field of ultrathin films already as shown by Figure 22. Particularly, for thermoelectrics, supercapacitors and catalysts 2D oxide materials show significant improvements over 3D bulk materials. On the laboratory scale, further possibilities of 2D oxide nanosheets and novel materials are expected to be continuously reported enhancing the research field even further. Especially hetero-nanostructures of oxide nanosheets with other oxides or non-oxides seem to be promising for combining advantages of different material classes and exploiting interface interactions.

An important topic for future applications is rooted in upscaling synthesis techniques for industrial purposes. Top-down approaches may have some benefit for industrial scale productions, but bottom-up approaches can cover a broader spectrum of material compositions. For the industrial scale application, not only the making of nanosheets needs to be scaled up, but also proper production technology for the transfer of 2D oxide nanosheets into devices needs to be developed. The goal in mass-producing 2D oxide nanosheets is to take advantage of unique physical properties found in these ultrathin materials, and to make them in a form that is easy to process with existing industrial methods.

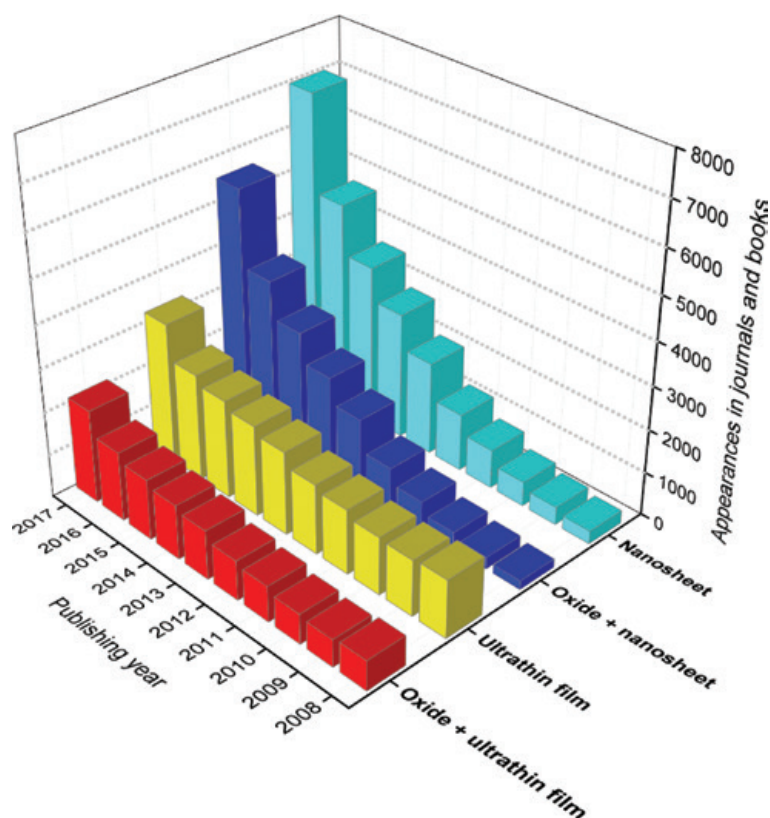


Fig. 22: Appearances of various 2D-correlated keywords in journals and books over the last 10 years. It should be mentioned, that with increasing publications in general, assumingly every keyword would show a raise over the recent years. Nevertheless, the drastically increasing interest in 2D nanosheets clearly outruns this trend by passing other keywords as ultrathin films. Data source for the graphical portrayal derived from Science Direct.

Copyright declaration: Some of the displayed figures were thankfully supplied from the open access Creative Commons Attribution 4.0 International License as denoted by CC BY 4.0 in the concerning figure captions. To view a copy of this licence, visit <http://creativecommons.org/licenses/by/4.0/>.

References

1. K. S. Novoselov, A. K. Geim, S. V. Morozov, D. Jiang, M. I. Katsnelson, I. V. Grigorieva, S. V. Dubonos, A. A. Firsov, *Nature* **438** (2005) 197.
2. A. Gupta, T. Sakhivel, S. Seal, *Prog. Mater. Sci.* **73** (2015) 44.
3. C. Bouet, M. D. Tessier, S. Ithurria, B. Mahler, B. Nadal, B. Dubertret, *Chem. Mater.* **25** (2013) 1262.
4. R. Mas-Ballesté, C. Gómez-Navarro, J. Gómez-Herrero, F. Zamora, *Nanoscale* **3** (2011) 20.
5. H. Zhang, *ACS Nano* **9** (2015) 9451.

6. C. Tan, X. Cao, X.-J. Wu, Q. He, J. Yang, X. Zhang, J. Chen, W. Zhao, S. Han, G.-H. Nam, M. Sindoro, H. Zhang, *Chem. Rev.* **117** (2017) 6225.
7. B. Mendoza-Sánchez, Y. Gogotsi, *Adv. Mater.* **28** (2016) 6104.
8. J. Y. Park, S. Kwon, J. H. Kim, *Adv. Mater. Interfaces* **1** (2014) 1300089.
9. M. Osada, T. Sasaki, *Adv. Mater.* **24** (2012) 210.
10. V. Nicolosi, M. Chhowalla, M. G. Kanatzidis, M. S. Strano, J. N. Coleman, *Science* **340** (2013) 1226419.
11. K. Shavanova, Y. Bakakina, I. Burkova, I. Shtepliuk, R. Viter, A. Ubelis, V. Beni, N. Starodub, R. Yakimova, V. Khranovskyy, *Sensors (Basel)* **16** (2016) 223.
12. R. Ma, T. Sasaki, *Adv. Mater.* **22** (2010) 5082.
13. J. E. ten Elshof, H. Yuan, P. G. Rodriguez, *Adv. Energy Mater.* **6** (2016) 1600355.
14. M. Aksit, D. P. Toledo, R. D. Robinson, *J. Mater. Chem.* **22** (2012) 5936.
15. L. Gao, Y. Li, M. Xiao, S. Wang, G. Fu, L. Wang, *2D Mater.* **4** (2017) 025031.
16. K. Fukuda, K. Akatsuka, Y. Ebina, R. Ma, K. Takada, I. Nakai, T. Sasaki, *ACS Nano* **2** (2008) 1689.
17. K. Fukuda, K. Akatsuka, Y. Ebina, M. Osada, W. Sugimoto, M. Kimura, T. Sasaki, *Inorg. Chem.* **51** (2012) 1540.
18. J. Qin, Y. Xing, G. Zhang, *J. Am. Ceram. Soc.* **96** (2013) 1617.
19. M. Reinelt, A. Allouche, M. Oberkofler, C. Linsmeier, *New J. Phys.* **11** (2009) 043023.
20. S. Valedbagi, J. Jalilian, S. M. Elahi, S. Majidi, A. Fathalian, V. Dalouji, *Electron. Mater. Lett.* **10** (2014) 5.
21. T. L. Chen, X. M. Li, W. D. Yu, X. Zhang, *Appl. Phys. A* **81** (2005) 657.
22. K. Matsuzaki, H. Hosono, T. Susaki, *Phys. Rev. B* **82** (2010) 033408.
23. A. Ma, L. Gu, Y. Zhu, M. Meng, J. Gui, Y. Yu, B. Zhang, *Chem. Commun. (Camb.)* **53** (2017) 8517.
24. M. Liu, J. Xu, B. Cheng, W. Ho, J. Yu, *Appl. Surf. Sci.* **332** (2015) 121.
25. M. M. J. Treacy, S. B. Rice, A. J. Jacobson, J. T. Lewandowski, *Chem. Mater.* **2** (1990) 279.
26. Y.-S. Han, I. Park, J.-H. Choy, *J. Mater. Chem.* **11** (2001) 1277.
27. Y. Ebina, T. Sasaki, M. Watanabe, *Solid State Ion.* **151** (2002) 177.
28. B.-W. Li, M. Osada, Y.-H. Kim, Y. Ebina, K. Akatsuka, T. Sasaki, *J. Am. Chem. Soc.* **139** (2017) 10868.
29. F. Hashemzadeh, *Water Sci. Technol.* **73** (2016) 1378.
30. R. E. Schaak, T. E. Mallouk, *Chem. Mater.* **12** (2000) 3427.
31. A. Takagaki, M. Sugisawa, D. Lu, J. N. Kondo, M. Hara, K. Domen, S. Hayashi, *J. Am. Chem. Soc.* **125** (2003) 5479.
32. S. Akbarian-Tefaghi, T. Rostamzadeh, T. T. Brown, C. Davis-Wheeler, J. B. Wiley, *ChemNano-Mat* **3** (2017) 538.
33. R. E. Schaak, T. E. Mallouk, *Chem. Commun. (Camb.)* (2002) 706.
34. P. Shen, H. T. Zhang, H. Liu, J. Y. Xin, L. F. Fei, X. G. Luo, R. Z. Ma, S. J. Zhang, *J. Mat. Chem. A* **3** (2015) 3456.
35. A. Takagaki, T. Yoshida, D. Lu, J. N. Kondo, M. Hara, K. Domen, S. Hayashi, *J. Phys. Chem. B* **108** (2004) 11549.
36. T.-G. Xu, C. Zhang, X. Shao, K. Wu, Y.-F. Zhu, *Adv. Funct. Mater.* **16** (2006) 1599.
37. H. Cao, X. Zhou, C. Zheng, Z. Liu, *ACS Appl. Mater. Interfaces* **7** (2015) 11984.
38. D. Zhang, W. Sun, Z. Chen, Y. Zhang, W. Luo, Y. Jiang, S. X. Dou, *Chem. Eur. J.* **22** (2016) 18060.
39. D. Wang, S. H. Vijapur, Y. Wang, G. G. Botte, *Int. J. Hydrogen Energy* **42** (2017) 3987.
40. F. Bao, X. Wang, X. Zhao, Y. Wang, Y. Ji, H. Zhang, X. Liu, *RSC Adv.* **4** (2014) 2393.

41. M. Al-Mamun, X. Su, H. Zhang, H. Yin, P. Liu, H. Yang, D. Wang, Z. Tang, Y. Wang, H. Zhao, *Small* **12** (2016) 2866.
42. Z. Li, W. Zhang, H. Wang, B. Yang, *Electrochim. Acta* **258** (2017) 561.
43. D. H. Sim, X. Rui, J. Chen, H. Tan, T. M. Lim, R. Yazami, H. H. Hng, Q. Yan, *RSC Adv.* **2** (2012) 3630.
44. S. Ida, C. Ogata, U. Unal, K. Izawa, T. Inoue, O. Altuntasoglu, Y. Matsumoto, *J. Am. Chem. Soc.* **129** (2007) 8956.
45. C. Guo, J. Xu, S. Wang, L. Li, Y. Zhang, X. Li, *CrystEngComm* **14** (2012) 3602.
46. J. Tian, P. Hao, N. Wei, H. Cui, H. Liu, *ACS Catal.* **5** (2015) 4530.
47. C. Zhao, H. Zhang, W. Si, H. Wu, *Nat. Commun.* **7** (2016) 12543.
48. H. Liu, M. Luo, J. Hu, T. Zhou, R. Chen, J. Li, *Appl. Catal. B* **140–141** (2013) 141.
49. Z. Zhang, D. Jiang, C. Xing, L. Chen, M. Chen, M. He, *Dalton Trans.* **44** (2015) 11582.
50. S. Ding, X. W. D. Lou, *Nanoscale* **3** (2011) 3586.
51. C. Wang, G. Du, K. Ståhl, H. Huang, Y. Zhong, J. Z. Jiang, *J. Phys. Chem. C* **116** (2012) 4000.
52. S. Takenaka, S. Miyake, S. Uwai, H. Matsune, M. Kishida, *J. Phys. Chem. C* **119** (2015) 12445.
53. D. Fu, C. Zhu, X. Zhang, C. Li, Y. Chen, *J. Mat. Chem. A* **4** (2016) 1390.
54. H. Kim, C. M. Gilmore, A. Piqué, J. S. Horwitz, H. Mattoussi, H. Murata, Z. H. Kafafi, D. B. Chrisey, *J. Appl. Phys.* **86** (1999) 6451.
55. D. R. Dreyer, S. Park, C. W. Bielawski, R. S. Ruoff, *Chem. Soc. Rev.* **39** (2010) 228.
56. Q. Dai, S. Bai, Y. Lou, X. Wang, Y. Guo, G. Lu, *Nanoscale* **8** (2016) 9621.
57. T. Sasaki, M. Watanabe, H. Hashizume, H. Yamada, H. Nakazawa, *J. Am. Chem. Soc.* **118** (1996) 8329.
58. I. Moriguchi, Y. Tsujigoi, Y. Teraoka, S. Kagawa, *Adv. Mater.* **11** (1999) 997.
59. T. Tanaka, K. Fukuda, Y. Ebina, K. Takada, T. Sasaki, *Adv. Mater.* **16** (2004) 872.
60. X. H. Yang, Z. Li, G. Liu, J. Xing, C. Sun, H. G. Yang, C. Li, *CrystEngComm* **13** (2011) 1378.
61. M. Ohwada, K. Kimoto, K. Suenaga, Y. Sato, Y. Ebina, T. Sasaki, *J. Phys. Chem. Lett.* **2** (2011) 1820.
62. T. Gao, H. Fjellvåg, P. Norby, *J. Mater. Chem.* **19** (2009) 787.
63. X. Jin, J. Lim, N.-S. Lee, S.-J. Hwang, *Electrochim. Acta* **235** (2017) 720.
64. F. Geng, R. Ma, Y. Ebina, Y. Yamauchi, N. Miyamoto, T. Sasaki, *J. Am. Chem. Soc.* **136** (2014) 5491.
65. H. Song, A. O. Sjøstad, H. Fjellvåg, H. Okamoto, Ø. B. Vistad, B. Arstad, P. Norby, *J. Solid State Chem.* **184** (2011) 3135.
66. X. Rui, Z. Lu, H. Yu, D. Yang, H. H. Hng, T. M. Lim, Q. Yan, *Nanoscale* **5** (2013) 556.
67. J. Schoiswohl, S. Surnev, M. Sock, M. G. Ramsey, G. Kresse, F. P. Netzer, *Angew. Chem. Int. Ed.* **43** (2004) 5546.
68. K. Kai, Y. Yoshida, H. Kageyama, G. Saito, T. Ishigaki, Y. Furukawa, J. Kawamata, *J. Am. Chem. Soc.* **130** (2008) 15938.
69. Y. Yuan, S. Wu, F. Shu, Z. Liu, *Chem. Commun. (Camb.)* **50** (2014) 1095.
70. J. Coelho, B. Mendoza-Sánchez, H. Pettersson, A. Pokle, E. K. McGuire, E. Long, L. McKeon, A. P. Bell, V. Nicolosi, *2D Mater.* **2** (2015) 025005.
71. X. Xiao, H. Song, S. Lin, Y. Zhou, X. Zhan, Z. Hu, Q. Zhang, J. Sun, B. Yang, T. Li, L. Jiao, J. Zhou, J. Tang, Y. Gogotsi, *Nat. Commun.* **7** (2016) 11296.
72. S.-J. Kim, I. Y. Kim, S. B. Patil, S. M. Oh, N.-S. Lee, S.-J. Hwang, *Chem. Eur. J.* **20** (2014) 5132.
73. L. Chen, C. Zhao, Y. Zhou, H. Peng, Y. Zheng, *J. Alloys Compd.* **504** (2010) L46.
74. M.-S. Wu, Y.-H. Ou, Y.-P. Lin, *J. Electrochem. Soc.* **158** (2011) A231.

75. T. W. Kim, E.-J. Oh, A.-Y. Jee, S. T. Lim, D. H. Park, M. Lee, S.-H. Hyun, J.-H. Choy, S.-J. Hwang, *Chem. Eur. J.* **15** (2009) 10752.
76. O. C. Compton, A. Abouimrane, Z. An, M. J. Palmeri, L. C. Brinson, K. Amine, S. T. Nguyen, *Small* **8** (2012) 1110.
77. K. Zhu, W. Hua, X. Wang, *Chem. Lett.* **40** (2011) 156.
78. B. Zhao, J. Song, T. Fang, P. Liu, Z. Jiao, H. Zhang, Y. Jiang, *Mater. Lett.* **67** (2012) 24.
79. X. Shu, H. Zheng, G. Xu, J. Zhao, L. Cui, J. Cui, Y. Qin, Y. Wang, Y. Zhang, Y. Wu, *Appl. Surf. Sci.* **412** (2017) 505.
80. G. Wang, J. Huang, S. Chen, Y. Gao, D. Cao, J. Power Sources **196** (2011) 5756.
81. J. Huang, H. Wu, D. Cao, G. Wang, *Electrochim. Acta* **75** (2012) 208.
82. D. Ju, H. Xu, J. Zhang, J. Guo, B. Cao, *Sens. Actuators B Chem.* **201** (2014) 444.
83. T. Sahoo, S. K. Nayak, P. Chelliah, M. K. Rath, B. Parida, *Mater. Res. Bull.* **75** (2016) 134.
84. B. Zhang, F. Wang, C. Zhu, Q. Li, J. Song, M. Zheng, L. Ma, W. Shen, *Nano-Micro Lett.* **8** (2016) 137.
85. T. Matsunaga, S. Takeshita, T. Isobe, *J. Lumin.* **165** (2015) 62.
86. D. Sticker, M. Rothbauer, V. Charwat, J. Steinkühler, O. Bethge, E. Bertagnolli, H. D. Wanzenboeck, P. Ertl, *Sens. Actuators B Chem.* **213** (2015) 35.
87. K. Nakagawa, T. Jia, W. Zheng, S. M. Fairclough, M. Katoh, S. Sugiyama, S. C. E. Tsang, *Chem. Commun. (Camb.)* **50** (2014) 13702.
88. K. Nakagawa, H. Yamashita, D. Saeki, T. Yoshioka, T. Shintani, E. Kamio, H. T. Kreissl, S. C. E. Tsang, S. Sugiyama, H. Matsuyama, *Chem. Commun. (Camb.)* **53** (2017) 7929.
89. N. Miyamoto, H. Yamamoto, R. Kaito, K. Kuroda, *Chem. Commun. (Camb.)* (2002) 2378.
90. K. Akatsuka, G. Takanashi, Y. Ebina, N. Sakai, M.-a. Haga, T. Sasaki, *J. Phys. Chem. Solids* **69** (2008) 1288.
91. D. S. Kim, T. C. Ozawa, K. Fukuda, S. Ohshima, I. Nakai, T. Sasaki, *Chem. Mater.* **23** (2011) 2700.
92. K. Fukuda, T. Saida, J. Sato, M. Yonezawa, Y. Takasu, W. Sugimoto, *Inorg. Chem.* **49** (2010) 4391.
93. S. Lee, X. Jin, I. Y. Kim, T.-H. Gu, J.-W. Choi, S. Nahm, S.-J. Hwang, *J. Phys. Chem. C* **120** (2016) 11786.
94. J. Bai, S.-H. Han, R.-L. Peng, J.-H. Zeng, J.-X. Jiang, Y. Chen, *ACS Appl. Mater. Interfaces* **9** (2017) 17195.
95. G. Cui, Z. Li, L. Gao, M. Zhang, *Phys. Chem. Chem. Phys.* **14** (2012) 16321.
96. A. A. Ibrahim, R. Ahmad, A. Umar, M. S. Al-Assiri, A. E. Al-Salami, R. Kumar, S. G. Ansari, S. Baskoutas, *Biosens. Bioelectron.* **98** (2017) 254.
97. A. Zavabeti, J. Z. Ou, B. J. Carey, N. Syed, R. Orrell-Trigg, E. L. H. Mayes, C. Xu, O. Kavehei, A. P. O'Mullane, R. B. Kaner, K. Kalantar-zadeh, T. Daeneke, *Science* **358** (2017) 332.
98. K. Fukuda, I. Nakai, Y. Ebina, R. Ma, T. Sasaki, *Inorg. Chem.* **46** (2007) 4787.
99. D. Takimoto, K. Fukuda, S. Miyasaka, T. Ishida, Y. Ayato, D. Mochizuki, W. Shimizu, W. Sugimoto, *Electrocat.* **8** (2017) 144.
100. H.-J. Kim, M. Osada, Y. Ebina, W. Sugimoto, K. Tsukagoshi, T. Sasaki, *Sci. Rep.* **6** (2016) 19402.
101. M. R. Waller, T. K. Townsend, J. Zhao, E. M. Sabio, R. L. Chamousis, N. D. Browning, F. E. Osterloh, *Chem. Mater.* **24** (2012) 698.
102. P. Ganter, C. Ziegler, A. T. Friedrichs, V. Duppel, C. Scheu, B. V. Lotsch, *ChemNanoMat* **3** (2017) 411.
103. K. S. Novoselov, A. K. Geim, S. V. Morozov, D. Jiang, Y. Zhang, S. V. Dubonos, I. V. Grigorieva, A. A. Firsov, *Science* **306** (2004) 666.

104. K. S. Novoselov, D. Jiang, F. Schedin, T. J. Booth, V. V. Khotkevich, S. V. Morozov, A. K. Geim, *Proc. Natl. Acad. Sci. USA* **102** (2005) 10451.
105. Y. Guo, C. Liu, Q. Yin, C. Wei, S. Lin, T. B. Hoffman, Y. Zhao, J. H. Edgar, Q. Chen, S. P. Lau, J. Dai, H. Yao, H.-S. P. Wong, Y. Chai, *ACS Nano* **10** (2016) 8980.
106. J. N. Coleman, M. Lotya, A. O'Neill, S. D. Bergin, P. J. King, U. Khan, K. Young, A. Gaucher, S. De, R. J. Smith, I. V. Shvets, S. K. Arora, G. Stanton, H.-Y. Kim, K. Lee, G. T. Kim, G. S. Duesberg, T. Hallam, J. J. Boland, J. J. Wang, J. F. Donegan, J. C. Grunlan, G. Moriarty, A. Shmeliov, R. J. Nicholls, J. M. Perkins, E. M. Grieveson, K. Theuwissen, D. W. McComb, P. D. Nellist, V. Nicolosi, *Science* **331** (2011) 568.
107. J. Rooze, E. V. Rebrov, J. C. Schouten, J. T. F. Keurentjes, *Ultrason. Sonochem.* **20** (2013) 1.
108. N. Zhang, J. Chu, Li, C., H. Chen, Q. Li, *J. Am. Ceram. Soc.* **93** (2010) 536.
109. L. Liu, Z. Shen, M. Yi, X. Zhang, S. Ma, *RSC Adv.* **4** (2014) 36464.
110. W.-J. Lee, Y.-M. Sung, *Cryst. Growth Des.* **12** (2012) 5792.
111. Z. Sun, T. Liao, Y. Dou, S. M. Hwang, M.-S. Park, L. Jiang, J. H. Kim, S. X. Dou, *Nat. Commun.* **5** (2014) 3813.
112. F. Wang, J.-H. Seo, G. Luo, M. B. Starr, Z. Li, D. Geng, X. Yin, S. Wang, D. G. Fraser, D. Morgan, Z. Ma, X. Wang, *Nat. Commun.* **7** (2016) 10444.
113. S. Ida, C. Ogata, M. Eguchi, W. J. Youngblood, T. E. Mallouk, Y. Matsumoto, *J. Am. Chem. Soc.* **130** (2008) 7052.
114. X. Cai, T. C. Ozawa, A. Funatsu, R. Ma, Y. Ebina, T. Sasaki, *J. Am. Chem. Soc.* **137** (2015) 2844.
115. J. Wang, Q. Liu, Q. Liu, *Opt. Mater. (Amst.)* **29** (2007) 593.
116. M. Aksit, B. C. Hoselton, H. J. Kim, D.-H. Ha, R. D. Robinson, *ACS Appl. Mater. Interfaces* **5** (2013) 8998.
117. J. Hou, Y. Zheng, Y. Su, W. Zhang, T. Hoshide, F. Xia, J. Jie, Q. Li, Z. Zhao, R. Ma, T. Sasaki, F. Geng, *J. Am. Chem. Soc.* **137** (2015) 13200.
118. Y. Liu, Z. Xu, W. Gao, Z. Cheng, C. Gao, *Adv. Mater.* **29** (2017) 1606794.
119. T. Hoshide, Y. Zheng, J. Hou, Z. Wang, Q. Li, Z. Zhao, R. Ma, T. Sasaki, F. Geng, *ACS Nano* **4** (2017) 3543.
120. M. Osada, K. Akatsuka, Y. Ebina, H. Funakubo, K. Ono, K. Takada, T. Sasaki, *ACS Nano* **4** (2010) 5225.
121. B.-W. Li, M. Osada, T. C. Ozawa, Y. Ebina, K. Akatsuka, R. Ma, H. Funakubo, T. Sasaki, *ACS Nano* **4** (2010) 6673.
122. I. Moriguchi, H. Maeda, Y. Teraoka, S. Kagawa, *Chem. Mater.* **9** (1997) 1050.
123. R. Brydson, S. Brooks, *Aberration-Corrected Analytical Transmission Electron Microscopy*, Royal Microscopical Society, Wiley-VCH, New Jersey (2011).
124. Z. Sun, T. Liao, L. Kou, *Sci. China Mater.* **60** (2017) 1.
125. C. Zhong, Y. Deng, W. Hu, J. Qiao, L. Zhang, J. Zhang, *Chem. Soc. Rev.* **44** (2015) 7484.
126. F. Wang, X. Wu, X. Yuan, Z. Liu, Y. Zhang, L. Fu, Y. Zhu, Q. Zhou, Y. Wu, W. Huang, *Chem. Soc. Rev.* **46** (2017) 6816.
127. C. A. Vincent, B. Scrosati, *Modern Batteries: An Introduction to Electrochemical Power Sources*, Butterworth-Heinemann, London, 2nd Edition (1997).
128. D. S. Ghosh, *Ultrathin Metal Transparent Electrodes for the Optoelectronics Industry*, Springer Theses, Springer, Heidelberg (2013).
129. R. Baetens, B. P. Jelle, A. Gustavsen, *Sol. Energy Mater. Sol. Cells* **94** (2010) 87.
130. C. G. Granqvist, *Sol. Energy Mater. Sol. Cells* **92** (2008) 203.
131. G. Cai, J. Wang, P. S. Lee, *Acc. Chem. Res.* **49** (2016) 1469.
132. K. Wang, P. Zeng, J. Zhai, Q. Liu, *Electrochem. Commun.* **26** (2013) 5.

133. M. Wagh, L. Patil, T. Seth, D. Amalnerkar, *Mater. Chem. Phys.* **84** (2004) 228.
134. H. van Luan, H. N. Tien, S. H. Hur, J. H. Han, W. Lee, *Nanomaterials (Basel)* **7** (2017) 313.
135. L. Sun, W. Fang, Y. Yang, H. Yu, T. Wang, X. Dong, G. Liu, J. Wang, W. Yu, K. Shi, *RSC Adv.* **7** (2017) 33419.
136. Y. Zhang, W. Zeng, *Mater. Lett.* **195** (2017) 217.
137. J. Xu, Z. Xue, N. Qin, Z. Cheng, Q. Xiang, *Sens. Actuators B Chem.* **242** (2017) 148.
138. M. M. Rahman, M. M. Alam, A. M. Asiri, M. A. Islam, *RSC Adv.* **7** (2017) 22627.
139. S. B. Upadhyay, R. K. Mishra, P. P. Sahay, *Ceram. Int.* **42** (2016) 15301.
140. L. Qi, Z. Yan, Y. Huo, X.-M. Hai, Z.-Q. Zhang, *Biosens. Bioelectron.* **87** (2017) 566.
141. M. R. Mahmoudian, W. J. Basirun, P. M. Woi, M. Sookhakian, R. Yousefi, H. Ghadimi, Y. Alias, *Mater. Sci. Eng. C Mater. Biol. Appl.* **59** (2016) 500.
142. W. Huang, L. Ge, Y. Chen, X. Lai, J. Peng, J. Tu, Y. Cao, X. Li, *Sens. Actuators B Chem.* **248** (2017) 169.
143. S. Balendhran, S. Walia, M. Alsaif, E. P. Nguyen, J. Z. Ou, S. Zhuiykov, S. Sriram, M. Bhaskaran, K. Kalantar-Zadeh, *ACS Nano* **7** (2013) 9753.
144. W.-Q. Wu, D. Chen, Y.-B. Cheng, R. A. Caruso, *Sol. RRL* **1** (2017) 1700117.
145. D. Bi, W. Tress, M. I. Dar, P. Gao, J. Luo, C. Renevier, K. Schenk, A. Abate, F. Giordano, J.-P. C. Baena, J.-D. Decoppet, S. M. Zakeeruddin, M. K. Nazeeruddin, M. Grätzel, A. Hagfeldt, *Sci. Adv.* **2** (2016) e1501170.
146. X. Li, D. Bi, C. Yi, J.-D. Decoppet, J. Luo, S. M. Zakeeruddin, A. Hagfeldt, M. Grätzel, *Science* **353** (2016) 58.
147. D. Zhong, Q. Jiang, B. Huang, W.-H. Zhang, C. Li, *J. Energy Chem.* **24** (2015) 626.
148. C. Li, Y. Li, Y. Xing, Z. Zhang, X. Zhang, Z. Li, Y. Shi, T. Ma, R. Ma, K. Wang, J. Wei, *ACS Appl. Mater. Interfaces* **7** (2015) 15117.
149. A. Kojima, K. Teshima, Y. Shirai, T. Miyasaka, *J. Am. Chem. Soc.* **131** (2009) 6050.
150. Y. Bai, Y. Fang, Y. Deng, Q. Wang, J. Zhao, X. Zheng, Y. Zhang, J. Huang, *ChemSusChem* **9** (2016) 2686.
151. A. Feldhoff, *Energy Harv. Sys.* **2** (2015) 517.
152. K. Koumoto, R. Funahashi, E. Guilmeau, Y. Miyazaki, A. Weidenkaff, Y. Wang, C. Wan, X.-D. Zhou, *J. Am. Ceram. Soc.* **96** (2013) 1.
153. K. Koumoto, Y. Wang, R. Zhang, A. Kosuga, R. Funahashi, *Annu. Rev. Mater. Res.* **40** (2010) 363.
154. L.-D. Zhao, J. He, D. Berardan, Y. Lin, J.-F. Li, C.-W. Nan, N. Dragoe, *Energy Environ. Sci.* **7** (2014) 2900.
155. F. Li, T.-R. Wei, F. Kang, J.-F. Li, *J. Alloys Compd.* **614** (2014) 394.
156. L. D. Hicks, M. S. Dresselhaus, *Phys. Rev. B* **47** (1993) 12727.
157. M. S. Dresselhaus, G. Chen, M. Y. Tang, R. G. Yang, H. Lee, D. Z. Wang, Z. F. Ren, J.-P. Fleurial, P. Gogna, *Adv. Mater.* **19** (2007) 1043.
158. Y. Sun, S. Gao, Y. Xie, *Chem. Soc. Rev.* **43** (2014) 530.
159. H. Ohta, S. Kim, Y. Mune, T. Mizoguchi, K. Nomura, S. Ohta, T. Nomura, Y. Nakanishi, Y. Ikuhara, M. Hirano, H. Hosono, K. Koumoto, *Nat. Mater.* **6** (2007) 129.
160. C. Xiao, Z. Li, K. Li, P. Huang, Y. Xie, *Acc. Chem. Res.* **47** (2014) 1287.
161. C. J. Vineis, A. Shakouri, A. Majumdar, M. G. Kanatzidis, *Adv. Mater.* **22** (2010) 3970.
162. Y. Sun, H. Cheng, S. Gao, Q. Liu, Z. Sun, C. Xiao, C. Wu, S. Wei, Y. Xie, *J. Am. Chem. Soc.* **134** (2012) 20294.
163. M. Hong, Z.-G. Chen, L. Yang, G. Han, J. Zou, *Adv. Electron. Mater.* **1** (2015) 1500025.
164. M. Samanta, S. N. Guin, K. Biswas, *Inorg. Chem. Front.* **4** (2017) 84.

165. D. O. Demchenko, D. B. Ameen, *Comput. Mater. Sci.* **82** (2014) 219.
166. P. Brinks, G. Rijnders, M. Huijben, *Appl. Phys. Lett.* **105** (2014) 193902.
167. M. Bittner, N. Kanas, F. Steinbach, D. Groeneveld, R. Hinterding, P. Wemhoff, K. Wiik, M.-A. Einarsrud, A. Feldhoff, manuscript in preparation.
168. J. Huang, J. Chen, T. Yao, J. He, S. Jiang, Z. Sun, Q. Liu, W. Cheng, F. Hu, Y. Jiang, Z. Pan, S. Wei, *Angew. Chem. Int. Ed.* **54** (2015) 8722.
169. J. Bao, X. Zhang, B. Fan, J. Zhang, M. Zhou, W. Yang, X. Hu, H. Wang, B. Pan, Y. Xie, *Angew. Chem. Int. Ed.* **54** (2015) 7399.
170. S. Ida, T. Ishihara, *J. Phys. Chem. Lett.* **5** (2014) 2533.
171. Y. Okamoto, S. Ida, J. Hyodo, H. Hagiwara, T. Ishihara, *J. Am. Chem. Soc.* **133** (2011) 18034.
172. G. Liu, L. Wang, C. Sun, Z. Chen, X. Yan, L. Cheng, H.-M. Cheng, G. Q. M. Lu, *Chem. Commun. (Camb.)* **11** (2009) 1383.
173. Y. Matsumoto, M. Koinuma, Y. Iwanaga, T. Sato, S. Ida, *J. Am. Chem. Soc.* **131** (2009) 6644.
174. S. Liang, R. Liang, L. Wen, R. Yuan, L. Wu, X. Fu, *Appl. Catal. B* **125** (2012) 103.
175. D. Jiang, T. Wang, Q. Xu, D. Li, S. Meng, M. Chen, *Appl. Catal. B* **201** (2017) 617.
176. X. Ma, D. Jiang, P. Xiao, Y. Jin, S. Meng, M. Chen, *Catal. Sci. Technol.* **7** (2017) 3481.
177. H. W. Kim, H. W. Yoon, S.-M. Yoon, B. M. Yoo, B. K. Ahn, Y. H. Cho, H. J. Shin, H. Yang, U. Paik, S. Kwon, J.-Y. Choi, H. B. Park, *Science* **342** (2013) 91.
178. H. Huang, Y. Ying, X. Peng, *J. Mat. Chem. A* **2** (2014) 13772.
179. W. L. Xu, C. Fang, F. Zhou, Z. Song, Q. Liu, R. Qiao, M. Yu, *Nano Lett.* **17** (2017) 2928.
180. M. Y. Jeon, D. Kim, P. Kumar, P. S. Lee, N. Rangnekar, P. Bai, M. Shete, B. Elyassi, H. S. Lee, K. Narasimharao, S. N. Basahel, S. Al-Thabaiti, W. Xu, H. J. Cho, E. O. Fetisov, R. Thyagarajan, R. F. DeJaco, W. Fan, K. A. Mkhoyan, J. I. Siepmann, M. Tsapatsis, *Nature* **543** (2017) 690.
181. L. Ding, Y. Wei, L. Li, T. Zhang, H. Wang, J. Xue, L.-X. Ding, S. Wang, J. Caro, Y. Gogotsi, *Nat. Commun.* **9** (2018) 155.
182. L. Ding, Y. Wei, Y. Wang, H. Chen, J. Caro, H. Wang, *Angew. Chem. Int. Ed.* **56** (2017) 1825.

List of Figures

1.1	Total worldwide energy consumption from 1971 to 2018 in kilo tons of oil equivalent (ktoe).	1
1.2	Waste heat in the year 2012 assigned to the relevant sectors.	2
1.3	Carrier concentration dependency of SEEBECK coefficient α , electrical conductivity σ , power factor PF , entropy conductivity Λ and figure-of-merit zT	8
1.4	Impact of band structure engineering on the DOS.	9
1.5	Schematic illustration of the electronic transport in an undoped material, a material with modulated doping and for uniform doping.	10
1.6	Schematic illustration of a material with an all-scale hierarchical structure.	11
1.7	Comparison of low- to mid-temperature thermoelectric materials with IOFFE plots and power factor vs. figure-of-merit plots.	14
1.8	Comparison of high-temperature thermoelectric materials with IOFFE plots and power factor vs. figure-of-merit plots.	15
1.9	Comparison of air and oxidation stability in dependence of the temperature.	16
1.10	Comparison of oxide thermoelectric materials with IOFFE plots and power factor vs. figure-of-merit plots.	17
1.11	Misfit-layered structure of $\text{Ca}_3\text{Co}_4\text{O}_9$	18
1.12	Step-wise procedure of the molten-flux synthesis.	54
2.1	General structure of the presented research in this thesis.	119

Bibliography

- [1] IEA, World Energy Balances: Overview (2020).
URL <https://www.iea.org/reports/world-energy-balances-overview>
- [2] C. Forman, I. K. Muritala, R. Pardemann, B. Meyer, Estimating the global waste heat potential, *Renewable and Sustainable Energy Reviews* 57 (2016) 1568–1579. doi:10.1016/j.rser.2015.12.192.
- [3] V. Vallem, Y. Sargolzaeiaval, M. Ozturk, Y.-C. Lai, M. D. Dickey, Energy harvesting and storage with soft and stretchable materials, *Advanced Materials* 33 (19) (2021) e2004832. doi:10.1002/adma.202004832.
- [4] R. A. Kishore, A. Marin, C. Wu, A. Kumar, S. Priya, *Energy Harvesting: Materials, Physics, and System Design with Practical Examples*, DEStech Publications, Lancaster, 2019.
- [5] T. J. Seebeck, *Magnetische Polarisation der Metalle und Erze durch Temperaturdifferenz 1822-1823*, Wilhelm Engelmann, Leipzig, 1895.
- [6] J. C. A. Peltier, *Nouvelles Expériences sur la Caloricité des Courans Électrique*, *Annales de Chimie et de Physique* (56) (1834) 371–386.
- [7] J. Yang, T. Caillat, Thermoelectric materials for space and automotive power generation, *MRS Bulletin* 31 (3) (2006) 224–229. doi:10.1557/mrs2006.49.
- [8] H. B. Callen, The application of Onsager’s reciprocal relations to thermoelectric, thermomagnetic, and galvanomagnetic effects, *Physical Review* 73 (11) (1948) 1349–1358. doi:10.1103/PhysRev.73.1349.
- [9] S. R. de Groot, *Thermodynamics of Irreversible Processes*, 1st Edition, North-Holland Publishing Company, Amsterdam, 1951.
- [10] A. Feldhoff, Thermoelectric material tensor derived from the Onsager-de Groot-Callen model, *Energy Harvesting and Systems* 2 (1-2) (2015). doi:10.1515/ehs-2014-0040.
- [11] H. U. Fuchs, *The Dynamics of Heat: A Unified Approach to Thermodynamics and Heat Transfer*, 2nd Edition, Graduate Texts in Physics, Springer Science+Business Media LLC, New York, 2010. doi:10.1007/978-1-4419-7604-8.
- [12] H. U. Fuchs, A direct entropic approach to uniform and spatially continuous dynamical models of thermoelectric devices, *Energy Harvesting and Systems* 1 (3-4) (2014). doi:10.1515/ehs-2014-0011.
- [13] C. Goupil, W. Seifert, K. Zabrocki, E. Müller, G. J. Snyder, Thermodynamics of thermoelectric phenomena and applications, *Entropy* 13 (8) (2011) 1481–1517. doi:10.3390/e13081481.
- [14] A. Feldhoff, Power conversion and its efficiency in thermoelectric materials, *Entropy* 22 (8) (2020). doi:10.3390/e22080803.

-
- [15] A. F. Ioffe, *Semiconductor Thermoelements and Thermoelectric Cooling*, 1st Edition, London: Info-search Ltd., 1957.
- [16] C. Zener, Putting electrons to work, *Transactions of American Society for Metals* (53) (1961) 1052–1068.
- [17] P. Drude, Zur Elektronentheorie der Metalle, *Annalen der Physik* 306 (3) (1900) 566–613. doi:10.1002/andp.19003060312.
- [18] P. Drude, Zur Elektronentheorie der Metalle; II. Teil. Galvanomagnetische und thermomagnetische Effekte, *Annalen der Physik* 308 (11) (1900) 369–402. doi:10.1002/andp.19003081102.
- [19] P. Drude, Zur Elektronentheorie der Metalle, *Annalen der Physik* 312 (3) (1902) 687–692. doi:10.1002/andp.19023120312.
- [20] R. Gross, A. Marx, *Festkörperphysik*, 2nd Edition, Walter de Gruyter, Berlin, 2014. doi:10.1524/9783110358704.
- [21] C. Kittel, *Introduction to Solid State Physics*, 8th Edition, John Wiley & Sons, Hoboken, 2005.
- [22] K. Seeger, *Semiconductor Physics: An Introduction*, 9th Edition, Advanced Texts in Physics, Springer Berlin Heidelberg, Heidelberg, 2004. doi:10.1007/978-3-662-09855-4.
- [23] H. J. Goldsmid, *Introduction to Thermoelectricity*, Vol. 121, Springer Berlin Heidelberg, Heidelberg, 2010. doi:10.1007/978-3-642-00716-3.
- [24] G. Tan, L.-D. Zhao, M. G. Kanatzidis, Rationally designing high-performance bulk thermoelectric materials, *Chemical Reviews* 116 (19) (2016) 12123–12149. doi:10.1021/acs.chemrev.6b00255.
- [25] Q. Zhu, E. M. Hopper, B. J. Ingram, T. O. Mason, Combined Jonker and Ioffe analysis of oxide conductors and semiconductors, *Journal of the American Ceramic Society* 94 (1) (2011) 187–193. doi:10.1111/j.1551-2916.2010.04047.x.
- [26] G. H. Jonker, The application of combined conductivity and Seebeck-effect plots for the analysis of semiconductor properties, *Philips Research Repts* (23) (1968) 131–138.
- [27] G. Job, R. Rüffler, *Physical Chemistry from a Different Angle: Introducing Chemical Equilibrium, Kinetics and Electrochemistry by Numerous Experiments*, 1st Edition, Springer International Publishing, New York, 2016.
- [28] H. Ibach, H. Lüth, *Festkörperphysik*, 7th Edition, Springer Berlin Heidelberg, Heidelberg, 2009. doi:10.1007/978-3-540-85795-2.
- [29] H.-S. Kim, Z. M. Gibbs, Y. Tang, H. Wang, G. J. Snyder, Characterization of Lorenz number with Seebeck coefficient measurement, *APL Materials* 3 (4) (2015) 041506. doi:10.1063/1.4908244.
-

- [30] R. B. Bird, W. E. Stewart, E. N. Lightfoot, *Transport Phenomena*, 2nd Edition, John Wiley & Sons, New York, 2007.
- [31] D. Narducci, Do we really need high thermoelectric figures of merit? A critical appraisal to the power conversion efficiency of thermoelectric materials, *Applied Physics Letters* 99 (10) (2011) 102104. doi:10.1063/1.3634018.
- [32] M. Wolf, R. Hinterding, A. Feldhoff, High power factor vs. high zT - A review of thermoelectric materials for high-temperature application, *Entropy* 21 (11) (2019) 1058. doi:10.3390/e21111058.
- [33] T. Zhu, Y. Liu, C. Fu, J. P. Heremans, J. G. Snyder, X. Zhao, Compromise and synergy in high-efficiency thermoelectric materials, *Advanced Materials* 29 (14) (2017). doi:10.1002/adma.201605884.
- [34] M. Bittner, N. Kanas, R. Hinterding, F. Steinbach, J. Räthel, M. Schrade, K. Wiik, M.-A. Einarsrud, A. Feldhoff, A comprehensive study on improved power materials for high-temperature thermoelectric generators, *Journal of Power Sources* 410-411 (2019) 143–151. doi:10.1016/j.jpowsour.2018.10.076.
- [35] Z. Dashevsky, S. Shusterman, M. P. Dariel, I. Drabkin, Thermoelectric efficiency in graded indium-doped PbTe crystals, *Journal of Applied Physics* 92 (3) (2002) 1425–1430. doi:10.1063/1.1490152.
- [36] S. A. Yamini, T. Ikeda, A. Lalonde, Y. Pei, S. X. Dou, G. J. Snyder, Rational design of p -type thermoelectric PbTe: Temperature dependent sodium solubility, *Journal of Materials Chemistry A* 1 (31) (2013) 8725. doi:10.1039/C3TA11654A.
- [37] K. H. Lee, S. Kim, H.-S. Kim, S. W. Kim, Band convergence in thermoelectric materials: theoretical background and consideration on Bi–Sb–Te alloys, *ACS Applied Energy Materials* 3 (3) (2020) 2214–2223. doi:10.1021/acsaem.9b02131.
- [38] K. Biswas, J. He, I. D. Blum, C.-I. Wu, T. P. Hogan, D. N. Seidman, V. P. Dravid, M. G. Kanatzidis, High-performance bulk thermoelectrics with all-scale hierarchical architectures, *Nature* 489 (7416) (2012) 414–418. doi:10.1038/nature11439.
- [39] L.-D. Zhao, V. P. Dravid, M. G. Kanatzidis, The panoscopic approach to high performance thermoelectrics, *Energy & Environmental Science* 7 (1) (2014) 251–268. doi:10.1039/c3ee43099e.
- [40] B. Abeles, Lattice thermal conductivity of disordered semiconductor alloys at high temperatures, *Physical Review* 131 (5) (1963) 1906–1911. doi:10.1103/PhysRev.131.1906.
- [41] X. Shi, J. Yang, S. Bai, J. Yang, H. Wang, M. Chi, J. R. Salvador, W. Zhang, L. Chen, W. Wong-Ng, On the design of high-efficiency thermoelectric clathrates through a systematic cross-substitution of framework elements, *Advanced Functional Materials* 20 (5) (2010) 755–763. doi:10.1002/adfm.200901817.

-
- [42] M. S. Dresselhaus, G. Chen, M. Y. Tang, R. G. Yang, H. Lee, D. Z. Wang, Z. F. Ren, J.-P. Fleurial, P. Gogna, New directions for low-dimensional thermoelectric materials, *Advanced Materials* 19 (8) (2007) 1043–1053. doi:10.1002/adma.200600527.
- [43] M. G. Kanatzidis, Nanostructured thermoelectrics: The new paradigm?, *Chemistry of Materials* 22 (3) (2010) 648–659. doi:10.1021/cm902195j.
- [44] X.-L. Shi, J. Zou, Z.-G. Chen, Advanced thermoelectric design: From materials and structures to devices, *Chemical Reviews* 120 (15) (2020) 7399–7515. doi:10.1021/acs.chemrev.0c00026.
- [45] D. J. Bergman, O. Levy, Thermoelectric properties of a composite medium, *Journal of Applied Physics* 70 (11) (1991) 6821–6833. doi:10.1063/1.349830.
- [46] D. J. Bergman, L. G. Fel, Enhancement of thermoelectric power factor in composite thermoelectrics, *Journal of Applied Physics* 85 (12) (1999) 8205–8216. doi:10.1063/1.370660.
- [47] Y. Lan, A. J. Minnich, G. Chen, Z. Ren, Enhancement of thermoelectric figure-of-merit by a bulk nanostructuring approach, *Advanced Functional Materials* 20 (3) (2010) 357–376. doi:10.1002/adfm.200901512.
- [48] A. Shakouri, Recent developments in semiconductor thermoelectric physics and materials, *Annual Review of Materials Research* 41 (1) (2011) 399–431. doi:10.1146/annurev-matsci-062910-100445.
- [49] Q. Zhang, X. Ai, L. Wang, Y. Chang, W. Luo, W. Jiang, L. Chen, Improved thermoelectric performance of silver nanoparticles-dispersed Bi_2Te_3 composites deriving from hierarchical two-phased heterostructure, *Advanced Functional Materials* 25 (6) (2015) 966–976. doi:10.1002/adfm.201402663.
- [50] M. Wolf, K. Menekse, A. Mundstock, R. Hinterding, F. Nietschke, O. Oeckler, A. Feldhoff, Low thermal conductivity in thermoelectric oxide-based multiphase composites, *Journal of Electronic Materials* 48 (11) (2019) 7551–7561. doi:10.1007/s11664-019-07555-2.
- [51] F. Delorme, P. Diaz-Chao, E. Guilmeau, F. Giovannelli, Thermoelectric properties of $\text{Ca}_3\text{Co}_4\text{O}_9\text{-Co}_3\text{O}_4$ composites, *Ceramics International* 41 (8) (2015) 10038–10043. doi:10.1016/j.ceramint.2015.04.091.
- [52] M. Acharya, S. S. Jana, M. Ranjan, T. Maiti, High performance ($\text{ZT} > 1$) *n*-type oxide thermoelectric composites from earth abundant materials, *Nano Energy* 84 (2021) 105905. doi:10.1016/j.nanoen.2021.105905.
- [53] C. Wan, X. Gu, F. Dang, T. Itoh, Y. Wang, H. Sasaki, M. Kondo, K. Koga, K. Yabuki, G. J. Snyder, R. Yang, K. Koumoto, Flexible *n*-type thermoelectric materials by organic intercalation of layered transition metal dichalcogenide TiS_2 , *Nature Materials* 14 (6) (2015) 622–627. doi:10.1038/NMAT4251.
- [54] C. Meng, C. Liu, S. Fan, A promising approach to enhanced thermoelectric properties using carbon nanotube networks, *Advanced Materials* 22 (4) (2010) 535–539. doi:10.1002/adma.200902221.
-

- [55] M. Bittner, N. Kanas, R. Hinterding, F. Steinbach, D. Groeneveld, P. Wemhoff, K. Wiik, M.-A. Einarsrud, A. Feldhoff, Triple-phase ceramic 2D nanocomposite with enhanced thermoelectric properties, *Journal of the European Ceramic Society* 39 (4) (2019) 1237–1244. doi:10.1016/j.jeurceramsoc.2018.10.023.
- [56] L. Pan, Y. Lang, L. Zhao, D. Berardan, E. Amzallag, C. Xu, Y. Gu, C. Chen, L.-D. Zhao, X. Shen, Y. Lyu, C. Lu, Y. Wang, Realization of *n*-type and enhanced thermoelectric performance of *p*-type BiCuSeO by controlled iron incorporation, *Journal of Materials Chemistry A* 6 (27) (2018) 13340–13349. doi:10.1039/c8ta03521k.
- [57] B. Zhu, X. Liu, Q. Wang, Y. Qiu, Z. Shu, Z. Guo, Y. Tong, J. Cui, M. Gu, J. He, Realizing record high performance in *n*-type Bi₂Te₃-based thermoelectric materials, *Energy & Environmental Science* 13 (7) (2020) 2106–2114. doi:10.1039/d0ee01349h.
- [58] Y. Liu, Y. Zhang, S. Ortega, M. Ibáñez, K. H. Lim, A. Grau-Carbonell, S. Martí-Sánchez, K. M. Ng, J. Arbiol, M. V. Kovalenko, D. Cadavid, A. Cabot, Crystallographically textured nanomaterials produced from the liquid phase sintering of Bi_{*x*}Sb_{2-*x*}Te₃ nanocrystal building blocks, *Nano Letters* 18 (4) (2018) 2557–2563. doi:10.1021/acs.nanolett.8b00263.
- [59] J. Zhang, Di Wu, D. He, D. Feng, M. Yin, X. Qin, J. He, Extraordinary thermoelectric performance realized in *n*-Type PbTe through multiphase nanostructure engineering, *Advanced Materials* 29 (39) (2017). doi:10.1002/adma.201703148.
- [60] G. Tan, F. Shi, S. Hao, L.-D. Zhao, H. Chi, X. Zhang, C. Uher, C. Wolverton, V. P. Dravid, M. G. Kanatzidis, Non-equilibrium processing leads to record high thermoelectric figure of merit in PbTe-SrTe, *Nature Communications* 7 (2016) 12167. doi:10.1038/ncomms12167.
- [61] X. Chen, H. Wu, J. Cui, Y. Xiao, Y. Zhang, J. He, Y. Chen, J. Cao, W. Cai, S. J. Pennycook, Z. Liu, L.-D. Zhao, J. Sui, Extraordinary thermoelectric performance in *n*-type manganese doped Mg₃Sb₂ Zintl: High band degeneracy, tuned carrier scattering mechanism and hierarchical microstructure, *Nano Energy* 52 (2018) 246–255. doi:10.1016/j.nanoen.2018.07.059.
- [62] X. Wang, J. Li, C. Wang, B. Zhou, L. Zheng, B. Gao, Y. Chen, Y. Pei, Orbital alignment for high performance thermoelectric YbCd₂Sb₂ alloys, *Chemistry of Materials* 30 (15) (2018) 5339–5345. doi:10.1021/acs.chemmater.8b02155.
- [63] G. Rogl, A. Grytsiv, P. Rogl, E. Bauer, M. Hohenhofer, R. Anbalagan, R. C. Mallik, E. Schafner, Nanostructuring of *p*- and *n*-type skutterudites reaching figures of merit of approximately 1.3 and 1.6, respectively, *Acta Materialia* 76 (2014) 434–448. doi:10.1016/j.actamat.2014.05.051.
- [64] Y. Liu, L.-D. Zhao, Y. Zhu, Y. Liu, F. Li, M. Yu, D.-B. Liu, W. Xu, Y.-H. Lin, C.-W. Nan, Synergistically optimizing electrical and thermal transport properties of BiCuSeO via a dual-doping approach, *Advanced Energy Materials* 6 (9) (2016) 1502423. doi:10.1002/aenm.201502423.

- [65] E. Woermann, A. Muan, Phase equilibria in the system CaO-cobalt oxide in air, *Journal of Inorganic and Nuclear Chemistry* 32 (5) (1970) 1455–1459. doi:10.1016/0022-1902(70)80631-5.
- [66] N. Kanas, G. Skomedal, T. D. Desissa, A. Feldhoff, T. Grande, K. Wiik, M.-A. Einarsrud, Performance of a thermoelectric module based on *n*-type $(\text{La}_{0.12}\text{Sr}_{0.88})_{0.95}\text{TiO}_{3-\delta}$ and *p*-type $\text{Ca}_3\text{Co}_{4-x}\text{O}_{9+\delta}$, *Journal of Electronic Materials* 49 (7) (2020) 4154–4159. doi:10.1007/s11664-020-08127-5.
- [67] S. Saini, H. S. Yaddanapudi, K. Tian, Y. Yin, D. Magginetti, A. Tiwari, Terbium ion doping in $\text{Ca}_3\text{Co}_4\text{O}_9$: A step towards high-performance thermoelectric materials, *Scientific Reports* 7 (2017) 44621. doi:10.1038/srep44621.
- [68] H. Zhu, J. Mao, Y. Li, J. Sun, Y. Wang, Q. Zhu, G. Li, Q. Song, J. Zhou, Y. Fu, R. He, T. Tong, Z. Liu, W. Ren, L. You, Z. Wang, J. Luo, A. Sotnikov, J. Bao, K. Nielsch, G. Chen, D. J. Singh, Z. Ren, Discovery of TaFeSb-based half-Heuslers with high thermoelectric performance, *Nature Communications* 10 (1) (2019) 270. doi:10.1038/s41467-018-08223-5.
- [69] N. Shutoh, S. Sakurada, Thermoelectric properties of the $\text{Ti}_x(\text{Zr}_{0.5}\text{Hf}_{0.5})_{1-x}\text{NiSn}$ half-Heusler compounds, *Journal of Alloys and Compounds* 389 (1-2) (2005) 204–208. doi:10.1016/j.jallcom.2004.05.078.
- [70] R. Basu, S. Bhattacharya, R. Bhatt, M. Roy, S. Ahmad, A. Singh, M. Navaneethan, Y. Hayakawa, D. K. Aswal, S. K. Gupta, Improved thermoelectric performance of hot pressed nanostructured *n*-type SiGe bulk alloys, *Journal of Materials Chemistry A* 2 (19) (2014) 6922. doi:10.1039/C3TA14259K.
- [71] S. Ahmad, A. Singh, A. Bohra, R. Basu, S. Bhattacharya, R. Bhatt, K. N. Meshram, M. Roy, S. K. Sarkar, Y. Hayakawa, A. K. Debnath, D. K. Aswal, S. K. Gupta, Boosting thermoelectric performance of *p*-type SiGe alloys through in-situ metallic YSi_2 nanoinclusions, *Nano Energy* 27 (2016) 282–297. doi:10.1016/j.nanoen.2016.07.002.
- [72] H. B. Kang, U. Saparamadu, A. Nozariasbmarz, W. Li, H. Zhu, B. Poudel, S. Priya, Understanding oxidation resistance of half-Heusler alloys for in-air high temperature sustainable thermoelectric generators, *ACS Applied Materials & Interfaces* 12 (32) (2020) 36706–36714. doi:10.1021/acsami.0c08413.
- [73] J. W. Fergus, Oxide materials for high temperature thermoelectric energy conversion, *Journal of the European Ceramic Society* 32 (3) (2012) 525–540. doi:10.1016/j.jeurceramsoc.2011.10.007.
- [74] Y. Yin, B. Tudu, A. Tiwari, Recent advances in oxide thermoelectric materials and modules, *Vacuum* 146 (2017) 356–374. doi:10.1016/j.vacuum.2017.04.015.
- [75] L.-D. Zhao, J. He, D. Berardan, Y. Lin, J.-F. Li, C.-W. Nan, N. Dragoe, Bi-CuSeO oxyselenides: New promising thermoelectric materials, *Energy & Environmental Science* 7 (9) (2014) 2900–2924. doi:10.1039/c4ee00997e.

- [76] J. Yang, F. R. Stabler, Automotive applications of thermoelectric materials, *Journal of Electronic Materials* 38 (7) (2009) 1245–1251. doi:10.1007/s11664-009-0680-z.
- [77] W. S. Liu, E. W. Lee, M.-A. Nicolet, V. Arbet-Engels, K. L. Wang, N. M. Abuhadba, C. R. Aita, Wet oxidation of GeSi at 700 °C, *Journal of Applied Physics* 71 (8) (1992) 4015–4018. doi:10.1063/1.350847.
- [78] J. Leszczynski, K. T. Wojciechowski, A. L. Malecki, Studies on thermal decomposition and oxidation of CoSb₃, *Journal of Thermal Analysis and Calorimetry* 105 (1) (2011) 211–222. doi:10.1007/s10973-011-1461-5.
- [79] S. H. Park, Y. Kim, C.-Y. Yoo, G. Yoon, Oxidation and sublimation suppression of PbTe thermoelectric legs by plasma coated ceramic layers, *Journal of Vacuum Science & Technology A: Vacuum, Surfaces, and Films* 34 (6) (2016) 061101. doi:10.1116/1.4964131.
- [80] D. Music, K. Chang, P. Schmidt, F. N. Braun, M. Heller, S. Hermsen, P. J. Pöllmann, T. Schulzendorff, C. Wagner, On atomic mechanisms governing the oxidation of Bi₂Te₃, *Journal of Physics: Condensed matter* 29 (48) (2017) 485705. doi:10.1088/1361-648X/aa945f.
- [81] F. Li, T.-R. Wei, F. Kang, J.-F. Li, Thermal stability and oxidation resistance of BiCuSeO based thermoelectric ceramics, *Journal of Alloys and Compounds* 614 (2014) 394–400. doi:10.1016/j.jallcom.2014.06.117.
- [82] C. Li, Q. Chen, Y. Yan, Effects of Pr and Yb dual doping on the thermoelectric properties of CaMnO₃, *Materials* 11 (10) (2018). doi:10.3390/ma11101807.
- [83] A. Ahmad, M. Umer, X. Tan, R. Liu, F. Mohmad, M. Hussain, G.-K. Ren, Y.-H. Lin, High-temperature electrical and thermal transport behaviors of In₂O₃-based ceramics by Zn-Sn co-substitution, *Journal of Applied Physics* 123 (24) (2018) 245108. doi:10.1063/1.5026492.
- [84] B. Zhang, J. Wang, T. Zou, S. Zhang, X. Yaer, N. Ding, C. Liu, L. Miao, Y. Li, Y. Wu, High thermoelectric performance of Nb-doped SrTiO₃ bulk materials with different doping levels, *Journal of Materials Chemistry C* 3 (43) (2015) 11406–11411. doi:10.1039/c5tc02016f.
- [85] M. Ohtaki, K. Araki, K. Yamamoto, High thermoelectric performance of dually doped ZnO ceramics, *Journal of Electronic Materials* 38 (7) (2009) 1234–1238. doi:10.1007/s11664-009-0816-1.
- [86] M. Ito, D. Furumoto, Microstructure and thermoelectric properties of Na_xCo₂O₄/Ag composite synthesized by the polymerized complex method, *Journal of Alloys and Compounds* 450 (1-2) (2008) 517–520. doi:10.1016/j.jallcom.2006.12.081.
- [87] Y. Miyazaki, Crystal structure and thermoelectric properties of the misfit-layered cobalt oxides, *Solid State Ionics* 172 (1-4) (2004) 463–467. doi:10.1016/j.ssi.2004.01.046.

-
- [88] Y. Miyazaki, M. Onoda, T. Oku, M. Kikuchi, Y. Ishii, Y. Ono, Y. Morii, T. Kajitani, Modulated structure of the thermoelectric compound $[\text{Ca}_2\text{CoO}_3]_{0.62}\text{CoO}_2$, *Journal of the Physical Society of Japan* 71 (2) (2002) 491–497. doi:10.1143/JPSJ.71.491.
- [89] T. Janssen, A. Janner, A. Looijenga-Vos, P. M. De Wolff, *International Tables for Crystallography: 9.8 Incommensurate and Commensurate Modulated Structures*, 3rd Edition, Kluwer Acad. Publ, Dordrecht, 2004.
- [90] T. Janssen, G. Chapuis, M. de Boissieu, *Aperiodic Crystals: From Modulated Phases to Quasicrystals*, Vol. 20 of *International Union of Crystallography monographs on crystallography*, Oxford University Press, Oxford, 2007.
- [91] M. Bittner, L. Helmich, F. Nietschke, B. Geppert, O. Oeckler, A. Feldhoff, Porous $\text{Ca}_3\text{Co}_4\text{O}_9$ with enhanced thermoelectric properties derived from sol-gel synthesis, *Journal of the European Ceramic Society* 37 (13) (2017) 3909–3915. doi:10.1016/j.jeurceramsoc.2017.04.059.
- [92] Y. Zhang, J. Zhang, Q. Lu, Synthesis of highly textured $\text{Ca}_3\text{Co}_4\text{O}_9$ ceramics by spark plasma sintering, *Ceramics International* 33 (7) (2007) 1305–1308. doi:10.1016/j.ceramint.2006.04.011.
- [93] N. Puri, R. P. Tandon, A. K. Mahapatro, Fully dense hot pressed calcium cobalt oxide ceramics, *Ceramics International* 44 (6) (2018) 6337–6342. doi:10.1016/j.ceramint.2018.01.024.
- [94] S. Funahashi, H. Guo, J. Guo, A. L. Baker, K. Wang, K. Shiratsuyu, C. A. Randall, Cold sintering and co-firing of a multilayer device with thermoelectric materials, *Journal of the American Ceramic Society* 100 (8) (2017) 3488–3496. doi:10.1111/jace.14852.
- [95] S. Bresch, B. Mieller, D. Schoenauer-Kamin, R. Moos, F. Giovanelli, T. Rabe, Influence of pressure assisted sintering and reaction sintering on microstructure and thermoelectric properties of bi-doped and undoped calcium cobaltite, *Journal of Applied Physics* 126 (7) (2019) 075102. doi:10.1063/1.5107476.
- [96] D. Kenfaui, M. Gomina, J. G. Noudem, D. Chateigner, Anisotropy of transport properties correlated to grain boundary density and quantified texture in thick oriented $\text{Ca}_3\text{Co}_4\text{O}_9$ ceramics, *Materials* 11 (7) (2018). doi:10.3390/ma11071224.
- [97] C.-H. Lim, W.-S. Seo, S. Lee, Y. S. Lim, J.-Y. Kim, H.-H. Park, S.-M. Choi, K. H. Lee, K. Park, Anisotropy of the thermoelectric figure of merit (ZT) in textured $\text{Ca}_3\text{Co}_4\text{O}_9$ ceramics prepared by using a spark plasma sintering process, *Journal of the Korean Physical Society* 66 (5) (2015) 794–799. doi:10.3938/jkps.66.794.
- [98] M. Schrade, T. Norby, T. G. Finstad, Hall effect measurements on thermoelectric $\text{Ca}_3\text{Co}_4\text{O}_9$: On how to determine the charge carrier concentration in strongly correlated misfit cobaltites, *Journal of Applied Physics* 117 (20) (2015) 205103. doi:10.1063/1.4921861.
-

- [99] J. J. Shen, L. P. Hu, T. J. Zhu, X. B. Zhao, The texture related anisotropy of thermoelectric properties in bismuth telluride based polycrystalline alloys, *Applied Physics Letters* 99 (12) (2011) 124102. doi:10.1063/1.3643051.
- [100] I. Terasaki, Y. Sasago, K. Uchinokura, Large thermoelectric power in NaCo_2O_4 single crystals, *Physical Review. B: Condensed Matter* 56 (20) (1997) R12685–R12687. doi:10.1103/PhysRevB.56.R12685.
- [101] K. Fujita, T. Mochida, K. Nakamura, High-temperature thermoelectric properties of $\text{Na}_x\text{CoO}_{2-\delta}$ single crystals, *Japanese Journal of Applied Physics* 40 (2001) 4644–4647. doi:10.1143/JJAP.40.4644.
- [102] Y. Lei, X. Li, L. Liu, G. Ceder, Synthesis and stoichiometry of different layered sodium cobalt oxides, *Chemistry of Materials* 26 (18) (2014) 5288–5296. doi:10.1021/cm5021788.
- [103] J. Sui, J. Li, J. He, Y.-L. Pei, D. Berardan, H. Wu, N. Dragoe, W. Cai, L.-D. Zhao, Texturation boosts the thermoelectric performance of BiCuSeO oxyselenides, *Energy & Environmental Science* 6 (10) (2013) 2916. doi:10.1039/C3EE41859F.
- [104] H. Zhang, Ultrathin two-dimensional nanomaterials, *ACS Nano* 9 (10) (2015) 9451–9469. doi:10.1021/acsnano.5b05040.
- [105] R. Hinterding, A. Feldhoff, Two-dimensional oxides: Recent progress in nanosheets, *Zeitschrift für Physikalische Chemie* 233 (1) (2019) 117–165. doi:10.1515/zpch-2018-1125.
- [106] L. D. Hicks, M. S. Dresselhaus, Effect of quantum-well structures on the thermoelectric figure of merit, *Physical Review. B: Condensed Matter* 47 (19) (1993) 12727–12731. doi:10.1103/PhysRevB.47.12727.
- [107] C. Xiao, Z. Li, K. Li, P. Huang, Y. Xie, Decoupling interrelated parameters for designing high performance thermoelectric materials, *Accounts of Chemical Research* 47 (4) (2014) 1287–1295. doi:10.1021/ar400290f.
- [108] C. J. Vineis, A. Shakouri, A. Majumdar, M. G. Kanatzidis, Nanostructured thermoelectrics: Big efficiency gains from small features, *Advanced Materials* 22 (36) (2010) 3970–3980. doi:10.1002/adma.201000839.
- [109] H. Ohta, S. Kim, Y. Mune, T. Mizoguchi, K. Nomura, S. Ohta, T. Nomura, Y. Nakanishi, Y. Ikuhara, M. Hirano, H. Hosono, K. Koumoto, Giant thermoelectric Seebeck coefficient of a two-dimensional electron gas in SrTiO_3 , *Nature Materials* 6 (2) (2007) 129–134. doi:10.1038/nmat1821.
- [110] M. Samanta, S. N. Guin, K. Biswas, Ultrathin few layer oxychalcogenide BiCuSeO nanosheets, *Inorganic Chemistry Frontiers* 4 (1) (2017) 84–90. doi:10.1039/C6QI00435K.
- [111] K. Koumoto, Y. Wang, R. Zhang, A. Kosuga, R. Funahashi, Oxide thermoelectric materials: A nanostructuring approach, *Annual Review of Materials Research* 40 (1) (2010) 363–394. doi:10.1146/annurev-matsci-070909-104521.

-
- [112] R. Wei, X. Tang, J. Yang, J. Dai, C. Liang, W. Song, X. Zhu, Y. Sun, $\text{Ca}_3\text{Co}_4\text{O}_9$ /polycrystalline Al_2O_3 : An effective template for *c*-axis oriented layered cobaltate thin films by chemical solution deposition, *RSC Advances* 5 (23) (2015) 17746–17750. doi:10.1039/c4ra15378b.
- [113] Z. D. Li, D. Wu, K. Y. Zhao, H. Zhang, Synthesis of the thermoelectric thin films of $\text{Ca}_3\text{Co}_4\text{O}_9$ and $\text{Ca}_3\text{Co}_2\text{O}_6$ using pulsed-laser deposition techniques, *Advanced Materials Research* 531 (2012) 484–488. doi:10.4028/www.scientific.net/AMR.531.484.
- [114] M. M. Seabaugh, G. L. Messing, M. D. Vaudin, Texture development and microstructure evolution in liquid-phase-sintered α -alumina ceramics prepared by templated grain growth, *Journal of the American Ceramic Society* 83 (12) (2000) 3109–3116. doi:10.1111/j.1151-2916.2000.tb01690.x.
- [115] J. Boltersdorf, N. King, P. A. Maggard, Flux-mediated crystal growth of metal oxides: Synthetic tunability of particle morphologies, sizes, and surface features for photocatalysis research, *CrystEngComm* 17 (11) (2015) 2225–2241. doi:10.1039/c4ce01587h.
- [116] D. Elwell, B. W. Neate, Mechanisms of crystal growth from fluxed melts, *Journal of Materials Science* 6 (12) (1971) 1499–1519. doi:10.1007/BF02403090.
- [117] D. G. Porob, P. A. Maggard, Synthesis of textured $\text{Bi}_5\text{Ti}_3\text{FeO}_{15}$ and $\text{LaBi}_4\text{Ti}_3\text{FeO}_{15}$ ferroelectric layered Aurivillius phases by molten-salt flux methods, *Materials Research Bulletin* 41 (8) (2006) 1513–1519. doi:10.1016/j.materresbull.2006.01.020.
- [118] D. Arney, L. Fuoco, J. Boltersdorf, P. A. Maggard, Flux synthesis of $\text{Na}_2\text{Ca}_2\text{Nb}_4\text{O}_{13}$: The influence of particle shapes, surface features, and surface areas on photocatalytic hydrogen production, *Journal of the American Ceramic Society* 96 (4) (2013) 1158–1162. doi:10.1111/jace.12122.
- [119] D. E. Bugaris, H.-C. zur Loye, Materials discovery by flux crystal growth: Quaternary and higher order oxides, *Angewandte Chemie International Edition* 51 (16) (2012) 3780–3811. doi:10.1002/anie.201102676.
- [120] M.-A. Einarsrud, T. Grande, 1D oxide nanostructures from chemical solutions, *Chemical Society Reviews* 43 (7) (2014) 2187–2199. doi:10.1039/C3CS60219B.
- [121] G. Wulff, XXV. Zur Frage der Geschwindigkeit des Wachstums und der Auflösung der Krystallflächen, *Zeitschrift für Kristallographie - Crystalline Materials* 34 (1-6) (1901) 449–530. doi:10.1524/zkri.1901.34.1.449.
- [122] M. v. Laue, Der Wulffsche Satz für die Gleichgewichtsform von Kristallen, *Zeitschrift für Kristallographie - Crystalline Materials* 105 (1-6) (1943) 124–133. doi:10.1524/zkri.1943.105.1.124.
- [123] A. A. Chernov, The kinetics of the growth forms of crystals, *Soviet Physics Crystallography* (7) (1963) 728–730.
-

- [124] M. R. Singh, D. Ramkrishna, A comprehensive approach to predicting crystal morphology distributions with population balances, *Crystal Growth & Design* 13 (4) (2013) 1397–1411. doi:10.1021/cg301851g.
- [125] C. Shivakumara, M. Hegde, A. Prakash, A. Khadar, G. Subbanna, N. Lalla, Low temperature synthesis, structure and properties of alkali-doped La_2NiO_4 , LaNiO_3 and $\text{LaNi}_{0.85}\text{Cu}_{0.15}\text{O}_3$ from alkali hydroxide fluxes, *Solid State Sciences* 5 (2) (2003) 351–357. doi:10.1016/S1293-2558(02)00056-0.
- [126] W. Paulus, A. Cousson, G. Dhalenne, J. Berthon, A. Revcolevschi, S. Hosoya, W. Treutmann, G. Heger, R. Le Toquin, Neutron diffraction studies of stoichiometric and oxygen intercalated La_2NiO_4 single crystals, *Solid State Sciences* 4 (5) (2002) 565–573. doi:10.1016/S1293-2558(02)01299-2.
- [127] M. Brunelli, M. Coduri, M. Ceretti, W. Paulus, Local apical oxygen disorder in oxygen rich $\text{La}_2\text{NiO}_{4.18}$, comparing neutron single crystal and n/X-PDF analysis from powder diffraction data, *Journal of Physics D: Applied Physics* 48 (50) (2015) 504009. doi:10.1088/0022-3727/48/50/504009.
- [128] S.-Y. Jeon, M.-B. Choi, J.-H. Hwang, E. D. Wachsman, S.-J. Song, Electrical Conductivity and Thermoelectric Power of $\text{La}_2\text{NiO}_{4+\delta}$, *Journal of The Electrochemical Society* 158 (5) (2011) B476. doi:10.1149/1.3559186.
- [129] M. Burriel, J. Santiso, M. D. Rossell, G. van Tendeloo, A. Figueras, G. Garcia, Enhancing total conductivity of $\text{La}_2\text{NiO}_{4+\delta}$ epitaxial thin films by reducing thickness, *The Journal of Physical Chemistry C* 112 (29) (2008) 10982–10987. doi:10.1021/jp7101622.
- [130] V. Kharton, A. Yaremchenko, E. Tsipis, A. Valente, M. Patrakeev, A. Shaula, J. Frade, J. Rocha, Characterization of mixed-conducting $\text{La}_2\text{Ni}_{0.9}\text{Co}_{0.1}\text{O}_{4+\delta}$ membranes for dry methane oxidation, *Applied Catalysis A: General* 261 (1) (2004) 25–35. doi:10.1016/j.apcata.2003.10.028.
- [131] T. Klande, K. Efimov, S. Cusenza, K.-D. Becker, A. Feldhoff, Effect of doping, microstructure, and CO_2 on $\text{La}_2\text{NiO}_{4+\delta}$ -based oxygen-transporting materials, *Journal of Solid State Chemistry* 184 (12) (2011) 3310–3318. doi:10.1016/j.jssc.2011.10.019.
- [132] K. Chiba, Structure of layered perovskite-type $\text{Na}_2\text{Ca}_2\text{Nb}_4\text{O}_{13}$ single crystals, *Solid State Ionics* 108 (1-4) (1998) 179–183. doi:10.1016/S0167-2738(98)00037-X.
- [133] K. Chiba, N. Ishizawa, S. Oishi, A Ruddlesden–Popper-type layered perovskite, $\text{Na}_2\text{Ca}_2\text{Nb}_4\text{O}_{13}$, *Acta Crystallographica Section C Crystal Structure Communications* 55 (7) (1999) 1041–1044. doi:10.1107/S0108270199001134.
- [134] Y.-S. Han, I. Park, J.-H. Choy, Exfoliation of layered perovskite, $\text{KCa}_2\text{Nb}_3\text{O}_{10}$, into colloidal nanosheets by a novel chemical process, *Journal of Materials Chemistry* 11 (4) (2001) 1277–1282. doi:10.1039/B006045N.

2. Thermoelectric oxide composites based on $\text{Ca}_3\text{Co}_4\text{O}_9$

In this chapter, various thermoelectric composite systems with $\text{Ca}_3\text{Co}_4\text{O}_9$ (CCO) as a base material are investigated. CCO is the most auspicious *p*-type oxide material and is suitable for high-temperature applications up to 1173 K in air. Its low toxicity in comparison to commonly used Bi_2Te_3 makes it even more interesting, wherefore an improvement of this material is desirable. Two different concepts were investigated within this thesis, which are schematically shown in Fig. 2.1. The first concept comprises three publications dealing with the synthesis of microdimensional plate-like oxide crystals, their embedding in a CCO matrix and reaction sintering. The second concept comprises two publications with a nanodimensional approach, where two-dimensional nanostructures originate from heavy doping or reaction sintering occurs with nanosheets. The results of the micro- and nanodimensional approaches are covered in the following sections 2.1 and 2.2.

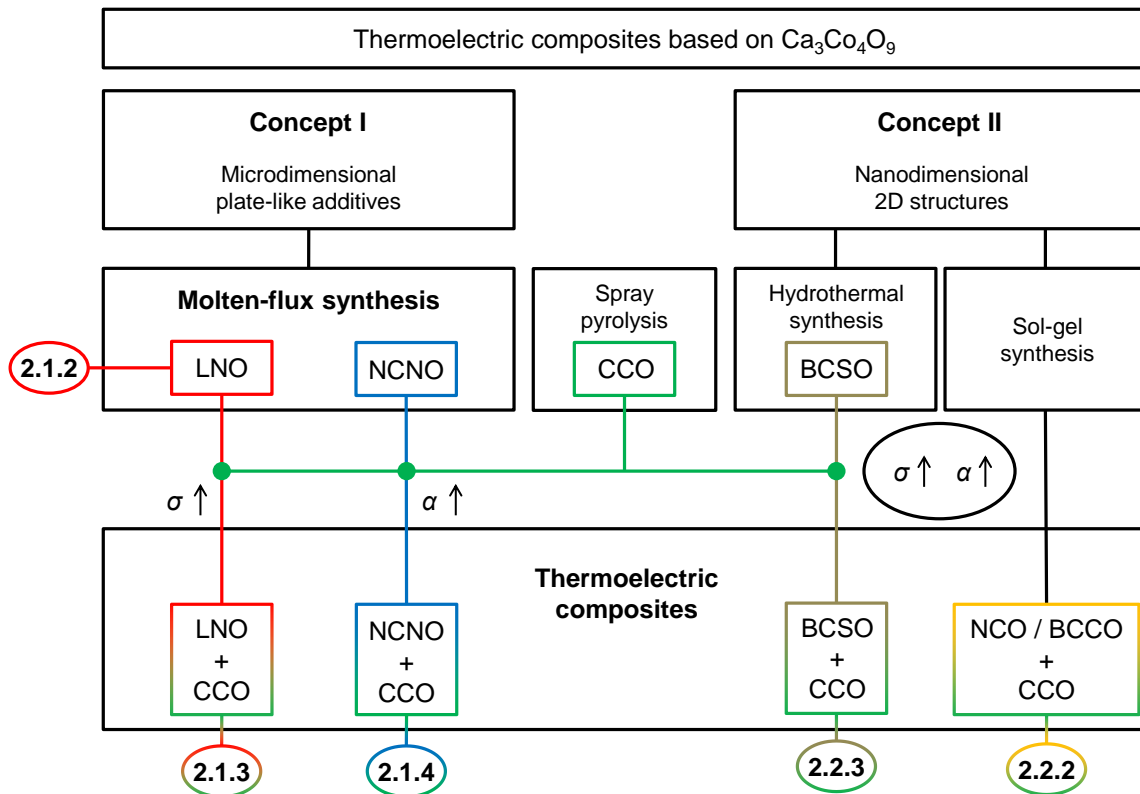


Figure 2.1: General structure of the presented research in this thesis. Investigated material combinations in a $\text{Ca}_3\text{Co}_4\text{O}_9$ (CCO) matrix are La_2NiO_4 (LNO), $\text{Na}_2\text{Ca}_2\text{Nb}_4\text{O}_{13}$ (NCNO), Na_xCoO_2 (NCO) with $\text{Bi}_2\text{Ca}_2\text{Co}_2\text{O}_9$ (BCCO) and BiCuSeO (BCSO). Concept I comprises investigations with microdimensional plate-like oxides and concept II deals with nanodimensional 2D structures.

2.1 Concept I: Microdimensional approach

2.1.1 Summary

The first concept deals with the embedding of microdimensional sheets in a CCO matrix. Molten-flux synthesis was chosen as a suitable synthesis method for gaining the desired crystal shape of the additives. The RUDDLESDEN-POPPER phase La_2NiO_4 (LNO) was considered as a mixing partner due to its interesting transport properties as a mixed ionic-electronic conductor. To ensure the proper crystal growth of microdimensional sheets, molten-flux synthesis for LNO was elaborated in section 2.1.2. Two different routes were investigated: the solid-state route and the sol-gel process. Both routes were concluded by a molten-flux synthesis using sodium hydroxide as a flux. The role of additional water turned out to be crucial for the outcome of the grown crystals. Analysis of the particles revealed the infrequent occurrence of higher RUDDLESDEN-POPPER phases on the plate surface. Both routes led to microdimensional plate-like particles, but they differed in purity and aspect ratio. While crystal growth along the a, b -plane was more pronounced for the sol-gel process, the solid-state route resulted in less impurities.

The LNO particles of the solid-state route were further processed to a thermoelectric composite material in section 2.1.3. Microstructural analysis by X-ray diffraction (XRD), electron diffraction patterns, energy-dispersive X-ray spectroscopy (EDXS), transmission electron microscopy (TEM) and scanning TEM (STEM) revealed reactions between LNO and CCO during the sintering at 1173 K. As a result, a complex system of multiple oxides emerged containing $\text{La}(\text{Co},\text{Ni})\text{O}_3$, $\text{Ca}_3\text{Co}_2\text{O}_6$, $(\text{Co},\text{Ni})\text{O}$ and the matrix material CCO. The samples containing 1 wt% and 5 wt% LNO were the most promising, because a higher power factor was achieved by an improved electrical conductivity. The enhanced electrical conductivity could be attributed to the $\text{La}(\text{Co},\text{Ni})\text{O}_3$ perovskite phase. Higher contents of LNO diminished the positive effect on the power factor, most likely due to imbalances of the reactant ratio and interconnecting grains of the added phases. Furthermore, the SEEBECK coefficient was lowered as expected. The thermal conductivity was improved at lower temperature, but slightly deteriorated at higher temperature in comparison to porous CCO. Finally, the best achieved figure-of-merit was 0.27 for the sample with 5 wt% LNO, while the average zT was increased by about 20% in the temperature range of 473 K to 1073 K.

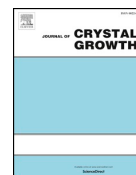
The introduction of LNO into a CCO system proved to be beneficial to the thermoelectric properties, mainly due to the increased electrical conductivity. Another system was investigated in section 2.1.4, where the SEEBECK coefficient had priority. Thus, a material with a low electrical conductivity and a large band gap was chosen, featuring large plate-like particles to follow the first concept. $\text{Na}_2\text{Ca}_2\text{Nb}_4\text{O}_{13}$ (NCNO) was the material of choice, which could be produced as microdimensional sheets with high aspect ratios. Similar to the LNO-CCO system, the NCNO was not thermodynamically stable besides CCO at high sintering temperature, which resulted in Nb-doped CCO and the formation of the perovskite $\text{Ca}(\text{Nb},\text{Co})\text{O}_3$. As expected, the electrical conductivity was reduced with increasing amounts of NCNO, but the SEEBECK coefficient was enhanced, resulting in an improved power factor for the samples with 1, 5 and 10 wt% NCNO. The thermal conductivity was lower for the composite systems, wherefore the figure-of-merit could also be increased by about 19% to 0.32 compared to pristine porous CCO.

2.1.2 Anisotropic growth of $\text{La}_2\text{NiO}_{4+\delta}$: Influential pre-treatment in molten-flux synthesis

Richard Hinterding, Zhijun Zhao, Chao Zhang and Armin Feldhoff

Journal of Crystal Growth, 523 **2019**, 125135

DOI: 10.1016/j.crysgro.2019.06.021



Anisotropic growth of $\text{La}_2\text{NiO}_{4+\delta}$: Influential pre-treatment in molten-flux synthesis



Richard Hinterding^{a,*}, Zhijun Zhao^a, Chao Zhang^b, Armin Feldhoff^{a,*}

^a Institute of Physical Chemistry and Electrochemistry, Leibniz University Hannover, Callinstrasse 3A, D-30167 Hannover, Germany

^b Institute for Mineralogy, Leibniz University Hannover, Callinstrasse 3, D-30167 Hannover, Germany

ARTICLE INFO

Communicated by R.S. Feigelson

Keywords:

- A1. Crystal morphology
- A2. Molten-flux
- A2. Solid-state synthesis
- A2. Sol-gel synthesis
- B1. La_2NiO_4
- B2. Mixed ionic-electronic conductor

ABSTRACT

Molten-flux synthesis was applied to the mixed ionic-electronic conducting oxide $\text{La}_2\text{NiO}_{4+\delta}$. Melt of NaOH was used to dissolve precursors, which were either coarse mixtures of the oxides La_2O_3 and NiO from a classical solid-state route or ultrafine mixtures of La_2CO_5 and NiO from a sol-gel process. To estimate optimum synthesis temperature for the sol-gel process, reaction sequence was monitored by in-situ X-ray diffraction. The molten-flux synthesis in ambient air was conducted at 400 °C for up to 14 h with variation of additional water content and the precursor stoichiometry. Purity and composition of products were investigated by ex-situ X-ray diffraction and wavelength dispersive X-ray spectroscopy. A maximum length of plate-like crystals of ca. 30 μm in the *a*, *b*-plane was observed at a thickness of ca. 2 μm in the *c*-axis (i.e. aspect ratio of 15). By varying several parameters of the molten-flux synthesis, both size and aspect ratio of $\text{La}_2\text{NiO}_{4+\delta}$ plate-like crystals could be varied over a wide range.

1. Introduction

Owing to their excellent dielectric properties, unique conductivities for electrons and ions as well as the long-term stability against CO_2 , $\text{La}_2\text{NiO}_{4+\delta}$ -based Ruddlesden-Popper (RP) phases have stimulated many researchers' interest over the last few decades. The properties result in potential applications as microelectronics and mixed ionic-electronic conductors (MIECs) in capacitors [1], gas sensors [2,3], catalytic reactors [4–6], solid oxide fuel cells (SOFCs) [7,8], solid oxide electrolyzer cells (SOECs) [9], and oxygen-transporting membranes (OTMs) [10–12]. Studies have found that $\text{La}_2\text{NiO}_{4+\delta}$ -related single crystals show greater colossal permittivity in the gigahertz range and better ionic transportation comparing to their polycrystals with arbitrary grain orientations [13–16]. The crystal structure of $\text{La}_2\text{NiO}_{4+\delta}$ is responsible for the aforementioned properties, although the physical mechanism behind the colossal permittivity in other materials is still generally controversial [17,18]. The structure of lanthanum nickelate $\text{La}_2\text{NiO}_{4+\delta}$, similar to the tetragonal K_2NiF_4 structure, is composed of LaO rock-salt layers and LaNiO_3 perovskite layers alternating along its crystallographic *c*-axis, while the interstitial oxygen species locate in rock-salt layers [19–21]. Depending on the oxygen excess δ , $\text{La}_2\text{NiO}_{4+\delta}$ adopts versatile orthorhombic and tetragonal phases at room temperature [19,22]. In stoichiometric La_2NiO_4 (i.e. $\delta = 0$), the NiO_6 octahedra are tilted to relieve structural stress caused by the interlayer

lattice mismatch [19,20]. In some La-site doped $\text{La}_2\text{NiO}_{4+\delta}$, e.g. $\text{La}_{1.8}\text{Ca}_{0.2}\text{NiO}_{4+\delta}$, the distortion of NiO_6 octahedra and LaO_9 dodecahedra is observed and supposed to be contributed to the colossal permittivity in the high frequency range [18]. In hyper-stoichiometric $\text{La}_2\text{NiO}_{4+\delta}$, the stress can also be accommodated by the interstitial oxygen in the rock-salt layers [23,24]. Theoretical simulations and experimental investigations on single crystals and thin films have shown that the oxygen transport is highly anisotropic and predominated by the interstitial oxygen [15,25–28]. Through accommodating interstitial oxygen, its structure is maintained at an average tetragonal symmetry $I4/mmm$ (conventional setting) or $F4/mmm$ [19,20]. The latter space group, thanks to its enlarged unit cell ($a\sqrt{2} \times a\sqrt{2} \times c$), is used for easier comparison of lattice parameters between orthorhombic and tetragonal structures [20].

From the aspect of applications, single crystals are favored due to their superb properties and they can be synthesized by a floating-zone method or by a skull-melting method [15,19,29,30]. Unfortunately, these single crystal syntheses have the disadvantage of high production costs, especially for large crystals [31]. An alternative way is preparing grain-oriented polycrystals. Recently, *c*-axis and *a*-axis orientated thin films with thicknesses up to 450 nm have been grown via chemical vapor deposition or pulsed laser deposition [26,32–35]. The orientated thin films provide deep insights into the oxygen surface exchange and diffusion kinetics, however, a structural reorientation from *c*-axis to *a*-

* Corresponding authors.

E-mail addresses: richard.hinterding@pci.uni-hannover.de (R. Hinterding), armin.feldhoff@pci.uni-hannover.de (A. Feldhoff).

<https://doi.org/10.1016/j.jcrysgro.2019.06.021>

Received 20 February 2019; Received in revised form 17 May 2019; Accepted 17 June 2019

Available online 24 June 2019

0022-0248/ © 2019 Elsevier B.V. All rights reserved.

axis was found for films thicker than 550 nm [35].

Another solution is synthesizing anisotropic particles, which can then be facily assembled to grain-oriented polycrystals via tape casting [36]. Comparing to the classic solid-state synthesis, reactions taking place in liquid phase usually create products with controllable morphology and specific texture when the products have highly anisotropic crystal lattices [37,38]. In a reverse micro-emulsion system, nanostructured $\text{La}_2\text{NiO}_{4+\delta}$ with adjusted sizes and different shapes have been created by varying the ratio of surfactant to water and have shown different oxygen transport properties regarding the terminated surfaces [39]. To obtain products in the range of micrometers and maintain their anisotropic morphology, the molten-flux synthesis (MFS) using salts or hydroxides can be applied [38,40]. Many complex oxides with various morphologies, including superconducting oxides such as La_2CuO_4 and $\text{EuBa}_2\text{Cu}_3\text{O}_{7-x}$ have been prepared via MFS, which however, rarely has been applied to $\text{La}_2\text{NiO}_{4+\delta}$ until now and is a promising route for gaining plate-like crystals with tunable sizes and aspect ratios [40–42].

Among the various fluxes, hydroxide melts are widely used to dissolve reactants owing to their adjustable solubility of metal oxides and relatively low melting temperatures, which can be as low as 170 °C for the NaOH-KOH eutectic mixture [40–43]. Similar to the auto-dissociation of water, there is also an auto-dissociation of molten hydroxides that can be described by the oxo-acidity established by Lux and Flood (Eq. 1) [44,45]. The dissociation constant K_d , just like the equilibrium constant of water K_w , depends on the type of hydroxides and the temperature. Analogous to the pH value, the acidity of molten hydroxides is depicted by the pH_2O value (see Eq. 2), which affects the solubility of metal oxides in hydroxides. At the beginning of a synthesis, reactants are dissolved in the wet (acidic) melt. As the synthesis proceeds, the content of water in the melt decreases, shifting the dissociation equilibrium to the product side and producing the target product.



$$\text{pH}_2\text{O} = -\log[\text{H}_2\text{O}] \quad (2)$$

In this work, $\text{La}_2\text{NiO}_{4+\delta}$ plate-like crystals with different sizes and aspect ratios were prepared in molten NaOH by using either oxide mixtures (La_2O_3 and NiO) or the nanocrystalline intermediates (La_2CO_5 and NiO) as reactants. Information concerning purity, structure, morphology, and chemical compositions was obtained by X-ray diffraction (XRD), (scanning) transmission electron microscopy ((S)TEM), scanning electron microscopy (SEM), and electron-probe micro-analysis (EPMA). The formation mechanism of plate-like morphologies formed in molten NaOH was discussed.

2. Experimental section

Fig. 1 shows the experimental procedures to synthesize $\text{La}_2\text{NiO}_{4+\delta}$ products. The precursors were prepared via two alternative ways, i.e. a solid-state route (SSR) and a sol-gel process (SGP).

2.1. Preparation of precursors

The precursors for SSR-based MFS were prepared by using La_2O_3 powder (99.99%) and NiO nanopowder (99.8%) purchased from Sigma-Aldrich without further purification. To prepare the oxide mixtures, La_2O_3 and NiO in specific stoichiometry were mixed and ground in an agate mortar at 25 °C for 15 min.

The precursors for SGP-based MFS were prepared by utilizing ethylene-diamine-tetraacetic-acid (EDTA, Alfa Aesar, 99.4%) and citric acid (Alfa Aesar, 99.5%) as organic ligands [46]. $\text{La}(\text{NO}_3)_3 \cdot 6 \text{H}_2\text{O}$ (Fluka, 99%) and $\text{Ni}(\text{NO}_3)_2 \cdot 6 \text{H}_2\text{O}$ (Sigma-Aldrich, 98.5%) in specific stoichiometry were dissolved in distilled water, followed by adding EDTA and citric acid under stirring. After introducing $\text{NH}_3 \cdot \text{H}_2\text{O}$ buffer,

the mixture turned into a blue sol. The pH value of the sol was maintained by the buffer during the heating process at 150 °C. At least 3 h later, a blue gel was obtained and transferred into a heating mantle for further heat treatment at around 300 °C. The amorphous powder was then ground and calcined at 500 °C for 2 h with a heating rate of 2 °C min^{-1} . Afterwards, the intermediate mixture was ground and ready for MFS.

2.2. Molten-flux synthesis

A typical procedure of the MFS started from adding 100 μL distilled water to 1.16 g NaOH pellets followed by oxide mixtures (from SSR) or intermediates (from SGP), resulting in the weight ratio of 1: 11.6: 1.16 in an alumina-crucible. The crucible was then transferred into a muffle furnace and heated at 400 °C with a heating rate of 10 °C min^{-1} for 8 h. After cooling to room temperature, distilled water was added into the crucible, followed by two times of filtration to remove NaOH and impurities. Subsequently, the product was washed with acetone and dried at 80 °C.

2.3. Characterization

The crystal structure and phase purity of products were examined by XRD (Bruker AXS GmbH, Bruker D8 Advance) and field-emission TEM (JEOL JEM-2100F-UHR). STEM and high-resolution TEM (HRTEM) were operated at 200 kV. For the ex-situ XRD measurements, Cu $K\alpha$ radiation was excited at 30 kV and 40 mA and data were collected in a step-scan mode between 10° and 50° (2θ) with a step size of 0.01° and 0.6 s per step without sample rotation. In-situ XRD measurements were made on the same diffractometer equipped with a high-temperature oven chamber (Anton-Paar) in the temperature range of 30–1000 °C in an air flow of 100 mL min^{-1} using Cu $K\alpha$ radiation excited at 40 kV and 40 mA. Temperatures were programmed step-wise with a delay time of 30 min before each measurement, which was set in the step-scan mode in the range of 10° and 50° (2θ) with a step size of 0.02° and 0.5 s per step. For TEM investigations, the powder was pressed under a force of 20 kN and then fixed with epoxy resin between two slices of silicon wafers, followed by several polishing processes and final Ar-ion thinning until the sample was electron transparent. The RPs mentioned in this work are $\text{La}_2\text{NiO}_{4+\delta}$ (PDF: 01-076-0055, tetragonal, $a = 3.86800 \text{ \AA}$, $c = 12.67900 \text{ \AA}$), $\text{La}_4\text{Ni}_3\text{O}_{10}$ (PDF: 01-070-5844, orthorhombic, $a = 5.41327 \text{ \AA}$, $b = 5.46233 \text{ \AA}$, $c = 27.96049 \text{ \AA}$), and LaNiO_3 (PDF: 01-070-5757, rhombohedral, $a = 5.45240 \text{ \AA}$, $c = 13.15720 \text{ \AA}$).

The morphology of products was observed by field-emission SEM (JEOL JSM-6700F) at an accelerating voltage of 2 kV. Chemical composition of the oxide mixtures and sol-gel intermediates were investigated by an energy dispersive X-ray spectrometer (EDXS, Oxford Instruments, INCA-300) located on the SEM with an excitation voltage of 15 kV, while the chemical compositions of plate-like crystals were determined by EPMA (CAMECA, SX100) equipped with five automated wavelength-dispersive X-ray spectrometers (WDXS) at 15 kV. Plate-like crystals in form of powder were embedded in epoxy and polished with diamond powder to obtain a flat and clean surface for EPMA. To avoid charging effects on the surface, a thin layer of carbon was coated. Each sampling point with a diameter of ca. 1 μm was on a flat surface of a plate-like crystal. The calibration materials used for EPMA were lanthanum phosphate (for La), jadeite (for Na), and nickel metal (for Ni).

3. Results and discussion

Many of the rare-earth-elements-containing complex oxides are synthesized from their corresponding binary oxides in molten alkali hydroxides [43,47]. The eutectic with the composition of 49 mol% NaOH and 51 mol% KOH is usually chosen owing to its low melting temperature [43]. However, for the metal oxides La_2O_3 and NiO, it has

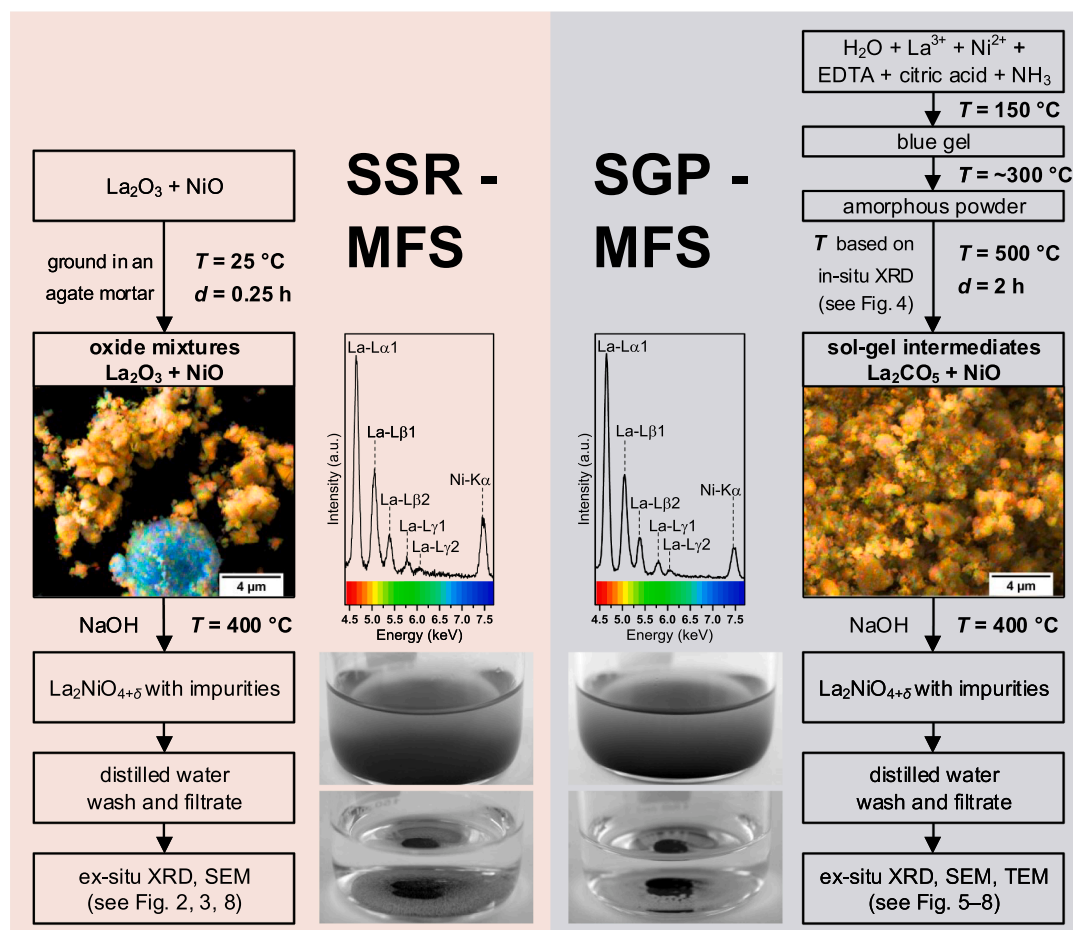


Fig. 1. Flow chart of the molten-flux synthesis (MFS) with precursors from a solid-state route (SSR-MFS) and a sol-gel process (SGP-MFS). The energy-dispersive X-ray spectra (EDXS) together with EDXS-based pseudocolor elemental mapping images show that nickel oxide disperses better in the sol-gel intermediates than in the oxide mixtures. In case of the SSR, an agglomerate of NiO particles with several microns in length is present as seen by the blue area. Integrated energy-pseudocolor range is shown by rainbows below the EDXS. Inserted photographs were shot before (top) and after filtration (bottom). The outer diameter of beakers equals 55 mm. (For interpretation of the references to colour in this figure legend, the reader is referred to the web version of this article.)

been reported that a mixture of La_2NiO_4 and LaNiO_3 (members of the RP phases with $m = 1$ and $m = \infty$ in the general formula $\text{La}_{m+1}\text{Ni}_m\text{O}_{3m+1}$) is produced in the NaOH-KOH eutectic due to the formation of superoxides in presence of KOH [42]. For this reason, only NaOH flux was chosen in this work to dissolve the precursors prepared via either SSR or SGP. Experimental parameters including the stoichiometric ratio of reactants, dwell time, and the water content within the flux during the crystal formation process were varied and optimized.

3.1. Solid-state route based molten-flux synthesis

The XRD patterns in Figs. 2 and 3 indicate that regardless of different synthesis parameters (see Table 1), all samples have the main phase of the body-centered tetragonal $\text{La}_2\text{NiO}_{4+\delta}$ in the $I4/mmm$ space group, which is expected since excess oxygen will be incorporated when prepared in air [19,20,48]. As mentioned in the introduction, the solubility of oxides in molten hydroxides depends highly on the pH_2O value. To demonstrate the influence of the water content, the pH_2O value was varied by alternating the water content in NaOH and by adding a certain amount of water to the NaOH. The SEM micrographs of SSR1 (Fig. 2b) clearly show that most plate-like crystals had lengths of

Table 1
Stoichiometry of precursors and synthesis parameters for SSR-MFS samples.

Sample	La/Ni-ratio	Added water (μL)	Dwell time ^a (h)
SSR1 ^b	2: 1	–	8
SSR2 ^b	2: 1	100	8
SSR3	2: 1	100	8
SSR4	2: 1.1	100	8
SSR5 ^c	2: 1.1	100	8
SSR6 ^c	2: 1	100	8

^a Dwell time: the time period that the oven keeps the reaction temperature at 400 °C.

^b Synthesized using waterless NaOH powder instead of NaOH pellets.

^c Synthesized in a nickel-crucible.

about 1 μm when no water was introduced into the system. Similar plate-like crystals were obtained when the reactant mixture was added after elimination of H_2O in NaOH at 400 °C for 30 min (SSR7, see Fig. S1 in the Supporting Information, SI). As the hydroxide melt became more acidic by adding 100 μL H_2O , larger plate-like crystals with lengths of about 15 μm were found in SSR2. No noticeable difference regarding the size of plate-like crystals was found in SSR3 when the

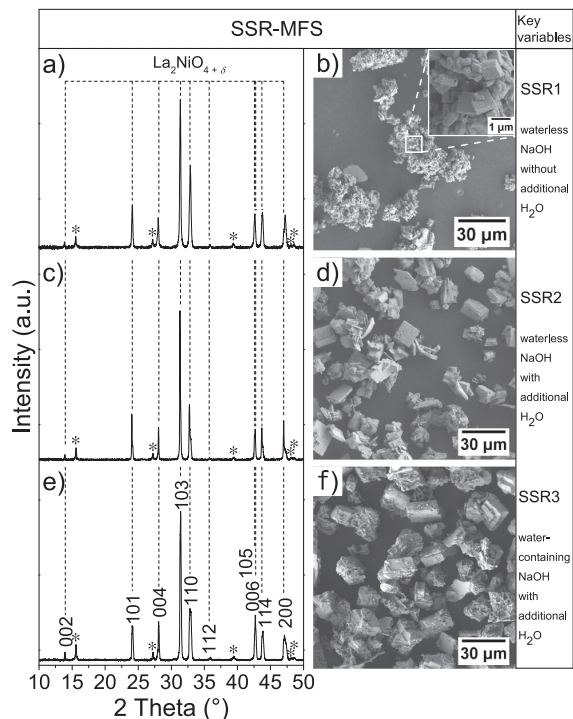
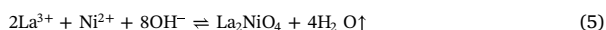


Fig. 2. Powder XRD patterns and SEM micrographs of (a,b) SSR1, (c,d) SSR2, and (e,f) SSR3 powders synthesized via the solid-state route based molten-flux synthesis (SSR-MFS) under different conditions influencing the water content. Asterisks: Bragg positions of $\text{La}(\text{OH})_3$ [PDF: 01-083-2034]. Reflections of the main product $\text{La}_2\text{NiO}_{4+\delta}$ [PDF: 01-076-0055] are indexed. The XRD data are normalized to the same height of the 103 reflection for a clear comparison. The waterless NaOH refers to NaOH powder stored in a refrigerator at -18°C .

pH_2O value was further increased by using water-containing NaOH. It should be mentioned that in order to provide sufficient water and counteract possible water evaporation during heating, more water (100 μL) was added than calculated below.

The water content in the reaction system is estimated as follows. For n mol La_2O_3 and NiO , as used in the SSR-based MFS, a total of $(3n + n) \times 18.00 = 72.00n$ g H_2O is needed (see Eqs. (3) and (4)) to fully dissolve the reactants. Considering the hygroscopic property, NaOH usually contains 1 wt.% H_2O [49]. It is reported, that after exposing to wet air for 8 h, 60% La_2O_3 is hydroxylated to $\text{La}(\text{OH})_3$, which means La_2O_3 contains 9 wt.% H_2O [50]. Since La_2O_3 was kept in a glove box filled with argon, the water content should be far less than 9 wt.%. That means, assuming La_2O_3 contains 9 wt.% H_2O , the flux still needs at least $(72.00n - 40.00 \times 100n \times 0.01 - 325.82 \times n \times 0.09) = 2.68n$ g additional H_2O to dissolve all reactants. The water loss via evaporation during the heating process is omitted in the calculation because this process only took nearly 40 min. Furthermore, water is held tightly by NaOH below 400°C , even under high vacuum [51].



Based on the observations above, a plausible mechanism about the formation of $\text{La}_2\text{NiO}_{4+\delta}$ is suggested as follows. Once the system reaches 323°C , NaOH starts to melt. La_2O_3 and NiO are then dissolved in acidic NaOH-flux (see Eqs. (3) and (4)). As a consequence of the gradual evaporation of water, a specific pH_2O value is reached and the

nucleation of $\text{La}_2\text{NiO}_{4+\delta}$ starts. The product formation is favored by the gradual evaporation of water as the equilibrium reaction shifts to the product side (see Eq. 5). The different size of plate-like crystals between SSR1 and SSR2 is caused by different nucleation sites and nuclei numbers. If the classical crystal growth theory in solution can be applied in molten hydroxides [47,52], the formation of small plate-like crystals in case of SSR1 can be explained by the heteronucleation on undissolved reactant particles owing to the shortage of water when the NaOH melts. The nucleation and crystal growth may be separated to some extent, which is similar to the formation of monodisperse nanocrystals [53]. On the contrary, if sufficient water is present to fully dissolve all reactants when NaOH turns into liquid (in cases of SSR2 and SSR3), homogeneous nucleation takes place at a specific pH_2O , resulting in less nuclei for crystal growth than in the case of the former sample (SSR1), which favors large plate-like crystals with lengths between ca. 10–20 μm .

It is worth noting that minor reflections from $\text{La}(\text{OH})_3$ impurity are found in the XRD patterns of SSR1 to SSR3 (Fig. 2a,c,e). Interestingly, the $\text{La}(\text{OH})_3$ also had a regular morphology. An example is shown in Fig. S3. Most likely, the reason for the $\text{La}(\text{OH})_3$ impurities lies within the solubilities of the reactants and the products in the molten NaOH. The reaction starts with a wet flux of NaOH and solvated metal oxides, and gradual evaporation of water leads to an increased pH_2O value (see Eq. 2), which influences the solubilities. Since La_2O_3 has a lower solubility than NiO in the molten NaOH at a specific pH_2O value, the La^{3+} precipitates alongside the $\text{La}_2\text{NiO}_{4+\delta}$, resulting in $\text{La}(\text{OH})_3$ with layered hexagonal morphology as shown in Fig. S3. Unreacted Ni^{2+} may precipitate as NiO , which could be removed from the product by washing and filtration steps as proven by the SEM micrographs and XRD patterns in Figs. 2, 3, 5. The non-stoichiometry caused by different solubilities is also reported in the synthesis of $\text{Ba}_6\text{Ti}_{17}\text{O}_{40}$ and KNbO_3 in molten alkali metal chlorides [54,55]. Apart from the solubility difference between La_2O_3 and NiO , the inhomogeneously mixed reactant mixture and the partial substitution of La by Na (see Section 3.3) are additional reasons for the presence of $\text{La}(\text{OH})_3$. The influence of the homogeneity of mixture on SSR-based MFS will be compared with SGP-based MFS and discussed later.

The formation of $\text{La}(\text{OH})_3$ was avoided by diminishing the stoichiometric ratio of La/Ni in the reactant mixture from 2: 1 to 2: 1.1 and utilizing a nickel-crucible as seen in Fig. 3c. In this way, the equilibrium in Eq. (5) shifts to the product side and there are less La^{3+} ions in the NaOH flux leading to $\text{La}(\text{OH})_3$. Interestingly, this impurity could be barely prevented neither by solely diminishing the La/Ni-ratio to 2: 1.1 (SSR4) nor by using a nickel-crucible (SSR6). Further raising the Ni-portion to a ratio of La/Ni = 2: 1.2 in an alumina-crucible (SSR9, see SI) built not only the hydroxide $\text{La}(\text{OH})_3$, but also the Ni-rich phase LaNiO_3 evidenced by its weak reflections in Fig. S2. Therefore, the bottom and wall of the nickel-crucible may also take part in the reaction, but the overall reaction rate is slow due to the relatively low temperature of 400°C [51,56]. The La/Ni ratio for getting pure $\text{La}_2\text{NiO}_{4+\delta}$ is therefore between 2: 1.1 and 2: 1.2. No changes regarding the morphology were found when the La/Ni-ratios were varied. The over-stoichiometric Ni element may form the NiO nanoparticles during the cooling process after the reaction and penetrate through filter papers during filtration.

3.2. Sol-gel process based molten-flux synthesis

After the heat treatment of the gel at around 300°C , the powder contained carbon-based compounds because of incomplete decomposition or residuals of EDTA and citric acid. To minimize their influence on the molten-flux synthesis, a calcination step was added and resulted in a mass loss up to 70%.

In-situ XRD measurements were performed on uncalcined sol-gel amorphous powder under an air flow from room temperature to 1000°C to estimate the optimum calcination temperature for getting sol-gel intermediates used in SGP-based MFS. As shown in Fig. 4, the

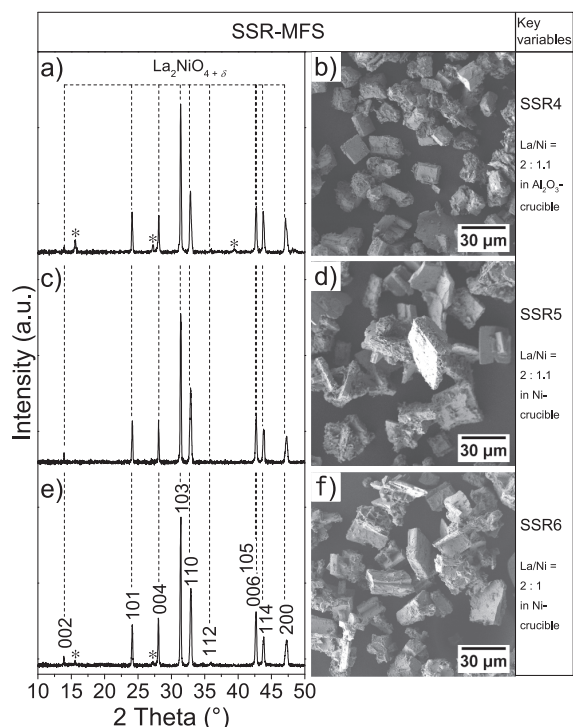


Fig. 3. Powder XRD patterns and SEM micrographs of (a,b) SSR4, (c,d) SSR5, and (e,f) SSR6 powders synthesized in alumina and nickel crucibles via the solid-state route based molten-flux synthesis (SSR-MFS). The stoichiometric ratios of La/Ni in reactants were 2: 1.1 for SSR4-5 and 2: 1 for SSR6. Asterisks: Bragg positions of $\text{La}(\text{OH})_3$ [PDF: 01-083-2034]. Reflections of the main product $\text{La}_2\text{NiO}_{4+\delta}$ [PDF: 01-076-0055] are indexed. The XRD data are normalized to the same height of the 103 reflection for a clear comparison.

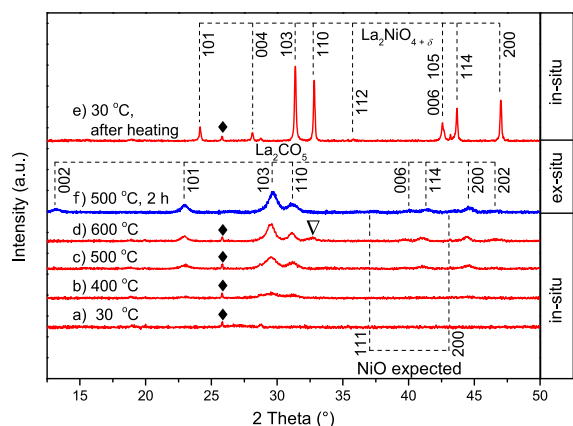


Fig. 4. In-situ (a–e) and ex-situ (f) powder XRD patterns of sol-gel intermediates. Diamond symbols: Bragg positions of Al_2O_3 from the in-situ XRD sample holder. Dotted vertical lines: Bragg positions of $\text{La}_2\text{NiO}_{4+\delta}$ [PDF: 01-076-0055], La_2CO_5 [PDF: 00-023-0320], and NiO [PDF: 01-071-4750]. The triangle indicates the broad reflection that covers the Bragg position of the 110 reflection from $\text{La}_2\text{NiO}_{4+\delta}$.

first crystalline intermediates were formed between 400 °C and 500 °C. These intermediates could be identified as lanthanum oxycarbonate La_2CO_5 and nickel oxide NiO , although the NiO reflections were not observed. The EDXS and the EDXS-based pseudocolor elemental

Table 2
Stoichiometry of precursors and synthesis parameters for SGP-MFS samples.

Sample	La/Ni-ratio	Added water (μL)	Dwell time ^a (h)
SGP1-MFS	2: 1	–	6
SGP2-MFS	2: 1	100	6
SGP3-MFS	2: 1	100	8
SGP4-MFS	2: 1	100	14

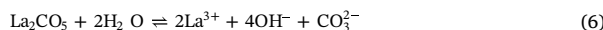
^a Dwell time: the time period that the oven keeps the reaction temperature at 400 °C.

mapping image in Fig. 1 confirm the presence of the Ni element. Since possible NiCO_3 already decomposes to NiO before the calcination process [57], NiO should be present in sol-gel intermediates. The NiO reflections are probably dispersed into the background for the reason that NiO particles are too small or still amorphous. A new broad reflection, marked by a triangle in Fig. 4d, appears at 600 °C. The broad reflection covers the Bragg position of the 110 reflection from $\text{La}_2\text{NiO}_{4+\delta}$ as illustrated by the XRD pattern measured at 30 °C after the sample was heated to 1000 °C (see Fig. 4e). As the temperature rises, this reflection becomes more intensive along with weakening of the intermediates reflections (not presented here).

Based on the in-situ XRD investigation, calcination of sol-gel amorphous powder was limited to 500 °C to obtain finely intermixed La_2CO_5 and NiO intermediates instead of $\text{La}_2\text{NiO}_{4+\delta}$. These SGP-derived intermediates were adopted as precursors for the SGP-based MFS, which was conducted at 400 °C in molten NaOH (see Fig. 1). The synthesis parameters are listed in Table 2.

Fig. 5 presents the XRD patterns and SEM micrographs of SGP1 to SGP4 synthesized by heating precursors (La/Ni-ratio of 2: 1) in molten NaOH with varied water content and dwell time. Similar to the SSR-based MFS, the SGP-based MFS also brought powder with the main phase of the body-centered tetragonal $\text{La}_2\text{NiO}_{4+\delta}$, accompanied by a minor phase of $\text{La}(\text{OH})_3$ as shown by the XRD patterns. One very weak reflection, possibly from the higher RP-phase LaNiO_3 , was detected around 23° in all four XRD patterns. This reflection could not be diminished by reducing the Ni-portion in precursors (La/Ni-ratio of 2: 0.95), whereas the reflections of $\text{La}(\text{OH})_3$, similar to the SSR-based MFS, were successfully avoided by using precursors with the La/Ni-ratio of 2: 1.1 in a nickel-crucible (SGP8) as presented by Fig. S5 in the SI. The formation of the trace amount of LaNiO_3 in SGP1 to SGP4 may be caused by few amorphous higher RP-phases ($n > 1$) in intermediates calcined at 500 °C.

The influence of water in molten-flux synthesis was verified in the SGP-based MFS. Fig. 5b,d depicts the SEM micrographs of SGP1 and SGP2, which were synthesized without and with additional water, respectively. Comparing SGP1 and SGP2 with SSR1 and SSR2, a similar effect of the water content was found for the SGP-based MFS: when no additional water was introduced, the resulting plate-like crystals (SGP1) had lengths of about 2 μm , whereas larger plate-like crystals with lengths of about 10 μm (SGP2) were formed by adding 100 μL water. The water content in the reaction system is estimated as follows. To fully dissolve n mol La_2CO_5 and NiO , as used in the SGP-based MFS, a total of $(n + 2n) \times 18.00 = 54.00n$ g H_2O (see Eqs. (4) and (6)) is needed. Considering the 1 wt.% H_2O in NaOH , at least $(54.00n - 40.00 \times 100n \times 0.01) = 14.00n$ g additional H_2O should be introduced.



Unlike the neglectable influence of the dwell time on the products synthesized via SSR-based MFS (see Fig. S4), distinct differences between SGP2 (dwell time 6 h) and SGP3-4 (dwell time 8 h and 14 h) were observed from the XRD patterns and SEM micrographs in Fig. 5 and from the statistical analysis of crystals' dimensions in Fig. S6. Along with extended dwell times, the XRD patterns of SGP3 and SGP4 present strong preferential orientation evidenced by the intensive 001

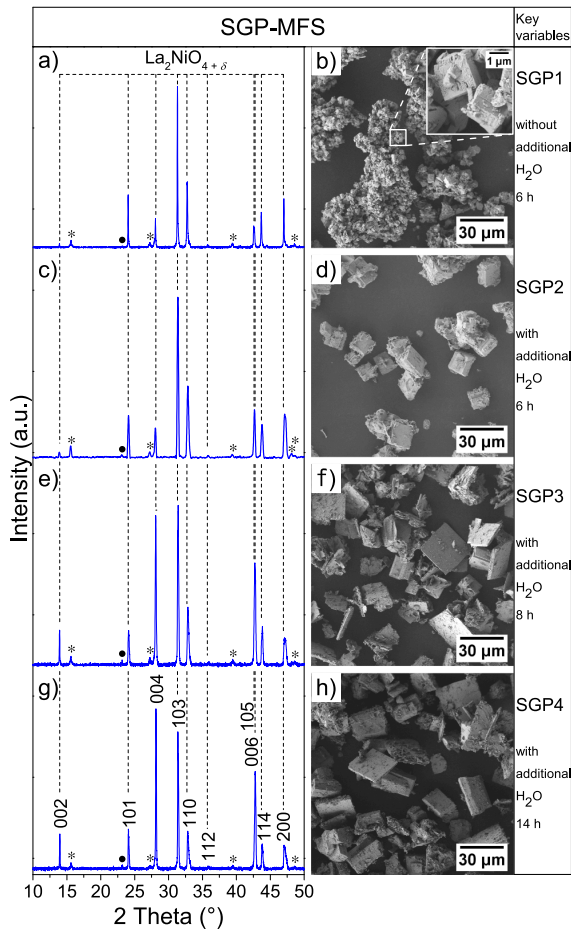


Fig. 5. Powder XRD patterns and SEM micrographs of (a,b) SGP1, (c,d) SGP2, (e,f) SGP3, and (g,h) SGP4 powders synthesized via the sol-gel process based molten-flux synthesis (SGP-MFS). SGP1 to SGP4 were synthesized in alumina-crucibles with the stoichiometric ratio of La/Ni 2: 1. Asterisks: Bragg positions of La(OH)₃ [PDF: 01-083-2034]. Solid points: the Bragg position 101 of LaNiO₃ [PDF: 01-070-5757]. Reflections of the main product La₂NiO_{4+δ} [PDF: 01-076-0055] are indexed. The XRD data are normalized to the same height of the 103 reflection.

reflections and the weak $hk0$ reflections in Fig. 5e,g, implying that the growth of plate-like crystals mainly occurs perpendicular to the c -axis. For SGP4, the intensity of the 004 reflection even exceeds the ones of the 103 reflection, which is the most intense reflection in the standard XRD pattern (PDF: 01-076-0055). The preferential orientation on the XRD sample holder can be attributed to the relatively large aspect ratios of plate-like crystals in SGP3 and SGP4. As shown in Fig. 5f,h, the thicknesses of SGP2 to SGP4 were all around 2 μm , whereas the lengths of SGP3 and SGP4 were greater than SGP2 (ca. 10 μm). The statistical analysis of crystals' dimensions shown in Fig. S6 indicates an elongation of length and a slight thinning of thickness for dwell times longer than 6 h, resulting in large aspect ratios correspondingly. The mechanism for the formation of large aspect ratios after long dwell time is not clear, perhaps the CO₃²⁻ ions produced by dissolution of La₂CO₃ in NaOH flux (see Eq. 6) have stronger ability to hinder the crystal growth along the c -axis than the OH⁻ ions because of the Coulomb interaction with the (LaO)⁺ layers at the surface of La₂NiO_{4+δ} particles. Meanwhile, the Ostwald ripening likely participated in the crystal growth process.

Fig. 6 demonstrates the information gained from TEM analysis

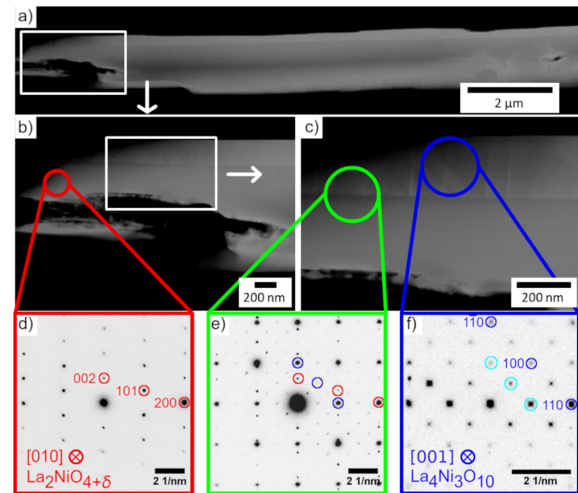


Fig. 6. Cross-sectional transmission electron microscopy characterization of a plate-like crystal from the SGP3-MFS batch. (a–c) STEM annular dark-field micrographs. (d) SAED pattern of main phase La₂NiO_{4+δ} along [010]_{m=1} zone axis. (e) SAED pattern at the interface of La₂NiO_{4+δ} and La₄Ni₃O₁₀ with corresponding Laue indices shown in (d) and (f). (f) SAED pattern of higher RP-phase La₄Ni₃O₁₀ along [001]_{m=3} zone axis with extra reflections colored in cyan. Note the enlarged scale bar in (f). (For interpretation of the references to colour in this figure legend, the reader is referred to the web version of this article.)

about the cross-section of La₂NiO_{4+δ} ($m = 1$) plate-like crystals from the SGP3-MFS batch. While most of the crystals consisted of pure La₂NiO_{4+δ} with no obvious irregularities as shown in Fig. S7, few of them featured a second phase at the surface as can be seen in Fig. 6a–c for a well crystallized plate-like crystal with the length of 12 μm and the height of 2 μm . This phase could be identified as the higher RP-phase La₄Ni₃O₁₀ ($m = 3$), which grew upon the (001)_{m=1} surface of the La₂NiO_{4+δ}. Identification was realized by selected-area electron diffraction (SAED) patterns of the La₂NiO_{4+δ}, the La₄Ni₃O₁₀ and the interface of both phases in Fig. 6d–f. In accordance with the observations of Gauquelin et al. [7], only the La₄Ni₃O₁₀ and no La₃Ni₂O₇ ($m = 2$) was found upon the (001)_{m=1} surface of the La₂NiO_{4+δ}. The SAED pattern of the La₄Ni₃O₁₀ shows additional spots colored in cyan, which cannot be indexed and are likely attributed to ordered oxygen interstitials or a displacement of the oxygen atom positions [7]. Varying intensity of the reflections between the pure phases and the interface is attributed to the thickness of the examined areas.

The SAED pattern in Fig. 6e at the interface of both phases allows the determination of the orientation relationship of the La₄Ni₃O₁₀ on the surface of the La₂NiO_{4+δ} plate-like crystal: $(002)_{m=1} \parallel (1\bar{1}0)_{m=3} \wedge [010]_{m=1} \parallel [001]_{m=3}$. A visualization of the orientation relationship with the relevant crystal structures is given in Fig. 7. The relationship shows a stacking of the two phases along the c -axis of the main phase La₂NiO_{4+δ} ($m = 1$), with $b_{m=1}$ and $c_{m=3}$ axes being parallel. Additionally, a rotation of 45° around the c -axis of La₄Ni₃O₁₀ results from the SAED patterns as can be seen in Fig. 7b. The concluding plan view in Fig. 7c shows the stacking of both phases upon each other, where the general structure of La₂NiO_{4+δ} can be recognized within the La₄Ni₃O₁₀ structure. However, displacements of atomic columns along the c -axis of La₄Ni₃O₁₀ may complicate the growth upon the La₂NiO_{4+δ}, which could be a reason for its unsteady appearance. The presence of the higher RP-phases may be attributed to small amounts of superoxides within the molten-flux, as it happens with KOH. Based on the low reaction temperature of 400 °C, evaporation of volatile lanthanum species can be excluded, but a segregation of nickel and lanthanum with ongoing nucleation could also be relevant. Since both La₄Ni₃O₁₀ and LaNiO₃ were identified besides the main product, the

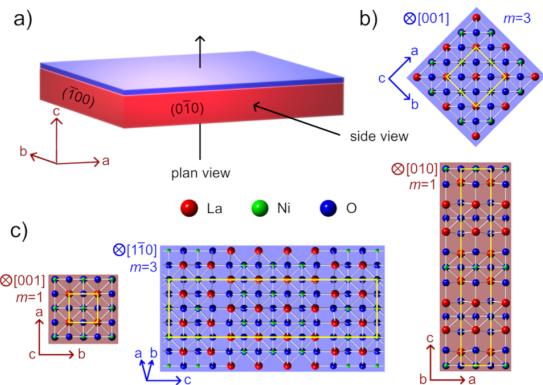


Fig. 7. Crystallographic information of the plate-like crystals based on TEM investigations in Fig. 6. (a) Scheme of a plate-like crystal with selected surfaces and coordinate system. (b) Side view of $\text{La}_2\text{NiO}_{4+\delta}$ [ICSD: 33536, $m = 1$] and $\text{La}_4\text{Ni}_3\text{O}_{10}$ [ICSD: 80279, $m = 3$] along $[010]_{m=1}$ and $[001]_{m=3}$ zone axes. (c) Plan view of $\text{La}_2\text{NiO}_{4+\delta}$ and $\text{La}_4\text{Ni}_3\text{O}_{10}$ along $[001]_{m=1}$ and $[110]_{m=3}$ zone axes. Note that unit cells of each compound are highlighted in yellow. (For interpretation of the references to colour in this figure legend, the reader is referred to the web version of this article.)

presence of other RP-phases such as $\text{La}_3\text{Ni}_2\text{O}_7$ can be assumed as well. Nevertheless, the amount of higher RP-phases within the batch was too small to investigate comprehensively, which means a rather pure $\text{La}_2\text{NiO}_{4+\delta}$.

Regarding the plate-like morphology of the $\text{La}_2\text{NiO}_{4+\delta}$, the SAED patterns verify the $\{001\}$ facets as dominating in comparison to the $\{100\}$ and $\{010\}$ facets, which can be explained by crystal growth mechanics. When the thermodynamic equilibrium during crystal growth is reached due to the rapid kinetic processes, the exposed crystal facets lead to a minimum overall surface energy, resulting in the Wulff-Curie shape [58,59]. However, according to the Wulff-Chernov theorem, the habitus of large crystals is usually determined by the facets with low growth velocities since the rate of equilibration is hindered by the small surface-to-volume ratio of large crystals [60,61]. As calculated by Read et al. [62], the surface energy of $\{001\}$ facets is 1.55 Jm^{-2} , which is greater than those of $\{100\}$ and $\{111\}$ facets (0.98 and 1.08 Jm^{-2}). Hence, the habitus of $\text{La}_2\text{NiO}_{4+\delta}$ plate-like crystals is governed by the growth velocities of facets instead of the surface energies.

Actually, $\text{La}_2\text{NiO}_{4+\delta}$ is composed of positively charged $(\text{LaO})^+$ layers and negatively charged $(\text{LaNiO}_3)^-$ layers alternating along its crystallographic c -axis. In molten NaOH , the $(\text{LaO})^+$ layers at the surface of $\text{La}_2\text{NiO}_{4+\delta}$ particles should be surrounded by plenty of OH^- . That means, greater energy must be applied for crystal growth along the c -axis than in the (a, b) -plane, since once the crystal is terminated with $(\text{LaO})^+$ layers, $(\text{LaNiO}_3)^-$ layers are hindered by the surrounding OH^- ions to some extent. In case of SGP-based MFS, another type of anion (i.e. CO_3^{2-}) is present in molten NaOH . The thermochemical radius of CO_3^{2-} equals 178 pm , which is larger than the one of OH^- (133 pm) [63]. Regarding the greater steric hindrance and stronger Coulomb interaction comparing to OH^- , the crystal growth along the c -axis becomes more difficult in the presence of CO_3^{2-} . As a result, the plate-like crystals synthesized by SGP-based MFS are thinner than the plate-like crystals via SSR-based MFS, and thus have larger aspect ratios as shown in Fig. 8.

3.3. Comparison of the products synthesized via the solid-state route and the sol-gel process

In all SGP-MFS samples, except the La-rich samples SGP5 and SGP6 (see SI), the $\text{La}(\text{OH})_3$ phase was only recognized in XRD patterns, but

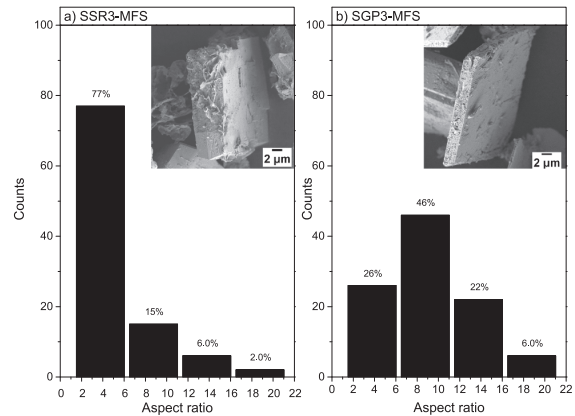


Fig. 8. Aspect ratio histograms of plate-like crystals synthesized via molten-flux synthesis based on (a) solid-state route and (b) sol-gel process. The insets present corresponding SEM micrographs of typical plate-like crystals. For each sample, 100 crystals from SEM micrographs were evaluated using the software ImageJ.

not in SEM micrographs. As a comparison, large hexagonal $\text{La}(\text{OH})_3$ particles with the length of tens of microns were observed in the SEM micrographs of all SSR-MFS samples except the Ni-rich samples SSR5 and SSR9. Examples of SEM micrographs containing large $\text{La}(\text{OH})_3$ are given in Fig. S3. This remarkable difference reveals one advantage of SGP-based MFS, namely less $\text{La}(\text{OH})_3$ impurity owing to the high homogeneity of precursors from the SGP. As shown in Fig. 1, NiO disperses well in sol-gel intermediates prepared via the SGP. In contrast to this, the oxide mixtures obtained via the SSR show an agglomerate of NiO with the length of $6 \mu\text{m}$. The diffusion path for the product formation via the SSR-based MFS is thus longer than the path via the SGP-based MFS. In addition, even at the temperature of 400°C , the dynamic viscosity of molten NaOH equals $3.3 \text{ mPa}\cdot\text{s}$, which is three times greater than that of H_2O at 20°C [64]. Hence, the combination rate of La^{3+} and Ni^{2+} through diffusion in some area may be slower than the rate of losing water in the SSR-based MFS. $\text{La}(\text{OH})_3$ is consequently nucleated and grows to large particles. The relatively slow combination rate caused by the inhomogeneity of the oxide mixtures is also the reason that both $\text{La}(\text{OH})_3$ and LaNiO_3 were found in SSR9, whose La/Ni-ratio of reactants equaled 1: 1.2.

In addition to the difference in the $\text{La}(\text{OH})_3$ impurity, the SGP-based MFS also produced $\text{La}_2\text{NiO}_{4+\delta}$ plate-like crystals with larger aspect ratios than the crystals synthesized by SSR-based MFS. The statistical analysis of products from the two methods under the same synthesis parameters is presented in Fig. 8. While 77% plate-like crystals from SSR-based MFS had aspect ratios in the range of 1–6, half of the crystals from the SGP-based MFS showed aspect ratios in the range of 6–11, and larger aspect ratios in the range of 16–21 were also present. The SEM micrographs in Fig. 8 illustrate typical plate-like crystals with the aspect ratio of 5 for SSR3-MFS and 9 for SGP3-MFS. As a result of large aspect ratio, the preferential orientation of plate-like crystals on a sample holder can be easily reached, which is proved by the $00l$ reflections (i.e. 002, 004, and 006) of the XRD pattern in Fig. 5e. Compared to the XRD pattern in Fig. 5e, the XRD pattern of SSR3 in Fig. 2 shows no deviation from the standard XRD pattern (PDF: 01-076-0055) regarding the intensity.

The chemical compositions of the two samples synthesized via SSR-based MFS and SGP-based MFS are listed in Table 3. Despite the plate-like crystals being formed via different precursors, their compositions were almost identical. Both samples had the sodium content of nearly 1.4 at.%, which was randomly placed at the La position due to similar ionic radii of 122 pm (La^{3+}) and 124 pm (Na^+) in contrast to 69 pm of Ni^{2+} [65]. This leads to A-site doped lanthanum nickelate, which is in

Table 3
Electron probe micro-analysis results of plate-like crystals from SSR3-MFS and SGP3-MFS.

Sample ^a	Atomic percent (%)				Stoichiometric ratio ^b			
	La	Na	Ni	O	La	Na	Ni	O
SSR3	28.13± 0.79	1.38± 0.62	13.80± 0.55	56.69± 0.35	2.04± 0.14	0.10± 0.04	1	4.12± 0.20
SGP3	27.94± 0.76	1.40± 0.65	14.02± 0.53	56.64± 0.35	2.00± 0.13	0.10± 0.04	1	4.04± 0.18

^a The samples were both heated to 400 °C with a heating rate of 10 °C min⁻¹ and held for 8 h in alumina-crucibles. Prior to heating, 100 µL H₂O were added.

^b Normalized by the atomic percent of Ni²⁺.

agreement with former observations by Shivakumara et al. [42]. The sum of stoichiometric ratios from metal ions was slightly larger than 3, but was in a reasonable range considering the standard deviation of repeated measurements and the presence of Ni³⁺ ions in La₂NiO_{4+δ} samples. The oxygen hyper-stoichiometry of the both samples reveals that oxygen is incorporated during the synthesis to release the structural stress.

4. Conclusions

Various synthesis parameters were investigated in this paper to prepare La₂NiO_{4+δ} plate-like crystals in molten NaOH based on two different kinds of precursors. As an important parameter, sufficient water content at the beginning of reactions led to larger crystals. An extended reaction time benefited the SGP-based MFS in the formation of large plate-like crystals (up to 30 µm in the *a*, *b*-plane) and textured structure, whereas negligible effects were determined for SSR-based MFS regarding the extended reaction time. Products obtained from the two kinds of precursors showed differences in the aspect ratio of plate-like crystals and in the size of La(OH)₃ impurity. Thanks to the molecular-level mixed precursors, SGP-based MFS produced less and smaller-sized La(OH)₃ impurity than SSR-based MFS when stoichiometric precursors were used. Pure La₂NiO_{4+δ} plate-like crystals were obtained in SSR-based MFS by employing Ni-rich precursors in a nickel-crucible. The work shows that the La₂NiO_{4+δ} plate-like crystals delivered by the molten-flux synthesis have adjustable lengths (1–30 µm) and large aspect ratios (> 10). For the flexibility in control over size and habitus, positive effects are expected for the use of La₂NiO_{4+δ} in potential applications.

Author Contributions

The manuscript was written through contributions of all authors. All authors have given approval to the final version of the manuscript.

Acknowledgments

This work was supported by the Deutsche Forschungsgemeinschaft (DFG, German Research Foundation) – FE 928/15-1. Z. Zhao acknowledges financial support by the Graduate Academy of the Leibniz University Hannover. Authors gratefully appreciate technical assistance by F. Steinbach.

Appendix A. Supplementary material

Supplementary data associated with this article can be found, in the online version, at <https://doi.org/10.1016/j.jcrysgro.2019.06.021>.

References

- [1] M.O. Orlandi, M.A. Ramirez, C.R. Foschini, A.A. Felix, J.A. Varela, Giant dielectric constant materials and their applications, in: M. Aparicio, A. Jitianu, L.C. Klein (Eds.), *Sol-Gel Processing for Conventional and Alternative Energy*, 1st ed., Springer, US, Boston, MA, 2012, pp. 123–146, https://doi.org/10.1007/978-1-4614-1957-0_7.
- [2] X. Hao, C. Ma, X. Yang, T. Liu, B. Wang, F. Liu, X. Liang, C. Yang, H. Zhu, G. Lu,

- YSZ-based mixed potential H₂S sensor using La₂NiO₄ sensing electrode, *Sens. Actu. B* 255 (2018) 3033–3039, <https://doi.org/10.1016/j.snb.2017.09.127>.
- [3] E.S. Raj, K.F.E. Pratt, S.J. Skinner, I.P. Parkin, J.A. Kilner, High conductivity La_{2-x}Sr_xCu_{1-y}(Mg, Al)_yO₄ solid state metal oxide gas sensors with the K₂NiF₄ structure, *Chem. Mater.* 18 (14) (2006) 3351–3355, <https://doi.org/10.1021/cm060520e>.
- [4] H.J.M. Bouwmeester, Dense ceramic membranes for methane conversion, *Catal. Today* 82 (1) (2003) 141–150, [https://doi.org/10.1016/S0920-5861\(03\)00222-0](https://doi.org/10.1016/S0920-5861(03)00222-0).
- [5] V.V. Kharton, A.A. Yaremchenko, E.V. Tsipis, A.A. Valente, M.V. Patrakeev, A.L. Shaula, J.R. Frade, J. Rocha, Characterization of mixed-conducting La₂Ni_{0.9}Co_{0.1}O_{4+δ} membranes for dry methane oxidation, *Appl. Catal., A* 261 (1) (2004) 25–35, <https://doi.org/10.1016/j.apcata.2003.10.028>.
- [6] P. Li, B. Wei, Z. Lü, Y. Wu, Y. Zhang, X. Huang, La_{1.7}Sr_{0.3}Co_{0.5}Ni_{0.5}O_{4+δ} layered perovskite as an efficient bifunctional electrocatalyst for rechargeable zinc-air batteries, *Appl. Surf. Sci.* 464 (2019) 494–501, <https://doi.org/10.1016/j.apsusc.2018.09.113>.
- [7] N. Gauquelin, T.E. Weirich, M. Ceretti, W. Paulus, M. Schroeder, Long-term structural surface modifications of mixed conducting La₂NiO_{4+δ} at high temperatures, *Monatsh. Chem.* 140 (9) (2009) 1095–1102, <https://doi.org/10.1007/s00706-009-0146-2>.
- [8] A.M. Hernández, L. Moggi, A. Caneiro, La₂NiO_{4+δ} as cathode for SOFC: reactivity study with YSZ and CGO electrolytes, *Int. J. Hydrogen Energy* 35 (11) (2010) 6031–6036, <https://doi.org/10.1016/j.ijhydene.2009.12.077>.
- [9] A. Egger, N. Schrödl, C. Gspan, W. Sitte, La₂NiO_{4+δ} as electrode material for solid oxide fuel cells and electrolyzer cells, *Solid State Ion.* 299 (2017) 18–25, <https://doi.org/10.1016/j.ssi.2016.10.002>.
- [10] V. Kharton, F. Marques, A. Atkinson, Transport properties of solid oxide electrolyte ceramics: a brief review, *Solid State Ion.* 174 (1–4) (2004) 135–149, <https://doi.org/10.1016/j.ssi.2004.06.015>.
- [11] A. Shaula, E. Naumovich, A. Viskup, V. Pankov, A. Kovalevsky, V. Kharton, Oxygen transport in La₂NiO_{4+δ}: assessment of surface limitations and multilayer membrane architectures, *Solid State Ion.* 180 (11) (2009) 812–816, <https://doi.org/10.1016/j.ssi.2009.01.005>.
- [12] T. Klande, K. Efimov, S. Cusenza, K.D. Becker, A. Feldhoff, Effect of doping, microstructure, and CO₂ on La₂NiO_{4+δ}-based oxygen-transporting materials, *J. Solid State Chem.* 184 (12) (2011) 3310–3318, <https://doi.org/10.1016/j.jssc.2011.10.019>.
- [13] S. Krohns, P. Lunkenheimer, C. Kant, A.V. Pronin, H.B. Brom, A.A. Nugroho, M. Diantoro, A. Loidl, Colossal dielectric constant up to gigahertz at room temperature, *Appl. Phys. Lett.* 94 (12) (2009), <https://doi.org/10.1063/1.3105993> 122903.
- [14] A. Podpirka, S. Ramanathan, Thin film colossal dielectric constant oxide La_{2-x}Sr_xNiO₄: synthesis, dielectric relaxation measurements, and electrode effects, *J. Appl. Phys.* 109 (1) (2011), <https://doi.org/10.1063/1.3528161> 014106.
- [15] J. Bassat, P. Odier, A. Villesuzanne, C. Marin, M. Pouchard, Anisotropic ionic transport properties in La₂NiO_{4+δ} single crystals, *Solid State Ion.* 167 (3–4) (2004) 341–347, <https://doi.org/10.1016/j.ssi.2003.12.012>.
- [16] M. Burriel, H. Tézlez, R.J. Chater, R. Castaing, P. Veber, M. Zaghioui, T. Ishihara, J.A. Kilner, J.-M. Bassat, Influence of crystal orientation and annealing on the oxygen diffusion and surface exchange of La₂NiO_{4+δ}, *J. Phys. Chem. C* 120 (32) (2016) 17927–17938, <https://doi.org/10.1021/acs.jpcc.6b05666>.
- [17] X.C. Fan, X.M. Chen, X.Q. Liu, Structural dependence of microwave dielectric properties of SrAlO₄ (R = Sm, Nd, La) ceramics: crystal structure refinement and infrared reflectivity study, *Chem. Mater.* 20 (12) (2008) 4092–4098, <https://doi.org/10.1021/cm703273z>.
- [18] C.-Y. Shi, Z.-B. Hu, Y.-M. Hao, Structural magnetic and dielectric properties of La_{2-x}Ca_xNiO_{4+δ} (x = 0, 0.1, 0.2, 0.3), *J. Alloys Compd.* 509 (4) (2011) 1333–1337, <https://doi.org/10.1016/j.jallcom.2010.10.030>.
- [19] W. Paulus, A. Cousson, G. Dhalenne, J. Berthon, A. Revcolevschi, S. Hosoya, W. Treutmann, G. Heger, R. Le Toquin, Neutron diffraction studies of stoichiometric and oxygen intercalated La₂NiO₄ single crystals, *Solid State Sci.* 4 (5) (2002) 565–573, [https://doi.org/10.1016/S1293-2558\(02\)01299-2](https://doi.org/10.1016/S1293-2558(02)01299-2).
- [20] M. Brunelli, M. Coduri, M. Ceretti, W. Paulus, Local apical oxygen disorder in oxygen rich La₂NiO_{4.18}, comparing neutron single crystal and n/X-PDF analysis from powder diffraction data, *J. Phys. D: Appl. Phys.* 48 (50) (2015) 504009, <https://doi.org/10.1088/0022-3727/48/50/504009>.
- [21] Z. Hiroi, T. Obata, M. Takano, Y. Bando, Y. Takeda, O. Yamamoto, Ordering of interstitial oxygen atoms in La₂NiO_{4+δ} observed by transmission electron microscopy, *Phys. Rev. B* 41 (16) (1990) 11665–11668, <https://doi.org/10.1103/PhysRevB.41.11665>.
- [22] S.J. Skinner, Characterisation of La₂NiO_{4+δ} using in-situ high temperature neutron powder diffraction, *Solid State Sci.* 5 (3) (2003) 419–426, <https://doi.org/10.1016/>

- s1293-2558(03)00050-5.
- [23] I.D. Brown, *The Chemical Bond in Inorganic Chemistry: The Bond Valence Model*, first ed., Oxford University Press, 2010 doi:10.1093/acprof:oso/9780199298815.001.0001.
- [24] N. Gauquelin, Impact of the structural anisotropy of $\text{La}_2\text{NiO}_{4+\delta}$ on high temperature surface modifications and diffusion of oxygen, Ph.D. thesis, RWTH Aachen University, 2010.
- [25] L. Minerchini, R.W. Grimes, J.A. Kilner, K.E. Sickafus, Oxygen migration in $\text{La}_2\text{NiO}_{4+\delta}$, *J. Mater. Chem.* 10 (10) (2000) 2349–2354, <https://doi.org/10.1039/b004212i>.
- [26] M. Burriel, G. Garcia, J. Santiso, J.A. Kilner, R.J. Chater, S.J. Skinner, Anisotropic oxygen diffusion properties in epitaxial thin films of $\text{La}_2\text{NiO}_{4+\delta}$, *J. Mater. Chem.* 18 (4) (2008) 416–422, <https://doi.org/10.1039/B711341B>.
- [27] M. Yashima, M. Enoki, T. Wakita, R. Ali, Y. Matsushita, F. Izumi, T. Ishihara, Structural disorder and diffusional pathway of oxide ions in a doped Pr_2NiO_4 -based mixed conductor, *J. Am. Chem. Soc.* 130 (9) (2008) 2762–2763, <https://doi.org/10.1021/ja711478h>.
- [28] Z. Du, Z. Zhang, A. Niemczyk, A. Olszewska, N. Chen, K. Świerczek, H. Zhao, Unveiling the effects of A-site substitutions on the oxygen ion migration in $\text{A}_2\text{NiO}_{4+\delta}$ by first principles calculations, *Phys. Chem. Chem. Phys.* 20 (33) (2018) 21685–21692, <https://doi.org/10.1039/c8cp04392b>.
- [29] W.-J. Jang, K. Imai, M. Hasegawa, H. Takei, Growth and structure of $\text{La}_2\text{NiO}_{4+\delta}$ ($0.19 \geq \delta \geq 0.12$) single crystals, *J. Cryst. Growth* 152 (3) (1995) 158–168, [https://doi.org/10.1016/0022-0248\(94\)01026-9](https://doi.org/10.1016/0022-0248(94)01026-9).
- [30] D.J. Buttrey, H.R. Harrison, J.M. Honig, R.R. Schartman, Crystal growth of Ln_2NiO_4 ($\text{Ln} = \text{La, Pr, Nd}$) by skull melting, *J. Solid State Chem.* 54 (3) (1984) 407–413, [https://doi.org/10.1016/0022-4596\(84\)90172-5](https://doi.org/10.1016/0022-4596(84)90172-5).
- [31] Y. Yan, L. Yang, Y. Zhou, K.-H. Cho, J.S. Heo, S. Priya, Enhanced temperature stability in $< 111 >$ textured tetragonal $\text{Pb}(\text{Mg}_{1/3}\text{Nb}_{2/3})\text{O}_3$ - PbTiO_3 piezoelectric ceramics, *J. Appl. Phys.* 118 (10) (2015), <https://doi.org/10.1063/1.4929958> 104101.
- [32] M. Burriel, J. Santiso, M.D. Rossell, G.V. Tendeloo, A. Figueras, G. Garcia, Enhancing total conductivity of $\text{La}_2\text{NiO}_{4+\delta}$ epitaxial thin films by reducing thickness, *J. Phys. Chem. C* 112 (29) (2008) 10982–10987, <https://doi.org/10.1021/jp7101622>.
- [33] N. Tsvetkov, Q. Lu, Y. Chen, B. Yildiz, Accelerated oxygen exchange kinetics on $\text{Nd}_2\text{NiO}_{4+\delta}$ thin films with tensile strain along c-axis, *ACS Nano* 9 (2) (2015) 1613–1621, <https://doi.org/10.1021/nm506279h>.
- [34] Y. Chen, H. Téllez, M. Burriel, F. Yang, N. Tsvetkov, Z. Cai, D.W. McComb, J.A. Kilner, B. Yildiz, Segregated chemistry and structure on (001) and (100) surfaces of $(\text{La}_{1-x}\text{Sr}_x)_2\text{CoO}_4$ override the crystal anisotropy in oxygen exchange kinetics, *Chem. Mater.* 27 (15) (2015) 5436–5450, <https://doi.org/10.1021/acs.chemmater.5b02292>.
- [35] D. Telesca, B.O. Wells, B. Sinkovic, Structural reorientation of PLD grown La_2NiO_4 thin films, *Surf. Sci.* 606 (9) (2012) 865–871, <https://doi.org/10.1016/j.susc.2012.02.001>.
- [36] T. Kimura, Microstructure development and texture formation in lead-free piezoelectric ceramics prepared by templated grain growth process, *J. Ceram. Soc. Jpn.* 124 (4) (2016) 268–282, <https://doi.org/10.2109/jcersj2.124.P4-1>.
- [37] X. Liu, N. Fechner, M. Antonietti, Salt melt synthesis of ceramics, semiconductors and carbon nanostructures, *Chem. Soc. Rev.* 42 (21) (2013) 8237–8265, <https://doi.org/10.1039/C3CS60159E>.
- [38] J. Boltersdorf, N. King, P.A. Maggard, Flux-mediated crystal growth of metal oxides: synthetic tunability of particle morphologies, sizes, and surface features for photocatalysis research, *CrystEngComm* 17 (11) (2015) 2225–2241, <https://doi.org/10.1039/c4ce01587h>.
- [39] X. Ma, B. Wang, E. Xhafa, K. Sun, E. Nikolla, Synthesis of shape-controlled $\text{La}_2\text{NiO}_{4+\delta}$ nanostructures and their anisotropic properties for oxygen diffusion, *Chem. Commun.* 51 (1) (2015) 137–140, <https://doi.org/10.1039/c4cc07364a>.
- [40] L.N. Marquez, S.W. Keller, A.M. Stacy, M. Fendorf, R. Gronsky, Synthesis of twin-free, orthorhombic europium barium copper oxide $\text{EuBa}_2\text{Cu}_3\text{O}_7$ superconductors at 450 °C by direct precipitation from molten sodium hydroxide and potassium hydroxide, *Chem. Mater.* 5 (6) (1993) 761–764, <https://doi.org/10.1021/cm00030a007>.
- [41] W.K. Ham, G.F. Holland, A.M. Stacy, Low-temperature synthesis of superconducting $\text{La}_{2-x}\text{M}_x\text{CuO}_4$: direct precipitation from NaOH/KOH melts, *J. Am. Chem. Soc.* 110 (15) (1988) 5214–5215, <https://doi.org/10.1021/ja00223a063>.
- [42] C. Shivakumara, M.S. Hegde, A.S. Prakash, A.M.A. Khadar, G.N. Subbanna, N.P. Lalla, Low temperature synthesis, structure and properties of alkali-doped La_2NiO_4 , LaNiO_3 and $\text{LaNi}_{0.85}\text{Cu}_{0.15}\text{O}_3$ from alkali hydroxide fluxes, *Solid State Sci.* 5 (2) (2003) 351–357, [https://doi.org/10.1016/S1293-2558\(02\)00056-0](https://doi.org/10.1016/S1293-2558(02)00056-0).
- [43] S.J. Mugavero, W.R. Gemmill, I.P. Roof, H.-C. zur Loye, Materials discovery by crystal growth: Lanthanide metal containing oxides of the platinum group metals (Ru, Os, Ir, Rh, Pd, Pt) from molten alkali metal hydroxides, *J. Solid State Chem.* 182 (7) (2009) 1950–1963, <https://doi.org/10.1016/j.jssc.2009.05.006>.
- [44] H. Lux, Acids and bases in a fused salt bath: the determination of oxygen-ion concentration, *Z. Elektrochem. Soc.* 45 (1939) 303–309.
- [45] H. Flood, T. Förland, The acidic and basic properties of oxides, *Acta Chem. Scand.* 1 (1947) 592–604.
- [46] A. Feldhoff, M. Arnold, J. Martynczuk, T.M. Gesing, H. Wang, The sol-gel synthesis of perovskites by an EDTA/citrate complexing method involves nanoscale solid state reactions, *Solid State Sci.* 10 (6) (2008) 689–701, <https://doi.org/10.1016/j.solidstatesciences.2007.11.030>.
- [47] D.E. Bugaris, H.-C. zur Loye, Materials discovery by flux crystal growth: quaternary and higher order oxides, *Angew. Chem. Int. Ed.* 51 (16) (2012) 3780–3811, <https://doi.org/10.1002/anie.201102676>.
- [48] D.E. Rice, D.J. Buttrey, An X-Ray diffraction study of the oxygen content phase diagram of $\text{La}_2\text{NiO}_{4+\delta}$, *J. Solid State Chem.* 105 (1) (1993) 197–210, <https://doi.org/10.1006/jssc.1993.1208>.
- [49] S.L. Stoll, A.M. Stacy, C.C. Torardi, Single-crystal growth, alkali metal ordering, and superconductivity in $\text{La}_{2-x}\text{M}_x\text{CuO}_4$ ($\text{M} = \text{Na, K}$), *Inorg. Chem.* 33 (13) (1994) 2761–2765, <https://doi.org/10.1021/ic00091a016>.
- [50] P. Fleming, R.A. Farrell, J.D. Holmes, M.A. Morris, The rapid formation of $\text{La}(\text{OH})_3$ from La_2O_3 powders on exposure to water vapor, *J. Am. Ceram. Soc.* 93 (4) (2010) 1187–1194, <https://doi.org/10.1111/j.1551-2916.2009.03564.x>.
- [51] D.D. Williams, J.A. Grand, R.R. Miller, The reactions of molten sodium hydroxide with various metals, *J. Am. Chem. Soc.* 78 (20) (1956) 5150–5155, <https://doi.org/10.1021/ja01601a004>.
- [52] C. Hu, Y. Xi, H. Liu, Z.L. Wang, Composite-hydroxide-mediated approach as a general methodology for synthesizing nanostructures, *J. Mater. Chem.* 19 (7) (2009) 858–868, <https://doi.org/10.1039/b816304a>.
- [53] J. Park, J. Joo, S.G. Kwon, Y. Jang, T. Hyeon, Synthesis of monodisperse spherical nanocrystals, *Angew. Chem. Int. Ed.* 46 (25) (2007) 4630–4660, <https://doi.org/10.1002/anie.200603148>.
- [54] T. Kimura, Y. Miura, K. Fuse, Texture development in barium titanate and PMN-PT using hexabarium 17-titanate heterotemplates, *Int. J. Appl. Ceram. Technol.* 2 (1) (2005) 15–23, <https://doi.org/10.1111/j.1744-7402.2005.02007.x>.
- [55] Y. Saito, H. Takao, Synthesis of polycrystalline plate-like KNbO_3 particles by the topochemical micro-crystal conversion method and fabrication of grain-oriented $(\text{K}_{0.5}\text{Na}_{0.5})\text{NbO}_3$ ceramics, *J. Eur. Ceram. Soc.* 27 (13) (2007) 4085–4092, <https://doi.org/10.1016/j.jeurceramsoc.2007.02.099>.
- [56] M. Komath, Hot corrosion of nickel in anhydrous sodium hydroxide, *Mater. Chem. Phys.* 45 (2) (1996) 171–175, [https://doi.org/10.1016/0254-0584\(96\)80098-8](https://doi.org/10.1016/0254-0584(96)80098-8).
- [57] K. Efimov, M. Arnold, J. Martynczuk, A. Feldhoff, Crystalline intermediate phases in the sol-gel-based synthesis of $\text{La}_2\text{NiO}_{4+\delta}$, *J. Am. Ceram. Soc.* 92 (4) (2009) 876–880, <https://doi.org/10.1111/j.1551-2916.2009.02943.x>.
- [58] G. Wulff, XXV. Zur Frage der Geschwindigkeit des Wachstums und der Auflösung der Kristallflächen, *Z. Krist.-Cryst. Mater.* 34 (1–6) (1901) 449–530, <https://doi.org/10.1524/zkri.1901.34.1.449>.
- [59] M.V. Laue, Der Wulffsche Satz für die Gleichgewichtsform von Kristallen, *Z. Krist.-Cryst. Mater.* 105 (1–6) (1943) 124–133, <https://doi.org/10.1524/zkri.1943.105.1.124>.
- [60] A.A. Chernov, The kinetics of the growth forms of crystals, *Sov. Phys. Cryst* 7 (1963) 728–730.
- [61] M.R. Singh, D. Ramkrishna, A comprehensive approach to predicting crystal morphology distributions with population balances, *Cryst. Growth Des.* 13 (4) (2013) 1397–1411, <https://doi.org/10.1021/cg301851g>.
- [62] M.S.D. Read, M.S. Islam, G.W. Watson, F.E. Hancock, Surface structures and defect properties of pure and doped La_2NiO_4 , *J. Mater. Chem.* 11 (10) (2001) 2597–2602, <https://doi.org/10.1039/b102678j>.
- [63] H. Jenkins, K. Thakur, Reappraisal of thermochemical radii for complex ions, *J. Chem. Educ.* 56 (9) (1979) 576–577.
- [64] Y. Zhang, S.-L. Zheng, H.-B. Xu, H. Du, Y. Zhang, Decomposition of chromite ore by oxygen in molten NaOH– NaNO_3 , *Int. J. Miner. Process.* 95 (1) (2010) 10–17, <https://doi.org/10.1016/j.minpro.2010.03.005>.
- [65] R.D. Shannon, Revised effective ionic radii and systematic studies of interatomic distances in halides and chalcogenides, *Acta Crystallogr. A* 32 (5) (1976) 751–767, <https://doi.org/10.1107/S0567739476001551>.

Supporting Information

Anisotropic growth of $\text{La}_2\text{NiO}_{4+\delta}$: Influential pre-treatment in molten-flux synthesis

Richard Hinterding,^{a,*} Zhijun Zhao,^a Chao Zhang,^b and Armin Feldhoff^{a,*}

^a Institute of Physical Chemistry and Electrochemistry, Leibniz University Hannover,
Callinstrasse 3A, D-30167 Hannover, Germany

^b Institute for Mineralogy, Leibniz University Hannover, Callinstrasse 3, D-30167
Hannover, Germany

Table S1: Summary of SSR-MFS and SGP-MFS samples presented in the supporting information.

Sample	La/Ni-ratio of precursors	Dwell time (h)	Crucible	Added water (μL)	Results shown in
SSR7	2 : 1	8	Al_2O_3	–	Figure S1
SSR8	2 : 1	8	Al_2O_3	100	Figure S1
SSR9	2 : 1.2	8	Al_2O_3	100	Figure S2
SSR10	2 : 1	6	Al_2O_3	100	Figure S3&S4
SSR11	2 : 1	14	Al_2O_3	100	Figure S4
SGP5	2 : 0.95	8	Al_2O_3	100	Figure S5
SGP6	2 : 0.95	8	Ni	100	Figure S3&S5
SGP7	2 : 1	8	Ni	100	Figure S5
SGP8	2 : 1.1	8	Ni	100	Figure S5
SGP9	2 : 1.1	8	Al_2O_3	100	Figure S5

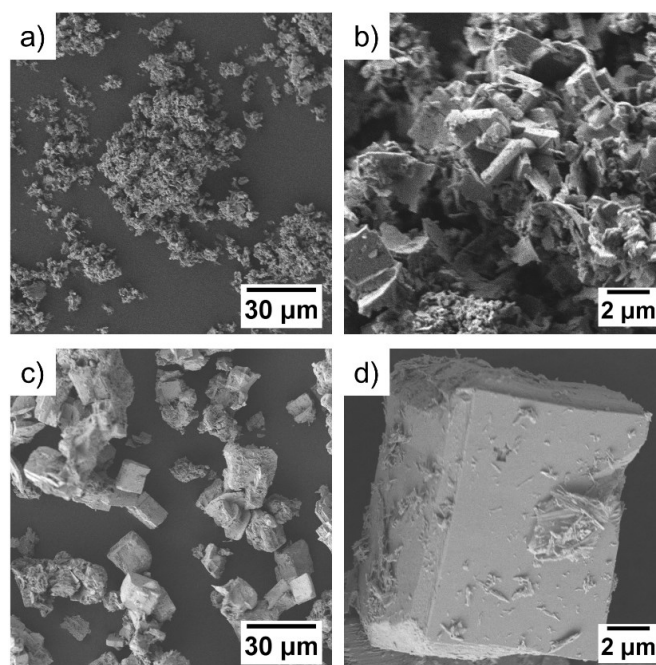


Figure S1: SEM of (a,b) SSR7 and (c,d) SSR8 powders synthesized via the solid-state route based molten-flux synthesis (SSR-MFS) by varying the water content in the molten NaOH.

Experiment conditions: For SSR7, NaOH was firstly heated to 400 °C at a heating rate of 10 °C/min. After 30 min, the reactant mixture was added and the system was held at 400 °C for 8 h; For SSR8, 100 μL H_2O was dropped on surfaces of NaOH at room temperature. After mixing reactants with NaOH, the system was placed in a preheated oven at 400 °C and maintained for 8 h.

In case of SSR7, part of the mixture was dissolved in the molten NaOH upon the addition of reactants. The rest, however, was not dissolved and sunk on the bottom of the crucible. As discussed in the main

text (manuscript), it is assumed to be caused by the shortage of water.

By adding 100 μL H_2O in the system, reactants mixture was fully dissolved in NaOH 5 min later after the NaOH melted. After about 10 min, the liquid was getting darker, presumably due to the formation of $\text{La}_2\text{NiO}_{4+\delta}$ particles with increasing loss of water.

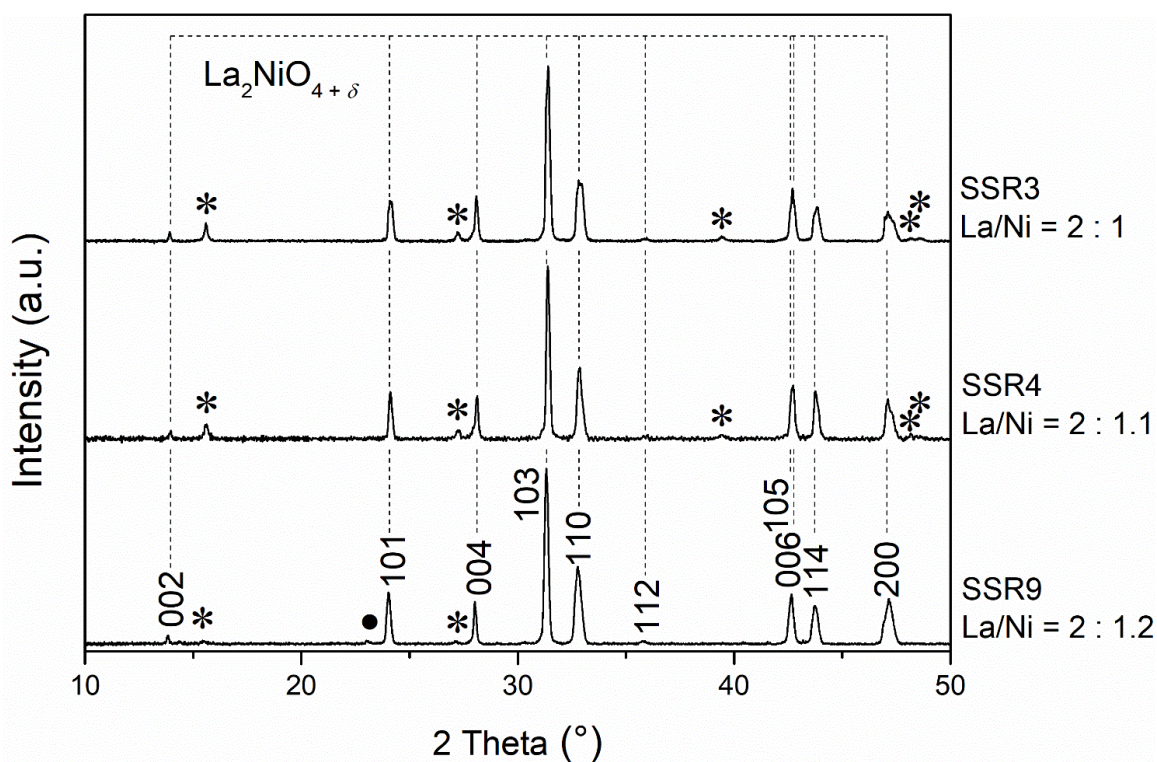


Figure S2: XRD of powders synthesized in alumina crucibles by increasing the Ni-portion in reactants via the solid-state route based molten-flux synthesis (SSR-MFS). Asterisks: Bragg positions of $\text{La}(\text{OH})_3$ [PDF: 01-083-2034]. Solid points: Bragg positions of LaNiO_3 [PDF: 01-070-5757]. Reflections of the main product $\text{La}_2\text{NiO}_{4+\delta}$ [PDF: 01-076-0055] are indexed. The XRD data are normalized to the same height of the 103 reflection for a clear comparison.

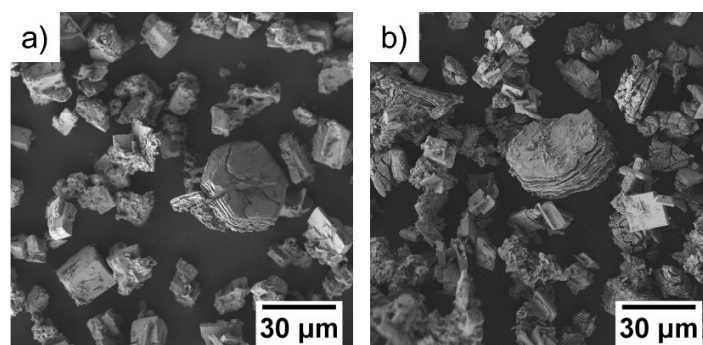


Figure S3: SEM micrographs of powder after the first of filtration of SSR10 and SGP6. Hexagon-shaped $\text{La}(\text{OH})_3$ particles with layered morphology are presented.

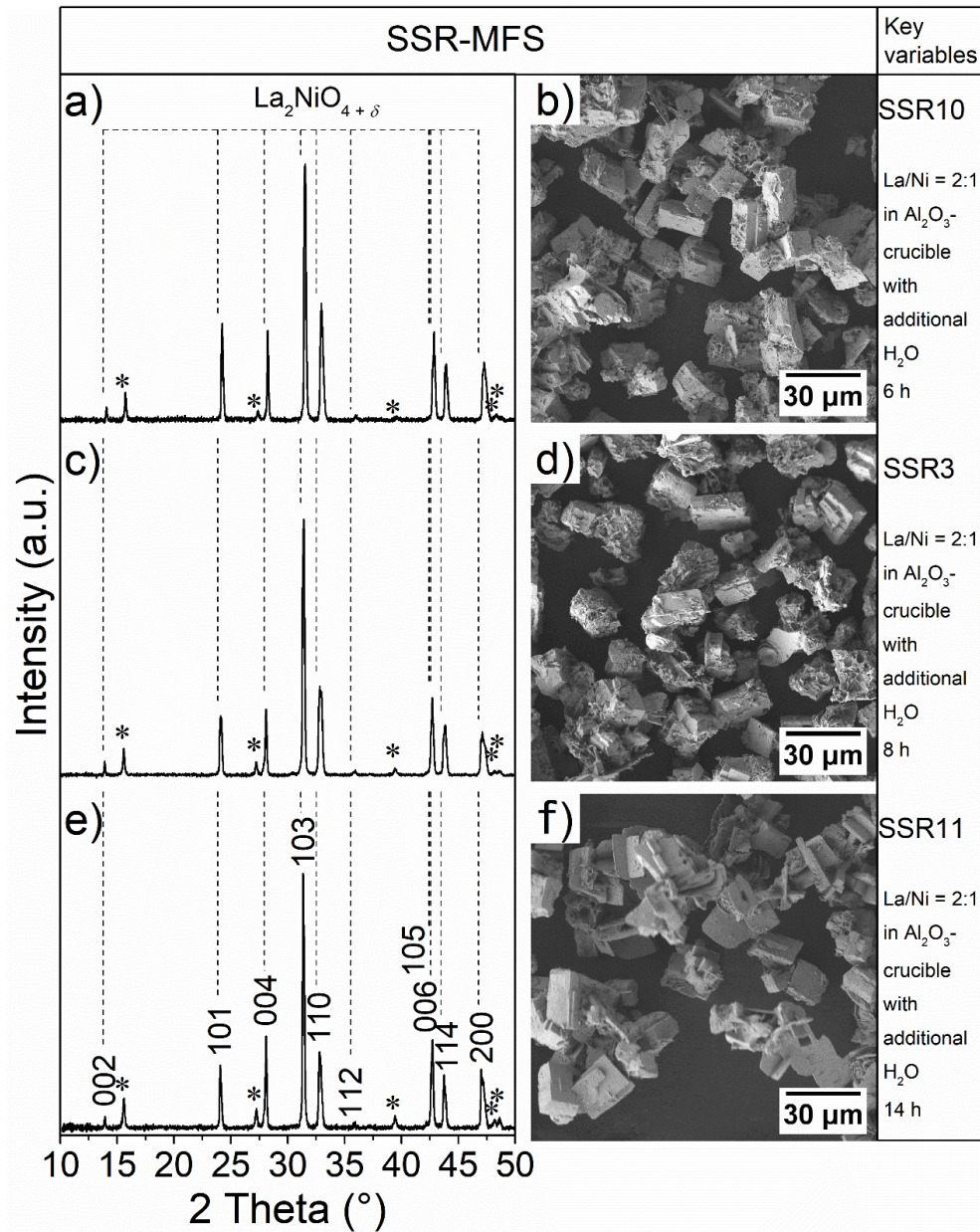


Figure S4: XRD and SEM of three powders synthesized via the solid-state route based molten-flux synthesis (SSR-MFS) with different dwell times at 400 °C: (a,b) 6 h, (c,d) 8 h, and (e,f) 14 h. Asterisks: Bragg positions of $\text{La}(\text{OH})_3$ [PDF: 01-083-2034]. Reflections of the main product $\text{La}_2\text{NiO}_{4+\delta}$ [PDF: 01-076-0055] are indexed. The XRD data have been normalized to the same height of the 103 reflection for a clear comparison.

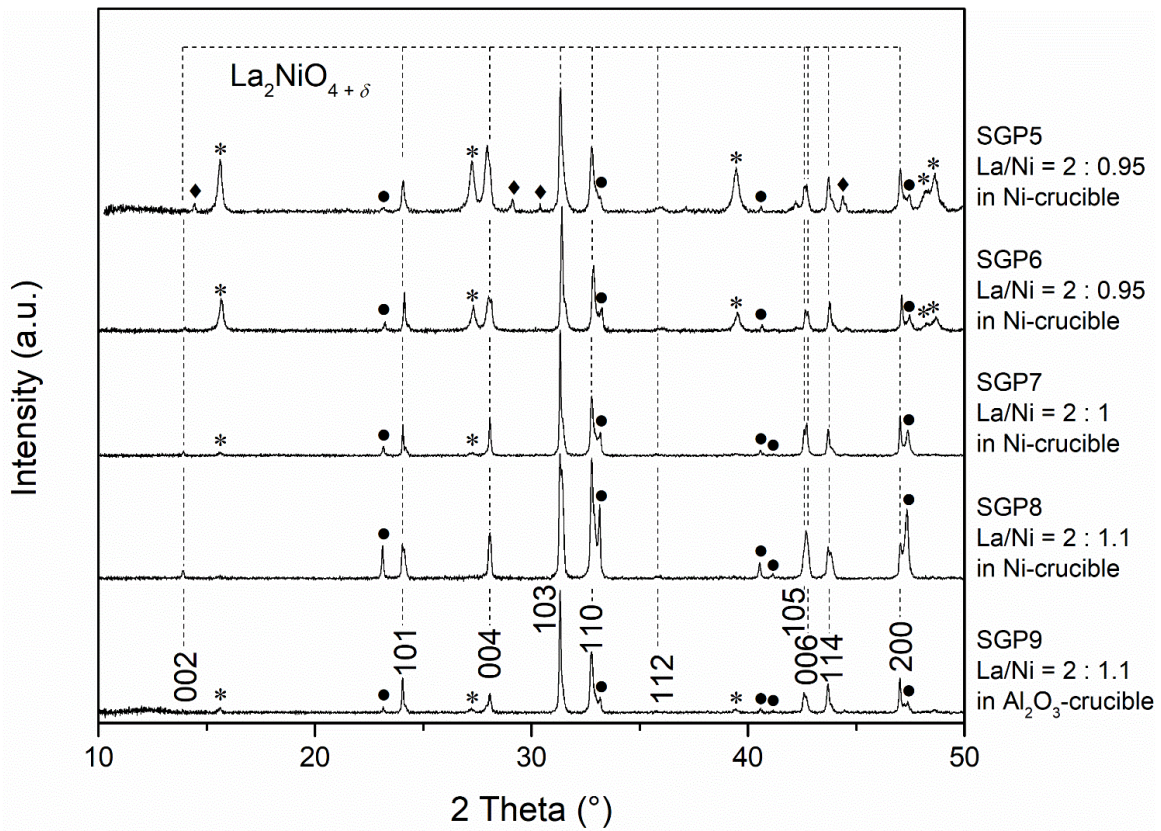


Figure S5: XRD of powders synthesized in alumina or nickel crucibles via the sol-gel process based molten-flux synthesis (SGP-MFS) at 400 °C for 8 h. Before heating, 100 μL H_2O was dropped on surfaces of NaOH. The La/Ni-ratios in precursors were varied from 2 : 0.95 to 2 : 1.1. Asterisks: Bragg positions of $\text{La}(\text{OH})_3$ [PDF: 01-083-2034]. Solid points: Bragg positions of LaNiO_3 [PDF: 01-070-5757]. Rhombuses: possible Bragg positions of LaOOH . Reflections of the main product $\text{La}_2\text{NiO}_{4+\delta}$ [PDF: 01-076-0055] are indexed. The XRD data are normalized to the same height of the 103 reflection for a clear comparison.

LaNiO_3 is present in SGP5 and SGP6 due to the higher RP-phase in the intermediates. As the Ni-portion in the intermediates increases (SGP6 to SGP8), the intensity of $\text{La}(\text{OH})_3$ reflections decrease while the intensity of LaNiO_3 reflections increase.

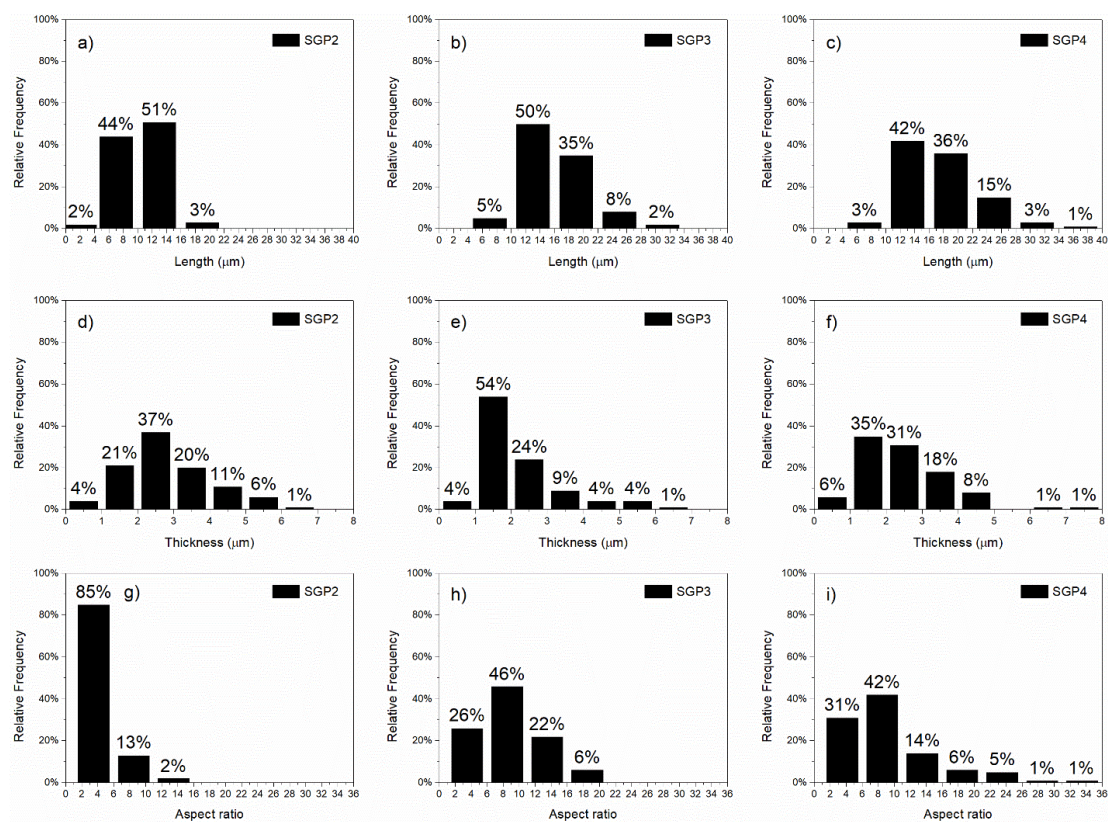


Figure S6: Histograms of (a-c) the length distribution, (d-f) the thickness distribution, and (g-i) the aspect ratio distribution of platelets synthesized with the dwell time of 6 h (SGP2), 8 h (SGP3), and 14 h (SGP4). For each sample, 100 platelets from corresponding SEM micrographs were evaluated using the software Image J.

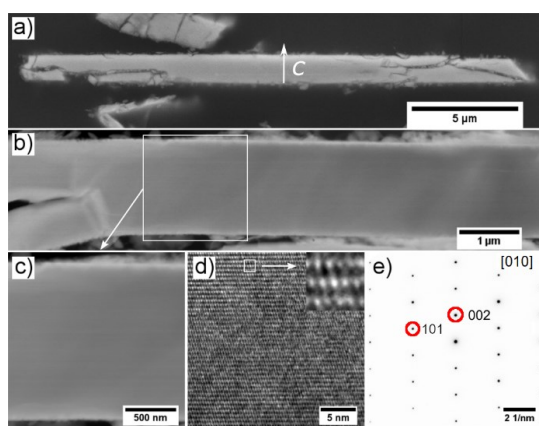


Figure S7: Electron microscopy characterization from cross-sections of a platelet from the SGP3-MFS batch. (a) SEM micrograph at 15kV. (b-c) STEM annular dark-field micrograph. (d) HRTEM micrograph. SAED pattern of main phase $\text{La}_2\text{NiO}_{4+\delta}$ along [010] zone axis. (e) SAED pattern of $\text{La}_2\text{NiO}_{4+\delta}$ along [010] zone axis.

2.1.3 Ceramic composites based on $\text{Ca}_3\text{Co}_{4-x}\text{O}_{9+\delta}$ and $\text{La}_2\text{NiO}_{4+\delta}$ with enhanced properties

Richard Hinterding, Zhijun Zhao, Mario Wolf, Matthias Jakob, Oliver Oeckler and Armin Feldhoff

Open Ceramics, 6 **2021**, 100103

DOI: 10.1016/j.oceram.2021.100103



Ceramic composites based on $\text{Ca}_3\text{Co}_{4-x}\text{O}_{9+\delta}$ and $\text{La}_2\text{NiO}_{4+\delta}$ with enhanced thermoelectric properties



R. Hinterding^{a,*}, Z. Zhao^a, M. Wolf^a, M. Jakob^b, O. Oeckler^b, A. Feldhoff^{a,**}

^a Leibniz University Hannover, Institute of Physical Chemistry and Electrochemistry, Callinstr. 3A, D-30167, Hannover, Germany

^b Leipzig University, Institute of Mineralogy, Crystallography and Materials Science, Scharnhorststr. 20, D-04275, Leipzig, Germany

ARTICLE INFO

Keywords:

Calcium cobalt oxide
Composite
Ceramic
Lanthanum nickelate
Reaction sintering
Thermoelectric
Power factor
Figure-of-merit

ABSTRACT

Ceramic composites were produced by combining the oxide materials $\text{Ca}_3\text{Co}_{4-x}\text{O}_{9+\delta}$ and $\text{La}_2\text{NiO}_{4+\delta}$. Both compounds were characterized by a plate-like crystal shape, but crystal sizes differed by around two orders of magnitude. The composite materials could be successfully prepared by using uniaxial pressing of powder mixtures and pressureless sintering to a porous ceramic. Possible reactions between both materials during sintering were analyzed. The ceramic composites with low amounts of $\text{La}_2\text{NiO}_{4+\delta}$ showed enhanced thermoelectric properties, caused by an increasing power factor and simultaneously decreasing thermal conductivity. For the evaluation of the thermoelectric properties, two different types of Ioffe plots were utilized. The maximum figure-of-merit zT at 1073 K was 0.27 for the pure $\text{Ca}_3\text{Co}_{4-x}\text{O}_{9+\delta}$ as well as for the sample containing 5 wt% $\text{La}_2\text{NiO}_{4+\delta}$. However, the average \overline{zT} in the temperature range of 373 K to 1073 K could be increased by 20% for the composite material.

1. Introduction

1.1. Thermoelectric energy conversion

In the light of limited resources, energy harvesting is a topic with increasing importance. A promising option is the conversion of wasted thermal energy into electrical energy via thermoelectric generators. However, the efficiency and performance of the latest thermoelectric materials still require further research to allow widespread application. There are various material classes such as tellurides [1], half-Heusler compounds [2], Zintl phases [3], polymers [4], oxides [5], oxy-selenides [6] and many more, which all have their advantages and disadvantages with respect to efficiency, energy conversion, chemical stability, application temperature or toxicity. Especially the working temperature and atmosphere are usually important criterions when choosing the proper thermoelectric materials for an application. For high-temperature applications with working conditions in air, the chemical stability of the used materials can be challenging. However, oxides typically show high temperature stability in air and especially the *p*-type cobalt oxide $\text{Ca}_3\text{Co}_{4-x}\text{O}_{9+\delta}$ (CCO) also shows remarkable thermoelectric properties based on its layered structure [5,7]. CCO is stable up to approximately 1200 K under air [8,9] and has a monoclinic crystal

structure built up from two incommensurate subsystems [10]. One subsystem contains CoO_2 as a misfit-layered CdI_2 structure type and the other subsystem consists of three Ca_2CoO_3 units as a layered cutout of the rock-salt type. Both subsystems alternate along the shared *c*-axis with same *a* and distinct *b* lattice parameters [11].

To discuss the performance of thermoelectric materials, some fundamental parameters appearing in the thermoelectric material tensor of Eq. (1) are indispensable [12–14].

$$\begin{pmatrix} I_q \\ I_s \end{pmatrix} = \frac{A}{L} \begin{pmatrix} \sigma & \sigma \cdot \alpha \\ \sigma \cdot \alpha & \sigma \cdot \alpha^2 + \Lambda \end{pmatrix} \cdot \begin{pmatrix} \Delta\phi \\ \Delta T \end{pmatrix} \quad (1)$$

The thermoelectric energy conversion of a thermoelectric material with a cross-sectional area *A* and a length *L* relies on the coupling of currents of electrical charge I_q and entropy I_s . Under the assumption of constant gradients, the electrical potential difference $\Delta\phi$ and the temperature difference ΔT may cause a thermally-induced electrical current, which is dependent on the three material parameters: the isothermal electrical conductivity σ , the Seebeck coefficient α and the electrically open-circuited entropy conductivity Λ . The entropy conductivity is directly related to the open-circuited heat conductivity λ via Eq. (2), and both can be addressed by the term thermal conductivity [15]. The thermoelectric parameters all reappear in Eq. (2), where the performance of a

* Corresponding author.

** Corresponding author.

E-mail addresses: richard.hinterding@pci.uni-hannover.de (R. Hinterding), armin.feldhoff@pci.uni-hannover.de (A. Feldhoff).

<https://doi.org/10.1016/j.oceram.2021.100103>

Received 14 October 2020; Received in revised form 19 March 2021; Accepted 6 April 2021

Available online xxx

2666-5395/© 2021 The Authors. Published by Elsevier Ltd on behalf of European Ceramic Society. This is an open access article under the CC BY license (<http://creativecommons.org/licenses/by/4.0/>).

thermoelectric material is given by the figure-of-merit zT .

$$zT = \frac{\sigma \cdot \alpha^2}{\lambda} \cdot T = \frac{\sigma \cdot \alpha^2}{\Lambda} = \frac{PF}{\Lambda} \quad (2)$$

One advantage of using the more fundamental entropy conductivity is making the figure-of-merit explicitly dependent on all three material parameters but only implicitly on temperature [14]. While the zT describes the maximum energy conversion efficiency, the power factor $PF = \sigma \cdot \alpha^2$ is proportional to the maximum electrical power output of a thermoelectric material. Both quantities are important to describe the thermoelectric performance of a material [15].

1.2. Thermoelectric composites

Composite materials can combine specific single phase properties into a superior heteromaterial. The influence of introducing one or multiple phases to a main matrix material is highly dependent on the chosen materials. In general, the introduction of heterointerfaces can affect the mean-free path of phonons and hence the thermal conductivity [16–18]. Material combinations comprising organic polymers and inorganic materials showed success in increasing the Seebeck coefficient of the system significantly [19–21]. Other composites introduce carbon nanotubes to benefit from a higher electrical conductivity [22,23]. Regarding CCO, the addition of Ag inclusions has shown beneficial effects on the thermoelectric performance [24–26]. Furthermore, adding polymers to gain a triple-phase CCO/Ag/polymer composite could reduce the thermal conductivity considerably, but the material combination made proper sintering difficult [27]. Another composite consisting of the three phases CCO, Na_xCoO_2 and $\text{Bi}_2\text{Ca}_2\text{Co}_2\text{O}_9$ was gained by using high dopant levels of Na and Bi during the synthesis [28]. This composite benefitted from similar layered crystal structures of the components and resulted in an increased power factor. It also shows the benefits of combining doping and composite materials, which was also investigated for Ag doping and Ag inclusions by Wang et al. [29]. Generally, doping is a powerful instrument for improving thermoelectric properties of CCO. The currently best figure-of-merit zT for polycrystalline CCO was reached by Saini et al. [30] with 0.74 at 800 K by Tb doping. Some other promising doping elements leading to improved thermoelectric properties are Bi [31], Ag [29], Fe [32], Eu [33] or Lu [34]. A zT value of 0.87 at 973 K was reached for the single-crystalline material [35], but polycrystalline materials are preferred in terms of synthesis effort.

Regarding the thermoelectric properties of a two-phase composite, Bergman et al. stated some theoretical limits [36]. While the figure-of-merit shall not be able to exceed the zT value of the pure single components, this is not applicable for the power factor [37]. However, these studies were made before the more recent development regarding influences on the nanoscale. Furthermore, partial reactions between the components may lead to a multiphase system, which impair the validity of these statements in that case.

Within this study, the combination of CCO and $\text{La}_2\text{NiO}_{4+\delta}$ (LNO) to CCO/LNO ceramic composites was investigated. While most research on CCO focuses on thermoelectrics, the mixed ionic-electronic conductivity and dielectric properties of LNO make it interesting for several potential applications in microelectronics, gas separation membranes or catalysis [38–40]. It is a p -type material with a moderate Seebeck coefficient of approximately $50 \mu\text{V K}^{-1}$ at 1273 K, which can increase significantly in dependence of oxygen partial pressure and hole doping [41,42]. The heat conductivity decreases with temperature and is about $5.5 \text{ W m}^{-1} \text{ K}^{-1}$ at 1000 K [43] while the electrical conductivity can reach values up to 200 S cm^{-1} [44]. The structure of LNO comprises LaO rock-salt layers and LaNiO_3 perovskite layers, which alternate along the c -axis [45,46]. Therefore, both mixing components are characterized by layered structures and anisotropic transport properties, making it important to combine the properties in the same direction. The good electrical conductivity and the shared p -type conductivity make the LNO suitable as a mixing partner

within a CCO matrix. As high sintering temperatures were used, reactions between the CCO and LNO phases are possible and were investigated. The aim of preparing the CCO/LNO ceramic composites was the increase of the thermoelectric properties in comparison to pure CCO. To evaluate these properties, two different Ioffe plots regarding the power factor and the entropy conductivity were used [15,47].

2. Experimental

2.1. Materials

Two different oxide powders were used to produce ceramic oxide composites. The calcium cobalt oxide $\text{Ca}_3\text{Co}_{4-x}\text{O}_{9+\delta}$ (CCO) powder was purchased from CerPoTech (Tiller, Norway). The lanthanum nickelate $\text{La}_2\text{NiO}_{4+\delta}$ (LNO) was synthesized by introducing oxide mixtures of La_2O_3 and NiO into an alumina crucible with NaOH pellets, followed by heating at 673 K for 8 h with a heating rate of 10 K min^{-1} . The mixture was cooled to room temperature and washed with distilled water and acetone. Since the LNO is based on a previous work, more detailed information about the synthesis process can be found there [38]. Composites of CCO and LNO were synthesized by mixing the powders in the respective weight ratios of 99:1, 95:5, 90:10, 80:20 and 60:40 to a total weight of 1 g. The mixture was ground in an agate mortar for approximately 15 min and uniaxially pressed in a 16 mm die with 250 MPa at room temperature. Afterwards, pressureless sintering to ceramic samples was processed at 1173 K for 10 h with a heating and cooling rate of 2 K min^{-1} under air. For thermoelectric measurements, the sintered disks were cut into bars with a length of 10 mm by using a precision vertical diamond wire saw from O'Well model 3242.

2.2. Analysis of microstructure

To investigate the phase purity of used powders and gained ceramics, X-ray diffraction (XRD, Bruker AXS GmbH, Bruker D8 Advance) measurements were operated in a step-scan mode between 10° and $80^\circ 2\theta$ with a step size of 0.01° and 1 s per step without sample rotation. Cu-K_α radiation was used at 40 kV and 40 mA. Powder diffraction data for identification and comparison within this work are used for the compounds $\text{Ca}_3\text{Co}_{4-x}\text{O}_{9+\delta}$ (Miyazaki et al. [11], monoclinic, $a = 4.834 \text{ \AA}$, $b_1 = 2.824 \text{ \AA}$, $b_2 = 4.558 \text{ \AA}$, $c = 10.844 \text{ \AA}$), $\text{Ca}_3\text{Co}_2\text{O}_6$ (PDF: [01-089-0630], rhombohedral, $a = 9.079 \text{ \AA}$, $c = 10.381 \text{ \AA}$), Co_3O_4 (PDF: [01-073-1701], cubic, $a = 8.084 \text{ \AA}$), $\text{La}_2\text{NiO}_{4+\delta}$ (PDF: [01-078-2186], tetragonal, $a = 5.502 \text{ \AA}$, $c = 12.504 \text{ \AA}$), $\text{La}(\text{Co,Ni})\text{O}_3$ (PDF: [00-054-0834], rhombohedral, $a = 5.465 \text{ \AA}$, $c = 13.125 \text{ \AA}$). The incommensurate structure of CCO required the approach of a four-dimensional superspace group for indexing the X-ray and electron diffraction patterns. Therefore, the superspace group $Cm(0\ 1\ -\ p\ 0)$ (equivalent to $Bm(0\ 0\ \gamma)$ No. 8.3) was applied in accordance with literature [11,48,49].

A field-emission scanning electron microscope (SEM, JEOL JSM-6700F) was used for micrographs at 2 kV and elemental mappings at 15 kV with the equipped energy dispersive X-ray spectrometer (EDXS, Oxford Instruments, INCA-200). In-depth analysis of the composition was accomplished by a field-emission transmission electron microscope (TEM, JEOL JEM-2100F-UHR), which was also equipped with an EDXS (Oxford Instruments, INCA-300). Scanning TEM (STEM), high-resolution TEM (HRTEM) and selected area electron diffraction (SAED) were made at 200 kV. Density and porosity of the sintered disks were determined by the Archimedes method (ISO 5018:1983). Isopropanol was used as a fluid and density values were averaged for three different disks resulting in deviations of up to 2%.

2.3. Analysis of thermoelectric properties

Measurements of the electrical conductivity σ , the Seebeck coefficient α and the heat conductivity λ were realized with respect to temperature

dependency and orientation of the samples. The sintered ceramics were cut into bars (10 mm, 2 mm, 1.6 mm) to measure the electrical conductivity and the Seebeck coefficient perpendicular to the pressing direction. The measurement of the electrical conductivity was accomplished by a 4-point probe method at equilibrium conditions within a horizontal three-heating-zone tube furnace from Carbolite Gero EVZ 12/450B. To measure the Seebeck coefficient, a ProboStat A setup from NorECs with a vertical furnace from Elite Thermal Systems Ltd. at equilibrium conditions was used. Measurements were done with KEITHLEY multimeters and gained data processed by using Lab VIEW software. Equilibrium conditions were reached by heating the samples to 1073 K and measuring downwards with set up heating plateaus every 100 K. A laser flash setup LFA 1000 from Linseis with an InSb detector was used to measure the thermal diffusivity D under an oxygen-helium mixed atmosphere (80% He, 20% O_2). Test measurements without oxygen partial pressure resulted in a decomposition of CCO between 773 K and 873 K [50], wherefore the mixture was necessary to gain reliable data. Values for the heat capacity of CCO were taken from a former publication [28] and the CCO/LNO ceramic composites were measured in relation to the CCO. Two different sample orientations as perpendicular and parallel to the pressing direction were investigated. The measurements perpendicular to the pressing direction were conducted up to 573 K. The limitation in temperature was caused by the used lamellar graphite holder from Linseis, which is not stable in an oxidic atmosphere at high temperatures. For using the lamellar holder, cut bars were rotated by 90° and aligned. The utilization of the holder was essential and enabled measurements of the thermal diffusivity in the same direction as the electrical conductivity and the Seebeck coefficient and therefore a determination of figure-of-merit zT . Values of thermal diffusivity above 573 K with orientation perpendicular to the pressing direction were estimated by calculating polynomial fits for the measurements parallel to the pressing direction. As these parallel measurements were conducted in the full temperature range of 373 K–1073 K, their fits were transferred to the measurements in the other direction assuming similar trends.

3. Results and discussion

3.1. Ceramic composite: microstructure

For obtaining the ceramic composites, two different oxide powders consisting of $\text{Ca}_3\text{Co}_{4-x}\text{O}_{9+\delta}$ (CCO) and $\text{La}_2\text{NiO}_{4+\delta}$ (LNO) were used. Phase purity and crystal shape of these compounds have been confirmed by powder XRD patterns and SEM micrographs (compare Fig. S1). The CCO showed 30 nm thin sheets with extensions about 200–500 nm and the LNO large plate-like or cuboidal particles with several microns in size. The XRD patterns showed the reflections of the desired phases with negligible impurities of Co_3O_4 in case of the CCO.

Regarding the CCO/LNO ceramic composites after sintering, the XRD patterns are displayed in Fig. 1a. For a more precise comparison, enlarged graphs are given in Fig. S2. No additional reflections could be detected for the samples with up to 10 wt% LNO, but for 20 wt% and 40 wt% LNO reflections of $\text{Ca}_3\text{Co}_2\text{O}_6$ and the perovskite phase $\text{La}(\text{Co,Ni})\text{O}_3$ became apparent. Together with the lack of $\text{La}_2\text{NiO}_{4+\delta}$ reflections in all samples, this indicates a reaction between CCO and LNO has occurred. The density measurements in Fig. 1b show a bulk density of 2.94 g cm^{-3} for pure CCO, which results in a relative density of 63% in comparison to the theoretical density of 4.68 g cm^{-3} [51]. The bulk density of the ceramic composites increased linearly with the added amount of LNO, which can be explained by the higher density of 7.32 g cm^{-3} for LNO or 7.23 g cm^{-3} for LaNiO_3 . By extrapolating the linear fit to 100% LNO, it does not reach a value of dense LNO, because higher sintering temperatures of at least 1473 K would be required [52], but CCO decomposes at temperatures above roughly 1200 K in air [8,9].

To examine the absence of LNO reflections in the XRD patterns after sintering, SEM-EDXS analysis of the sample with 5 wt% LNO was done. Fig. 2 shows the microstructural characterization of a single LNO particle

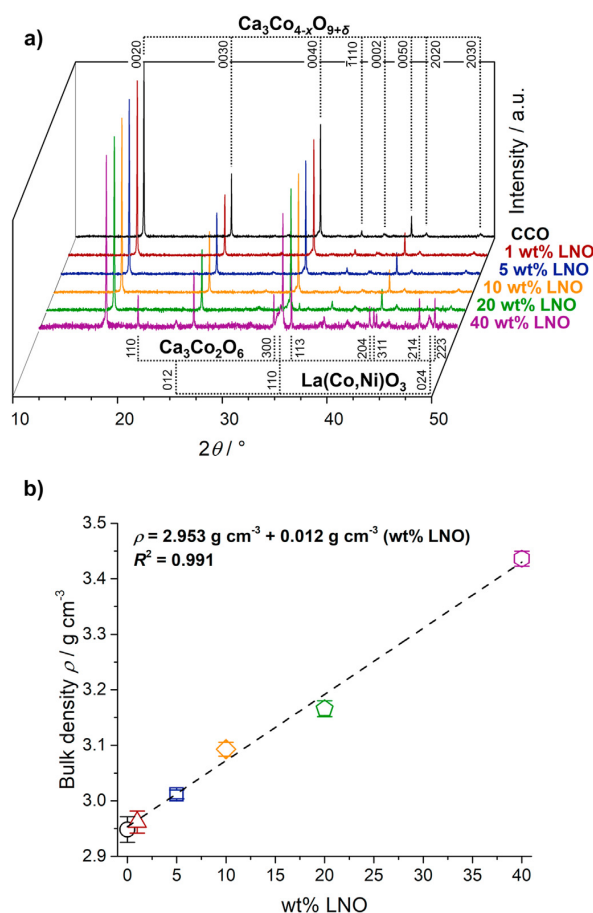


Fig. 1. Composition and density of the CCO/LNO ceramic composites after sintering. a) Background-corrected and normalized XRD patterns of the matrix material CCO and the composites with indexed reflections for the CCO and the phases of reaction sintering $\text{Ca}_3\text{Co}_2\text{O}_6$ and $\text{La}(\text{Co,Ni})\text{O}_3$. Reflections of CCO were indexed with the four-dimensional superspace group approach [11]. b) Densities of the CCO and the composites determined by Archimedes method. The bulk density shows a linear dependency on the added amount of LNO.

inside the CCO matrix (compare Fig. S3 for an overview of the LNO distribution). Concerning the elemental distributions in Fig. 2d–h several things are worth highlighting. First of all, the lanthanum is solely located within the original LNO particle and did not diffuse into the CCO matrix. Cobalt on the other hand did penetrate the LNO particles and some cobalt-nickel inclusions are visible as well. Depending on the penetration depth from the polishment, these inclusions could also be located at the surface of the particle. This assumption is encouraged by the same cobalt-nickel rich phase surrounding the particle. The calcium is mainly located within the CCO matrix. With the knowledge from the XRD patterns, the newly formed $\text{La}(\text{Co,Ni})\text{O}_3$ has to be located within the LNO particle and the $\text{Ca}_3\text{Co}_2\text{O}_6$ most likely in its vicinity. The formation of $\text{La}(\text{Co,Ni})\text{O}_3$ is confirmed by comparing the La:Ni ratio before and after the sintering by a quantitative EDXS analysis. A detailed description of the investigated areas and resulting elemental compositions is given in Fig. S4. Before sintering the ratio was about 2:1 as confirmed by previous studies [38], but afterwards it changed significantly to 2:0.7. Interestingly, the La:Co ratio even reached a value of 2:1.5, wherefore the La:(Co,Ni) ratio is roughly 1 and therefore matching to the perovskite compound. The loss of Ni within the particle could also be the reason for the formation of the cobalt-nickel rich phase, which was not detected by XRD and needs

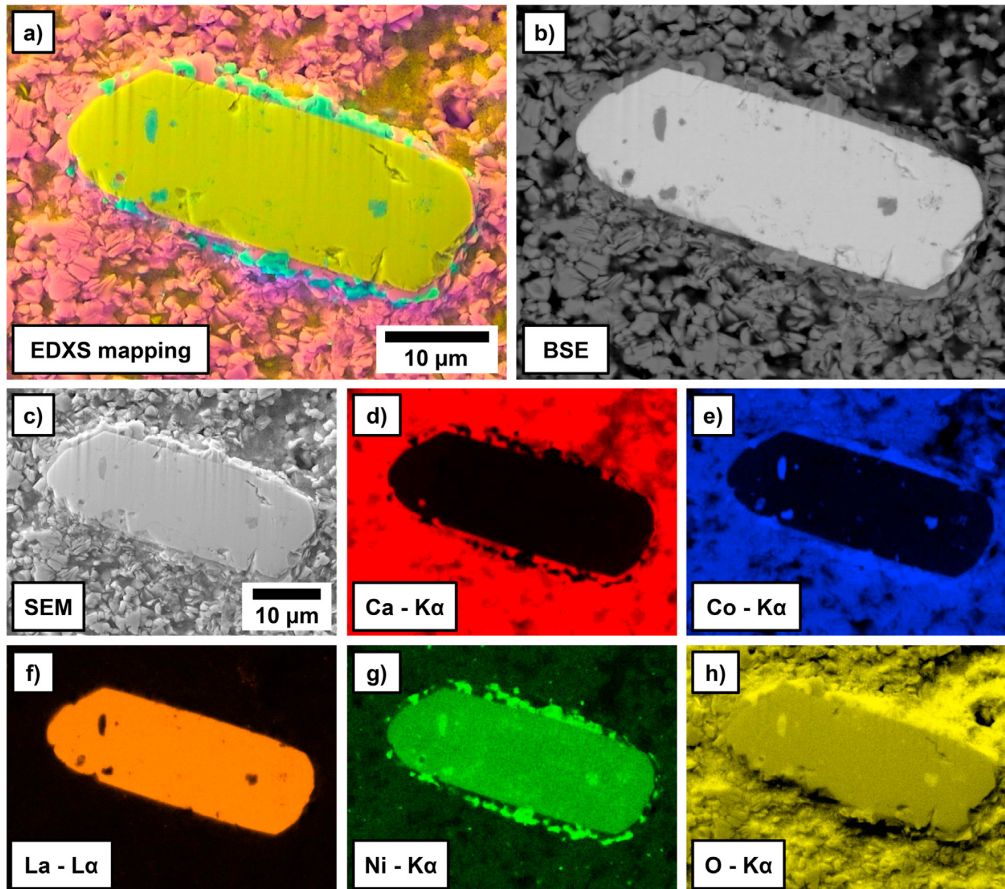


Fig. 2. Cross-sectional SEM-EDXS analysis of the 5 wt% LNO sample after sintering showing a single LNO plate-like crystal embedded in a CCO matrix. a) Overlay EDXS mapping and corresponding SEM micrograph summarizing the results from c-h. b) Backscattered-electron (BSE) micrograph showing the elemental contrasts. c) SEM micrograph as basis for EDXS analysis. d-h) Elemental distributions of the respective elements Ca, Co, La, Ni and O. Note, for the oxygen distribution shading effects are visible, caused by surface irregularities.

further analysis provided by TEM measurements in the following.

Firstly, the CCO matrix within the 5 wt% LNO sample was investigated by TEM and its results can be seen in Fig. 3. The STEM micrographs in Fig. 3a and b shows lamellar contrasts, which are attributed to stacking faults. The EDXS mapping in Fig. 3c shows a homogeneous distribution of calcium and cobalt and therefore no unwanted inclusions. The HRTEM micrograph in Fig. 3d shows stacked layers, fitting to the layered structure of CCO along the *c*-axis. The stacking faults become apparent in the SAEDs of Fig. 3e-g along the [1100] zone axis. The SAED pattern becomes distinct when a single lamella is investigated in Fig. 3e, but at the interface of the lamellae the reflections of the $\bar{1}100$ zone axis also appear. This is typical for microtwins, where the stacking order is inverted [53]. A direct comparison between the experimental and the simulated SAED patterns for the microtwin is given in Fig. 3g and h. The resulting orientation relationship between the two grains called A and B is therefore $[1100]_A \parallel [\bar{1}100]_B \wedge (0010)_A \wedge (0010)_B$. This characteristic was found frequently within the sample and is to our best knowledge not yet reported for CCO. It is most likely attributed to the synthesis technique, wherefore it could not be further influenced. The investigation of the matrix shows the CCO being unimpaired from the LNO as long as its not in direct contact with it.

Secondly, the CCO-LNO interface has been analyzed via STEM, EDXS and SAED, shown in Fig. 4a-e. The EDXS analysis confirms the results

from the SEM in terms of cobalt diffusing into the LNO. Since CCO is the only possible cobalt source within the composite, the CCO has to decompose into $\text{Ca}_3\text{Co}_2\text{O}_6$ by releasing CoO and O_2 [54,55]. Surprisingly, not only the direct interface but the whole LNO particle shows significant amounts of cobalt. This explains the disappearing XRD reflections of LNO and the appearing reflections of $\text{La}(\text{Co,Ni})\text{O}_3$ discussed formerly in Fig. 1a. As the oxidation state of Ni is increased in $\text{La}(\text{Co,Ni})\text{O}_3$ compared to $\text{La}_2\text{NiO}_{4+\delta}$, the involvement of atmospheric oxygen is likely. Furthermore, the polycrystalline nature of the $\text{La}(\text{Co,Ni})\text{O}_3$ /LNO particles become evident by looking at the SAEDs of Fig. 4d and e. While some distinct patterns could be detected for $\text{La}(\text{Co,Ni})\text{O}_3$ and LNO along the [001] zone axis, several other reflections are visible as well. This means the introduction of cobalt into the LNO led to a breakdown of the original crystal structure and the formation of a polycrystalline system with $\text{La}(\text{Co,Ni})\text{O}_3$ as the main phase and LNO as a minor phase existing next to each other. Another phase needing clarification from Fig. 2 is the nickel-cobalt rich phase. In Fig. 4f-i, this phase could be identified as NiO with high amounts of Co, resulting in $(\text{Ni,Co})\text{O}$ with a Ni:Co ratio of 1:0.6 based on the EDXS analysis. The phase was located close to the LNO particles, but not at the direct interface of CCO-LNO, which means it could be caused by nanocrystalline NiO particles on the compound LNO, which were not detectable by XRD. A more reasonable explanation supported by the EDXS results of Fig. 2 is the formation of NiO as a result of the reduced La:Ni ratio within $\text{La}(\text{Co,Ni})\text{O}_3$ in comparison to LNO. The

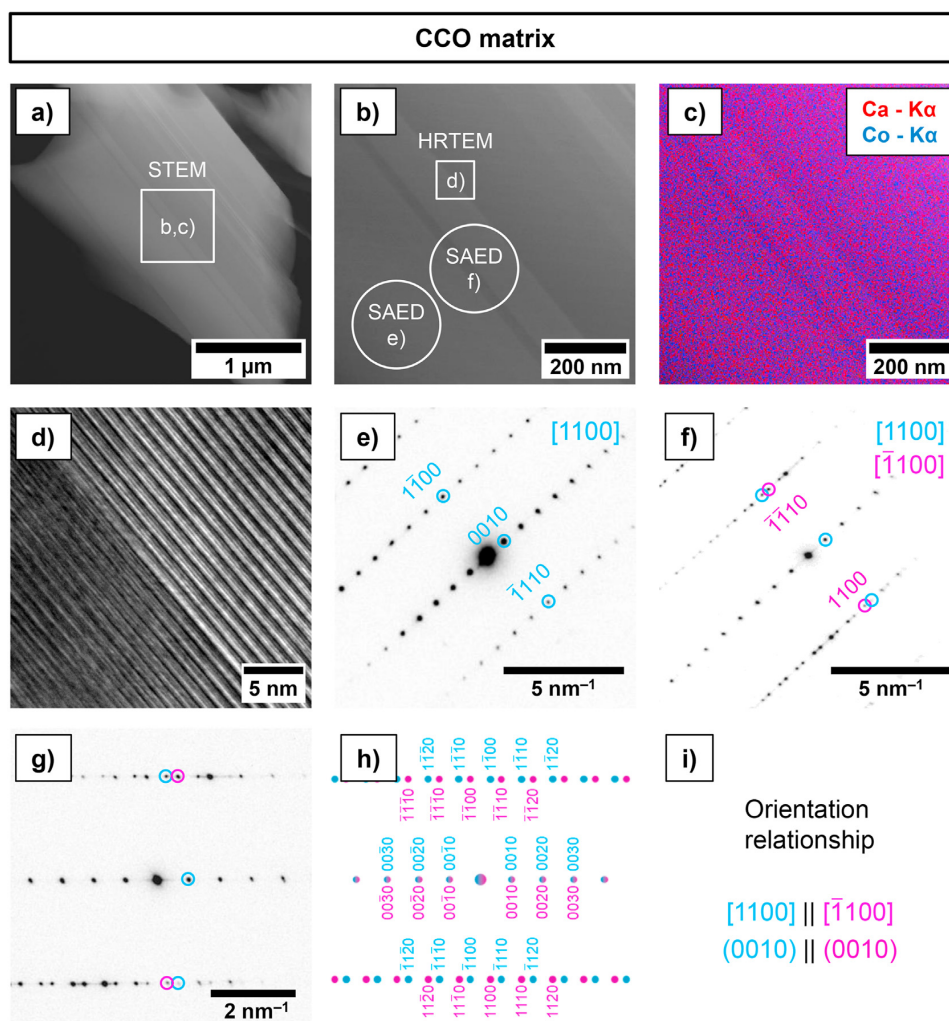


Fig. 3. Cross-sectional TEM characterization of the CCO matrix within the sample of 5 wt% LNO. a,b) STEM annular dark-field micrographs showing lamellar contrasts and the SAED scanning area size. c) EDXS mapping of the CCO to prove the homogeneous distribution of the elements Ca and Co. d) High-resolution TEM highlighting the stacking of the layered structure at the grain boundary. e) SAED pattern of the [1100] zone axis with given Laue indices. f) SAED pattern at the grain boundary, which shows reflections along the [1100] and $[\bar{1}100]$ zone axes, indicating microtwins. g) Enlarged and rotated SAED pattern of f) for an easy comparison with the simulated pattern in h). h) Simulated SAED patterns of the [1100] and $[\bar{1}100]$ zone axes. i) Resulting orientation relationship at the grain boundary. Reflections of CCO were indexed with the four-dimensional superspace group approach [11].

segregated Ni could therefore be responsible for the NiO formation in the vicinity of the original LNO particles.

Summarizing the results from XRD, SEM, EDXS and TEM the reaction scheme given in Fig. 5 can be derived. The CCO in vicinity of the LNO partially decomposes to $\text{Ca}_3\text{Co}_2\text{O}_6$, CoO and O_2 during the sintering process at 1173 K. Usually, this decomposition of CCO only occurs at temperatures exceeding roughly 1200 K [8,9,54], wherefore the presence of LNO seems conditional. The LNO on the other hand reacted mainly to the perovskite $\text{La}(\text{Co},\text{Ni})\text{O}_3$ and $(\text{Ni},\text{Co})\text{O}$. The formation of the perovskite is associated with an oxidation of the Ni in LNO and a structural change. The structural change from LNO to higher Ruddlesden-Popper phases ($\text{La}_{n+1}\text{Ni}_n\text{O}_{3n+1}$ with $n > 1$) is not yet fully understood [56,57]. However, the formation of the perovskite from LNO is proven to be possible as demonstrated by Adachi et al. [58] for post-sintering oxidation, where a high partial pressure of O_2 and additional NiO was necessary. Hence, the oxygen and the CoO formed by the

decomposition of CCO as well as the high porosity of the system could play an important role. The La:Ni ratio in the perovskite requires more Ni or less La in comparison to the LNO. The EDXS results showed that excess La was compensated with the introduction of Co and some Ni even segregated from the compound. The presence of $(\text{Ni},\text{Co})\text{O}$ could be a result of the segregated Ni and the formed CoO.

3.2. Ceramic composite: thermoelectric properties

The analysis of the microstructure in section 3.1 confirmed the presence of several phases within the CCO/LNO ceramic composites, namely CCO, LNO, $\text{La}(\text{Co},\text{Ni})\text{O}_3$, $\text{Ca}_3\text{Co}_2\text{O}_6$ and marginal $(\text{Ni},\text{Co})\text{O}$. Their overall influence on the thermoelectric properties was determined by measuring the electrical conductivity σ , Seebeck coefficient α and heat conductivity λ of the CCO/LNO ceramic composites in Fig. 6.

Beginning with the electrical conductivity in Fig. 6a, increasing

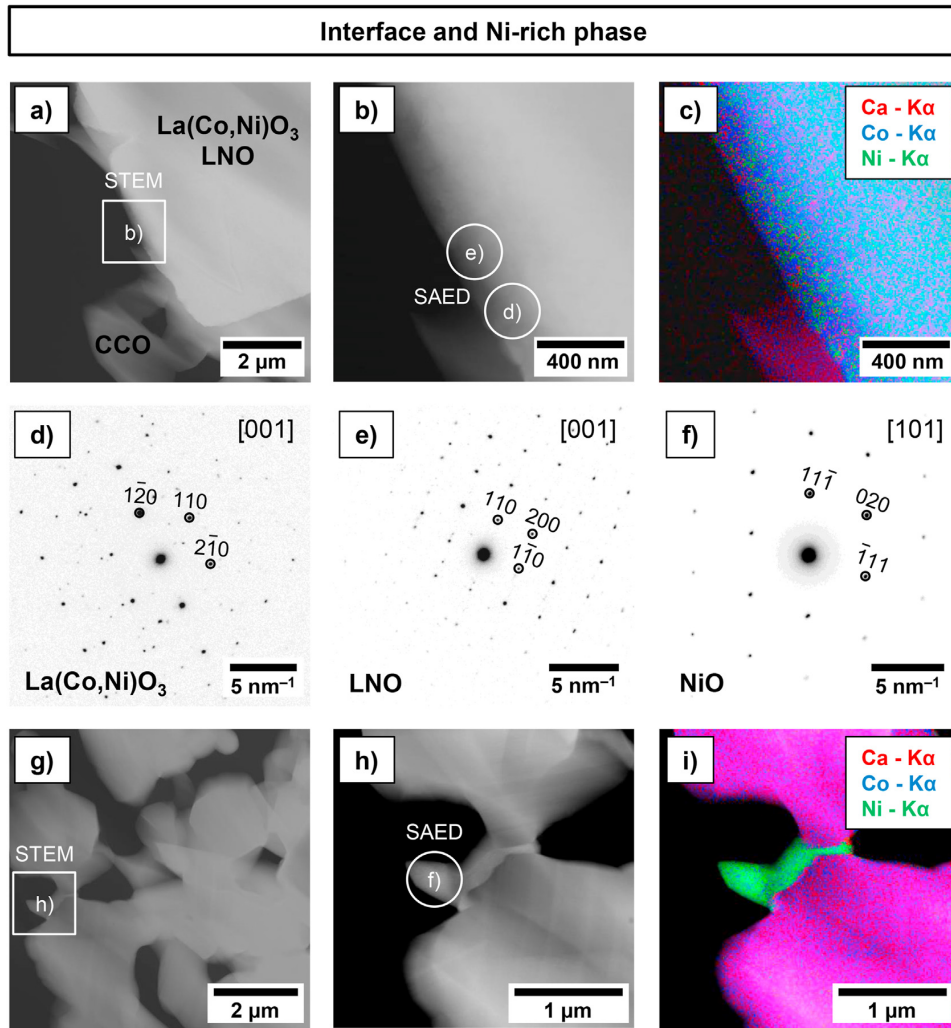


Fig. 4. Cross-sectional TEM characterization of the LNO-CCO interface and the Ni-rich phase within the sample of 5 wt% LNO. a,b) STEM annular dark-field micrographs of a large plate-like LNO grain surrounded by CCO. c) EDXS mapping of the CCO-LNO interface showing the homogeneous introduction of Co into the LNO. d,e) SAED patterns of the [001] zone axes of La(Co,Ni)O₃ and LNO with various different patterns indicating a polycrystalline material. f) SAED pattern of the Ni-rich phase NiO along the [101] zone axis. g,h) STEM annular dark-field micrographs of the NiO surrounded by CCO matrix. i) EDXS mapping of the NiO with no signs of Ni transport into the CCO.

values were measured for the 1–10 wt% LNO samples in comparison to CCO. At 1073 K the highest value of 76 S cm^{-1} was reached by the 5 wt% LNO composite, which is 17% higher than of CCO, but with further increasing amounts of LNO the electrical conductivity diminished. The improved values can be explained by the occurrence of the La(Co,Ni)O₃ phase, which is known for its comparatively high electrical conductivity [59]. The decreasing values after 5 wt% LNO could be caused by an unfavorable ratio of CCO to LNO leading to more contacts between LNO particles and more incomplete reactions. A deeper insight on the temperature dependency of the electrical conductivity is given in Fig. S5 in terms of an Arrhenius plot. A comparison of the activation energies of the electronic transport showed a general increase with higher amounts of LNO and a significant rise for the samples with 20 wt% and 40 wt% LNO. This means the transport behavior becomes more sensitive to temperature with increasing amounts of LNO. The nearly unchanged activation energy for the 1 wt% and 5 wt% samples could mean that low amounts do not hinder the electronic transport and can even be beneficial concerning

the electrically conductive La(Co,Ni)O₃ phase. A metallic-to-semiconducting transition at roughly 600 K was also noticed, which corresponds to reported values for CCO [60,61]. The Seebeck coefficient in Fig. 6b is usually inversely coupled with the electrical conductivity and is decreasing for all the CCO/LNO ceramic composites. This is caused by the lower Seebeck coefficients of the additional phases besides CCO. While LNO is also a *p*-type material, undoped LaNiO₃ is an *n*-type material with low negative Seebeck coefficients. Although, by substituting Ni with Co as it is the case here, the perovskite material becomes *p*-type and fits better with the CCO [59]. The reaction product Ca₃Co₂O₆ on the other hand has a higher Seebeck coefficient than the CCO but a lower electrical conductivity [62,63]. The combination of electrical conductivity and Seebeck coefficient results in the power factor shown in Fig. 6c. The 1 wt% and 5 wt% LNO samples both show a higher power factor while higher amounts of LNO lead to lower values. This means in both cases the increase in electrical conductivity outweighed the decrease of the Seebeck coefficient. For a complete picture of the

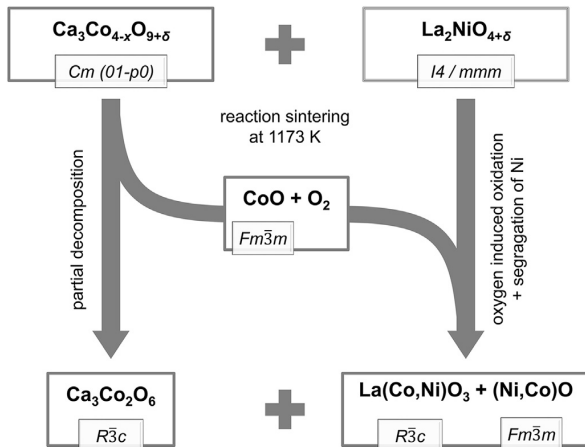


Fig. 5. Reaction scheme for the reaction sintering. The matrix CCO partially decomposes and the LNO mainly reacts to $\text{La}(\text{Co,Ni})\text{O}_3$ and $(\text{Ni,Co})\text{O}$.

thermoelectric properties, the heat conductivity λ is displayed in Fig. 6d. Overall, the heat conductivities of all measured samples are relatively low, which can be attributed to their high porosity [64]. The 1 wt% and 5 wt% samples show a decreased heat conductivity for temperatures below 873 K and 973 K respectively, while for the 10 wt% sample the values did deviate only slightly with the temperature and stay around the best value of CCO at 1073 K. This results in better average values for the CCO/LNO ceramic composites in comparison to CCO concerning the temperature range. Note that the values of λ above 573 K were fitted to the measurements parallel to the pressing direction, because the oxygen-helium atmosphere did not allow higher temperatures with the used setup (compare Fig. S6). A comparison of measurements in both

directions from the literature validates this method, as the temperature dependent trend is comparable [65,66]. The fact that all measured values for the heat conductivity parallel and perpendicular to the pressing direction differ proves anisotropy to some extent within the ceramic samples and the importance of combining the thermoelectric properties with the same direction.

The overall picture of the thermoelectric properties perpendicular to the pressing direction including two different Ioffe plots and the figure-of-merit zT is given in Fig. 7. The type-I Ioffe plot in Fig. 7a shows the power factor against the electrical conductivity. By this portrayal, the reason for the increased power factors of the 1 wt% and 5 wt% LNO samples gets obvious as the electrical conductivity increases. The type-II Ioffe plot in Fig. 7b on the other hand shows the thermal properties in terms of entropy conductivity Λ against the electrical conductivity. The minimum value of CCO could not be lowered in the ceramic composites, but the decreasing maximum value resulted in a better average value. The figure-of-merit zT is the combination of power factor and entropy conductivity and displayed in Fig. 7c as a function of the temperature. The 1 wt% LNO sample showed a higher power factor, but the increased entropy conductivity at 973 K and 1073 K led to a lower maximum zT than the CCO. The even higher power factor and slightly lower entropy conductivity of the 5 wt% LNO sample led to a similar maximum zT of 0.27 as the CCO. At the same time, the average zT was increased significantly by about 20% from 473 K to 1073 K. The average and maximum zT of the 10 wt% sample both decrease in comparison to CCO due to the shrinking power factor. Overall, the maximum zT could not be increased by the CCO/LNO ceramic composites, but a significantly higher average value was reached by the 5 wt% LNO sample for a temperature range of 373 K to 1073 K.

4. Conclusions

The combination of undoped $\text{Ca}_3\text{Co}_{4-x}\text{O}_{9+\delta}$ and $\text{La}_2\text{NiO}_{4+\delta}$ in ceramic composites with varying ratios was investigated with respect to

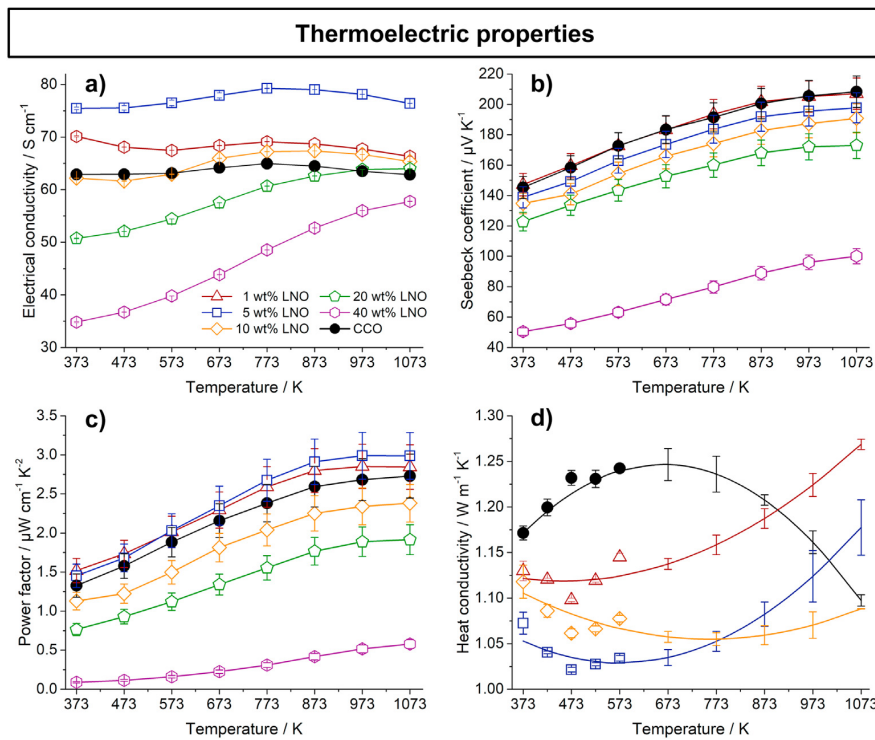


Fig. 6. Thermoelectric properties of the CCO/LNO ceramic composites perpendicular to the pressing direction in dependence on temperature with standard deviations. a) Electrical conductivity σ with increased values for the 1 wt% and 5 wt% LNO samples in comparison to CCO. b) Seebeck coefficient α with decreasing values for all ceramic composites. c) Power factor with increased values for the 1 wt% and 5 wt% LNO samples. d) Heat conductivity λ with increased values at high temperatures and decreased values at lower temperatures for the ceramic composites. Values above 573 K for the heat conductivity were gained by transferring fits and error bars for measurements parallel to the pressing direction (see Fig. S4).

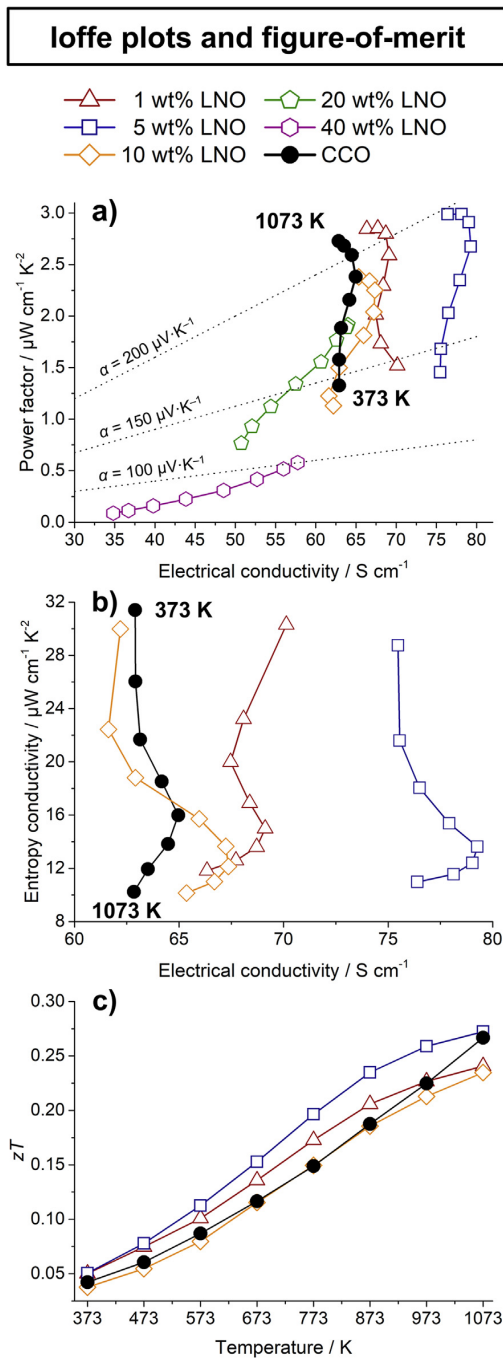


Fig. 7. Ioffe plots with 100 K temperature steps and figure-of-merit zT of the CCO/LNO ceramic composites. a) Type-I Ioffe plot with the power factor against the electrical conductivity σ . The samples with 1 wt% and 5 wt% LNO show a higher power factor than the CCO. b) Type-II Ioffe plot with the entropy conductivity Λ against the electrical conductivity σ . No composite has a lower entropy conductivity in comparison to CCO, but the overall range diminishes. c) Combined power factor and entropy conductivity in figure-of-merit zT against the temperature. The 5 wt% LNO sample shows the best properties with an increased average zT in the temperature range of 373 K to 1073 K.

the thermoelectric properties. The choice of undoped $\text{Ca}_3\text{Co}_{4-x}\text{O}_{9+\delta}$ enabled the determination of reasons for changing thermoelectric properties, but future research could include a doped matrix or additional phases for possible improvements. Microstructure analysis by XRD, SEM, EDXS and TEM showed both compounds reacting with each other during the sintering, resulting in the partial formation of $\text{Ca}_3\text{Co}_2\text{O}_6$ and $\text{La}(\text{Co,Ni})\text{O}_3$. The matrix material without contact to $\text{La}_2\text{NiO}_{4+\delta}$ was apparently not influenced and showed microtwins as stacking faults. The power factor of the 1 wt% and 5 wt% $\text{La}_2\text{NiO}_{4+\delta}$ composites were improved despite a diminishing Seebeck coefficient, because of the increased electrical conductivity resulting from the $\text{La}(\text{Co,Ni})\text{O}_3$ phase. Thermal conductivity of these samples was not lowered at higher temperatures, but the average value was improved. This resulted in a similar maximum figure-of-merit zT of 0.27 for the best composite with 5 wt% $\text{La}_2\text{NiO}_{4+\delta}$ in comparison to pure $\text{Ca}_3\text{Co}_{4-x}\text{O}_{9+\delta}$, but the average zT in the temperature range of 373 K to 1073 K could be increased by about 20%.

Declaration of interest

The authors declare that they have no known competing financial interests or personal relationships that could have appeared to influence the work reported in this paper.

Acknowledgements

This work was supported by the Deutsche Forschungsgemeinschaft (DFG, German Research Foundation) - project number 325156807. Authors gratefully appreciate technical assistance by F. Steinbach.

Appendix A. Supplementary data

Supplementary data to this article can be found online at <https://doi.org/10.1016/j.oceram.2021.100103>.

References

- [1] G. Tan, L.-D. Zhao, M.G. Kanatzidis, Rationally designing high-performance bulk thermoelectric materials, *Chem. Rev.* 116 (2016) 12123–12149, <https://doi.org/10.1021/acs.chemrev.6b00255>.
- [2] S.J. Poon, Recent advances in thermoelectric performance of half-Heusler compounds, *Metals* 8 (2018) 989, <https://doi.org/10.3390/met8120989>.
- [3] J. Shuai, J. Mao, S. Song, Q. Zhang, G. Chen, Z. Ren, Recent progress and future challenges on thermoelectric Zintl materials, *Mater. Today Phys.* 1 (2017) 74–95, <https://doi.org/10.1016/j.mtphys.2017.06.003>.
- [4] Q. Zhang, Y. Sun, W. Xu, D. Zhu, Organic thermoelectric materials: emerging green energy materials converting heat to electricity directly and efficiently, *Adv. Mater.* 26 (2014) 6829–6851, <https://doi.org/10.1002/adma.201305371>.
- [5] Y. Yin, B. Tudu, A. Tiwari, Recent advances in oxide thermoelectric materials and modules, *Vacuum* 146 (2017) 356–374, <https://doi.org/10.1016/j.vacuum.2017.04.015>.
- [6] L.-D. Zhao, J. He, D. Berardan, Y. Lin, J.-F. Li, C.-W. Nan, N. Drago, BiCuSeO oxyselenides: new promising thermoelectric materials, *Energy Environ. Sci.* 7 (2014) 2900–2924, <https://doi.org/10.1039/c4ee00997e>.
- [7] J.W. Fergus, Oxide materials for high temperature thermoelectric energy conversion, *J. Eur. Ceram. Soc.* 32 (2012) 525–540, <https://doi.org/10.1016/j.jeurceramsoc.2011.10.007>.
- [8] E. Woermann, A. Muan, Phase equilibria in the system CaO-cobalt oxide in air, *J. Inorg. Nucl. Chem.* 32 (1970) 1455–1459, [https://doi.org/10.1016/0022-1902\(70\)80631-5](https://doi.org/10.1016/0022-1902(70)80631-5).
- [9] N. Kanas, S.P. Singh, M. Rotan, M. Saleemi, M. Bittner, A. Feldhoff, T. Norby, K. Wiik, T. Grande, M.-A. Einarsrud, Influence of processing on stability, microstructure and thermoelectric properties of $\text{Ca}_3\text{Co}_{4-x}\text{O}_{9+\delta}$, *J. Eur. Ceram. Soc.* 38 (2018) 1592–1599, <https://doi.org/10.1016/j.jeurceramsoc.2017.11.011>.
- [10] Y. Miyazaki, Crystal structure and thermoelectric properties of the misfit-layered cobalt oxides, *Solid State Ionics* 172 (2004) 463–467, <https://doi.org/10.1016/j.ssi.2004.01.046>.
- [11] Y. Miyazaki, M. Onoda, T. Oku, M. Kikuchi, Y. Ishii, Y. Ono, Y. Morii, T. Kajitani, Modulated structure of the thermoelectric compound $[\text{Ca}_2\text{CoO}_3]_{0.62}\text{CoO}_2$, *J. Phys. Soc. Jpn.* 71 (2002) 491–497, <https://doi.org/10.1143/JPSJ.71.491>.
- [12] H.U. Fuchs, A direct entropic approach to uniform and spatially continuous dynamical models of thermoelectric devices, *Energy Harvesting and Systems* 1 (2014), <https://doi.org/10.1515/ehs-2014-0011>.

- [13] A. Feldhoff, Thermoelectric material tensor derived from the Onsager–de Groot–Callen model, *Energy Harvesting and Systems* 2 (2015), <https://doi.org/10.1515/ehs-2014-0040>.
- [14] A. Feldhoff, Power conversion and its efficiency in thermoelectric materials, *Entropy* 22 (2020) 803, <https://doi.org/10.3390/e22080803>.
- [15] M. Wolf, R. Hinterding, A. Feldhoff, High power factor vs. high zT —A review of thermoelectric materials for high-temperature application, *Entropy* 21 (2019) 1058, <https://doi.org/10.3390/e21111058>.
- [16] Q. Zhang, X. Ai, L. Wang, Y. Chang, W. Luo, W. Jiang, L. Chen, Improved thermoelectric performance of silver nanoparticles-dispersed Bi_2Te_3 composites deriving from hierarchical two-phased heterostructure, *Adv. Funct. Mater.* 25 (2015) 966–976, <https://doi.org/10.1002/adfm.201402663>.
- [17] W. Liu, X. Yan, G. Chen, Z. Ren, Recent advances in thermoelectric nanocomposites, *Nano Energy* 1 (2012) 42–56, <https://doi.org/10.1016/j.nanoen.2011.10.001>.
- [18] K. Kato, K. Kuriyama, T. Yabuki, K. Miyazaki, Organic-inorganic thermoelectric material for a printed generator, *J. Phys. Conf. Ser.* 1052 (2018), <https://doi.org/10.1088/1742-6596/1052/1/012008>, 012008.
- [19] B. Zhang, J. Sun, H.E. Katz, F. Fang, R.L. Opila, Promising thermoelectric properties of commercial PEDOT:PSS materials and their Bi_2Te_3 powder composites, *ACS Appl. Mater. Interfaces* 2 (2010) 3170–3178, <https://doi.org/10.1021/am100654p>.
- [20] N. Toshima, Recent progress of organic and hybrid thermoelectric materials, *Synth. Met.* 225 (2017) 3–21, <https://doi.org/10.1016/j.synthmet.2016.12.017>.
- [21] M. Culebras, A. García-Barberá, J.F. Serrano-Claumarchirant, C.M. Gómez, A. Cantarero, Hybrids composites of NCCO/PEDOT for thermoelectric applications, *Synth. Met.* 225 (2017) 103–107, <https://doi.org/10.1016/j.synthmet.2016.12.016>.
- [22] J.N. Coleman, M. Lotya, A. O'Neill, S.D. Bergin, P.J. King, U. Khan, K. Young, A. Gaucher, S. De, R.J. Smith, I.V. Shvets, S.K. Arora, G. Stanton, H.-Y. Kim, K. Lee, G.T. Kim, G.S. Duesberg, T. Hallam, J.J. Boland, J.J. Wang, J.F. Donegan, J.C. Grunlan, G. Moriarty, A. Shmeliov, R.J. Nicholls, J.M. Perkins, E.M. Grievson, K. Theuwissen, D.W. McComb, P.D. Nellist, V. Nicolosi, Two-dimensional nanosheets produced by liquid exfoliation of layered materials, *Science* 331 (2011) 568–571, <https://doi.org/10.1126/science.1194975>.
- [23] Q. Yao, L. Chen, W. Zhang, S. Liufu, X. Chen, Enhanced thermoelectric performance of single-walled carbon nanotubes/polyaniline hybrid nanocomposites, *ACS Nano* 4 (2010) 2445–2451, <https://doi.org/10.1021/nn1002562>.
- [24] Y. Song, Q. Sun, L. Zhao, F. Wang, Z. Jiang, Synthesis and thermoelectric power factor of $(\text{Ca}_{0.95}\text{Bi}_{0.05})_3\text{Co}_4\text{O}_9/\text{Ag}$ composites, *Mater. Chem. Phys.* 113 (2009) 645–649, <https://doi.org/10.1016/j.matchemphys.2008.08.029>.
- [25] F. Kahraman, M.A. Madre, S. Rasekh, C. Salvador, P. Bosque, M.A. Torres, J.C. Diez, A. Sotelo, Enhancement of mechanical and thermoelectric properties of $\text{Ca}_3\text{Co}_4\text{O}_9$ by Ag addition, *J. Eur. Ceram. Soc.* 35 (2015) 3835–3841, <https://doi.org/10.1016/j.jeurceramsoc.2015.05.029>.
- [26] Z. Shi, C. Zhang, T. Su, J. Xu, J. Zhu, H. Chen, T. Gao, M. Qin, P. Zhang, Y. Zhang, H. Yan, F. Gao, Boosting the thermoelectric performance of calcium cobaltite composites through structural defect engineering, *ACS Appl. Mater. Interfaces* 12 (2020) 21623–21632, <https://doi.org/10.1021/acami.0c03297>.
- [27] M. Wolf, K. Menekse, A. Mundstock, R. Hinterding, F. Nietschke, O. Oeckler, A. Feldhoff, Low thermal conductivity in thermoelectric oxide-based multiphase composites, *J. Electron. Mater.* 48 (2019) 7551–7561, <https://doi.org/10.1007/s11664-019-07555-2>.
- [28] M. Bittner, N. Kanas, R. Hinterding, F. Steinbach, D. Groeneveld, P. Wemhoff, K. Wiik, M.-A. Einarsrud, A. Feldhoff, Triple-phase ceramic 2D nanocomposite with enhanced thermoelectric properties, *J. Eur. Ceram. Soc.* 39 (2019) 1237–1244, <https://doi.org/10.1016/j.jeurceramsoc.2018.10.023>.
- [29] Y. Wang, Y. Sui, J. Cheng, X. Wang, W. Su, Comparison of the high temperature thermoelectric properties for Ag-doped and Ag-added $\text{Ca}_3\text{Co}_4\text{O}_9$, *J. Alloys Compd.* 477 (2009) 817–821, <https://doi.org/10.1016/j.jallcom.2008.10.162>.
- [30] S. Saini, H.S. Yaddanapudi, K. Tian, Y. Yin, D. Maggini, A. Tiwari, Terbium ion doping in $\text{Ca}_3\text{Co}_4\text{O}_9$: a step towards high-performance thermoelectric materials, *Sci. Rep.* 7 (2017) 44621, <https://doi.org/10.1038/srep44621>.
- [31] S. Li, R. Funahashi, I. Matsubara, K. Ueno, S. Sodeoka, H. Yamada, Synthesis and thermoelectric properties of the new oxide materials $\text{Ca}_{3-x}\text{Bi}_x\text{Co}_4\text{O}_{9+\delta}$ ($x = 0.75$), *Chem. Mater.* 12 (2000) 2424–2427, <https://doi.org/10.1021/cm000132r>.
- [32] F. Delorme, P. Diaz-Chao, F. Giovannelli, Effect of Ca substitution by Fe on the thermoelectric properties of $\text{Ca}_3\text{Co}_4\text{O}_9$ ceramics, *J. Electroceram.* 40 (2018) 107–114, <https://doi.org/10.1007/s10832-018-0109-2>.
- [33] D. Wang, L. Chen, Q. Yao, J. Li, High-temperature thermoelectric properties of $\text{Ca}_3\text{Co}_4\text{O}_{9+\delta}$ with Eu substitution, *Solid State Commun.* 129 (2004) 615–618, <https://doi.org/10.1016/j.ssc.2003.11.045>.
- [34] N.V. Nong, C.-J. Liu, M. Ohtaki, High-temperature thermoelectric properties of late rare earth-doped $\text{Ca}_3\text{Co}_4\text{O}_{9+\delta}$, *J. Alloys Compd.* 509 (2011) 977–981, <https://doi.org/10.1016/j.jallcom.2010.09.150>.
- [35] M. Shikano, R. Funahashi, Electrical and thermal properties of single-crystalline $(\text{Ca}_2\text{Co}_2\text{O}_7)_n\text{CoO}_2$ with a $\text{Ca}_3\text{Co}_4\text{O}_9$ structure, *Appl. Phys. Lett.* 82 (2003) 1851–1853, <https://doi.org/10.1063/1.1562337>.
- [36] D.J. Bergman, O. Levy, Thermoelectric properties of a composite medium, *J. Appl. Phys.* 70 (1991) 6821–6833, <https://doi.org/10.1063/1.349830>.
- [37] D.J. Bergman, L.G. Fel, Enhancement of thermoelectric power factor in composite thermoelectrics, *J. Appl. Phys.* 85 (1999) 8205–8216, <https://doi.org/10.1063/1.370660>.
- [38] R. Hinterding, Z. Zhao, C. Zhang, A. Feldhoff, Anisotropic growth of $\text{La}_2\text{NiO}_{4+\delta}$: influential pre-treatment in molten-flux synthesis, *J. Cryst. Growth* 523 (2019) 125135, <https://doi.org/10.1016/j.jcrysgro.2019.06.021>.
- [39] T. Klände, K. Efimov, S. Cusenza, K.-D. Becker, A. Feldhoff, Effect of doping, microstructure, and CO_2 on $\text{La}_2\text{NiO}_{4+\delta}$ -based oxygen-transporting materials, *J. Solid State Chem.* 184 (2011) 3310–3318, <https://doi.org/10.1016/j.jssc.2011.10.019>.
- [40] V. Kharton, A. Yaremchenko, E. Tsipis, A. Valente, M. Patrakeev, A. Shaula, J. Frade, J. Rocha, Characterization of mixed-conducting $\text{La}_2\text{NiO}_9\text{Co}_{0.1}\text{O}_{4+\delta}$ membranes for dry methane oxidation, *Appl. Catal. Gen.* 261 (2004) 25–35, <https://doi.org/10.1016/j.apcata.2003.10.028>.
- [41] S.-Y. Jeon, M.-B. Choi, J.-H. Hwang, E.D. Wachsman, S.-J. Song, Electrical conductivity and thermoelectric power of $\text{La}_2\text{NiO}_{4+\delta}$, *J. Electrochem. Soc.* 158 (2011) B476, <https://doi.org/10.1149/1.3559186>.
- [42] V. Pardo, A.S. Botana, D. Baldomir, Enhanced thermoelectric response of hole-doped $\text{La}_2\text{NiO}_{4+\delta}$ from ab initio calculations, *Phys. Rev. B* 86 (2012), <https://doi.org/10.1103/PhysRevB.86.165114>.
- [43] C.G.S. Pillai, A.M. George, Thermal conductivity of La_2CuO_4 , La_2NiO_4 , and Nd_2CuO_4 in the semiconducting and metallic phases, *Int. J. Thermophys.* 7 (1986) 1091–1100, <https://doi.org/10.1007/BF00502380>.
- [44] M. Burriel, J. Santiso, M.D. Rossell, G. van Tendeloo, A. Figueras, G. Garcia, Enhancing total conductivity of $\text{La}_2\text{NiO}_{4+\delta}$ epitaxial thin films by reducing thickness, *J. Phys. Chem. C* 112 (2008) 10982–10987, <https://doi.org/10.1021/jp7101622>.
- [45] W. Paulus, A. Cousson, G. Dhalleen, J. Berthon, A. Revcolevschi, S. Hosoya, W. Treutmann, G. Heger, R. Le Toquin, Neutron diffraction studies of stoichiometric and oxygen intercalated La_2NiO_4 single crystals, *Solid State Sci.* 4 (2002) 565–573, [https://doi.org/10.1016/S1293-2558\(02\)01299-2](https://doi.org/10.1016/S1293-2558(02)01299-2).
- [46] M. Brunelli, M. Coduri, M. Ceretti, W. Paulus, Local apical oxygen disorder in oxygen rich $\text{La}_2\text{NiO}_{4.18}$, comparing neutron single crystal and n/χ -PDF analysis from powder diffraction data, *J. Phys. Appl. Phys.* 48 (2015) 504009, <https://doi.org/10.1088/0022-3727/48/5/040009>.
- [47] A.F. Ioffe, *Semiconductor Thermoelements and Thermoelectric Cooling*, first ed., Info-search Ltd., London, 1957.
- [48] T. Janssen, A. Janner, A. Looijenga-Vos, P.M. De Wolff, *International Tables for Crystallography: 9.8 Incommensurate and Commensurate Modulated Structures*, vol. 3, Kluwer Acad. Publ. Dordrecht, 2004.
- [49] T. Janssen, G. Chapuis, M. de Boissieu, *Periodic Crystals: from Modulated Phases to Quasicrystals*, Volume 20 of International Union of Crystallography Monographs on Crystallography, Oxford University Press, Oxford and New York, 2007.
- [50] N. Kanas, G. Skomedal, T.D. Desissa, A. Feldhoff, T. Grande, K. Wiik, M.-A. Einarsrud, Performance of a thermoelectric module based on n -type $(\text{La}_{0.12}\text{Sr}_{0.88})_{0.95}\text{TiO}_{3-\delta}$ and p -type $\text{Ca}_3\text{Co}_{4-x}\text{O}_{9+\delta}$, *J. Electron. Mater.* 49 (2020) 4154–4159, <https://doi.org/10.1007/s11664-020-08127-5>.
- [51] A.C. Masset, C. Michel, A. Maignan, M. Hervieu, O. Toulemonde, F. Studer, B. Raveau, J. Hejtmanek, Misfit-layered cobaltite with an anisotropic giant magnetoresistance: $\text{Ca}_3\text{Co}_4\text{O}_9$, *Phys. Rev. B* 62 (2000) 166–175, <https://doi.org/10.1103/PhysRevB.62.166>.
- [52] K. Efimov, T. Klände, N. Juditzki, A. Feldhoff, Ca-containing CO_2 -tolerant perovskite materials for oxygen separation, *J. Membr. Sci.* 389 (2012) 205–215, <https://doi.org/10.1016/j.memsci.2011.10.030>.
- [53] C.B. Carter, Electron diffraction from microtwins and long-period polytypes, *Philos. Mag.* A 50 (1984) 133–141, <https://doi.org/10.1080/01418618408244217>.
- [54] D. Sedmidubský, V. Jakes, O. Jankovský, J. Leitner, Z. Sofer, J. Hejtmanek, Phase equilibria in Ca–Co–O system, *J. Solid State Chem.* 194 (2012) 199–205, <https://doi.org/10.1016/j.jssc.2012.05.014>.
- [55] G. Constantinescu, A.R. Sarabando, S. Rasekh, D. Lopes, S. Sergiienko, P. Amirkhizi, J.R. Frade, A.V. Kovalevsky, Redox-promoted tailoring of the high-temperature electrical performance in $\text{Ca}_3\text{Co}_4\text{O}_9$ thermoelectric materials by metallic cobalt addition, *Materials* 13 (2020), <https://doi.org/10.3390/ma13051060>.
- [56] N. Gauquelin, T.E. Weirich, M. Ceretti, W. Paulus, M. Schroeder, Long-term structural surface modifications of mixed conducting $\text{La}_2\text{NiO}_{4+\delta}$ at high temperatures, *Monatshfte für Chemie - Chemical Monthly* 140 (2009) 1095–1102, <https://doi.org/10.1007/s00706-009-0146-2>.
- [57] R. Sayers, S.J. Skinner, Evidence for the catalytic oxidation of $\text{La}_2\text{NiO}_{4+\delta}$, *J. Mater. Chem.* 21 (2011) 414–419, <https://doi.org/10.1039/c0jm02419h>.
- [58] Y. Adachi, N. Hatada, K. Hirota, M. Kato, T. Uda, Preparation of pure and fully dense lanthanum nickelates $\text{La}_{n+1}\text{Ni}_n\text{O}_{3n+1}$ ($n = 2, 3, \infty$) by post-sintering oxidation process, *J. Am. Ceram. Soc.* 102 (2019) 7077–7088, <https://doi.org/10.1111/jace.16611>.
- [59] P. Migiaakis, J. Androulakis, J. Giapintzakis, Thermoelectric properties of $\text{LaNi}_{1-x}\text{Co}_x\text{O}_3$ solid solution, *J. Appl. Phys.* 94 (2003) 7616, <https://doi.org/10.1063/1.1629393>.
- [60] Y.-H. Lin, J. Lan, Z. Shen, Y. Liu, C.-W. Nan, J.-F. Li, High-temperature electrical transport behaviors in textured $\text{Ca}_3\text{Co}_4\text{O}_9$ -based polycrystalline ceramics, *Appl. Phys. Lett.* 94 (2009), <https://doi.org/10.1063/1.3086875>, 072107.
- [61] G. Constantinescu, S.M. Mikhalev, A.D. Lisenkov, D.V. Lopes, A.R. Sarabando, M.C. Ferro, T.F.d. Silva, S.A. Sergiienko, A.V. Kovalevsky, Prospects for electrical performance tuning in $\text{Ca}_3\text{Co}_4\text{O}_9$ materials by metallic Fe and Ni particles additions, *Materials* 14 (2021), <https://doi.org/10.3390/ma14040980>.
- [62] M. Tahashi, K. Ogawa, M. Takahashi, H. Goto, Effect of compositional ratio of cobalt to calcium on crystal phase and thermoelectric properties of oxide thermoelectric material composed of sintered $\text{Ca}_3\text{Co}_4\text{O}_9/\text{Ca}_2\text{Co}_2\text{O}_6$ mixture, *J. Ceram. Soc. Jpn.* 121 (2013) 444–447, <https://doi.org/10.2109/jcersj2.121.444>.
- [63] N. Kanas, S. Singh, M. Rotan, T. Desissa, T. Grande, K. Wiik, T. Norby, M.-A. Einarsrud, Thermoelectric properties of $\text{Ca}_3\text{Co}_{2-x}\text{Mn}_x\text{O}_6$ ($x = 0.05, 0.2, 0.5, 0.75, \text{ and } 1$), *Materials* 12 (2019) 497, <https://doi.org/10.3390/ma12030497>.

- [64] M. Bittner, L. Helmich, F. Nietschke, B. Geppert, O. Oeckler, A. Feldhoff, Porous $\text{Ca}_3\text{Co}_4\text{O}_9$ with enhanced thermoelectric properties derived from sol-gel synthesis, *J. Eur. Ceram. Soc.* 37 (2017) 3909–3915, <https://doi.org/10.1016/j.jeurceramsoc.2017.04.059>.
- [65] D. Kenfaoui, B. Lenoir, D. Chateigner, B. Ouladdiaf, M. Gomina, J.G. Noudem, Development of multilayer textured $\text{Ca}_3\text{Co}_4\text{O}_9$ materials for thermoelectric generators: influence of the anisotropy on the transport properties, *J. Eur. Ceram. Soc.* 32 (2012) 2405–2414, <https://doi.org/10.1016/j.jeurceramsoc.2012.03.022>.
- [66] C.-H. Lim, W.-S. Seo, S. Lee, Y.S. Lim, J.-Y. Kim, H.-H. Park, S.-M. Choi, K.H. Lee, K. Park, Anisotropy of the thermoelectric figure of merit (ZT) in textured $\text{Ca}_3\text{Co}_4\text{O}_9$ ceramics prepared by using a spark plasma sintering process, *J. Kor. Phys. Soc.* 66 (2015) 794–799, <https://doi.org/10.3938/jkps.66.794>.

Supporting information:**Ceramic composites based on $\text{Ca}_3\text{Co}_{4-x}\text{O}_{9+\delta}$ and $\text{La}_2\text{NiO}_{4+\delta}$ with enhanced thermoelectric properties**R. Hinterding^a, Z. Zhao^a, M. Wolf^a, M. Jakob^b, O. Oeckler^b, A. Feldhoff^a^aLeibniz University Hannover, Institute of Physical Chemistry and Electrochemistry, Callinstr. 3A, D-30167 Hannover, Germany^bLeipzig University, Institute of Mineralogy, Crystallography and Materials Science, Scharnhorststr. 20, D-04275 Leipzig, Germany

For gaining the ceramic composites, two different oxide powders consisting of $\text{Ca}_3\text{Co}_{4-x}\text{O}_{9+\delta}$ (CCO) and $\text{La}_2\text{NiO}_{4+\delta}$ (LNO) were used. To ensure phase purity of these components, XRD patterns and SEM micrographs of both were measured and are displayed in Fig. S1. The XRD in Fig. S1a confirms the identity of the CCO phase, but also some minor impurities of Co_3O_4 . Since the Co_3O_4 is not detectable anymore after sintering as shown in the section 3.1, its role should be negligible. The relatively low signal to noise ratio is caused by the small crystal size as displayed in Fig. S1b. The SEM micrograph shows sheets, which are typical for CCO, with a thickness of ca. 30 nm and a lateral extension about 200-500 nm. The XRD of the LNO powder in Fig. S1c on the other hand shows only reflections of the desired phase and has a way higher signal to noise ratio, indicating a larger crystal size. The crystals in Fig. S1d show plate-like and cuboidal shapes, which means they are not completely uniform.

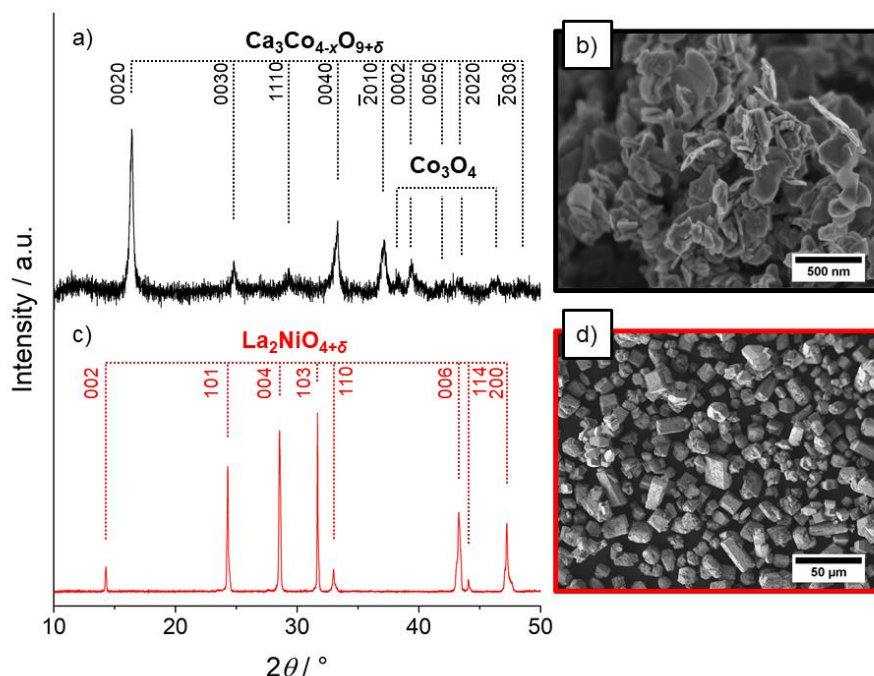


Figure S1: XRD patterns and SEM micrographs of the composite compounds a-b) $\text{Ca}_3\text{Co}_{4-x}\text{O}_{9+\delta}$ and c-d) $\text{La}_2\text{NiO}_{4+\delta}$ as powder materials.

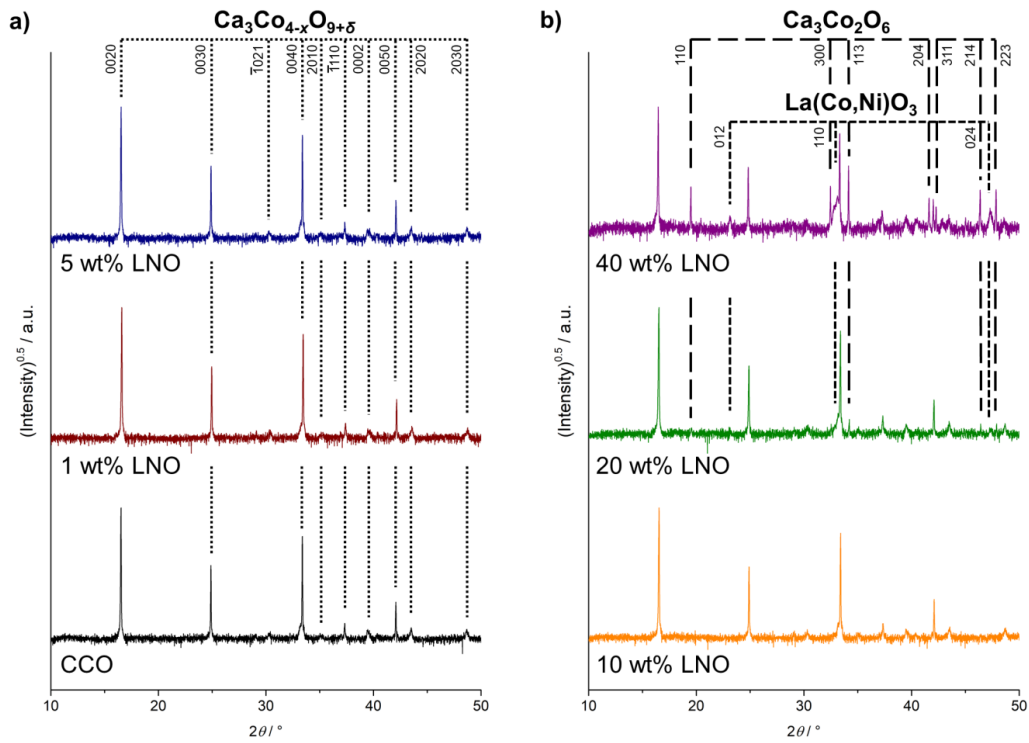


Figure S2: XRD patterns of the CCO/LNO ceramic composites after sintering. Samples with a) 0, 1 and 5 wt% LNO or b) 10, 20 and 40 wt% LNO. Intensity is given as a square root to make the identification of small additional reflections easier.

Fig. S2 shows the XRD patterns of the ceramic composites after sintering. For the 0-10 wt% LNO composites, the XRD patterns show only the reflections for CCO. At 20 and 40 wt% the signals of $\text{La}(\text{Co,Ni})\text{O}_3$ and $\text{Ca}_3\text{Co}_2\text{O}_6$ become apparent.

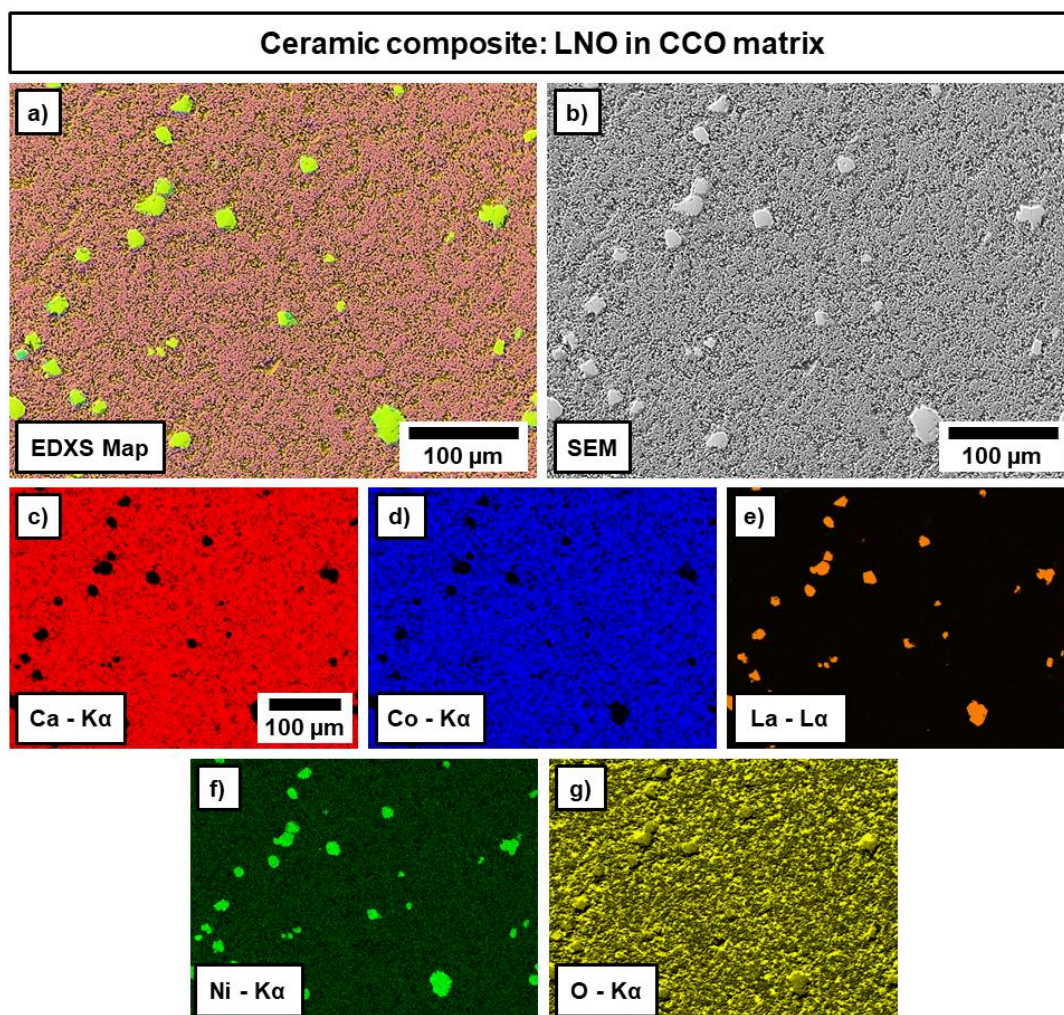


Figure S3: Cross-sectional SEM-EDXS analysis of the 5 wt% LNO sample showing the distribution of LNO within the CCO matrix. a) Overlay EDXS mapping summarizing the results from b-g. b) SEM micrograph as basis for EDXS analysis. d-g) Elemental distributions of the respective elements Ca, Co, La, Ni and O.

An overview for the distribution of LNO within the CCO matrix is given in Fig. S3. The elemental mapping in Fig. S3a shows the LNO particles mostly not in contact to each other. Calcium and cobalt are mostly located within the CCO matrix, while lanthanum and nickel remain in the LNO particles. Oxygen appears in all visible phases as they are oxides.

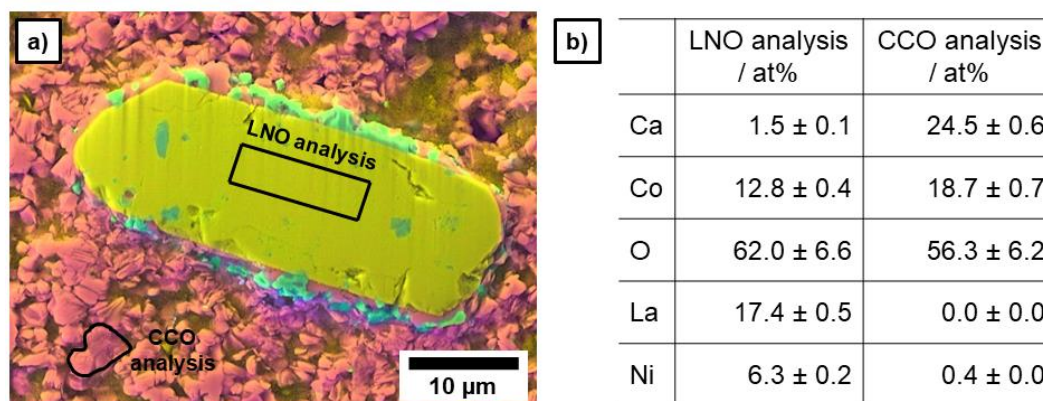


Figure S4: Cross-sectional SEM-EDXS analysis of the 5 wt% LNO sample. a) Overlay EDXS mapping extracted from Fig. 2 with marked areas used for quantitative analysis. b) Results of the quantitative EDXS analysis for the relevant elements Ca, Co, O, La and Ni.

Fig. S4 shows the corresponding quantitative EDXS analysis for Fig. 2. Within the LNO particle the La:Ni ratio in the LNO was reduced from 2:1 to 2:0.72, which means that Ni segregated from the particle and possibly formed the surrounding (Ni,Co)O. The La:Co ratio increased from 2:0 to 2:1.47 and the final La:(Ni,Co) ratio resulted in 2:2.2, which is roughly about 1:1 and therefore supports the formation of $\text{La}(\text{Ni,Co})\text{O}_3$.

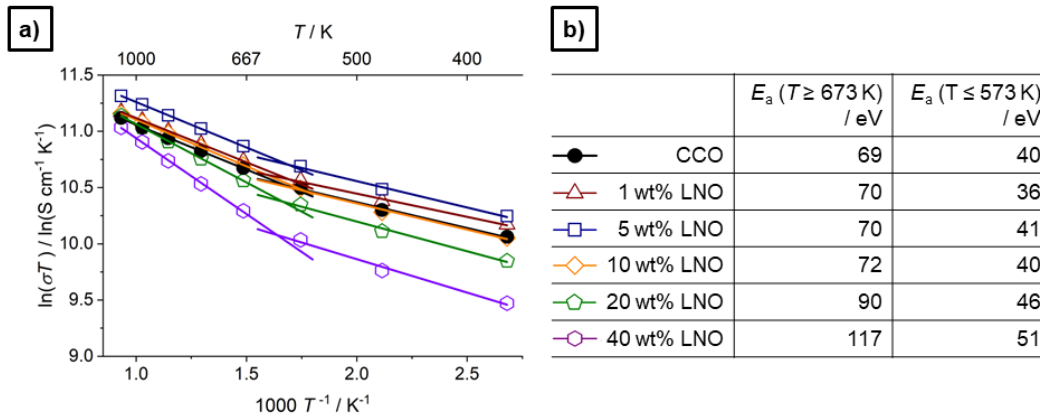


Figure S5: a) Arrhenius plot of the electrical conductivity measurements given in Fig. 6a. and b) the calculated activation energies for the high-temperature and low-temperature regions.

Fig. S5 shows the temperature dependency of the electrical conductivity in an Arrhenius plot. For this, the assumption of $\sigma \cdot T \propto \exp(-E_a/k_B T)$ was made [60,61]. The five data points with the highest temperatures (673-1073 K) were used for linear regression at high temperatures and the three remaining data points (373-573 K) for another linear regression at low temperatures. Two linear regressions were made for each sample as there is a clear change of the slope from 673 K to 573 K. This change can be attributed to a metallic-to-semiconducting transition regarding the transport behavior [60]. The slope of the lines can be used to calculate the activation energy of the electronic transport. A comparison of the measured samples shows a nearly constant activation energy for the pure CCO and the samples with 1-10 wt% LNO. This could mean that the additive does not hinder the electronic transport at these amounts and is even beneficial as long as it does not exceed 5 wt%. However, the activation energy is significantly rising for the 20 wt% and 40 wt% sample. Together with the lower values of the electrical conductivity this means the additive plays a major role for the electronic transport and also corresponds to a higher temperature sensitivity.

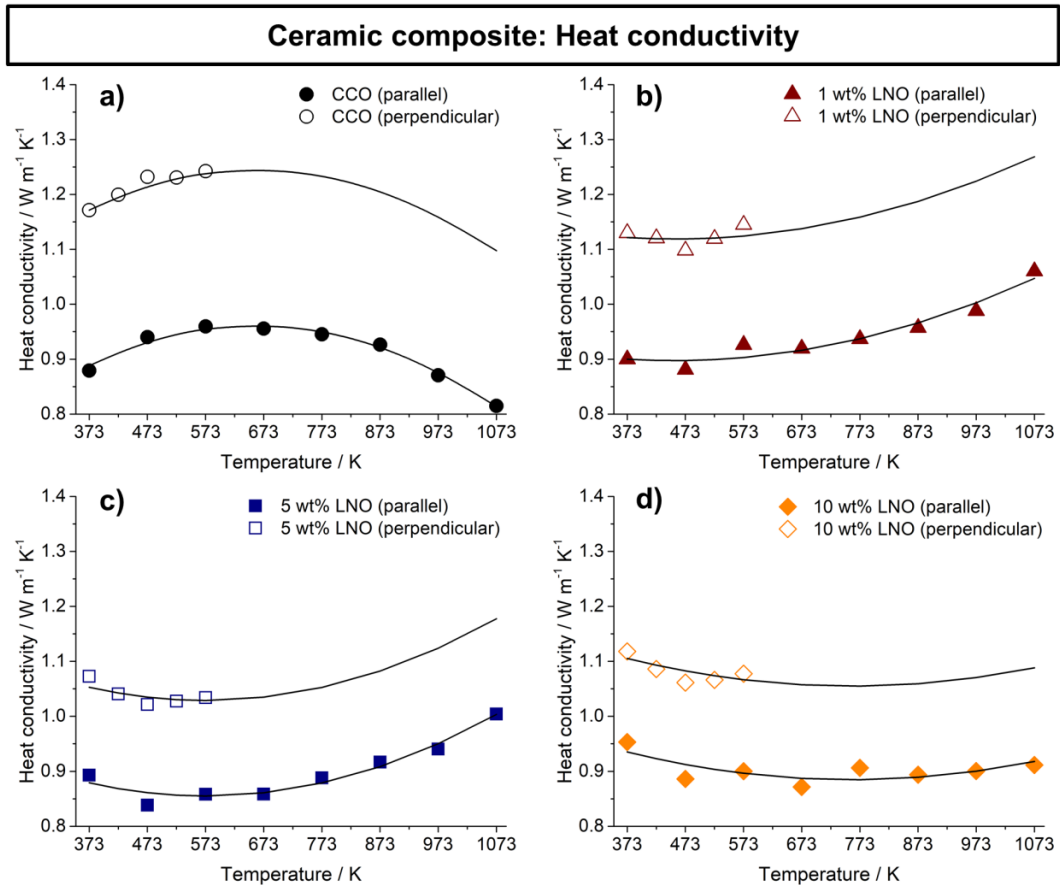


Figure S6: Heat conductivity measurements parallel and perpendicular to the pressing direction. The measurements were conducted for a) CCO, b) 1 wt% LNO, c) 5 wt% LNO and d) 10 wt% LNO samples. The fits were calculated for the parallel measurements and transferred to the perpendicular measurements to estimate the missing values at higher temperatures.

Fig. S6 shows the heat conductivity measurements parallel and perpendicular to the pressing direction. Both directions were necessary to see if the CCO/LNO ceramic composites show anisotropic transport properties. The higher heat conductivities perpendicular to the pressing direction are caused by a preferred orientation of the CCO and possibly by of the additional phases. As the heat conductivity of CCO is lower along the *c*-axis of the material, the CCO sheets were orientated partly by uniaxial pressing. The measurements parallel to the pressing direction required a graphite holder with a temperature limit of 573 K in the oxygen/helium atmosphere. Therefore, similar behaviors along both directions were assumed with good agreement to the measurements and fits for the parallel direction were calculated. These fits were transferred to the measurements perpendicular to the pressing direction to gain values for 673-1073 K.

2.1.4 Improved thermoelectric properties in ceramic composites based on $\text{Ca}_3\text{Co}_4\text{O}_9$ and $\text{Na}_2\text{Ca}_2\text{Nb}_4\text{O}_{13}$

Richard Hinterding, Mario Wolf, Matthias Jakob, Oliver Oeckler and Armin Feldhoff

Open Ceramics, 8 **2021**, 100198

DOI: 10.1016/j.oceram.2021.100198



Improved thermoelectric properties in ceramic composites based on $\text{Ca}_3\text{Co}_4\text{O}_9$ and $\text{Na}_2\text{Ca}_2\text{Nb}_4\text{O}_{13}$

R. Hinterding^{a,*}, M. Wolf^a, M. Jakob^b, O. Oeckler^b, A. Feldhoff^{a,**}

^a Leibniz University Hannover, Institute of Physical Chemistry and Electrochemistry, Callinstr. 3A, D-30167, Hannover, Germany

^b Leipzig University, Institute of Mineralogy, Crystallography and Materials Science, Scharnhorststr. 20, D-04275, Leipzig, Germany

ARTICLE INFO

Keywords:

Calcium cobalt oxide
Composite
Ceramic
Sodium calcium niobate
Reaction sintering
Thermoelectrics
Power factor
Figure-of-merit

ABSTRACT

The oxide materials $\text{Ca}_3\text{Co}_4\text{O}_9$ and $\text{Na}_2\text{Ca}_2\text{Nb}_4\text{O}_{13}$ were combined in a new ceramic composite with promising synergistic thermoelectric properties. Both compounds show a plate-like crystal shape and similar aspect ratios but the matrix material $\text{Ca}_3\text{Co}_4\text{O}_9$ with lateral sizes of less than 500 nm is about two orders of magnitude smaller. Uniaxial pressing of the mixed compound powders was used to produce porous ceramics after conventional sintering. Reactions between both compounds and their compositions were thoroughly investigated. In comparison to pure $\text{Ca}_3\text{Co}_4\text{O}_9$, mixing with low amounts of $\text{Na}_2\text{Ca}_2\text{Nb}_4\text{O}_{13}$ proved to be beneficial for the overall thermoelectric properties. A maximum figure-of-merit of $zT = 0.32$ at 1073 K and therefore an improvement of about 19% was achieved by the ceramic composites.

1. Introduction

1.1. Thermoelectric energy harvesting

Energy harvesting is a topic with great significance to a mindful handling of limited resources. One possible route is the utilization of the thermoelectric effect to convert thermal energy into electrical energy. Apart from the aspects of processing and optimization of thermoelectric generators, the thermoelectric performance of the underlying materials still needs to be improved. Many different material classes are relevant in thermoelectrics, which differentiate in maximum efficiency, electrical power output, optimum temperature, chemical stability or toxicity. Among the most promising there are tellurides [1], half-Heusler compounds [2], Zintl phases [3], polymers [4], oxides [5] and oxy-selenides [6]. Discussing the performance of thermoelectric materials requires the introduction of the fundamental thermoelectric material tensor in Eq. (1) [7–9].

$$\begin{pmatrix} I_q \\ I_S \end{pmatrix} = \frac{A}{L} \begin{pmatrix} \sigma & \sigma \cdot \alpha \\ \sigma \cdot \alpha & \sigma \cdot \alpha^2 + \Lambda \end{pmatrix} \cdot \begin{pmatrix} \Delta\varphi \\ \Delta T \end{pmatrix} \quad (1)$$

The tensor shows the coupling of currents of electrical charge I_q and entropy I_S for the energy conversion in a thermoelectric material with a cross-sectional area A and a length L [9]. The electrical potential

difference $\Delta\varphi$ and the temperature difference ΔT may cause a thermally-induced electrical current, which is dependent on the three material parameters: the isothermal electrical conductivity σ , the Seebeck coefficient α and the electrically open-circuited entropy conductivity Λ . The more fundamental entropy conductivity is related to the open-circuited heat conductivity λ as shown in Eq. (2). Both terms can be condensed by using the term thermal conductivity [10].

$$zT = \frac{\sigma \cdot \alpha^2}{\lambda} \cdot T = \frac{\sigma \cdot \alpha^2}{\Lambda} = \frac{PF}{\Lambda} \quad (2)$$

The thermoelectric parameters all reappear in Eq. (2), where the performance of a thermoelectric material is given by the figure-of-merit zT . While the zT rules over the maximum energy conversion efficiency, the power factor $PF = \sigma \cdot \alpha^2$ is proportional to the maximum power output of a thermoelectric material. Both quantities are important to describe the thermoelectric performance of a material [10].

1.2. Composite materials

Specific single phase properties can be combined within a composite material. Depending on the characteristics of the combined materials, they can either coexist or interact with each other. Some theoretical limits of a coexisting two-phase composite were stated by Bergman et al.

* Corresponding author.

** Corresponding author.

E-mail addresses: richard.hinterding@pci.uni-hannover.de (R. Hinterding), armin.feldhoff@pci.uni-hannover.de (A. Feldhoff).

<https://doi.org/10.1016/j.oceram.2021.100198>

Received 6 May 2021; Received in revised form 20 October 2021; Accepted 4 November 2021

Available online 19 November 2021

2666-5395/© 2021 The Author(s). Published by Elsevier Ltd on behalf of European Ceramic Society. This is an open access article under the CC BY license

(<http://creativecommons.org/licenses/by/4.0/>).

[11]. The figure-of-merit zT of the single phase components shall not be exceeded by the composites, although it is possible concerning the power factor [12]. However, these studies do not take the more recently investigated interactions on the nanoscale into account. Furthermore, the transferability to a multiphase system is uncertain, which could be created by reactions between the mixing partners. The addition of one or multiple phases generally leads to heterointerfaces, which can decrease the mean-free path of phonons and thus reduce the thermal conductivity [13–15]. Note that depending on the additional phase, the overall thermal conductivity is not necessarily enhanced [16]. Mixing organic polymers and inorganic materials could improve the Seebeck coefficient effectively [17–19]. For $\text{Ca}_3\text{Co}_4\text{O}_9$ (CCO) in particular, Ag inclusions have proven to positively influence the thermoelectric performance [20–22]. Other metallic additions such as Co particles were beneficial for porous CCO systems by increasing the power factor [23]. Further adding polymers to a CCO/Ag system could reduce the thermal conductivity, but led to problems concerning the application temperature [24]. The power factor of a CCO composite was also increased by utilizing high dopant levels of Ca and Bi leading to a triple-phase composite [25]. Another study investigating the influence of adding La_2NiO_4 to a CCO matrix also revealed improved thermoelectric properties [26].

The present study investigates the influence on the thermoelectric properties of adding $\text{Na}_2\text{Ca}_2\text{Nb}_4\text{O}_{13}$ (NCNO) into a CCO matrix. CCO functions as the matrix material as it is well-known for its excellent thermoelectric properties. Furthermore, it is stable up to 1198 K in air [5,27], which makes it suitable for high-temperature applications. The thermoelectric properties of CCO are directly linked to its layered structure built up from two incommensurate subsystems [28]. CoO_2 constitutes one subsystem with a misfit-layered CdI_2 structure type while the other subsystem consists of three Ca_2CoO_3 units as a layered cutout of the rock-salt type [28]. Both subsystems alternate along the shared c -axis with same a and distinct b lattice parameters [29]. The layered structure results in strongly anisotropic thermoelectric properties [30,31]. NCNO on the other hand is mainly investigated with respect to the flux synthesis of single crystals [32] and its photocatalytic activity [33]. Structurally, the NCNO consists of $[(\text{Ca}_2\text{Na})\text{Nb}_4\text{O}_{13}]$ perovskite-type layers linked by Na^+ cations [34,35]. The structure can be categorized as a Ruddlesden-Popper type and belongs to the Dion-Jacobson series of $\text{Na}[\text{Ca}_2\text{Na}_{n-3}\text{Nb}_n\text{O}_{3n+1}]$. The Na located between the layers should have a higher mobility and could therefore interact with the CCO during sintering. The obvious reason for NCNO not being used for thermoelectrics is the large bandgap of 3.3 eV [33], which results in electronically insulating characteristics. On the other hand, the inversely coupled Seebeck coefficient should be considerably large and surpass the one of CCO. Hence, an increased Seebeck coefficient and a decreasing electrical conductivity were expected from introducing NCNO into a CCO matrix with unknown consequences on the figure-of-merit. The usage of large plate-like particles of NCNO also allowed a preferred orientation during the uniaxial pressing. The final goal of preparing these CCO/NCNO ceramics was the improvement of the thermoelectric properties in comparison to pure CCO. To evaluate these properties, two different Ioffe plots with respect to the power factor and the entropy conductivity were applied [10,36].

2. Experimental

2.1. Materials

The composite materials were obtained by combining two different oxide powders. The oxide material $\text{Ca}_3\text{Co}_4\text{O}_9$ (CCO) functioned as a matrix and was purchased from CerPoTech (Tiller, Norway). The additive oxide material was $\text{Na}_2\text{Ca}_2\text{Nb}_4\text{O}_{13}$ (NCNO), which was synthesized by a molten-flux synthesis based on research from Arney et al. [33]. A stoichiometric mixture of water-free Na_2CO_3 , $\text{Ca}(\text{NO}_3)_2 \cdot 4 \text{H}_2\text{O}$ and Nb_2O_5 was mixed in a mortar and grinded for about 15 min. Afterwards, Na_2SO_4 was added in a 20:1 flux-to-reactant molar ratio and grinded

again for about 15 min. The mixture was transferred into an alumina crucible and heated to 1373 K with a heating rate of 0.8 K/min in a muffle furnace. After a 10 h holding time, it was cooled to room temperature with a rate of 2 K/min. The white product powder was washed with hot deionized water in an ultrasonic bath to remove the flux and smaller particles. Ceramic composites containing CCO and NCNO were synthesized by grinding the precursor powders in a mortar for about 15 min with the respective weight ratios of 99:1, 95:5, 90:10 and 80:20 and a total weight of 1 g. The mixture was uniaxially pressed in a 16 mm steel die with 250 MPa at room temperature in air. Sintering was performed at ambient pressure at 1173 K for 10 h with a heating and cooling rate of 2 K min^{-1} in air. For thermoelectric measurements, the sintered disks were cut into bars with a length of 10 mm by using a precision vertical diamond wire saw from O'Well model 3242.

2.2. Analysis of microstructure

Phase purity of powders and ceramics was investigated by X-ray diffraction (XRD, Bruker AXS GmbH, Bruker D8 Advance) measurements, which were operated at 40 kV and 40 mA with Cu-K_α radiation. Powder diffraction data for identification and comparison within this work are used for the compounds $\text{Ca}_3\text{Co}_4\text{O}_9$ (Miyazaki et al. [29], monoclinic, $a = 4.834 \text{ \AA}$, $b_1 = 2.824 \text{ \AA}$, $b_2 = 4.558 \text{ \AA}$, $c = 10.844 \text{ \AA}$), $\text{Na}_2\text{Ca}_2\text{Nb}_4\text{O}_{13}$ (PDF: [01-089-6576], orthorhombic, $a = 5.474 \text{ \AA}$, $b = 5.510 \text{ \AA}$, $c = 36.151 \text{ \AA}$), CaNbO_3 (PDF: [01-089-0718], orthorhombic, $a = 5.448 \text{ \AA}$, $b = 5.526 \text{ \AA}$, $c = 7.758 \text{ \AA}$). The approach of a four-dimensional superspace group was used for CCO due to its incommensurate structure. Therefore, indexing of CCO in XRDs was realized with the superspace group $Cm(0\ 1\ -\ p\ 0)$ (equivalent to $Bm(0\ 0\ \gamma)$) in accordance with literature [29,37,38]. A field-emission scanning electron microscope (FE-SEM, JEOL JSM-6700F) was used for secondary electron micrographs of the powders at 2 kV. Elemental mappings were measured at 15 kV with another FE-SEM (JEOL JSM-7610FPlus) equipped with two energy dispersive X-ray spectrometers (EDXS, Bruker, XFlash 6/60). Quantifications of elemental mappings were evaluated by the software Esprit version 2.2 from Bruker using the ZAF correction method. In-depth analysis of the composition was accomplished by a field-emission transmission electron microscope (TEM, JEOL JEM-2100F-UHR), which was also equipped with an EDXS (Oxford Instruments, INCA-300). Scanning TEM (STEM), high-resolution TEM (HRTEM) and selected area electron diffraction (SAED) were performed at 200 kV. Density and porosity of the sintered disks were determined by the Archimedes method (ISO 5018:1983). Isopropanol was used as a fluid and density values were averaged for three different disks.

2.3. Analysis of thermoelectric properties

Measurements of the electrical conductivity, Seebeck coefficient and heat conductivity were realized with respect to temperature dependency and orientation of the samples. The sintered ceramics were cut into bars (10 mm, 2 mm, 1.6 mm) to measure the electrical conductivity and the Seebeck coefficient perpendicular to the pressing direction. The measurement of the electrical conductivity was accomplished by a 4-point probe method at equilibrium conditions within a horizontal three-heating-zone tube furnace from Carbolite Gero EVZ 12/450B. The samples were heated to 1073 K with a heating rate of 3 K min^{-1} and maintained at this temperature for 4 h. Afterwards, the temperature program included cooling steps of 100 K with a dwell time of 2 h up to 873 K and 1 h up to 373 K. In total, the samples were exposed to a temperature above 373 K for more than 20 h. To measure the Seebeck coefficient, a ProboStat A setup from NorECs with a vertical furnace from Elite Thermal Systems Ltd. was used. Measurements were done with KEITHLEY multimeters and gained data processed by using Lab VIEW software. To gain values at equilibrium conditions, the temperature program included heating to 1073 K with a heating rate of 3 K min^{-1} and cooling steps of 100 K with dwell times of 1.5 h up to 773 K and 2 h

up to 373 K. A laser flash setup LFA 1000 from Linseis with an InSb detector was used to measure the thermal diffusivity D . Under helium (standard conditions), CCO started decomposing between 773 K and 873 K by releasing oxygen in accordance with literature [39]. Therefore, an oxygen-helium mixed atmosphere (20% O_2 , 80% He) was used and values were averaged for three subsequent heating and cooling cycles to gain reliable data. Heat capacity c_p of each composite was measured in comparison to a pure CCO sample via the equations $\Delta T = E \cdot m^{-1} \cdot c_p^{-1}$ (ΔT = temperature difference in K; E = energy in J; m = mass of the sample in g; c_p = heat capacity in $\text{J g}^{-1} \text{K}^{-1}$) and $c_{p,\text{sample}} = c_{p,\text{reference}} \cdot \Delta T_{\text{reference}} \cdot m_{\text{reference}}$. Values for c_p of CCO were taken from literature [25]. Two different sample orientations i.e. perpendicular and parallel to the pressing direction were investigated. The measurements perpendicular to the pressing direction were conducted up to 573 K. Values of thermal diffusivity above 573 K with orientation perpendicular to the pressing direction were estimated by calculating polynomial fits for the measurements parallel to the pressing direction (compare another study using this method for more information [26]). As these parallel measurements were conducted in the full temperature range of 373 K to 1073 K, their calculated fits were transferred to the measurements in the other direction assuming similar trends with respect to the temperature.

3. Results and discussion

3.1. Compound powders

Two oxide powders with large differences in crystal sizes were used as base materials for the composites. As shown in Fig. 1, the CCO matrix powder was characterized by small particles with a plate-like shape. Its lateral extensions were about 200–500 nm and its thickness about 30 nm. The additive NCNO on the other hand showed the crystal morphology of microsheets with lateral extensions of up to 80 μm and a thickness of up to 8 μm . Therefore, both phases had a similar aspect ratio around 10 but were distinguished by two to three orders of magnitude respecting their crystal size. The small particle size of the CCO qualified it as a suitable matrix material for embedding the second phase. The plate-like crystal shape of both phases facilitate a preferred orientation when pressed, which can result in a ceramic with anisotropic transport properties.

3.2. Ceramic composite: composition and microstructure

The composition of the CCO/NCNO ceramic composites after sintering was investigated by XRD. For the NCNO compound powder, the sintered CCO and the sintered composites XRD patterns are displayed in Fig. 2. For the samples with low amounts of weighed NCNO (1 and 5 wt %), only the reflections for the matrix material CCO are visible. However, for the samples with 10 wt% and 20 wt% weighed NCNO, reflections of CaNbO_3 (CNO) became apparent. Since the original reflections of NCNO are not detected anymore, a reaction to CNO accompanied by a segregation of sodium is reasonable. The XRD patterns give no hint about a third phase containing sodium in the composites, although it could be nanocrystalline, only formed in minor amounts or integrated in the CCO matrix.

The formed CNO phase was further analyzed by SEM-EDXS in Fig. 3 for the sample with 5 wt% NCNO (compare Fig. S1 for an overview mapping). One single CNO particle is shown within the CCO matrix to analyze its composition. A morphological transformation at least at the surface of the particle is evident, which is now irregularly shaped. This is most likely due to reaction sintering and the newly formed phase. The EDX spectrum in Fig. 3b and the elemental distributions in Fig. 3d–h shows that the particles mainly consist of Ca, Nb and O, but also some Co and residual Na are noticeable. In the original NCNO, the Ca:Nb ratio is presumably 1:2 but in CNO it is 1:1, which means there should be an excess of Nb. The EDXS results suggest an even lower Ca:Nb ratio of 1:0.76 and therefore a segregation of Nb. There are no Nb-rich inclusions

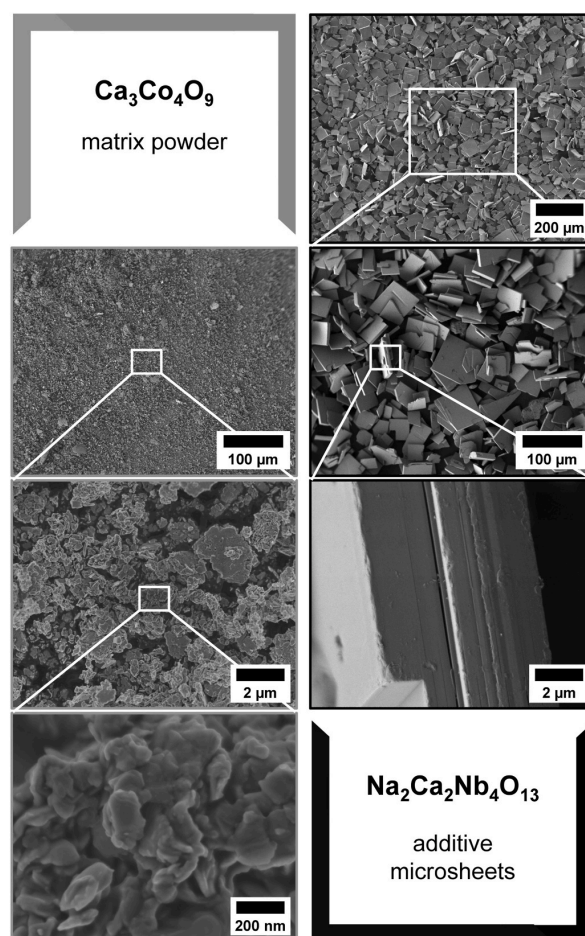


Fig. 1. SEM micrographs of the precursors powders $\text{Ca}_3\text{Co}_4\text{O}_9$ and $\text{Na}_2\text{Ca}_2\text{Nb}_4\text{O}_{13}$ used for the ceramic composites.

around the particle, but the surrounding CCO shows small amounts of approximately 1 at% Nb. This could mean that an integration of excess Nb into the CCO has occurred by exchanging Co from the CCO into the CNO particle. This cation exchange of $\text{Co}^{2+}/\text{Co}^{3+}/\text{Co}^{4+}$ and Nb^{5+} seems reasonable when the ionic radii are compared. For a coordination number of 6 (Co positions in CCO), the ionic radii are 65/55/53 pm for Co^{2+} (low-spin)/ Co^{3+} (low-spin)/ Co^{4+} (high-spin) and 64 pm for Nb^{5+} [40]. Based on the two subsystems of CCO, all three different valences occur, but the average value is between +3 and +4 in dependence of the variable oxygen amount [41,42]. The CoO_2 subsystem only features Co^{3+} and Co^{4+} , while the Ca_2CoO_3 contains Co^{2+} to some extent [43]. Comparing the ionic radii of Co and Nb ions, the substitution of Co^{2+} seems favored. However, substitution experiments involving Mn^{3+} (65 pm) or Fe^{2+} (61 pm) ions with similar radii to Nb^{5+} resulted in the substitution of Co^{3+} or Co^{4+} [42]. Investigations concerning Nb doping of CCO assume the same behavior [44]. Therefore, a substitution is clearly possible in this case, but the position is uncertain. The different charges of the ions suggest that the presence of oxygen is also essential for the cation exchange. The Ca:Co ratio in the CNO is 1:0.37 and together with the Nb amount this fits to $\text{Ca}(\text{Nb},\text{Co})\text{O}_3$ as the newly formed phase. Residual Na is left with a Ca:Na ratio of 1:0.12 and is most likely located on the Ca-position of the CNO. The Na within the original NCNO, which is partly located in between the NbO_6 octahedra, can be removed to gain the perovskite structure. This is well investigated for

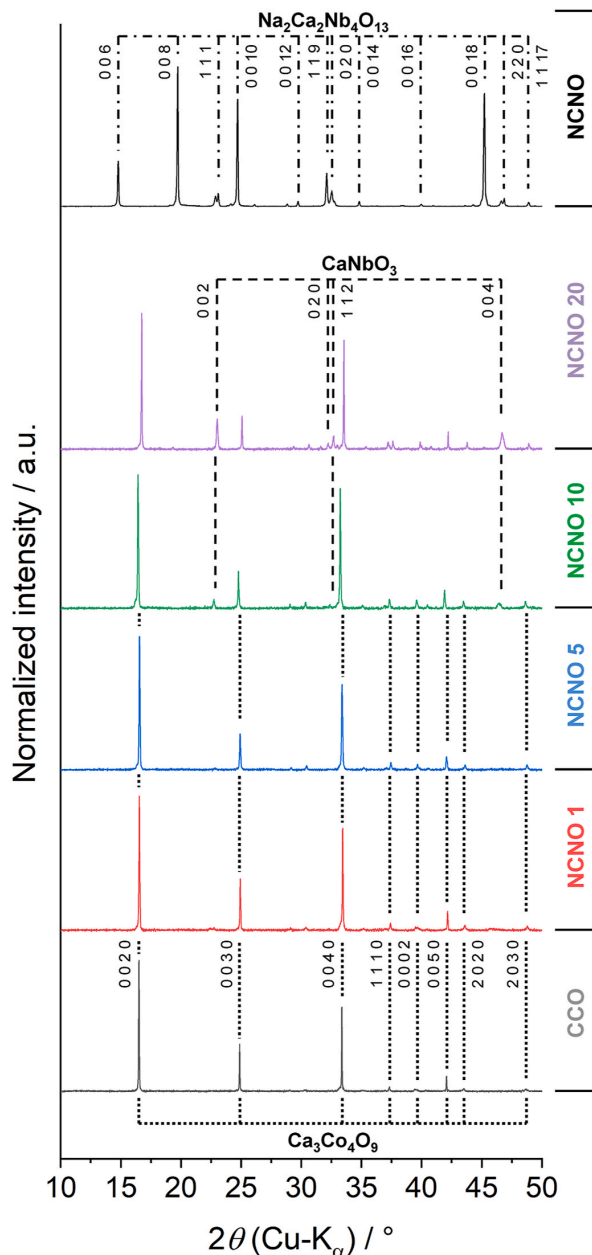


Fig. 2. XRD patterns of the compound NCNO powder, the sintered CCO/NCNO ceramic composites and the sintered CCO. All patterns were background-corrected and normalized for an easy comparison. Original phases of CCO and NCNO were indexed as well as the newly formed CaNbO_3 . Reflections of the CCO were indexed with the four-dimensional superspace group approach [29,38].

the Dion-Jacobson series of $\text{A}[\text{Ca}_2\text{Na}_{n-3}\text{Nb}_n\text{O}_{3n+1}]$ in terms of ion intercalation and production of perovskite nanosheets [45–48]. Here, the introduction of Co and the high temperature during sintering could be the reason for the phase transformation. The structurally different atom positions of Na could also explain why there is still some Na left in the newly formed CNO. It is not entirely clear in which form the segregated Na remains, but the overview EDXS mapping in Fig. S1

suggests the formation of CoO containing Na and Ca to some extent. The main observations during the sintering were summarized and illustrated by the reaction scheme given in Fig. 4.

Further analysis regarding the newly formed CNO was performed by TEM measurements in Fig. 5. The cross-section of a former NCNO plate and the respective EDXS mapping are given in Fig. 5a,d. The irregular shape at the surface and the introduction of Co into the CNO as found in the SEM results can be recognized. The elemental distribution of Ca, Co and Nb is also rather homogeneous within the CNO particle. The CCO plate crossing the CNO particle also shows a loss of Co and a gain of Nb, resulting in a Ca:Co ratio of 1.08 and a Ca:Nb ratio of 1:0.17. This supports the assumption of a cation exchange between the CCO and the NCNO as the Ca:(Co,Nb) ratio is at 1:1.25 and therefore close to the original Ca:Co ratio of 1:1.33. Again, no new phase with Na as a major element was found in the close vicinity of the CNO particle. EDXS showed only trace amounts of Na within the CNO and no Na within the CCO particle. Therefore, the Na is most likely located within some CoO in the CCO matrix as suggested by Fig. S1 or evaporated to some extent during sintering. The CNO phase was also investigated by SAED and HRTEM for the zone axes [112] in Fig. 5b and c and for [001] in Fig. 5e and f. Both zone axes gave a clear diffraction pattern at the marked location of Fig. 5a, which allowed the distinct indexing of them. As not the whole particle was oriented simultaneously, polycrystallinity seems reasonable. Furthermore, the [001] orientation in Fig. 5f allowed the determination of the a - and b -axis lattice parameters (5.57 Å and 5.66 Å respectively), which are only slightly larger than the literature data for pure CaNbO_3 (5.45 Å and 5.53 Å respectively for ICSD 01-089-0718).

3.3. Ceramic composite: thermoelectric properties

The microstructure analysis in section 3.2 revealed that CCO and NCNO do not coexist at high temperatures and the formation of CNO is induced with the loss of Na. The influence of the new phases within the CCO matrix was investigated by measuring the electrical conductivity σ , Seebeck coefficient α and heat conductivity λ of the CCO/LNO ceramic composites in Fig. 6.

The electrical conductivity (see Fig. 6a) shows the expected decreasing trend with increasing amounts of NCNO. However, the sample with 1 wt% NCNO shows even slightly higher values and the 5 wt % only a small decrease. This behavior could be linked to the cation exchange between the CCO and NCNO, which leads to a Nb-doped CCO. A similar trend was found by Zhu et al. [44] for targeted Nb-doping of CCO, where low amounts of Nb lowered the electrical resistivity and higher amounts increased it. The decrease in electrical conductivity is also caused by the $\text{Ca}(\text{Nb},\text{Co})\text{O}_3$ phase, which originates from the CaNbO_3 with really low values of $10^{-5} \text{ S cm}^{-1}$ at 750 K [49]. No significant or sudden changes of the electrical conductivity were observed during the measurement time of more than 20 h above 373 K for the composites as well as for the pure CCO. As incomplete reactions can be an issue for the long-term stability of composites, these changes would be unfavorable. Based on the measurements, complete reactions and stable composites are suggested. More details about the electrical conductivity were observed by the Arrhenius plot in Fig. S3. A metallic-to-semiconducting transition between 573–673 K was found for CCO in accordance with literature [50,51]. For high temperatures, the composites also show an increase of the activation energy for the electronic transport, which is caused by hindered transport across the additional phases. The Seebeck coefficient is usually inversely coupled to the electrical conductivity, which is also the case for the investigated composites. The main reason for the increasing Seebeck coefficient is most likely the additional $\text{Ca}(\text{Nb},\text{Co})\text{O}_3$ phase within the system. Although no systematical studies of the electronic properties of the $\text{Ca}(\text{Nb},\text{Co})\text{O}_3$ system and the consequences of substituting Nb with Co were available, the undoped CaNbO_3 and CaCoO_3 can give some information. On the one hand the CaNbO_3 shows p -type conductivity by a positive Seebeck coefficient and electrically insulating characteristics [49]. On

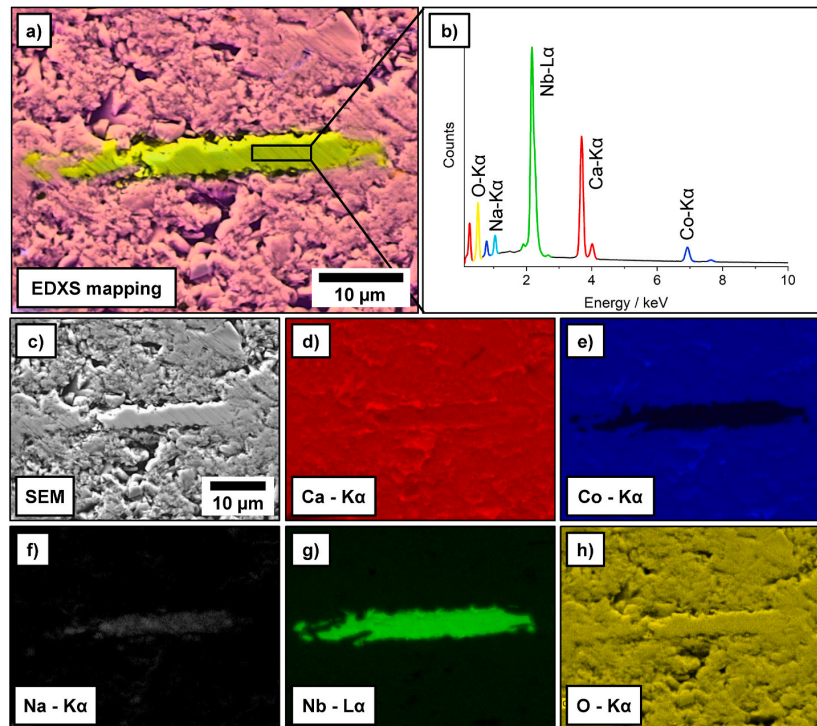


Fig. 3. Cross-sectional SEM-EDXS analysis of the 5 wt% NCNO sample after sintering showing a single CNO plate-like particle embedded in a CCO matrix. a) Overlay EDXS mapping summarizing the results from c-h. b) EDX spectrum shows exemplarily the composition of the CNO phase. c) SEM micrograph as basis for EDXS analysis. d-h) Elemental distributions of the respective elements Ca, Co, Na, Nb and O.

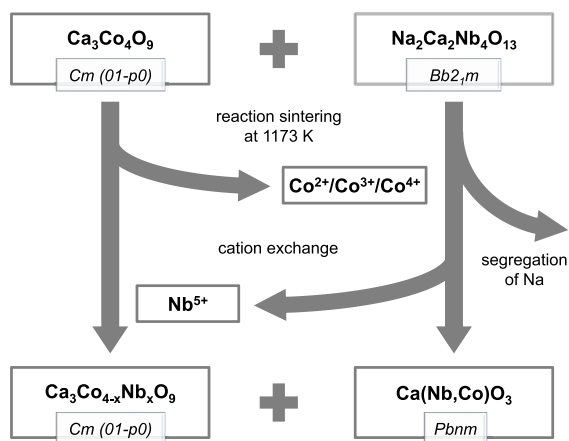


Fig. 4. Reaction scheme of CCO and NCNO during reaction sintering. A cation exchange between CCO and the newly formed $\text{Ca}(\text{Co,Nb})\text{O}_3$ occurred and Na partly segregated.

the other hand the CaCoO_3 shows a nonmetallic behavior regarding the temperature dependency of the electrical conductivity despite showing large values of 333 S cm^{-1} at room temperature [52]. Therefore, a higher electrical conductivity but lower Seebeck coefficient of $\text{Ca}(\text{Nb,Co})\text{O}_3$ in comparison to CaNbO_3 are reasonable. It should be noted that the amount of initial NCNO could also have an impact on the Nb:Co ratio and therefore the thermoelectric properties. This could explain why the sample containing 20 wt% NCNO shows a different slope than the

samples containing less amounts. Another subordinate factor concerning the Seebeck coefficient is the introduction of Nb into the CCO, where a higher Nb amount led to increased values [53]. Combining the electrical conductivity and the Seebeck coefficient gives the power factor in Fig. 6c. The samples containing 1–10 wt% NCNO all show an increase, especially towards higher temperatures. The maximum value is reached by the 5 wt% sample and the decreasing electrical conductivity becomes prevalent for the 20 wt% sample. The last part for a complete picture of the thermoelectric properties is the thermal conductivity, which is given as the heat conductivity in Fig. 6d. All investigated ceramic composites showed a decreased heat conductivity for the whole temperature range. This could be caused by the additional phonon scattering sites coming from the $\text{Ca}(\text{Nb,Co})\text{O}_3$ phase, but the larger atomic mass of Nb in comparison to Co and the Nb-doping could also play a significant role. Interestingly, the heat conductivity between the 1–10 wt% samples did not differ by much and shows if anything an increasing trend. This could be caused by a higher heat conductivity of the additional phase, which balances out with the increased phonon scattering at interfaces. It should be noted that the values of λ above 573 K were fitted to the measurements parallel to the pressing direction (compare Fig. S2). The reason for this was the applied oxygen-helium atmosphere, which did not allow higher temperatures with the used setup. A comparison of measurements for CCO in both directions from the literature validates this method, as the temperature dependent trend is comparable [30,54]. The same method was also used in a previous study investigating CCO composites [26]. By comparing the heat conductivity parallel and perpendicular to the pressing direction differences become obvious (compare Fig. S2), which are most likely caused by some anisotropy of the ceramic samples. This anisotropy comes from the preferred orientation of CCO and the CNO due to uniaxial pressing. This underlines the importance of combining the thermoelectric properties within the same

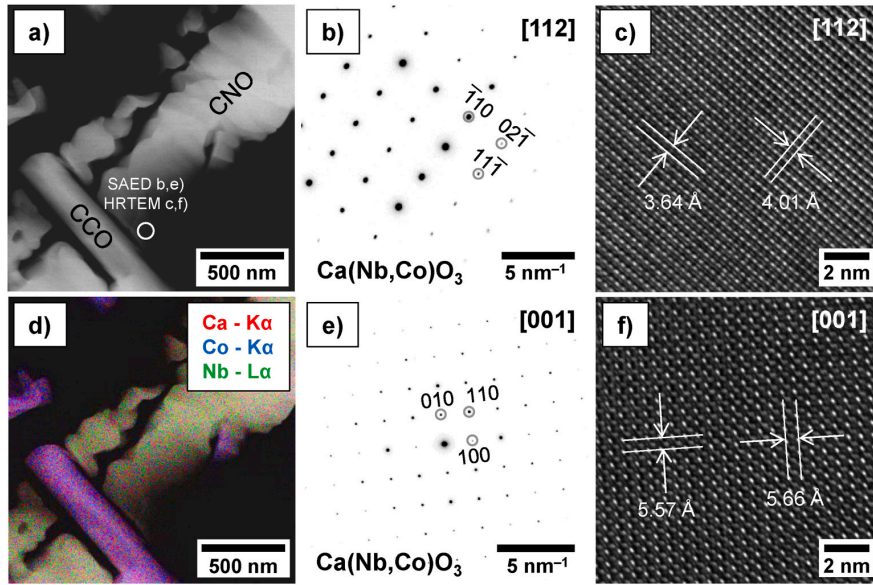


Fig. 5. Cross-sectional TEM characterization of the sample with 5 wt% NCNO. a,d) STEM annular dark-field micrograph of a large plate-like $\text{Ca}(\text{Co,Nb})\text{O}_3$ (CNO) grain partly surrounded by CCO and the EDXS mapping of the CNO grain showing a homogeneous distribution of Ca and Nb as well as the introduction of Co. b,c,e,f) SAED pattern and corresponding high-resolution TEM micrographs along the [112] and the [100] zone axes of the newly formed CNO phase.

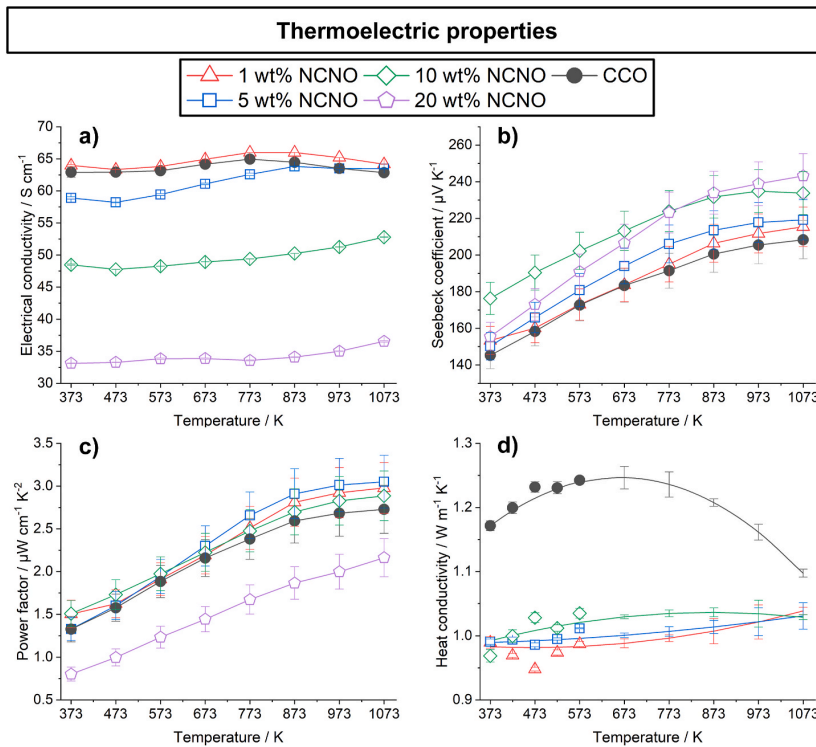


Fig. 6. Thermoelectric properties of the CCO/NCNO ceramic composites perpendicular to the pressing direction in dependence on temperature with standard deviations. a) Electrical conductivity with similar values for the 1 wt% and decreasing values for higher amounts of NCNO in comparison to CCO. b) Seebeck coefficient with increasing values for all investigated composites. c) Power factor with increased values for all investigated composites except the 20 wt% NCNO sample. d) Heat conductivity with decreased values for the ceramic composites. Values above 573 K for the heat conductivity were gained by transferring fits and error bars for measurements parallel to the pressing direction (see Fig. S2).

direction.

Two different Ioffe plots and the figure-of-merit zT displayed in Fig. 7 were derived from the thermoelectric properties in Fig. 6. The type-I Ioffe plot in Fig. 7a gives the power factor in dependence of the

electrical conductivity, which allows a clear comparison between the different samples. Increased power factors at high temperatures are noticed for the 1–10 wt% samples. The decreasing electrical conductivity correlates with the increasing Seebeck coefficient and becomes

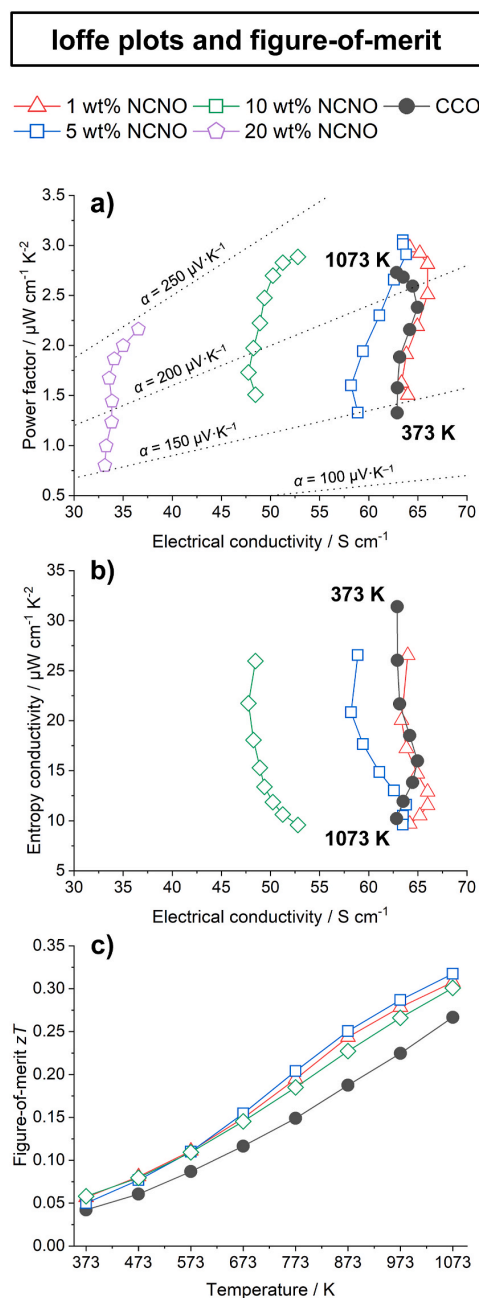


Fig. 7. Ioffe plots with 100 K temperature steps and figure-of-merit zT of the CCO/NCNO ceramic composites. a) Type-I Ioffe plot with the power factor against the electrical conductivity. The samples with 1 wt%, 5 wt% and 10 wt% NCNO show a higher power factor than the CCO. b) Type-II Ioffe plot with the entropy conductivity against the electrical conductivity. Slightly lower values were reached at high temperatures in comparison to pure CCO. c) Figure-of-merit zT against the temperature. All investigated composites show an increased average and maximum zT .

dominant for 20 wt% NCNO. The type-II Ioffe plot in Fig. 7b shows the thermal properties in terms of entropy conductivity Λ in dependence of the electrical conductivity. Slightly lower values at high temperatures were reached by the composites. Additionally, the maximum entropy

conductivity could effectively be reduced for lower temperatures. Finally, the figure-of-merit zT was determined perpendicular to the pressing direction by combining the power factor and the entropy conductivity. The corresponding plot against the temperature is given in Fig. 7c. The samples with 1–10 wt% NCNO all show improved values with the 1 wt% and 5 wt% sample being the best. This results from the increased power factor and the simultaneously low entropy conductivity. The 1 wt% sample has a slightly lower figure-of-merit in comparison to the 5 wt%, but the electrical conductivity is higher. The difference of the figure-of-merit between composites with low amounts of NCNO and the pure CCO becomes more pronounced with increasing temperatures and reaches its maximum value at 1073 K with 0.32 against 0.27, which is equivalent to an improvement of approximately 19%.

4. Conclusions

Ceramic composites based on the undoped $\text{Ca}_3\text{Co}_4\text{O}_9$ and $\text{Na}_2\text{Ca}_2\text{Nb}_4\text{O}_{13}$ were produced with varying ratios between both compounds. Using undoped $\text{Ca}_3\text{Co}_4\text{O}_9$ allowed the determination of the reasons in changing thermoelectric properties, but future research could benefit further from a doped CCO. Analysis of the microstructure by XRD, SEM, EDXS and TEM suggested a cation exchange of Co and Nb between the matrix material and the additive material as well as a newly formed $\text{Ca}(\text{Nb},\text{Co})\text{O}_3$ phase. The Seebeck coefficient was increased for the ceramic composites but the electrical conductivity was reduced, with the exception of sample containing 1 wt% of the additive. Both values combined led to an improved power factor for the samples containing 1–10 wt% additive. The introduction of additional phases also led to a small reduction of the thermal conductivity. As a result, the maximum figure-of-merit zT at 1073 K was increased by about 19% for the composite with 5 wt% $\text{Na}_2\text{Ca}_2\text{Nb}_4\text{O}_{13}$ in comparison to pure $\text{Ca}_3\text{Co}_4\text{O}_9$. These results underline the potential of composite materials concerning improved thermoelectric properties.

Declaration of competing interest

The authors declare that they have no known competing financial interests or personal relationships that could have appeared to influence the work reported in this paper.

Acknowledgements

This work was supported by the Deutsche Forschungsgemeinschaft (DFG, German Research Foundation) - project number 325156807. Authors gratefully appreciate technical assistance by F. Steinbach.

Appendix A. Supplementary data

Supplementary data to this article can be found online at <https://doi.org/10.1016/j.oceram.2021.100198>.

References

- [1] G. Tan, L.-D. Zhao, M.G. Kanatzidis, Rationally designing high-performance bulk thermoelectric materials, *Chem. Rev.* 116 (2016) 12123–12149, <https://doi.org/10.1021/acs.chemrev.6b00255>.
- [2] S.J. Poon, Recent advances in thermoelectric performance of half-Heusler compounds, *Metals* 8 (2018) 989, <https://doi.org/10.3390/met8120989>.
- [3] J. Shuai, J. Mao, S. Song, Q. Zhang, G. Chen, Z. Ren, Recent progress and future challenges on thermoelectric Zintl materials, *Materials Today Physics* 1 (2017) 74–95, <https://doi.org/10.1016/j.mtphys.2017.06.003>.
- [4] Q. Zhang, Y. Sun, W. Xu, D. Zhu, Organic thermoelectric materials: emerging green energy materials converting heat to electricity directly and efficiently, *Adv. Mater.* 26 (2014) 6829–6851, <https://doi.org/10.1002/adma.201305371>.
- [5] Y. Yin, B. Tudu, A. Tiwari, Recent advances in oxide thermoelectric materials and modules, *Vacuum* 146 (2017) 356–374, <https://doi.org/10.1016/j.vacuum.2017.04.015>.
- [6] L.-D. Zhao, J. He, D. Berardan, Y. Lin, J.-F. Li, C.-W. Nan, N. Dragoe, BiCuSeO oxyselenides: new promising thermoelectric materials, *Energy Environ. Sci.* 7 (2014) 2900–2924, <https://doi.org/10.1039/c4ee00997e>.

- [7] H.U. Fuchs, A direct entropic approach to uniform and spatially continuous dynamical models of thermoelectric devices, *Energy Harvest. Syst.* 1 (2014), <https://doi.org/10.1515/ehs-2014-0011>.
- [8] A. Feldhoff, Thermoelectric material tensor derived from the Onsager–de Groot–Callen model, *Energy Harvest. Syst.* 2 (2015), <https://doi.org/10.1515/ehs-2014-0040>.
- [9] A. Feldhoff, Power conversion and its efficiency in thermoelectric materials, *Entropy* 22 (2020) 803, <https://doi.org/10.3390/e22080803>.
- [10] M. Wolf, R. Hinterding, A. Feldhoff, High power factor vs. high zT —a review of thermoelectric materials for high-temperature application, *Entropy* 21 (2019) 1058, <https://doi.org/10.3390/e21111058>.
- [11] D.J. Bergman, O. Levy, Thermoelectric properties of a composite medium, *J. Appl. Phys.* 70 (1991) 6821–6833, <https://doi.org/10.1063/1.349830>.
- [12] D.J. Bergman, L.G. Fel, Enhancement of thermoelectric power factor in composite thermoelectrics, *J. Appl. Phys.* 85 (1999) 8205–8216, <https://doi.org/10.1063/1.370660>.
- [13] Q. Zhang, X. Ai, L. Wang, Y. Chang, W. Luo, W. Jiang, L. Chen, Improved thermoelectric performance of silver nanoparticles-dispersed Bi_2Te_3 composites deriving from hierarchical two-phased heterostructure, *Adv. Funct. Mater.* 25 (2015) 966–976, <https://doi.org/10.1002/adfm.201402663>.
- [14] W. Liu, X. Yan, G. Chen, Z. Ren, Recent advances in thermoelectric nanocomposites, *Nano Energy* 1 (2012) 42–56, <https://doi.org/10.1016/j.nanoen.2011.10.001>.
- [15] K. Kato, K. Kuriyama, T. Yabuki, K. Miyazaki, Organic-inorganic thermoelectric material for a printed generator, *J. Phys. Chem.* 1052 (2018), 012008, <https://doi.org/10.1088/1742-6596/1052/1/012008>.
- [16] F. Delorme, P. Diaz-Chao, E. Guilmeau, F. Giovannelli, Thermoelectric properties of $\text{Ca}_3\text{Co}_4\text{O}_9$ - Co_3O_4 composites, *Ceram. Int.* 41 (2015) 10038–10043, <https://doi.org/10.1016/j.ceramint.2015.04.091>.
- [17] B. Zhang, J. Sun, H.E. Katz, F. Fang, R.L. Opila, Promising thermoelectric properties of commercial PEDOT:PSS materials and their Bi_2Te_3 powder composites, *ACS Appl. Mater. Interfaces* 2 (2010) 3170–3178, <https://doi.org/10.1021/am100654p>.
- [18] N. Tushima, Recent progress of organic and hybrid thermoelectric materials, *Synth. Met.* 225 (2017) 3–21, <https://doi.org/10.1016/j.synthmet.2016.12.017>.
- [19] M. Culebras, A. García-Barberá, J.F. Serrano-Claumarchirant, C.M. Gómez, A. Cantarero, Hybrids composites of NCCO/PEDOT for thermoelectric applications, *Synth. Met.* 225 (2017) 103–107, <https://doi.org/10.1016/j.synthmet.2016.12.016>.
- [20] Y. Song, Q. Sun, L. Zhao, F. Wang, Z. Jiang, Synthesis and thermoelectric power factor of $(\text{Ca}_{0.95}\text{Bi}_{0.05})_3\text{Co}_4\text{O}_9/\text{Ag}$ composites, *Mater. Chem. Phys.* 113 (2009) 645–649, <https://doi.org/10.1016/j.matchemphys.2008.08.029>.
- [21] F. Kahraman, M.A. Madre, S. Rasekh, C. Salvador, P. Bosque, M.A. Torres, J. C. Diez, A. Sotelo, Enhancement of mechanical and thermoelectric properties of $\text{Ca}_3\text{Co}_4\text{O}_9$ by Ag addition, *J. Eur. Ceram. Soc.* 35 (2015) 3835–3841, <https://doi.org/10.1016/j.jeurceramsoc.2015.05.029>.
- [22] Z. Shi, C. Zhang, T. Su, J. Xu, J. Zhu, H. Chen, T. Gao, M. Qin, P. Zhang, Y. Zhang, H. Yan, F. Gao, Boosting the thermoelectric performance of calcium cobaltite composites through structural defect engineering, *ACS Appl. Mater. Interfaces* 12 (2020) 21623–21632, <https://doi.org/10.1021/acami.0c03297>.
- [23] G. Constantinescu, A.R. Sarabando, S. Rasekh, D. Lopes, S. Sergienko, P. Amirkhizi, J.R. Frade, A.V. Kovalevsky, Redox-promoted tailoring of the high-temperature electrical performance in $\text{Ca}_3\text{Co}_4\text{O}_9$ thermoelectric materials by metallic cobalt addition, *Materials* 13 (2020), <https://doi.org/10.3390/ma13051060>.
- [24] M. Wolf, K. Menekse, A. Mundstock, R. Hinterding, F. Nietschke, O. Oeckler, A. Feldhoff, Low thermal conductivity in thermoelectric oxide-based multiphase composites, *J. Electron. Mater.* 48 (2019) 7551–7561, <https://doi.org/10.1007/s11664-019-07555-2>.
- [25] M. Bittner, N. Kanas, R. Hinterding, F. Steinbach, D. Groeneveld, P. Wemhoff, K. Wiik, M.-A. Einarsrud, A. Feldhoff, Triple-phase ceramic 2D nanocomposite with enhanced thermoelectric properties, *J. Eur. Ceram. Soc.* 39 (2019) 1237–1244, <https://doi.org/10.1016/j.jeurceramsoc.2018.10.023>.
- [26] R. Hinterding, Z. Zhao, M. Wolf, M. Jakob, O. Oeckler, A. Feldhoff, Ceramic composites based on $\text{Ca}_3\text{Co}_4\text{O}_9$ and $\text{La}_2\text{NiO}_{4.5}$ with enhanced thermoelectric properties, *Open Ceramics* 6 (2021) 100103, <https://doi.org/10.1016/j.oceram.2021.100103>.
- [27] J.W. Fergus, Oxide materials for high temperature thermoelectric energy conversion, *J. Eur. Ceram. Soc.* 32 (2012) 525–540, <https://doi.org/10.1016/j.jeurceramsoc.2011.10.007>.
- [28] Y. Miyazaki, Crystal structure and thermoelectric properties of the misfit-layered cobalt oxides, *Solid State Ionics* 172 (2004) 463–467, <https://doi.org/10.1016/j.ssi.2004.01.046>.
- [29] Y. Miyazaki, M. Onoda, T. Oku, M. Kikuchi, Y. Ishii, Y. Ono, Y. Morii, T. Kajitani, Modulated structure of the thermoelectric compound $[\text{Ca}_2\text{CoO}_3]_{0.62}\text{CoO}_2$, *J. Phys. Soc. Jpn.* 71 (2002) 491–497, <https://doi.org/10.1143/JPSJ.71.491>.
- [30] D. Kenfaui, B. Lenoir, D. Chateigner, B. Ouladdiaf, M. Gomia, J.G. Noudem, Development of multilayer textured $\text{Ca}_3\text{Co}_4\text{O}_9$ materials for thermoelectric generators: influence of the anisotropy on the transport properties, *J. Eur. Ceram. Soc.* 32 (2012) 2405–2414, <https://doi.org/10.1016/j.jeurceramsoc.2012.03.022>.
- [31] S. Bresch, B. Mieller, D. Schoenauer-Kamin, R. Moos, F. Giovannelli, T. Rabe, Influence of pressure assisted sintering and reaction sintering on microstructure and thermoelectric properties of bi-doped and undoped calcium cobaltite, *J. Appl. Phys.* 126 (2019), 075102, <https://doi.org/10.1063/1.5107476>.
- [32] S. Oishi, Y. Nagai, K. Chiba, N. Ishizawa, Growth of layered perovskite-type $\text{Na}_2\text{Ca}_2\text{Nb}_4\text{O}_{13}$ crystals by the Na_2SO_4 flux method, *Chem. Lett.* 27 (1998) 439–440, <https://doi.org/10.1246/cl.1998.439>.
- [33] D. Arney, L. Fuoco, J. Boltersdorf, P.A. Maggard, Flux synthesis of $\text{Na}_2\text{Ca}_2\text{Nb}_4\text{O}_{13}$: the influence of particle shapes, surface features, and surface areas on photocatalytic hydrogen production, *J. Am. Ceram. Soc.* 96 (2013) 1158–1162, <https://doi.org/10.1111/jace.12122>.
- [34] K. Chiba, Structure of layered perovskite-type $\text{Na}_2\text{Ca}_2\text{Nb}_4\text{O}_{13}$ single crystals, *Solid State Ionics* 108 (1998) 179–183, [https://doi.org/10.1016/S0167-2738\(98\)00037-X](https://doi.org/10.1016/S0167-2738(98)00037-X).
- [35] K. Chiba, N. Ishizawa, S. Oishi, A. Ruddlesden–Popper-type layered perovskite, $\text{Na}_2\text{Ca}_2\text{Nb}_4\text{O}_{13}$, *Acta Crystallogr. Sect. C Cryst. Struct. Commun.* 55 (1999) 1041–1044, <https://doi.org/10.1107/S0108270199001134>.
- [36] A.F. Ioffe, *Semiconductor Thermoelements and Thermoelectric Cooling*, first ed., Info-search Ltd., London, 1957.
- [37] T. Janssen, A. Janner, A. Looijenga-Vos, P.M. De Wolff, *International Tables for Crystallography Volume C: 9.8 Incommensurate and Commensurate Modulated Structures*, vol. 3, Kluwer Acad. Publ, Dordrecht, 2004.
- [38] T. Janssen, G. Chapuis, M. de Boissieu, *Aperiodic Crystals: from Modulated Phases to Quasicrystals*, Volume 20 of *International Union of Crystallography Monographs on Crystallography*, Oxford University Press, Oxford and New York, 2007.
- [39] N. Kanas, G. Skomedal, T.D. Desissa, A. Feldhoff, T. Grande, K. Wiik, M.-A. Einarsrud, Performance of a thermoelectric module based on n -type $(\text{La}_{0.12}\text{Sr}_{0.88})_{0.95}\text{TiO}_{3-\delta}$ and p -type $\text{Ca}_3\text{Co}_4\text{O}_9$, *J. Electron. Mater.* 49 (2020) 4154–4159, <https://doi.org/10.1007/s11664-020-08127-5>.
- [40] R.D. Shannon, Revised effective ionic radii and systematic studies of interatomic distances in halides and chalcogenides, *Acta Crystallogr. A* 32 (1976) 751–767, <https://doi.org/10.1107/S0567739476001551>.
- [41] U. Hira, L. Han, K. Norrman, D.V. Christensen, N. Pryds, F. Sher, High-temperature thermoelectric properties of Na- and W-doped $\text{Ca}_3\text{Co}_4\text{O}_9$ system, *RSC Adv.* 8 (2018) 12211–12221, <https://doi.org/10.1039/c8ra01691g>.
- [42] Y. Wang, Y. Sui, P. Ren, L. Wang, X. Wang, W. Su, H. Fan, Strongly correlated properties and enhanced thermoelectric response in $\text{Ca}_3\text{Co}_{4-x}\text{M}_x\text{O}_9$ ($\text{M} = \text{Fe}, \text{Mn}, \text{and Cu}$), *Chem. Mater.* 22 (2010) 1155–1163, <https://doi.org/10.1021/cm902483a>.
- [43] S. Lambert, H. Leligny, D. Grebille, Three forms of the misfit layered cobaltite $[\text{Ca}_2\text{CoO}_3][\text{CoO}_2]_{1.62} \cdot \text{A}$ 4D structural investigation, *J. Solid State Chem.* 160 (2001) 322–331, <https://doi.org/10.1006/jssc.2001.9235>.
- [44] C. Zhu, H. An, W. Ge, Z. Li, G. Tang, Enhancing the thermoelectric properties of $\text{Ca}_3\text{Co}_4\text{O}_9$ thin films by Nb ion injection, *J. Alloys Compd.* 567 (2013) 122–126, <https://doi.org/10.1016/j.jallcom.2013.03.069>.
- [45] M.M.J. Treacy, S.B. Rice, A.J. Jacobson, J.T. Lewandowski, Electron microscopy study of delamination in dispersions of the perovskite-related layered phases $\text{K}[\text{Ca}_2\text{Na}_{0.3}\text{Nb}_{0.7}\text{O}_{3n-1}]$: evidence for single-layer formation, *Chem. Mater.* 2 (1990) 279–286, <https://doi.org/10.1021/cm00009a018>.
- [46] Y.-S. Han, I. Park, J.-H. Choy, Exfoliation of layered perovskite, $\text{KCa}_2\text{Nb}_3\text{O}_{10}$, into colloidal nanosheets by a novel chemical process, *J. Mater. Chem.* 11 (2001) 1277–1282, <https://doi.org/10.1039/B006045N>.
- [47] B.-W. Li, M. Osada, Y.-H. Kim, Y. Ebina, K. Akatsuka, T. Sasaki, Atomic layer engineering of high- κ ferroelectricity in 2D perovskites, *J. Am. Chem. Soc.* 139 (2017) 10868–10874, <https://doi.org/10.1021/jacs.7b05665>.
- [48] R. Hinterding, A. Feldhoff, Two-dimensional oxides: recent progress in nanosheets, *Z. Phys. Chem.* 233 (2019) 117–165, <https://doi.org/10.1515/zpch-2018-1125>.
- [49] E. Oz, S. Demirel, S. Altin, E. Altin, O. Baglayan, A. Bayri, S. Avci, Fabrication of Ca-Mn-Nb-O compounds and their structural, electrical, magnetic and thermoelectric properties, *Mater. Res. Express* 5 (2018), 036304, <https://doi.org/10.1088/2053-1591/aab3af>.
- [50] D. Sedmidubský, V. Jákš, O. Jankovský, J. Leitner, Z. Sofer, J. Hejtmánek, Phase equilibria in Ca–Co–O system, *J. Solid State Chem.* 194 (2012) 199–205, <https://doi.org/10.1016/j.jssc.2012.05.014>.
- [51] G. Constantinescu, S.M. Mikhalev, A.D. Lisenkov, D.V. Lopes, A.R. Sarabando, M. C. Ferro, T.F.d. Silva, S.A. Sergienko, A.V. Kovalevsky, Prospects for electrical performance tuning in $\text{Ca}_3\text{Co}_4\text{O}_9$ materials by metallic Fe and Ni particles additions, *Materials* 14 (2021), <https://doi.org/10.3390/ma14040980>.
- [52] T. Osaka, H. Takahashi, H. Sagayama, Y. Yamasaki, S. Ishiwata, High-pressure synthesis of an unusual antiferromagnetic metal CaCoO_3 with GdFeO_3 -type perovskite structure, *Phys. Rev. B* 95 (2017), <https://doi.org/10.1103/PhysRevB.95.224440>.
- [53] K. Fujie, S. Horii, I. Matsubara, W. Shin, N. Murayama, J. Shimoyama, K. Kishio, Effect of high valence metal doping on thermoelectric properties of $[\text{Ca}_2\text{CoO}_3]_{0.62}\text{CoO}_2$, *MRS Proceedings* 793 (2003), <https://doi.org/10.1557/PROC-793-SS.34>.
- [54] C.-H. Lim, W.-S. Seo, S. Lee, Y.S. Lim, J.-Y. Kim, H.-H. Park, S.-M. Choi, K.H. Lee, K. Park, Anisotropy of the thermoelectric figure of merit (zT) in textured $\text{Ca}_3\text{Co}_4\text{O}_9$ ceramics prepared by using a spark plasma sintering process, *J. Kor. Phys. Soc.* 66 (2015) 794–799, <https://doi.org/10.3938/jkps.66.794>.

Supporting information:

Improved thermoelectric properties in ceramic composites based on $\text{Ca}_3\text{Co}_4\text{O}_9$ and $\text{Na}_2\text{Ca}_2\text{Nb}_4\text{O}_{13}$

R. Hinterding^a, M. Wolf^a, M. Jakob^b, O. Oeckler^b, A. Feldhoff^a

^aLeibniz University Hannover, Institute of Physical Chemistry and Electrochemistry, Callinstr. 3A, D-30167 Hannover, Germany
^bLeipzig University, Institute of Mineralogy, Crystallography and Materials Science, Scharnhorststr. 20, D-04275 Leipzig, Germany

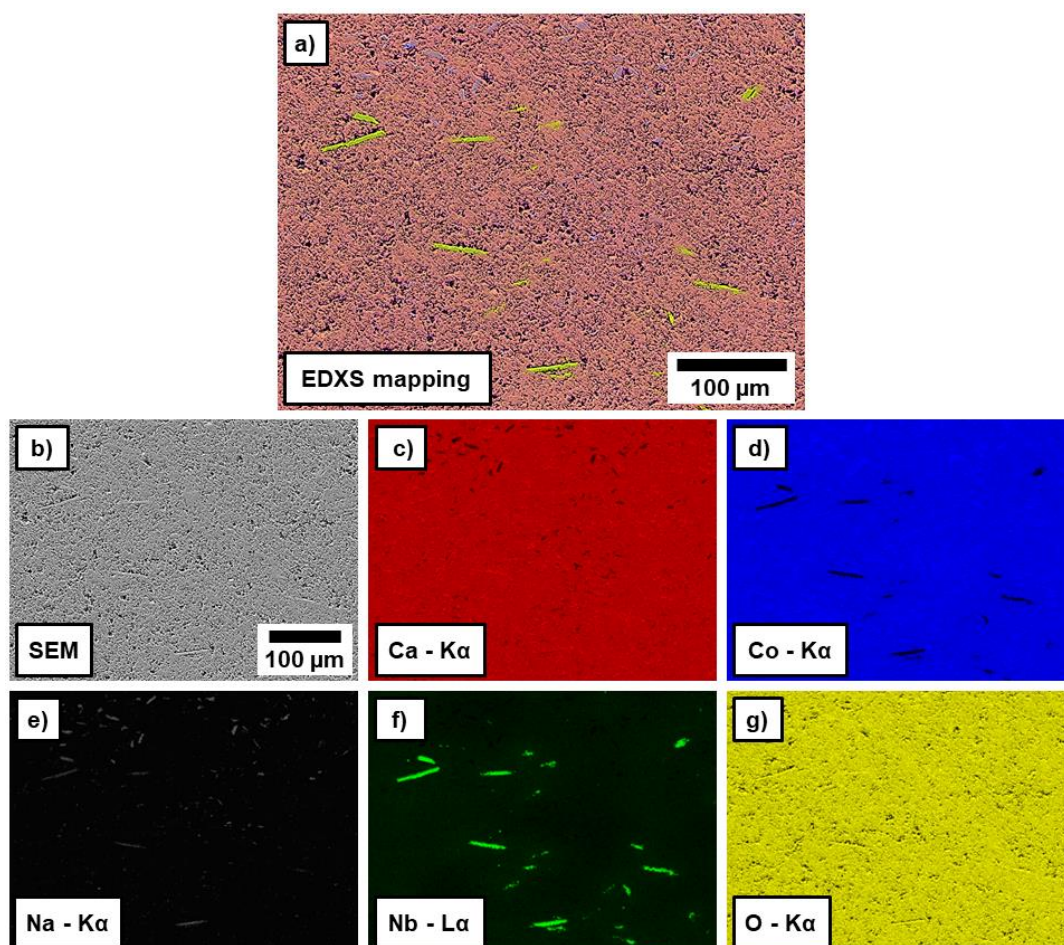


Figure S1: Cross-sectional SEM-EDXS analysis of the 5 wt% NCNO sample showing the distribution of NCNO within the CCO matrix. a) Overlay EDXS mapping summarizing the results from b-g. b) SEM micrograph as basis for EDXS analysis. c-g) Elemental distributions of the respective elements Ca, Co, Na, Nb and O.

The $\text{Na}_2\text{Ca}_2\text{Nb}_4\text{O}_{13}$ reacts to $\text{Ca}(\text{Nb},\text{Co})\text{O}_3$ during sintering. Therefore, an overview for the distribution of CNO within the $\text{Ca}_3\text{Co}_4\text{O}_9$ (CCO) matrix is given in Fig. S1. The elemental mapping in Fig. S1a shows the CNO particles mostly not in contact to each

other and with a preferred orientation. Calcium and cobalt are mostly located within the CCO matrix, while niobium mainly remains within the CNO particles. Some remaining sodium is located within CNO but there is also a Co-, Na- and O-rich phase located within the CCO matrix. The quantitative EDXS results show a Co:Ca ratio of 0.3 and a Co:Na ratio of 0.2, which suggests the formation of CoO with some Ca and Na on the Co position.

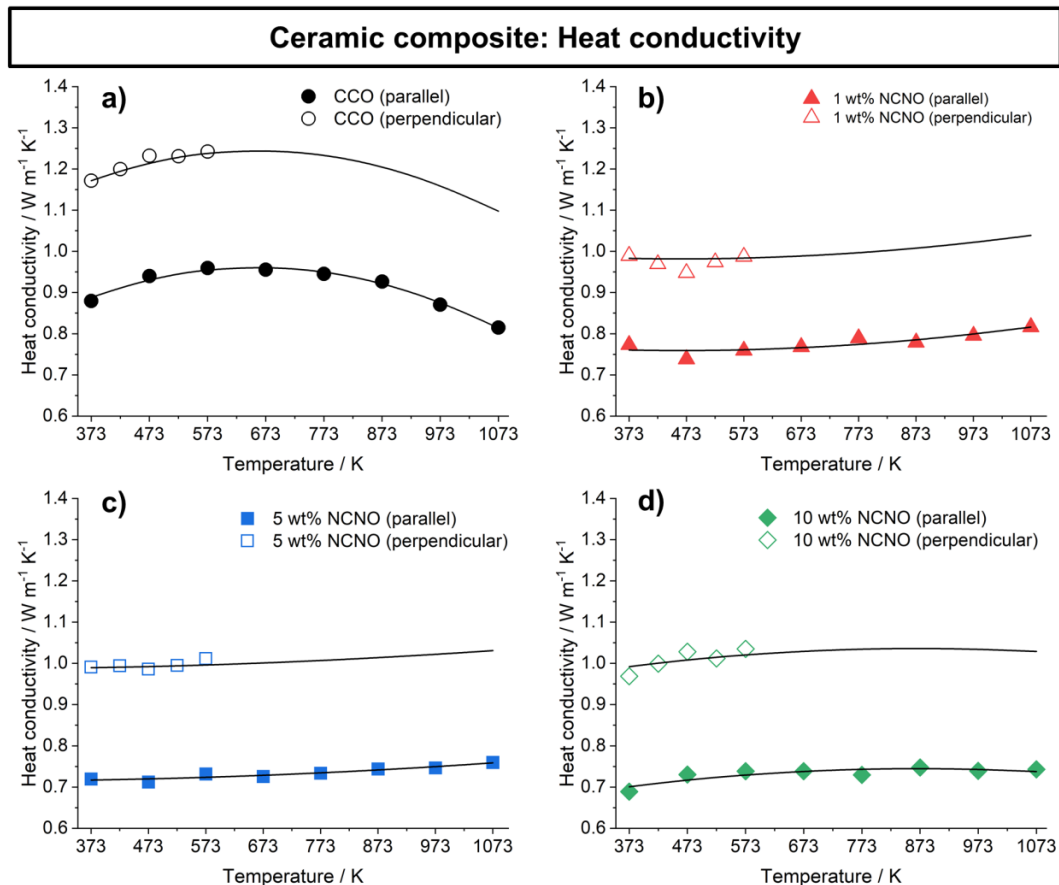


Figure S2: Heat conductivity measurements parallel and perpendicular to the pressing direction. The measurements were conducted for a) CCO, b) 1 wt% NCNO and c) 5 wt% NCNO and d) 10 wt% NCNO samples. The fits were calculated for the parallel measurements and transferred to the perpendicular measurements to estimate the missing values at higher temperatures.

Fig. S2 shows the heat conductivity measurements parallel and perpendicular to the pressing direction. Both directions were necessary to see if the CCO/NCNO ceramic composites show anisotropic transport properties. The higher heat conductivities perpendicular to the pressing direction are caused by a preferred orientation of the CCO and possibly by the additional phases. As the heat conductivity of CCO is lower along the *c*-axis of the material, the CCO sheets were oriented partly by uniaxial pressing. The measurements parallel to the pressing direction required a graphite holder with a temperature limit of 573 K in the oxygen/helium atmosphere. Therefore, similar behaviors along both directions were assumed with good agreement to the

measurements and fits for the parallel direction were calculated. These fits were transferred to the measurements perpendicular to the pressing direction to gain values for 673-1073 K.

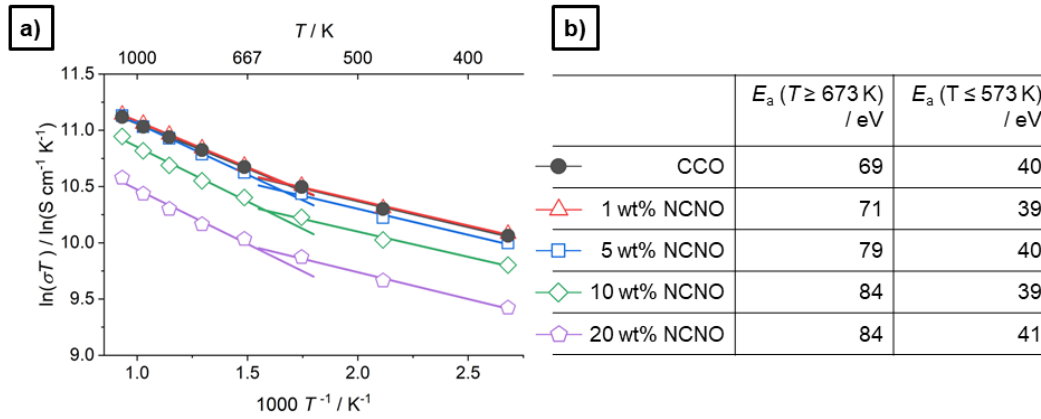


Figure S3: a) Arrhenius plot of the electrical conductivity measurements (compare Fig. 6a) and b) the calculated activation energies for the high-temperature and low-temperature regions.

Fig. S3 shows the Arrhenius plot for the electrical conductivity measurements given in Fig. 6a. For the calculation of the activation energies, the assumption of $\sigma \cdot T \propto \exp(-E_a/k_B T)$ was made [23,50,51]. The five data points with the highest temperatures (673-1073 K) were used for linear regression at high temperatures and the three remaining data points (373-573 K) for linear regression at low temperatures. Two linear regressions were made for each sample as there is a clear change of the slope from 673 K to 573 K. This change can be attributed to a metallic-to-semiconducting transition regarding the transport behavior [23]. The calculated activation energies were extracted by the slope of the lines. While the activation energy at low temperatures stays nearly the same for all samples, the activation energy at high temperatures shows increasing values in dependence on the amount of NCNO.

2.2 Concept II: Nanodimensional approach

2.2.1 Summary

The second concept towards ceramic composites based on $\text{Ca}_3\text{Co}_4\text{O}_9$ involves nanodimensional compounds. As a first approach, two-dimensional (2D) structures within a CCO matrix were formed by heavy doping in a sol-gel synthesis and sintering at 1173 K. Co-doping with sodium, bismuth and terbium on the calcium position beyond the solubility limit resulted in three co-existing phases CCO, Na_xCoO_2 (NCO) and $\text{Bi}_2\text{Ca}_2\text{Co}_2\text{O}_9$ (BCCO). High-resolution TEM (HRTEM) revealed the emergence of semi-coherently aligned 2D layers due to similarities in lattice parameters of the components. The NCO with superior thermoelectric properties but weaker thermal stability in comparison to CCO was stabilized at higher temperature as usual by embedding it in the CCO matrix. Hence, the power factor could be more than doubled in comparison to CCO, but the thermal conductivity was significantly increased as well. Therefore, the overall figure-of-merit was slightly lowered compared to CCO, but considering the importance of the power factor the results are promising nonetheless.

In the second nanodimensional approach, the oxyselenide BiCuSeO (BCSO) was mixed with CCO and reaction sintering resulted in a multiphase oxide composite. Similar to concept I, the crystal shape of the additive was plate-like, but this time nanosheets were used. As expected, the BCSO did not withstand high temperature in air and decomposed. Various compositions in the range of 0 wt% to 30 wt% BCSO in the initial mixture were investigated and the 20 wt% sample showed the best thermoelectric properties. The electrical conductivity was increased to 144 S cm^{-1} at 1173 K while maintaining a high SEEBECK coefficient. This resulted in an 127% increase of the power factor in comparison to pristine CCO and was caused by multiple factors. First of all, elemental EDXS mappings revealed crystal growth of CCO to microdimensional sheets and being doped with Bi and Cu after sintering, which explains the altering properties. Furthermore, the formation of cobalt oxides Co_3O_4 and CoO to a great extent was confirmed as a result of Co leaving CCO. In-situ XRD monitoring of the unsintered mixture revealed Bi_2O_3 as an intermediate phase and supported the assumption of restructured CCO. The formation of Bi_2O_3 was also observed for the 30 wt% BCSO sample due to doping limitations within the CCO. As a result, the electrical conductivity and the power factor were clearly diminished. Finally, thermogravimetric analyses of the sintered ceramics confirmed the thermal stability of the composites up to 20 wt% BCSO and unfinished oxidation for 30 wt% BCSO. Overall, the nanosheets decomposed during the sintering leading to crystal growth of doped CCO and other oxides. The significantly enhanced power factor shows great potential as an oxide composite system.

2.2.2 Triple-phase ceramic 2D nanocomposite with enhanced thermoelectric properties

Michael Bittner, Nikola Kanas, Richard Hinterding, Frank Steinbach, Dennis Groeneveld, Piotr Wemhoff, Kjell Wiik, Mari-Ann Einarsrud, Armin Feldhoff

Journal of European Ceramic Society, 39 **2019**, 1237-1244

DOI: 10.1016/j.jeurceramsoc.2018.10.023



Contents lists available at ScienceDirect

Journal of the European Ceramic Society

journal homepage: www.elsevier.com/locate/jeurceramsoc

Original Article

Triple-phase ceramic 2D nanocomposite with enhanced thermoelectric properties

Michael Bittner^{a,*}, Nikola Kanas^b, Richard Hinterding^a, Frank Steinbach^a, Dennis Groeneveld^a, Piotr Wemhoff^a, Kjell Wiik^b, Mari-Ann Einarsrud^b, Armin Feldhoff^{a,*}^a Institute of Physical Chemistry and Electrochemistry, Leibniz University Hannover, DE-30167 Hannover, Germany^b Department of Materials Science and Engineering, NTNU Norwegian University of Science and Technology, Sem Saelands vei 12, N-7491 Trondheim, Norway

ARTICLE INFO

Keywords:

Thermoelectricity
All-scale hierarchical architecture
2D nanostructures
Nanocomposite
 $\text{Ca}_3\text{Co}_4\text{O}_9$

ABSTRACT

A thermoelectric triple-phase p-type $\text{Ca}_3\text{Co}_4\text{O}_9$ - Na_xCoO_2 - $\text{Bi}_2\text{Ca}_2\text{Co}_2\text{O}_9$ (CCO–NCO–BCCO) 2D nanocomposite was obtained from pressureless sintering in air. The anisotropic thermoelectric properties of the nanocomposite exhibit a high electrical conductivity of 116 S cm^{-1} and a power factor of $6.5 \mu\text{W cm}^{-1} \text{ K}^{-2}$ perpendicular to the pressing direction at 1073 K in air. A corresponding zT value of 0.35 was obtained. Three co-doped, thermoelectrically active misfit-layered materials were stacked to form a triple-phase nanocomposite, which combines the advantages of all three materials. The resulting nanocomposite enables simultaneous increases of the isothermal electrical conductivity σ and the Seebeck coefficient α by charge carrier concentration engineering and synergistic effects. The $\text{Bi}_2\text{Ca}_2\text{Co}_2\text{O}_9$ and Na_xCoO_2 phases were stabilized in a $\text{Ca}_3\text{Co}_4\text{O}_9$ matrix at high temperatures. To evaluate the application of the nanocomposite in high-temperature thermoelectric generators, the representation of the electrical conductivity and power factor in a Ioffe plot was more appropriate than the zT value.

1. Introduction

1.1. Thermoelectric power conversion

Interest in thermoelectric materials (TE) for energy harvesting arises from their ability to convert thermal power directly into electrical power without moving parts. This is mediated by the coupling of currents of entropy I_S and electrical charge I_q in the solid, which can cause a thermally-induced electrical current (Seebeck effect). Under steady state conditions and the assumption of weak temperature dependence of the electron chemical potential as well as of the Seebeck coefficient α , the basic transport equation [1,2] can be expressed by the difference in temperature ΔT and the electrical voltage U over the thermoelectric material of cross-sectional area A and length L as follows:

$$\begin{pmatrix} I_q \\ I_S \end{pmatrix} = \frac{A}{L} \begin{pmatrix} \sigma & \sigma\alpha \\ \sigma\alpha & \sigma\alpha^2 + \Lambda \end{pmatrix} \begin{pmatrix} U \\ \Delta T \end{pmatrix} \quad (1)$$

The thermoelectric material tensor in Eq. (1) is composed of three quantities, which are the isothermal electrical conductivity σ , the Seebeck coefficient α and the entropy conductivity at electrical open circuit Λ (i.e., at vanishing electrical current). Note that each quantity σ , α and

Λ itself is a tensor. The entropy conductivity Λ is related to the traditional heat conductivity λ by the absolute temperature T , as given in Eq. (2).

$$\lambda = T \cdot \Lambda \quad (2)$$

The maximum of the second-law power conversion efficiency $\eta_{II,max}$ is determined solely by the thermoelectric figure-of-merit zT , as given by Eq. (3), which results from tensor element 22 in the thermoelectric material tensor in Eq. (1) [1].

$$zT = \frac{\sigma\alpha^2}{\Lambda} = \frac{\sigma\alpha^2}{\lambda} \cdot T \quad (3)$$

Maximum electrical power output of a thermoelectric material $P_{el,max,mat}$, as shown in Eq. (4), is determined by the geometry (A , L), the power factor $\sigma\alpha^2$ and the temperature difference to the square $(\Delta T)^2$.

$$P_{el,max,mat} = \frac{1}{4} \cdot \frac{A}{L} \cdot \sigma\alpha^2 \cdot (\Delta T)^2 \quad (4)$$

The laws of classical physics restrict the scope for enhancing the power factor $\sigma\alpha^2$ and figure-of-merit zT due to the interrelation of the parameters σ , α and λ . These values depend on the carrier concentration n and the mobility of the carriers μ , which correlate with each other [3].

* Corresponding authors.

E-mail addresses: michael.bittner@pci.uni-hannover.de (M. Bittner), armin.feldhoff@pci.uni-hannover.de (A. Feldhoff).<https://doi.org/10.1016/j.jeurceramsoc.2018.10.023>

Received 30 July 2018; Received in revised form 22 October 2018; Accepted 23 October 2018

Available online 03 November 2018

0955-2219/© 2018 Elsevier Ltd. All rights reserved.

To overcome these limits, several approaches have been postulated and tested during recent years. Previously, the thermoelectric community was focused on reducing λ and thereby optimizing zT . This was performed by tuning the micro- and nanostructure to scatter phonons on all length scales [7,8]. The best material would possess an all-scale hierarchical architecture that scatters phonons on the mesoscale by its microstructure, on the nanoscale by nanoprecipitates or nanostructures and on the atomic scale by point defects (co-doping, cross substitution) [9,10]. The structures should be coherent (endotaxy) and possess electronic band energies matching those of the host material to avoid electron scattering, which would result in reduced electron mobility [11–13].

Recently, more attention has been paid to enhancing the power factor $\sigma \cdot \alpha^2$ [14–17]. Carrier concentration engineering and co-doping can be used to increase the electrical conductivity σ [10]. The approaches of compositionally alloyed nanostructures and band-structure engineering are able to increase the Seebeck coefficient α [11,13]. The most promising approach to enhance the power factor in an almost temperature-independent manner is band-structure engineering with resonant levels or resonant impurities and the introduction of additional electronic bands [14,18]. The goals of this effort are the distortion and increase of the electronic density of states (DOS) in the vicinity of the Fermi level as much as possible. Hicks and Dresselhaus forecasted nanostructures such as 2-dimensional (2D) quantum wells and 1D quantum wires to be suitable for tuning the DOS in the vicinity of the Fermi level by the aforementioned techniques [19].

1.2. Oxides

State-of-the-art commercially available bulk thermoelectric materials include alloys, tellurides and half-Heusler or Zintl phases, such as Bi_2Te_3 [20], PbTe-PbS [16], SiGe [21], SnSe [22], FeNbSb [17] and $\text{Yb}_{14}\text{MnSb}_{11}$ [23]. These materials exhibit inferior stability at high temperature and in oxidizing atmospheres, are toxic, or include expensive and rare elements. However, thermoelectric oxides are expected to be viable materials for addressing these problems due to their benefits, such as non-toxicity, mechanical, thermal and chemical stability at high temperatures in air [24–26].

Recently, a new thermoelectric oxide material was discovered: BiCuSeO oxyselenides possess excellent thermoelectric properties in the moderate-temperature range (up to 650 °C), being comparable to alloys, Half-Heusler and Zintl phase materials [27–29]. However, BiCuSeO oxyselenides are not stable at high temperatures under oxidizing conditions [30]. In terms of the figure-of-merit zT , oxides which are stable in air cannot compete with other material classes. For this reason, the development of oxides should focus on high power factors and electrical conductivity, to enhance the electrical power output of thermoelectric generators at high temperatures. Narducci postulated that if an infinite heat source is available for thermoelectric energy conversion, a high power factor and a moderate heat conductivity are beneficial for high electrical power outputs [31].

The layer-structured cobalt oxide $\text{Ca}_3\text{Co}_4\text{O}_9$ (CCO), based on CaO , has already been investigated and sustains high temperatures up to 1198 K [32–34]. CCO possesses a monoclinic crystal structure formed by a misfit-layered structure of a CdI_2 -type CoO_2 subsystem with a triangular lattice and a layered rock-salt subsystem of three Ca_2CoO_3 units, which alternate along the c -axis. The two subsystems of the monoclinic system have different b -axis parameters and form an incommensurate structure, as shown in Fig. 1a [4]. The synthesis of doped CCO via the well known sol-gel technique, reveals several advantages such as homogeneity, grain size and stoichiometric control [33]. The layered crystal structure affects also grain shape and has significant impact on anisotropy, degree of compacting and thereby on thermoelectric properties, especially on isothermal electrical conductivity and heat conductivity.

In this work, sol-gel synthesis is used as a “bottom-up” technique to

co-dope Na, Bi and Tb to the Ca-site of the Ca_2CoO_3 subsystem, which is visualized in Fig. 1a. Table S 1† in the supplementary information shows the ionic radii of the substituted elements and dopants. According to the similarity of the ionic radii, doping should be possible. Co-doping can adjust carrier concentrations and introduce resonant impurities to enhance the thermoelectric properties σ and α . According to Eq. (4), this directly improves the electrical power outputs of the obtained materials. Thus, σ can be enhanced by Na and Bi doping [10,35,36], while α can be improved by rare-earth doping (Tb) due to the hybridization of electronic bands with sp character [13,26,37,38].

Increasing the doping level of Na and Bi leads to the formation of a triple-phase nanocomposite of co-doped CCO, Na_xCoO_2 (NCO) and $\text{Bi}_2\text{Ca}_2\text{Co}_2\text{O}_9$ (BCCO). NCO and BCCO also have monoclinic misfit-layered crystal structures, revealed in Fig. 1b and c, which are comparable to that of CCO [4,6,39,40]. The three structures simply differ in stacking and composition of the rock salt layer. Compared to CCO, BCCO possesses a higher α but a lower σ and NCO vice versa [6,41,42]. Overall, a nanocomposite (CCO–NCO–BCCO) of a co-doped CCO phase and “compositionally alloyed nanostructures” [10] of NCO and BCCO with partially coherent layered structures promise enhanced thermoelectric properties compared to those of the single materials. The formation of a high power triple-phase nanocomposite stabilizes the NCO and BCCO phases at elevated temperatures and hence enables application in thermoelectric generators for energy conversion.

2. Materials and methods

2.1. Synthesis

Different elements like Li, Ce, Sm and Yb next to Na, Bi and Tb were tested as dopants for CCO. The best combination was found to be Na, Bi and Tb. Na, Bi and Tb co-doped CCO powders were synthesized via a sol-gel route, which provides fine-grained particles of homogenous composition as described by [43] for perovskites and by [33] for pure CCO. Calcium(II) nitrate tetrahydrate 99.98%, cobalt(II) nitrate hexahydrate ACS 98–102.00%, bismuth(III) nitrate hydrate 99.999%, terbium(III) nitrate hydrate 99.9% and sodium nitrate $\geq 99.5\%$ from Alfa Aesar were used as sources. The calcined powder samples were uniaxially cold pressed at 200 MPa and pressurelessly sintered in air for 20 h at 1173 K. Reference samples of CCO, BCCO and NCO phases were cold pressed at 200 MPa and sintered for 10 h at 1173, 1123 and 1073 K, respectively. Table 1 shows the stoichiometry and abbreviation of synthesized samples. All steps, synthesis, calcination and sintering, were conducted under ambient air conditions.

2.2. Microstructure analysis

The phase compositions of the synthesized powders and sintered ceramics were characterized via X-ray diffraction (XRD) using a Bruker D8 Advance with $\text{Cu-K}\alpha$ radiation. Microstructural characterization and elemental analysis of polished ceramic samples were performed using a JEOL JSM-6700F field-emission scanning electron microscope (FE-SEM) equipped with an Oxford Instruments INCA 300 (energy-dispersive X-ray spectroscopy, EDXS). Transmission electron microscopy (TEM) was performed at 200 kV using a JEOL JEM-2100F-UHR equipped with an Oxford Instruments INCA 300 (EDXS) for elemental analysis. Elemental distribution information of analyzed materials were obtained from Na- $\text{K}\alpha$, Ca- $\text{K}\alpha$, Bi- $\text{L}\alpha$, Co- $\text{K}\alpha$, Tb- $\text{L}\alpha$ and O- $\text{K}\alpha$ transitions. Density and porosity were measured by Archimedes method (ISO 5018:1983) using isopropanol. Density values were averaged from 3 measurements with less than 2% deviation. The heat capacity C_p , was estimated by differential scanning calorimetry (DSC) with a Netzsch STA 409 PC/PG in a synthetic air atmosphere with a flow of 30 mL min^{-1} and a heating rate of 5 K min^{-1} within the range of 313–1173 K.

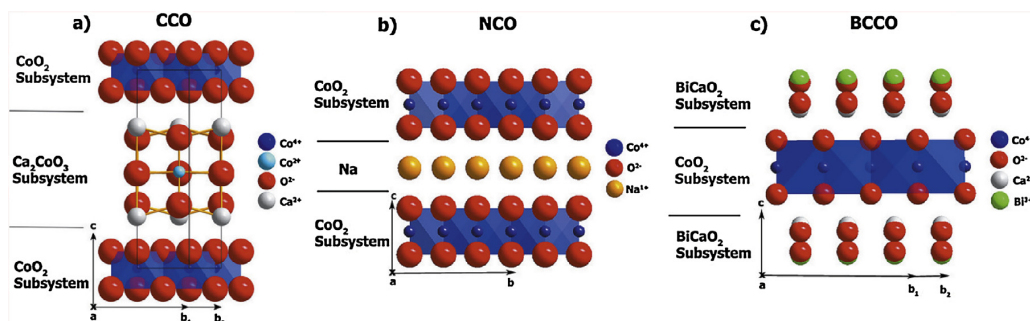


Fig. 1. Crystal structures of (a) $\text{Ca}_3\text{Co}_4\text{O}_9$ (CCO), (b) Na_xCoO_2 (NCO) and (c) $\text{Bi}_2\text{Ca}_2\text{Co}_2\text{O}_9$ (BCCO) along the a -axis. The ions involved are indicated by spheres of different size and colour: cobalt (small) in blue and turquoise, oxygen (large) in red, calcium (medium) in grey, bismuth (large) in green and sodium (large) in orange. Note b_1 and b_2 in (a), (b) form an irrational ratio, and the aperiodic crystal structure is described by superspace groups. Crystal structure data were taken from [4–6]. (For interpretation of the references to color in this figure legend, the reader is referred to the web version of this article.)

Table 1

Stoichiometry and abbreviation of synthesized nanocomposites (CCO-30-35-6, CCO-30-35-8, CCO-30-35-10) and reference samples (CCO, BCCO, NCO).

Stoichiometry	Abbreviation
$\text{Ca}_3\text{Co}_4\text{O}_9$	CCO
Na_xCoO_2	NCO
$\text{Bi}_2\text{Ca}_2\text{Co}_2\text{O}_9$	BCCO
$\text{Ca}_{2.29}\text{Na}_{0.3}\text{Bi}_{0.35}\text{Tb}_{0.06}\text{Co}_4\text{O}_9$	CCO-30-35-6
$\text{Ca}_{2.27}\text{Na}_{0.3}\text{Bi}_{0.35}\text{Tb}_{0.08}\text{Co}_4\text{O}_9$	CCO-30-35-8
$\text{Ca}_{2.25}\text{Na}_{0.3}\text{Bi}_{0.35}\text{Tb}_{0.1}\text{Co}_4\text{O}_9$	CCO-30-35-10

2.3. Measurement of thermoelectric properties

To investigate the thermoelectric properties of the manufactured oxide materials, σ , α and λ were measured as functions of temperature and pressing direction. To obtain a large ceramic sample (CCO-30-35-6, 30-35-8 and 30-35-10), the green body was pressed at 200 MPa using a 16 mm die and reground and pressed again, followed by a sintering process of 20 h at 1173 K. Samples were cut from large ceramic pellets (cylindrical, 16 mm \times 16 mm) in bar shape (10 mm \times 1.2 mm \times 1.2 mm and 10 mm \times 2.5 mm \times 2.5 mm) parallel and perpendicular to the pressing direction. The σ values were estimated by a pseudo 4-point measurement at equilibrium conditions, utilizing a horizontal three-heating-zone tube furnace from Carbolite Gero EVZ 12/450B and a home-made measurement cell. The α values were measured using a ProboStat A setup from NorECs at equilibrium conditions in a furnace from Elite Thermal Systems Ltd. The values were logged using KEITHLEY 2100 6 $\frac{1}{2}$ Digital Multimeters. Data were acquired and converted using Lab VIEW software. The measurements of σ and α (heated to 1073 K and measured down with equilibrium at every temperature) were repeated from samples cut perpendicular and parallel to the pressing direction with less than 5% deviation. The uncertainties of 5 and 2% for α and of 10 and 4% for the power factor (the latter obtained from samples cut parallel to the pressing direction), were averaged from 5 values. The values of λ were estimated using $\lambda = D \cdot C_p \cdot \rho$ and a LFA 457 MicroFlash laser flash setup from Netzsch under synthetic air atmosphere. Measurements of the thermal diffusivity D , averaged from 3 values, showed less than 5% deviation. Accordingly, the uncertainties for the zT value were calculated to be 10 and 5% (the latter obtained from samples cut parallel to the pressing direction). More details are given in the supporting information[†].

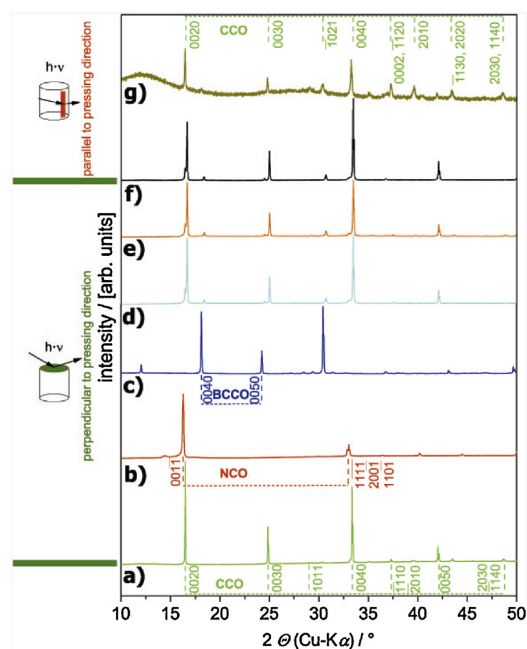


Fig. 2. X-ray diffraction patterns of ceramic samples: (a) CCO (taken from [33]), (b) NCO, (c) BCCO, (d) CCO-30-35-6, (e) CCO-30-35-8, (f) CCO-30-35-10 (perpendicular to pressing direction), (g) CCO-30-35-10 (parallel to pressing direction). CCO (green) and BCCO (blue) reflections were indexed in superspace group Cm (0 1 – p 0, equivalent to Bm (0 0 γ), no. 8.3 [44,40]). NCO (red) reflections were indexed in superspace group C2/m [6]. The main NCO reflections (001-1 and 22-1-1, 200-1, 110-1) overlap with CCO (green) reflections. Difference in texture was obtained from samples, which were cut perpendicular (d–f) and parallel to the pressing direction (g). Additional XRD patterns of NCO and BCCO are given in S1 \ddagger . (For interpretation of the references to color in this figure legend, the reader is referred to the web version of this article.)

3. Results and discussion

3.1. Composition of triple-phase nanocomposites

The XRD patterns of all three phases (CCO, NCO, BCCO) within the triple-phase nanocomposite are shown as individual references in Fig. 2a–c. With increasing doping level above the solubility limit of the CCO matrix, the formation of a composite material consisting of CCO, NCO and BCCO phases during sintering at 1173 K was enabled, as

shown in Fig. 2d–g.

As the Tb content was increased, the ceramics became slightly more textured and oriented compared with the CCO reference in Fig. 2a (weaker 0020, 2010 and stronger 0040, 0050 CCO reflections). Furthermore, the reflections were less shifted to lower angles with increasing Tb-content. Hence, Tb was assumed to facilitate the formation of the CCO–NCO–BCCO nanocomposite, and smaller amounts of Bi were integrated into the CCO structure. Reflections of the NCO (001-1) and BCCO (0040, 0050) phases can be found within the nanocomposites, as shown in Fig. 2d–g. Depending on the direction of cold pressing and cutting of the ceramic green body, different texture was obtained, as displayed in Fig. 2d–f (perpendicular) and Fig. 2g (parallel). Parallel to the direction of cold pressing of the green body, the ceramic showed a more variegated mixture of reflections from different planes, although the reflections 0010 (0020, 0030, 0040, etc.) remained the most intense.

Supplementing the XRD patterns, microstructural characterization by SEM revealed the NCO phase and confirmed the CCO and BCCO phases within the composite material. The microstructure of NCO and BCCO phases are displayed in Fig. S 2†, while SEM micrographs and elemental distributions of polished cross-sections of CCO–NCO–BCCO nanocomposites are shown in Fig. 3. The representation of the elemental Tb content in the SEM mappings was resigned due to the homogenous distribution on the microscale and therefore missing scientific information. Values of the density of NCO and BCCO are given in Table 2. Co-doping with Na, Bi and Tb resulted in a nanocomposite material of CCO, BCCO and NCO grains with pores in between. Increasing the doping level of Tb led to the formation of a denser

nanocomposite, as shown in Fig. 3a–f, and subsequently decreased porosity, given in Table 2. This porosity has a strong impact on thermal and electrical conductivity, because both values are decreasing with increased thermal and electrical contact resistances [33,34]. The values of both, thermal and electrical conductivity, are also influenced by the degree of grain orientation, since the grains have anisotropic transport characteristics. Moreover, the higher the grain orientation, the lower is the porosity.

The CCO-30-35-10 nanocomposite was further examined by TEM. Fig. 4a–f identifies semi-coherently aligned 2D nanostructures. The material was pervaded by NCO, BCCO and CCO 2D layers, revealed in Fig. 4a and b. These layers were homogeneously distributed throughout the material, alternating in thickness and sequence. As shown in Fig. 4b and c, the different layers were co-doped with Na, Bi and Tb in the CCO phase, Ca, Bi and Tb in the NCO phase, and Na and Tb in the BCCO phase, respectively. The Tb content was enriched in the CCO and BCCO, while decreased in the NCO phase.

These co-doped layers of NCO and BCCO seemed to be stabilized at high temperatures by the interdiffusion of the doped elements and surrounding phases, represented in the linescan of Fig. 4c. The NCO phase, not implemented in the nanocomposite, exhibited the lowest chemical and thermal stability at high temperatures. As illustrated in Fig. 5a, the NCO reference phase began decomposing in air at approximately 963 K. Although, the interdiffusion of Ca, Bi and Tb, as shown in Fig. 4c, could stabilize this phase (Bi and Tb may occupy Na positions). The effect of the interdiffusion of Ca into the NCO phase also seemed to depend on its thickness and surroundings. Fig. 4d–f reveals the three feasible heterophase interfaces, BCCO–CCO, CCO–NCO and BCCO–NCO within the nanocomposite. The different phases grew semi-coherently on each other, facilitated by their similar, layered structure. The lattice parameters, given in Table 3, show similar values for the *a*-axis, while the *c*-parameter within the different phases was slightly lower than a multiple of the *c*-parameter in NCO. The NCO phase also exhibited areas of amorphous-like character with many defects, as displayed in Fig. 4f. This phase was naturally less stable, but the amorphous-like phase formation could be either attributed to very thin layers, a cation-deficient metastable phase or damage from Ar-ion polishing during specimen preparation. Analyses from SEM and TEM, as shown in Figs. 3 and 4, revealed structures on the micro- and nanoscale. Fig. 4c confirmed point defects on the atomic scale, which were introduced by interdiffusion and co-doping. Overall, structural investigations verified an all-scale hierarchical structure of the nanocomposites. Hence, phonons could be scattered on the microscale, nanoscale and atomic scale, while at the same time, semi-coherently aligned, misfit-layered materials were present as shown.

3.2. Thermoelectric properties

The thermoelectric properties of reference NCO and BCCO materials are shown in Fig. 5. The NCO material shows a high electrical conductivity of 142 S cm^{-1} at 963 K, but low Seebeck coefficient of $175 \mu\text{V K}^{-1}$ at 873 K. The NCO material decomposes at about 963 K in air, leading to a decreased conductivity. In contrast to this, the BCCO material has a high Seebeck coefficient of $274 \mu\text{V K}^{-1}$ at 973 K, but a low electrical conductivity of 18 S cm^{-1} at 1023 K. The BCCO material is stable up to 1023 K in air.

The thermoelectric properties of CCO and nanocomposites are based on an anisotropic character, as shown in Fig. 6. This anisotropy is caused by the crystal structures of the three basic materials CCO, NCO and BCCO, as illustrated in Fig. 1a–c, and by compression and sintering, which led to grain orientation, as shown in Figs. 2, 3 and 4. The thermoelectric properties σ , α and power factor of CCO and the nanocomposite ceramics, are illustrated in Fig. 6a and b as a function of temperature and depend on the pressing direction. The trend for σ for all samples, displayed in Fig. 6b, was almost constant throughout the temperature range and reached 116 S cm^{-1} at 1073 K for CCO-30-35-

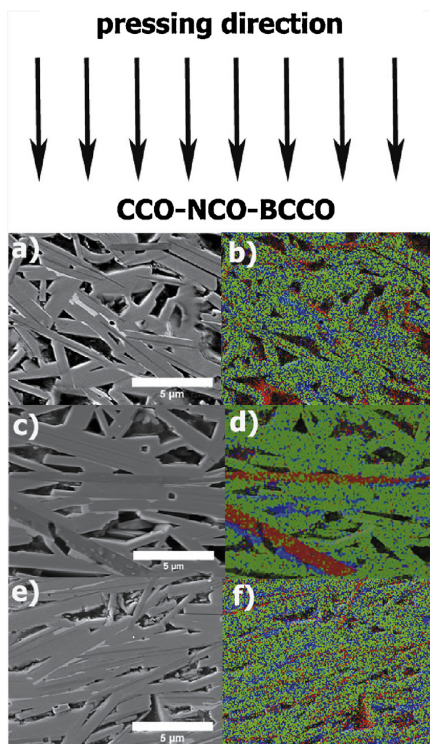


Fig. 3. Cross-sectional SEM micrographs and EDXS elemental distributions of CCO–NCO–BCCO nanocomposite ceramics: (a, b) CCO-30-35-6; (c, d) CCO-30-35-8; (e, f) CCO-30-35-10. The CCO phase is dominated by Ca (green), the NCO phase by Na (red) and the BCCO phase by Bi (blue). The direction of uniaxial cold pressing is indicated by black arrows. Additional SEM sites of NCO and BCCO are shown in Fig. S 2†. (For interpretation of the references to color in this figure legend, the reader is referred to the web version of this article.)

Table 2

Density and porosity of reference ceramics (CCO, NCO, BCCO) and nanocomposite ceramics. References were sintered for 10 h at 1173, 1123, 1073 K and nanocomposites for 20 h at 1173 K. Values of the density were measured using ISO (International Organization for Standardization) 5018:1983. Reference values for CCO are taken from [33]. True density of composite ceramics is unknown.

Material abbreviation	Bulk density (g cm^{-3})	True density (g cm^{-3})	Open porosity (%)	True porosity (%)	Closed porosity (%)	Theoretical density (%)
CCO	3.2 ± 0.1	4.68	33.3 ± 0.7	33.5 ± 1.1	0.2 ± 0.7	67.7 ± 1.5
NCO	3.2 ± 0.0	4.65	15.7 ± 2.6	30.6 ± 0.2	14.9 ± 2.8	69.4 ± 0.0
BCCO	5.5 ± 0.0	6.82	1.6 ± 0.9	19.8 ± 0.6	18.1 ± 0.4	80.2 ± 0.0
CCO-30-35-6	3.9 ± 0.0		21.5 ± 0.3			
CCO-30-35-8	3.9 ± 0.0		22.1 ± 0.9			
CCO-30-35-10	3.9 ± 0.0		19.2 ± 0.7			

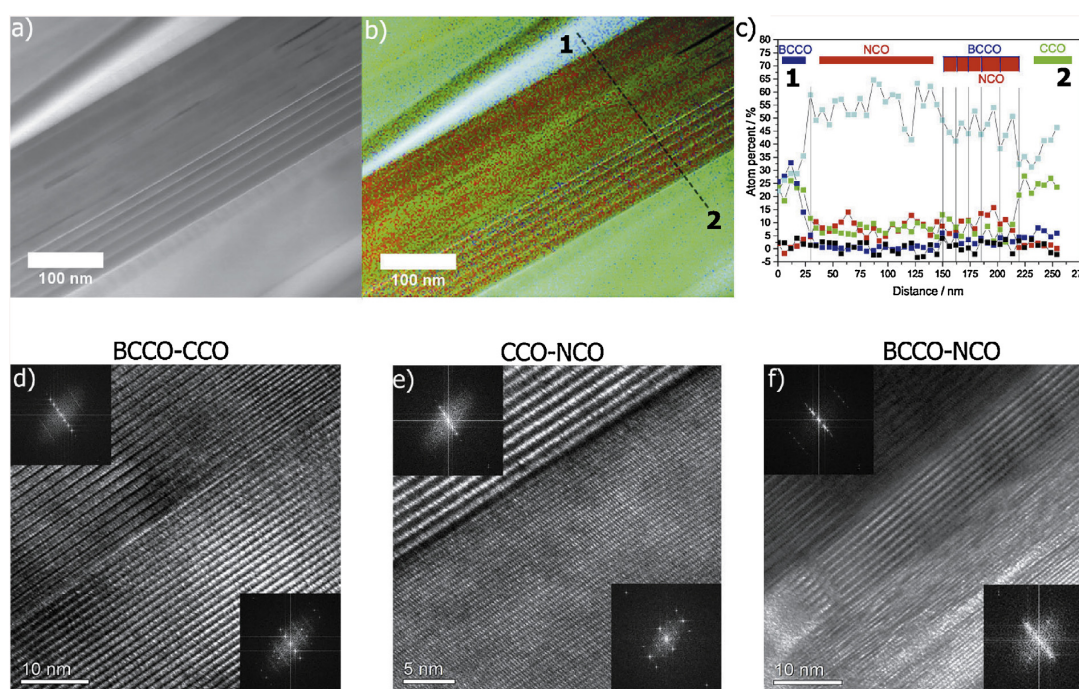


Fig. 4. TEM analysis of a CCO-30-35-10 nanocomposite ceramic: (a, b) Scanning transmission electron microscopy (STEM) dark-field micrograph and EDXS elemental distribution (more detail in Fig. S 3, 4†). The CCO phase is dominated by Ca, the NCO phase by Na and the BCCO phase by Bi. (c) Linescan of 5.7 nm point-to-point distance of the elemental distribution of Na (red), Ca (green), Bi (blue), Tb (black) and Co (turquoise) in the area shown in (b) and along the indicated dotted line. (d–f) High-resolution transmission electron microscopy (HRTEM) micrographs of the heteromaterial interfaces BCCO–CCO, CCO–NCO and BCCO–NCO. Insets show the reduced fast Fourier transformation (rFFT), which are shown in more detail in Fig. S 5†. Additional TEM sites are shown in Figs. S 6–8†. (For interpretation of the references to color in this figure legend, the reader is referred to the web version of this article.)

10 perpendicular to the pressing direction. The σ values of CCO and of CCO-30-35-10 were also measured parallel to the pressing direction and reached 48 S cm^{-1} and 51 S cm^{-1} , respectively, at 1073 K. These materials showed similar behavior because of the enhanced orientation and nanocomposite composition in CCO-30-35-10. As shown in Fig. 3, the nanocomposite ceramics contained not only a Na, Bi and Tb co-doped CCO phase, but also NCO phase [6,45], which is electrically highly conductive, as indicated in Fig. 5a. It is concluded, that the incorporated and stabilized, co-doped NCO phase further increased the σ value of the nanocomposite material. Both, the formation of a BCCO phase, which has a high α value [41,42], as illustrated in Fig. 5b, and the integration of Bi and Tb [38] at Ca-site positions, increased the α value of the nanocomposite. The NCO and BCCO materials show inferior stability at temperatures above 963 and 1023 K in air, respectively, as shown in Fig. 5. However, the incorporation of NCO and BCCO into a stable matrix like CCO stabilized these materials at high temperatures (above 963 K, 1023 K) in air. As long as nanocomposites are used up to 1073 K, they show good cycle stability. A different

manuscript, which addresses stability and thermoelectric generators is going to be published soon. The generators were annealed at least two times up to 1073 K and subsequently tested from 973 to 1173 K in air. The results were stable and in accordance with the thermoelectric properties of the single materials. For this reason, the microstructure of the nanocomposites is assumed to be stable and unchanged. The behavior of α for all nanocomposites, shown in Fig. 6a, was likewise similar, starting from different values and increased with temperature, reaching 236 and $250 \mu\text{V K}^{-1}$ at 1073 K for a CCO-30-35-10 nanocomposite ceramic perpendicular and parallel to the pressing direction, respectively. The absolute values of σ for the different materials increased with doping content of Tb. The simultaneous increases in σ and α indicate an increased charge carrier density n and carrier mobility μ in the nanocomposite ceramics. The impact of Bi on the thermoelectric properties of c -axis-oriented CCO thin films was reported by Sun et al. [46], and Saini et al. [38] showed that Tb-doping increased the value of μ .

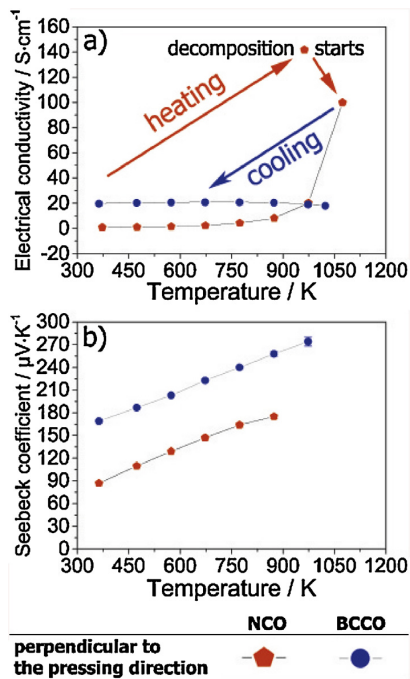


Fig. 5. Thermoelectric parameters of NCO (pentagon, red) and BCCO (circle, blue) as a function of temperature in air: (a) Isothermal electrical conductivity σ , direction of heating, cooling, start of NCO decomposition and highest value of NCO before decomposition are indicated. (b) Seebeck coefficient α . Samples were cut and measured perpendicular to the pressing direction. Uncertainties are indicated by error bars. (For interpretation of the references to color in this figure legend, the reader is referred to the web version of this article.)

Table 3

Lattice parameters (in Å) of the CCO, NCO and BCCO phases at the interfaces BCCO–CCO, BCCO–NCO and CCO–NCO within a CCO-30-35-10 nanocomposite, as analyzed by HRTEM (Fig. 4). Values were measured from reduced fast Fourier transformations (rFFT). Semi-coherent lattice parameters are in bold.

Interfaces			
	(1) BCCO–CCO	(3) BCCO–NCO	(2) CCO–NCO
BCCO	$c = 15.02$	$b_1 = 3.13, c = 14.81$	
CCO	$a = 5.11, b_2 = 4.55$ $c = 10.96$	$c = 10.67$	
NCO		$a = 5.26, c = 5.47$	$a = 5.07, b_1 = 2.82$ $c = 5.74$

3.3. Challenges in manufacturing

The manufacturing of a large, crack-free and homogeneous ceramic sample from uniaxially pressing and pressureless sintering in air, in order to measure the transport properties parallel to the pressing direction, is challenging. For this reason, thermoelectric properties parallel to the pressing direction were solely reported for the CCO-30-35-10 sample, which showed best values perpendicular to the pressing direction. In previous reports about the anisotropic properties of CCO, large and dense materials were obtained from cold isostatically pressing (CIP) [48], spark plasma sintering (SPS) [49] and hot-pressing (HP) [50,51].

3.4. Figure-of-merit zT vs. Ioffe plot

The zT values of CCO and CCO-30-35-10 nanocomposite, shown in

Fig. 6d, were determined according to Eq. (3), from the calculated power factor and the corresponding values of the heat conductivity λ perpendicular and parallel to the pressing direction, respectively. The λ values of the CCO-30-35-10 nanocomposite, as shown in Fig. 6c, reached 1.96 and 1.1 W m⁻¹ K⁻¹, respectively, at 1073 K perpendicular and parallel to the pressing direction. The anisotropy in the thermal transport properties is illustrated by the difference of the heat conductivity perpendicular and parallel to the pressing direction. Fig. 59† illustrates the measured values of the heat capacity C_p as a function of temperature in the range from 313 K to 1173 K. The heat capacity C_p reached approximately 0.83 J K⁻¹ g⁻¹ at 1073 K for a CCO-30-35-10 nanocomposite. The trend and values of C_p as a function of temperature were similar to the values for pure CCO reported by Jankovsky et al. [52] and were consistent with phononic Debye–Einstein behavior. Values of the figure-of-merit zT at 1073 K, as shown in Fig. 6d, were as follows: 0.4 (parallel to the pressing direction, CCO), 0.35 (perpendicular, CCO-30-35-10) and 0.31 (parallel, CCO-30-35-10). A very low heat conductivity λ , which is given in Fig. 6c, led to a high zT value of CCO in the direction parallel to the pressing direction. However, CCO shows low values in the Ioffe plot of Fig. 6b of both thermoelectric power factor $\sigma \cdot \alpha^2$ and electrical conductivity σ [33], which is detrimental for power generation.

The thermoelectric power factor of nanocomposites, calculated from σ and α perpendicular and parallel to the pressing direction, is shown in a Ioffe plot in Fig. 6b as a function of the electrical conductivity. The Ioffe plot is suitable to estimate the capability of a thermoelectric material in power generation applications, due to the combined presentation of electrical conductivity σ and the power factor $\sigma \cdot \alpha^2$ [47]. A large improvement was observed due to the simultaneous enhancement of σ and α by Na, Bi and Tb co-doping and the formation of a nanocomposite material, which is, according to Eq. (4), beneficial for power generation. The thermoelectric power factor of the CCO-30-35-10 nanocomposite, represented in Fig. 6b, reached 6.5 and 3.2 $\mu\text{W cm}^{-1} \text{K}^{-2}$ at 1073 K, perpendicular and parallel to the pressing direction, respectively. The consideration of all parameters within the figure-of-merit zT , according to Eq. (3), conceals the specific properties of the materials, a thermal isolator with low electrical conductivity can provide a high zT value. However, a thermal isolator, which has a high figure-of-merit zT , but poor electrical properties, is not useful for high electrical power generation. The Ioffe plot, illustrated in Fig. 6b, which considers the thermoelectric power factor and the electrical conductivity, is more appropriate according to Eq. (4), to evaluate the applicability of a material for high-temperature power generation.

3.5. Comparison and evaluation

Nanocomposites from pressureless sintering in air exhibited similar trends of the heat conductivity λ , but absolute values of 1.83, 1.79 and 1.96 W m⁻¹ K⁻¹ at 1073 K differed, as shown in Fig. 6c. Solely based on this figure, the inclusions of NCO and BCCO appear to enhance the thermal conductivity. However, dense CCO materials from SPS [49] and HP [50] showed much higher λ values of 3.0 and 2.8 W m⁻¹ K⁻¹ perpendicular to the pressing direction than dense nanocomposites presumably would. As a result, different microstructures, values of density and electrical conductivity of the pure CCO and CCO–NCO–BCCO nanocomposite ceramics make a comparison difficult. As shown in Fig. 6c, the nanocomposite revealed a λ value of 1.1 W m⁻¹ K⁻¹ at 1073 K parallel to the pressing direction. Previous reports about anisotropic transport properties in highly oriented CCO revealed a heat conductivity of 1.5 and 1.2 W m⁻¹ K⁻¹ parallel to the pressing direction [49,50]. Concerning the electrical conductivity σ and the Seebeck coefficient α , Nong et al. were able to enhance σ to about 130 S cm⁻¹ and α to approximately 235 $\mu\text{V K}^{-1}$ at 1073 K perpendicular to the pressing direction by co-doping with Ag, Lu and spark plasma sintering of a dense material [26]. Saini et al. showed a significant increase in α by Tb-doping up to 325 $\mu\text{V K}^{-1}$ at 800 K for a

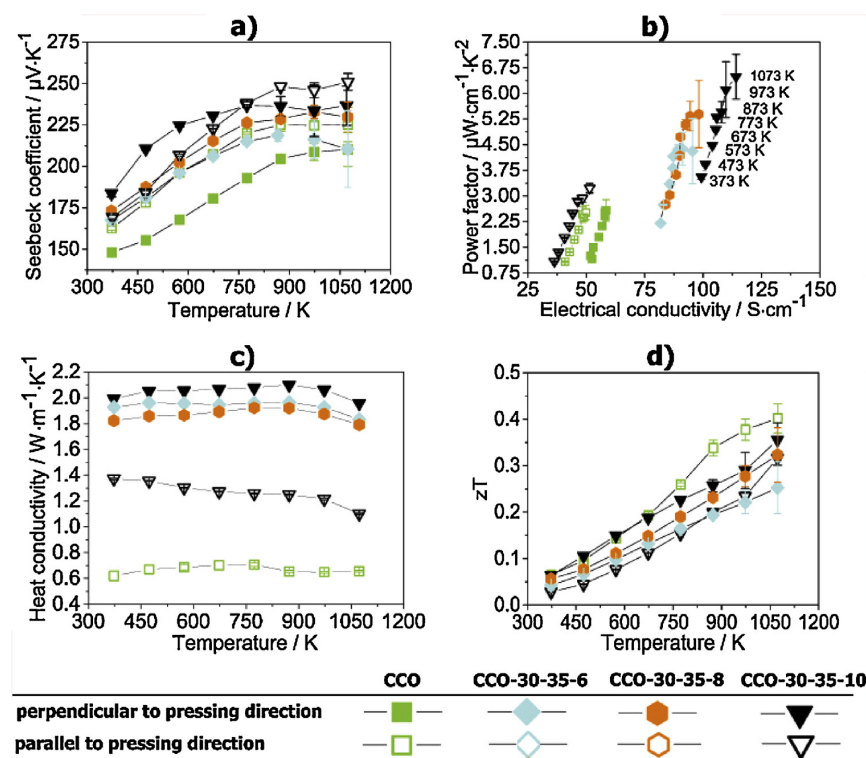


Fig. 6. Thermoelectric parameters of CCO (square, green, taken from [33]), CCO-30-35-6 (diamond, turquoise), CCO-30-35-8 (hexagon, orange) and CCO-30-35-10 (reverse rectangle, black) as a function of temperature: (a) Seebeck coefficient α , (b) Ioffe plot, power factor $\sigma \cdot \alpha^2$ as a function of σ [47], (c) heat conductivity λ and (d) figure-of-merit zT . Closed and open symbols represent values measured from samples perpendicular and parallel to the pressing direction, respectively. Uncertainties are indicated by error bars. (For interpretation of the references to color in this figure legend, the reader is referred to the web version of this article.)

$\text{Ca}_{3-x}\text{Tb}_x\text{Co}_4\text{O}_9$, $x = 0.5$ ceramic, perpendicular to the pressing direction [38]. By comparing the thermoelectric properties of the stacked 2D nanocomposite with the aforementioned reports, further improvements could be achieved with enhanced density, for example by utilization of alternative processing techniques. However, the comparison of the anisotropic thermoelectric properties of manufactured nanocomposites with CCO-based materials from literature is difficult. According to the used synthesis route and processing technique, the obtained properties like density, microstructure and degree of orientation of the materials are different. As a consequence, the obtained thermoelectric properties of these materials can not be easily compared to each other.

The pure phases of CCO [49], NCO [53] and BCCO [41] show a thermoelectric power factor of about 5, 3 and $1 \mu\text{W}\cdot\text{cm}^{-1}\cdot\text{K}^{-2}$ at 1073 K, 900 K and 1000 K, respectively. These lower values of the thermoelectric power factors, compared to the triple-phase CCO–NCO–BCCO nanocomposite, were obtained from much higher polycrystalline bulk densities of 96–99%.

Strong anisotropy was also observed for σ and α , however, the values perpendicular and parallel to the pressing direction were enhanced due to co-doping and composite formation. The highest power factor and zT value were obtained perpendicular to the pressing direction for the CCO-30-35-10 nanocomposite. The high thermoelectric power factor $\sigma \cdot \alpha^2$, electrical conductivity σ , shown in the Ioffe plot in Fig. 6b, and the moderate heat conductivity λ are beneficial for power generation at high temperatures from infinite heat sources [31]. Thermoelectric materials should be designed and utilized in consideration of their application area, for example high energy conversion efficiency or high power generation. In this work, a high power material of semi-coherent 2D nanostructures was developed. This triple-phase nanocomposite has simultaneously enhanced thermoelectric properties and is applicable in the high-temperature range in air for thermoelectric power generation.

4. Conclusions

A material design of semi-coherently layered 2D nanostructures appears promising. Co-doping with suitable dopants can enhance the thermoelectric properties, but a triple-phase nanocomposite of co-doped phases provides synergistic effects and increases the thermoelectric properties. The formation of semi-coherent 2D nanostructures enabled the simultaneous enhancement of the thermoelectric properties σ and α . The BCCO and NCO phases are stabilized at elevated temperatures within a co-doped CCO–NCO–BCCO nanocomposite and beneficial properties were extended to the high-temperature range. The integration of materials that are unstable at high temperatures into a stable matrix could utilize synergistic effects and presents new alternatives in material development. The high electrical conductivity and power factor, revealed by the Ioffe plot, offer the application in a thermoelectric generator for waste heat recovery at high temperatures in air. The evaluation of thermoelectric materials for power generation at high temperatures should be discussed critically, since the figure-of-merit zT is misleading to determine the applicability. The Ioffe plot, which shows the thermoelectric power factor as a function of the electrical conductivity, is more suitable to evaluate the ability for high-temperature power generation.

Acknowledgments

This work has been funded by the Deutsche Forschungsgesellschaft (DFG, German Research Foundation) – FE928/17-1. Financial support from The Research Council of Norway is appreciated under the program Nano2021 to the project (Number 228854) “Thermoelectric materials: Nanostructuring for improving the energy efficiency of thermoelectric generators and heat-pumps” (THELMA). Thanks are to the E.ON Stipendienfonds (T0087 – ESF) for financing the academic exchange between the Norwegian University for Science and Technology (NTNU)

and the Gottfried Wilhelm Leibniz University Hannover.

Appendix A. Supplementary data

Supplementary data associated with this article can be found, in the online version, at <https://doi.org/10.1016/j.jeurceramsoc.2018.10.023>.

References

- [1] H.U. Fuchs, A direct entropic approach to uniform and spatially continuous dynamical models of thermoelectric devices, *EHS* 1 (3–4) (2014) 253–265.
- [2] A. Feldhoff, Thermoelectric material tensor derived from the Onsager–de Groot–Callen model, *EHS* 2 (1) (2015) 5–13.
- [3] A.F. Ioffe, *Physics of Semiconductors*, 1st ed., Infosearch Ltd., London, 1960.
- [4] Y. Miyazaki, M. Onoda, T. Oku, M. Kikuchi, Y. Ishii, Y. Ono, Y. Morii, T. Kajitani, Modulated structure of thermoelectric compound $[\text{Ca}_2\text{CoO}_3]_x \text{CoO}_2$, *J. Phys. Soc. Jpn.* 71 (2002) 491–497.
- [5] H. Muguerra, D. Grebille, E. Guilmeau, R. Cloots, Modulated misfit structure of the thermoelectric $[\text{Bi}_{0.84}\text{CoO}_2]_{1.69} \text{CoO}_2$ cobalt oxide, *Inorg. Chem.* 47 (2008) 2464–2471.
- [6] L. Viciu, J.W.G. Bos, H.W. Zandbergen, Q. Huang, M.L. Foo, S. Ishiwata, A.P. Ramirez, M. Lee, N.P. Ong, R.J. Cava, Crystal structure and elementary properties of Na_xCoO_2 ($x = 0.32, 0.51, 0.6, 0.75, \text{ and } 0.92$) in the three-layer NaCoO_2 family, *Phys. Rev. B* 73 (2006) 174104-1–174104-10.
- [7] M.G. Kanatzidis, Nanostructured thermoelectrics: the new paradigm? *Chem. Mater.* 22 (2010) 648–659.
- [8] M. Martín-González, O. Caballero-Calero, P. Díaz-Chao, Nanoengineering thermoelectrics for 21st century: energy harvesting and other trends in the field, *Renew. Sustain. Energy Rev.* 24 (2013) 288–305.
- [9] J. Yang, H.-L. Yip, A.K.-Y. Jen, Rational design of advanced thermoelectric materials, *Adv. Energy Mater.* 3 (2013) 549.
- [10] G. Tan, L.-D. Zhao, M. Kanatzidis, Rationally designing high-performance bulk thermoelectric materials, *Chem. Rev.* 116 (2016) 12123–12149.
- [11] M.S. Dresselhaus, G. Chen, M.Y. Tang, R. Yang, H. Lee, D. Wang, Z. Ren, J.P. Fleurial, P. Gogna, New directions for low-dimensional thermoelectric materials, *Adv. Mater.* 19 (2007) 1043–1053.
- [12] D.L. Medlin, G.J. Snyder, Interfaces in bulk thermoelectric materials a review for current opinion in colloid and interface science, *Curr. Opin. Colloid Interfaces* 14 (2009) 226–235.
- [13] J.P. Heremans, B. Wondoloch, A.M. Chamoire, Resonant levels in bulk thermoelectric semiconductors, *Energy Environ. Sci.* 5 (2012) 5510–5530.
- [14] Y. Pei, X. Shi, A. Lalonde, H. Wang, L. Chen, G.J. Snyder, Convergence of electronic bands for high performance bulk thermoelectrics, *Nature* 473 (2011) 66–69.
- [15] R.J. Korkosz, T.C. Chasapis, S.-H. Lo, J.W. Doak, Y.J. Kim, C.-I. Wu, E. Hatzikraniotis, T.P. Hogan, D.N. Seidman, D. Wolverton, V.P. Dravid, M.G. Kanatzidis, High ZT in p-type $(\text{PbTe})_{1-2x}(\text{PbSe})_x(\text{PbS})_x$ thermoelectric materials, *J. Am. Chem. Soc.* 136 (2014) 3225–3237.
- [16] D. Wu, L.-D. Zhao, J. He, Superior thermoelectric performance in PbTe-PbS pseudobinary: extremely low thermal conductivity and modulated carrier concentration, *Energy Environ. Sci.* 8 (2015) 2056–2068.
- [17] C. Fu, T. Zhu, Y. Liu, H. Xie, X. Zhao, Band engineering of high performance p-type FeNbSb based half-Heusler thermoelectric materials for figure of merit $zT > 1$, *Energy Environ. Sci.* 8 (2015) 216–220.
- [18] J.P. Heremans, V. Jovicic, E.S. Toberer, A. Saramat, K. Kurosaki, A. Charoenphakdee, S. Yamanaka, G.J. Snyder, Enhancement of thermoelectric efficiency in PbTe by distortion of the electronic density of states, *Science* 321 (2008) 554–557.
- [19] L.D. Hicks, M.S. Dresselhaus, Thermoelectric figure of merit of a one-dimensional conductor, *Phys. Rev. B* 47 (1993) 16631–16634.
- [20] G.J. Snyder, E.S. Toberer, Complex thermoelectric materials, *Nat. Mater.* 7 (2008) 105–114.
- [21] G. Joshi, H. Lee, Y. Lan, X. Wang, G. Zhu, D. Wang, R. Gould, D.C. Cuff, M.Y. Tang, M.S. Dresselhaus, G. Chen, Z. Ren, Enhanced thermoelectric figure-of-merit in nanostructured p-type silicon germanium bulk alloys, *Nano Lett.* 8 (2008) 4670–4674.
- [22] L.-D. Zhao, S.-H. Lo, Y. Zhang, H. Sun, G. Tan, C. Uher, C. Wolverton, V.P. Dravid, M.G. Kanatzidis, Ultralow thermal conductivity and high thermoelectric figure of merit in SnSe crystals, *Nature* 508 (2014) 373–377.
- [23] S.R. Brown, S.M. Kauzlarich, F. Gascoin, G.J. Snyder, $\text{Yb}_{14}\text{MnSb}_{11}$: new high efficiency thermoelectric material for power generation, *Chem. Mater.* 18 (2006) 1873–1877.
- [24] D.M. Rowe, *CRC Handbook of Thermoelectrics*, 89th Edition, CRC Press, Boca Raton, FL, 1995.
- [25] M. Ohtaki, K. Araki, K. Yamamoto, High thermoelectric performance of dually doped ZnO ceramics, *J. Electron. Mater.* 38 (2009) 1234–1238.
- [26] N.V. Nong, N. Pryds, S. Lineroth, M. Ohtaki, Enhancement of the thermoelectric performance of p-type layered oxide $\text{Ca}_3\text{Co}_4\text{O}_{9+\delta}$ through heavy doping and metallic nano-inclusions, *Adv. Mater.* 23 (2011) 2484–2490.
- [27] J. Sui, J. Li, J. He, Y.-L. Pei, D. Berardan, H. Wu, N. Dragoe, W. Cai, L.-D. Zhao, Texturation boosts the thermoelectric performance of BiCuSeO oxyselelenides, *Energy Environ. Sci.* 6 (2013) 2916–2920.
- [28] Y. Liu, L.-D. Zhao, Y. Zhu, Y. Liu, F. Li, M. Yu, D.-B. Liu, W. Xu, Y.-H. Lin, C.-W. Nan, Synergistically optimizing electrical and thermal transport properties of BiCuSeO via a dual-doping approach, *Adv. Energy Mater.* 6 (2016) 1502423.
- [29] G.-K. Ren, S.-Y. Wang, Y.-C. Zhu, K.J. Ventura, X. Tan, W. Xu, Y.-H. Lin, J. Yang, C.-W. Nan, Enhancing thermoelectric performance in hierarchically structured BiCuSeO by increasing bond covalency and weakening carrier-phonon coupling, *Adv. Energy Mater.* 10 (2017) 1590–1599.
- [30] C. Barreteau, D. Berardan, N. Dragoe, Studies on the thermal stability of BiCuSeO , *J. Solid State Chem.* 222 (2015) 53–59.
- [31] D. Narducci, Wo we really need high thermoelectric figure of merit? A critical appraisal to the power conversion efficiency of thermoelectric materials, *Appl. Phys. Lett.* 99 (2011) 102104-1–102104-3.
- [32] Y. Miyazaki, Crystal structure and thermoelectric properties of the misfit-layered cobalt oxides, *Solid State Ionics* 172 (2004) 463–467.
- [33] M. Bittner, L. Helmich, F. Nietschke, B. Geppert, O. Oeckler, A. Feldhoff, Porous $\text{Ca}_3\text{Co}_4\text{O}_9$ with enhanced thermoelectric properties derived from sol-gel synthesis, *J. Eur. Ceram. Soc.* 37 (2017) 3909–3915.
- [34] N. Kanas, S.P. Singh, M. Rotan, M. Saleemi, M. Bittner, A. Feldhoff, T. Norby, K. Wiik, T. Grande, M.-A. Einarsrud, Influence of processing on stability, microstructure and thermoelectric properties of $\text{Ca}_3\text{Co}_4\text{O}_{9+\delta}$, *J. Eur. Ceram. Soc.* 38 (2018) 1592–1599.
- [35] G. Xu, R. Funahashi, M. Shikano, I. Matsubara, Y. Zhou, Thermoelectric properties of the Bi- and Na-substituted $\text{Ca}_3\text{Co}_4\text{O}_9$ system, *Appl. Phys. Lett.* 80 (2002) 3760–3762.
- [36] Y. Masuda, D. Nagahama, H. Itahara, T. Tani, W.S. Seo, K. Koumoto, Thermoelectric performance of Bi- and Na-substituted $\text{Ca}_3\text{Co}_4\text{O}_9$ improved through ceramic texturing, *J. Mater. Chem.* 13 (2003) 1094–1099.
- [37] A.I. Klyndyuk, I.V. Matsukevich, Synthesis and properties of $\text{Ca}_{2.8}\text{Ln}_{0.2}\text{Co}_4\text{O}_{9+\delta}$ ($\text{Ln} = \text{La, Nd, Sm, Tb-Er}$) solid solutions, *Inorg. Mater.* 48 (2012) 1052–1057.
- [38] S. Saini, H.S. Yaddanapudi, K. Tian, Y. Yin, D. Maggini, A. Tiwari, Terbium ion doping in $\text{Ca}_3\text{Co}_4\text{O}_9$: A step towards high-performance thermoelectric materials, *Sci. Rep.-UK* 7 (2017) 44621.
- [39] H. Leiginy, D. Grebille, O. Pérez, A.C. Masset, M. Hervieu, B. Raveau, A five-dimensional structural investigation of the misfit layer compound $[\text{Bi}_{0.87}\text{SrO}_2]_2[\text{CoO}_2]_{1.82}$, *Acta Cryst. B* 56 (2000) 173–182.
- [40] E. Guilmeau, M. Pollet, D. Grebille, M. Hervieu, M. Muguerra, R. Cloots, M. Mikami, R. Funahashi, Nanoblock coupling effect in iodine intercalated $[\text{Bi}_{0.82}\text{CaO}_2]_2[\text{CoO}_2]_{1.69}$ layered cobaltite, *Inorg. Chem.* 46 (2007) 2124–2131.
- [41] A. Sotelo, E. Guilmeau, S. Rasekh, M.A. Madre, S. Marinel, J.C. Diez, Enhancement of the thermoelectric properties of directionally grown Bi–Ca–Co–O through Pb for Bi substitution, *J. Eur. Ceram. Soc.* 30 (2010) 1815–1820.
- [42] I.V. Matsukevich, A.I. Klyndyuk, E.A. Tugova, A.N. Kovalenko, A.A. Marova, N.S. Krasutska, Thermoelectric properties of $\text{Ca}_{3-x}\text{Bi}_x\text{Co}_4\text{O}_{9+\delta}$ ($0.0 \leq x \leq 1.5$) ceramics, *Inorg. Mater.* 52 (2016) 644–650.
- [43] A. Feldhoff, M. Arnold, J. Martynczuk, T.M. Gesing, H. Wang, The sol-gel synthesis of perovskites by EDTA/citric complexing method involves nanoscale solid state reactions, *Solid State Sci.* 10 (2008) 689–701.
- [44] T. Janssen, A. Janner, A. Looijenga-Vos, P.M. De Wolff, International Tables for Crystallography: 9. 8 Incommensurate and commensurate modulated structures, Volume C Edition, Kluwer Academic Publishers, Dordrecht/Boston/London, 2004.
- [45] M. Lee, L. Viciu, Y. Wang, M.L. Foo, S. Watauchi, R.A. Pascal JR, R.J. Cava, N.P. Ong, Large enhancement of the thermopower in Na_xCoO_2 at high Na doping, *Nat. Mater.* 5 (2006) 537–540.
- [46] T. Sun, H.H. Hng, Q.Y. Yan, J. Ma, Enhanced high temperature thermoelectric properties of Bi-doped c-axis oriented $\text{Ca}_3\text{Co}_4\text{O}_9$ thin films by pulsed laser deposition, *J. Appl. Phys.* 108 (8) (2010) 3709.
- [47] Q. Zhu, E.M. Hopper, B.J. Ingram, T.O. Mason, Combined Jonker and Ioffe analysis of oxide conductors and semiconductors, *J. Am. Ceram. Soc.* 94 (2011) 187–193.
- [48] J.-W. Moon, D. Nagahama, Y. Masuda, W.-S. Seo, K. Koumoto, Anisotropic thermoelectric properties of crystal-axis oriented ceramics of layer-structured oxide in the Ca–Co–O system, *J. Ceram. Soc. Jpn.* 109 (2001) 647–650.
- [49] C.-H. Lim, H.-H. Park, S.-M. Choi, K.-H. Lee, K. Park, Anisotropy of the thermoelectric figure of merit (ZT) in textured $\text{Ca}_3\text{Co}_4\text{O}_9$ ceramics prepared by using a spark plasma sintering process, *J. Korean Phys. Soc.* 66 (2015) 794–799.
- [50] D. Kenfai, B. Lenoir, D. Chateigner, B. Ouladidaf, M. Gomina, J.G. Noudem, Development of multilayer textured $\text{Ca}_3\text{Co}_4\text{O}_9$ materials for thermoelectric generators: Influence of the anisotropy on the transport properties, *J. Eur. Ceram. Soc.* 32 (2012) 2405–2414.
- [51] D. Kenfai, D. Chateigner, M. Gomina, J.G. Noudem, B. Ouladidaf, A. Dauschner, B. Lenoir, Volume texture and anisotropic thermoelectric properties in $\text{Ca}_3\text{Co}_4\text{O}_9$ bulk materials, *Mater. Today* 2 (2015) 637–646.
- [52] O. Jankovsky, D. Sedmidubsky, Z. Sofer, J. Hejtmanek, Thermodynamic behavior of $\text{Ca}_3\text{Co}_4\text{O}_{9+\delta}$ ceramics, *Ceram-Silikaty* 56 (2) (2012) 139–144.
- [53] J.-Y. Tak, K.H. Lee, J.-Y. Kim, C.-H. Lim, W.-S. Seo, Y.S. Lim, H.K. Cho, S.-M. Choi, Optimization of synthesis conditions of $\text{Na}_{0.7}\text{CoO}_2$ for high thermoelectric performance, *J. Electron. Mater.* 44 (2014) 1408–1412.

**Supplementary information for
"Triple-phase ceramic 2D nanocomposite with
enhanced thermoelectric properties"**

Michael Bittner¹, Nikola Kanas², Richard Hinterding¹, Frank Steinbach¹,
Dennis Groeneveld¹, Piotr Wemhoff¹, Kjell Wiik², Mari-Ann Einarsrud²,
Armin Feldhoff¹

¹Institute of Physical Chemistry and Electrochemistry,
Leibniz University Hannover, Germany

²Department of Materials Science and Engineering,
Norwegian University of Science and Technology, Norway

1 Supplementary

Schemes, diagrams both SEM and TEM micrographs were created using OriginPro 9.1G, ImageJ, Diamond and Digital Micrograph. Figures were arranged, merged and saved using PowerPoint 2010 and Photoshop CS5. Table S 1 shows the ionic radii of the substituted elements and inserted dopants. According to the similarity of the ionic radii of the elements used, doping should be possible. The XRD patterns of the Na_xCoO_2 (NCO) and $\text{Bi}_2\text{Ca}_2\text{Co}_2\text{O}_9$ (BCCO) phases, shown in Figure S 1 refer to Figure 2 in the main text. A step size of 0.003942, a time per step of 1.1 seconds, a voltage of 40 kV and a current of 40 mA were used in the XRD experiments. Pure NCO and nearly pure BCCO phases were subjected to SEM and elemental distribution analyses of polished cross-sections, as shown in Figure S 2a-d. Vibration-polished cross-section specimens were prepared by a multistep (30 μm , 15 μm , 6 μm , 3 μm and 1 μm diamond lapping films) polishing program using a Techprep from Allied - High Tech Products, Inc., followed by vibration polishing using a Buehler Vibromet-2 and a 50 nm colloidal alumina suspension. TEM specimens were prepared similar to SEM specimens and put on a TEM grid. The specimens were pinched out using a precision ion polishing system (Ar-ion) Model 691 from Gatan. The BCCO phase decomposes at approximately 1023 K, and Ca-containing phases are formed; see Figure S 1^[1]. Figure S 3 gives detailed elemental distribution information referring to Figure 4a-c in the main document. The interdiffusion of Ca into the NCO phase is clearer, and the very thin layers of NCO and BCCO are clearly visible in the Na, Ca and Bi signals shown in Figure S 3d-f. The insets of Figure 4d-f in the main document are enlarged for a better readability in Figure S 4a-f. Additional TEM micrographs of other sites of the CCO-30-35-10 nanocomposite ceramic are shown in Figures S 5, 6 and 7. These other sites clarify the composition and thickness of different layers within the material. These sequences continue throughout the ceramic. Comparing Figure S 5 and Figure S 6 shows that the amount of interdiffusion of Ca into the NCO phase is not constant, suggesting that the degree of interdiffusion might also depends on thickness and surroundings (e.g., being embedded between BCCO phases). Figure S 8 illustrates the measured heat capacities C_P of CCO and nanocomposite ceramics as a function of temperature in the range from 313 K to 1173 K. The C_P values reached approximately $0.83 \text{ J} \cdot \text{g}^{-1} \cdot \text{K}^{-1}$ at 1073 K for a CCO-30-35-10 nanocomposite ceramic. The nanocomposite ceramics showed only small differences in C_P from those of undoped CCO. The system was calibrated and the sapphire method was used. The sensitivity S and heat capacity C_P were calculated as described by Jankovsky et al.^[2]. Samples of bar geometry were

cut from a ceramic pellet using an O'Well model 3242 precision vertical diamond wire saw.

1.1 Figures

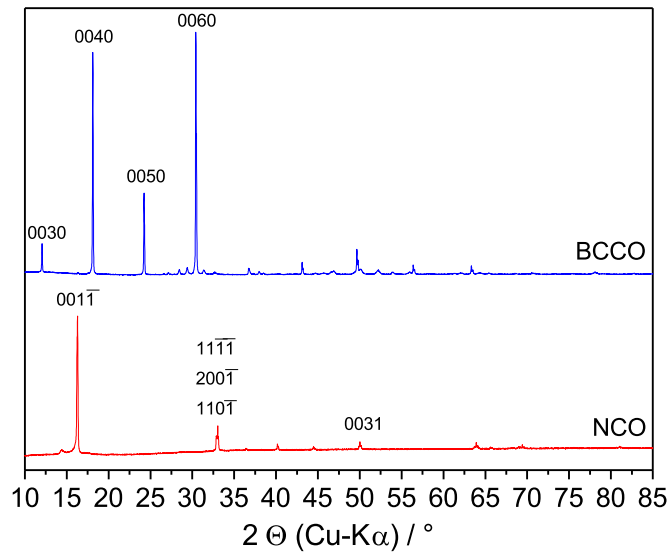


Figure S 1: XRD patterns of **NCO** and **BCCO** with indexed reflections according to superspace group $C2/m$ ^[3] and $P2/m$ ^[4]. NCO and BCCO were obtained after sintering at 1073 and 1123 K for 10 hours, respectively.

3

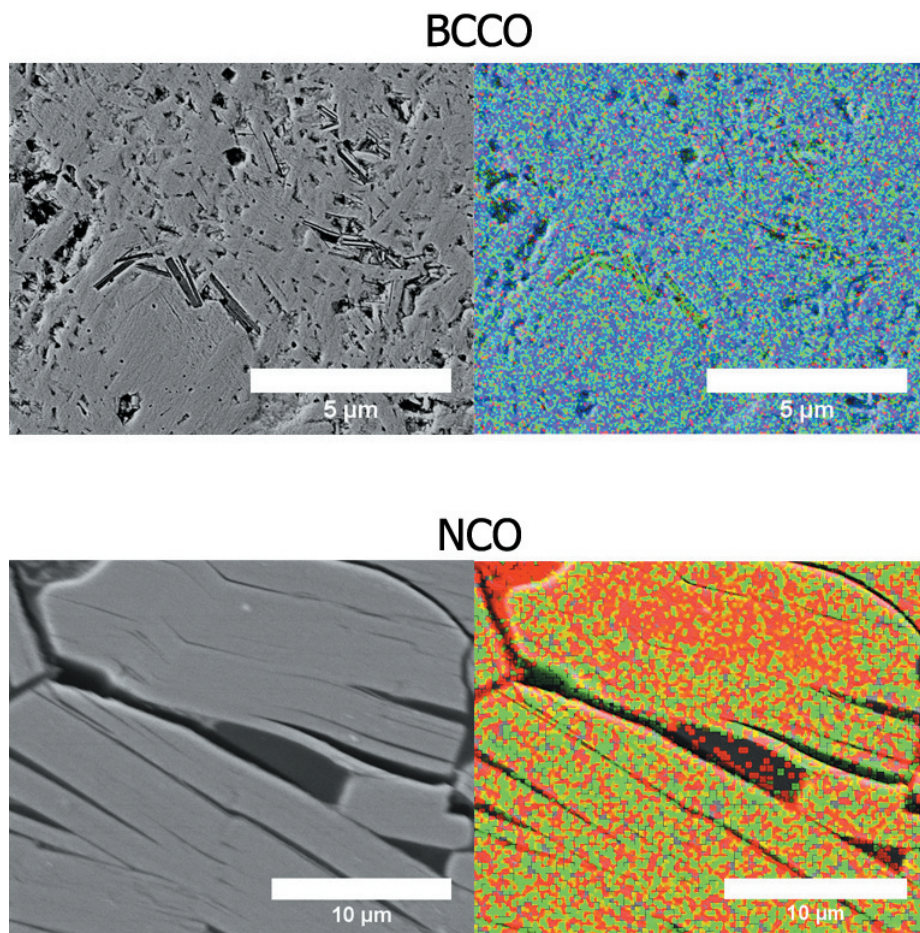


Figure S 2: SEM cross-sectional micrographs and EDXS elemental distributions of a, b) **BCCO** ceramic (Ca-green, Bi-blue and Co-red) and c, d) **NCO** ceramic (Na-green and Co-red).

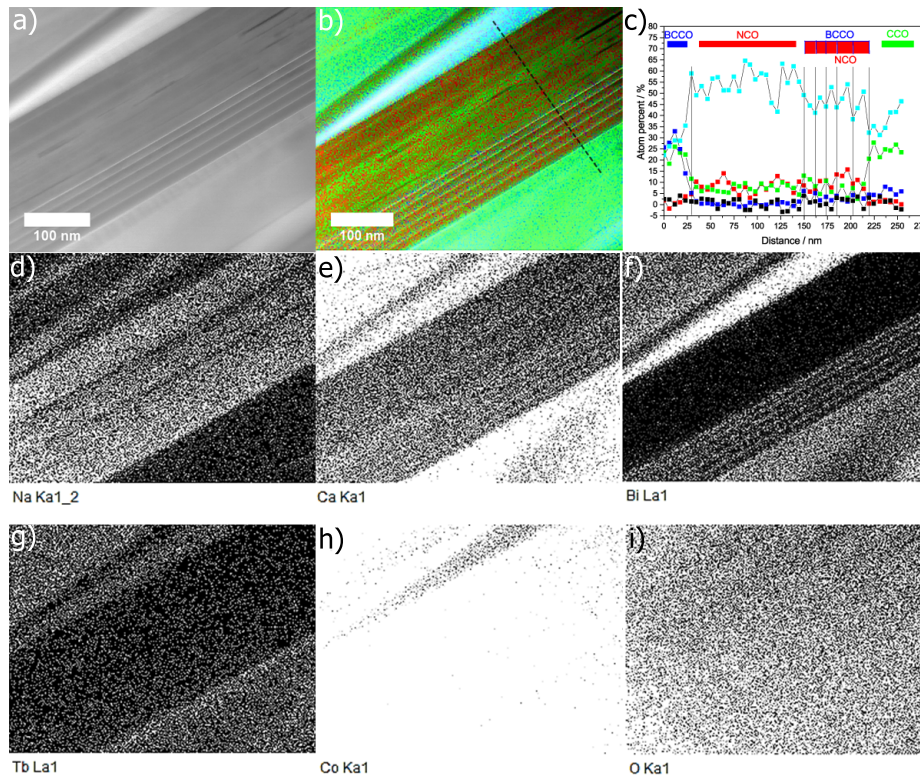


Figure S 3: TEM analysis of a **CCO-30-35-10** nanocomposite ceramic, supplementing Figure 4a-c) of the main document. a, b) STEM dark-field micrograph and EDXS elemental distribution of the region shown. c) Linescan of the elemental distribution of Na (red), Ca (green), Bi (blue), Tb (black) and Co (turquoise) shown in b). Along the indicated direction (dotted line), different phases and their compositions along the linescan are indicated. d-i) Detailed elemental distribution information for Na, Ca, Bi, Co, Tb and O.

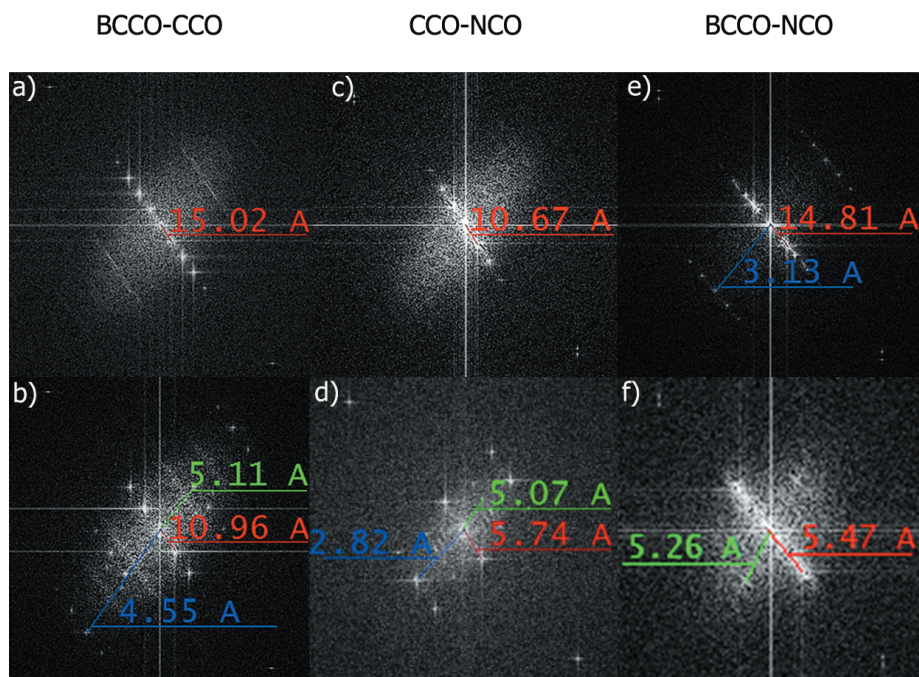


Figure S 4: Enlarged presentation of reduced fast Fourier transformations in insets of Figure 4d-f) showing the TEM analysis of a **CCO-30-35-10** nanocomposite ceramic: a, b) BCCO-CCO-interface; c, d) CCO-NCO-interface; and e, f) BCCO-NCO-interface with indicated lattice parameters of a (green), b (blue) and c (red).
 BCCO-CCO: BCCO - $c = 15.02 \text{ \AA}$, CCO - $a = 5.11 \text{ \AA}$, $b_2 = 4.55 \text{ \AA}$, $c = 10.96 \text{ \AA}$
 CCO-NCO: CCO - $c = 10.67 \text{ \AA}$, NCO - $a = 5.07 \text{ \AA}$, $b_1 = 2.82 \text{ \AA}$, $c = 5.74 \text{ \AA}$
 BCCO-NCO: BCCO - $b_1 = 3.13 \text{ \AA}$, $c = 14.81 \text{ \AA}$, NCO - $a = 5.26 \text{ \AA}$, $c = 5.47 \text{ \AA}$

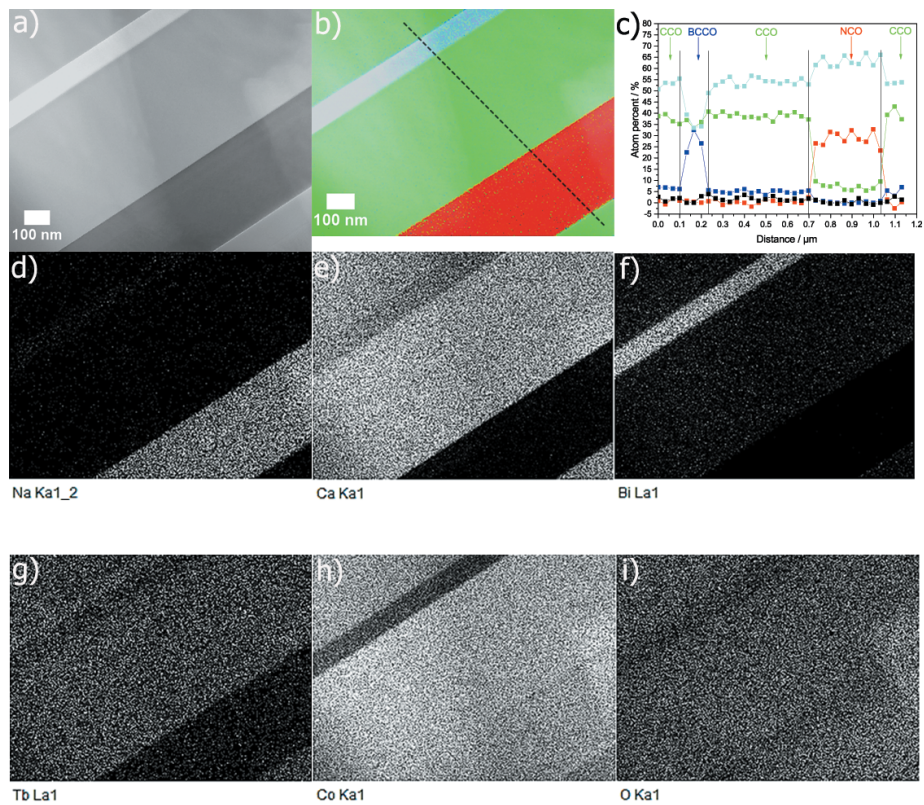


Figure S 5: TEM analysis of a second site of a **CCO-30-35-10** nanocomposite ceramic, a, b) STEM dark-field micrograph and EDXS elemental distribution of the area shown. c) Linescan of the elemental distribution of Na (red), Ca (green), Bi (blue), Tb (black) and Co (turquoise) shown in b). Along the indicated direction (dotted line), different phases and their compositions along the linescan are indicated. d-i) Detailed elemental distribution information for Na, Ca, Bi, Co, Tb and O.

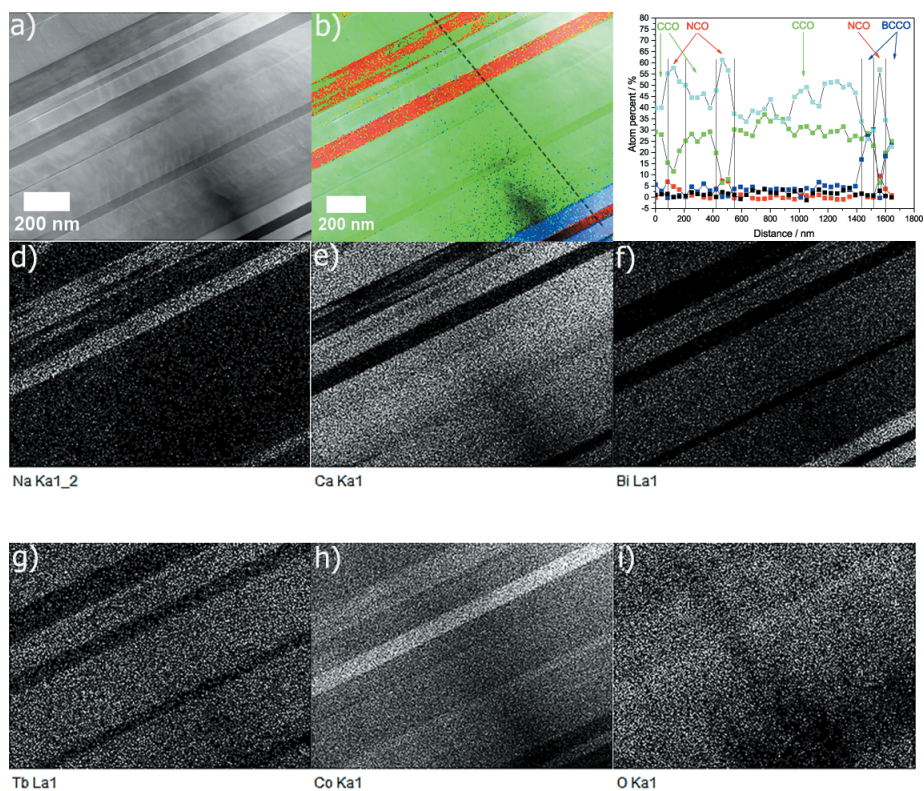


Figure S 6: TEM analysis of a third site of a **CCO-30-35-10** nanocomposite ceramic, a, b) STEM dark-field micrograph and EDXS elemental distribution of the area shown. c) Linescan of the elemental distribution of Na (red), Ca (green), Bi (blue), Tb (black) and Co (turquoise) shown in b). Along the indicated direction (dotted line), different phases and their compositions along the linescan are indicated. d-i) Detailed elemental distribution information for Na, Ca, Bi, Co, Tb and O.

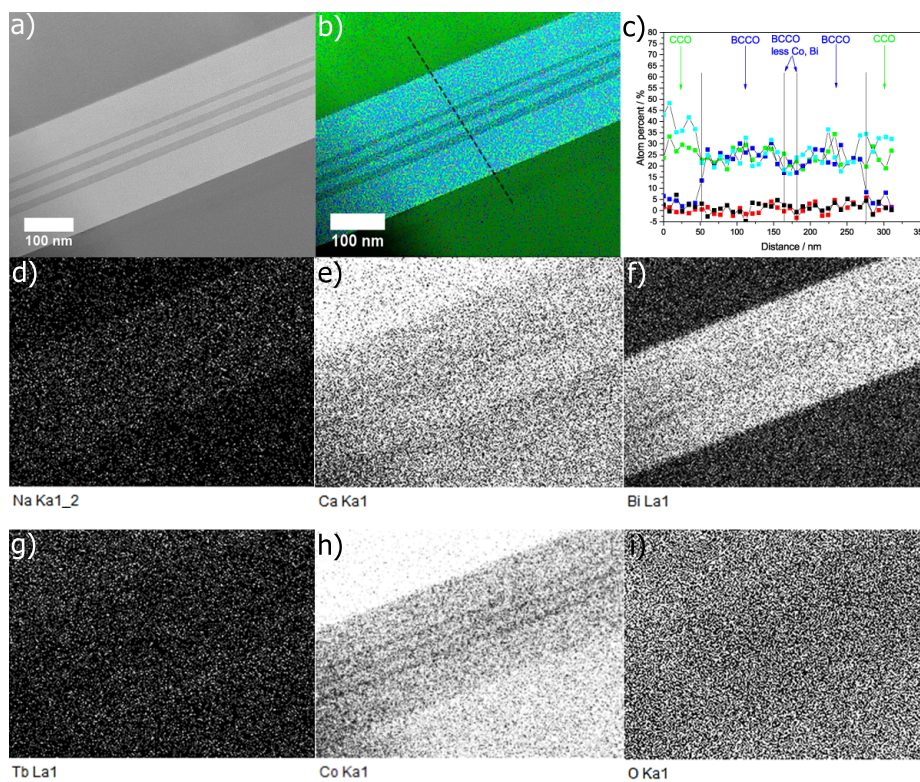


Figure S 7: TEM analysis of a fourth site of a **CCO-30-35-10** nanocomposite ceramic, a, b) STEM dark-field micrograph and EDXS elemental distribution of the area shown. c) Linescan of the elemental distribution of Na (red), Ca (green), Bi (blue), Tb (black) and Co (turquoise) shown in b). Along the indicated direction (dotted line), different phases and their compositions along the linescan are indicated. d-i) Detailed elemental distribution information for Na, Ca, Bi, Co, Tb and O.

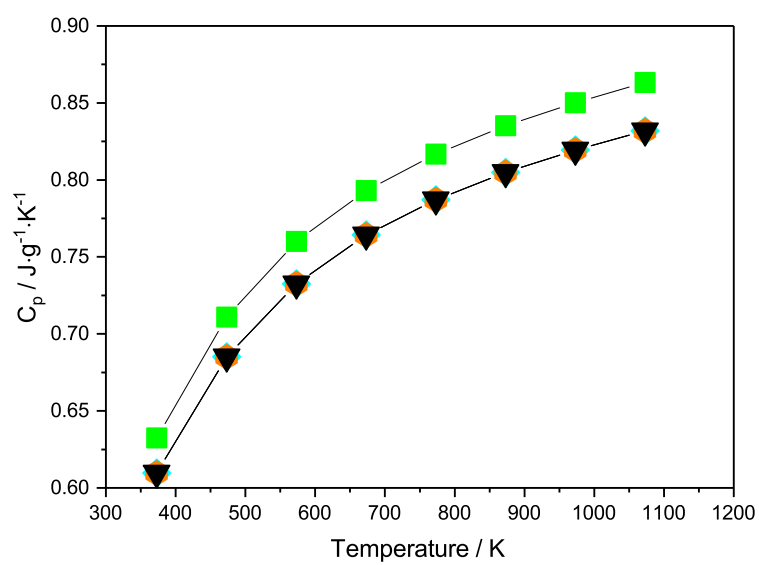


Figure S 8: Heat capacity C_p as a function of temperature of **CCO** (squares, green, taken from^[5]), **CCO-30-35-6** (diamonds, turquoise), **CCO-30-35-8** (hexagons, orange) and **CCO-30-35-10** (inverted triangles, black) ceramics.

1.2 Tables

Table S 1: Ionic radii of cations and dopants in $\text{Ca}_{3-x-y-z}\text{Na}_x\text{Bi}_y\text{Tb}_z\text{Co}_4\text{O}_9$ ^[6].

Element	Ca	Na	Bi	Tb	Co		
coordination number	6	6	6	6	8		
ionic charge	+2	+1	+3	+3	+4	+3	+4
ionic radii / Å	1.12	1.18	1.17	1.04	0.88	0.61	0.53

References

- [1] A. Sotelo, E. Guilmeau, S. Rasekh, M. A. Madre, S. Marinel, J. C. Diez, Enhancement of the thermoelectric properties of directionally grown Bi-Ca-Co-O through Pb for Bi substitution, *J. Eur. Ceram. Soc.* 30 (2010) 1815–1820.
- [2] O. Jankovsky, D. Sedmidubsky, Z. Sofer, J. Hejtmanek, Thermodynamic behavior of $\text{Ca}_3\text{Co}_4\text{O}_{9+\delta}$ ceramics, *Ceram-Silikaty* 56(2) (2012) 139–144.
- [3] L. Viciu, J. W. G. Bos, H. W. Zandbergen, Q. Huang, M. L. Foo, S. Ishiwata, A. P. Ramirez, M. Lee, N. P. Ong, R. J. Cava, Crystal structure and elementary properties of Na_xCoO_2 ($x = 0.32, 0.51, 0.6, 0.75,$ and 0.92) in the three-layer NaCoO_2 family, *Phys. Rev. B* 73 (2006) 174104–1–174104–10.
- [4] E. Guilmeau, M. Pollet, D. Grebille, M. Hervieu, M. Muguerra, R. Cloots, M. Mikami, R. Funahashi, Nanoblock coupling effect in iodine intercalated $[\text{Bi}_{0.82}\text{CaO}_2]_2[\text{CoO}_2]_{1.69}$ layered cobaltite, *Inorg. Chem.* 46 (2007) 2124–2131.
- [5] M. Bittner, L. Helmich, F. Nietschke, B. Geppert, O. Oeckler, A. Feldhoff, Porous $\text{Ca}_3\text{Co}_4\text{O}_9$ with enhanced thermoelectric properties derived from sol-gel synthesis, *J. Eur. Ceram. Soc.* 37 (2017) 3909–3915.
- [6] R. D. Shannon, Revised effective ionic radii and systematic studies of interatomic distances in halides and chalcogenides, *Acta Cryst.* A32 (1976) 751–767.

2.2.3 Reaction sintering of $\text{Ca}_3\text{Co}_4\text{O}_9$ with BiCuSeO nanosheets for high-temperature thermoelectric composites

Richard Hinterding, Desiree Rieks, Patrick A. Kießling, Lukas Steinbach, Nadja C. Bigall, Armin Feldhoff

Journal of Electronic Materials, **2021**

DOI: 10.1007/s11664-021-09336-2



Reaction Sintering of $\text{Ca}_3\text{Co}_4\text{O}_9$ with BiCuSeO Nanosheets for High-Temperature Thermoelectric Composites

Richard Hinterding¹ · Desiree Rieks¹ · Patrick A. Kißling¹ · Lukas Steinbach¹ · Nadja C. Bigall¹ · Armin Feldhoff¹ Received: 20 September 2021 / Accepted: 8 November 2021
© The Author(s) 2021

Abstract

Ceramic composites composed of oxide materials have been synthesized by reaction sintering of $\text{Ca}_3\text{Co}_4\text{O}_9$ with BiCuSeO nanosheets. *In situ* x-ray diffraction and thermogravimetric analyses of the compound powders were conducted to understand the phase transformations during heating up to 1173 K. Further thermogravimetric analyses investigated the thermal stability of the composites and the completion of reaction sintering. The microstructure of the formed phases after reaction sintering and the composition of the composites were investigated for varying mixtures. Depending on the amount of BiCuSeO used, the phases present and their composition differed, having a significant impact on the thermoelectric properties. The increase of the electrical conductivity at a simultaneously high Seebeck coefficient resulted in a large power factor of $5.4 \mu\text{W cm}^{-1} \text{K}^{-2}$, more than twice that of pristine $\text{Ca}_3\text{Co}_4\text{O}_9$.

Keywords Thermoelectrics · composites · $\text{Ca}_3\text{Co}_4\text{O}_9$ · BiCuSeO · oxides

Introduction

Thermoelectric Principles

Thermoelectricity is the conversion of thermal energy into electrical energy and vice versa. As one method of energy harvesting, the thermoelectric effect can help in the face of limited resources and a growing need for sustainable energy. To utilize thermoelectricity to a greater extent, further improvements regarding the power output and conversion efficiency of thermoelectric materials are necessary. The basic principles of thermoelectric energy conversion in a material are described by the transport equation in Eq. 1.^{1–3}

$$\begin{pmatrix} I_q \\ I_S \end{pmatrix} = \frac{A}{L} \begin{pmatrix} \sigma & \sigma \cdot \alpha \\ \sigma \cdot \alpha & \sigma \cdot \alpha^2 + \Lambda_{OC} \end{pmatrix} \cdot \begin{pmatrix} \Delta\varphi \\ \Delta T \end{pmatrix} \quad (1)$$

This integral form of the transport equation includes the coupling of the electrical charge I_q and entropy I_S currents of a material with a cross-sectional area A and a length L . A thermally induced electrical current emerges due to the electrical potential difference $\Delta\varphi$ and the temperature difference ΔT . The magnitude of the electrical current depends on three material parameters, viz. the electrical conductivity σ , the Seebeck coefficient α , and the electrically open-circuited entropy conductivity Λ_{OC} . All three parameters as well as their relationship with the heat conductivity λ_{OC} appear in Eq. 2, which defines the figure of merit $f^{3,4}$ or zT .^{3,5}

$$f = \frac{\sigma \cdot \alpha^2}{\Lambda_{OC}} = \frac{\sigma \cdot \alpha^2}{\lambda_{OC}} \cdot T := zT \quad (2)$$

The figure of merit of a thermoelectric material reflects the maximum energy conversion efficiency, while the power factor $PF = \sigma \cdot \alpha^2$ dominates the maximum electrical power output.⁶ Especially for high-temperature applications, where the provided heat is abundant, the power factor is at least equally important as the figure of merit.⁷

✉ Richard Hinterding
richard.hinterding@pci.uni-hannover.de

✉ Armin Feldhoff
armin.feldhoff@pci.uni-hannover.de

¹ Institute of Physical Chemistry and Electrochemistry,
Callinstr. 3A, 30167 Hannover, Germany

Thermoelectric Materials

Many different material classes compete with or complement each other in thermoelectrics. Tellurides,⁸ skutterudites,⁹ half-Heusler compounds,¹⁰ Zintl phases,¹¹ polymers¹² as well as oxides¹³ are among the most prominent ones. This work focuses on oxides and oxyselenides as components for thermoelectric composites. The greatest advantage of oxides in comparison with most other materials is their high thermal stability in air, which is important for actual applications.⁶ Within the class of *p*-type oxides, $\text{Ca}_3\text{Co}_4\text{O}_9$ (CCO) is nearly uncontested with respect to its thermoelectric performance. Its thermal stability up to 1220 K in air¹⁴ allows applications at high temperature, and its thermoelectric properties originate from the layered structure. Two incommensurate subsystems build up CCO, one consisting of CoO_2 and one of Ca_2CoO_3 . The CoO_2 unit with a misfit-layered CdI_2 structure type alternates with the Ca_2CoO_3 unit with a cutout rocksalt-type structure.¹⁵ The incommensurate structure results from the same *a* but distinct *b* parameters of the two subsystems being stacked along the shared *c*-axis.¹⁶ As a result of the layered structure, anisotropic transport properties with favorable thermoelectric characteristics within the *a*–*b*-plane emerge.^{17,18} BiCuSeO (BCSO) on the other hand is a layered oxyselenide with limited thermal stability up to 573 K in air.¹⁹ Its layered structure with alternating Bi_2O_2 and Cu_2Se_2 layers along the *c*-axis²⁰ also results in highly anisotropic transport properties.²¹ Moreover, the anisotropy is even more pronounced in nanosheets because of the quantum confinement effect,²² which can improve the thermoelectric properties substantially.²³ Despite its limited oxidation stability, the thermoelectric properties of BCSO result in a figure of merit above 1 when doped properly, mainly owing to a low thermal conductivity.²⁴ Due to the oxidation tendency of BCSO, the combination of CCO with BCSO at the high sintering temperature of CCO in air is expected to result in reaction sintering accompanied by phase transformations. These phase transformations may result in ceramic composites with enhanced thermoelectric properties. A selection of other reported materials for composite materials based on CCO are silver inclusions,^{25,26} silver with polymer,²⁷ Na_xCoO_2 ,²⁸ Na_xCoO_2 with $\text{Bi}_2\text{Ca}_2\text{Co}_2\text{O}_9$,²⁹ La_2NiO_4 ,³⁰ ZrO_2 ,³¹ Co_3O_4 ,³² or Fe with Ni particles³³ to name a few. Generally, the added heterointerfaces in composite systems can lead to a decreased mean free path of phonons and hence a reduced thermal conductivity,^{34,35} although this depends on the added phases. The performance outcome after reaction sintering is difficult to predict, and changes of the transport properties in the composites must be related to newly formed phases or altering compositions. Therefore, scanning electron microscopy

(SEM), x-ray diffraction (XRD) analysis, thermogravimetric analysis (TGA), transmission electron microscopy (TEM), and energy-dispersive x-ray spectroscopy (EDXS) were used in this work to understand the changes of the CCO-BCSO system during and after sintering.

Experimental Procedures

Chemicals

The chemicals used included calcium cobaltite ($\text{Ca}_3\text{Co}_4\text{O}_9$, CerPoTech, Norway), bismuth nitrate hydrate [$\text{Bi}(\text{NO}_3)_3 \cdot x \text{H}_2\text{O}$, Alfa Aesar, 99.999%], selenourea [$\text{SeC}(\text{NH}_2)_2$, Alfa Aesar, 99%], copper nitrate hemipentahydrate [$\text{Cu}(\text{NO}_3)_2 \cdot 2.5\text{H}_2\text{O}$, Aldrich Chemistry, $\geq 99.99\%$], potassium hydroxide (KOH, $\geq 85\%$), sodium hydroxide (NaOH, Carl Roth, $\geq 99\%$), and ethanol (Carl Roth, $\geq 99.8\%$).

Synthesis

CCO and BCSO powders were used to form the ceramic composites. Pristine CCO powder was purchased from CerPoTech (Tiller, Norway). Further processing of the CCO powder involved grinding in an agate mortar for 15 min and uniaxial pressing in a 16-mm die at 250 MPa and room temperature. The gained disks were sintered at 1173 K for 10 h with a heating rate of 2 K min^{-1} and cooling rate of 10 K min^{-1} under air. The sintered CCO was ground again and then ready to form composite mixtures. BCSO nanosheets were synthesized hydrothermally according to the instructions given by Samanta et al.³⁶ The declared amounts of chemicals were added to a large 200-ml Teflon-lined stainless-steel autoclave. To obtain the composites, washed BCSO and presintered CCO were mixed in an agate mortar at weight ratios of 5:95, 10:90, 20:80, and 30:70 for 15 min. The pressing and sintering processes were analogous to those described for pristine CCO.

Microstructure Analysis

Identification of phases and their purity was achieved by x-ray diffraction (XRD) analysis (Bruker AXS GmbH, Bruker D8 Advance) with Cu K_α radiation. *In situ* measurements were performed with an equipped heating chamber HTK1200N (Anton Paar). The heating and cooling rate as well as the total dwell time at 1173 K were programmed to be equal to the sintering conditions of the pressed disks. A synthetic air gas flow of 50 ml min^{-1} was applied. Differences occurred because of the use of noncompacted powder and additional dwell times at lower temperature due to the measurement duration. Powder diffraction files from the

ICDD database were used to evaluate the measured XRD patterns for the following compounds: $\text{Ca}_3\text{Co}_4\text{O}_9$ (Miyazaki et al.¹⁵ and PDF 00-058-0661), CoO (PDF 01-071-1178), Co_3O_4 (PDF 01-074-1657), CaCo_2O_4 (PDF 00-051-1760), BiCuSeO (PDF 01-076-6689), Bi_2SeO_2 (PDF 01-070-1549), Bi_2O_3 (PDF 01-075-4627), and $\text{Ca}_3\text{Co}_2\text{O}_6$ (PDF 01-089-2466). The four-dimensional superspace group $Cm(0\ 1 - p\ 0)$ (equivalent to $Bm(0\ 0\ \gamma)$) was used for CCO in accordance with literature^{15,37,38} to account for the incommensurate structure. Further analyses were carried out by electron microscopy. Cross-sections were prepared by embedding the samples in epoxy resin and applying a multistep polishing program completed by vibration polishing using a 50-nm Al_2O_3 suspension. Elemental maps were obtained by scanning electron microscopy (SEM, JEOL JSM-7610FPlus) at 15 kV with two energy-dispersive x-ray spectrometers (EDXS, XFlash 6/60). Further analyses of the powders were conducted using a different SEM (JEOL JSM-6700F) at 2 kV. Scanning transmission electron microscopy (STEM, JEOL JEM-2100F-UHR) equipped with EDXS (Oxford Instruments, INCA-200 TEM) was used to analyze the main phase CCO. High-resolution TEM (HRTEM) and selected-area electron diffraction (SAED) were carried out at 200 kV. Thermogravimetric characteristics were measured with a TGA/DSC3+ from Mettler Toledo at a heating rate of $2\ \text{K}\ \text{min}^{-1}$ and air flow of $20\ \text{ml}\ \text{min}^{-1}$. The density of the sintered disks was determined by using the Archimedes method (ISO 5018:1983) with isopropanol as fluid.

Thermoelectric Analysis

The electrical conductivity and Seebeck coefficient were measured perpendicular to the pressing direction by cutting the sintered disks into bars with length of 10 mm and width of 3 mm. The electrical conductivity was measured by the four-point probe method at equilibrium conditions within a horizontal three-heating-zone tube furnace (Carbolite Gero EVZ 12/450B). The Seebeck coefficient was determined by using a ProboStat A setup from NorECs with a vertical furnace from Elite Thermal Systems Ltd. at equilibrium conditions. Values were recorded after heating to the maximum temperature of 1073 K and cooling in steps of 100 K to room temperature with intermediate dwell times to maintain stable conditions. The measurement setup included Keithley multimeters and LabVIEW data processing software.

Results and Discussion

CCO and BCSO powders were mixed to obtain the ceramic composites. The CCO was presintered and then ground to achieve higher crystallinity (compare the XRD and SEM measurements in Supplementary Fig. S1) and increased

density (Fig. S2) in the sintered ceramics with positive effects on the electrical conductivity. Only presintered CCO powder was used for the composites. BCSO was synthesized hydrothermally with minor Bi_2SeO_2 impurities, as proven by the XRD results in Supplementary Fig. S1a. The crystal habitus of BCSO was examined by SEM, and nanosheets with thickness of approximately 50 nm and lateral extension of up to 1000 nm were observed (cf. Supplementary Fig. S1b).

As BCSO is not stable at high temperature in air, changes in the composition of the sintered CCO-BCSO composites were expected. Beginning with the EDXS analysis, the elemental overlay maps in Fig. 1 provide more information on the resulting phases. The first difference between the CCO and the sample with 10 wt.% BCSO is the crystal growth of CCO to large plate-like particles with lateral size of roughly $10\ \mu\text{m}$. This effect became even more pronounced with increasing BCSO amount and is likely caused by extensive restructuring of the CCO. Furthermore, a secondary cobalt oxide phase arises with particle size of approximately $1\ \mu\text{m}$

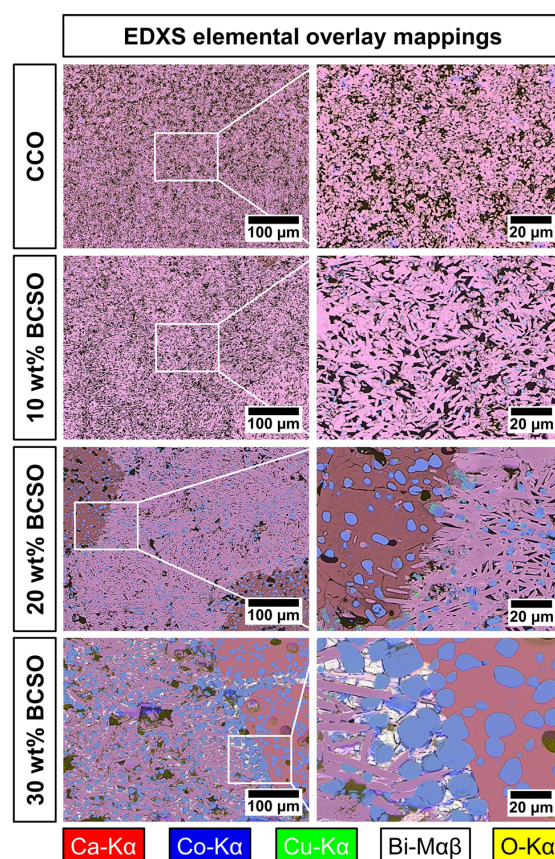


Fig. 1 Cross-sectional EDXS elemental overlay maps of CCO and composites with 10 wt.%, 20 wt.%, and 30 wt.% BCSO. See Supplementary Figs. S3–S10 for more details.

for the sample with 10 wt.% BCSO. These cobalt oxide particles grew to size of up to 20 μm when the amount of BCSO was increased to 20 wt.% and 30 wt.%. A third phase of $\text{Ca}_3\text{Co}_2\text{O}_6$ emerged at 20 wt.% BCSO, which also incorporated cobalt oxide particles but did not show distinct crystal grains, which could indicate amorphous structure. Finally, a fourth phase of Bi_2O_3 became obvious for the 30 wt.% sample, being located between the CCO grains. The phases were identified by evaluating the quantitative EDXS results in Fig. 2, based on the average value of five particles for each phase and mapping. All the cross-sectional EDXS mappings performed at various magnifications are shown in Supplementary Fig. S3–S10. Note that no Se was detected in any of the composites, indicating evaporation or sublimation of a Se species during sintering.

The elemental composition of the CCO shows where Bi from the original BCSO remains. However, a doping limit seems to be reached at 20 wt.% BCSO as the amount of Bi does not increase further for the 30 wt.% sample. This explains the occurrence of the $\text{Bi}_2\text{O}_3\text{:Co,Ca}$ phase only for high amounts of BCSO because excess Bi cannot be incorporated into the CCO anymore. The substitution of Co with Bi in CCO leads to formation of $\text{Co}_3\text{O}_4\text{:Co,Ca}$. Co_3O_4 and cubic CoO are both thermodynamically stable cobalt oxides in air at room temperature^{39,40} and cannot easily be distinguished by EDXS. Both phases can transfer reversibly into each other depending on the oxidation or reduction conditions.⁴⁰ At temperatures above 513 K in air, cubic CoO usually transforms rapidly into Co_3O_4 .³⁹ As the composites were sintered for several hours at this temperature in air, one can assume that only Co_3O_4 will be left. As the sintering temperature of 1173 K is slightly above the decomposition temperature of 1170 K for Co_3O_4 into CoO,⁴¹ both oxides can be expected in the sintered ceramic. This is proven by the XRD patterns of the 20 wt.% and 30 wt.% BCSO samples shown in Supplementary Fig. S11, which clearly show

the presence of CoO as well as Co_3O_4 within the composites. Furthermore, the amount of Cu in the cobalt oxides clearly increased with the amount of BCSO introduced. As only Cu but no Bi was found in the cobalt oxides, initial formation of CoO can be concluded based on the oxidation states of the metals, followed by partial oxidation to Co_3O_4 . $\text{Ca}_3\text{Co}_2\text{O}_6$ is a typical decomposition product of CCO,¹⁴ and its composition does not alter with increasing amounts of BCSO. Such decomposition could be caused by exothermic reactions during sintering, locally increasing the temperature above the decomposition temperature of CCO when agglomerates of BCSO are present. This is reasonable since the sintering temperature of 1173 K is close to the decomposition temperature of 1220 K.¹⁴ Another explanation is oxidation and decomposition of BCSO during sintering. The oxygen required for the formation of oxides could be derived from CCO, facilitating decomposition of CCO. This is especially the case when atmospheric oxygen cannot move freely within the compacted disk during sintering. As cobalt oxides are also decomposition products of CCO, this further explains the growth of these particles for the samples with 20 wt.% and 30 wt.% BCSO.

To understand the process during reaction sintering, *in situ* XRD analysis of the powder with 20 wt.% BCSO and 80 wt.% CCO was performed in air. The results (Fig. 3) show the progression of the phases formed during the whole sintering process. Noteworthy changes in reflections are highlighted, and the CCO and BCSO reflections are indexed at the starting temperature of 303 K. As expected, the BCSO decomposes at 573 K, which becomes obvious when looking at the vanishing 102 and 200 reflections. With the decomposition of BCSO, formation of Bi_2O_3 begins, and at 773 K, this phase even shows the most intense reflection of the composite (see $2\theta = 27.5^\circ$). At 873 K, the bismuth oxide also decomposes until it completely disappears at 1073 K. Another intermediate phase is CuO, which becomes

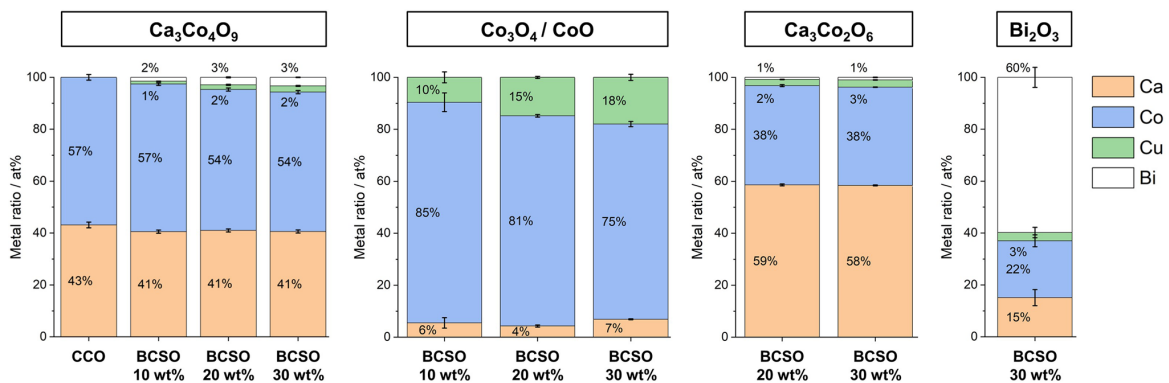


Fig. 2 EDXS-based quantification of compounds occurring in pristine CCO and composites with 10 wt.%, 20 wt.%, and 30 wt.% BCSO. Values are averages from five different spots within the elemental mappings of Fig. 1.

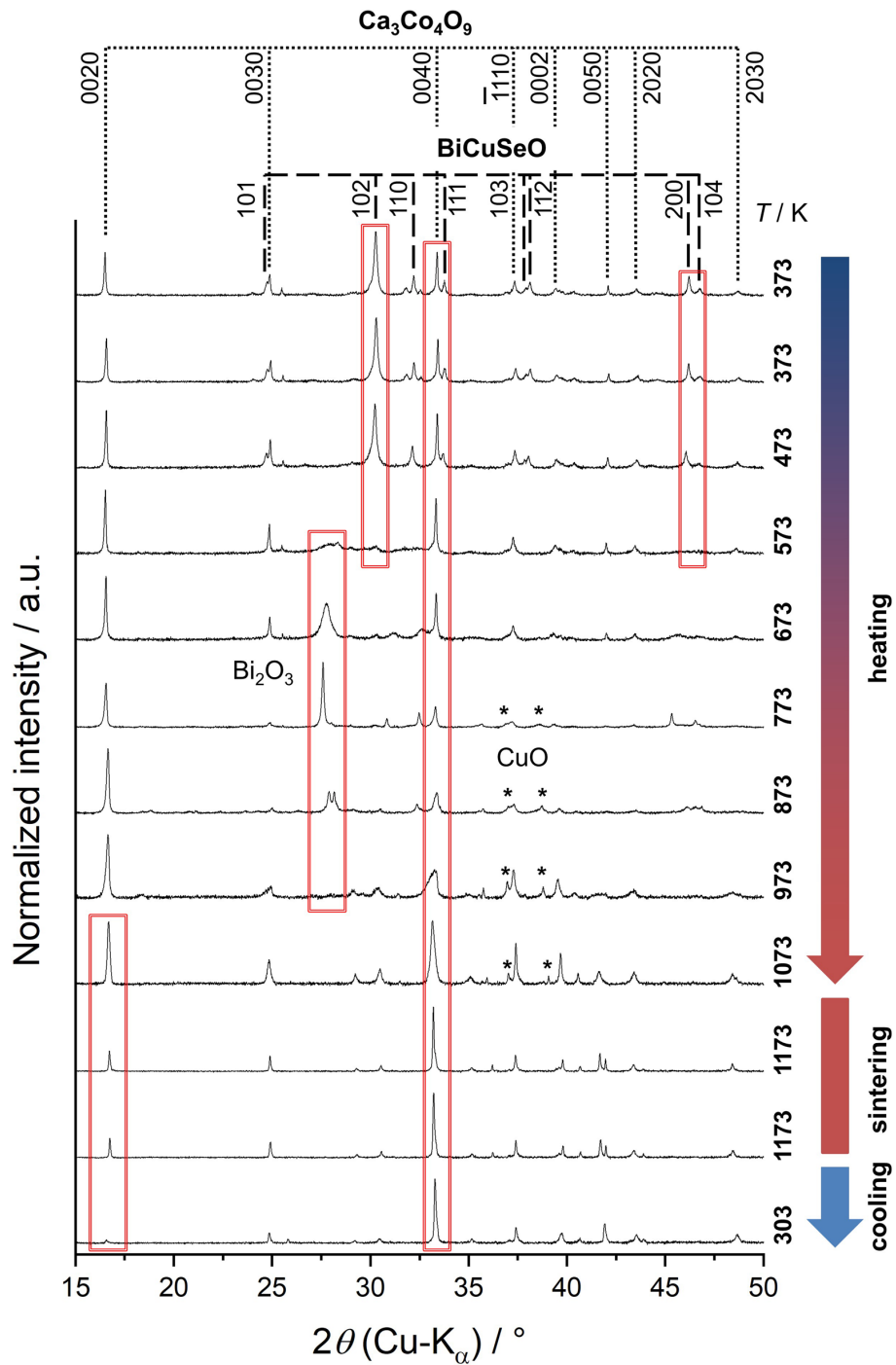


Fig. 3 *In situ* powder XRD monitoring of reaction sintering of the sample containing 20 wt.% BCSO and 80 wt.% CCO. From top to bottom, the temperature increases from room temperature to the max-

imum temperature of 1173 K in steps of 100 K followed by cooling. Starting materials CCO and BCSO are indexed, and domains with noteworthy alteration are highlighted.

distinct at 773 K but vanishes at the maximum temperature of 1173 K. No crystalline selenium phases apart from BCSO at the beginning could be detected at any temperature step. The diffraction pattern when first reaching 1173 K is almost identical to that after the full sintering duration of 10 h, indicating that the phase transformations were completed. In the final product after sintering and cooling to 303 K, mainly reflections of CCO remain, but the intensity ratio is shifted in comparison with sintered CCO disks (cf. Supplementary Fig. S11). The main reason for this is the random orientation of the powder in comparison with the preferred orientation after uniaxial pressing. It is also related to the growth process of CCO to large plate-like CCO particles as depicted in the EDXS mappings. The 0040 reflection of CCO first diminishes compared with the 0020 reflection

until a temperature of 773 K is reached. At 873 K, the 0040 reflection intensifies and becomes the most intense during sintering. This indicates massive rearrangement within the CCO during the heating process and is related to the integration of Bi and Cu into the CCO structure. Generally, a strong preferred orientation or even texture is beneficial for CCO, because of its better thermoelectric properties along the a - b -plane.^{17,18}

Further information about the phases present during and after sintering was acquired by thermogravimetric analyses (Fig. 4a, b). The mass gain at 573 K can be attributed to the decomposition temperature of BCSO¹⁹ as confirmed by *in situ* XRD analysis and suggests the formation of oxides. The maximum mass occurs at 773 K, where Bi₂O₃ is the dominant crystalline phase according to the *in situ* XRD

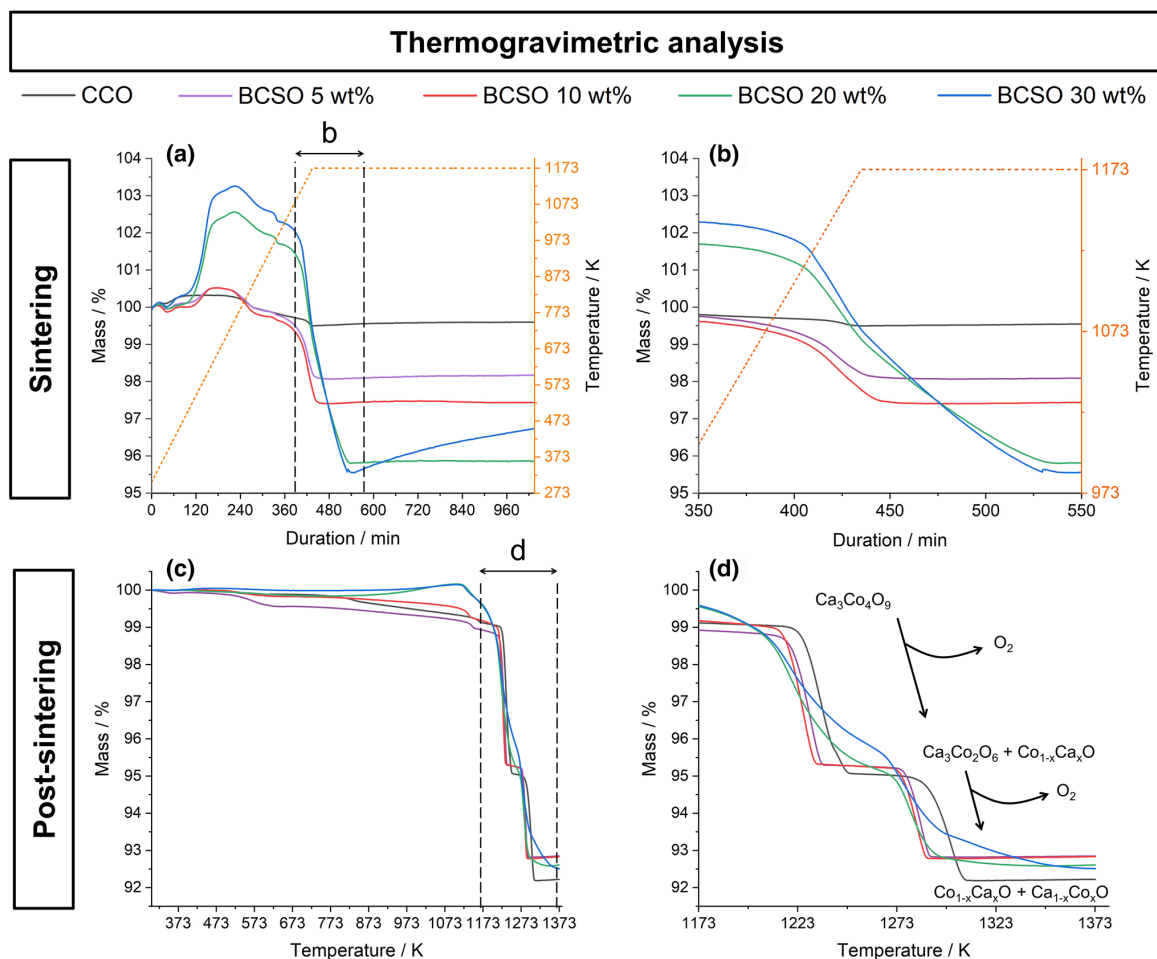


Fig. 4 Thermogravimetric analyses of unsintered powders and sintered ceramics of pristine CCO and composites. (a, b) Mass change and temperature against the duration of the applied sintering method

for the compound powders. (c, d) Mass change against the temperature for the sintered ceramics.

analysis. The decomposition of Bi_2O_3 between 873 K and 973 K is accompanied by a mass loss of approximately 1 wt.%. This mass loss is likely related to the incorporation of Bi into the CCO structure under release of oxygen. The most intense mass loss occurs between 973 K and 1173 K, being due to evaporation or sublimation of the Se species. As confirmed by the elemental mappings before, no Se was present in the sintered ceramics. Therefore, the loss of 4 wt.% for the sample with 20 wt.% BCSO in Fig. 4b must be attributed to a Se species with Cu and Bi still present within the composites. Furthermore, CCO shows only a small loss of less than 0.5 wt.% in this region, which is an expected phenomenon and linked to the variable and temperature-dependent amount of oxygen within the structure.⁴² For the samples with 5 wt.% to 20 wt.% BCSO, a plateau is reached at the sintering temperature of 1173 K, indicating that the reactions were completed and a stable composite resulted. However, the sample with 30 wt.% BCSO showed steady mass gain during the dwell time, indicating that oxygen was incorporated. As Bi_2O_3 is only found in significant amounts in this sample after sintering, the mass gain is likely caused by its formation. To prove the stability and decomposition temperature of the sintered composites, further thermogravimetric investigations were performed (Fig. 4c, d). Until 1173 K, only a small loss of up to 1 wt.% occurs for all the composites and the CCO, which can be attributed to oxygen reordering in CCO. The decomposition of CCO occurs at roughly 1223 K, in good agreement with literature data.¹⁴ For the composites, the decomposition temperature range widens due to the structural changes of CCO by incorporating Bi and Cu. Another mass loss is located at 1298 K, where $\text{Ca}_3\text{Co}_2\text{O}_6$ fully decomposes into calcium oxide and cobalt oxide, in agreement with literature¹⁴. The presence of both steps in all the composites supports the assumption that CCO is still the main phase.

The CCO within the sample with 20 wt.% BCSO was further investigated by TEM to verify its crystallinity after the growth to large plate-like particles. As shown in Fig. 5, the CCO showed high crystallinity as confirmed by the SAED results in Fig. 5b. No other phases or different orientations were observed for the investigated grain along the [0100] zone axis. The pairwise occurrence of reflections close to each other can be explained by microtwins, which have been observed for CCO previously.³⁰ The high-resolution TEM results in Fig. 5c, d clearly show the stacking order along the *c*-axis, while the bright lines are associated with the CoO_2 layers.⁴³ The dimension of the *c*-axis at 11.00 Å is slightly larger in comparison with the value of 10.84 Å for pure CCO,¹⁵ which can be attributed to the incorporation of Bi into the structure. The ionic radius of Bi^{3+} of 103 pm is clearly larger than the value of 0.55 pm for Co^{3+} , thus the expansion of the unit cell to some extent seems reasonable and further confirms the doping of CCO.

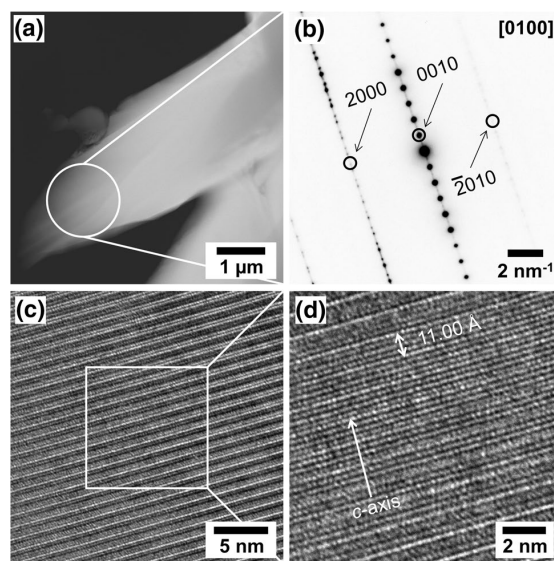


Fig. 5 Cross-sectional TEM characterization of the 20 wt.% BCSO sample. (a) STEM annular dark-field micrograph showing cross-section of a CCO sheet and the investigated area for SAED. (b) SAED pattern of CCO along the [0100] zone axis. Reflections were indexed by the four-dimensional superspace group approach.¹⁵ (c, d) High-resolution TEM showing the stacking order along the crystallographic *c*-axis and its dimension.

Based on the results of the analyses described so far, the outcome of reaction sintering of CCO and BCSO at different weight ratios is presented in Fig. 6. During the sintering process, the BCSO oxidizes and the Se species leaves the composite. While the CCO restructures and grows, Bi and Cu are incorporated and doped CCO results. The substituted Co and Ca form doped cobalt oxides with atmospheric oxygen. Further reactions occur for the same with 20 wt.% BCSO, where the CCO decomposition product $\text{Ca}_3\text{Co}_2\text{O}_6\text{:Bi,Cu}$ appears. Finally, $\text{Bi}_2\text{O}_3\text{:Co,Ca}$ emerges at 30 wt.% BCSO as the solubility limits of Bi are reached within the CCO.

Finally, the thermoelectric properties in terms of the electrical conductivity and Seebeck coefficient were measured and are shown in Fig. 7. The electrical conductivity in Fig. 7a increases with the amount of BCSO until reaching a maximum of 144 S cm^{-1} at 20 wt.% and 1073 K. The substantial decrease observed for the 30 wt.% sample is likely caused by the more dominant Bi_2O_3 phase, which even at high temperature has a relatively low electrical conductivity below 1 S cm^{-1} .⁴⁴ However, small amounts of Bi_2O_3 between CCO grains have proven to be beneficial to the thermoelectric properties by decreasing the grain-boundary resistivity.⁴⁵ The noticeable increase in density for the 20 wt.% BCSO sample (Supplementary Fig. S2) could also be linked to the Bi_2O_3 formation during the sintering process caused by liquification during sintering

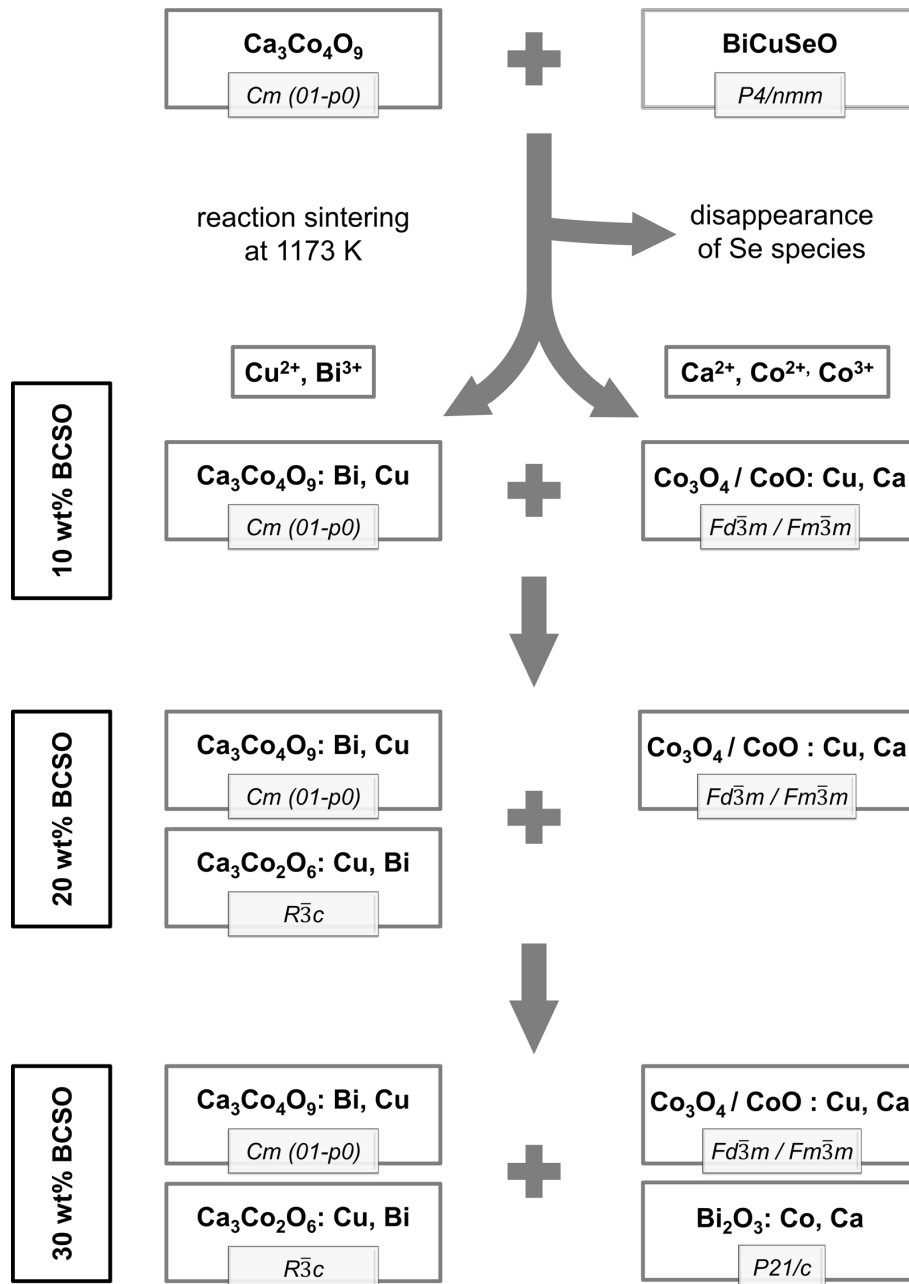


Fig. 6 Schematic of reaction sintering between CCO and BCSO. Depending on the amount of BCSO added, different phases emerge.

and reducing the sintering temperature.⁴⁶ Furthermore, the temperature dependence of the electrical conductivity increases with the amount of BCSO, which is also reflected in the Arrhenius plot in Supplementary Fig. S12 and the corresponding rise of the activation energies. The general progression of the Seebeck coefficient with

temperature is similar for all the investigated composites, but increased values can be noted despite the increasing electrical conductivity. This can be explained by the doping of CCO with Bi and Cu, which independently from each other have been proven to enhance the Seebeck coefficient and even the electrical conductivity.^{45,47} The

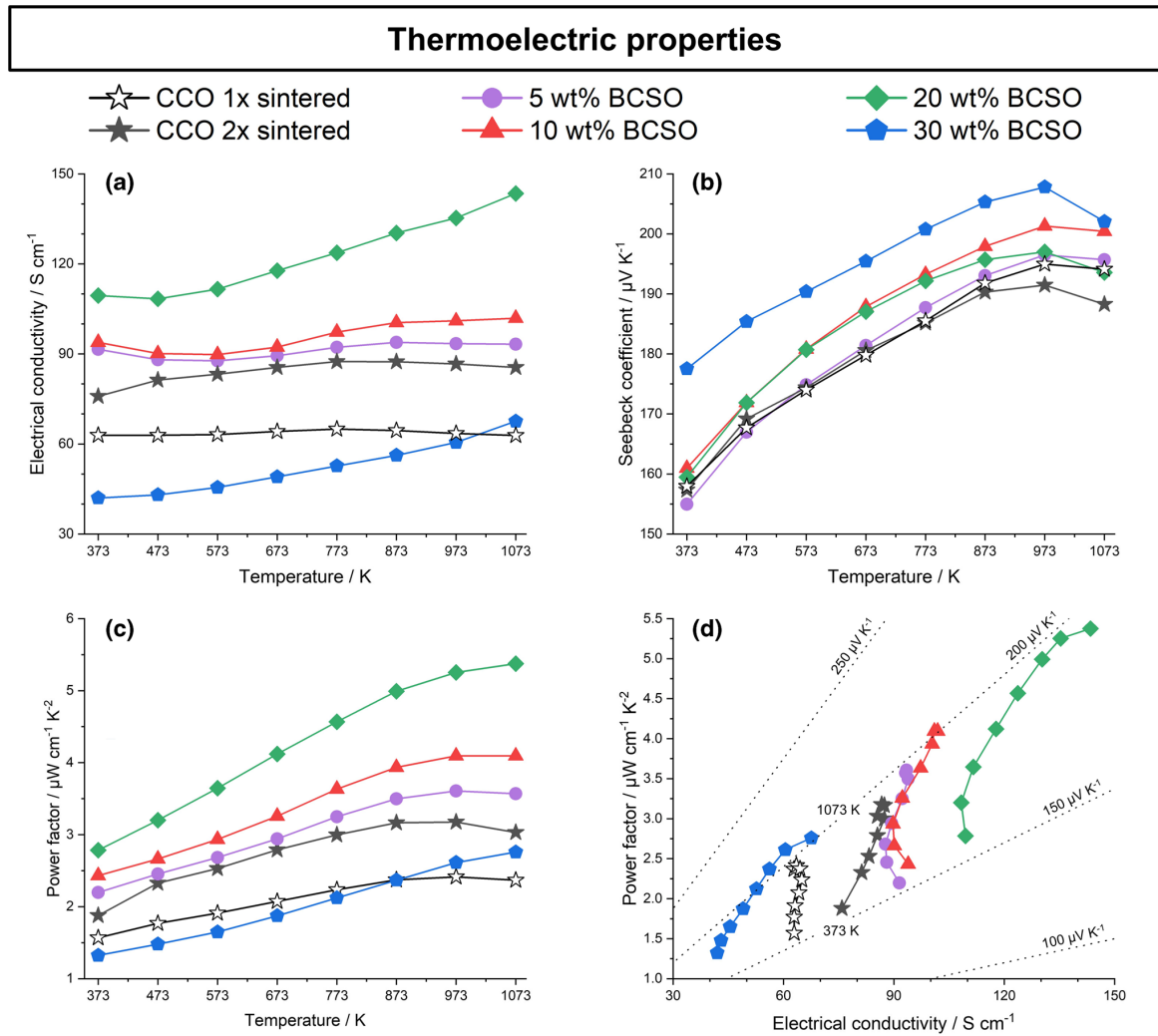


Fig. 7 Thermoelectric properties of sintered CCO and respective composites with 5 wt.%, 10 wt.%, 20 wt.%, and 30 wt% BCSO. (a) Electrical conductivity with maximum value for 20 wt.% BCSO at 1073 K. (b) Seebeck coefficient with higher values for all investigated

composites in comparison with pristine CCO. (c) Power factor with maximum values for the 20 wt.% BCSO sample. (d) Type I Ioffe plot showing the power factor against electrical conductivity, condensing the results of a–c into one clear graph.

resulting power factor in Fig. 7c shows an improved value of $5.4 \mu\text{W cm}^{-1} \text{K}^{-2}$ for 20 wt.% BCSO in comparison with $2.9 \mu\text{W cm}^{-1} \text{K}^{-2}$ for double-sintered CCO and $2.37 \mu\text{W cm}^{-1} \text{K}^{-2}$ at 1073 K. Hence, the power factor is more than doubled. This becomes more obvious in the type I Ioffe plot in Fig. 7d. The plot of the power factor against the electrical conductivity summarizes the previous diagrams in Fig. 7a–c in one diagram. The improved power factor can clearly be attributed to the increase of the electrical conductivity as the Seebeck coefficient does not alter significantly. As stated by Narducci⁷, the power factor is an equally important value as the figure of merit zT for

limitless energy sources, which are more likely to have high temperature⁶.

Conclusions

$\text{Ca}_3\text{Co}_4\text{O}_9$ and BiCuSeO were combined for the first time to create composites after reaction sintering. Presintering of $\text{Ca}_3\text{Co}_4\text{O}_9$ before use as a component enabled a higher density and increased electrical conductivity. As expected, the BCSO did not withstand the high sintering temperature of 1173 K in air, but the resulting reactions enabled *in situ*

doping of $\text{Ca}_3\text{Co}_4\text{O}_9$ with Bi and Cu as well as the formation of other doped oxide phases. XRD, SEM, EDXS, TGA, and TEM analyses revealed the phases in the final ceramic composites and possible intermediates during sintering. The high-temperature stability of the sintered ceramics was confirmed by TGA. Overall, the composites with up to 20 wt.% BiCuSeO were superior to pristine $\text{Ca}_3\text{Co}_4\text{O}_9$ in terms of the thermoelectric power factor. Formation of unfavorable Bi_2O_3 was observed at a share of 30 wt.% due to the solubility limits in $\text{Ca}_3\text{Co}_4\text{O}_9$. The best power factor of $5.4 \mu\text{W cm}^{-1} \text{K}^{-2}$ was achieved for the 20 wt.% BiCuSeO sample at 1073 K because of a substantial increase of the electrical conductivity while maintaining a high Seebeck coefficient. This resulted in a value more than twice as high as that of pristine $\text{Ca}_3\text{Co}_4\text{O}_9$ and shows the great potential of these composite systems based on more subtle adjustment of the weight ratio in the future.

Supplementary Information The online version contains supplementary material available at <https://doi.org/10.1007/s11664-021-09336-2>.

Acknowledgments The authors gratefully appreciate access to the JSM-6700FPLUS by Dr. Renat Almeev and technical assistance by Frank Steinbach. The study was partly funded by Deutsche Forschungsgemeinschaft (DFG, German Research Foundation) projects FE 928/21-1 and BI 1708/5-1.⁴⁸ In addition, the project leading to these results has in part received funding from the European Research Council (ERC) under the European Union's Horizon 2020 research and innovation program (grant agreement no. 714429).

Funding Open Access funding enabled and organized by Projekt DEAL.

Conflict of interest The authors declare that they have no conflicts of interest.

Open Access This article is licensed under a Creative Commons Attribution 4.0 International License, which permits use, sharing, adaptation, distribution and reproduction in any medium or format, as long as you give appropriate credit to the original author(s) and the source, provide a link to the Creative Commons licence, and indicate if changes were made. The images or other third party material in this article are included in the article's Creative Commons licence, unless indicated otherwise in a credit line to the material. If material is not included in the article's Creative Commons licence and your intended use is not permitted by statutory regulation or exceeds the permitted use, you will need to obtain permission directly from the copyright holder. To view a copy of this licence, visit <http://creativecommons.org/licenses/by/4.0/>.

References

- H.U. Fuchs, *The dynamics of heat: A unified approach to thermodynamics and heat transfer*, 2nd edn. Graduate Texts in Physics (Springer Science+Business Media LLC, New York, 2010). <https://doi.org/10.1007/978-1-4419-7604-8>
- A. Feldhoff, *Energy Harvest. Syst.* **2**(1–2), 1 (2015). <https://doi.org/10.1515/ehs-2014-0040>
- A. Feldhoff, *Entropy* **22**(8), 1 (2020). <https://doi.org/10.3390/e22080803>
- C. Zener, *Trans. Am. Soc. Met.* **53**, 1052 (1961)
- A.F. Ioffe, *Semiconductor Thermoelements and Thermoelectric Cooling*, 1st edn. (Info-search Ltd., London, 1957)
- M. Wolf, R. Hinterding, A. Feldhoff, *Entropy* **21**(11), 1058 (2019). <https://doi.org/10.3390/e21111058>
- D. Narducci, *Appl. Phys. Lett.* **99**(10), 102104 (2011). <https://doi.org/10.1063/1.3634018>
- G. Tan, L.D. Zhao, M.G. Kanatzidis, *Chem. Rev.* **116**(19), 12123 (2016). <https://doi.org/10.1021/acs.chemrev.6b00255>
- J.Q. Guo, H.Y. Geng, T. Ochi, S. Suzuki, M. Kikuchi, Y. Yamaguchi, S. Ito, *J. Electron. Mater.* **41**(6), 1036 (2012). <https://doi.org/10.1007/s11664-012-1958-0>
- S.J. Poon, *Metals* **8**(12), 989 (2018). <https://doi.org/10.3390/met8120989>
- J. Shuai, J. Mao, S. Song, Q. Zhang, G. Chen, Z. Ren, *Mater. Today Phys.* **1**, 74 (2017). <https://doi.org/10.1016/j.mtphys.2017.06.003>
- Q. Zhang, Y. Sun, W. Xu, D. Zhu, *Adv. Mater.* **26**(40), 6829 (2014). <https://doi.org/10.1002/adma.201305371>
- J.W. Fergus, *J. Eur. Ceram. Soc.* **32**(3), 525 (2012). <https://doi.org/10.1016/j.jeurceramsoc.2011.10.007>
- O. Jankovsky, D. Sedmidubsky, Z. Sofer, P. Simek, J. Hejtmanek, *Ceramics-Silikáty* **56**(2), 139 (2012)
- Y. Miyazaki, M. Onoda, T. Oku, M. Kikuchi, Y. Ishii, Y. Ono, Y. Morii, T. Kajitani, *J. Phys. Soc. Jpn.* **71**(2), 491 (2002). <https://doi.org/10.1143/JPSJ.71.491>
- Y. Miyazaki, *Solid State Ionics* **172**(1–4), 463 (2004). <https://doi.org/10.1016/j.ssi.2004.01.046>
- C.H. Lim, W.S. Seo, S. Lee, Y.S. Lim, J.Y. Kim, H.H. Park, S.M. Choi, K.H. Lee, K. Park, *J. Korean Phys. Soc.* **66**(5), 794 (2015). <https://doi.org/10.3938/jkps.66.794>
- D. Kenfaui, M. Gomina, J.G. Noudem, D. Chateigner, *Materials* **11**(7), 1 (2018). <https://doi.org/10.3390/ma11071224>
- F. Li, T.R. Wei, F. Kang, J.F. Li, *J. Alloys Compd.* **614**, 394 (2014). <https://doi.org/10.1016/j.jallcom.2014.06.117>
- L.D. Zhao, J. He, D. Berardan, Y. Lin, J.F. Li, C.W. Nan, N. Dragoe, *Energy Environ. Sci.* **7**(9), 2900 (2014). <https://doi.org/10.1039/c4ee00997e>
- J. Sui, J. Li, J. He, Y.L. Pei, D. Berardan, H. Wu, N. Dragoe, W. Cai, L.D. Zhao, *Energy Environ. Sci.* **6**(10), 2916 (2013). <https://doi.org/10.1039/C3EE41859F>
- M.S. Dresselhaus, G. Chen, M.Y. Tang, R.G. Yang, H. Lee, D.Z. Wang, Z.F. Ren, J.P. Fleurial, P. Gogna, *Adv. Mater.* **19**(8), 1043 (2007). <https://doi.org/10.1002/adma.200600527>
- H. Ohta, S. Kim, Y. Mune, T. Mizoguchi, K. Nomura, S. Ohta, T. Nomura, Y. Nakanishi, Y. Ikuhara, M. Hirano, H. Hosono, K. Koumoto, *Nat. Mater.* **6**(2), 129 (2007). <https://doi.org/10.1038/nmat1821>
- Y. Liu, L.D. Zhao, Y. Zhu, Y. Liu, F. Li, M. Yu, D.B. Liu, W. Xu, Y.H. Lin, C.W. Nan, *Adv. Energy Mater.* **6**(9), 1502423 (2016). <https://doi.org/10.1002/aenm.201502423>
- M. Mikami, N. Ando, R. Funahashi, *J. Solid State Chem.* **178**(7), 2186 (2005). <https://doi.org/10.1016/j.jssc.2005.04.027>
- F. Kahraman, M.A. Madre, S. Rasekh, C. Salvador, P. Bosque, M.A. Torres, J.C. Diez, A. Sotelo, *J. Eur. Ceram. Soc.* **35**(14), 3835 (2015). <https://doi.org/10.1016/j.jeurceramsoc.2015.05.029>
- M. Wolf, K. Menekse, A. Mundstock, R. Hinterding, F. Nietschke, O. Oeckler, A. Feldhoff, *J. Electron. Mater.* **48**(11), 7551 (2019). <https://doi.org/10.1007/s11664-019-07555-2>
- C. Chen, T. Zhang, R. Donelson, D. Chu, R. Tian, T.T. Tan, S. Li, *Acta Mater.* **63**, 99 (2014). <https://doi.org/10.1016/j.actamat.2013.10.011>

29. M. Bittner, N. Kanas, R. Hinterding, F. Steinbach, D. Groeneveld, P. Wemhoff, K. Wiik, M.A. Einarsrud, A. Feldhoff, *J. Eur. Ceram. Soc.* **39**(4), 1237 (2019). <https://doi.org/10.1016/j.jeurceramsoc.2018.10.023>
30. R. Hinterding, Z. Zhao, M. Wolf, M. Jakob, O. Oeckler, A. Feldhoff, *Open Ceramics* **6**, 100103 (2021). <https://doi.org/10.1016/j.oceram.2021.100103>
31. R.K. Gupta, R. Sharma, A.K. Mahapatro, R.P. Tandon, *Physica B* **483**, 48 (2016). <https://doi.org/10.1016/j.physb.2015.12.028>
32. F. Delorme, P. Diaz-Chao, E. Guilmeau, F. Giovannelli, *Ceram. Int.* **41**(8), 10038 (2015). <https://doi.org/10.1016/j.ceramint.2015.04.091>
33. G. Constantinescu, S.M. Mikhalev, A.D. Lisenkov, D.V. Lopes, A.R. Sarabando, M.C. Ferro, T.F.d. Silva, S.A. Sergiienko, A.V. Kovalevsky, *Materials* **14**(4) (2021). <https://doi.org/10.3390/ma14040980>
34. Q. Zhang, X. Ai, L. Wang, Y. Chang, W. Luo, W. Jiang, L. Chen, *Adv. Funct. Mater.* **25**(6), 966 (2015). <https://doi.org/10.1002/adfm.201402663>
35. W. Liu, X. Yan, G. Chen, Z. Ren, *Nano Energy* **1**(1), 42 (2012). <https://doi.org/10.1016/j.nanoen.2011.10.001>
36. M. Samanta, S.N. Guin, K. Biswas, *Inorg. Chem. Front.* **4**(1), 84 (2017). <https://doi.org/10.1039/C6QI00435K>
37. T. Janssen, A. Janner, A. Looijenga-Vos, P.M. De Wolff, *International Tables for Crystallography: 9.8 Incommensurate and Commensurate Modulated Structures*, 3rd edn. (Kluwer Acad. Publ, Dordrecht, 2004)
38. T. Janssen, G. Chapuis, M. de Boissieu, *Aperiodic Crystals: From Modulated Phases to Quasicrystals*, *International Union of Crystallography monographs on crystallography*, vol. 20 (Oxford University Press, Oxford, 2007)
39. K.M. Nam, J.H. Shim, D.W. Han, H.S. Kwon, Y.M. Kang, Y. Li, H. Song, W.S. Seo, J.T. Park, *Chem. Mater.* **22**(15), 4446 (2010). <https://doi.org/10.1021/cm101138h>
40. F.C. Kong, Y.F. Li, C. Shang, Z.P. Liu, *J. Phys. Chem. C* **123**(28), 17539 (2019). <https://doi.org/10.1021/acs.jpcc.9b02842>
41. M. Chen, B. Hallstedt, L.J. Gauckler, *J. Phase Equilibria* **24**(3), 212 (2003). <https://doi.org/10.1361/105497103770330514>
42. K.T. Jacob, P. Gupta, *J. Solid State Chem.* **221**, 57 (2015). <https://doi.org/10.1016/j.jssc.2014.09.013>
43. T. Paulauskas, R.F. Klie, *J. Undergr. Res. Univ. Ill. Chicago* **5**(1), 1 (2017). <https://doi.org/10.5210/jur.v5i1.7511>
44. C. Ftikos, B. Steele, *J. Eur. Ceram. Soc.* **14**(6), 501 (1994). [https://doi.org/10.1016/0955-2219\(94\)90119-8](https://doi.org/10.1016/0955-2219(94)90119-8)
45. J.Y. Cho, O.J. Kwon, Y.K. Chung, J.S. Kim, W.S. Kim, K.J. Song, C. Park, *J. Electron. Mater.* **44**(10), 3621 (2015). <https://doi.org/10.1007/s11664-015-3924-0>
46. M. Liu, C. He, J. Wang, W.G. Wang, Z. Wang, *J. Alloys Compd.* **502**(2), 319 (2010). <https://doi.org/10.1016/j.jallcom.2009.12.134>
47. Y. Huang, B. Zhao, X. Hu, S. Lin, R. Ang, W. Song, Y. Sun, *Dalton Trans.* **41**(36), 11176 (2012). <https://doi.org/10.1039/c2dt31346d>
48. DFG SPP 2005: Priority Programm Opus Fluidum Futurum-Rheology of Reactive, Multiscale, Multiphase Construction Materials. www.spp2005.de

Publisher's Note Springer Nature remains neutral with regard to jurisdictional claims in published maps and institutional affiliations.

Supporting Information:

Reaction sintering of $\text{Ca}_3\text{Co}_4\text{O}_9$ with BiCuSeO nanosheets for high-temperature thermoelectric composites

R. Hinterding¹, D. Rieks¹, P. A. Kißling¹, L. Steinbach¹, N. C. Bigall¹, A. Feldhoff¹

¹Leibniz University Hannover, Institute of Physical Chemistry and Electrochemistry, Callinstr. 3A, D-30167 Hannover, Germany

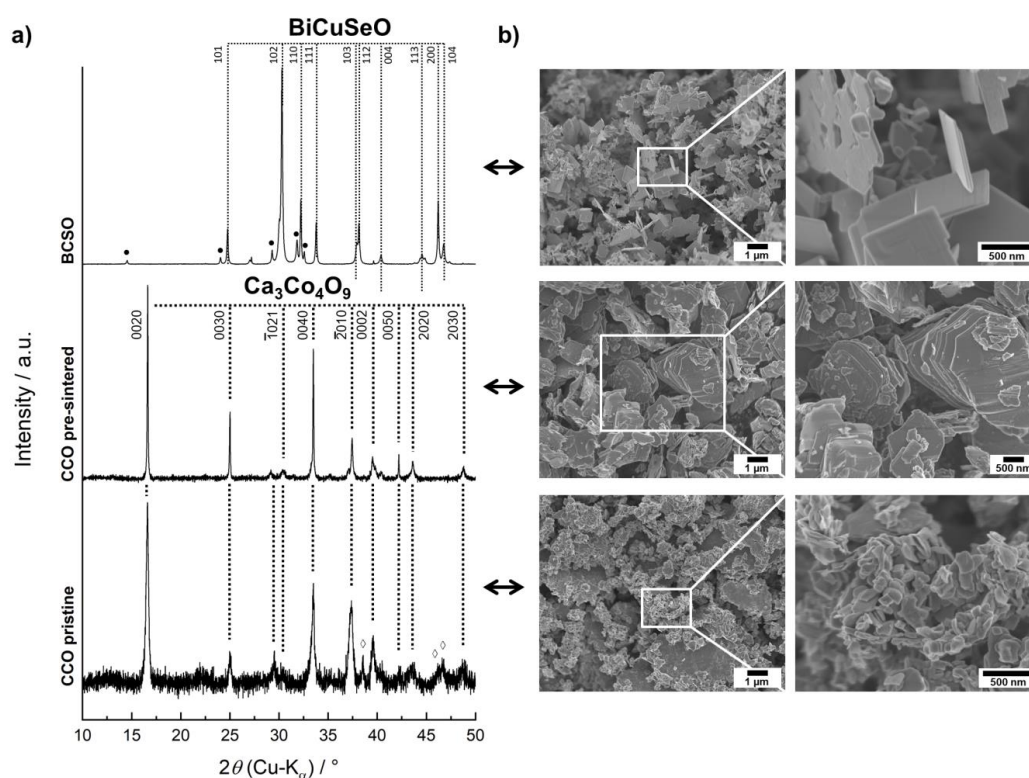


Figure S1: a) XRD patterns of the hydrothermally synthesized BCSO powder, the pre-sintered CCO and the pristine CCO with indexed reflections. For the BCSO powder, the minor phase Bi₂SeO₂ is marked by the spot symbol and for pristine CCO the minor phase CaCo₂O₄ is identified marked by the diamond symbol. b) SEM micrographs of the BCSO nanosheets, the pre-sintered CCO and the pristine CCO.

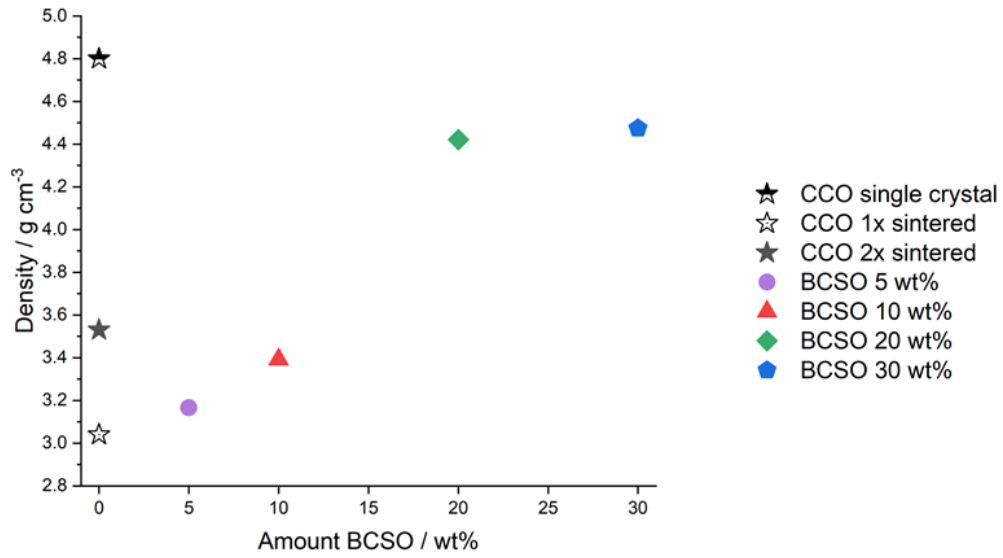


Figure S2: Density of sintered CCO and respective BCSO composites in comparison to the measured value of $4.80 \text{ g}\cdot\text{cm}^{-3}$ [1] for single crystalline CCO. The values were determined by Archimedes method.

[1]: M. Mikami, E. Guilmeau, R. Funahashi, K. Chong, D. Chateigner, *Journal of Materials Research* 20 (2005) 2491-2497. DOI 10.1557/jmr.2005.0298

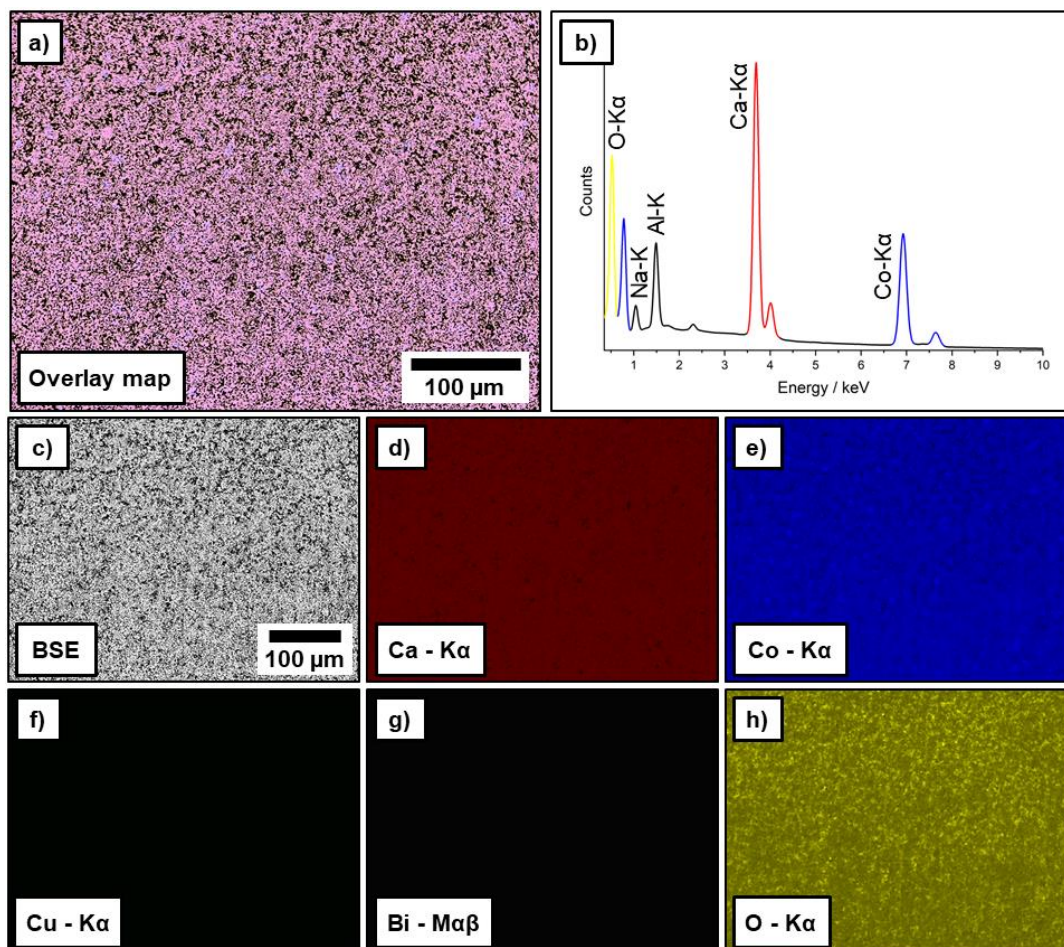


Figure S3: Overview cross-sectional SEM-EDXS analysis of the CCO matrix after sintering. a) Overlay EDXS mapping condensing the results from c-h. b) Sum spectrum of the elemental mapping with assigned peaks. c) Back-scattered electron (BSE) micrograph as basis for EDXS analysis. c-g) Elemental distributions of the respective elements Ca, Co, Cu, Bi and O. Oxygen accumulations are caused by Al_2O_3 nanoparticles introduced by vibration polishing and indicate porosity.

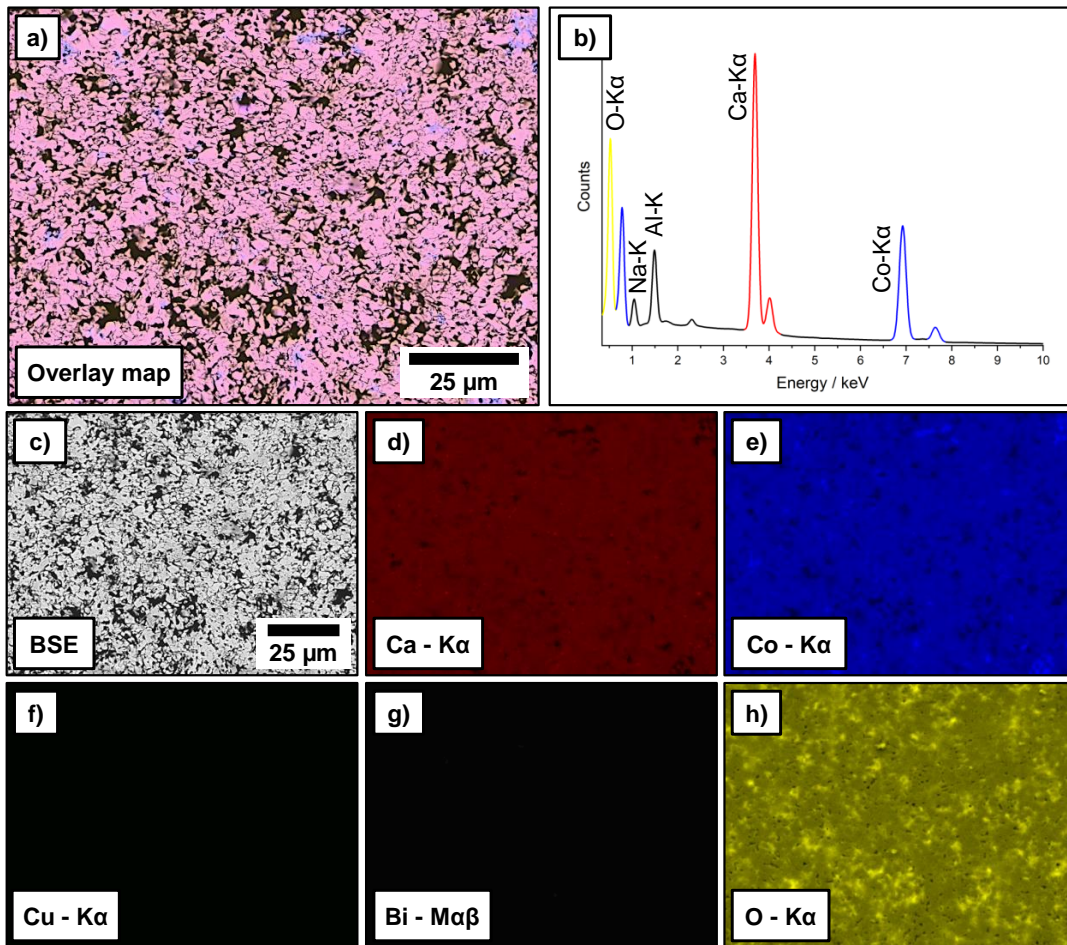


Figure S4: In-depth cross-sectional SEM-EDXS analysis of the CCO matrix after sintering. a) Overlay EDXS mapping condensing the results from c-h. b) Sum spectrum of the elemental mapping with assigned peaks. c) Back-scattered electron (BSE) micrograph as basis for EDXS analysis. c-g) Elemental distributions of the respective elements Ca, Co, Cu, Bi and O. Oxygen accumulations are caused by Al_2O_3 nanoparticles introduced by vibration polishing and indicate porosity.

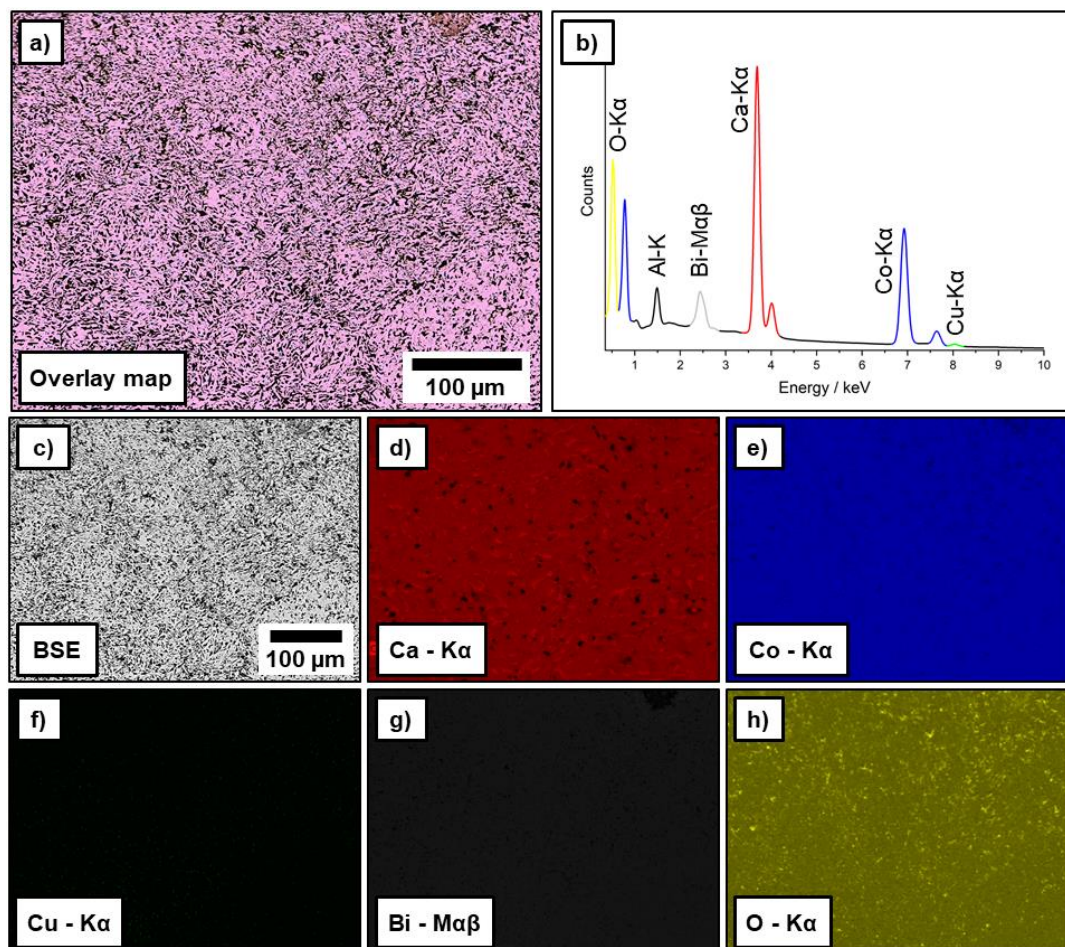


Figure S5: Overview cross-sectional SEM-EDXS analysis of the composite ceramic with 10 wt% BCSO after sintering. a) Overlay EDXS mapping condensing the results from c-h. b) Sum spectrum of the elemental mapping with assigned peaks. c) Back-scattered electron (BSE) micrograph as basis for EDXS analysis. c-g) Elemental distributions of the respective elements Ca, Co, Cu, Bi and O. Oxygen accumulations are caused by Al_2O_3 nanoparticles introduced by vibration polishing and indicate porosity.

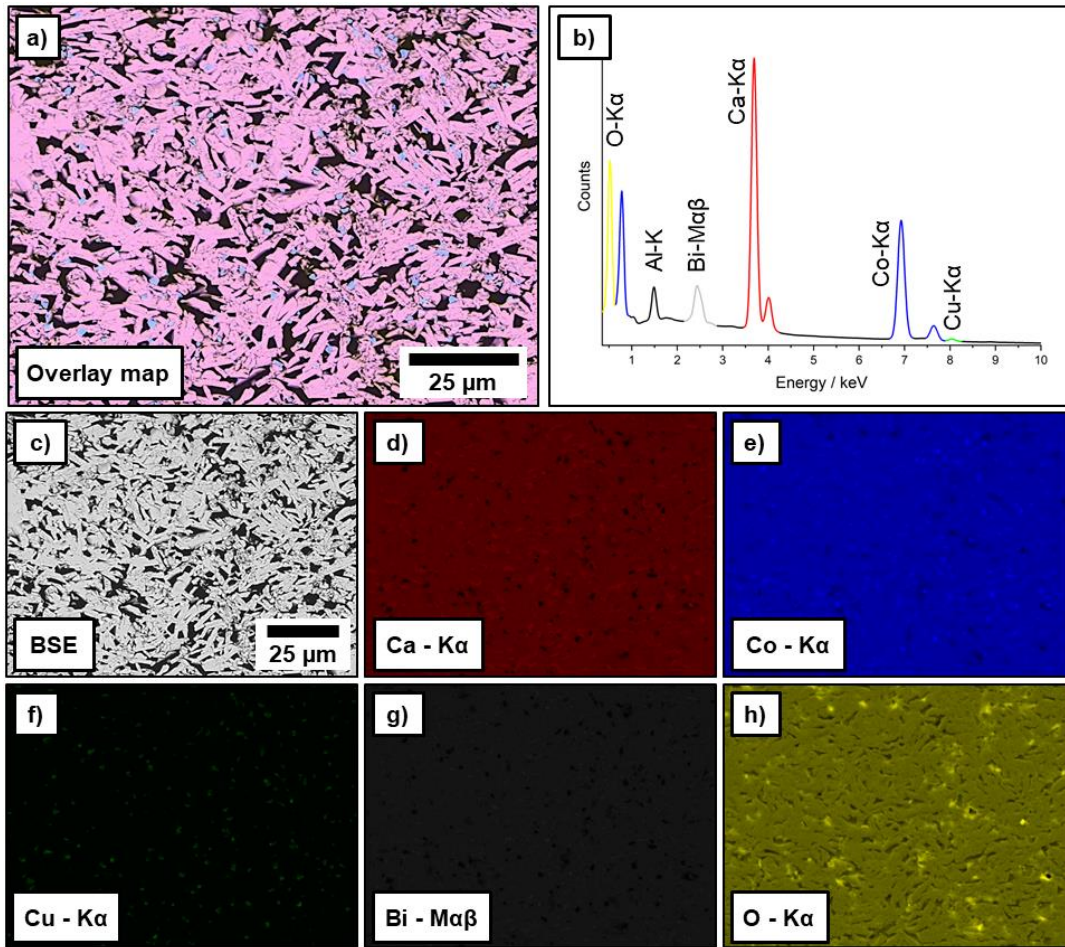


Figure S6: in-depth cross-sectional SEM-EDXS analysis of the composite ceramic with 10 wt% BCSO after sintering. a) Overlay EDXS mapping condensing the results from c-h. b) Sum spectrum of the elemental mapping with assigned peaks. c) Back-scattered electron (BSE) micrograph as basis for EDXS analysis. c-g) Elemental distributions of the respective elements Ca, Co, Cu, Bi and O. Oxygen accumulations are caused by Al_2O_3 nanoparticles introduced by vibration polishing and indicate porosity.

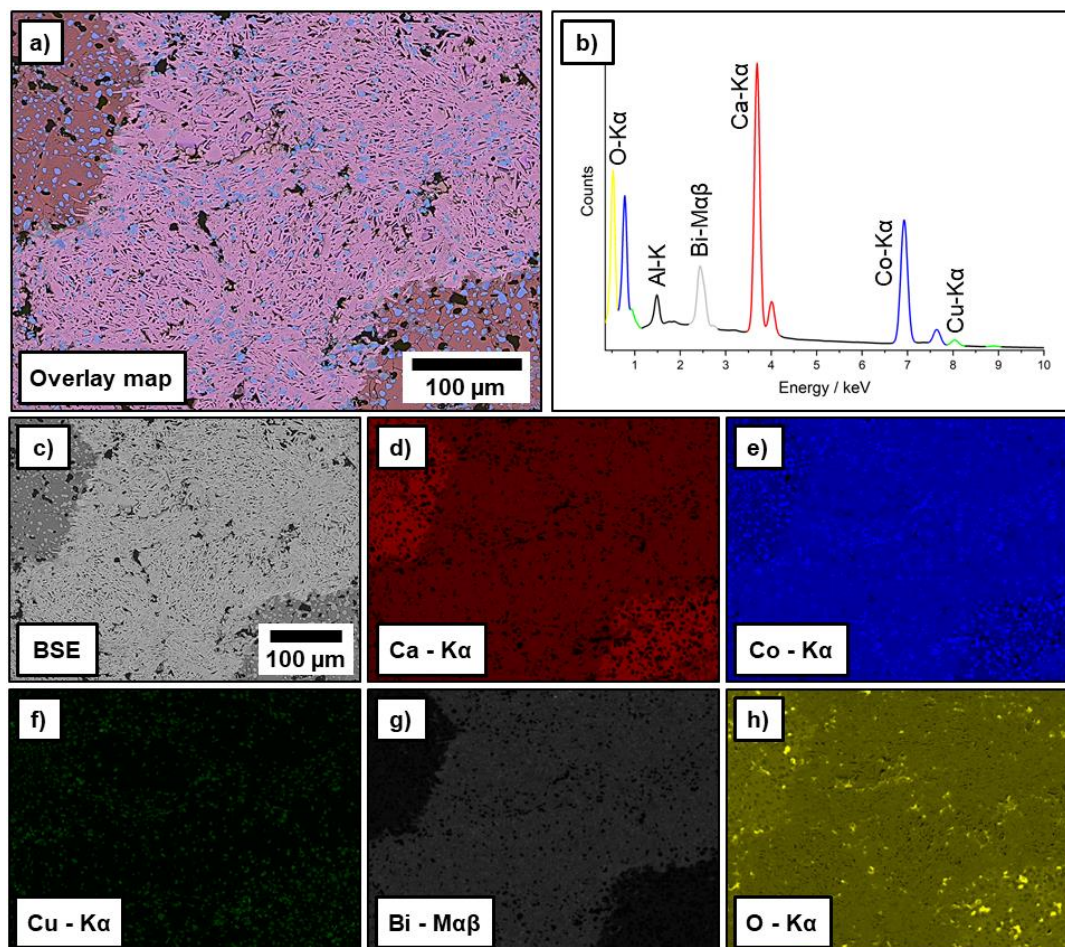


Figure S7: Overview cross-sectional SEM-EDXS analysis of the composite ceramic with 20 wt% BCSO after sintering. a) Overlay EDXS mapping condensing the results from c-h. b) Sum spectrum of the elemental mapping with assigned peaks. c) Back-scattered electron (BSE) micrograph as basis for EDXS analysis. c-g) Elemental distributions of the respective elements Ca, Co, Cu, Bi and O. Oxygen accumulations are caused by Al_2O_3 nanoparticles introduced by vibration polishing and indicate porosity.

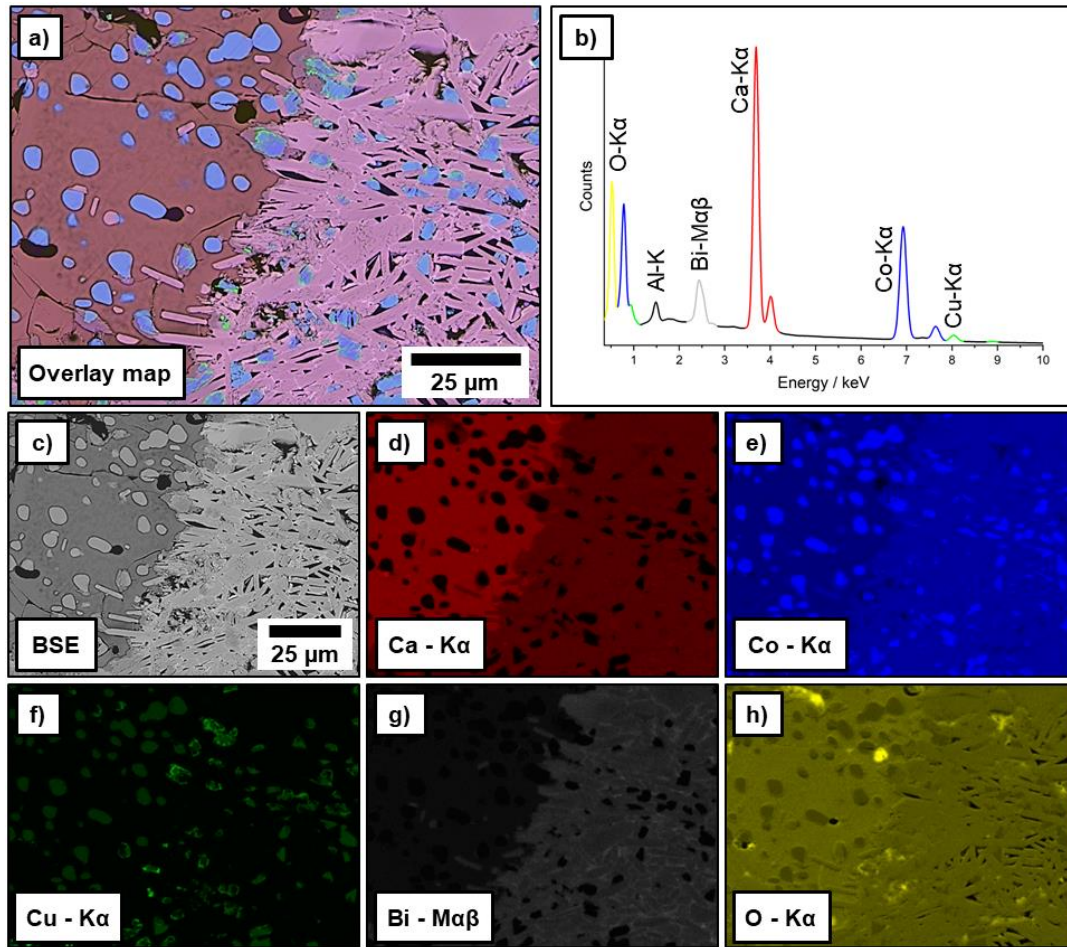


Figure S8: In-depth cross-sectional SEM-EDXS analysis of the composite ceramic with 20 wt% BCSO after sintering. a) Overlay EDXS mapping condensing the results from c-h. b) Sum spectrum of the elemental mapping with assigned peaks. c) Back-scattered electron (BSE) micrograph as basis for EDXS analysis. c-g) Elemental distributions of the respective elements Ca, Co, Cu, Bi and O. Oxygen accumulations are caused by Al_2O_3 nanoparticles introduced by vibration polishing and indicate porosity.

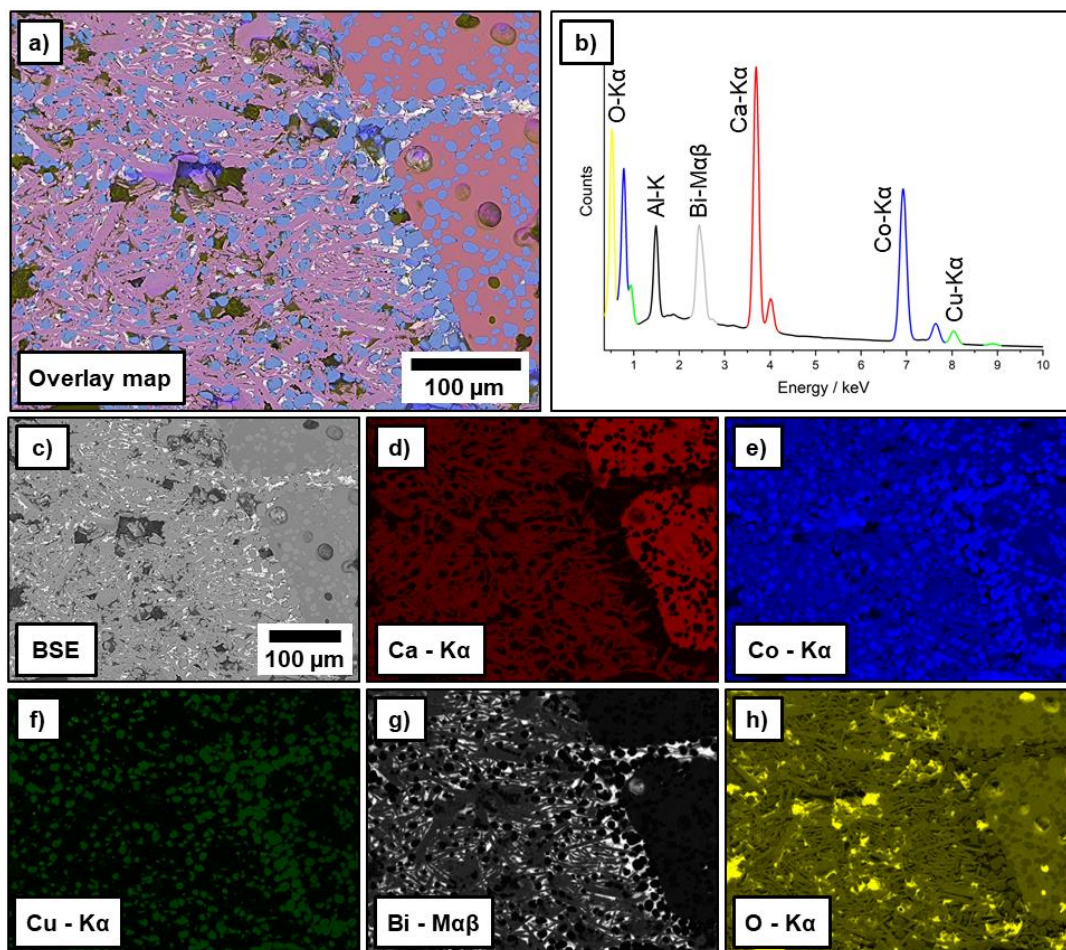


Figure S9: Overview cross-sectional SEM-EDXS analysis of the composite ceramic with 30 wt% BCSO after sintering. a) Overlay EDXS mapping condensing the results from c-h. b) Sum spectrum of the elemental mapping with assigned peaks. c) Back-scattered electron (BSE) micrograph as basis for EDXS analysis. c-g) Elemental distributions of the respective elements Ca, Co, Cu, Bi and O. Oxygen accumulations are caused by Al_2O_3 nanoparticles introduced by vibration polishing and indicate porosity.

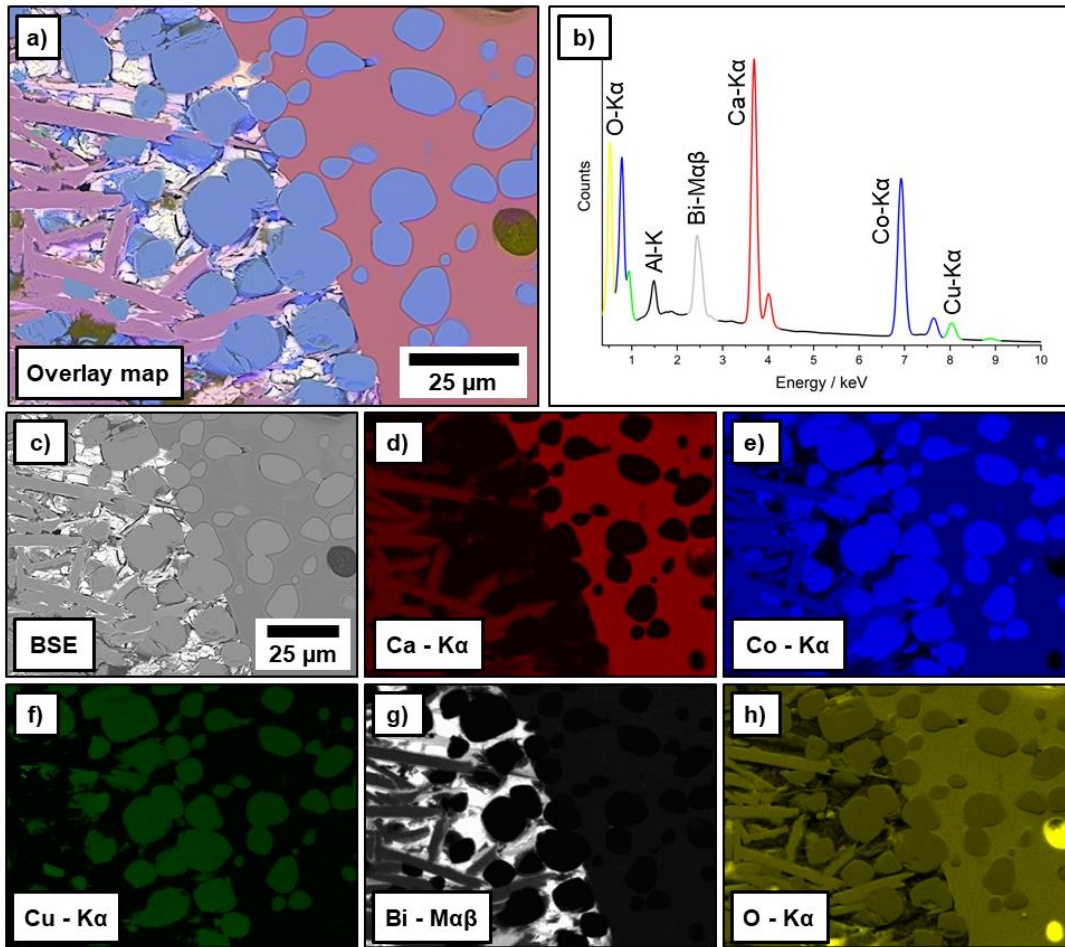


Figure S10: In-depth cross-sectional SEM-EDXS analysis of the composite ceramic with 30 wt% BCSO after sintering. a) Overlay EDXS mapping condensing the results from c-h. b) Sum spectrum of the elemental mapping with assigned peaks. c) Back-scattered electron (BSE) micrograph as basis for EDXS analysis. c-g) Elemental distributions of the respective elements Ca, Co, Cu, Bi and O. Oxygen accumulations are caused by Al_2O_3 nanoparticles introduced by vibration polishing and indicate porosity.

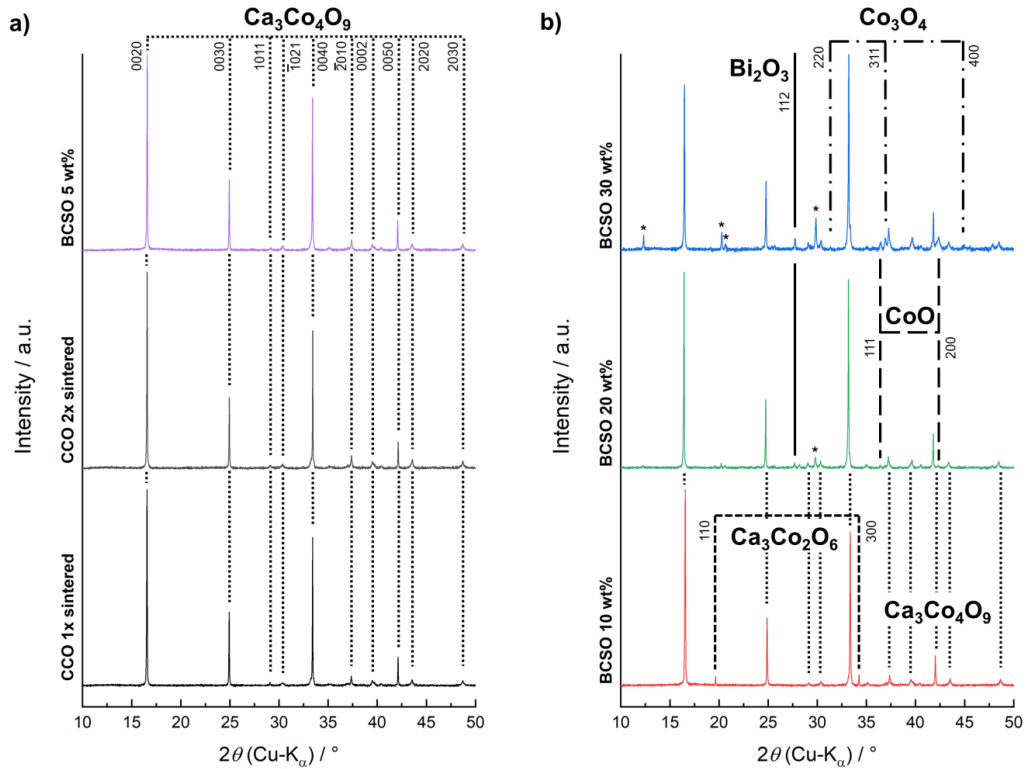


Figure S11: XRD patterns of the CCO/BCSO ceramic composites after sintering and surface polishing. Samples with a) 0 (CCO 1x sintered), 0 (CCO 2x sintered) and 5 wt% BCSO or b) 10, 20 and 30 wt% BCSO. Reflections of the respective compounds are indexed or else marked by the star symbol.

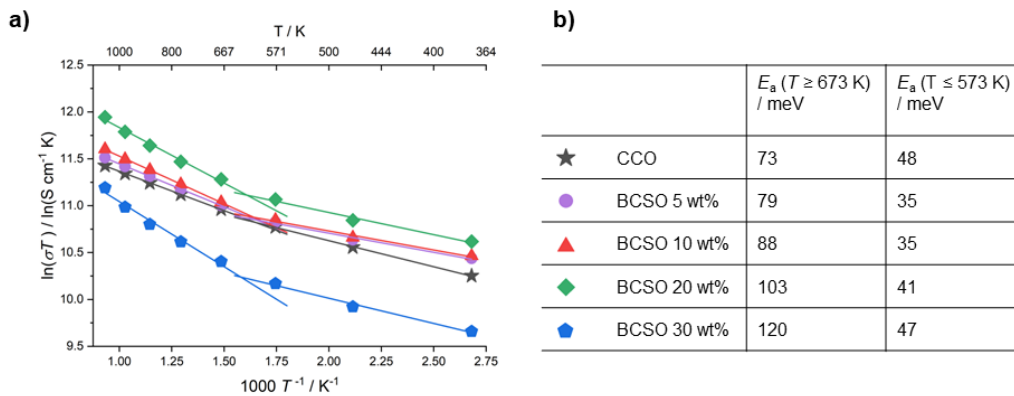


Figure S12: a) Arrhenius plot of the electrical conductivity measurements and b) the calculated activation energies for the high-temperature and low-temperature regions.

3. Conclusions and Outlook

The focus of this thesis was the investigation of oxide-based composites and exploring their possibilities for thermoelectric energy conversion. $\text{Ca}_3\text{Co}_4\text{O}_9$ (CCO) was chosen as a matrix material for the composites, because it is the best performing oxide material to date in terms of thermoelectrics. Therefore, improving the thermoelectric properties of this material is of great interest for the thermoelectric research community.

As a first innovative concept, the introduction of microdimensional oxide sheets with a plate-like crystal shape into composite systems was examined. Furthermore, relatively unusual materials for thermoelectrics, such as La_2NiO_4 (LNO) and $\text{Na}_2\text{Ca}_2\text{Nb}_4\text{O}_{13}$ (NCNO), were used as mixing partners to widen the field of known thermoelectric composites. A second concept followed a nanodimensional approach. One route investigated the in-situ formation of nanocomposites by doping beyond the solubility limit. As a result, a new triple-phase composite consisting of CCO, Na_xCoO_2 (NCO) and $\text{Bi}_2\text{Ca}_2\text{Co}_2\text{O}_9$ (BCCO) was formed with an exceptionally high power factor. Another route dealt with reaction sintering between BiCuSeO (BCSO) nanosheets and a CCO matrix. The resulting multiphase composite achieved a remarkable increase of the electrical conductivity and the power factor.

The most exceptional feature of oxides in comparison to other thermoelectric materials is their good stability at high temperature under air. Therefore, oxides are extremely important for actual applications, although competing material classes may be more advanced at pushing the boundaries of power factor and figure-of-merit. To provide an overview of the relevant high-temperature materials, a review was composed revitalizing IOFFE plots as a superb tool for evaluating thermoelectric properties. The IOFFE plot is highlighting the often overlooked importance of the electrical conductivity and the power factor within thermoelectrics in comparison to the usual focus on the energy conversion efficiency represented by the figure-of-merit. Based on the observations of the review, CCO is the outstanding *p*-type oxide material for high-temperature applications with enormous potentials for thermoelectric composites. As commonly used additives such as silver were already sufficiently investigated, other oxides such as LNO were chosen as a mixing partner.

The anisotropic transport properties of LNO with a high in-plane electrical conductivity were the motivation for designing microdimensional sheets, which can orientate during uniaxial pressing. Hence, the usage of a molten-flux synthesis to gain the desired habitus was elaborated. The amount of water in the molten flux turned out to be crucial to the crystal growth. Careful analysis by transmission electron microscopy verified the occasional growth and the orientation relationship of higher RUDDLESDEN-POPPER phases on the surface of LNO caused by oxidizing reaction species within the molten flux. Both, the solid-state route and the sol-gel process successfully led to plate-like particles. While the sol-gel process resulted in a higher aspect ratio, the solid-state route benefitted from a higher product purity. On that account, the LNO of the solid-state route was chosen for further processing in a thermoelectric composite.

Sophisticated investigations of the microstructure and the composition of the CCO-LNO composite revealed that both phases are not co-existing at the high sintering temperature of 1173 K. Instead, the perovskite $\text{La}(\text{Co,Ni})_3$, the CCO decomposition product $\text{Ca}_3\text{Co}_2\text{O}_6$ and $(\text{Ni,Co})\text{O}$ were formed with favorable effects on the thermoelectric properties. For low amounts of LNO, the electrical conductivity was enhanced due to the perovskite phase, while the SEEBECK coefficient was only slightly lowered. The resulting increase of the power factor was accompanied by an altered thermal conductivity of the composite in comparison to pristine CCO. Main reasons for this effect are most likely additional phonon scattering at interfaces and a different thermal conductivity of newly formed phases. Although the maximum figure-of-merit at 1073 K was similar for CCO and the best performing LNO-CCO composite, the higher values at lower temperature for the composite resulted in a rise of 19% concerning the average zT from 473 K to 1073 K. Therefore, this composite system is especially beneficial for applications where the maximum temperature may vary or is rather below 1073 K.

In another composite system, the combination of NCNO with CCO was investigated following the same approach as with LNO. However, in contrast to LNO, NCNO is characterized by a very low electrical conductivity due to its large band gap and thus large SEEBECK coefficient. While the CCO-LNO composite should benefit from an enhanced electrical conductivity, the CCO-NCNO composite should take advantage of an increased SEEBECK coefficient. This aim was successfully achieved by NCNO reacting to the perovskite $\text{Ca}(\text{Nb,Co})\text{O}_3$ during sintering and an in-situ cation exchange between Nb from NCNO and Co from CCO. Again, low amounts of 1 wt% to 5 wt% additive proved to be more efficient than higher amounts, indicating an optimum ratio of matrix and additional phases for the transport properties. The increase of the SEEBECK coefficient was accompanied by a diminishing electrical conductivity, but the power factor could be increased nonetheless. As the thermal conductivity was lowered by the additional phases, the maximum figure-of-merit benefitted by about 18% in comparison to pristine CCO. Since the SEEBECK coefficient is included by square within the power factor, changed values are more potent compared to the electrical conductivity. Thus, not only the average zT as by LNO, but also the maximum zT could effectively be enhanced in the CCO-NCNO system.

For the second concept, the size reduction of the introduced additives was considered. In a review comprising oxide nanosheets, the synthesis methods and advantages such as the quantum confinement effect of nanodimensional sheets were emphasized. Difficulties of extending the extraordinary transport properties of two-dimensional oxides to bulk materials were approached by two different routes. The first route followed an in-situ formation of a CCO-NCO-BCCO triple phase ceramic emerged by heavy doping. The thermal stabilization of the thermoelectrically auspicious NCO within the CCO matrix led to a high electrical conductivity and the BCCO could increase the SEEBECK coefficient simultaneously. As a result, the power factor could be more than doubled, even when the figure-of-merit was not increased. However, this is not necessarily a drawback considering the importance of the power factor for high-temperature applications.

As a second route of the nanodimensional approach, reaction sintering between CCO and BCSO was investigated. Before mixing the compounds, the pristine CCO was improved regarding electrical conductivity and density by using a double sintering method. As expected, the BCSO was not stable in air at high temperature and de-

composed completely. Various oxides were formed as a consequence during the sintering process, but doped cobalt oxides $\text{Co}_3\text{O}_4/\text{CoO}:\text{Cu},\text{Ca}$ and doped $\text{CCO}:\text{Bi},\text{Cu}$ were identified as main phases in the final composites. Depending on the initial amount of BCSO, the crystal growth of CCO and the additional phases was intensified. The electrical conductivity increased with the BCSO amount up to 20 wt%, until the solubility limit of Bi within CCO was reached and the formation of Bi_2O_3 became prevalent. The SEEBECK coefficient remained stable or even slightly increased in comparison to pristine CCO. Hence, the power factor was increased by 127% compared to pristine CCO as a consequence of in-situ doping of CCO and the formation of additional oxide phases.

Comparing all four investigated systems, the one involving the triple-phase nanocomposite was able to reach the highest power factor, most likely due to doping and the embedding of NCO. The systems involving ex-situ microdimensional or nanodimensional sheets, on the other hand, highlighted the reactivity of CCO and the new possibilities coming along with it. While it is difficult to predict the outcome of adding comparable oxide materials, LNO and NCNO clearly showed the prospects of simultaneously modifying the power factor as well as the figure-of-merit by reaction sintering. The potential of in-situ doping by introducing a thermally unstable compound was demonstrated with BCSO and a power factor comparable to the triple-phase nanocomposite was reached. Note that undoped CCO was used for the systems with ex-situ addition of plate-like additives to clarify the reaction characteristics, wherefore further improvements are expected for doped CCO within thermoelectric composites in the future. Even a combination of microdimensional and nanodimensional sheets or other nanostructures is conceivable, resulting in all-scale hierarchical structures. Hereby, the conducted research may function as a foundation stone for thermoelectric composites utilizing reaction sintering as a prospective method.

Curriculum Vitae

Personal data

Name Richard Hinterding
Date of birth 10.02.1992
Place of birth Greven, Germany
ORCID <https://orcid.org/0000-0002-7604-458>



Education

2017-2021 **Doctoral student** at the Leibniz University Hannover,
Institute of Physical Chemistry and Electrochemistry
Topic: Physico-Chemical Development of Oxide-Based Ceramics for
Thermoelectric Energy Harvesting

2015-2017 Leibniz University Hannover
M. Sc. in Material and Nanochemistry (**Grade: 1.4**)

2011-2015 Leibniz University Hannover
B. Sc. in Chemistry (**Grade: 1.6**)

2004-2011 Gymnasium Himmelsthür
A-levels, high school graduation (**Grade: 1.9**)

Secondary business

2017 Research assistant at the Leibniz University Hannover
Institute of Physical Chemistry and Electrochemistry

2015-2016 Research assistant at the Leibniz University Hannover
Institute of Inorganic Chemistry

Publications and Conferences

Publications included in this work

1. High power factor vs. high zT - A review of thermoelectric materials for high-temperature application
M. Wolf, R. Hinterding, A. Feldhoff
Entropy, 21 (11) **2019**, 1058
2. Two-dimensional oxides: Recent progress in nanosheets
R. Hinterding, A. Feldhoff
Zeitschrift für Physikalische Chemie, 233 (1) **2019**, 117-165
3. Anisotropic growth of $\text{La}_2\text{NiO}_{4+\delta}$: Influential pre-treatment in molten-flux synthesis
R. Hinterding, Z. Zhao, C. Zhang, A. Feldhoff
Journal of Crystal Growth, 523 **2019**, 125135
4. Ceramic composites based on $\text{Ca}_3\text{Co}_{4-x}\text{O}_{9+\delta}$ and $\text{La}_2\text{NiO}_{4+\delta}$ with enhanced thermoelectric properties
R. Hinterding, Z. Zhao, M. Wolf, M. Jakob, O. Oeckler, A. Feldhoff
Open Ceramics, 6 **2021**, 100103
5. Enhanced thermoelectric properties in ceramic composites based on $\text{Ca}_3\text{Co}_4\text{O}_9$ and $\text{Na}_2\text{Ca}_2\text{Nb}_4\text{O}_{13}$
R. Hinterding, M. Wolf, M. Jakob, O. Oeckler, A. Feldhoff
Open Ceramics, 8 **2021**, 100198
6. Triple-phase ceramic 2D nanocomposite with enhanced thermoelectric properties
M. Bittner, N. Kanas, R. Hinterding, F. Steinbach, D. Groeneveld, P. Wemhoff, K. Wiik, M.-A. Einarsrud, A. Feldhoff
Journal of European Ceramic Society, 39 (4) **2019**, 1237-1244
7. Reaction sintering of $\text{Ca}_3\text{Co}_4\text{O}_9$ with BiCuSeO nanosheets for high-temperature thermoelectric composites
R. Hinterding, D. Rieks, P.A. Kießling, L. Steinbach, N.C. Bigall, A. Feldhoff
Journal of Electronic Materials, **2021**

Publications not included in this work

1. Low thermal conductivity in thermoelectric oxide-based multiphase composites
M. Wolf, K. Menekse, A. Mundstock, R. Hinterding, F. Nietschke, O. Oeckler, A. Feldhoff
Journal of Electronic Materials, 48 (11) **2019**, 7551-7561
2. A comprehensive study on improved power materials for high-temperature thermoelectric generators
M. Bittner, N. Kanas, R. Hinterding, F. Steinbach, J. Räthel, M. Schrade, K. Wiik, M.-A. Einarsrud, A. Feldhoff
Journal of Power Sources, 410-411 **2019**, 143-151
3. Geometry optimization of thermoelectric modules: Deviation of optimum power output and conversion efficiency
M. Wolf, A. Rybakov, R. Hinterding, A. Feldhoff
Entropy, 22 **2020**, 1233
4. Combination of laser and thermal sintering of thermoelectric $\text{Ca}_3\text{Co}_4\text{O}_9$ films
M. Wolf, L. Rehder, F. Steinbach, M. Abt, R. Hinterding, L. Overmeyer, A. Feldhoff
Chemie Ingenieur Technik, 94 **2022**, 1-10

Contributions to conferences

1. Molten-flux synthesis of $\text{La}_2\text{NiO}_{4+\delta}$
Z. Zhao, R. Hinterding, C. Zhang, A. Feldhoff
Bunsentagung 2018 - Kinetics in the Real World, Deutsche Bunsen-Gesellschaft, May 10th-12th, **2018**, Hannover, Germany (Poster)
2. Self-assembly of a thermoelectric nanocomposite in a complex oxide system
M. Bittner, N. Kanas, F. Steinbach, D. Groeneveld, R. Hinterding, P. Wemhoff, K. Wiik, M.-A. Einarsrud, A. Feldhoff
Bunsentagung 2018 - Kinetics in the Real World, Deutsche Bunsen-Gesellschaft, May 10th-12th, **2018**, Hannover, Germany (Poster)
3. Self-assembled oxide 2D nanocomposite with enhanced thermoelectric power factor and reduced thermal conductivity
A. Feldhoff, M. Bittner, N. Kanas, F. Steinbach, D. Groeneveld, R. Hinterding, P. Wemhoff, K. Wiik, M.-A. Einarsrud
Electroceramics XVI, European Ceramic Society, July 9th-12th, **2018**, Hasselt, Belgium (Talk)

-
4. Triple-phase ceramic nanocomposite with enhanced thermoelectric power factor
A. Feldhoff, M. Bittner, N. Kanas, F. Steinbach, D. Groeneveld, R. Hinterding,
P. Wemhoff, K. Wiik, M.-A. Einarsrud
The 2nd Annual Energy Harvesting Society Conference, The American Ceramic
Society, September 5th-7th, **2018**, Philadelphia, USA (Talk)
 5. Multifunctional nano- and macroporous bioactive glass-composites for bone-
replacement
N. Ehlert, M. Lietzow, K. Besecke, R. Hinterding, J. Schaeske, M. Stiesch,
L. Burmeister, A. Hoffmann, S. Gniesmer, A. Kampmann
DGBM - Deutsche Gesellschaft für Biomaterialien, November 8th-10th, **2018**,
Braunschweig, Germany (Talk)
 6. Crystal growth of large anisotropic $\text{La}_2\text{NiO}_{4+\delta}$ platelets via molten-flux
R. Hinterding, A. Feldhoff
*MGCTF 2019 - Mechanisms and non-linear problems of nucleation and growth
of crystals and thin films*, July 1st-5th, **2019**, St. Petersburg, Russia (Talk)
 7. Elastic polymer-coated nano- and macroporous bioactive glass-composites for
bone regeneration
M. Lietzow, K. Besecke, R. Hinterding, L. Burmeister, A. Hoffmann, A. Kamp-
mann, M. Stiesch, N. Ehlert
*BioMAT 2019 - European Symposium and Exhibition on Biomaterials and Re-
lated Areas*, May 8th-9th, **2019**, Weimar, Germany (Poster)
 8. Crystal growth of large anisotropic $\text{La}_2\text{NiO}_{4+\delta}$ platelets via molten-flux
R. Hinterding, A. Feldhoff
ZFM - Zentrum für Festkörperchemie und Neue Materialien, July 19th, **2019**,
Braunschweig, Germany (Talk)
 9. Thermoelectric composite ceramics based on anisotropic oxides
R. Hinterding, Z. Zhao, M. Wolf, M. Jakob, O. Oeckler, A. Feldhoff
VCT 2020 - Virtual Conference on Thermoelectrics, International Thermoelec-
tric Society, July 21st-23rd, **2020** (Online poster)
 10. Thermoelectric composite ceramics based on a $\text{Ca}_3\text{O}_4\text{O}_9$ matrix and large aniso-
tropic oxides
R. Hinterding, Z. Zhao, M. Wolf, M. Jakob, O. Oeckler, A. Feldhoff
Electroceramics XVII, European Ceramic Society, August 24th-28th, **2020**, Darm-
stadt, Germany (Online talk)
 11. Combination of $\text{Ca}_3\text{O}_4\text{O}_9$ with anisotropic oxides in thermoelectric composite
ceramics
R. Hinterding, Z. Zhao, M. Wolf, M. Jakob, O. Oeckler, A. Feldhoff

ICACC 2021 - International Conference and Exposition on Advanced Ceramics and Composites, The American Ceramic Society, February 8th-12th, **2020** (Online talk)

12. Thermoelectric properties of composite ceramics based on $\text{Ca}_3\text{O}_4\text{O}_9$ and large plate-like oxides

R. Hinterding, Z. Zhao, M. Wolf, M. Jakob, O. Oeckler, A. Feldhoff

CERAMICS 2021 - 96th DKG Annual Meeting, Deutsche Keramische Gesellschaft, April 19th-21st, **2021** (Online talk)

13. Importance of material's working points to assess thermoelectric power conversion

A. Feldhoff, M. Wolf, R. Hinterding

MCARE 2021 joint with EHS 2021 - Materials Challenges in Alternative & Renewable Energy joint with the 4th Annual Energy Harvesting Society Meeting, The American Ceramic Society, July 19th-22nd, **2021**, (Online talk)

14. Tuning the thermoelectric performance of CaMnO_3 -based ceramics by controlled exsolution and micro-structuring

N. Kanas, B. Williamson, R. Hinterding, M.-A. Einarsrud, S.M. Selbach, A. Feldhoff, K. Wiik

MS & T21 - Materials Science & Technology, The American Ceramic Society, October 17th-21st, **2021**, Columbus, Ohio, USA (Online talk)